E-ISSN: 2687 - 6167
NUMBER 51
DECEMBER 2022

JSR A

JOURNAL OF SCIENTIFIC REPORTS A

JOURNAL OF SCIENTIFIC REPORTS-A DECEMBER 2022 NUMBER 51

Kutahya Dumlupinar University Scientific Reports A
Evliya Celebi Campus Tavsanli Road 10 KM. 43270 Kutahya
Phone : (0274) 443 11 42
E-mail : joursra@gmail.com
gipra.com

Dumlupinar University Press

gate of science

Kütahya Dumlupınar University
Institute of Graduate Studies

Journal of Scientific
Reports-A
E-ISSN: 2687-6167
Number 51, December 2022

Journal of Scientific Reports-A started its publication life in 2000 as name of Journal of Science and Technology of Dumlupınar University and is a national peer-reviewed journal published regularly twice a year in June and December. The language of the journal is English. Articles submitted to the journal are evaluated by at least two referees who are experts in the subject and selected by the editorial board. All articles submitted to the journal are evaluated by the double-blind method. Articles submitted to our journal for review should not be previously published, accepted for publication and in the process of being evaluated for publication in another journal. All responsibility for the articles published in the journal belongs to the author(s).

The journal aims to share scientific studies carried out in the fields of science and engineering at national and international level with scientists and the public. Original research articles, review articles and short notes in science and engineering disciplines are accepted for the journal. Original research articles are expected to contain theoretical and experimental results and should not be published in other journals. In the review articles, it is expected that scientific, technological and current developments on a specific subject are reflected by using an extensive bibliography and made a satisfying evaluation of these. Short notes should be brief writings prepared to announce the first findings of an original study.

Editorial Policy

The journal is open access and the article evaluation period is between 1-2 months.

Correspondence Address: Kütahya Dumlupınar Üniversitesi Evliya Çelebi Yerleşkesi Fen Bilimleri Enstitüsü 43270 KÜTAHYA
E-mail: joursra@gmail.com
Webpage: gsjsra.com
Phone: 0 274 443 19 42
Fax: 0 274 265 20 60

JSR A
Journal of Scientific Reports

JSR A
Journal of Scientific Reports

JSR A
Journal of Scientific Reports

JOURNAL OF SCIENTIFIC REPORTS-A
E-ISSN: 2687-6167

CONTENTS

RESEARCH ARTICLES

JSR A
Journal of Scientific Reports

JSR A
Journal of Scientific Reports

Journal of Scientific Reports-A, Number 51, December 2022

Kütahya Dumlupınar University
Institute of Graduate Studies

Journal of Scientific
Reports-A
E-ISSN: 2687-6167
Number 51, December 2022

RESEARCH ARTICLE

MAJOR and TRACE ELEMENT GEOCHEMISTRY of the MALKARA (TEKIRDAĞ, TURKEY) COALS

Cevdet Bertan GÜLLÜDAĞ[1,*], Mehmet ALTUNSOY[2]

[1*]Akdeniz University, Vocational School of Technical Science, Department of Construction Technology, Antalya, bgulludag@akdeniz.edu.tr, ORCID: 0000-0001-5777-1808
[2]Akdeniz University, Faculty of Engineering, Department of Geological Engineering, Antalya, altunsoy@akdeniz.edu.tr, ORCID: 0000-0002-3140-6682

Receive Date:19.04.2022 *Accepted Date: 21.06.2022*

ABSTRACT

Coal, which contains various amounts of major and trace elements, has the feature of being a mineral deposit according to the accumulation rate of certain elements. The types and quantities of inorganic components are important to the chemical, geological and technological properties of coal. If the necessary precautions were not taken during the extraction, transportation, and coal combustion, some negative effects could occur to the environment and human health. A total of 54 coal, roof, floor, and parting samples were taken from 8 boreholes in the Tekirdağ, Malkara lignite field in the Northwest of Turkey. The samples were prepared in accordance with all the procedures of mineralogical and geochemical analyses. Quartz, ankerite, pyrite, calcite, mica, aragonite, dolomite, feldspar minerals and smectite, illite, cholinite, and chlorite among clay minerals were detected out. Trace elements, including V (8-212 ppm), Co (5.3-31 ppm), Ni (0.1-257 ppm), Cu (1.5-109.6 ppm), Rb (0.2-125.8 ppm), Sr (193.8-615.3 ppm), Y (5.4-28 ppm), Zr (13.6-495.1), Ba (120-436 ppm), and W (7.1-226 ppm) are enriched. The enriched elements in the coal are largely associated with inorganic matter. However, Be, Sr and W are related to organic and inorganic substances. Due to its high concentrations, Se, Be, Cu, Mo, Ni, Pb, Th, U, V, Zn, Ba, Co, and Sn might have negative effects on the environment and human health. Therein, Be, Co, Pb, Ni, and Se are potential air pollutants in the use of coal.

Keywords: *Coal, Enrichment Factor, Major and Trace Element, Malkara (Tekirdağ, Turkey)*

1. INTRODUCTION

China performed the largest coal production around the world in 2018 with a share of %44.7, while India ranked second, accounting for %9.7. In addition, almost half of the world's coal consumption was also made by China. Germany is in the first place in lignite consumption, also with the effect of industrial development. Turkey is rich in coal resources, especially the lignite. The lignite reserve of Turkey reached up to 8.3 billion tons in 2005, and was further estimated to reach over 20 billion tons

JSR A
Journal of Scientific Reports

in 2022 with the exploration of new fields. The lignite production in Turkey accounts for %8.9 of the world's lignite production [1]. With the increasing energy demand, coal is intensively exploited in new fields and widely used in many fields, dominated by electricity generation. Coal combustion by power generation brings various negative results. The damages of coal come into view in its removal, transport and combusted. Although it cannot be prevented completely, it is necessary to keep this damage to a minimum. Coal quality parameters include the economic and technological importance of trace elements in the content of coal and their effects on the environment and human health [2-7]. The concentrations of trace element in coal are key parameters to evaluate the coal quality [8]. The Malkara lignites (with a reserve of 206 million tons) accounts large part of the Thrace Basin coals (639,17 million tons) [9]. The reason for choosing the research area in this study is that it is located in or near residential areas. The purpose of this study is to determine the element content of the Malkara coals, to interpret the sources of these elements, and to evaluate its possible environmental effects.

2. GEOLOGICAL SETTING

The Malkara coal mine is located in the Thrace Basin (Fig. 1). The Thrace Basin is the Tertiary intermontane basin, where the Middle Eocene-Pliocene strata is exposed [10,11]. The studied coal seams are hosted in the Danişmen Formation of Yenimuhacir Group, which is 300-1000 meters in thickness. It hosts three members of Armutburnu, Pınarhisar, and Taşlısekban. It is composed of limestone, sandstone, tuffite, siltstone, claystone, and is intercalated with coal. Above the Danişmen Formation and under the discordant Hisarlıdağ Formation is the Osmancık Formation which is a member of the same group as the Danişmen Formation (Fig. 2).

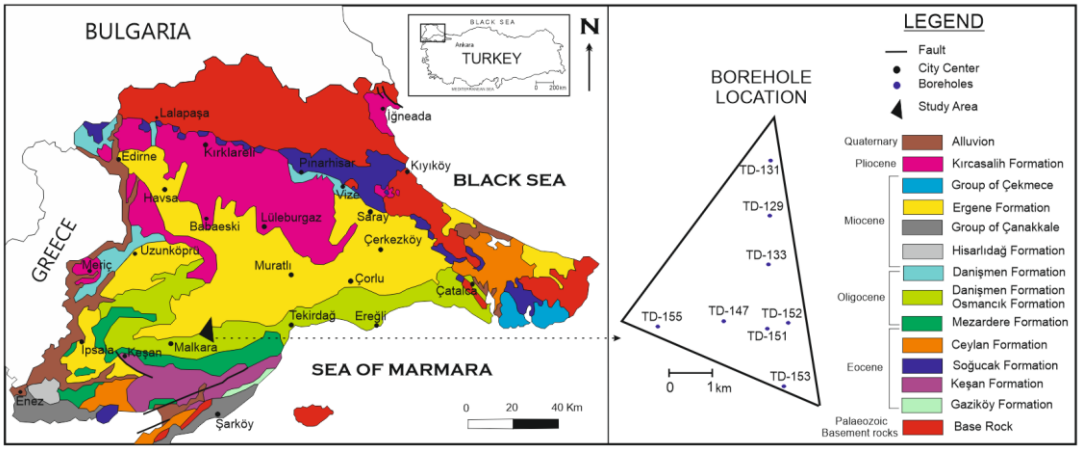

Figure 1. Geological map of the Thrace Basin in Turkey (modified from Perinçek et al. [11]) and location of study area.

JSR A
Journal of Scientific Reports

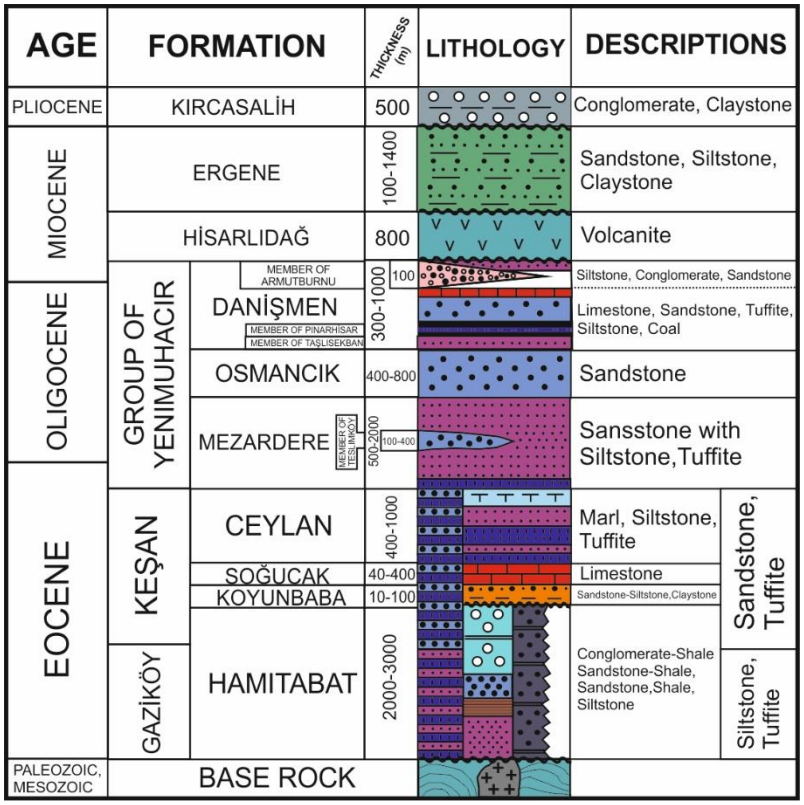

Figure 2. Generalized stratigraphic section of the Thrace Tertiary Basin (Modeified from [12]).

3. MATERIALS and METHODS

The major and trace element determination was conducted in a total of 54 samples, including 26 coal samples taken from 8 boreholes [TD-151 (n=2), TD-147 (n=4), TD-153 (n=2), TD-133 (n=3), TD-152 (n=3), TD-155 (n=4), TD-131 (n=3), and TD-129 (n=5)], 28 non-coal roof, floor, and parting rock samples [TD-151 (n=3), TD-147 (n=5), TD-153 (n=2), TD-133 (n=4), TD-152 (n=4), TD-155 (n=3), TD-131 (n=4), and TD-129 (n=3)] (Fig. 3). Lignite veins start at 25 meters and continue to a depth of 550 meters. The thicknesses of lignite veins vary between 25-100 centimeters. The measurement of major and trace elements were performed in the ACME laboratory (Canada). In a total of 25 samples (organic and inorganic), all XRD rock and clay fraction shots were performed in TPAO (Turkish Petroleum Corporation) Laboratory, being all XRD rocks and clay in 18 samples and all XRD rocks in 7 samples. The whole XRD rock and clay analyses were accredited with TÜRKAK (Turkey Accreditation Agency) TS EN ISO/IEC 17025: 2005 standards.

JSR A
Journal of Scientific Reports

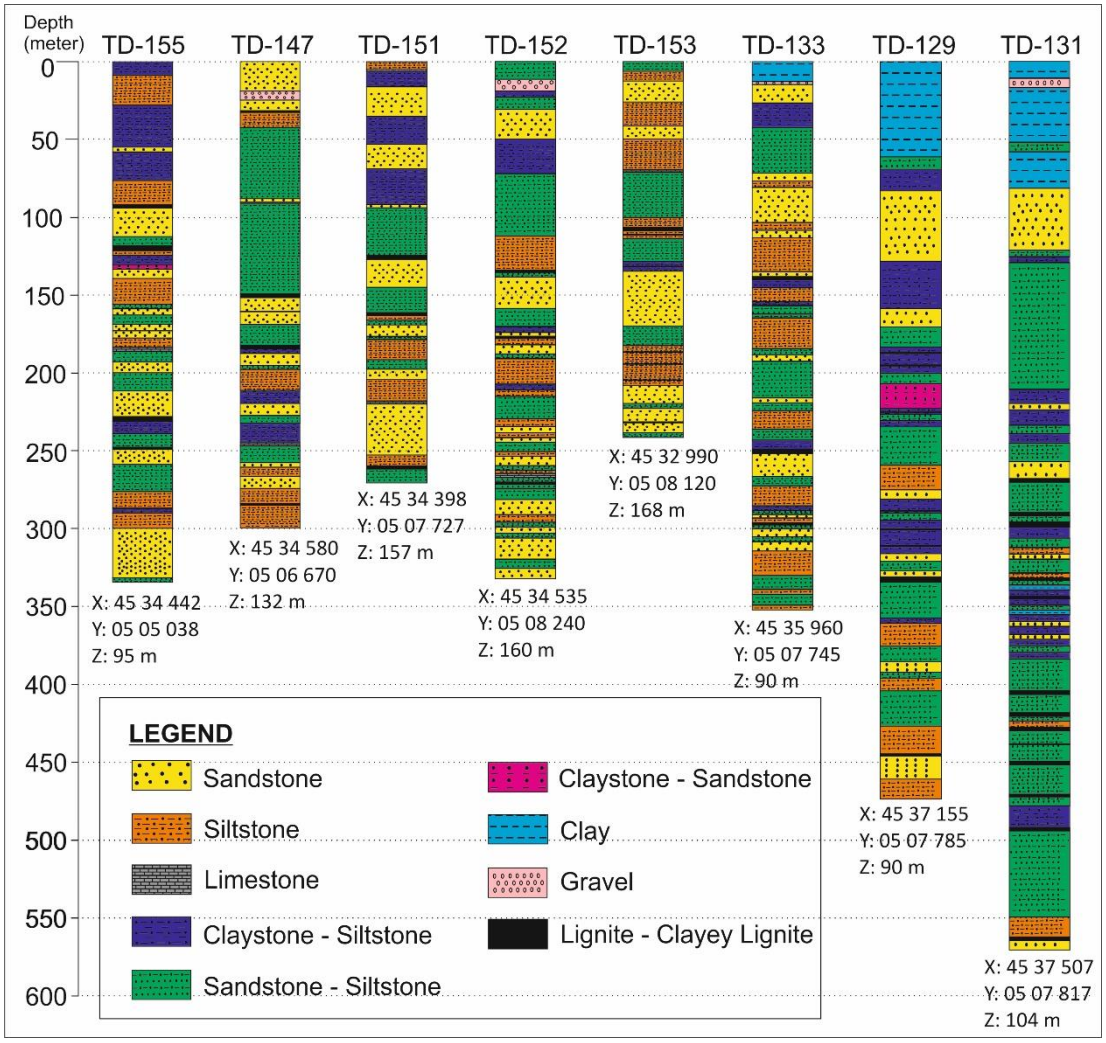

Figure 3. Changes of the lithology in the boreholes.

4. RESULT and DISCUSSION

4.1. Mineralogical Composition of Coal, Roof and Floor of the Coal Seams

The results of the analysis were evaluated in two parts as organic and inorganic materials. Similar mineral descriptions were found in both sample types. Clastic materials continue to be transported into the basin during sedimentation.

JSR A
Journal of Scientific Reports

The mica, quartz, clay minerals, calcite, dolomite, feldspar group minerals, ankerite, aragonite, pyrite and amorphous materials were found in the semi-quantitative XRD analysis. The clay minerals were abundant in these samples. The calcite, one carbonate mineral, is more abundant than that of dolomite and aragonite. Aragonite is more enriched than dolomite (Table 1).

The most abundant mineral in the analyzed coal and rock samples is quartz. Such a high content of quartz in samples at every seams that indicates the clastical of detrius material in the mine during peat-accumulation. Pyrite is detected at all seams. It can be concluded that pyrite occurs mostly syngenetically during burial and carbonization in the diagenesis phase. K-feldspar is available at almost all levels and in small quantities. Plagioclase is in small quantities and very rarely. Feldspars are of a detrital origin and usually weathered to clays. The presence of mica group minerals is also at a moderate level. The ankerite was present at all levels with a small amount.

As in the whole rock, in the clay fraction, a similar mineral type and abundance is observed in both coal and sandstone, siltstone, claystone samples. The dominant clay minerals are illite, and smectite, and the amount of smectite is higher than that of other clay minerals. Chlorite was rarely detected in few samples. Chlorite occurs only in a few examples, indicating that it was transported from source region (Table 2). The amount of smectite is very high, showing that it has not been transformed into illite. The coexistence of smectite with kaolinite and chlorite indicates that the feldspar was altered in a hot and semi-dry climates [13].

Table 1. Whole rock and clay components of the Malkara coal samples.

Sample Number	Group of Clayey Minerals				TCQ	Q	Ank	P	Cal	Mica	Arg	D	Felds	Pl
	Kln	I	Sm	Ch										
2152-20	#	#	###		XXX	XX	X	XX	XX		X	X		
152-42	#	#	##		XXX	XXX	X	XX	X	X	X			
133-21	#	#	###		XXX	XXX	X	XX	XX	X	X	X	X	X
133-30	#	#	##		XXX	XXX		XX	X	X	X		X	
129-18						XXX		XX	XX	X	X	X	X	
129-36						XXX	XX	XX	XX				X	X
147-14	#	#	##		XXX	XXX	X	XX	XX	X	X		X	X
147-26						XXX		XX	XX	XX			X	
153-6	#	#	##		XXX	XXX	X	XX	XX	X			X	
153-18						XXX	X	X	X	X	X		X	
151-13		#	###		XX	X	X		X	X		X	X	
151-30						XXX		X	XX	X			X	X
155-12						XXX	X	XX	XX	X	X	X	X	X
155-28	#	##	##		XX	XXX		XXX	XX	X			X	X
131-27		#	##	#	XXX	XXX	X	XX	XXX	X		X	X	
131-39		#	###		XXX	XX		XX	XXX	XX			X	

JSR A
Journal of Scientific Reports

Kln (Kaolinite), I (Illite), Sm (Smectite), Ch (Chlorite), TCQ (Total Clay Quantity), Q (Quartz), Ank (Ankerite), P (Pyrite), Cal (Calcite), Arg (Aragonite), D (Dolomite), Felds (Feldspar), Pl (Plagioclase), "#", "X" Relative abundance of minerals

Table 2. Whole rock and clay components of roof, floor, and parting samples of the Malkara coal measure.

Sample Number	Group of Clayey Minerals				TCQ	Q	Ank	P	Cal	Mica	Arg	D	Felds	Pl
	Kln	I	Sm	Ch										
152-19		#	#	##	X	XX X	X	X X	XX	X	X	X		
133-23	#	#	##		XXX	XX X	X	X	XX		X			
129-19	#	#	##		XXX	XX	X	X	XX	X	X		X	
147-15	#	#	##		XXX	XX X	X	X	XX	X	X	X	X	
153-7		#	##	#	XXX	XX	X	X	X	XX	X		X	X
151-12	#	#	##		XX	XX	X	X	XX	X	X		X	
151-14						XX X	X	X X	XX X	X	X	X	X	
155-13	#	#	#		XX	XX	X	X	XX X	X	X			
131-38	#	#	##		XXX	XX	X	X	XX	XX	X		X	

Kln (Kaolinite), I (Illite), Sm (Smectite), Ch (Chlorite), TCQ (Total Clay Quantity), Q (Quartz), Ank (Ankerite), P (Pyrite), Cal (Calcite), Arg (Aragonite), D (Dolomite), Felds (Feldspar), Pl (Plagioclase), "#", "X" Relative abundance of minerals

4.2. Major Element Relations in Coal

The average contents of the major elements in the coal samples are below %1, except for Si, Al, Fe, Mg, and Ca (Table 3). All major elements presented comparable concentrations to the upper continental crust. Only Cr is at the same concentration as the upper continental crust. All major elements have higher concentrations than that of world coals. Compared to the Turkey and U.S. coals, only Ca, and P and Mn are at lower concentrations. Compared to the Chinese coals, Fe, P, and Mn are in low concentration. The statistical analysis was utilized to infer the major elements hosted in coal samples and the origin of these elements. Precision and relative standard deviation (RSD) values were calculated for the quality control elements. The statistical analysis was utilized to develop an approach about the main elements included in coal samples and the origins of these elements and the correlation matrix formed is given in Table 4.

Table 3. Arithmetic means of the major elements' concentrations of in the Malkara coal, UCC (Upper Continental Crust), world, Turkey, U.S. and China coals.

Malkara Coals	UCC [14]	World [15]	Turkey [17-19]	U.S. [20]	China [21]

JSR A
Journal of Scientific Reports

Element (%)	RSD %	Min.	Max.	Avr.					
Silicium	13.25	0.16	19.49	10.09	31.10	-[16]	5.10	2.40	3.96
Aluminum	4.14	0.19	33.40	5.26	8.15	1.00[16]	2.10	1.50	3.16
Ferrum	3.45	0.52	6.10	3.17	3.92	1.00[16]	2.30	1.30	3.39
Magnesium	0	0.28	2.19	1.22	1.50	0.02[16]	0.50	0.11	0.13
Calcium	0.92	0.55	6.65	1.41	2.57	1.00[16]	1.80	0.46	0.88
Natrium	1.91	0.10	0.96	0.46	2.43	0.02[16]	0.10	0.08	0.12
Kalium	0	0.01	1.95	0.77	2.32	0.01[16]	0.30	0.18	0.16
Titanium	0	0.02	0.38	0.21	0.38	0.05[16]	0.10	0.08	0.20
Phosphorus	0	-	0.32	0.03	0.07	-[16]	-	0.04	0.04
Manganum	0	-	0.05	0.02	0.08	0.05[16]	-	0.05	0.01
Chromium	12.86	-	0.06	0.01	0.01	-[16]	-	-	-
TOT-C	-	10.12	55.85	31.28	-	-	-	-	-
TOT-S	-	-	7.01	1.88	-	-	-	-	-

TOT-C: Total Carbon, TOT-S: Total Sulfur.

Table 4. Major element correlation of Malkara coals [22].

	Si	**Al**	**Fe**	**Mg**	**Ca**	**Na**	**K**	**Ti**	**P**	**Mn**	**Cr**	**TOT C**	**TOT S**	**TOC**
Si	1	,831**	,618**	,895**	-,199	0,177	,919**	,968**	0,348	,543**	,634**	-,977**	-0,2	-0,3
Al		1	,388*	,759**	-0,207	0,054	,718**	,864**	0,172	0,3	0,383	-,812**	-0,194	-0,095
Fe			1	,587**	-0,072	-0,148	,660**	,575**	0,21	,684**	,662**	-,697**	,511**	-0,303
Mg				1	0,054	-0,059	,920**	,848**	,441*	,654**	,525**	-,911**	0,999	-,438*
Ca					1	0,036	-0,129	-0,178	0,362	0,283	-0,031	0,11	0,182	-0,297
Na						1	-0,024	0 ,16	0,24	-0,164	0,01	-0,11	0,053	0,012
K							1	,873**	,516**	,631**	,669**	-,902**	0,061	-0,379
Ti								1	0,308	,507**	,547**	-,956**	-0,243	-0,25
P									1	,452*	0,31	-0,367	0,156	-,582**
Mn										1	,494*	-,647**	0,334	-,403*

Cr											1	-,662**	0,286	-,521**
TOT C												1	-0,075	0,361
TOT S													1	-,077
TOC														1
** Correlation is significant at 0,01 level														
* Correlation is significant at 0,05 level														

The high availability rate of the Si is a clastic source indicator and indicates diagenetic silica precipitation. Thus, Si may be associated with silica with biological origin or detritic quartz. The positive correlation between Al - Si (r=0.831), Si -Ti (r=0.968) and Al - Ti (r=0.864) indicates a terrestrial origin of these elements and the presence of detritic clays into the basin. The presence of illite accounts for the high positive correlation between Al and K (r=0.718) [24]. Fe is found in the structure of clay and iron minerals. The positive correlation to elements with a detritic source, such as Al (r=0.388), Si (r=0.618) and Ti (r=0.575), suggests that Fe is related to clay minerals (Table 4). Its positive correlation with total sulfur (r=0.511) and the presence of pyrite minerals in almost all samples show that Fe may also associated from pyrite.

Mg is found in clay minerals and dolomite. In addition, it can also be found in a small amount of organic matter [24]. Dolomite was only detected in a small amounts in certain samples. When evaluated together with the negative correlation relationship it has with TOC (r=-0.438), the presence of Mg mineral in the study area is thought to be related to clay minerals rather than organic matter. K in coal is usually associated with aluminosilicate minerals. K, Na, and Al are mostly associated with phases containing Al-Si (analcime, clay minerals, feldspar) and are rarely associated with halite [25]. The absence of analcime and halite minerals in the coals in the study area suggests that most of K is related to clay minerals and less of it is related to feldspar. Mn is mostly found in the structure of organic matter but can also be found together with carbonate, clay and pyrite minerals. When the correlation between the presence of Mn in the study area and TOC (r=-0.403) was evaluated, it was determined that it points to inorganic origin. Cr can be adsorbed on iron and manganese oxides, clays, apatites and organic matter [26]. There is a negative correlation between Cr and TOC (r=-0.521) in the samples in the study area. When XRD analyzes are also evaluated, Cr's source is thought to be clay minerals. When all the data are evaluated together, considering the positive correlation between Si, Al, Fe, Mg, K, Ti, Mn and Cr, it was determined that these elements come from the same origin and represent the clastic origin.

In the study area, a significant correlation relationship between Ca and Na and other main elements and TOC, TOT S, TOT C could not be established. Ca can be found in different forms such as clay minerals, sulphate, carbonate and organic origin in coals [27, 28]. It is thought that the source of Ca is largely calcite in the study area, and also that the fossil shells observed in the coal samples may be a source of some Ca. Although the Na in the coal samples is known to be related to clay minerals and feldspars, no significant relation was found with the elements pointing to clastic origin such as Al, Si, and T. While P had a negative correlation with TOC (r=-0.582), it showed a positive correlation with

JSR A
Journal of Scientific Reports

Mg (r=0.441), K (r=0.516) and Mn (r=-0.452). No significant relationship was found between TOT C and TOT S and other major elements. Although a certain amount of P is present in organic matter, apatite mineral can also be a source of phosphorus [29]. Considering its negative correlation with TOC, the source of element P in the study area is largely calcite mineral.

4.3. Mode of Occurrence and Element Enrichment

Trace elements in coals occur both in organic and inorganic matter [4]. In coals with low ash content, elements are generally found in relation to organic matter [2]. As the ash yield increases, the amount of elements associated with organic material decreases, while the amount of elements associated with minerals increases [30]. Concentrations of the elements Be, Sc, V, Co, Ni, Cu, Zn, Ga, As, Se, Rb, Sr, Y, Zr, Nb, Mo, Ag, Cd, Sn, Sb, Cs, Ba, La, Ce, Pr, Nd, Sm, Eu, Gd, Tb, Dy, Ho, Er, Tm, Yb, Lu, Hf, Ta, W, Au, Hg, Tl, Pb, Bi, Th, U were presented (Table 5). The concentration of Ag was below the detection limit in most of the samples. Correlation coefficients were calculated in order to determine the relationship of trace elements with each other and TOC contents and to evaluate them in terms of their origin. Cluster analysis was performed to classify the elements according to their similarities in the ungrouped data matrix (Fig. 4).

Table 5. Arithmetic means of trace elements' concentrations of the Malkara coals, UCC, World, lignite, Turkey, U.S. and China coals.

Element (ppm)	RSD %	Malkara Coals			UCC[14]	World[15]	Lignite[16]	Turkey[17-19]	U.S.[20]	China[21]	Element (ppm)	RSD %	Malkara Coals			UCC[14]	World[15]	Lignite[16]	Turkey[17-19]	U.S.[20]	China[21]
		Min.	Max.	Avr.									Min.	Max.	Avr.						
Be	12.86	-	7.00	2.68	2.10	1.60	1.20	1.30	2.20	2.10	Ce	0	3.50	50.60	26.46	63.00	23.00	22.00	-	21.00	46.70
Sc	0	-	21.00	10.56	14.00	3.90	4.10	4.80	4.20	4.38	Pr	1.43	0.49	5.77	3.13	7.10	3.50	3.50	-	2.40	6.42
V	2.12	8.00	212.0	109.7	97.00	25.00	22.00	65.00	22.00	35.10	Nd	3.29	2.20	21.90	12.31	27.00	12.00	11.00	-	9.50	22.30
Co	2.32	5.30	31.00	15.83	17.30	5.10	4.20	10.00	6.10	7.08	Sm	6.53	0.68	4.40	2.48	4.70	2.00	1.90	-	1.70	4.07
Ni	5.94	-	257.0	116.9	47.00	13.00	9.00	150.0	14.00	13.70	Eu	8	0.23	1.02	0.61	1.00	0.47	0.50	-	0.40	0.84
Cu	-	1.50	109.6	36.69	28.00	16.00	15.00	20.00	16.00	17.50	Gd	8.32	0.94	4.49	2.60	4.00	2.70	2.60	-	1.80	4.65
Zn	-	2.00	77.00	41.04	67.00	23.00	18.00	40.00	53.00	41.40	Tb	5.9	0.14	0.70	0.41	0.70	0.32	0.30	-	0.30	0.62
Ga	2.6	0.70	41.50	9.78	17.50	5.80	5.50	5.80	5.70	6.55	Dy	6.94	0.85	4.56	2.56	3.90	2.10	2.00	-	1.90	3.74
As	-	0.80	24.50	8.88	4.80	8.30	7.60	65.00	24.00	3.79	Ho	4.46	0.20	0.98	0.55	0.83	0.54	0.50	-	0.35	0.96
Se	-	-	6.00	1.64	0.09	1.30	1.00	-	2.80	2.47	Er	4.47	0.55	2.87	1.64	2.30	0.93	0.90	-	1.00	1.79
Rb	-	0.20	125.8	52.37	84.00	14.00	10.00	25.00	21.00	9.25	Tm	6.15	0.08	0.41	0.23	0.30	0.31	0.30	-	0.15	0.64
Sr	2.45	193.8	615.3	351.2	320.0	110.0	120.0	210.0	130.0	140.0	Yb	1.71	0.52	2.68	1.51	2.00	1.00	1.00	-	0.95	2.08
Y	9.26	5.40	28.00	15.25	21.00	8.40	8.60	8.30	8.50	18.20	Lu	0	0.08	0.44	0.24	0.31	0.20	0.20	-	0.14	0.38
Zr	0.04	13.60	495.1	83.18	193.0	36.00	35.00	-	27.00	89.50	Hf	6.15	0.30	3.60	1.80	5.30	1.20	1.20	-	0.73	3.71
Nb	2.14	0.40	10.50	4.55	12.00	3.70	3.30	4.00	2.90	9.44	Ta	0	-	0.60	0.32	0.90	0.28	0.30	-	0.22	0.62
Mo	-	-	4.50	1.56	1.10	2.20	2.20	9.80	3.30	3.08	W	4.3	7.10	226.0	42.98	1.90	1.10	1.20	-	1.00	1.08

JSR A
Journal of Scientific Reports

Güllüdağ, C. B. and Altunsoy, M., Journal of Scientific Reports-A, Number 51, 1-25, December 2022.

Ag	-	-	-	-	53.00	0.10	0.10	-	-	-	Au*	-	-	2.70	1.81	1.50	3.70	3.00	-	-	-
Cd	-		0.40	0.20	0.09	0.22	0.20	-	0.47	0.25	Hg	-	0.02	0.31	0.08	0.05	0.10	0.10	0.10	0.17	0.16
Sn	0	-	3.00	1.50	2.10	1.10	0.80	-	1.30	2.11	Tl	-	-	0.50	0.18	0.90	0.63	0.70	-	1.20	0.47
Sb	-	-	2.00	0.40	0.40	0.92	0.80	2.70	1.20	0.84	Pb	-	1.80	19.20	10.10	17.00	7.80	6.60	9.30	11.00	15.10
Cs	0	-	7.90	3.62	4.9	1.00	1.00	4.90	1.10	1.13	Bi	-	-	0.50	0.26	0.16	0.97	0.80	-	<1.00	0.79
Ba	1.18	120.0	436.0	256.3	624.0	150.0	150.0	130.0	170.0	159.0	Th	-	0.40	10.70	6.09	10.5	3.30	3.30	-	3.20	5.84
La	0	1.70	26.80	13.82	31.00	11.00	10.00	-	12.00	22.50	U	0.92	0.20	8.30	4.12	2.70	2.40	2.90	13.00	2.10	2.43

**ppb*

The average concentration levels of the trace element contents of coal samples were compared with the World, Turkey, lignite, U. S. and China coals. Mo, Cd, Sb, Au, Hg, Tl, Bi elements presented low values, while Scandium, Vanadium, Cobalt, Cupric, Gallium, Rubidium, Strontium, Barium, Tungsten, Thorium elements presented high values, considering all coals of study area. While Be had close values with Chinese coals, it showed lower values than U. S. coals and higher values than other coals. Se, Zn and Pb are concentrations, which are lower than U. S. and Chinese coals and higher than the World and lignite coals. The average concentration of U, Cs and Ni elements is lower than Turkish coals and higher than other coal values. Y, Zr, Nb, Sn, Hf and Ta were measured at higher values than other coals, excluding Chinese coals. The median concentration of as element is below lignite, Turkey and U. S. coals. Rare earth elements (REE) are composed of La, Ce, Pr, Nd, Sm, Eu, Gd, Tb, Dy, Ho, Er, Tm, Yb, Lu trace elements, and they present higher values than U. S. coals and lower values than Chinese coals. All rare earth elements other than Pr, Gd and Tm are found in high concentrations in lignite and other world coals. No average values of rare earth elements were determined for Turkish coals. While Sb offers close values according to the upper continental crust averages, other elements except Beryllium,Vanadium, Nickel, Cupric, Arsenic, Selenium, Strontium, Molybdenum, Cadmium, Tungsten, Mercury, Bismuth and Uranium have low concentration values.

It was stated that Be is found in coals with quartz and clay minerals [31]. Based on the XRD analysis, it was determined that in wells numbered TD-131 and TD-133 where Be presented relatively higher values, clay minerals and quartz were also abundant. In addition, Be is largely associated with organic matter in coals, but no significant correlation was found between Be and TOC in the correlation matrix (Table 6). However, there is a close relationship between Be and TOC in the dendrogram (Fig. 4). It is reported that As [32], which is generally related to pyrite in coals and is seen in a small amount in organic structure, also originates from clay minerals and phosphates. Phosphate minerals were not found in XRD analyses. Clay minerals and pyrite determined in almost all coal samples constitute the source of As in the study area. Se formation is stated to be largely of organic origin [33, 34]. However, it has been reported that some Se originates from pyrite and accessory minerals, claustalite and galena [35]. The correlation between Se and TOC could not be established in the correlation matrix. Clausthalite and galena minerals were not found in XRD analysis. However, some Se may be caused by the pyrite mineral set at almost any level. Sr coals are generally together with sulphate, carbonate and phosphate minerals [35]. They have a less amount of organic associations [32]. Since no meaningful relationship was established with TOT S, it is not possible to make a definite judgement about its stemming from sulfates. The absence of phosphate minerals in the XRD

analysis eliminates this possibility. When its relationship with carbonate related elements was examined, no significant increase or decrease was detected. However, the carbonate minerals observed in all coal samples may be a source of some Sr. Although there was no significant correlation between Sr and TOC in the correlation matrix, a close relationship was found between the two in the dendrogram. Mo has a strong relationship with organic and inorganic substances [35, 36, 37]. Increased anoxic conditions also causes the concentration of Mo to increase. Mo element is related to humic acids as well as sulphide [38]. The correlation between Mo and TOC could not be establised in the correlation matrix. It is stated that the element W is related to organic matter in coals, but some W can also be found in the wolframite and scheelite minerals [39]. W is also found in carbonate minerals [31]. In XRD analysis, wolframite and scheelite minerals could not be determined. In the study area, no relationship was detected with carbonates. In the correlation matrix, although a significant relationship could not be established between W and TOC, their close relationship in the dendrogram reveals the association of W with organic matter. Although U coals can have both organic and inorganic origin, they are generally related to organic matter [35, 36]. It is also stated that it is found in silicate, carbonate, oxide, vanadate and sulfate minerals. A small amount of U can also be found in clay minerals through adsorption [40, 35]. There is no data in the study area indicating that U may be of organic origin. U is thought to be largely inorganic in origin.

Ni is largely related to sulfides but can also be found in relation to organic matter [35, 2]. Since no significant relationship could be established with total sulphur, it is thought that the presence of Ni in the study area is not caused by sulphides. When evaluated together with XRD analysis, it was determined that Ni in the coals originated from clay minerals and carbonates. Co can be found in relation to pyrite, clay, linnaite, other sulphides and organic matter in coals [33, 41, 35]. When the amount of pyrite minerals determined in the wells where Co offers high values are evaluated, it is determined that Co in the study area is associated with inorganic matter, especially clay minerals and a small amount of pyrite. The association of the element Y with organometallics [42], organic matter [43] and mineral matter [35] are indicated. Its negative relationship with TOC (r=-0.527) decreases the possibility of organic matter association. The high concentration it offers in samples rich in elements associated with detritic minerals indicates that Y is associated with mineral material, and most probably clays, in the study area. REEs, whose organic association is very rare, are generally found in coals in relation to mineral substances [44, 45, 46, 47]. In the study area, the negative correlation between REEs and TOC reveals that REEs belong to inorganic fraction. Considering its similar tendency with elements indicating a detritic source such as AI, K and Ti, it was concluded that REEs originate from clay minerals. A negative correlation was found between Ni, Co, Y, REE and TOC. No relation was determined between these elements and TOC in the dendrogram, which confirms the relationship of Ni, Co, Y and REE with inorganic association.

No significant relation was found between the elements of Barium, Scandium, Caesium, Hafnium, Niobium, Rubidium, Thorium, Vanadium, Cuprum, Zincum, Gallium, Stannum, Tantalum, Zirconium, Plumbum, Cadmium, Antimonium, Bisemutum, Aurum, Hydrargyrum, Thallium and TOC either in correlation matrix or in dendrogram. The source of these elements is also thought to be related to the inorganic material. Finkelman [36] stated that Ba is present in the barite minerals occurring in coal samples, while Goodarzi [48] showed its association with organic matter and clay. Since a significant relationship with TOC could not be determined, an approach regarding association

with organic matter could not be made. Barite mineral was not found in XRD analysis. Swaine [35] reported that there is also Ba in ankerite mineral. It is thought that the Ba in the study area is related to clay minerals and ankerite. Although association with organic and inorganic materials in coals was stated, no relationship could be established with TOC in the study area; therefore, its relationship with organic matter could not be determined. Inorganically, it can be found in silicates, clays and phosphate minerals [31]. Phosphate minerals were not found in the study area and it was determined that the presence of Sc is related to silicate and clay minerals. In the evaluation of the correlation matrix of element V, it was found to have the same characteristics as Sc element. Dendrogram also shows the close relationship between Sc and V element. Since no significant relationship was established with TOC, V is thought to be related to clay minerals rather than organic matter. Cs is found in coals in clays, mica minerals, feldspars and organic matter. The presence of clay, mica and feldspar minerals detected in XRD analysis in wells numbered TD-133 and TD-153, where the Cs concentration is high, supporting this association. Zr is always present with a certain amount of Hf element [41]. When the correlation matrix and dendrogram are examined, it is seen that Zr has a high positive correlation with Hf (r=0.960), Nb (r=0.693) and Ga (r=0.684). Hf and Nb are considered indicative of detritic material input into the storage medium. Therefore, it was determined that Zr, together with Hf and Nb, originated from detritic minerals. Cd is generally observed in coals of inorganic origin and possibly sphalerite formation [35, 34, 36]. It can also be found to be related with carbonates, clays and organic matter [48]. It was stated that pyrite may also contain some Cd [35]. In the study area, no data could be determined indicating that Cd may be of organic origin. No sphalerite mineral was found in the XRD analysis. The positive relationship it presents with Hf (r=0.527) and Zr (r=0.475) in the correlation matrix was monitored in dendrogram and it was determined that Cd element was mostly caused by detritic minerals, especially clay minerals. It is stated that Rb stems from clay minerals in coals [45]. In the study area, clay minerals, which are intensely observed in most of the coal samples, are thought to be the source of Rb. Pb may be associated with organic matter in coals of low maturity [49, 35, 36]. However, Pb no significant relationship with TOC in the study area, and considering the correlation with W (r=0.602), which was found to be of organic origin, it was determined that it is not related to organic matter. Finkelman [32] states that Pb originates from sulphite minerals. Although no significant relationship was established with TOT S, it suggests that almost any level of pyrite minerals may be the source of Pb. Bi is found in coals in relation to sulfide minerals. The characteristics of Bi in the correlation matrix are similar to Pb. There is a close relationship between these two elements in the dendrogram. Like Pb, Bi is thought to be of inorganic origin. Th is thought to be found together with mineral material, mostly monazite and zircon [45], as well as xenotimel [41]. Swaine [35] also stated that Th can be found together with iron oxides and clay minerals. Monazite, zircon and xenotime were not detected in XRD analysis. Th is probably related to clay minerals in the study area. Pyrite in coals can contain some Au [35]. Very low amounts of Au can also be found in detritic origin. The pyrite mineral determined at almost all levels in the study area is thought to be the source of Au in coal. It is stated that Cu source in coals is related to sulphides, generally pyrite, chalcopyrite and organic matter [35, 50, 48]. When the correlation matrix is evaluated, no significant relationship is observed between Cu and TOT S. No significant relationship could be established with TOC either and a close relationship between Cu and TOC could not be found in the dendrogram. This shows that the presence of Cu is related to inorganic matter rather than organic matter. The source of Cu is thought to be mainly clay minerals. It was maintained that Zn [36], the organic associations of which is mentioned in low rank coals, is generally associated with

sulfite minerals, sphalerite, carbonate and clay minerals [25, 48]. No sphalerite was found in the XRD analysis of coals. Since a significant relationship could not be determined with TOT S and TOC, a significant relationship could not be established with organic matter and sulfide minerals. Considering the XRD analyses in the well numbered TD-153, where Zn is the most intense, it is thought that the element in question largely stems from carbonate minerals and some clay minerals contribute. Ga element can be found in the structure of sphalerite, feldspar, clay and sulphite minerals. No sphalerite mineral was found in the XRD analysis. Since no meaningful relationship could be established with TOC, there is no organic association either. The Ga concentration in the study area is thought to be largely related to clay minerals and feldspar. Especially the high amounts of these minerals in the well numbered TD-133 support this view. It was reported that most of Sn in coal is found as Sn-oxides and Sn-sulfites such as disseminated cassiterite [3]. It is generally accepted that Sn is associated with minerals in coal. Ta is found in coal in relation to mineral matter, and possibly in relation to Ti, Zr and phosphates [41, 45]. Phosphate minerals could not be determined in the study area. In the well number TD-153, where the elements associated with the detritic input are concentrated, the Ta element shows its highest values. Therefore, when the correlation matrix and dendrogram are evaluated together, Ta is associated with detritic minerals in the study area. Sb is together with organic matter and sulfides in coals [35]. Since a meaningful relationship with TOC could not be determined, an original approach could not be developed. Sb is thought to be related to sulfites in the coals in the study area. In coals, Hg is generally related to selenite and sulfites [36, 48]. Pyrite is largely the source of Hg. Its positive correlation with TOT S (r=0.417) also confirms this. It is known that Tl is associated with pyrite in coals. Although no significant relationship could be established between Tl and TOT S in the correlation matrix, their close relationship in the dendrogram shows that the source of Tl is the pyrite mineral in the study area as well (Table 6).

Table 6. Trace element correlation matrix values of study area coals [22].

	Ba	Ni	Sc	Co	Cs	Hf	Nb	Rb	Sr	Th	U	V	Y	La	Ce	Pr	Nd	Sm	Gd	Tb	Dy	Ho	Er	Tm	Yb	Lu	Cu	Zn
Ba	1,00	0,28	,520*	0,32	0,31	0,29	0,26	0,36	,416*	,530*	0,08	,419*	,510*	,546*	,569*	,599*	,611*	,651*	,646*	,612*	,578*	,541*	,509*	,495*	,495*	,490*	,641*	,594*
Ni		1,00	,737*	,758*	,797*	0,37	,749*	,798*	-0,24	,616*	,512*	,564*	,617*	,701*	,747*	,728*	,727*	,712*	,711*	,727*	,693*	,676*	,649*	,649*	,636*	,594*	0,29	,730*
Sc			1,00	,836*	,738*	,618*	,804*	,841*	-0,11	,682*	0,27	,850*	,542*	,785*	,829*	,825*	,830*	,811*	,769*	,761*	,708*	,658*	,661*	,634*	,653*	,637*	,558*	,868*
Co				1,00	,688*	,553*	,788*	,739*	-0,16	,505*	0,29	,705*	,409*	,627*	,687*	,658*	,667*	,619*	,582*	,574*	,549*	,515*	,506*	,509*	,536*	,515*	,414*	,751*
Cs					1,00	,454*	,818*	,950*	-0,34	,755*	0,18	,428*	,482*	,805*	,822*	,789*	,759*	,707*	,655*	,643*	,576*	,554*	,527*	,521*	,535*	,510*	0,21	,792*
Hf						1,00	,719*	,475*	-0,25	,540*	0,28	,611*	0,31	,502*	,512*	,524*	,515*	,468*	,444*	,446*	,427*	,440*	,447*	,462*	,488*	,478*	0,16	,515*
Nb							1,00	,869*	-	,672*	0,30	,586*	,543*	,772*	,794*	,770*	,751*	,698*	,684*	,682*	,649*	,640*	,640*	,644*	,666*	,653*	0,11	,745*
Rb								1,00	-0,33	,777*	0,14	,524*	,570*	,883*	,894*	,868*	,850*	,801*	,763*	,745*	,678*	,646*	,633*	,609*	,626*	,605*	0,27	,873*
Sr									1,00	-0,13	-0,01	-0,10	-0,08	-0,20	-0,16	-0,12	-0,09	-0,05	-0,02	-0,04	-0,05	-0,07	-0,09	-0,07	-0,11	-0,05	0,38	-0,14
Th										1,00	0,20	,502*	,491*	,906*	,900*	,908*	,888*	,841*	,752*	,708*	,599*	,569*	,515*	,496*	,497*	,476*	0,37	,851*
U											1,00	,399*	,443*	0,24	0,28	0,29	0,30	0,33	,395*	,438*	,482*	,511*	,480*	,528*	,511*	,511*	0,12	0,23
V												1,00	0,35	,570*	,616*	,632*	,643*	,653*	,576*	,570*	,525*	,469*	,473*	,445*	,459*	,439*	,694*	,703*
Y													1,00	,706*	,707*	,715*	,734*	,790*	,891*	,921*	,959*	,978*	,974*	,967*	,959*	,938*	0,18	,582*
La														1,00	,991*	,988*	,979*	,954*	,910*	,877*	,803*	,767*	,734*	,712*	,723*	,706*	0,38	,929*
Ce															1,00	,996*	,989*	,969*	,923*	,894*	,821*	,779*	,745*	,724*	,734*	,712*	,425*	,941*
Pr																1,00	,996*	,979*	,935*	,904*	,831*	,788*	,753*	,730*	,738*	,720*	,463*	,945*
Nd																	1,00	,986*	,949*	,920*	,850*	,805*	,771*	,748*	,753*	,735*	,486*	,945*
Sm																		1,00	,974*	,953*	,895*	,849*	,817*	,789*	,793*	,769*	,514*	,912*
Gd																			1,00	,993*	,967*	,937*	,912*	,892*	,891*	,873*	,431*	,849*
Tb																				1,00	,985*	,961*	,944*	,927*	,922*	,902*	,390*	,811*
Dy																					1,00	,989*	,978*	,968*	,965*	,945*	0,33	,730*
Ho																						1,00	,991*	,987*	,984*	,968*	0,25	,675*
Er																							1,00	,992*	,990*	,977*	0,22	,641*
Tm																								1,00	,994*	,986*	0,19	,609*

Yb																									1,00	,991*	0,18	,629*
Lu																										1,00	0,19	,612*
Cu																											1,00	,587*
Zn																												1,00

Table 6 continues.

	TOC	TOT/C	TOT/	Be	Ga	Sn	Ta	W	Zr	Eu	Mo	Pb	As	Cd	Sb	Bi	Au	Hg	Tl	Se
Ba	-0,16	-,576**	-0,11	-0,20	0,20	0,34	,454*	-0,15	,511*	,727*	0,12	,594*	-0,02	0,33	-0,24	0,37	-0,12	0,27	0,15	0,20
Ni	-,443*	-,754**	0,19	-0,05	,709*	,591*	,698*	-,399*	0,37	,702*	0,12	,674*	,490*	0,31	,517*	,669*	0,17	0,22	0,34	0,13
Sc	-0,34	-,859**	0,02	-0,11	,803*	,724*	,775*	-,452*	,566*	,793*	-0,01	,705*	0,27	,526*	0,22	,663*	0,28	0,08	0,16	0,00
Co	-,437*	-,725**	-0,04	0,00	,759*	,662*	,702*	-0,28	,516*	,597*	-0,12	,545*	0,26	,486*	0,31	,588*	,445*	-0,04	0,12	-0,08
Cs	-0,37	-,854**	0,14	-0,31	,628*	,621*	,782*	-,419*	0,37	,646*	0,04	,646*	0,24	0,30	0,16	,733*	0,03	0,10	0,34	0,00
Hf	0,07	-,544**	-0,22	-0,20	,793*	,558*	,750*	-0,14	,960*	,514*	-0,06	,519*	-0,01	,527*	0,09	,525*	0,14	0,14	0,12	-0,27
Nb	-0,25	-,788**	0,05	-0,19	,833*	,691*	,843*	-0,27	,693*	,595*	-0,06	,587*	0,35	,395*	0,34	,614*	0,15	0,06	0,27	-0,25
Rb	-0,38	-,908**	0,13	-0,31	,676*	,699*	,767*	-,475*	0,37	,723*	0,00	,681*	0,28	0,30	0,18	,751*	0,08	0,00	0,26	-0,07
Sr	-0,05	0,06	0,23	0,08	-,492*	-0,22	-0,29	0,22	-0,20	-0,01	0,20	-0,10	-0,13	-,420*	-0,08	-0,25	0,05	0,37	-0,27	0,34
Th	-0,19	-,865**	-0,11	-0,39	,639*	,598*	,757*	-	,552*	,754*	0,18	,888*	-0,01	0,31	0,03	,882*	-0,07	0,14	,419	-0,01
U	-0,26	-0,22	0,25	0,28	,473*	0,15	0,18	-0,37	0,22	,453*	,645*	,456*	,629*	,394*	,690*	0,37	0,06	,395*	,413	0,35
V	-0,11	-,628**	-0,09	-0,04	,684*	,566*	,551*	-,433*	,459*	,577*	0,05	,539*	0,16	,553*	0,23	,491*	0,37	0,07	0,19	0,11
Y	-	-,575**	-0,02	0,09	,519*	,542*	,489*	-0,34	0,37	,859*	0,18	,686*	,431*	0,29	,416*	,514*	-0,19	0,20	0,29	0,19
La	-0,36	-,917**	-0,09	-0,32	,676*	,699*	,750*	-	,528*	,888*	0,14	,865*	0,12	,411*	0,07	,854*	-0,04	0,05	0,33	-0,04
Ce	-,390*	-,927**	-0,07	-0,25	,681*	,734*	,775*	-	,531*	,917*	0,15	,884*	0,16	,414*	0,12	,825*	-0,03	0,10	0,33	0,05
Pr	-0,38	-,931**	-0,06	-0,27	,687*	,722*	,755*	-	,507*	,923*	0,15	,883*	0,16	,428*	0,11	,825*	-0,02	0,06	0,32	0,05
Nd	-,402*	-,924**	-0,08	-0,25	,669*	,734*	,755*	-	,512*	,939*	0,12	,883*	0,16	,421*	0,11	,809*	0,01	0,10	0,31	0,06
Sm	-,416*	-,884**	-0,06	-0,25	,602*	,641*	,667*	-	,434*	,973*	0,21	,865*	0,22	,418*	0,14	,744*	-0,09	0,13	0,37	0,17
Gd	-,469*	-,832**	0,00	-0,13	,595*	,603*	,600*	-	,430*	,986*	0,24	,829*	0,35	,407*	0,28	,689*	-0,07	0,18	0,36	0,19
Tb	-,476*	-,797**	0,01	-0,09	,625*	,617*	,605*	-	,445*	,980*	0,22	,823*	0,37	,396*	0,32	,664*	-0,03	0,21	0,34	0,19
Dy	-	-,716**	0,03	-0,01	,637*	,603*	,564*	-,393*	,470*	,942*	0,18	,725*	,449*	,407*	,389*	,562*	-0,04	0,19	0,29	0,15
Ho	-	-,671**	0,02	0,03	,622*	,571*	,523*	-0,35	,477*	,901*	0,22	,689*	,462*	0,38	,453*	,525*	-0,08	0,19	0,27	0,14
Er	-,485*	-,642**	-0,02	0,05	,627*	,603*	,516*	-0,35	,499*	,880*	0,17	,663*	,440*	0,36	,444*	,496*	-0,05	0,15	0,20	0,09
Tm	-	-,620**	-0,02	0,06	,596*	,580*	,496*	-0,31	,471*	,855*	0,18	,630*	,454*	0,34	,457*	,463*	-0,08	0,16	0,22	0,09
Yb	-	-,630**	-0,03	0,06	,636*	,591*	,515*	-0,32	,503*	,840*	0,17	,618*	,444*	0,38	,458*	,455*	-0,07	0,14	0,23	0,04
Lu	-	-,622**	-0,01	0,07	,624*	,627*	,505*	-0,35	,472*	,847*	0,16	,615*	,438*	0,32	,465*	,460*	-0,02	0,12	0,16	0,03
Cu	-0,18	-,517**	0,01	-0,19	0,32	,473*	0,38	-,489*	0,18	,626*	0,20	,599*	0,02	0,39	-0,06	,579*	0,21	0,11	0,23	,412*
Zn	-0,37	-,958**	-0,09	-0,31	,658*	,688*	,759*	-	,436*	,841*	0,07	,855*	0,10	,495*	0,03	,811*	0,18	0,01	0,28	0,06
TOC	1,00	0,36	-0,08	-0,19	-0,23	-0,29	-0,18	0,31	0,17	-,428*	-0,08	-0,22	-0,29	0,00	-0,36	-0,23	0,09	0,08	-0,14	-0,17
TOT/C		1,00	-0,07	0,30	-	-	-	,465*	-	-	-0,05	-	-0,14	-0,38	-0,11	-	-0,15	-0,12	-0,24	0,01
TOT/S			1,00	0,25	-0,03	-0,28	-0,06	0,20	-0,20	-0,03	0,36	-0,06	,602*	-0,07	0,31	-0,04	0,03	,417*	0,15	0,38
Be				1,00	-0,03	-0,15	-0,29	0,16	-0,14	-0,15	0,09	-0,16	,447*	0,08	,449*	-0,16	0,13	0,15	-0,08	0,19
Ga					1,00	,638*	,738*	-,399*	,684*	,557*	-0,08	,589*	0,30	,490*	,433*	,636*	0,30	-0,04	0,17	-0,31
Sn						1,00	,699*	-	,449*	,615*	-0,24	,539*	-0,03	0,23	0,08	,521*	0,20	-0,18	-0,03	-0,36
Ta							1,00	-0,33	,648*	,585*	-0,19	,691*	0,05	0,35	0,09	,643*	0,14	0,18	0,19	-0,19
W								1,00	-0,01	-	-0,31	-	0,06	-0,17	-0,11	-	0,02	0,29	-0,15	0,00
Zr									1,00	,445*	-0,02	,455*	0,00	,475*	0,04	,408*	0,10	0,14	0,04	-0,29
Eu										1,00	0,22	,835*	0,26	,390*	0,18	,684*	-0,05	0,18	0,30	0,21
Mo											1,00	0,23	0,31	0,19	0,25	0,20	-0,38	0,25	0,36	,512*
Pb												1,00	0,18	0,35	0,15	,840*	0,03	0,24	,396	0,21
As													1,00	0,19	,762*	0,14	0,12	0,38	0,30	0,31
Cd														1,00	-0,01	,391*	0,08	0,05	0,28	0,15
Sb															1,00	0,18	0,18	0,25	0,23	0,10
Bi																1,00	-0,01	0,11	,416	0,09
Au																	1,00	-0,03	-0,22	-0,24
Hg																		1,00	,463	,568*
Tl																			1,00	0,35
Se																				1,00

JSR A
Journal of Scientific Reports

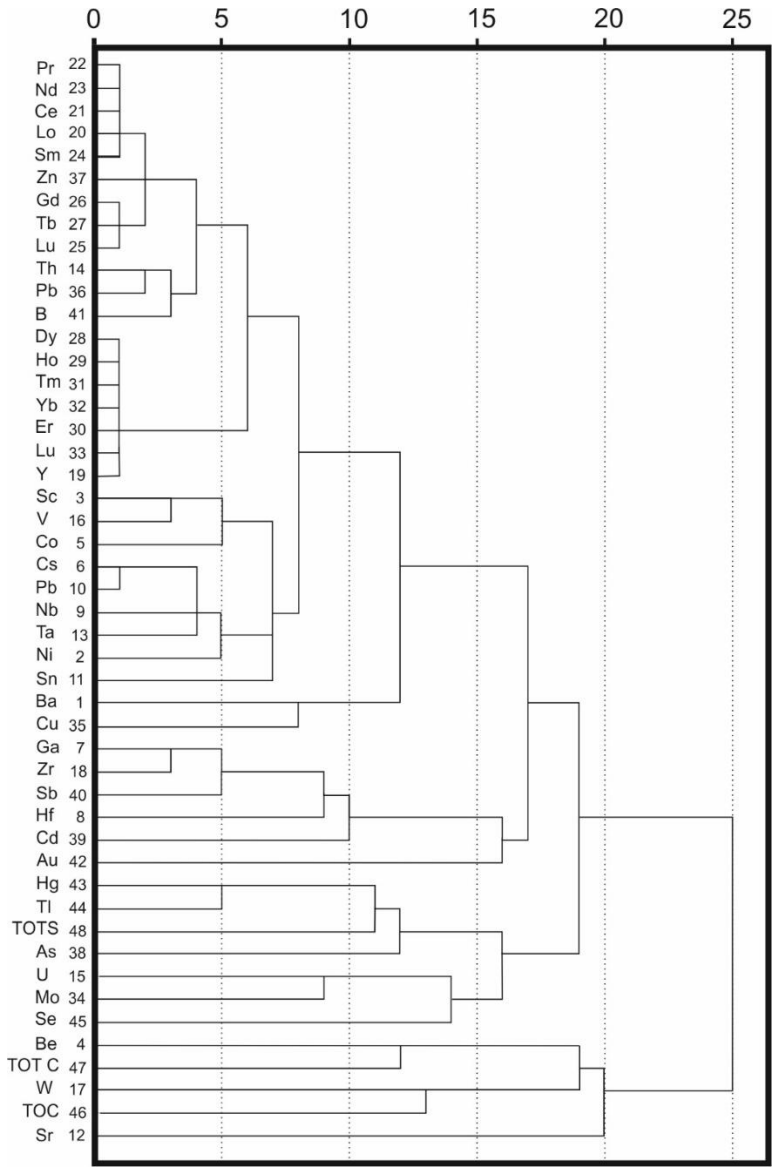

Figure 4. Dendrogram of trace elements in the Malkara coals.

4.4. Element Enrichment

The enrichment factors of the main and trace elements of Malkara coals were calculated according to the average UCC values [51] with the formula given below, values less than 1 were depleted, and values greater than 1 were considered enriched. While the main elements Si, Na, K and Mn were

JSR A
Journal of Scientific Reports

consumed in all coal samples, Fe, Mg and Cr were enriched in all samples except for the samples taken from the well numbered TD-151. Ca was enriched in the samples taken from the wells numbered TD-155 and TD-129; Ti was enriched in the wells other than the samples taken from the wells numbered TD-151 and TD-131 and P was only enriched in the samples taken from the well numbered TD-129 and consumed in all the other wells (Fig. 5).

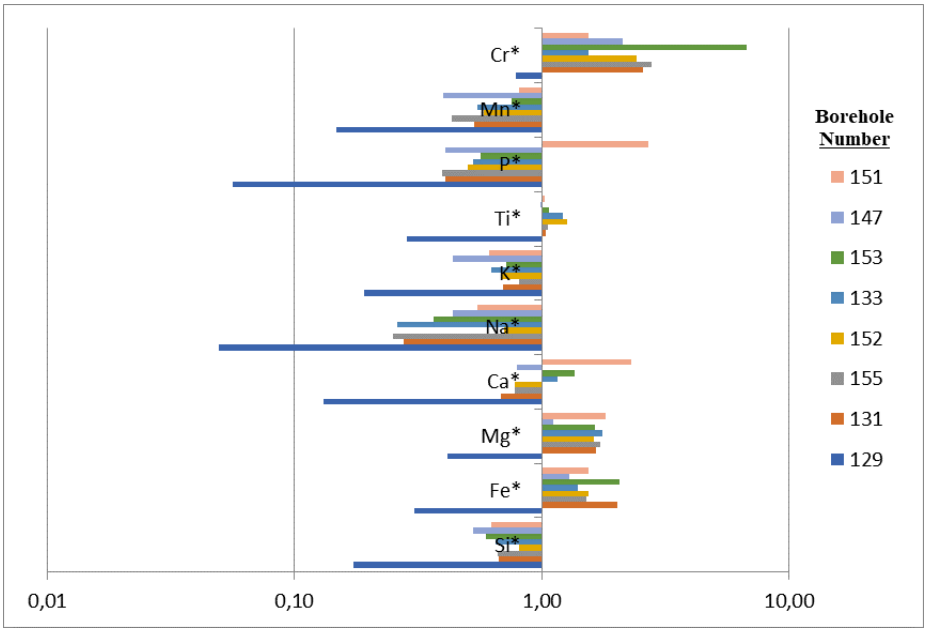

Figure 5. Well-based enrichment factors of major elements relative to the UCC. (Enrichment Factor (EF) = (element/Al)sample / (element/Al)average shale [52], *Major elements)

In trace elements, Barium, Beryllium, Cobaltum, Caesium, Gallium, Hafnium, Niobium, Rubidium, Stannum, Strontium, Tantalum, Thorium, Uranium, Vanadium, Zirconium, Yttrium, REE, Molybdenum, Cuprum, Plumbum, Zincum, Antimonium, Bisemutum, Aurum, Hydrargyrum and Thallium elements were found to be consumed both in the averages taken on the basis of wells and in general average (Fig. 6). W and Se elements were enriched in all coal samples both on general average and on a well basis. Ni was enriched in the samples taken from wells numbered TD (151,147 and 153), and consumed in samples taken from the wells numbered TD (133, 152, 155, 131 and 129). While As was enriched only in the samples taken from the well numbered TD-153, Cd was enriched only in the samples taken from the wells numbered TD (131 and 133). When the enriched elements were evaluated throughout the study area, it was found that the enrichments in question are related to organic matter.

JSR A
Journal of Scientific Reports

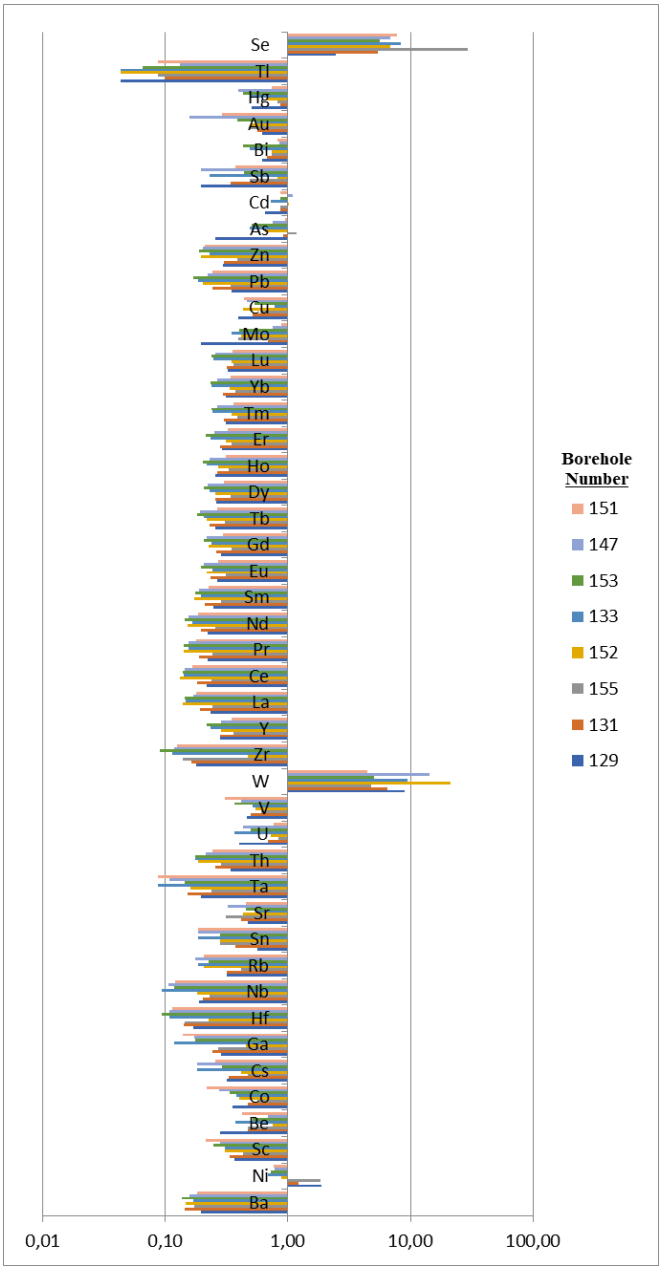

Figure 6. Well-based enrichment factors of trace elements relative to the UCC.

Element contents of coal base, ceiling and intercalation samples were compared with elemental contents of coal samples. As expected, the main elements increased in floor, ceiling and intercalation samples. In trace elements, an increase was determined in the amounts of Beryllium, Uranium, Vanadium, Molybdenum, Cuprum, Cadmium, Antimonium, Bisemutum, Hydrargyrum, Thallium and Selenium in coal samples. When the correlation matrix obtained by statistical analysis was evaluated, the elements Uranium, Vanadium, Cuprum, Cadmium, Antimonium, Bisemutum, Hydrargyrum and Thallium were associated with minerals content. However, the fact that these elements are found in coal samples in higher amounts reveals the relation of these elements to organic matters of sedimentation environment (Fig. 7).

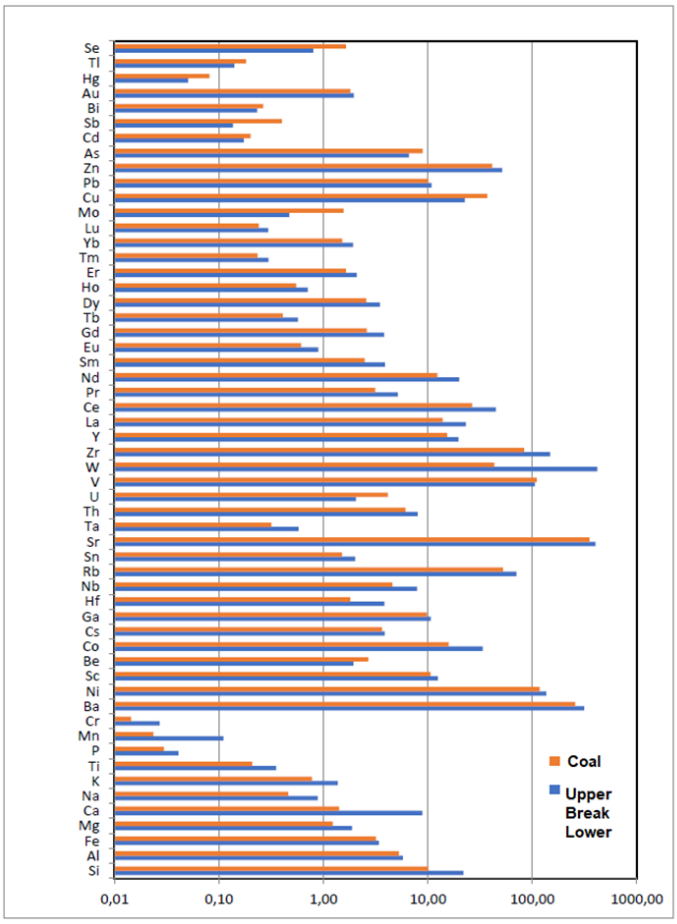

Figure 7. Comparison between the elemental contents of coal and rock samples.

4.5. Environmental Aspects of Trace Elements in the Malkara Coals

The environmental effects of the trace elements depend on their content and way of formation [53]. Toxic effects of trace elements may arise from the combustion of coal in domestic or industrial form [32]. Trace element content in coal has a great effect on the environment, economy and living beings [3].

Trace elements in coal are divided into three groups in terms of their environmental effects [2]. The elements in the first group consist of As, Cd, Hg and Se, and these elements are considered toxic. The elements in the second group consist of B, Be, Cu, Mo, Ni, Pb, Th, U, V and Zn, and these elements have environmental effects. The elements in the third group consist of Ba, Co, Sb, Sn and Tl and have the least environmental risk. Among the elements examined in the study area, Se in the first group, Be, Cu, Mo, Ni, Pb, Th, U, V, Zn in the second group, and Ba, Co, Sn elements in the third group presented values above the world coal averages. Due to the fact that especially Se element is a volatile element, due to its use in thermal power plants and for thermal purposes, it may have negative impact on environment and human health as a result of its emission to the atmosphere [54, 55, 56]. Although elements that may be environmentally hazardous such as Cd, Sb, Hg and Tl remain below world averages in coal samples, these elements also pose risks because there will be an increase in concentrations that will form in case of using coal due to the high amount of coal ceiling-floor and intercalation samples. On the other hand, As, Be, Cd, Cr, Co, Hg, Pb, Mn, Ni, Sb and Se elements are anthropogenic sourced air pollutants depending on coal use according to Clean Air Act Amendments. In the study area, Be, Co, Pb, Ni, and Se, which are among these elements offer values above the world average. Therefore, they are potential air pollutants in the use of coal.

5. CONCLUSIONS

As a result of the major and trace element analysis applied to 54 coal, coal ceiling base and intercalation samples taken from Malkara (Tekirdağ) region, XRD all rock and clay analyses, similar results were obtained from coal and roof, floor, and parting samples in mineralogical investigation of Malkara lignites. Quartz, ankerite, pyrite, calcite, mica, aragonite, dolomite, feldspar were detected. Smectite, illite, kaolinite, and chlorite were the clay minerals that are detected from big to small amounts.

In the value comparison of Malkara lignites, all elements other than Manganum, Molybdenum, Cadmium, Antimonium, Praseodymium, Gadolinium, Thulium, Aurum, Hydrargyrum, Thallium, Bisemutum were found to be above the world coal average; Vanadium, Nichelium, Cuprum, Arsenicum, Selenium, Strontium, Wolframium, Aurum, Hydrargyrum, Bisemutum, Uranium, above the upper continental crust average, Silicium, Aluminium, Ferrum, Magnesium, Natrium, Kalium, Titanium, Barium, Scandium, Vanadium, Cobaltum, Zincum, Cuprum, Gallium, Rubidium, Strontium, Yttrium, Niobium, Barium, Plumbum above the Turkey coal average, all elements other than Phosphorus, Manganum, Chromium, Zincum, Arsenicum, Selenium, Molybdenum, Cadmium, Antimonium, Aurum, Hydrargyrum, Thallium, Plumbum, Bisemutum above the U. S. coal average and Silicium, Aluminium, Magnesium, Calcium, Natrium, Kalium, Titanium, Manganum, Beryllium, Scandium, Vanadium, Cobaltum, Nichelium, Cuprum, Gallium, Arsenicum, Rubidium, Strontium, Caesium, Barium, Wolframium, Thorium is above the average of Chinese coals. All of the major

elements other than Cr are below the UCC concentration. It was determined that the major elements largely stem from inorganic matter. It was found that Be, Sr and W which are related to trace elements are not only related to inorganic substances but also the organic origin and no relation was determined between other trace elements and organic matter.

Element enrichment factors were calculated and consumed and enriched elements were determined. Among the major elements, Silicium, Natrium and Kalium were consumed in all wells and Phosphorus was consumed in all the wells other than TD-129. Ferrum, Magnesium, Chromium were enriched in all wells except TD-151, and Ti was enriched in all wells except TD-151 and TD-131. Among the minor elements, Barium, Beryllium, Cobaltum, Caesium, Gallium, Hafnium, Niobium, Rubidium, Stannum, Strontium, Tantalum, Thorium, Uranium, Vanadium, Zirconium, Yttrium, REE, Molybdenum, Cuprum, Plumbum, Zincum, Antimonium, Bisemutum, Aurum, Hydrargyrum, Thallium were consumed in all wells, and Wolframium and Sulphurium elements were enriched in all wells.

Among the coal samples in the study area, Selenium, Beryllium, Cuprum, Molybdenum, Niccolum, Plumbum, Thorium, Uranium, Vanadium, Zincum, Barium, Cobaltum, Stannum, which are among the elements that may create an adverse environmental effect, offered values above the world coal averages. Among these elements, Beryllium, Cobaltum, Plumbum, Niccolum and Selenium are potential air pollutants in the use of coal. The average samples of coal, coal ceiling, floor and intercalation were compared. When the environmentally sensitive elements were examined, Chromium, Arsenicum, Manganum, Niccolum, Plumbum, Phosphorus, Zincum, Thorium, Titanium, Cobaltum, Stannum, Barium, roof, floor and parting samples exhibited an increase compared to coal.

ACKNOWLEDGEMENTS

The authors acknowledge that some part of the data presented in this article is related to the PhD thesis of Cevdet Bertan Güllüdağ, entitled "GIS-supported investigation of organic geochemistry, main-trace element contents and environmental effects of Malkara (Tekirdağ) Coals ".This study was supported by the Research Unit of Akdeniz University (Project Number: FDK 2016-2042). The authors would like to thank the General Directorate of Mineral Research and Exploration (MTA) (Turkey) (for sampling and chemical analysis), Turkish Petroleum Corporation (TPAO), and Research Unit of Akdeniz University for contributions.

REFERENCES

[1] Chamber Of Mining Engineers Of Turkey, (2020), Coal and Energy Report 2020, Ankara, Turkey, pp. 48. (in Turkish)

[2] Swaine, D.J., (1995), The Contents and Some Related Aspects of Trace Elements in Coals, In: Environmental Aspects of Trace Elements in Coal, London: Kluwer Academic Publishers, pp. 312.

[3] Finkelman, R.B., Grosss, P.M.K., (1999), The types of data needed for assessing the environmental and human health ımpacts of coal, International Journal of Coal Geology, 40, 91-101.

[4] Gürdal, G., (2008), Geochemistry of trace elements in Çan coal (Miocene), Çanakkale, Turkey, International Journal of Coal Geology, 74 (1), 28-40.

[5] Altunsoy, M., Özçelik, O., Özdoğan, M., Güllüdağ, C.B., (2015), Major and trace element contents in coaly units of the Pliocene Dursunlu Formation, Procedia Earth and Planetary Science, 15, 774-780.

[6] Özçelik O., Yavuz Pehlivanlı B., Sarı A., Altunsoy M., Hökerek S., Ünal N., (2016), Geochemical characteristics of major and trace elements in Şahinali Coals, Aydın, Turkey, Energy Sources Part A-Recovery Utilization and Environmental Effects, 38 (10), 1435-1447.

[7] Altunsoy, M., Sarı, A., Özçelik, O., Engin, H., Hökerek, S., (2016), Major and trace-element enrichments in the Karapınar Coals (Konya, Turkey), Energy Sources Part A-Recovery Utilization And Envıronmental Effects, 38, 88-99.

[8] Koca, D., Altunsoy, M., Sarı, A., Güllüdağ, C.B., (2015), Pamucakyayla (Antalya) civarı organik kayaçlarındaki majör ve iz elementlerin jeokimyasal davranışları, Selçuk University Journal of Engineering, Sciences and Technology, 3 (4), 13-26. (in Turkish)

[9] Turkey Lignite Inventory, (2010), General Directorate of Mineral Research and Exploration Inventory series, Ankara, Turkey, pp. 371.

[10] Keskin, C., (1974), Kuzey Trakya havzası'nın stratigrafisi, Türkiye İkinci Petrol Kongresi Tebliğleri Kitabı, pp. 137-163. (in Turkish)

[11] Perinçek, D., Ataş, N., Karatut, Ş., Erensoy, E., (2015), Trakya Havzasında, Danişmen Formasyonu ıçindeki linyit katmanlarının potansiyelini kontrol eden jeolojik faktörler, Maden Tetkik ve Arama Dergisi, 150, 79-110. (in Turkish)

[12] Siyako, M. (2006). Lignite sandstones of the Thrace Basin. Mineral Research and Exploration Journal, 132, 63-73.

[13] Koca, D., (2011), Nallıhan (Ankara, Türkiye) civarı bitümlü şeyllerinde organik madde ve iz element zenginleşmeleri. Unpublished Ph.D. Dissertation. Ankara University, Turkey. Pp. 411. (in Turkish)

[14] Ketris, M.P., Yudovich, Y.E., (2009), Estimations of clarkes for carbonaceous biolithes: World averages fortrace element contents in black shales and coals, International Journal of Coal Geology, 78, 135-148.

[15] Palmer, C.A., Tuncalı, E., Dennen, K.O., Coburn, T.C., Finkelman R.B., (2004), Characterization of Turkish Coals: a Nation Wide Perspective, International Journal of Coal Geology, 60, 85-115.

[16] Finkelman, R.B., (1993), Trace and minor elements in coal, In: Organic Geochemistry, New York: Plenum, pp. 593–607.

[17] Dai, S.F., Zhou, Y.P., Ren, D.Y., Wang, X.B., Li, D., Zhao, L., (2007), Geochemistry and mineralogy of the Late Permian coals from the Songzao Coalfield, Chongqing, Southwestern China, Science in China Series D: Earth Science, 50, 678-688.

[18] Dai, S.F., Li, D., Chou, C.L., Zhao, L., Zhang, Y., Ren, D.Y., Ma, Y.W., Sun, Y.Y., (2008), Mineralogy and geochemistry of Boehmite-Richcoals: New insights from the Haerwusu Surface Mine, Jungar Coalfield, Inner Mongolia, China, International Journal of Coal Geology, 74, 185-202.

[19] Dai, S.F., Ren, D.Y., Chou, C.L., Finkelman, R.B., Seredin, V.V., Zhou, Y.P., (2012), Geochemistry of trace elements in Chinese coals: A Review of Abundances, Genetic Types, Impacts on Human Health, and Industrial Utilization, International Journal of Coal Geology, 94, 3-21.

[20] Rudnick, R.L., Gao, S., (2003), Treatise on geochemistry. Elsevier-Pergamon, Oxford. pp. 683.

[21] Valkovic, V., (1983), Trace elements in coal. Boca Raton, FL, CRC Press, pp. 210–281.

[22] Güllüdağ, C.B., (2019), GIS-supported investigation of organic geochemistry, main-trace element contents and environmental effects of Malkara (Tekirdağ) Coals, Dissertation, University of Akdeniz (in Turkish).

[23] Lo Mónaco, S., López, L., Rojas, H., Garcia, D., Premovic, P., Briceño, H., (2002), Distribution of major and trace elements in la luna formation, Southwestern Venezuelan Basin, Organic Geochemistry, 33, 1593-1608.

[24] Kortenski, J., Sotirov, A., (2002), Trace and major elements content and distribution in neogene lignite from the Sofia Basin, Bulgaria, International Journal of Coal Geology, 52, 63-82.

[25] Karayiğit, A.İ., Gayer, R.A., Querol, X., Onocak, T., (2000), Contents of major and trace elements in feed coals from Turkish coal-fired power plants, International Journal of Coal Geology 44 (2), 169-184.

[26] Prevot, L., (1990), Geochemistry, petrography, genesis of Cretaceous-Eocene Phosphorites; The Ganntour deposit (Morocco), a type example, Societe Geologique de France, Paris, pp. 232.

[27] Mukhopadhyay, P.K., (1986), Petrography of selected Wilcox and Jackson group lignites from the Tertiary of Texas, Geology of Golf Coast Lignites, Field Trip Guide Book, Geological Society of America.

[28] Karayiğit, A.İ., (2003), Mineralogy and trace element contents of the Upper Carboniferous Coals from the Asma-Dilaver and Gelik mines in Zonguldak, Turkey, Energy Sources, 25 (7), 689-702.

[29] Koralay, D.B., (2009), Bolu Havzası Eosen bitümlü şeyllerinin hidrokarbon potansiyeli ve iz element dağılımlarının belirlenmesi, Unpublished Ph.D. Dissertation, Ankara University, Turkey, 198 pp. (in Turkish)

[30] Song, D., Qin, Y., Zhang, J., Wang, W., Zheng, C., (2007), Concentration and distribution of trace elements in some coals from Nothern China, International Journal of Coal Geology, 69, 179-191.

[31] Singh, R.M., Singh, M.P., Chandra, D., (1983), Occurence, distribution and probable source of trace elements in Ghugas Coals, Wardha Valley, District Chandrapur and Yeotmal, Maharashtra, India, International Journal of Coal Geology, 2, 371-381.

[32] Finkelman, R.B., (1994a), Modes of occurence of potantially hazardous elements in coal: level of confidence, Fuel Processing Technology, 39 (1-3), 21-34.

[33] Gluskoter, H.J., Ruch, R.R., Miller, W.G., Cahill, R.A., Dreher, G.B., Kuhn, J.K., (1977), Trace elements in coal: Occurrence and distribution, III. State Geol. Surv. Circ, 499, pp. 154.

[34] Finkelman, R.B., (1994b), Theuse of modes of occurence information to predict the removal of the hazardous air pollutants, International Journal of Coal Geology, 124, 132-134.

[35] Swaine, D.J., (1990), Trace elements in coal. Butterwarh, London, pp. 278.

[36] Finkelman, R.B., (1995), Modes of occurrences of environmentally-sensitive trace elements in coal, In: Environmental aspects of trace elements in coal, The Netherlands: Kluwer Academic Publishers, pp. 24-44.

[37] Orem, W.H., Finkelman, R.B., (2003), Coal formation and geochemistry, In: Treatise on geochemistry, Elsevier, Amsterdam, pp. 191-222.

[38] Yavuz Pehlivanlı, B., (2011), Hırka Formasyonu (Beypazarı, Ankara, Türkiye) bitümlü şeyllerinin inorganik element depolanmaları ve organik- inorganik elementler arasındaki kökensel ilişkiler. Unpublished Ph.D. Dissertation. Ankara University, Turkey, 332 pp. (in Turkish)

[39] Eskenazy, G.M., (1982), The geochemistry of Tungsten in Bulgarian Coals, International Journal of Coal Geology, 2, 99-111.

[40] Wedepohl, K.H., (1969), Handbook of geochemistry, Berlin, Springer-Verlag, pp. 422.

[41] Finkelman, R.B., (1980), Modes of occurrence of trace elements in coal. Unpublished Ph.D. Dissertation. University of Maryland, Maryland, 301 pp.

[42] Ershov, V.M., (1962), Rare earth elements in coals of the Kizel Coal Basin, Geochemistry (USSR) 3, 306-308.

[43] Given P.H., Miller R.N., (1987), The association of major, minor and trace inorganic elements with lignites, Geochim. Cosmochim. Acta 51, 1843-1853.

[44] Shpirt, M.Y., Ratynskii, V.M., Zharov, Y.N., Zekel, L.A., (1984), Forms of trace element compounds and their behaviour in processing coals, Razvit, Uglekhim, 50, 224-235.

[45] Palmer, C.A., Filby, R.H., (1984), Distribution of trace elements in coal from the Powhatan No. 6 mine, Ohio, Fuel, 63, 318-328.

[46] Eskenazy, G.M., (1987), Rare Earth Elements and Yttrium in lithotypes of Bulgarian coal, Organic Geochemistry, 11, 83-89.

[47] Goodarzi, F., Van der Flier-Keller, E., (1988), Distribution of major, minor and trace elements in Hat Creek Deposit, No.2, British Columbia, Canada, Chemical Geology, 70, 313-333.

[48] Goodarzi, F., (2002), Elemental composition and modes of occurrence of elements in Canadian Feed-Coals, Fuel, 81, 1199-1213.

[49] Zubovic, P., Stadnichenko, T., Sheffey, N.B., (1960), The association of some minor elements with organic and ınorganic phases of coal, US Geol. Surv. Prof. Rap., No. 400-B, B84-B87.

[50] Querol, X., Finkelman, R.B., Alastuey, A., Huerta, A., Palmer, C.A., Mroczkowski, S., Kolker, A., Chenery, S.N.R., Robinson, J.J., Juan, R., Lopez-soler, A., (1998), Quantitative determination of modes of occurrence of major, minor and trace elements in coal: Comparison of results from different methods, AIE 8th Australian Coal Science Conference, pp. 51-56.

[51] Li, Y.H., (2000), A compendium of geochemistry: From solar nebula to the human brain. princeton, NJ: Princeton University Press.

[52] Brumsack, H.J., (2006), The trace metal content of recent organic carbon-rich sediments: Implications for Cretaceous Black Shale Formation, Palaeogeography, Palaeocimatology, Palaeoecology, 232, 344-361.

[53] Sun, R., Liu, G., Zheng, L., Chou, C.L., (2010), Geochemistry of trace elements in coals from the Zhuji Mine, Huainan Coalfield, Anhui, China, International Journal of Coal Geology, 81, 81-96.

[54] Zheng, B., Ding, Z., Huang, R., Zhu, J., Yu, X., Wang, A., Zhou, D., Mao, D., Su, H., (1999), Issues of health and disease relating to coal use in Southwestern China, International Journal of Coal Geology, 40, 119-132.

[55] Finkelman, R.B., (2004), Potential health ımpacts of burning coal beds and waste banks, International Journal of Coal Geology, 59 (1-2), 19-24.

[56] Dai, S., Ren, D., Tang, Y., Yue, M., Hao, L., (2005), Concentration and distribution of elements in Late Permian Coals from Western Guizhou Province, China, International Journal of Coal Geology, 61, 119-137.

Kütahya Dumlupınar University
Institute of Graduate Studies

Journal of Scientific
Reports-A
E-ISSN: 2687-6167
Number 51, December 2022

RESEARCH ARTICLE

ANTIOXIDANT RESPONSES TO DROUGHT STRESS IN PENNYROYAL (*Mentha pulegium* L.)

Funda ULUSU[1*], Kader TÜMER[2], Yakup ULUSU[3]

[1*]Karamanoglu Mehmetbey University, Vocational School of Technical Sciences, Department of Crop and Animal Production, Karaman, fulusu@kmu.edu.tr, ORCID: 0000-0002-0321-2602
[2]Karamanoglu Mehmetbey University, Faculty of Engineering, Department of Bioengineering, Karaman, kadertumer96@gmail.com, ORCID: 0000-0001-6392-0785
[3]Karamanoglu Mehmetbey University, Faculty of Engineering, Department of Bioengineering, Karaman, yakupulusu@kmu.edu.tr, ORCID: 0000-0002-8755-2822

Receive Date:21.07.2022 *Accepted Date: 19.08.2022*

ABSTRACT

Mentha pulegium L. (Lamiacea) is a valuable medicinal and aromatic plant found in humid and arid bioclimatic regions of Turkey. Drought stress is a growing concern for the future of agriculture, as well as the most common abiotic stress factor affecting the biochemical processes of plants and seriously damaging crop productivity. The aim of the study was to evaluate the effects of drought stress on the activity of enzymatic antioxidants (polyphenol oxidase - PPO, peroxidase - POD, ascorbate peroxidase - ASPX, catalase - CAT) and some ecophysiological (total chlorophyll content, chlorophyll a and b, carotenoid) responses in *M. pulegium* grown in pots under greenhouse conditions. In addition, oxidative stress markers were analysed to determine whether drought stress causes oxidative damage in pennyroyal. The plants were exposed to water stress during the 3rd, 6th and 10th days. All enzymatic antioxidant activities of plants under stress were increased compared to control plants. While there was a significant increase in PPO and POD activities in the first days of drought treatment, the prolongation of the treatment period resulted in a significant decrease in these activities. In addition, drought significantly increased lipid peroxidation (294%), hydrogen peroxide (158%) and proline (3172%) content compared to controls. These results show that drought treatment and duration significantly affect antioxidant enzyme activities, lipid peroxidation, hydrogen peroxide and proline content. DPPH (2-diphenyl-1-picrylhydrazyl), ABTS (2,20'-azino-bis (3-ethylbenzothiazoline-6-sulphonic acid)) radical scavenging activity, Fe^{+2} (FRAP) reducing activity and total phenolic content analysis were performed to analyse the effects of drought stress on antioxidant properties of pennyroyal plant. In addition, the decrease in photosynthetic pigment content in parallel with the prolongation of the drought period due to oxidative damage shows that this valuable medicinal and aromatic plant has low tolerance to drought.

Keywords; *Mentha pulegium, Drought stress, Enzymatic antioxidants, Proline, MDA*

JSR A
Journal of Scientific Reports

1. INTRODUCTION

In nature, plants are frequently exposed to biotic and abiotic stress conditions that cause negative effects in terms of growth, development and productivity. Environmental stressors have a limiting effect on plant growth and food production in many regions. Drought, which is accompanied by changing climatic conditions, is one of the most important abiotic factors limiting plant growth and production [1]. Drought is increasing rapidly on a global scale and affects approximately 55% (~7.8 million km^2) of the total arable land, with the Asian continent having the highest level with 39% (3.03 million km^2) [2]. In this respect, determining the drought stress tolerance mechanisms of plants is a very important ecological goal. In plants exposed to drought stress, many vital biochemical reactions such as stomatal closure at the molecular level, decrease in photosynthesis rate, increase in reactive oxygen species (ROS) are adversely affected, and this generally results in a decrease in crop productivity [3]. These negative effects of drought vary depending on the length, degree, frequency, plant species and growth period (vegetative- generative) of the plant [4].

Plants have developed a complex array of mechanisms to deal with biotic and abiotic stresses. One of the stress defense mechanisms in plants is the defense system, which includes enzymatic antioxidants [5]. It is known as a toxic problem for plants that hydrogen peroxide (H_2O_2), superoxide radicals and hydroxide ions (OH^-) that occur in plants under environmental stress cause ROS accumulation [6]. ROS can cause protein degradation, lipid peroxidation, DNA and cell damage and ultimately cell death [7,8]. In order to improve plant tolerance to environmental stresses, protect homeostasis and reduce the harmful effects of oxidative stress, these ROS are cleaned by some enzymatic such as PPO (polyphenol oxidase), SOD (superoxide dismutase), ASPX (ascorbate peroxidase), POD (peroxidase), CAT (catalase) and non-enzymatic (phenolic compounds, proline and ascorbic acid) antioxidants [9,10].

The degree of increase in antioxidant enzyme activities and amount under drought stress varies considerably drought severity, different plant species and even between two varieties of the same species [11]. In this respect, since the effects of drought stress on plants can vary significantly between species, investigating the genetic and physiological mechanisms that cause this stress difference is an important approach to increase the yield of plants with high medicinal and aromatic value [12,13]. To overcome drought stress, some studies are carried out to increase plant productivity by selecting plant species with high tolerance ability or applying biostimulators [14].

Mentha pulegium L. (Lamiaceae) is a perennial medicinal and aromatic plant with highly valuable essential oil (pulegone, piperitenon) [15] and phenolic compounds (apigenin, luteolin, kaempferol) [16]. In addition to the many pharmacological properties of this plant such as antiparasitic [17], antimicrobial [18], antioxidant [19], antimutagenic [20], it is also frequently used in agricultural food industries. It is known that many phytochemicals are synthesized that protect the plant against some negative environmental factors such as drought, ultraviolet, salt or pathogen experienced during the growth and production of this plant [21]. Therefore, it is important to investigate how this plant, which has an important potential for the pharmaceutical industry with its valuable secondary metabolites, can develop a defense mechanism against abiotic stress factors with enzymatic antioxidants. The effects of drought stress on growth and yields of pennyroyal plants have been reported in some studies [22,23].

However, there are few reports on how drought stress may affect parameters such as photosynthetic pigments, antioxidant defense system, protein content and lipid peroxidation.

In this study, we analyzed the effects of three different levels of drought stress (under controlled greenhouse conditions) on the activity of various antioxidant enzymes (PPO, POD, ASPX, CAT), total phenolic compounds (TPC), ABTS, DPPH, FRAP radical scavenging activity and some ecophysiological responses to understand the adaptation of pennyroyal to environmental stresses. The results obtained will guide future studies on the understanding of drought tolerance mechanisms in both *M. pulegium* and other medicinal and aromatic plant species.

2. MATERIAL and METHODS

2.1. Plant Material, Cultivation and Drought Treatments

M. pulegium seed samples were purchased from Zengarden (Turkey), an ecological certified and commercial seed company. Seeds were sterilized with 10% (v/v) sodium hypochlorite (20 min) and washed with distilled water, Then, seeds were sown in pots prepared with half peat-garden soil according to a completely random block design (with three replications). The seedlings that developed after germination were grown in the research greenhouse 20-25°C, 60-65% relative humidity and under natural light conditions. When the *M. pulegium* seedlings reached a sufficient size, the leaves were weighed and frozen in liquid nitrogen and stored at -80 °C until analysis.

2.2. Enzyme Activity Assays

For protein and antioxidant enzyme assays, control (well-watered) and drought-treated Pennyroyal Mint (*M. pulegium*) leaves (0.2 g) were pulverized with liquid nitrogen and extracted in 3 mL buffer containing 50 mM KH_2PO_4 (pH 7.0) buffer, 0.1 mM EDTA and 1% PVPP (w/v). The homogenate was filtered and then centrifuged at 4°C for 15 min at 15000 g. The supernatant was used for CAT, POD, ASPX and PPO activity assay [24].

Catalase (CAT, EC 1.11.1.6) activity was tested in a reaction mixture (final volume: 3 mL) containing 1450 µl of 50 mM KH_2PO_4 buffer (pH:7), 1500 µl of 30% H_2O_2 and 50 µl of plant extract. The disappearance of H_2O_2 was followed at 240 nm (3 min) (Schimadzu UV-1800, Japan) (H_2O_2: 0.036 $\mu mol^{-1}cm^{-1}$) [24].

Peroxidase (POD, EC 1.11.1.7) activity was measured according to the guaiacol method with minor modifications to the procedure of Sharma [25]. The reaction mixture in a total volume of 3 mL contained 970 µl of 50 mM KH_2PO_4 buffer (pH:6), 1000 µl of guaiacol (2-ethoxyphenol), 30% 1000 µl of H_2O_2 and 30 µl of plant extract. The increase in absorbance due to guaiacol oxidation was measured at 470 nm for 3 min.

Ascorbate peroxidase activity (ASPX, EC 1.11.1.11) was analyzed according to the method of Karabal [26] by monitoring a decrease in the absorbance at 290 nm for 3 min. The reaction mixture in a total volume of 3 mL consisted of 1450 µl of 50 mM phosphate buffer (pH: 7), 750 µl of ascorbic acid, 750 µl of 30% H_2O_2 and 50 µl plant extract. The enzyme activity was calculated using the extinction coefficient of ascorbate (2.8 mM^{-1} cm^{-1} at 290 nm).

Polyphenol oxidase activity (PPO, EC 1.10.3.1) was assayed according to the method of Flurkey [27]. The 3 mL substrate mixture contained 50 µl of crude extract, 0.20 M sodium phosphate buffer (pH: 6.5), 25 mM catechol. The increase in absorbance was recorded at 420 nm at 30 °C. Enzyme activity was calculated from the slope of absorbance–time curve. The PPO activity was defined as the amount of enzyme that caused an increase in absorbance of 0.001/min under assay conditions. Enzyme activities were expressed as enzymatic unit g^{-1} fresh weight (EU g^{-1} FW).

2.3. Determination of Proline Content

The proline (Pro) content (in µg g^{-1} FW of leaf) was determined by the method of Öztürk and Demir [28]. The 0.4 g leaf sample was homogenized in 4% sulfosalicylic acid and the homogenate was filtered through Whatman filter paper. The filtrate (0.5 mL) was 10 times diluted with distilled water. Then, the reaction mixture consisted of 1 mL of diluted sample, 1 mL of 96% glacial acetic acid and 1 mL of acid ninhydrin, which was incubated at 100 °C in a water bath for 1 h. The reaction was stopped by keeping it in an ice bath for 10 min. and 2 mL toluene was added to the reaction mixture and vortexed. After 5 min. of incubation, the absorbance was read at 520 nm. Pro concentration was determined by comparison with a standard graph constructed using known amounts of Pro and expressed as µg Pro g^{-1} fresh weight.

2.4. Oxidative Stress Markers (MDA, H_2O_2)

Malondialdehyde (MDA) content was determined in terms of thiobarbituric acid reactive (TBARS) substances produced according to the Sreenivasulu [29] method. 0.5 g fresh weight (FW) was homogenized with 5 mL of 0.1% trichloroacetic acid (TCA). The homogenate was centrifuged at 10.000 × g for 20 min. and 0.5 mL of supernatant was mixed with 1 mL of 0.5% (w/v) TBA in 20% (w/v) TCA. The mixture was heated at 95°C for 30 min. and then quickly cooled in an ice bath. Then the mixture was centrifuged at 10.000 × g for 5 min., the supernatant measured at 532 nm and optical density (absorbance) was corrected by a nonspecific absorbance read at 600 nm. MDA concentration was calculated using molar extinction coefficient of MDA-TBA product (1.55×105 M^{-1} cm^{-1}) and the results were expressed as µmol MDA g^{-1} FW.

The content of H_2O_2 was measured according to the method of Velikova [30] as follows: 0.5 g leaf tissue was homogenized with 5 ml of 0.1% (w/v) TCA. The mixture was centrifuged at 12.000 × g for 15 min. 0.5 mL of the resulting supernatant was mixed with 0.5 mL of 50 mM potassium phosphate (pH: 7) buffer and 1 mL of 1 M KI. The absorbance of the reaction mixture was measured at 390 nm.

2.5. Measurement of Photosynthetic Pigment Contents

Chlorophyll a (Chl a), chlorophyll b (Chl b), total chlorophyll contents were calculated according to Arnon [31] (Eş. 1, 2, 3) total carotenoid content according to Witham [32] (Eş. 4) and reported as mg of each pigment per g leaf FW. Leaf tissue samples (4 g) were homogenized with 15 mL of 80% (v/v) of acetone and ground for 1h on an ice bath. Then, the samples were centrifuged at 3000 × g for 5 min at 4 °C. Chlorophyll in the supernatant was measured immediately at wavelengths of 450, 645 and 663 nm to avoid interference from pigment degradation. Photosynthetic pigment amounts were calculated according to the following equations.

$$\text{Chlorophyll a (mg } g^{-1} \text{ FW)} = 12.7\ A_{663} - 2.69\ A_{645} \quad (1)$$

JSR A
Journal of Scientific Reports

Chlorophyll b (mg g^{-1} FW) = 22.9 A_{645} – 4.68 A_{663} (2)

Total chlorophyll (mg g^{-1} FW) = 20.2 A_{645} + 8.02 A_{663} (3)

Total caroteonids (mg g^{-1} FW) = 4.07 A_{450} - (0.0435 Chl a amount + 0.3367 Chl b amount) (4)

2.6. Total Protein Determination

The analysis of total protein was based on the procedure of Bradford [33]. 0.25 g of leaf tissue was homogenized with 2.5 mL of 50 mM KH_2PO_4 (pH:7) and the homogenate was centrifuged at 15.000 g for 20 min. at +4 °C. 2.5 mL of Coomassie Brilliant Blue G-250 was added to 20 µl supernatant and vortexed. After incubation (10 min), samples were measured at 595 nm. Bovine serum albumin (BSA; Sigma A7906) was used as the standard protein for the total protein amount calculation in the leaves.

2.7. Analysis of Total Phenolic Compounds and Antioxidant Properties

DPPH (2-diphenyl-1-picrylhydrazyl), ABTS (2,20'-azino-bis (3-ethylbenzothiazoline-6-sulphonic acid)) radical scavenging activity, Fe^{+2} (FRAP) reducing activity and total phenolic content analysis were performed to analyze the effects of drought stress on antioxidant properties of pennyroyal plant. For the analysis, 0.3 g of plant leaf sample was ground in liquid nitrogen and suspended in 5 mL of 80% methanol. After this suspension was mixed gently on a magnetic stirrer for 24 hours, it was centrifuged at 3000 rpm for 10 min., filtered through cellulose, and the supernatant was used for analysis.

Total phenolic content was determined by comparison with the gallic acid standard. For analysis, 250 µL of 10% Folin-Ciocalteu reagent and 500 µL of 1M Na_2CO_3 were added to 250 µL of extract and the final volume was made up to 3 mL with distilled water. After the prepared reaction mixtures were incubated in the dark for 20 min., absorbances were recorded at 765 nm. The total amounts of phenolic substances in the samples were calculated using the standard graph prepared with gallic acid [24].

In order to determine the ABTS radical scavenging activity, firstly, the 7mM stock ABTS solution was incubated with 2.45 mM $K_2S_2O_8$ for 12 hours at room temperature in the dark to produce radicals. Then, 50 µL of sample was mixed with 2 mL of ABTS radical solution and incubated for about 10 min., and then its absorbance at 734 nm was recorded. ABTS removal activity was calculated using the difference between the initial absorbance and the absorbance at the end of the reaction. ABTS radical scavenging activity calculated by the graph prepared using Trolox in the range of 0.1 to 0.8 mM as a standard, was expressed in µmol g^{-1} FW [34].

In order to determine the DPPH radical scavenging activity, 127 µM DPPH was prepared in methanol. Then, the reaction mixture consisting of 100 µL of pennyroyal extract, 400 µL of methanol and 1 mL of DPPH solution was prepared. After incubation at room temperature for 15 min for the reaction to take place, absorbances were recorded at 515 nm. DPPH removal activity calculated using the calibration curve prepared with standard Trolox was expressed as µmol g^{-1} FW [35].

JSR A
Journal of Scientific Reports

The FRAP method is an antioxidant activity determination method based on the reduction of ferric ions to ferrous ions. To perform this analysis, a working solution containing 40 mM HCl in 300 mM pH 3.6 acetate buffer, and 10 mM TPTZ (2,4,6-tripyridyl-s-triazine) prepared in 20 mM $FeCl_3$ x $6H_2O$ solution was prepared. 20 µL of sample extract was added to 3 mL of working solution and incubated in the dark for 30 min. The color change (ferrous tripyridyl-triazine complex) resulting from the reaction was recorded at 593 nm. FRAP radical scavenging activity calculated by the calibration graph obtained by using the $Fe_2(SO_4)_3$ solution prepared in the range of 0.005-0.5 mM as a standard was expressed as µmol g^{-1} FW [36].

2.7. Statistical Analysis

The results shown in the figures were evaluated as the mean of three replicates (n = 3) for each group. Data were analyzed and processed using SPSS Standard Version package program. The significance of differences between control and treatment groups was statistically evaluated by one-way ANOVA ($p<0.05$ as significant level) [37]. Figures were illustrated using GraphPad Prism 8.4.3.

3. RESULTS and DISCUSSION

3.1. Antioxidant Enzyme Activities

Enzyme (CAT, ASPX, POD, PPO) activities were measured in pennyroyal leaves under different drought stress and compared with the values of well-watered plants. The CAT activity of pennyroyal plants under drought stress increased by 122% at the end of the 3rd day compared to the control, and this increase was fourfold at the end of the 6th day. Although the CAT level increased in parallel with the continuation of drought stress, a rapid decrease occurred after 10 days due to oxidative damage. The increase in this enzyme activity during the early drought period can be evaluated as a physiological response to activating the antioxidant defense system and providing hemostasis in the pennyroyal plant. The absence of a statistically significant increase in H_2O_2 levels, which is the substrate of the catalase enzyme, in the 3rd and 6th day drought applications can be considered as a response of the plant to the increase in CAT activity (Figure 1). However, the decrease in CAT activity on the 10th day is an indication that the plants cannot tolerate the adverse effects of drought. In previous studies, it was determined that in moderate and severe drought conditions, drought stress significantly increased the CAT activities of *M. pulegium* compared to the control [38]. Similar results have been reported in *Cicer arietinum* L. [39,40], *Oryza sativa* L. [41], olive trees [42]. Again, like our study, Chakraborty and Pradhan [43] reported that CAT activity increased on the 3rd day of 5 different wheat cultivars, in which drought stress was applied for 3rd, 6th and 9th days. However, the continuation of drought stress in the following days, it was determined that the CAT activities in the same cultivars fell below the control values. This suggests that the applied drought stress is above the tolerance capacity of the cultivars in question.

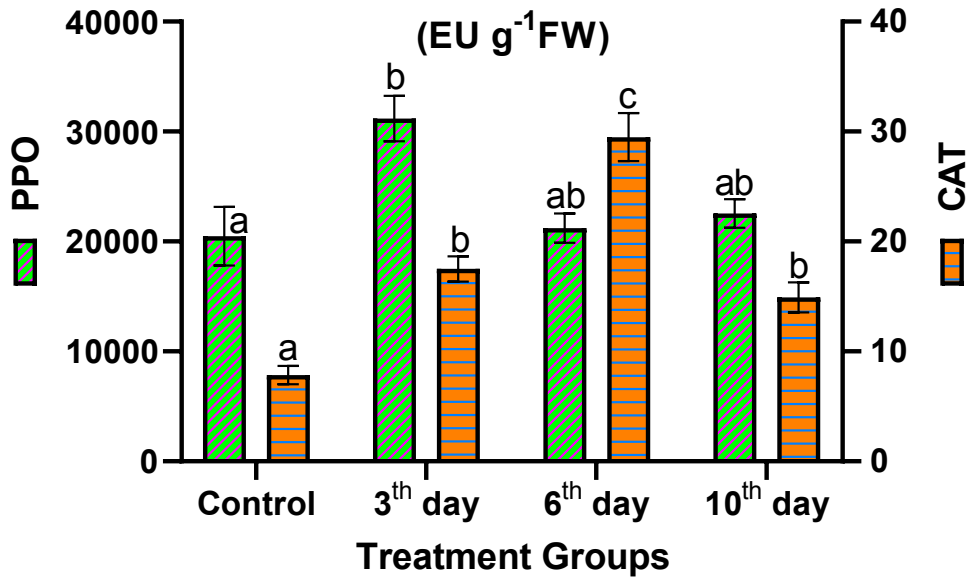

Figure 1. Effect of drought treatment on activity of PPO and CAT enzymes in leaves of *M. Pulegium.*

ASPX activity did not differ significantly between the first two drought treatments and control, but this activity was two times higher than control after ten days (Figure 2). In other words, while drought stress in the early stage did not affect ASPX activity in pennyroyal, the activity of this antioxidant enzyme increased significantly with the prolongation of stress. In previous studies, sweet pepper plants showed high enzyme activities against 30% and 60% drought stress, and ASPX activities increased 1.29 and 1.69-fold, respectively [44]. Again, Naderi [45] reported similar results in examining wheat genotypes under different drought stress conditions. ASPX are enzymes responsible for the H_20_2-dependent oxidation of ascorbate in plants in general [46]. Increases in CAT and ASPX activities because of drought treatments can be characterized as a defensive response related to excessive ROS production and damage, possibly resulting from drought stress.

JSR A
Journal of Scientific Reports

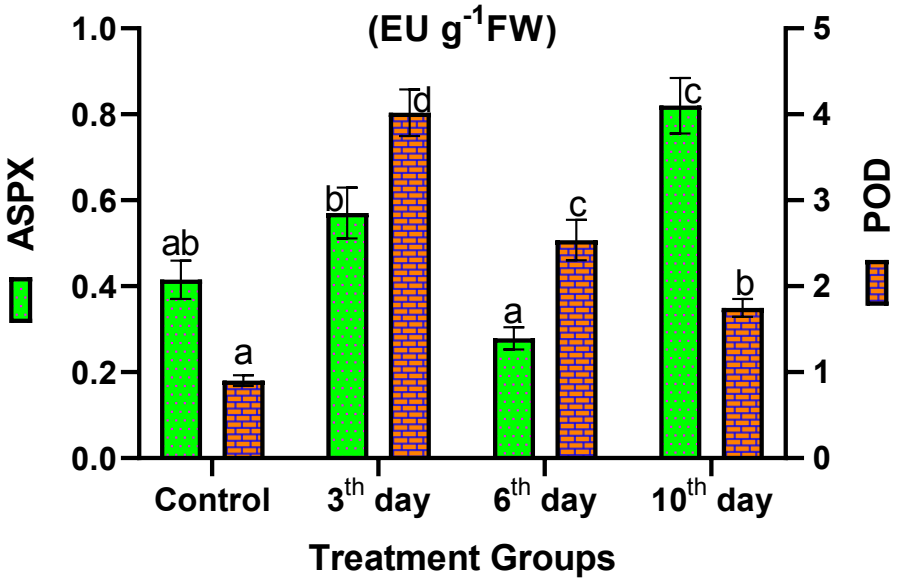

Figure 2. Effect of drought treatment on activity of ASPX and POD enzymes in leaves of *M. pulegium.*

Another antioxidant enzyme group that has a significant effect on preventing the harmful effects of ROS derivatives such as H_2O_2, which is formed as a result of plant metabolic reactions, is known as POD. POD activity in all drought-treated plants in the current study was higher than in control. In addition, POD activity reached its highest level in the early drought period (day 3) but started to decrease in the long term due to the negative effects of prolonged stress conditions on plant metabolism (such as H_2O_2 level, which can be kept under control thanks to increases in CAT activity). POD activity decreased ~40% on day 6 and ~60% on day 10 compared to day 3 but increased 2.7-fold and 1.8-fold compared to control, respectively (Figure 2). In physiological studies carried out by different research groups regarding POD activity, it was determined that this activity of *M. pulegium* exposed to drought stress decreased compared to the control [23], while exogenous application of penconazole to pennyroyal increased the same enzyme activity [47]. Again, *Brassica napus* L. showed low POD activity against drought stress [48], Chugh [49] reported an increase in POD activities of drought-resistant maize varieties under 72 h drought stress, while this enzyme activity decreased in drought-sensitive maize varieties. Similarly, it was determined that peroxidase activity in the leaves of drought-resistant and sensitive soybean varieties exposed to drought stress increased significantly in resistant varieties and decreased in susceptible varieties [50]. The susceptibility or tolerance ability of plants to drought stress is associated with enzymatic antioxidant responses synthesized in the biochemical process. As a result of the studies, drought-tolerant varieties try to minimize the damage that may be caused by oxidative stress (reducing H_2O_2 content, eliminating MDA, maintaining cell membrane integrity, etc.) because of physiological drought by increasing antioxidant enzyme activity

while under water stress [51]. Prolonged drought in plants can promote the accumulation of ROS, which causes cell damage or death and suppresses POD activity. The fact that peroxidases oxidize various substrates in the presence of H_2O_2 and take part in a hydroxylic cycle that can lead to the formation of ROS shows that these enzymes can work in two directions [52,53].

PPO activity in plants under drought stress, increased 1.5 times on day 3 compared to control, but at the end of day 6 and day 10, this rate decreased to 1.05 and 1.1 times, respectively (Figure 1). It has been reported that the drought stress applied by Khazaei and Estaji [44] to *Capsicum annuum* L. plant caused a significant increase in PPO activity compared to normal conditions, and the application of abscisic acid significantly increased the PPO activities in all drought levels. Again, drought stress applied in two drought tolerant (Bolani) and sensitive (Sistan) wheat varieties increased the PPO activity, and even severe drought stress caused this enzyme activity to reach the maximum level with 4.9 and 2.3 times compared to the control, respectively [45]. During stress, the increase in PPO activity, in addition to scavenging ROS and mitigating cell damage, is extremely important for plants' tolerance to oxidative stress [54,55]. In addition, thanks to the increase in PPO activity in plants exposed to stress, some harmful effects (reducing the amount of H_2O_2 and maintaining membrane integrity, etc.) that may occur can be minimized [44].

Plants with high antioxidant activities can be used as a source of natural medicine and therefore can be called medicinal plants [56]. These antioxidant properties in pennyroyal seedlings show that this plant has the potential for further use as a nutraceutical in the field of pharmacology.

3.2. Proline Content

The proline content in plants increased in parallel with the prolongation of the trial period in drought treatment ($p < 0.05$). On the 3^{rd}, 6^{th} and 10^{th} days of drought, the amount of proline in the plant increased by ~194%, 3172%, 479% compared to the control treatment, respectively (Figure 3). The pennyroyal plant was able to cope with drought stress at an early stage thanks to its antioxidant defense systems, but prolonged stress conditions caused almost 32 times more proline accumulation in the plant. Similarly, in other studies, it was noted that proline accumulation increased significantly in rice [57,58], cotton [59], tall fescue [60] and wheat genotypes [61] with increasing drought stress. Proline is very important for actively dividing cells, as it ensures the maintenance of sustainable growth (vegetative and generative) in plants under long-term environmental stress conditions. Therefore, accumulation of proline, which is used as a stress marker, in plant cells under biotic and abiotic stress conditions (heavy metal accumulation, pathogens, drought, salinity, UV, etc.) is associated with stress avoidance mechanisms [62-66]. In addition, proline, as a ROS scavenger and a molecule with the capacity to regulate many cellular homeostasis, is estimated to protect against cellular damage caused by stress factors such as salinity and drought [67, 68]. Plant tissues have the ability to accumulate proline, which is a powerful osmoprotectant, and to rapidly decompose it when necessary. The conversion of pyrroline-5-carboxylate (P5C) to proline during proline synthesis may cause an increase in the amount of ROS derivatives, followed by apoptosis and programmed cell death. For this reason, proline accumulated during a stress period is reduced to provide an energy source for growth and development after the stress is relieved, thus trying to prevent it from showing toxic effects [69, 70].

JSR A
Journal of Scientific Reports

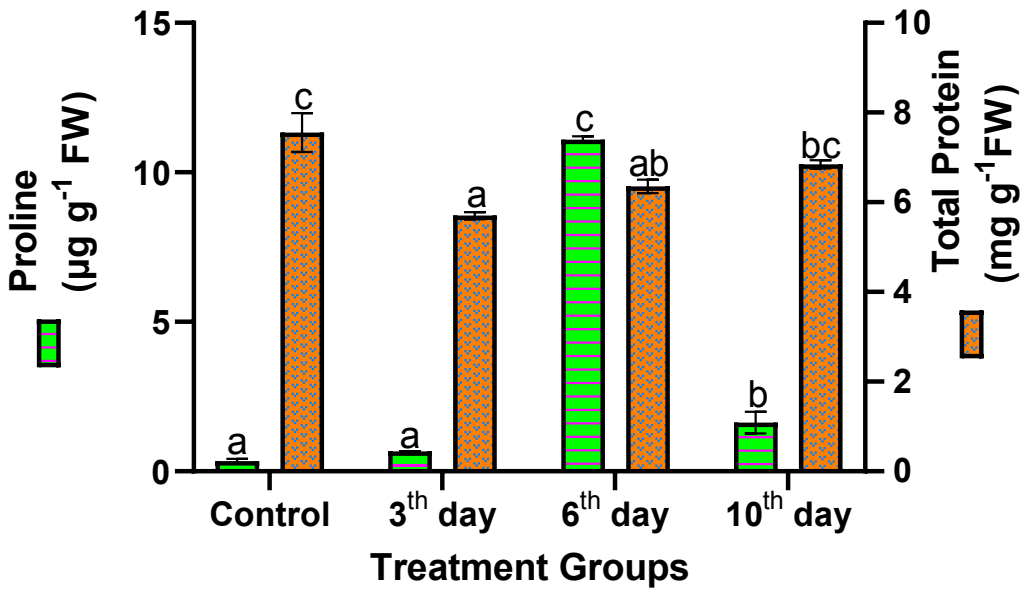

Figure 3. Effect of drought treatment on proline and total protein contents in leaves of *M. Pulegium.*

3.3. Changes in H_2O_2 and MDA Content

H_2O_2 and MDA content, two important indicators of oxidative stress, were measured to determine oxidative damage in *M. pulegium* exposed to different drought periods. In the study, H_2O_2 and MDA content of plants under drought stress showed a positive correlation with each other (Figure 4). The H_2O_2 content after 3, 6, and 10 days of drought increased 1.01, 1.21 and 1.32 times compared to the control plants, respectively (Figure 4). In addition, this treatment caused a significant increase in the MDA content of the plants. After 3, 6, and 10 days, MDA content increased 1.61, 2.92 and 2.61 times, respectively, and this increase was statistically significant ($p<0.05$) (Figure 4). The results obtained in H_2O_2 and MDA content are similar to Azad [23] and Siswoyo [71] studies.

JSR A
Journal of Scientific Reports

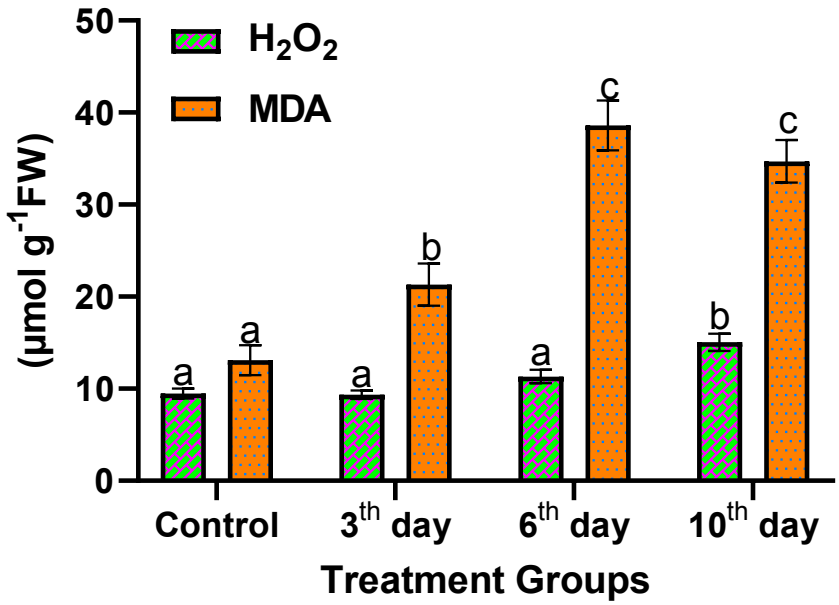

Figure 4. Effect of drought treatment on H_2O_2 and MDA contents in leaves of *M. pulegium.*

One of the most important problems that occur in plants under stress conditions is lipid peroxidation, which leads to deterioration of membrane stability. Despite the increase in the activities of antioxidant defense systems, the unavoidable increase in the amount of ROS derivatives such as H_2O_2 causes damage to the biological membrane structure. In cases where the antioxidant defense system cannot prevent the harmful effects of ROS, which attacks the double bonds in the phospholipid layer containing unsaturated fatty acids, a complex structure called malondialdehyde (MDA) emerges with the deterioration of lipids in the membranes [25]. Therefore, determining the amount of MDA allows us to have an idea about a measure of tissue and cell membrane damage. The data obtained show that a high level of cellular damage occurs in parallel with the long stress period with the accumulation of ROS and lipid peroxidation in *M. pulegium*, which is experiencing drought stress. It is also known that this deterioration in biological membranes releases the precursor compounds used in the synthesis of herbal stimulants and hormones that activate the antioxidant defense system in plants. These messenger structures, called phytohormone/plant growth regulators (PGR) and acting as signal molecules in cells, regulate the responses of plants to physiological conditions and can function even at very low concentrations. For example, jasmonic acid (JA), a signaling molecule, is currently considered as an endogenous phytohormone that regulates plant reproduction and growth, nutrient storage. Besides this important role in plant growth, JA also facilitates the adaptation of plants to different environmental stresses [72]. The release of precursors for the synthesis of plant defense hormones such as JA, due to the deterioration of the membranes, can be considered important in terms of combating stress conditions when considered from a different perspective.

JSR A
Journal of Scientific Reports

3.4. Chlorophyll (chlorophyll a, b and total chlorophyll) and Carotenoid Content

It has been reported in many studies that biotic and abiotic stress conditions reduce the photosynthetic efficiency of plants and therefore the hemostasis of the plant is impaired. Chl a, Chl b, total chlorophyll (total Chl) and carotenoid (Car) analysis were carried out to determine how the pigment degradations, which decrease the photosynthesis efficiency such as chlorosis and break the plant's defense power against stress conditions, change with drought. In parallel with the prolongation of drought stress in pennyroyal plants, the pigment content decreased significantly. Even, Chl a, Chl b, total Chl and Car contents decreased by 69%, 52%, 62% and 65%, respectively, compared to the control after 10 days of drought application. These results showed that the water stress experienced had to reduce the rate of photosynthesis due to the loss of chlorophyll in plants. The results obtained from the present study showed that the chlorophyll content of the pennyroyal plant decreased as a result of the suppression or degradation of chlorophyll biosynthesis by drought stress (Figure 5). Oxidative stress in plants causes disruption of chloroplast and can lead to a decrease in chlorophyll content [73]. Therefore, the results obtained can be considered as a distinctive symptom of oxidative stress [74]. Similar to our results, the gradual increase in drought stress resulted in decreased pigment contents in chickpeas [75, 76], maize [77], and peanuts [78].

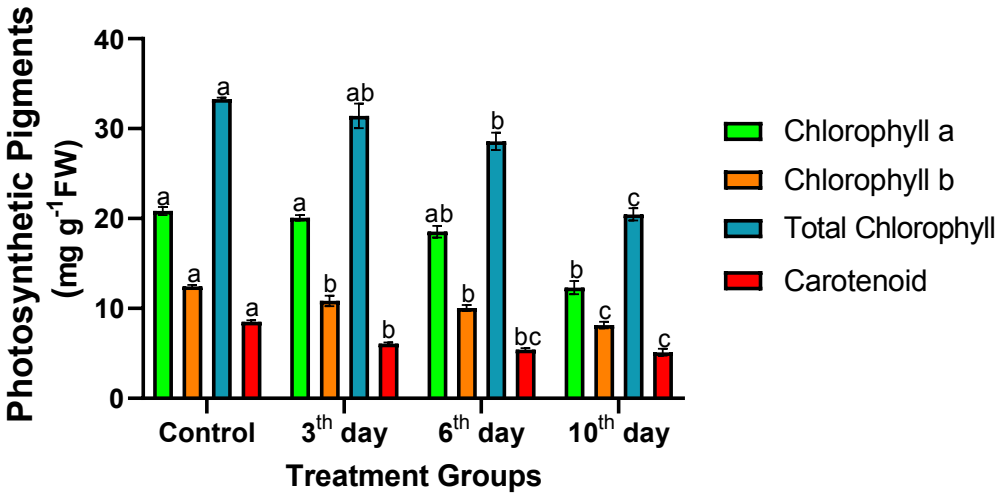

Figure 5. Effect of drought treatment on photosynthetic pigment contents in leaves of *M. pulegium.*

3.5. Total Protein Content

There was a gradual decrease in total protein content of the watermelon plant due to water stress. Variations of total protein content in leaves of *M. pulegium* plants subjected to drought stress for 10 days are shown in the Figure 3. With the onset of drought stress, the total protein content decreased by about 30%, while this decrease was more limited in the following days. Due to water stress, the total protein content initially decreased compared to the control and increased again in parallel with the increases in the synthesis of antioxidant enzymes triggered by the continuation of these adverse

conditions. In addition, the increased viscosity due to water loss in the cell cytoplasm under prolonged drought stress can be considered as the reason for the increase in the amount of protein per tissue compared to the early period. While there was a significant decrease in the total protein content of the drought-sensitive (Bahar) wheat variety among the 2 different wheat cultivars tested for drought stress, this decrease was slight in the drought-resistant (Kavir) variety [79]. Again, the total protein content of *Zea mays* L. [80], *Pistacia vera* L. [81] and *Levisticum officinale* Koch. [82] plants decreased under drought stress, which is consistent with our results.

3.6. Total Phenolic Compounds and Antioxidant Properties

Plants activate their antioxidant defense systems against biotic and abiotic stress conditions. This situation usually manifests itself in the form of an increase in antioxidant enzyme activities until plant homeostasis deteriorates in parallel with the increase in stress conditions. Herbal antioxidant defense systems first cope with stress conditions by increasing the activity of antioxidant enzymes, eliminating free oxygen radicals or converting them to less harmful molecules. In the present study, there is an increase in the activity of PPO, CAT, APX and POD enzymes in parallel with increasing drought stress. In addition to enzymatic antioxidants in plants, there are also non-enzymatic antioxidants such as ascorbic acid, phenolic compounds and carotenoids. With the increase in stress conditions, enzymes that eliminate the damages of peroxides such as CAT, APX, GPX first come into play and try to prevent the damages. In this study, besides enzymatic antioxidants, DPPH, FRAP, ABTS radical scavening activity and TPC amount were analyzed in pennyroyal plant. As can be seen from Figure 6, 7, while there was no significant change in these activities during the early drought period, the relative decrease in stress markers parallel to the increase in the activity of both enzymatic antioxidants during prolonged drought stress conditions; In addition, plant hemostasis, which started to deteriorate under 10 days of drought stress, caused a decrease in these activities.

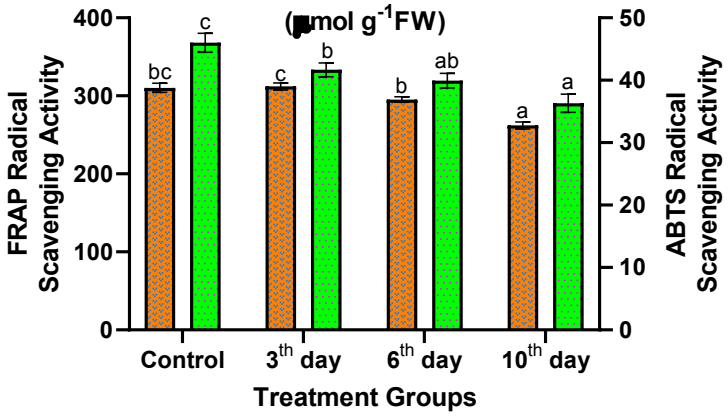

Figure 6. Effect of drought treatment on FRAP and ABTS radical scavenging activity in leaves of *M. pulegium.*

JSR A
Journal of Scientific Reports

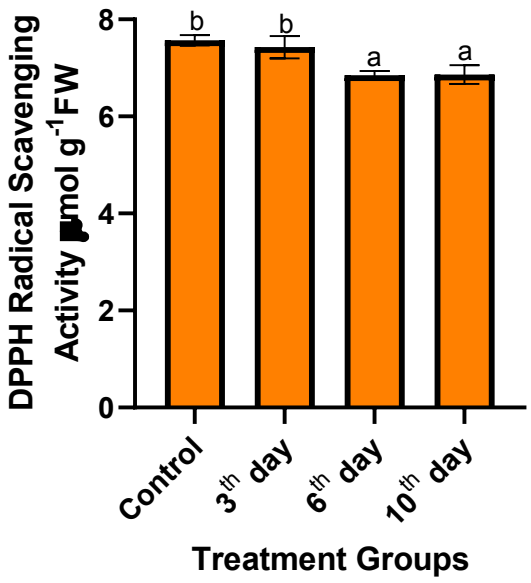

Figure 7. Effect of drought treatment on DPPH radical scavenging activity in leaves of *M. pulegium.*

The amount of TPC changed with drought conditions, especially during the long drought period. TPC content started to decrease from the 6th day, and this decrease became statistically significant on the 10th drought day (Figure 8). There are many studies conducted on plants such as wheat, pepper and *Amaranthus*, in which abiotic stress conditions cause the TPC content to increase and decrease [83-85]. In these studies, it has been reported that stress conditions may produce different results in plants with different genotypes. In our study, although a relative increase was observed in proline and antioxidant enzyme activities with long-term drought stress, the reason for the long-term decrease in total phenolic content may be due to the insufficient prevention of lipid peroxidation and stabilization of cell membranes [45].

JSR A
Journal of Scientific Reports

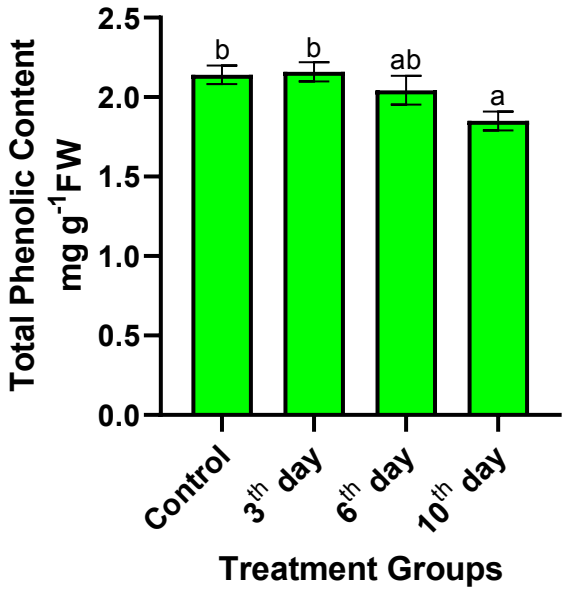

Figure 8. Effect of drought treatment on total phenolic content in leaves of *M. pulegium.*

Three different tests, DPPH, FRAP and ABTS removal activity, were performed as antioxidant activity test in the pennyroyal plant exposed to drought stress. No significant change was observed in all three activity tests, especially in the early drought period. Here, it can be thought that the increase in the activities of enzymatic antioxidants has a more dominant effect on creating normal physiological conditions in the plant. However, increased stress conditions caused a decrease in all three activities during the prolonged drought period.

4. CONCLUSION

Overall, drought stress caused an increase in antioxidant enzyme activities of *M. pulegium*, while prolongation of water stress caused a decrease in these enzyme activities. The significant decrease after an increase in CAT activity was compensated by an increase in ASPX and PPO activities. The significant positive correlation of PPO with ASPX and proline activities confirmed its important role in ROS scavenging. In terms of changes in lipid peroxidation (MDA content) and H_2O_2 amounts, it has been determined that the antioxidant defense system can slow down ROS production and membrane damage to a certain level. In addition, a rapid increase was observed in the amount of proline in the early stress period, but following this, proline levels decreased through the activation of the defense system triggered by the induced PGRs (plant growth regulators). Water stress increased chlorosis and caused a decrease in the amount of all photosynthetic pigments. Our results show that the antioxidant abilities in the medicinal and aromatic plant *M. pulegium* act as a defense mechanism

against drought stress. The use of these natural antioxidant sources as additives in food and cosmetics is increasing day by day, and therefore, the information obtained about the adaptive mechanisms of medicinal and aromatic plants exposed to drought, which poses a global threat, continues to attract attention from both an agricultural ecology and an economic point of view.

ACKNOWLEDGEMENT

The authors declare that they have no conflict of interest.

REFERENCES

[1] Hassan, F.A.S. and Ali, E.F., (2014), Impact of different water regimes based on class-A pan on growth, yield and oil content of *Coriandrum sativum* L. plant. Journal of the Saudi Society of Agricultural Sciences, 13(2), 155-161.

[2] Prăvălie, R., Patriche, C., Borrelli, P., Panagos, P., Roșca, B., Dumitrașcu, M. and Bandoc, G., (2021), Arable lands under the pressure of multiple land degradation processes. A global perspective. Environmental Research, 194, 110697.

[3] Anjum, S. A., Ashraf, U., Tanveer, M., Khan, I., Hussain, S., Zohaib, A. and Wang, L., (2017), Drought tolerance in three maize cultivars is related to differential osmolyte accumulation, antioxidant defense system, and oxidative damage. Frontiers in Plant Science, 8, 69.

[4] Alharby, H.F. and Fahad, S., (2020), Melatonin application enhances biochar efficiency for drought tolerance in maize varieties: Modifications in physio-biochemical machinery. Agronomy Journal, 112(4), 2826-2847.

[5] Foyer, C.H. and Noctor, G., (2005), Oxidant and antioxidant signalling in plants: a re-evaluation of the concept of oxidative stress in a physiological context. Plant, Cell & Environment, 28(8), 1056-1071.

[6] Saleem, M.H., Ali, S., Rehman, M., Hasanuzzaman, M., Rizwan, M., Irshad, S. and Qari, S.H., (2020), Jute: a potential candidate for phytoremediation of metals—a review. Plants, 9(2), 258.

[7] Gill, S.S. and Tuteja, N., (2010), Reactive oxygen species and antioxidant machinery in abiotic stress tolerance in crop plants. Plant physiology and biochemistry, 48(12), 909-930.

[8] Anjum, S. A., Wang, L., Farooq, M., Khan, I. and Xue, L., (2011), Methyl jasmonate-induced alteration in lipid peroxidation, antioxidative defence system and yield in soybean under drought. Journal of Agronomy and Crop Science, 197(4), 296-301.

[9] Azarabadi, S., Abdollahi, H., Torabi, M., Salehi, Z. and Nasiri, J., (2017), ROS generation, oxidative burst and dynamic expression profiles of ROS-scavenging enzymes of superoxide

dismutase (SOD), catalase (CAT) and ascorbate peroxidase (ASPX) in response to *Erwinia amylovora* in pear (*Pyrus communis* L). European Journal of Plant Pathology, 147(2), 279-294.

[10] Rehman, M., Liu, L., Bashir, S., Saleem, M.H., Chen, C., Peng, D. and Siddique, K.H., (2019), Influence of rice straw biochar on growth, antioxidant capacity and copper uptake in ramie (*Boehmeria nivea* L.) grown as forage in aged copper-contaminated soil. Plant Physiology and Biochemistry, 138, 121-129.

[11] Reddy, A.R., Chaitanya, K.V. and Vivekanandan, M., (2004), Drought-induced responses of photosynthesis and antioxidant metabolism in higher plants. Journal of plant physiology, 161(11), 1189-1202.

[12] Kamoshita, A., Babu, R. C., Boopathi, N. M. and Fukai, S., (2008), Phenotypic and genotypic analysis of drought-resistance traits for development of rice cultivars adapted to rainfed environments. Field crops research, 109(1-3), 1-23.

[13] Muscolo, A., Junker, A., Klukas, C., Weigelt-Fischer, K., Riewe, D. and Altmann, T., (2015), Phenotypic and metabolic responses to drought and salinity of four contrasting lentil accessions. Journal of experimental botany, 66(18), 5467-5480.

[14] Pourghasemian, N., Moradi, R., Naghizadeh, M. and Landberg, T., (2020), Mitigating drought stress in sesame by foliar application of salicylic acid, beeswax waste and licorice extract. Agricultural Water Management, 231, 105997.

[15] Mahboubi, M. and Haghi, G., (2008), Antimicrobial activity and chemical composition of *Mentha pulegium* L. essential oil. Journal of ethnopharmacology, 119(2), 325-327.

[16] Bakour, M., Campos, M. D.G., Imtara, H. and Lyoussi, B., (2020), Antioxidant content and identification of phenolic/flavonoid compounds in the pollen of fourteen plants using HPLC-DAD. Journal of Apicultural Research, 59(1), 35-41.

[17] Di Stasi L.C., Oliveira G.P., Carvalhaes M.A., Queiroz-Junior M. and Tien OS., (2002), Medicinal plants popularly used in the Brazilian tropical Atlantic forest. Fitoterapia 73: 69-91.

[18] Mahboubi, M. and Haghi, G., (2008), Antimicrobial activity and chemical composition of Mentha pulegium L. essential oil. Journal of ethnopharmacology, 119(2), 325-327.

[19] Teixeira B., Marques A., Ramos C., Batista I., and Serrano C., (2012), European pennyroyal (*Mentha pulegium*) from Portugal: Chemical composition of essential oil and antioxidant and antimicrobial properties of extracts and essential oil. Industrial Crops and Products 36: 81-87.

[20] Yumrutas O. and Saygıdeger S.D., (2012), Determination of antioxidant and antimutagenic activities of Phlomis armeniaca and Mentha pulegium. J Appl Pharm Sci 2012: 36-40.

[21] Karray-Bouraoui, N.A.J.O.U.A., Ksouri, R., Falleh, H., Rabhi, M., Jaleel, C.A., Grignon, C. and Lachaal, M., (2010), Effects of environment and development stage on phenolic content and antioxidant activities of *Mentha pulegium* L. Journal of Food Biochemistry, 34, 79-89.

[22] Hassanpour, H., Khavari-Nejad, R.A., Niknam, V., Razavi, K. and Najafi, F., (2014), Effect of penconazole and drought stress on the essential oil composition and gene expression of *Mentha pulegium* L. (Lamiaceae) at flowering stage. Acta physiologiae plantarum, 36(5), 1167-1175.

[23] Azad, N., Rezayian, M., Hassanpour, H., Niknam, V. and Ebrahimzadeh, H., (2021), Physiological Mechanism of Salicylic Acid in *Mentha pulegium* L. under salinity and drought stress. Brazilian Journal of Botany, 44(2), 359-369.

[24] Ulusu, Y., Öztürk, L. and Elmastaş, M., (2017), Antioxidant capacity and cadmium accumulation in parsley seedlings exposed to cadmium stress. Russian journal of plant physiology, 64(6), 883-888.

[25] Sharma, P., Jha, A.B., Dubey, R.S. and Pessarakli, M., (2012), Reactive oxygen species, oxidative damage, and antioxidative defense mechanism in plants under stressful conditions. Journal of botany, 2012.

[26] Karabal, E., Yücel, M. and Öktem, H.A., (2003), Antioxidant responses of tolerant and sensitive barley cultivars to boron toxicity. Plant Science, 164(6), 925-933.

[27] Flurkey, W.H., (1989), Polypeptide composition and amino-terminal sequence of broad bean polyphenoloxidase. Plant physiology, 91(2), 481-483.

[28] Öztürk, L. and Demir, Y., (2003), Effects of putrescine and ethephon on some oxidative stress enzyme activities and proline content in salt stressed spinach leaves. Plant Growth Regulation, 40(1), 89-95.

[29] Sreenivasulu, N., Ramanjulu, S., Ramachandra-Kini, K., Prakash, H.S., Shekar-Shetty, H., Savithri, H.S. and Sudhakar, C., (1999), Total peroxidase activity and peroxidase isoforms as modified by salt stress in two cultivars of fox-tail millet with differential salt tolerance. Plant Science, 141(1), 1-9.

[30] Velikova, V., Yordanov, I. and Edreva, A., (2000), Oxidative stress and some antioxidant systems in acid rain-treated bean plants: protective role of exogenous polyamines. Plant science, 151(1), 59-66.

[31] Arnon, D.I., (1949), Copper enzymes in isolated chloroplasts. Polyphenoloxidase in *Beta vulgaris*. Plant physiology, 24(1), 1.

[32] Witham, F.H., Blaydes, D.F. and Devlin, R.M., (1971), Experiments in plant physiology. Van Nostrand Reinhold Co, New York, c1971

[33] Bradford, M.M., (1976), A rapid and sensitive method for the quantitation of microgram quantities of protein utilizing the principle of protein-dye binding. Analytical biochemistry, 72(1-2), 248-254.

[34] Re, R., Pellegrini, N., Proteggente, A., Pannala, A., Yang, M. and Rice-Evans, C., (1999), Antioxidant activity applying an improved ABTS radical cation decolorization assay. Free radical biology and medicine, 26(9-10), 1231-1237.

[35] Sharma, O. P. and Bhat, T. K., (2009), DPPH antioxidant assay revisited. Food chemistry, 113(4), 1202-1205.

[36] Benzie, I.F. and Strain, J.J., (1996), The ferric reducing ability of plasma (FRAP) as a measure of "antioxidant power": the FRAP assay. Analytical biochemistry, 239(1), 70-76.

[37] Duncan, D.B., (1955), Multiple range and multiple F tests. Biometrics, 11(1), 1-42.

[38] Asghari, B., Khademian, R. and Sedaghati, B., (2020), Plant growth promoting rhizobacteria (PGPR) confer drought resistance and stimulate biosynthesis of secondary metabolites in pennyroyal (*Mentha pulegium* L.) under water shortage condition. Scientia Horticulturae, 263, 109132.

[39] Mafakheri, A., Siosemardeh, A., Bahramnejad, B., Struik, P.C. and Sohrabi, Y., (2011), Effect of drought stress and subsequent recovery on protein, carbohydrate contents, catalase and peroxidase activities in three chickpea (*Cicer arietinum*) cultivars. Australian Journal of Crop Science, 5(10), 1255-1260.

[40] Mohammadi, A., Habibi, D., Rohami, M. and Mafakheri, S., (2011), Effect of drought stress on antioxidant enzymes activity of some chickpea cultivars. Am-Euras. J. Agric. Environ. Sci, 11(6), 782-785.

[41] Lum, M.S., Hanafi, M.M., Rafii, Y.M. and Akmar, A.S.N., (2014), Effect of drought stress on growth, proline and antioxidant enzyme activities of upland rice. J. Anim. Plant Sci, 24(5), 1487-1493.

[42] Sofo, A., Dichio, B., Xiloyannis, C. and Masia, A., (2005), Antioxidant defenses in olive trees during drought stress: changes in activity of some antioxidant enzymes. Functional Plant Biology, 32(1), 45-53.

[43] Chakraborty, U. and Pradhan, B., (2012), Oxidative stress in five wheat varieties (*Triticum aestivum* L.) exposed to water stress and study of their antioxidant enzyme defense system, water stress responsive metabolites and H_2O_2 accumulation. Brazilian Journal of Plant Physiology, 24, 117-130.

[44] Khazaei, Z. and Estaji, A., (2020), Effect of foliar application of ascorbic acid on sweet pepper (*Capsicum annuum*) plants under drought stress. Acta Physiologiae Plantarum, 42(7), 1-12.

[45] Naderi, S., Fakheri, B.A., Maali-Amiri, R. and Mahdinezhad, N., (2020), Tolerance responses in wheat landrace Bolani are related to enhanced metabolic adjustments under drought stress. Plant Physiology and Biochemistry, 150, 244-253.

[46] Raven, E.L., (2003), Understanding functional diversity and substrate specificity in haem peroxidases: what can we learn from ascorbate peroxidase? Natural product reports, 20(4), 367-381.

[47] Hassanpour, H., Khavari-Nejad, R.A., Niknam, V., Najafi, F. and Razavi, K., (2012), Effects of penconazole and water deficit stress on physiological and antioxidative responses in pennyroyal (*Mentha pulegium* L.). Acta physiologiae plantarum, 34(4), 1537-1549.

[48] Branch, K., (2009), Effect of super absorbent application on antioxidant enzyme activities in canola (*Brassica napus* L.) cultivars under water stress conditions. American Journal of Agricultural and Biological Sciences, 4(3), 215-223.

[49] Chugh, V., Kaur, N. and Gupta, A.K., (2011), Evaluation of oxidative stress tolerance in maize (*Zea mays* L.) seedlings in response to drought. Indian J Biochem Biophys, 48(1), 47-53.

[50] Han, Y. H., (1997), Effect of high temperature and/or drought stress on the activities of SOD and POD of intact leaves in two soybean (G. max) cultivars. Soybean Genetics Newsletter, 24, 39-40

[51] Jaleel, C.A., Ragupathi, G.O.P.I. and Panneerselvam, R., (2008), Biochemical alterations in white yam (*Dioscorea rotundata* Poir.) under triazole fungicides: impacts on tuber quality. Czech J. Food Sci. Vol, 26(4), 297-307.

[52] Liszkay, A., Kenk, B. and Schopfer, P., (2003), Evidence for the involvement of cell wall peroxidase in the generation of hydroxyl radicals mediating extension growth. Planta, 217(4), 658-667.

[53] Passardi, F., Penel, C. and Dunand, C., (2004), Performing the paradoxical: how plant peroxidases modify the cell wall. Trends in plant science, 9(11), 534-540.

[54] Jaleel, C.A., Manivannan, P., Kishorekumar, A., Sankar, B., Gopi, R., Somasundaram, R. and Panneerselvam, R., (2007), Alterations in osmoregulation, antioxidant enzymes and indole alkaloid levels in Catharanthus roseus exposed to water deficit. Colloids and Surfaces B: Biointerfaces, 59(2), 150-157.

[55] Mittler, R., (2002), Oxidative stress, antioxidants and stress tolerance. Trends in plant science, 7(9), 405-410.

[56] Tlili, N., Elfalleh, W., Hannachi, H., Yahia, Y., Khaldi, A., Ferchichi, A. and Nasri, N., (2013), Screening of natural antioxidants from selected medicinal plants. International journal of food properties, 16(5), 1117-1126.

[57] Mostajeran, A. and Rahimi-Eichi, V., (2009), Effects of drought stress on growth and yield of rice (*Oryza sativa* L.) cultivars and accumulation of proline and soluble sugars in sheath and blades of their different ages leaves. Agric. & Environ. Sci, 5(2), 264-272.

[58] Dien, D.C., Mochizuki, T. and Yamakawa, T., (2019), Effect of various drought stresses and subsequent recovery on proline, total soluble sugar and starch metabolisms in Rice (*Oryza sativa* L.) varieties. Plant Production Science, 22(4), 530-545.

[59] Parida, A.K., Dagaonkar, V.S., Phalak, M.S. and Aurangabadkar, L.P., (2008), Differential responses of the enzymes involved in proline biosynthesis and degradation in drought tolerant and sensitive cotton genotypes during drought stress and recovery. Acta Physiologiae Plantarum, 30(5), 619-627.

[60] Man, D., Bao, Y.X., Han, L.B. and Zhang, X., (2011), Drought tolerance associated with proline and hormone metabolism in two tall fescue cultivars. HortScience, 46(7), 1027-1032.

[61] Sultan, M.A.R.F., Hui, L., Yang, L.J. and Xian, Z.H., (2012), Assessment of drought tolerance of some Triticum L. species through physiological indices. Czech Journal of Genetics and Plant Breeding, 48(4), 178-184.

[62] Siripornadulsil, S., Traina, S., Verma, D.P.S. and Sayre, R.T., (2002), Molecular mechanisms of proline-mediated tolerance to toxic heavy metals in transgenic microalgae. The Plant Cell, 14(11), 2837-2847.

[63] Mattioli, R., Marchese, D., D'Angeli, S., Altamura, M.M., Costantino, P. and Trovato, M., (2008), Modulation of intracellular proline levels affects flowering time and inflorescence architecture in Arabidopsis. Plant Molecular Biology, 66(3), 277-288.

[64] Miller, G., Honig, A., Stein, H., Suzuki, N., Mittler, R. and Zilberstein, A., (2009), Unraveling Δ1-pyrroline-5-carboxylate-proline cycle in plants by uncoupled expression of proline oxidation enzymes. Journal of Biological Chemistry, 284(39), 26482-26492.

[65] Kishor, P.K., Sangam, S., Amrutha, R.N., Laxmi, P.S., Naidu, K.R., Rao, K.S. and Sreenivasulu, N., (2005), Regulation of proline biosynthesis, degradation, uptake and transport in higher plants: its implications in plant growth and abiotic stress tolerance. Current science, 424-438.

[66] Furlan, A.L., Bianucci, E., Giordano, W., Castro, S. and Becker, D.F., (2020), Proline metabolic dynamics and implications in drought tolerance of peanut plants. Plant Physiology and Biochemistry, 151, 566-578.

[67] Szabados, L., Savouré, A., (2010), Proline: a multifunctional amino acid. Trends in plant science, 15(2), 89-97.

[68] Natarajan, S.K., Zhu, W., Liang, X., Zhang, L., Demers, A.J., Zimmerman, M.C. and Becker, D.F., (2012), Proline dehydrogenase is essential for proline protection against hydrogen peroxide-induced cell death. Free radical biology and medicine, 53(5), 1181-1191.

[69] Kavı Kıshor, P.B. and Sreenivasulu, N., (2014), Is proline accumulation per se correlated with stress tolerance or is proline homeostasis a more critical issue?. Plant, Cell & Environment, 37(2), 300-311.

[70] Dar, M.I., Naikoo, M.I., Rehman, F., Naushin, F. and Khan, F.A., (2016), Proline accumulation in plants: roles in stress tolerance and plant development. In Osmolytes and plants acclimation to changing environment. Emerging Omics Technologies (pp. 155-166). Springer, New Delhi.

[71] Siswoyo, T.A., Arum, L.S., Sanjaya, B.R.L. and Aisyah, Z.S., (2021), The growth responses and antioxidant capabilities of melinjo (*Gnetum gnemon* L.) in different durations of drought stress. Annals of Agricultural Sciences, 66(1), 81-86.

[72] Wang F., Yu G. and Liu P., (2019), Transporter-mediated subcellular distribution in the metabolism and signaling of jasmonates. Front Plant Sci 10, 390.

[73] Arora, A., Sairam, R.K. and Srivastava, G.C., (2002), Oxidative stress and antioxidative system in plants. Current Science, 82(10), 1227-1238.

[74] Smirnoff, N., (1993), The role of active oxygen in the response of plants to water deficit and desiccation. New phytologist, 125, 27-58.

[75] Mafakheri, A., Siosemardeh, A.F., Bahramnejad, B., Struik, P.C. and Sohrabi, Y., (2010), Effect of drought stress on yield, proline and chlorophyll contents in three chickpea cultivars. Australian Journal of Crop Science, 4(8), 580-585.

[76] Sohrabi, Y., Heidari, G., Weisany, W., Golezani, K.G. and Mohammadi, K., (2012), Changes of antioxidative enzymes, lipid peroxidation and chlorophyll content in chickpea types colonized by different Glomus species under drought stress. Symbiosis, 56(1), 5-18.

[77] Khayatnezhad, M. and Gholamin, R., (2012), The effect of drought stress on leaf chlorophyll content and stress resistance in maize cultivars (*Zea mays*). African Journal of Microbiology Research, 6(12), 2844-2848.

[78] Meher, P.S., Reddy, K.A. and Rao, D.M., (2018), Effect of PEG-6000 imposed drought stress on RNA content, relative water content (RWC), and chlorophyll content in peanut leaves and roots. Saudi Journal of Biological Sciences, 25(2), 285.

[79] Michaletti, A., Naghavi, M. R., Toorchi, M., Zolla, L., Rinalducci, S., (2018), Metabolomics and proteomics reveal drought-stress responses of leaf tissues from spring-wheat. Scientific reports, 8(1), 1-18.

[80] Mohammadkhani, N. and Heidari, R., (2008), Effects of drought stress on soluble proteins in two maize varieties. Turkish Journal of Biology, 32(1), 23-30.

[81] Khoyerdi, F.F., Shamshiri, M. H. and Estaji, A., (2016), Changes in some physiological and osmotic parameters of several pistachio genotypes under drought stress. Scientia horticulturae, 198, 44-51.

[82] Akhzari, D. and Pessarakli, M., (2016), Effect of drought stress on total protein, essential oil content, and physiological traits of Levisticum officinale Koch. Journal of Plant Nutrition, 39(10), 1365-1371.

[83] Kopta, T., Sekara, A., Pokluda, R., Ferby, V. and Caruso, G., (2020), Screening of chilli pepper genotypes as a source of capsaicinoids and antioxidants under conditions of simulated drought stress. Plants, 9(3), 364.

[84] Sarker, U. and Oba, S., (2018), Drought stress enhances nutritional and bioactive compounds, phenolic acids and antioxidant capacity of Amaranthus leafy vegetable. BMC Plant biology, 18(1), 1-15.

[85] Sahitya, U.L., Krishna, M.S.R., Deepthi, R., Prasad, G.S. and Kasim, D., (2018), Seed antioxidants interplay with drought stress tolerance indices in chilli (*Capsicum annuum* L.) seedlings. BioMed Research International, 2018.

Kütahya Dumlupınar University
Institute of Graduate Studies

Journal of Scientific
Reports-A
E-ISSN: 2687-6167
Number 51, December 2022

RESEARCH ARTICLE

DETERMINATION of SOME ANTIOXIDANT ACTIVITIES and OXIDATIVE STRESS LEVES in PATIENTS with LIP and ORAL CAVITY CANCER

Ali Hussein MER[1], Halil ÖZKOL[2], Halit DEMİR[3*], Şeyda BELLİ[4], Canan DEMİR[5], Ali ASLAN[6,7]

[1]Yüzüncü Yil University, Faculty of Science, Department of Biochemistry, Van, alihusseinmer@gmail.com,
ORCID: 0000-0002-6678-7999
[2]Yüzüncü Yıl University, Facukty of Medicine, Department of Medical Biology, Van, halilozkol@yyu.edu.tr,
ORCID:0000-0002-7563-1347
[3]Yüzüncü Yıl University, Faculty of Science, Department of Biochemistry, Van, halitdemir@yyu.edu.tr,
ORCID:0000-0001-5598-2601
[4]Bagcilar Training and Research Hospital, Department of Otorhinolaryngology, Istanbul, drseydabelli@gmail.com,
ORCID: 0000-0002-9132-4419
[5]Yüzüncü Yıl University, Vocational School of Health Sciences, Van, canandemir@yyu.edu.tr, ORCID:0000-0002-4204-9756
[6]Kyrgyz-Turkish Manas University, Faculty of Science, Department of Biology, Bishkek, Kyrgyzstan, aliaslan@yyu.edu.tr,
ORCID: 0000-0002-5122-6646
[7]Yüzüncü Yıl University, Faculty of Pharmacy, Department of Pharmacology, Van, aliaslan@yyu.edu.tr,
ORCID: 0000-0002-5122-6646

Receive Date:26.04.2022 *Accepted Date: 26.07.2022*

ABSTRACT

Squamous cell carcinomas constitute the majority of oral cavity tumors. Poor oral hygiene, smoking, chronic irritation and alcohol consumption are counted as etiological factors. In study, it was aimed to determine oxidative stress levels and some antioxidant activities such as superoxide dismutase (SOD), reduced glutathione (GSH) and catalase (CAT) in cancer of the lip and oral cavity. Malondialdehyde (MDA) levels, SOD, GSH and CAT activities were measured using the spectrophotometric method. The results showed that SOD, CAT and GSH levels decreased significantly in the patient group ($p<0.05$), while MDA levels increased significantly ($p<0.05$). Lack of antioxidants can increase the development of oral and lip cancers.

Keywords: *Lip and oral cavity cancers, SOD, GSH, CAT, MDA*

1. INTRODUCTION

Cancer is a state of excessive proliferation of cells. There are factors that predispose to the formation of cancer. Many factors such as environmental and family family history can be counted among the causes of cancer. Apart from free radicals, reactive oxygen nitrogen species (RONS) also participate in the initiation of carcinogenesis. Free radicals are formed from nitrogen, sulfur and oxygen molecules inside the cell [1]. ROS consists of oxygen molecules such as O2•_, •OH, 1O2), O3, RO2 and H_2O_2. ROS and Reactive Nitrogen Species (RNS) are two important agents of DNA damage [1].

JSR A
Journal of Scientific Reports

Oral cavity cancer with an incidence of more than 300,000 cases per year; It is defined as cancers of the hard and soft palate, lips, cheeks, tongue, floor of the mouth, sinuses and pharynx. Oral cavity cancer, whose prognosis is improved with early diagnosis, has a survival rate of 75% at 5 years for stage 1 [2]. Oral cavity cancer is more common in men than women in many countries. The increased risk with aging can lead to death in those aged 50 and above. Although oral cavity cancer is seen in all parts of the world, it is more in the south of Asia,especially in Pakistan, Sri Lanka, Taiwan, India, France in Europe, Slovenia, Slovakia, Hungary and the Latin region of America. It has been reported that the incidence of lip cancer is higher in Caucasians than in blacks in Australia and Canada. [3]. Excessive alcohol, tobacco consumption and exposure to ultraviolet sun rays are among the causes of oral cavity cancer. On the other hand, another risk factor for oral cavity cancer has been reported to be human papillomavirus [4].
ROS can control many cellular tasks. Lipid peroxidation is a chain reaction controlled by free radicals and causes the oxidation of unsaturated lipids. MDA can accelerate the increase of cell damage. It is a highly reactive substance [5,6,7].
In this study, we aimed to determine oxidative stress levels and some antioxidant activities such as GSH, CAT and SOD in cancer of the lip and oral cavity.

2. MATERIALS and METHODS

2.1. Materials

This study consisted of a total of 50 individuals: 25 were made up of patients diagnosed with lip and oral cavity cancer and 25 were from the healthy control group. Patient and healthy control groups were selected from clinic Urology Van Yuzuncu Yil University and Istanbul Bagcılar Training and Research Hospital. The study started with the decision of the Ethics Committee dated 31.05.2016 and numbered 2016/13
.

2.2. Methods

For measurements, blood was taken from sick and healthy individuals (4cc). Blood samples were separated from plasma by centrifugation at 4000 rpm for 5 minutes in the biochemistry laboratory, and the obtained serums were preserved until processed (at 20°C).

2.2.1. Determination of SOD activity

SOD was measured or analyzed with the system prepared by “Marklund et al” [8].

2.2.2. Determination of CAT activity

CAT activity was measured according to the method developed by Aebi [9].

2.2.3. Determination of level (GSH

GSH was performed using the Beutler method [10].

2.2.4. Determination of level MDA

MDA level was measured according to the method developed by Gutteridge [11].

JSR A
Journal of Scientific Reports

2.2.5. Statistical analysis

Mean±standard deviation were used as descriptive statistics. In two-group comparisons in terms of continuous variables; The t test was used when the normal distribution was provided, and the Mann-Whitney U statistics were used when it was not. In addition, The cutoff value that separates the patient was determined by performing the ROC curve analysis. For the level of significance, $p<0.05$ was taken and SPSS (ver: 13) statistical package program was preferred for analysis.

3. RESULTS

This study consisted of a total of 50 subjects, 25 of whom were healthy controls and 25 cancer of the lip and oral cavity. When Table 1 is examined for SOD, CAT and GSH enzyme activities, mean of the patient group was statistically lower than the average of the control group (Figure 1). When Table 1 was examined for MDA, the mean of the patient group was higher than the mean of the control group ($p<0.05$) (Figure 2).

Table 1. Values of healthy individuals with cancer of the lip and oral cavity.

Parameters	Controls (n= 25) Mean±SD	Patients (n=25) Mean±SD	p
SOD (U/L)	31.0943 ± 1.8198	16.0459 ± 1.6496	0.001
GSH (µmol/L)	0.0204 ± 0.0011	0.0066 ± 0.0004	0.001
CAT (U/L)	0.2908 ± 0.0901	0.0733 ± 0.0219	0.001
MDA (µmol/L)	0.5011 ± 0.1473	1.3607 ± 0.2053	0.001

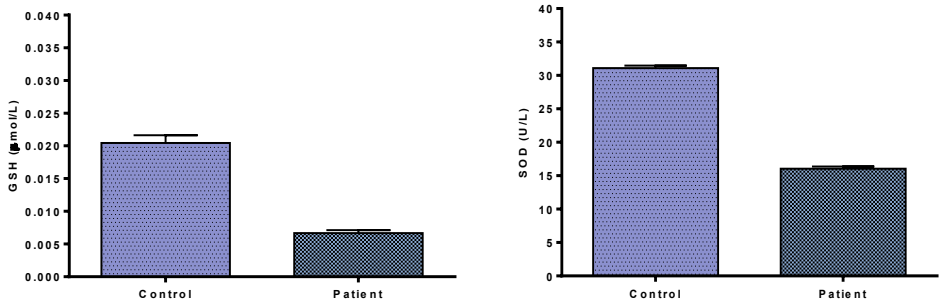

Figure 1. SOD activity and GSH level for patient and control groups.

JSR A
Journal of Scientific Reports

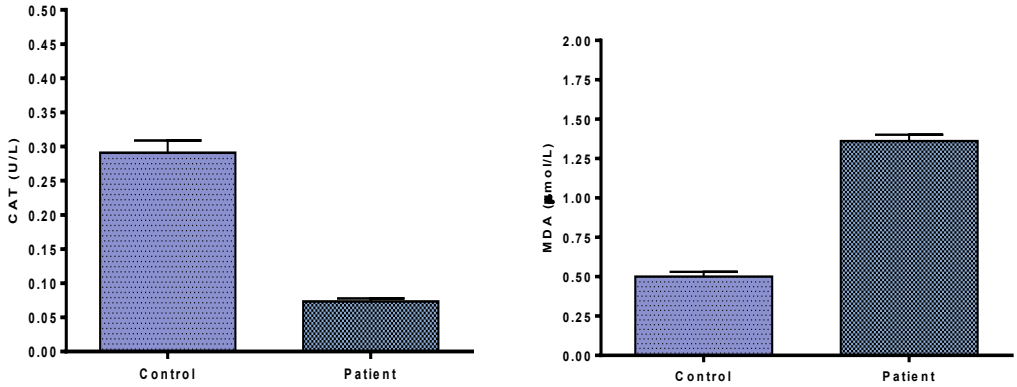

Figure 2. CAT activity and MDA level for patient and control groups.

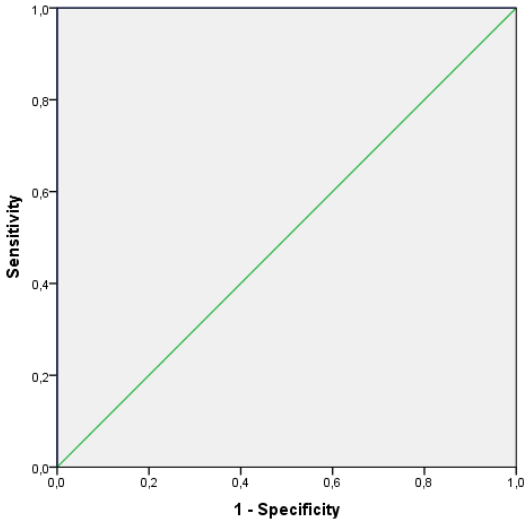

Figure 3. ROC Curve.

In the study, according to the results of ROC curve analysis, in separating the patient and control groups; The area under the curve was found to be 1.000±0.001 for MDA (Table 2). The cut-off value for MDA is seen as 0.86500 (Sensitivity 100%, Specificity 100%) (Figure 3).

Table 2: ROC analysis.

	Group	cut-off value	area under the curve	St. Error	Sensitivity	Specificity	p
MDA	Patient-	0.8650	1.000	0.001	1.000	1.000	0.001

JSR A
Journal of Scientific Reports

(µmol/L)	Control

4. DISCUSSION and CONCLUSION

Oral cavity cancers, which are among the head and neck cancers, attract more attention due to their high incidence. There are complications and mortality resulting from the diagnosis of squamous cell carcinoma diagnosed, reaching 40% in the lip and mouth cavity, 25% in the larynx and 15% in the throat with a low incidence. Lesions mostly seen on the lower lip may originate from the skin and basal cell carcinomas may migrate to the lip [12].

Head and neck cancers (HNC) cover important organs of the body. It can be diagnosed very easily. It is a region that includes all parts of the mouth [13].

Cancer occurs with oxidative stress as a result of incompatibility between antioxidants and oxidants in the body. Oxidative stress causes some diseases. High ROS level creates lipid hydroperoxides (LHP) and lipid peroxidation (MDA). MDA causes damage to the structure of the cell. They are known to be mutagenic and carcinogenic [14,15]. In some of the studies, it was determined that lipid peroxidation decreased and antioxidant levels increased after radiotherapy in patients. However, in a related study, no difference was found between the levels of antioxidant enzymes and MDA in smokers and non-smokers with lip-mouth cancer groups and healthy non-smokers. It is known that the level of antioxidants and oxidants varies depending on the phase of the cancer during the enlargement of tumors [16]. MDA level was found to be higher in patients with oral cavity cancer than in the control group ($p < 0.05$). ROC curve analysis was performed in the study. According to this; The area under the curve for MDA was 1.000±0.001 and the cut-off value were found as 0.8650 (sensitivity 100%, specificity 100%). In this case, the height of the MDA may be a marker in cancer lips and oral cavity.

In this study, we found that serum MDA levels increased and SOD, CAT and GSH levels decreased in patients with lip and oral cavity cancer. The increase in lipid peroxidation may increase the malignancy in the cell by increasing the radicals [17]. Antioxidant enzymes protect the cell against reactive oxygen radicals. GSH and CAT convert H_2O_2 to water, while SOD converts superoxide to H_2O_2 [17]. Selenium removes H_2O_2 from the environment with the help of GSH. Thus, cellular damage is prevented [18].

GSH, represented by a gene in humans, is a flavoenzyme and exposure to oxidative stress has also been shown to result in an increase in mRNA content. [19]. In a study in which GSH level was determined for oral cavity cancer risk, iron deficiency and low GSH level were associated with oxidative stress. [20]. In this study, the low GSH level of the patient group ($p < 0.05$) may be a marker for cancer lips and oral cavity.

CAT has a tremendous impact. It works well on metabolic systems. In a study examining the antioxidant levels in the serum of oral cavity cancer patients, it was determined that the CAT level was low [21]. In a study in which the role of oxidative stress and the activities of antioxidant enzymes were determined in patients, CAT level was found to be low [22]. In this study, CAT activity was also

lower than the control group ($p < 0.05$). In this case, low CAT activity may be a marker of cancer in the lips and oral cavity.

SOD constitutes the defense system, which is valuable in metabolic systems. Contributes to repair systems in metabolism [23]. SOD works effectively against cancers that may occur [6]. In a study evaluating oxidative damage in patients with oral submucous fibrosis, SOD level was decreased compared to healthy individuals [24]. In this study, low SOD activity ($p < 0.05$) of the patient group may be a marker of cancer in the lips and oral cavity.

In our study, it was concluded that activities antioxidant such as SOD, CAT and GSH decreased, while oxidative stress levels such as MDA increased in patients compared to controls. According to the ROC analysis, it can be said that the discrimination power of MDA is quite high and accordingly, it can be used as a diagnostic test to distinguish patients with lip and oral cavity cancer from the control group. Findings show that oxidative stress is associated with cancer of the lips and oral cavity, and increased oxidative stress can cause to rise of this disease. This study is a study showing the relationships between antioxidant enzymes and oxidative stress in cancer of the lip and oral cavity. In addition, more studies are needed in patients with lip and oral cavity cancer.

ACKNOWLEDGEMENT

The author declares that there are no conflict of interests.

REFERENCES

[1] Sun, Y., (1990), Free radicals, antioxidant enzymes, and carcinogenesis, *Free Radic. Biol. Med.*, 8, 583-599.

[2] Essat, M., Cooper, K., Bessey, A., Clowes, M., Chilcott, J.B., Hunter, K.D., (2022), Diagnostic accuracy of conventional oral examination for detecting oral cavity cancer and potentially malignant disorders in patients with clinically evident oral lesions: Systematic review and meta-analysis, Head & Neck, 44, 998-1013. https://doi.org/10.1002/hed.26992

[3] Petersen, P.E., (2005), Oral cancer prevention and control the approach of the World Health Organization, Oral oncology, 45, 454-460.

[4] Radoï, L., Luce, D., (2013), A review of risk factors for oral cavity cancer: the importance of a standardized case definition, Community Dent. Oral Epidemiol., 41, 97-109.

[5] Cerutti, P.A., (2006), Oxy-radicals and cancer, Lancet, 344, 862-863.

[6] Valko, M., Rhodes, C.J., Moncol, J., Izakovic, M., Mazur, M., (2006), Free radicals, metals and antioxidants in oxidative stress-induced cancer, Chemico-Biological Interactions, 160, 1-40.

[7] Salganik, R.I., (2001), The benefits and hazards of antioxidants: controlling apoptosis and other protective mechanisms in cancer patients and the human population, J. Am. Coll. Nutr., 20, 464-472.

[8] Marklund, S.L., Holme, E., Hellner, L., (1982), Superoxide dismutase in extracellular fluids, Clin. Chim. Acta, 126, 41-51.

[9] Aebi, H., (1984), Catalase. (in) methods in enzymology, L. Packer(Editör), Academic Pres, Orlando, 105, 121-126.

[10] Beutler, E., Duron, O., Kelly, B.M., (1963), Improved method for the determination of blood glutathione, J. Lab. Clin. Med., 61, 882-888.

[11] Gutteridge, J.M., (1995), Lipit peroxidation and antioxidants as biomarkers of tissue damage, Clin. Chem., 41(12), 1819-1828.

[12] Zitsch, R.P., Park, C.W., Renner, G.J., Rea, J.L., (1995), Outcome analysis for lip carcinoma, Otolaryngol. Head. Neck Surg., 113, 589-96.

[13] Stich, H.F., Anders, F., (1989), The involvement of reactive oxygen species in oral cancers of betel quid/tobacco chewers, Mutat. Res. Fundam. Mol. Mech. Mutagen, 214, 47-61.

[14] Zhang, Y., Chen, S.Y., Hsu, T., Santella, R.M., (2002), Immunohistochemical detection of malondialdehyde-DNA adducts in human oral mucosa cells, Carcinogenesis, 23, 207-211.

[15] Cerutti, P.A., (1985), Prooxidant states and tumor promotion, Science, 22, 375-81.

[16] Guyton, Z., Kensler, T.W., (1993), Oxidative mechanisms in carcinogenesis, Br. Med. Bull., 49, 523-544.

[17] Malathi, M., Vijaya, M., Shivashankara, A.R., (2011), The role of oxidative stress and the effect of radiotherapy on the plasma oxidant-antioxidant status in head and neck cancer, J. Clin. Diagnostic Res., 5, 249-251.

[18] Stohs, S.J., Al-Bayati, Z.F., Hassan, M.Q., Murray, W.J., Mohammedpeur, H.A., (1986), Glutathione peroxidase and reactive oxygen species in TCDD-induced lipid peroxidation, Adv. Exp. Med. Biol., 197, 357-65.

[19] Masella, R., Di-Benedetto, R., Vari, R., Filesi, C., Giovannini, C., (2005), Novel mechanisms of natural antioxidant compounds in biological systems: involvement of glutathione and glutathione-related enzymes, J. Nutr. Biochem., 16, 577-586.

[20] Richie, J. P., Kleinman, W., Marina, P., Abraham, P., Wynder, E. L., Muscat, J. E., (2008), Blood iron, glutathione, and micronutrient levels and the risk of oral cancer, Nutrition and cancer, 60(4), 474-482.

[21] Das, S., Kar Mahapatra, S., Gautam, N., Das, A., Roy, S., (2007), Oxidative stress in lymphocytes, neutrophils, and serum of oral cavity cancer patients: modulatory array of L-glutamine, Supportive care in cancer, 15(12), 1399-1405.

[22] Nuszkiewicz, J., Czuczejko, J., Maruszak, M., Pawłowska, M., Woźniak, A., Małkowski, B., Szewczyk-Golec, K., (2021), Parameters of oxidative stress, vitamin d, osteopontin, and melatonin in patients with lip, oral cavity, and pharyngeal cancer, Oxidative Medicine and Cellular Longevity, 2021, 13.

[23] Crapo, J.D., Oury, T., Rabouille, C., Slot, J.W., Chang, L.Y., (1992), Copper, zinc superoxide dismutase is primarily a cytosolic protein in human cells, Proc. Natl. Acad. Sci. USA, 89, 10405-10409.

[24] Bale, R., Kattappagari, K. K., Vidya, D., Vuddandi, S., Gummalla, C., & Baddam, V. R. R., (2017), Oral submucous fibrosis: A quantitative assessment of serum malondialdehyde, superoxide dismutase and correlation with clinical staging. Journal of Oral and Maxillofacial Pathology: JOMFP, 21(1), 41.

Kütahya Dumlupınar University
Institute of Graduate Studies

Journal of Scientific
Reports-A
E-ISSN: 2687-6167
Number 51, December 2022

RESEARCH ARTICLE

INVESTIGATION of REMOVAL of METHYL VIOLET 2B DYE USING TEA WASTE NANOPARTICLES PRODUCED by GREEN SYNTHESIS METHOD

Cansu KELEŞ[1*], Meltem SARIOĞLU CEBECİ [2], Ünsal AÇIKEL[3]

[1]Sivas Cumhuriyet University, Environmental Engineering Department, Sivas, 20199220012@cumhuriyet.edu.tr, ORCID:000-0003-4844-9360
[2]Sivas Cumhuriyet University, Environmental Engineering Department, Sivas, sarioglu@cumhuriyet.edu.tr,ORCID: 0000-0002-3636-0388
[3]Sivas Cumhuriyet University, Environmental Engineering Department, Sivas, uacikel@cumhuriyet.edu.tr, ORCID: 0000-0003-4969-8502

Receive Date:23.06.2022 *Accepted Date: 23.09.2022*

ABSTRACT

This study investigates the usability of $FeCl_3$ nanoparticles synthesized with tea waste by green synthesis method as an adsorbent in the removal of methyl violet 2B, a widely used cationic dyestuff, from wastewater.
Characterization analyzes of $FeCl_3$ nanoparticles synthesized with tea waste were performed with SEM/EDX and FTIR.
pH, adsorbent dose, initial dyestuff concentration parameters were studied in batch system and optimum conditions were determined. According to the experimental results, the best adsorption efficiency was obtained at the pH of 4.5, adsorbent dose of 1 g/L and initial dyestuff of 50 mg/L.
Equilibrium data obtained using different initial dyestuff concentrations and temperatures were applied to the Freundlich, Langmuir, Dubinin-Radushkevich and Temkin adsorption isotherms. The experimental results best fitted to the Langmuir isotherm. The separation factor (RL) calculated using Langmuir isotherm equations is between 0 and 1 at all temperatures, also showing that adsorption fits the isotherm.
In kinetic studies, experiments were performed at an initial dye concentration of 50 mg/L and the adsorption was found that adsorption was in fiting the pseudo second order kinetic model. Negative ΔG values (-5.703, -5.226, -5.148 kj/mol) determined in thermodynamic studies showed that adsorption was spontaneous and feasible. A negative ΔH value (-13.898 kj/mol) means adsorption is exothermic.
It has been shown that $FeCl_3$ nanoparticles synthesized with tea waste can be used as an effective adsorbent in the removal of methyl violet 2B from aqueous solutions with approximately 80% efficiency.

Keywords: *Methyl violet 2B, Adsorption, Kinetic, Isotherm, Nanoparticle, Green synthesis*

JSR A
Journal of Scientific Reports

1. INTRODUCTION

As a result of the increase in the needs of people, an increase in production has begun to meet this need. Paints started to be used in many areas and this situation started to create environmental risks. Dyes are divided into three groups according to their chemical structures as anionic, cationic and nonionic. The most harmful dye group is cationic dyes and methyl violet 2B is in this group. This dye can cause various diseases by making a great toxic effect on living things. Considering this dangerous nature of paints, dismantling is required to protect the environment and human health. Methyl violet 2B dyestuff used in the study, dyestuff in textile and printing industry, indicator in the range of pH 0-1.6 in chemistry, fingerprinting in forensic medicine, classification of bacteria in medicine by gram staining technique, treatment of skin injuries and serious burns, prevention and treatment of fungal diseases, antibiotic It has a wide range of uses as an alternative. Methyl violet 2B dyestuff also has some damages like most chemicals. In case of short-term inhalation, such as respiratory tract irritation, vomiting, diarrhea, headache and dizziness in case of long-term exposure, it causes damage to the mucous membranes and digestive system [1]. For these reasons, it should be removed from wastewater. Ultrafiltration, ion exchange and adsorption methods can be used as removal methods. Due to its easy operation and low cost, the most preferred method among these removal methods is the adsorption method. Different adsorbents can be used to reduce sewage pollution [2,3].

Nanotechnology has emerged as one of the basic concepts supported by technological developments and advanced research in various scientific fields. The properties of nanoparticles such as shape and size are due to the different methods used in the synthesis phase. Green synthesis is a method in which plant extracts or biomolecules are used as reducing and stabilizing agents to synthesize nanoparticles without the need for external stabilizers, which further reduces environmental waste. Plant biomass/extract has several inert advantages over other microscopic organisms in the synthesis of nanoparticles from various biological materials. In addition to the synthesis method, the techniques used are also an important element that ensures nanoparticles are in the nanoscale range. In addition to these, nanoparticles composed of various particles can have different catalytic, magnetic, optical properties compared to nanoparticles composed of a single type of particle. Since approximately 40-50% of nanoparticle atoms are on the surface, its reactivity is high. These features increase the importance of nanoparticles compared to other materials [4,5]. Nanoparticles are frequently used in adsorption due to their high adsorption capacity and small size [6,7]. Due to its low cost, it was focused on researching plant extracts. [8]. The main aim of this study is to investigate the effectiveness of $FeCl_3$ nanoparticles synthesized with tea waste in the effective removal of methyl violet 2B dye. In this study, pH, adsorbent dose, initial dyestuff concentration tests were performed and optimum conditions were found. In order to understand the adsorption mechanism, isotherm, kinetic and thermodynamic studies were carried out and results were obtained for the removal of methyl violet 2B dyestuff of $FeCl_3$ nanoparticles synthesized with tea waste. Similar studies are given in Table 1.

JSR A
Journal of Scientific Reports

Table 1. Similar studies.

Dye	Adsorbents	Processing conditions	Efficiency	References
Methyl violet	Fe_3O_4-Clinoptilolite	pH: 7 Time: 150 min Ad. dosage: 2 g/L Temperature(°K): 298	% 92-% 97	[9]
Methyl violet	Acorn inner shells - Fe_3O_4	pH: 6 Time: 180 min Ad. dosage:1 g/L Temperature(°K): 298	% 95	[10]
Methyl violet	Chitosan coated Clinoptilolite	pH: 6 Time: 60 min Ad. dosage: 5 g/L Temperature(°K): 298	% 93-% 98	[11]
Methyl violet	Ground olive kernel	pH: 7 Time: 90 min Ad. dosage: 0.25 mg/L Temperature(°K): 300	% 96	[12]
Methyl violet	Apricot kernel husk modified with tartaric acid	pH: 4 Time: 120 min Ad. dosage: 1 g/L Temperature(°K): 298	% 79	[13]

In this study, the adsorption efficiency of $FeCl_3$ nanoparticles synthesized with tea waste with methyl violet 2B aqueous solution was investigated. The reason why methyl violet 2B dyestuff is preferred is that it has a toxic effect on the environment and living things. In the study, firstly, tea extract was obtained by using the green synthesis method and synthesized with $FeCl_3$, and then the characterization and adsorption potential of these nanoparticles were investigated. This study provided an innovation to the literature in terms of the use of $FeCl_3$ nanoparticles synthesized using green synthesis method in the adsorption of methyl violet 2B solution. In the study, both detailed characterization analyses and the use of the nanoparticle synthesized in the adsorption stages have contributed to the literature.

2. MATERIAL and METHOD

2.1. Material

The methyl violet 2B ($C_{24}H_{28}CIN_3$) chemical (CAS: 8004-87-3) used to prepare the stock solution was obtained from HiMedia Lab. Iron (III) chloride ($FeCl_3$ 95%) chemical and sodium hydroxide (NaOH 99%) chemical were obtained from Tekkim Lab. Information on the characterization of $FeCl_3$ nanoparticles synthesized with tea waste has been reported using FTIR (Bruker Model: Tensor II, 4000-400 cm-1), SEM/EDX (TESCAN MIRA3 XMU), UV-Spectrophotometer (Hach DR3900) devices.

JSR A
Journal of Scientific Reports

2.2. Preparation of Tea Extract

In this study, black tea extract was used at a concentration of 60 g/L. To prepare black tea extract at the indicated concentration 60 g of black tea was weighed, 1000 mL of distilled water was added and mixed for 1 hour at 80 °C and precipitated at room temperature. The precipitate and the tea extract were separated from each other with the help of a filter.

2.3. Synthesis of $FeCl_3$ Nanoparticles

$FeCl_3$ nanoparticles synthesized using tea waste were obtained by green synthesis method. 0.1 M anhydrous $FeCl_3$ solution was dissolved in a 3:2 ratio of 100 mL of pure water-tea extract mixture and stirred at 80°C for 30 minutes. pH adjustment was made with NH_4OH. After pH adjustment, the temperature was kept constant and stirred on a magnetic stirrer for 2 hours. Later then the solution was allowed to settle at room temperature and the precipitate was washed with ethanol followed by distilled water. The washed precipitate was dried in a vacuum oven at 90°C for 12 hours.

2.4. Characterization of $FeCl_3$ Nanoparticles

Scanning Electron Microscopy - Energy Dispersive X-Ray Spectrometer (SEM/EDX, TESCAN MIRA3 XMU) and Fourier transform infrared (FTIR, Bruker Model: TensorII) were used for the characterization of $FeCl_3$ nanoparticles synthesized using tea waste.

2.5. Adsorption Experiments

Experiments were carried out in a batch system on the removal of methyl violet 2B dyestuff with $FeCl_3$ nanoparticles synthesized using tea waste. For adsorption experiments, 1000 mg/L stock methyl violet 2B solution was prepared. The stock solution was diluted and a dyestuff solution was prepared at a concentration of 50 mg/L. pH, adsorbent dose, initial dyestuff concentration tests were carried out and optimum conditions were determined. NaOH (0.1 M) and HCl (0.1 M) were used for pH adjustment. In order to determine the removal, dye concentrations were determined using a UV spectrophotometer at a wavelength of 575 nm.
The removal equations for the adsorption experiments are given in equations 1 and 2. [14].

$$qe = \frac{(Co-Ce)V}{m} \quad (1)$$

$$\text{Removal}(\%) = \frac{(Co-Ce)}{Co} x100 \quad (2)$$

3. RESULTS and DISCUSSION

3.1. Charactarization of $FeCl_3$ nanoparticles

3.1.1. SEM/EDX results

500, 5000, 1000 and 2000 kx SEM images of $FeCl_3$ nanoparticles synthesized by green synthesis method using tea waste before adsorption and after adsorption are given in Figure 1.

JSR A
Journal of Scientific Reports

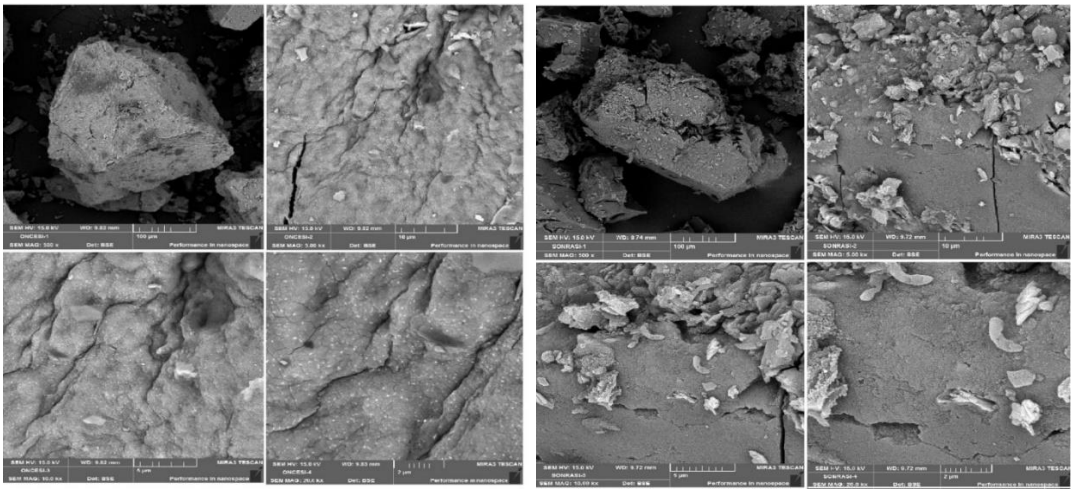

(a) (b)

Figure 1. SEM images of $FeCl_3$ nanoparticles synthesized with tea waste (a)before adsorption, (b)after adsorption.

As seen from the pre-adsorption SEM images $FeCl_3$ nanoparticles synthesized using tea waste have a porous and nano-sized structure. The white dots seen in Figure 1a are proof that the nanoparticle contains iron. If these white dots are not visible in Figure 1b This is the proof that the nanoparticle is adsorbed with the dye.

EDX analyzes were performed using the backscattered electron detector (BSE) of the SEM (TESCAN MIRA3 XMU). Elemental analysis results of $FeCl_3$ nanoparticles synthesized using tea waste before adsorption are given in Table 2. Figure 2 shows the EDX image of $FeCl_3$ nanoparticles synthesized using tea waste before and after adsorption.

Table 2. Elemental analysis results of $FeCl_3$ nanoparticles synthesized using tea waste before adsorption.

Element	Weight(%)	Atomic(%)
C	34.23	48.30
O	32.40	34.33
Na	10.16	7.49
Cl	15.11	7.22
K	1.60	0.69
Fe	6.51	1.97

JSR A
Journal of Scientific Reports

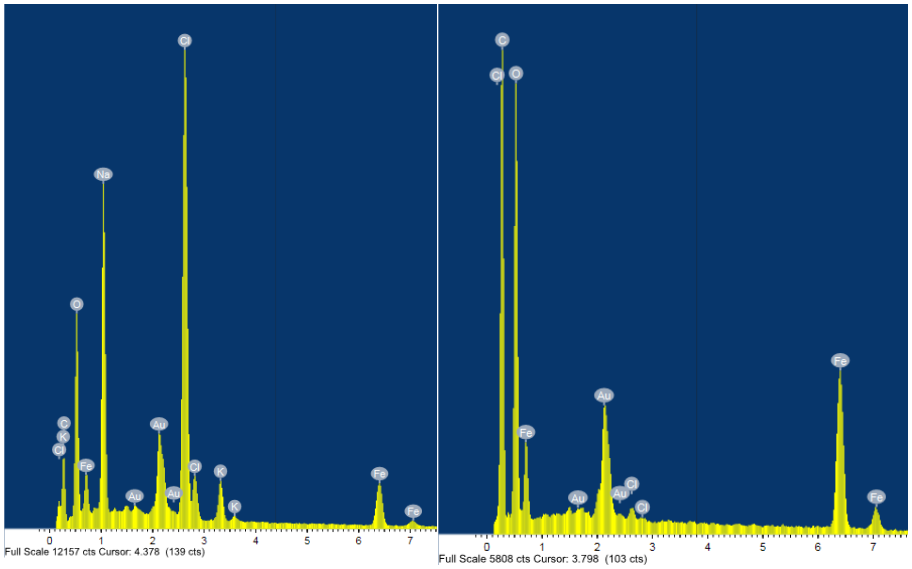

a b

Figure 2. EDX image of $FeCl_3$ nanoparticles synthesized using tea waste (a)before adsorption, (b)after adsorption.

The EDX analysis results given in Table 2 show that the elemental and quantitative weight composition of $FeCl_3$ nanoparticles synthesized using tea waste before adsorption It has been shown that it consists of 34.23% C, 32.40% O, 10.16% Na, 15.11% Cl, 1.60% K, 6.51% Fe elements. The EDX analysis results given in Table 3 show that the elemental and quantitative weight composition of $FeCl_3$ nanoparticles synthesized using tea waste after adsorption It showed that it consists of 45.99% C, 38.30% O, 0.27% Cl, 15.44% Fe elements. The presence of K in the nanoparticles before adsorption indicates that this may be due to the tea extract. The absence of some elements in the nanoparticles after adsorption can be explained by the fact that these elements have passed into the water. In addition, the increase in element C after adsorption is due to the adsorption of dye molecules with $FeCl_3$ nanoparticles synthesized using tea waste. Elemental analysis results of $FeCl_3$ nanoparticles synthesized using tea waste after adsorption are given in Table 3.

Table 3. Elemental analysis results of $FeCl_3$ nanoparticles synthesized using tea waste before adsorption.

Element	Weight(%)	Atomic(%)
C	34.23	48.30
O	32.40	34.33
Na	10.16	7.49
Cl	15.11	7.22
K	1.60	0.69

JSR A
Journal of Scientific Reports

Fe	6.51	1.97

3.1.2. FTIR analysis results

FTIR is used to understand the bonding of compounds in the substance and to determine adsorption and desorption [15]. Spectra Bruker Model: It was taken between 400-4000 cm^{-1} using Tensor FTIR Spectrum Device.

In Figure 3 The peaks around 2958 cm^{-1} and 2898 cm^{-1} may be due to the presence of CH_3 groups that cause C-H stretching [16]. The peaks at 2264 cm^{-1} and 2303 cm^{-1} can be attributed to stretching of the single bond CH group [5]. The adsorption band around 1728 cm^{-1}, 1634 cm^{-1}, 1581 cm^{-1}, 1544 cm^{-1}, 1497 cm^{-1} can correspond to C=C double bond stretching vibrations. The peaks formed in the fingerprint region, ie the band around 1342 cm^{-1}, 1205 cm^{-1}, 1169 cm^{-1}, 1040 cm^{-1} and 1034 cm^{-1}, may correspond to C-N stretching and bending vibrations [16].

The spectrum obtained after the adsorption of $FeCl_3$ nanoparticles synthesized using tea waste with methyl violet 2B solution showed spectral properties at 1582 cm^{-1}, which is proof that adsorbents are adsorbed with dye [17]. FTIR analysis result of $FeCl_3$ nanoparticle synthesized using tea waste is given in Figure 3.

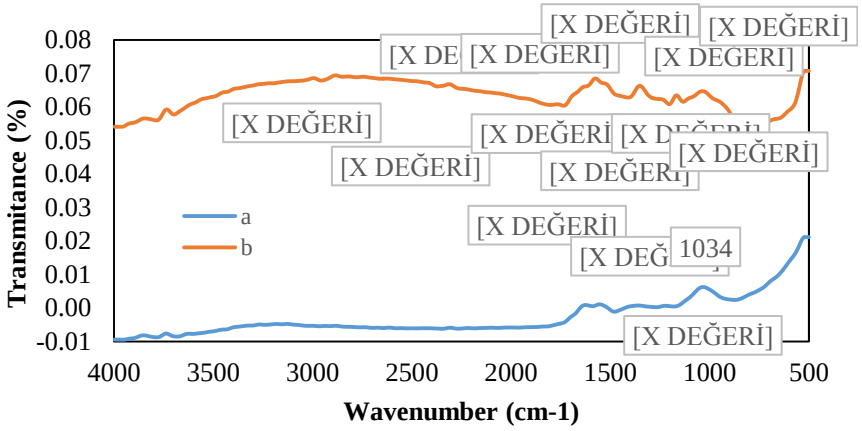

Figure 3. FTIR spectrum of $FeCl_3$ nanoparticles synthesized using tea waste a) Before adsorption of $FeCl_3$ nanoparticles synthesized using tea waste with methyl violet 2B b) After adsorption of $FeCl_3$ nanoparticles synthesized using tea waste with methyl violet 2B.

3.2. Adsorption Studies

3.2.1. Effect of pH

In order to observe the adsorption of methyl violet 2B solution with $FeCl_3$ nanoparticles synthesized using tea waste, pH values were changed and ambient conditions were kept constant (100 mL working volume, 50 mg/L dye concentration, 30°C temperature, 125 rpm stirring speed, 2 hours waiting time,

JSR A
Journal of Scientific Reports

1 g/L adsorbent dosage). Different pH adjustments were made and it was observed that the solution was more efficient at low pH, but the optimum pH was determined as 4.5 due to the loss of the produced material in acidic conditions. pH adjustments were made with HCl¬ and NaOH. The effect of pH on the adsorption is given in Figure 4.

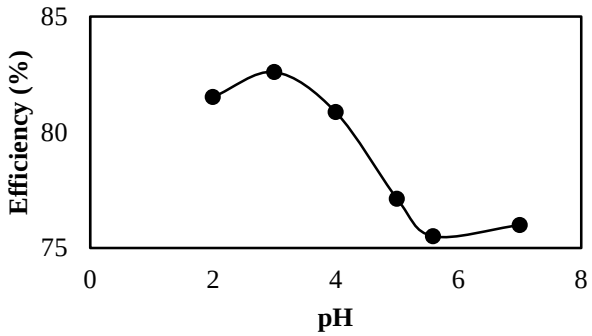

Figure 4. Effect of pH on adsorption efficiency.

3.2.2. Adsorbent dosage effect

To examine the effect of $FeCl_3$ nanoparticles synthesized using tea waste on methyl violet 2B dyestuff, the dye concentration was kept constant (50 mg/L) at a stirring speed of 125 rpm at 0.5-1-2-4-6 g/L adsorbent dosages, 100 mL working volume, pH 4.5 at 30 °C and time held constant (2 hours).When the graph below is examined, the removal efficiency is 92% at 2 g/L adsorbent dosage, while the efficiency is 82% at 1 g/L adsorbent dosage. Effect of adsorbent dosage on the adsorption is given in Figure 5.

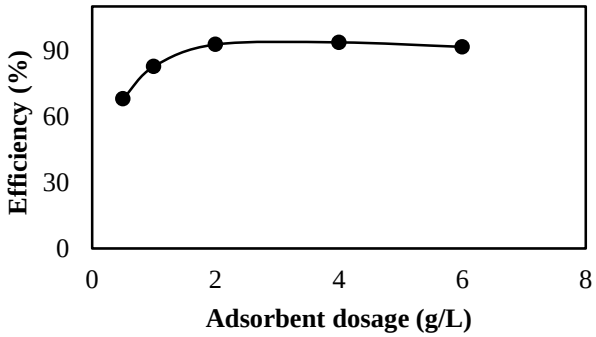

Figure 5. Effect of adsorbent dosage on adsorption efficiency.

JSR A
Journal of Scientific Reports

3.2.3. Initial dye effect

Methyl violet 2B solutions were prepared at 20, 40, 60, 80 and 100 mg/L concentrations by keeping the experimental conditions constant (125 rpm stirring speed, 30 °C temperature, 1 g/L adsorbent dosage, pH 4.5, 100 mL working volume, 2 hours waiting time). In the Figure below, it was observed that the percentage yield increased as dye concentration increased, while a decrease in yield was observed after a certain concentration. The adsorption reached equilibrium at initial concentration of 50 mg/L, and thus the optimum concentration was determined as 50 mg/L The effect of dye concentration on the adsorption is given in Figure 6.

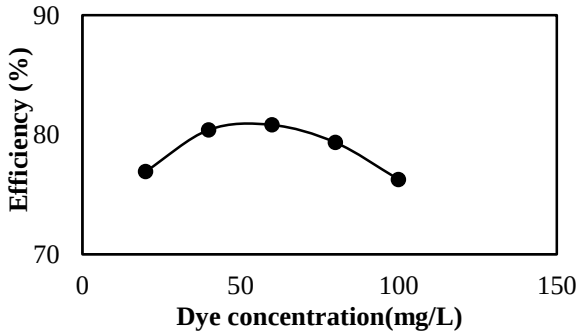

Figure 6. Effect of dye concentration on the adsorption efficiency.

3.3. Adsorption Kinetic

The velocity graphs of $FeCl_3$ nanoparticles synthesized with tea waste were analyzed in 4 different models as pseudo first order, pseudo second order, intraparticle diffusion and Elovich model. These models are it was investigated at optimum pH (4.5), 50 mg/L initial pollutant concentration, 1 g/L adsorbent dosage, 100 mL working volume, 240 min contact time and 125 rpm mixing speed. Graphs of kinetics were drawn and desired values were obtained from these graphs.

A plot of t/qt versus t was drawn to determine the pseudo second-order kinetic model. The R^2 value was found to be 1. However, it is seen that the adsorption capacity obtained experimentally and the calculated from the kinetic equation are very close to each other. Therefore, as a result of the data obtained, the removal of methyl violet 2B dye with FeCl3 nanoparticles synthesized using tea waste was found to be compatible with the pseudo second order kinetic model. The plots for the Pseudo first-order (a) and Pseudo second-order, (b) Intraparticle diffusion model (c) and Elovich model (d) are given in Figure 7. The data of methyl violet 2B adsorption with $FeCl_3$ nanoparticle synthesized using tea waste are given in Table 4.

JSR A
Journal of Scientific Reports

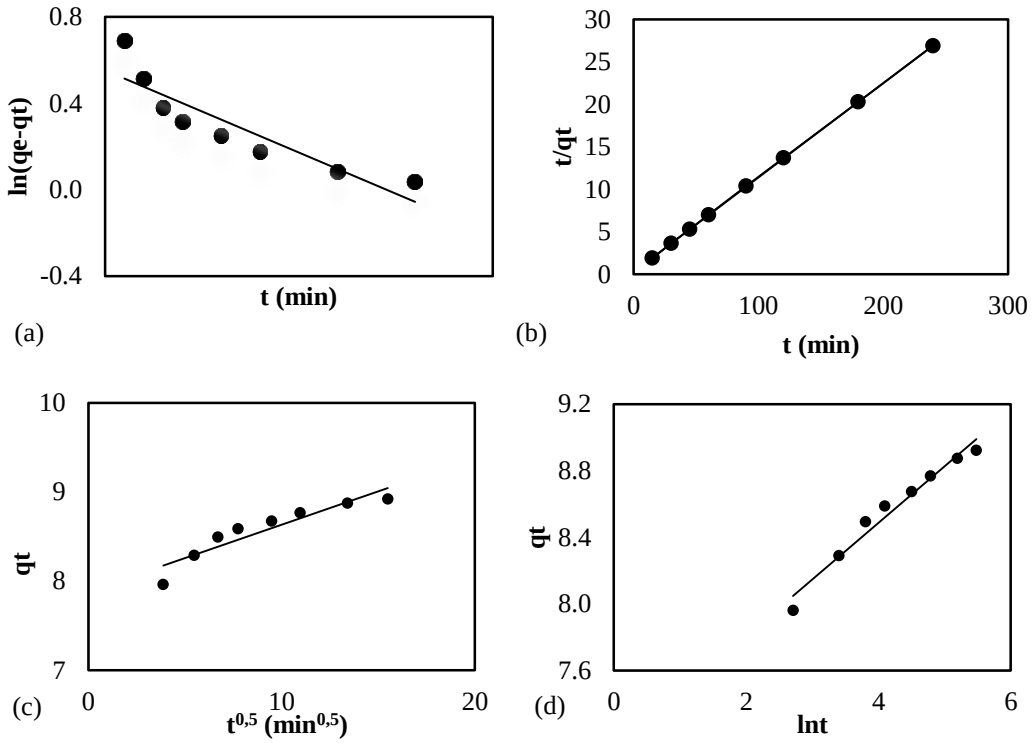

Figure 7. The plots for the (a) Pseudo first-order and (b) Pseudo second-order velocity graph, (c) Intraparticle diffusion model and (d) Elovich model.

Table 4. Kinetic data of methyl violet 2B adsorption with $FeCl_3$ nanoparticle synthesized using tea waste.

Pseudo first-order		**Pseudo second-order**		**Intraparticle diffusion model**		**Elovich**	
R^2	0.8161	**R^2**	1.0	**R^2**	0.865	**R^2**	0.9684
k_1 (min^{-1})	0.0001	**k_2 ((mg/g).min))**	0.0402	**C**	7.8852	**β**	1.187
$qe_{(cal)}$ (mg/g)	1.738	**$qe_{(cal)}$ (mg/g)**	9.009	**K_2**	0.0757	**α**	2.949
$qe_{(exp)}$ (mg/g)	9.058	**$qe_{(exp)}$ (mg/g)**	9.058				

3.4. Adsorption Isotherms

The Langmuir isotherm is a homogeneous, monolayer and physical isotherm [18]. Adsorption isotherms are used to determine the adsorption capacity. Curves that relate the solute concentration (Ce) remaining in the solution after being adsorbed at equilibrium and the amount of substance adsorbed per unit weight of the adsorbent at equilibrium (qe) [19].

JSR A
Journal of Scientific Reports

The dye adsorption of $FeCl_3$ nanoparticle synthesized with tea waste was investigated by Freundlich, Langmuir, Dubinin-Radushkevich and Temkin isotherms in the Figures below. These isotherms were investigated at different temperatures (20-30-40 °C), optimum pH (pH 4.5), 100 mL working volume, different dye concentrations (25-50-100-200 mg/L), 1440 min contact time and 125 rpm stirring speed. The curves given below are plotted with data obtained at 20°C.

When the correlation numbers of the Langmuir isotherm model at 20-40 °C temperatures given in Table 5 are examined, it is seen that the adsorption of $FeCl_3$ nanoparticles synthesized using tea waste is compatible with this isotherm model. The RL value, which is the separation factor defined by Webber and Chakkravorti based on the Langmuir equation, is an important parameter that indicates whether adsorption will occur or not. A low RL value is more suitable for the adsorption process [20]. Looking at Table 5, the low RL values and correlation number prove that this adsorption is compatible with the Langmuir isotherm model. Linear isotherm graphs of adsorption of methyl violet 2B from aqueous solution by $FeCl_3$ nanoparticle synthesized using tea waste Langmuir(a), Freundlich(b), Temkin(c) and Dubinin-Radushkevich(d) are given in figure 8.

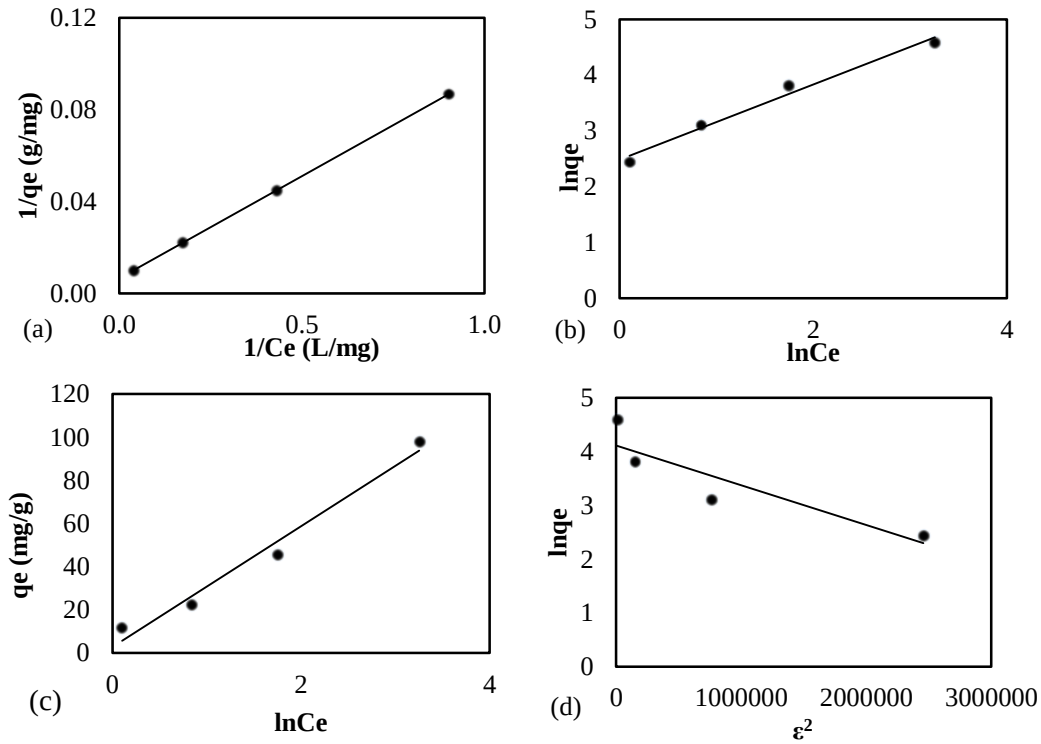

Figure 8. Linear isotherm plots of adsorption of methyl violet 2B from aqueous solution by $FeCl_3$ nanoparticle synthesized using tea waste (a) Langmuir, (b) Freundlich, (c) Temkin and (d) Dubinin-Radushkevich.

Freundlich isotherm is considered a multilayered process in which the amount of solute absorbed per unit mass of adsorbent gradually increases [21]. When looking at temperatures of 20-40 °C in Table 5, it is seen that the value of n is between 1 and 10. This shows a suitable sorption process [22]. Adsorption of $FeCl_3$ nanoparticles synthesized using tea waste may also be suitable for Freundlich isotherm.

It is accepted that the adsorption energy decreases linearly in the Temkin isotherm model as the active centers on the surface of the adsorbent are filled [23].

Dubinin-Radushkevich isotherm is used to understand whether the adsorption takes place with Gaussian energy over a heterogeneous surface [22]. The isotherm data of methyl violet 2B adsorption with $FeCl_3$ nanoparticle synthesized using tea waste are given in Table 5.

Table 5. Isotherm data of methyl violet 2B adsorption with $FeCl_3$ nanoparticle synthesized using tea waste.

Isotherm model	**Temperature (°C)**		
	20	**30**	**40**
Langmuir			
q_m (mg/g)	149.254	200.0	166.67
K_L (L/mg)	0.076	0.0437	0.049
R_L	0.344	0.477	0.449
R^2	1.0	0.9871	0.9752
Freundlich			
n	1.487	1.412	1.45
K_F	12.03	10.14	9.569
R^2	0.9819	0.982	0.9794
Temkin			
B	28.013	29.171	27.87
A	1.09	0.88	0.82
b_T (J/mol)	0.086	0.086	0.093
R^2	0.9754	0.9656	0.9459
Dubinin- Radushkevich			
q_m(mg/g)	61,06	64	63.18
K_D (mol^2/kJ^2)	22.225	8.718	8.718
E (kj/mol)	$2.67*10^{-4}$	$2.89*10^{-4}$	$2,89*10^{-4}$
R^2	0.8113	0.8563	0.8609

3.5. Adsorption Thermodynamics

Thermodynamic studies of the adsorption of $FeCl_3$ nanoparticles synthesized with tea waste with methyl violet 2B It was investigated at temperatures of 20-30-40 °C, optimum pH (pH 4.5), 100 mL working volume, adsorbent dosage of 1 g/L, initial dye concentration of 25 mg/L, contact time of

JSR A
Journal of Scientific Reports

1440 min and stirring speed of 125 rpm. Shape ΔH, ΔS and ΔG data were calculated from the Van't Hoff graph shown in Figure 17 and are given in Table 5. The adsorption process is thermodynamically feasible or not feasible and can be estimated from the sign of the standard free energy change (ΔG). If $\Delta G < 0$ adsorption is always possible and spontaneous, if $\Delta G > 0$. The adsorption process is not convenient and not spontaneous. Looking at Table 5, it is seen that the ΔG value obtained from the Van't Hoff plot is negative, indicating that the adsorption process is spontaneous and feasible. The ΔH value was calculated as -13,898 kj/mol, indicating that the adsorption is exothermic. The ΔS value was calculated as -28.18 kj/mol.K, which indicates a decrease in irregularity at the solid liquid interface [24]. Previous studies have shown that the ΔG° value ranges from -20 to 0 kj/mol for physical adsorption and -80 to -400 kJ/mol for chemical adsorption [25]. The ΔG values at all temperatures are respectively since -5.703, -5.226 and -5.148 kj/mol, we can say that adsorption is physical. A negative ΔG value (-5.703, -5.226, -5.148 kj/mol) indicates that adsorption is spontaneous and feasible, a negative ΔH value (-13.898 kj/mol) indicates adsorption is exothermic. The Van't Hoff linear graph is given in Figure 9.

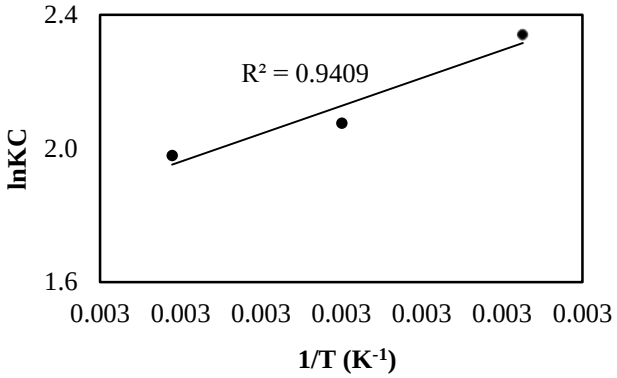

Figure 9. Van't Hoff linear graph.

4. RESULTS

In this study, $FeCl_3$ nanoparticles were prepared by green synthesis method using tea extract. The adsorption of methyl violet 2B dyestuff with $FeCl_3$ nanoparticles synthesized using tea extract was investigated in batch system. In 2 hours, the adsorption experiments reached equilibrium. The adsorbent dosege was studied in the range of 0.5-6 g/L and the optimum dose was determined as 1 g/L. pH was studied in the range of 2-7 and the optimum pH was determined as 4.5. The initial dyestuff concentration was studied in the range of 20-100 mg/L and the optimum concentration was determined as 50 mg/L. The equilibrium data obtained were applied to the isotherm equations and when the correlation numbers were examined, it was determined that the adsorption was in accordance with the Langmuir isotherm model. In the isotherm studies performed at 20 °C, 30 °C and 40 °C and the q_{max} values were found to be 149.254, 200 and 166.67 mg/g, respectively. The removal efficiency was calculated as 82 % at 30 °C where the highest q_{max} was obtained. According to the Langmuir isotherm, adsorption takes place physically. The separation factor (RL) for the Langmuir

isotherm was determined between 0.344-0.349, indicating that the process is suitable for the Langmuir isotherm. The adsorption kinetic equations were examined and it was seen that the adsorption was suitable for the pseudo second order kinetic model since the correlation number was 1. In addition, the relatively small relative error between the qe values obtained from the pseudo second order equation and the experimental qe values also supports this. The pseudo second order kinetic model assumes that the rate of adsorption is determined by the amount of sites remaining on the adsorption surface [26]. In the data obtained from thermodynamic studies, the adsorption enthalpy (ΔH) and Gibbs free energy were found to be -13.898kj/mol and -5.226kj/mol (30 °C), respectively. This shows that the adsorption process is exothermic, spontaneous and feasible. ΔS was found to be -28.18 kj/mol. A negative entropy indicates that the disorder at the solid-liquid interface is reduced. Characterization of $FeCl_3$ nanoparticles synthesized using tea extract was performed using SEM/EDX and FTIR devices. As a result of SEM/EDX analysis, it was observed that $FeCl_3$ nanoparticles synthesized using tea waste were adsorbed with methyl violet 2B dye. According to the results of the FTIR analysis, a peak showing methyl violet 2B was observed, which is proof that $FeCl_3$ nanoparticles synthesized using tea waste were adsorbed with dye. It was found that $FeCl_3$ nanoparticles synthesized with tea extract were effective in removing methyl violet 2B dye solution.

ACKNOWLEDGMENT

The authors would like to thank Duygu Anaklı and Halil İbrahim Çetintaş.

REFERENCES

[1] Saygı, S. (2017). Kil Katkili Poli(Hipe) Adsorban Üzerinde Metil Moru Boyar Maddesinin Adsorpsiyonu: Kinetik, Izoterm Ve Termodinamik Incelemeler. Master's Thesis Yıldız Technical University Graduate School of Natural and Applied Sciences, İstanbul, 124p.

[2] You, X., Zhou, R., Zhu, Y., Bu, D., Cheng, D. (2022). Adsorption of dyes methyl violet and malachite green from aqueous solution on multi-step modified rice husk powder in single and binary systems: characterization, adsorption behavior and physical interpretations, Journal of Hazardous Materials, 430, 128445.

[3] Foroutan, R., Mohammadi, R., Ahmadi, A., Bikhabar, G., Babaei, F., Ramavandi, B. (2022). Impact of Zno and Fe_3O_4 magnetic nanoscale on the methyl violet 2b removal efficiency of the activated carbon oak wood, Chemosphere, 286, 131632.

[4] Çiftçi, H., Er Çalişkan, Ç., Öztürk, K., Yazici, B. (2020). Bioactive nanoparticules synthesized via biogenic. Black Sea Journal of Engineering and Science 1: 29-42.

[5] Sharma, G., Kumar, A., Sharma, S., Al-Muhtaseb, A. H., Naushad, Mu., Ghfar, A. A., Ahamad, T., Stadler, F. J. (2019). Fabrication and characterization of novel Fe0@guar gum-crosslinked-soya lecithin nanocomposite hydrogel for photocatalytic degradation of methyl violet dye. Separation And Purification Technology, 211, 895-908.

[6] Sarangi, B., Mishra, S. P., Behera, N. (2022). Advances in green synthesis of ZnS nanoparticles: An overview, Materials Science in Semiconductor Processing, 147, 106723.

[7] Sun, Y., Gu, Y., Li, X., Singh, R. P. (2022). Synthesis of novel thiol-modified lysozyme coated magnetic nanoparticles for the high selective adsorption of Hg(II), Reactive and Functional Polymers, 170, 105129.

[8] Wang, G., Zhao, K., Gao, C., Wang, J., Mei, Y., Zheng, X., Zhu, P. (2021). Green synthesis of copper nanoparticles using green coffee bean and their applications for efficient reduction of organic dyes. Journal of Environmental Chemical Engineering, *9*(4), 105331.

[9] Alsancak, A. (2019). Demir Ile Zenginleştirilmiş Doğal Zeolitler Ile Sulu Çözeltilerden Metil Violet Giderimi. Master's Thesis Sakarya University Graduate School of Natural and Applied Sciences, Sakarya, 77p.

[10] Yakan, İ. (2019). Manyetik Yüklü Meşe Palamut Bazli Aktif Karbon Ile Sulu Çözeltilerden Metil Viyole Giderimi. Master's Thesis Sakarya University Graduate School of Natural and Applied Sciences, Sakarya, 103p.

[11] Kabadayı, O. (2018). Kitosan Kapli Zeolit Ile Sulu Çözeltilerden Boyar Madde Giderimi. Master's Thesis Sakarya University Graduate School of Natural and Applied Sciences, Sakarya, 84p.

[12] Özer, A. (2020). Öğütülmüş Zeytin Çekirdeği Kullanılarak Metil Viyolet Adsorpsiyonunun Incelenmesi. Master's Thesis Sakarya Unıversıty Graduate School of Natural and Applied Sciences, Sakarya, 69p.

[13] Tasmakıran, A., F. (2010). Zirai Yan Ürünlerin Modifiye Edilerek Yeni Adsorbanların Hazırlanması Ve Boyaların Adsorpsiyonu. Master's Thesis Selçuk Unıversıty Graduate School of Natural and Applied Sciences, Konya, 86p.

[14] Ivanets, A., Prozorovich, V., Roshchina, M., Sychova, O., Srivastava, V., Sillanpää, M. (2022). Methylene blue adsorption on magnesium ferrite: Optimization study, kinetics and reusability. Materials Today Communications, 31, 103594.

[15] Liu, J., Zhang, F., Dou, S., Zhu, M., Ding, L., Yang, Y. (2022). Adsorption of serine at the anatase TiO_2/water interface: A combined ATR-FTIR and DFT study. Science of The Total Environment, 807, 150839.

[16] Sarkar, S., Tiwari, N., Behera, M., Chakrabortty, S., Jhingran, K., Sanjay, K., Banerjee, S., Tripathy, S. K. (2022). Facile synthesis, characterization and application of magnetic Fe_3O_4-coir pith composites for the removal of methyl violet from aqueous solution: kinetics, isotherm, thermodynamics and parametric optimization. Journal of the Indian Chemical Society, *99*(5), 100447.

[17] *Methyl violet 2B - FTIR - Spectrum—SpectraBase*. (t.y.). Arrival date 28 May 2022, sender https://spectrabase.com/spectrum/7yZ9m0LwIPB

[18] Guo, X., Wang, J. (2019). Comparison of linearization methods for modeling the Langmuir adsorption isotherm. Journal of Molecular Liquids, 296, 111850.

[19] Kamath Miyar, H., Pai, A. (2021). Adsorption of malachite green by extracellular polymeric substance of *Lysinibacillus* sp. SS1: kinetics and isotherms. Heliyon, 7(6), e07169.

[20] Salihoğlu, Ö. (2020). Pirinç Kabuğu Ve Pirinç Kabuğu Silikası Adsorbanları Ile Parlak Yeşil Boyarmaddesinin Adsorpsiyonu: Karakterizasyon Ve Kinetik Çalışmalar. Master's Thesis Yıldız Technical University Graduate School of Natural and Applied Sciences, İstanbul, 129p.

[21] Chung, H. K., Kim, W. H., Park, J., Cho, J., Jeong, T. Y., Park, P. K. (2015). Application of Langmuir and Freundlich isotherms to predict adsorbate removal efficiency or required amount of adsorbent. Journal of Industrial and Engineering Chemistry, *28*, 241-246.

[22] A, O. D. (2012). Langmuir, Freundlich, Temkin and Dubinin–Radushkevich isotherms studies of equilibrium sorption of Zn^{2+} unto phosphoric acid modified rice husk. *IOSR* Journal of Applied Chemistry, 3(1), 38-45.

[23] Rona, E., B. (2019). Endüstriyel Atıksulardaki Ağır Metallerin Çeşitli Adsorbanlar Kullanılarak Giderilmesi. Master's Thesis Yıldız Technical University Graduate School of Natural and Applied Sciences, İstanbul, 90p.

[24] Doke, K. M., Khan, E. M. (2013). Adsorption thermodynamics to clean up wastewater, critical review. Reviews in Environmental Science and Bio/Technology, 12(1), 25-44.

[25] Kiziltaş, H. (2021). Orange G'nin sulu çözeltilerden uzaklaştırılması için α-Fe_2O_3 nanopartiküllerinin adsorban olarak kullanılması; adsorpsiyon, kinetik ve termodinamik özellikleri. European Journal of Science and Technology 21, 43-52.

[26] Li, H., Budarin, V. L., Clark, J. H., North, M., Wu, X. (2022). Rapid and efficient adsorption of methylene blue dye from aqueous solution by hierarchically porous, activated starbons®: mechanism and porosity dependence. Journal of Hazardous Materials, 129174.

Kütahya Dumlupınar University
Institute of Graduate Studies

Journal of Scientific
Reports-A
E-ISSN: 2687-6167
Number 51, December 2022

RESEARCH ARTICLE

WAVELENGTH TUNABLE PASSIVELY Q-SWITCHED FIBER RING LASER USING GALLIUM ARSENIDE BASED MICROCHIP SATURABLE ABSORBER

Thoalfeqar Ali Razaq ALYASIRI[1], Aşkınnur AŞKIN[2], Bünyamin KAYA[3], Şerif Ali SADIK[4*,] Fırat Ertaç DURAK[5], Ahmet ALTUNCU[6]

[1]Kütahya Dumlupınar University, Photonics Technologies Application and Research Center (FOTAM), Kütahya, thoalfeqar.alyasiri@ogr.dpu.edu.tr ,ORCID: 0000-0002-8379-0751
[2]Kütahya Dumlupınar University, Photonics Technologies Application and Research Center (FOTAM), Kütahya, askinnur.askin@org.dpu.edu.tr, ORCID: 0000-0003-0953-0246
[3]Kütahya Dumlupınar University, Photonics Technologies Application and Research Center (FOTAM), Kütahya, bunyamin.kaya2@ogr.dpu.edu.tr, ORCID: 0000-0002-9907-2826
[4]Kütahya Dumlupınar University, Photonics Technologies Application and Research Center (FOTAM), Kütahya, serifali.sadik@dpu.edu.tr, ORCID: 0000-0003-2883-1431
[5]Kütahya Dumlupınar University, Photonics Technologies Application and Research Center (FOTAM), Kütahya, firat.durak@dpu.edu.tr, ORCID: 0000-0002-4278-6561
[6]Kütahya Dumlupınar University, Photonics Technologies Application and Research Center (FOTAM), Kütahya, altuncu@dpu.edu.tr, ORCID: 0000-0002-3753-9515

Receive Date:31.08.2022 *Accepted Date: 05.10.2022*

ABSTRACT

The work presented in this study is focused on developing a widely wavelength tunable Q-switched pulsed erbium doped fiber ring laser (EDFRL) source operating in microsecond regime in Telecom wavelength spectrum of 1.55 μm (C and L bands). A commercial Gallium arsenide (GaAs) based microchip saturable absorber (SA) is used in the proposed EDFRL configuration to passively initiate Q-switching for stable pulse generation. Unless low damage threshold of the commercial GaAs based SA and non-optimized cavity length and losses, sufficiently stable pulse trains were obtained for a wide wavelength tuning range of 50 nm from 1520 nm to 1570 nm with high repeatability and long-term stability. The Q-switched output pulses of the proposed EDFRL have output average powers varying from +0.65 dBm to +1.53 dBm, the pulse widths varying from 4.27 μs to 7.16 μs and the repetition rates varying from 51.51 kHz to 31.42 kHz for different tuning wavelengths.

Keywords: *fiber laser, saturable absorber, Q-switched, wavelength tunable*

1. INTRODUCTION

Q-switched fiber lasers can generate high-energy pulses by modulating optical losses in the laser cavity using active or passive modulation elements. Therefore, studies on Q-switched fiber lasers have increased recently. Many modulators such as electro-optic modulators (EOM) [1], acousto-optic modulators (AOM) [2], semiconductor saturable absorber mirrors (SESAMs) [3], microchip saturable absorbers [4], and film saturable absorbers [5], carbon nanotubes [6], topological insulators (TIs) [7],

graphene [8], transition metal dichalcogenides (TMDs) [9] have been utilized to achieve Q-switching pulses. In contrast with the mode-locked ones, Q-switched fiber lasers have the ability to generate much higher pulse energy with microsecond or nanosecond pulses. Also, it is necessary to balance the dispersion and control the non-linear effects in the mode-locking process, which requires precise calculations and are not needed in the Q-switching process. Therefore, Q-switched fiber lasers have the advantages of efficiency, low cost, and ease of construction. The Q-switched lasers have many potential applications in various fields, such as sensing applications [10, 11], medicine [12] and material processing [13] owing to their advantages such as fast recovery time and low saturation intensity.

Passively Q-switched microchip lasers have many advantages, simplicity of implementation, pulse generation with a well-defined energy and duration, highly stable operation and easier to obtain single-frequency operation in a passively Q-switched laser than in an actively Q-switched device. The pulse duration from a Q-switched laser generally decreases with decreasing cavity length [14] and its central lasing wavelength can be passively tuned over a wide spectrum in C and L bands as soon as providing a positive gain spectrum using a wideband erbium doped fiber amplifier inside the cavity.

In this work, we demonstrate a widely tunable Q-switched erbium doped fiber ring laser with a gallium arsenide (GaAs) based saturable absorber (SA) as a passive Q-switching element, and an optical tunable band pass filter (OTBPF) as a wavelength tuning element. Stable Q-switched pulses are obtained in a 50 nm wide wavelength tuning range, which can be tuned from 1520 nm to 1570 nm. The obtained pulses have pulse widths ranging from 4.27 μs to 7.16 μs and repetition rates from 51.51 to 31.42 kHz.

2. EXPERIMENTAL DESIGN

In the experimental design utilized in this work, one backward pump laser diode and one forward pump laser diode with operating wavelengths of 980 nm were used to provide high pump power (Optical output power of the both of the laser diodes were set to 150 mW). An active fiber (Liekki Er-30) with the length of 6 m was utilized in the experimental setup. The length of the erbium doped fiber (EDF) was chosen to obtain a wideband CW operation in EDFRL using our previous results [15]. An isolator was utilized inside the ring cavity to ensure unidirectional lasing operation. To select the lasing wavelength of EDFRL, a MEMS-based C+L band OTBPF (TF1C100) was used in the cavity. A commercial GaAs microchip based SA is used as saturable absorber medium for pulse generation. The commercial SA used was 150 μm in thickness and had an absorbance of 58%, modulation depth of 35% and saturation fluence of 300μJ/cm2 at 1550 nm. The output of EDFRL was taken from the 10% port of the tap coupler with a 90% - 10% splitting ratio and then split into two ports, to observe the optical spectrum of the output signal and the electrical pulse forms simultaneously. The optical signal was analyzed at the optical spectrum analyzer (OSA Anritsu MS9710B). At the other port of the coupler, the optical signal was detected via an InGaAs 5 GHz photodiode (Thorlabs-DET08CFC/M), and the pulse waveforms were analyzed with an oscilloscope (Keysight-DSOX2002A). In the experimental setup, a manual polarization controller (PC) was used to optimize the polarization state of the light in the ring cavity, to eliminate the unwanted polarization effects. The schematic representation of the experimental setup was given in Fig.1.

JSR A
Journal of Scientific Reports

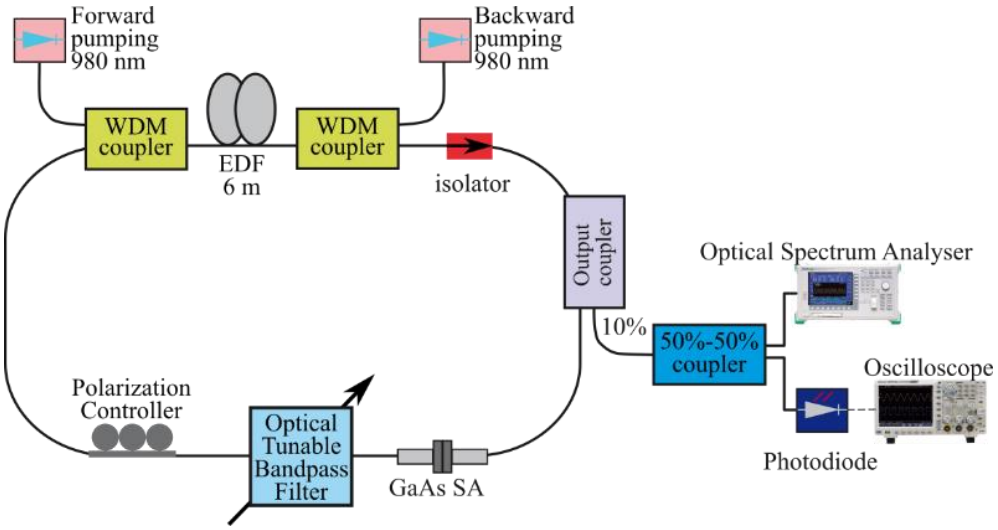

Figure 1. The proposed Q-switched EDFRL cavity used in experiments.

3. EXPERIMENTAL RESULTS

In the first experiment, the gain spectrum of the EDFA used in the setup was characterized using a commercial widely tunable (1520 nm-1607 nm) laser source (TLS) as the input light source. In these measurements, the forward and backward pump laser powers were set to 140 mW and the center wavelength of the TLS was tuned in the range of 1520-1607 nm. The gain spectrum of the bidirectional pumped EDFA is shown in Fig.2, which shows sufficient positive gains for a Q switched operation in our EDFRL design.

JSR A
Journal of Scientific Reports

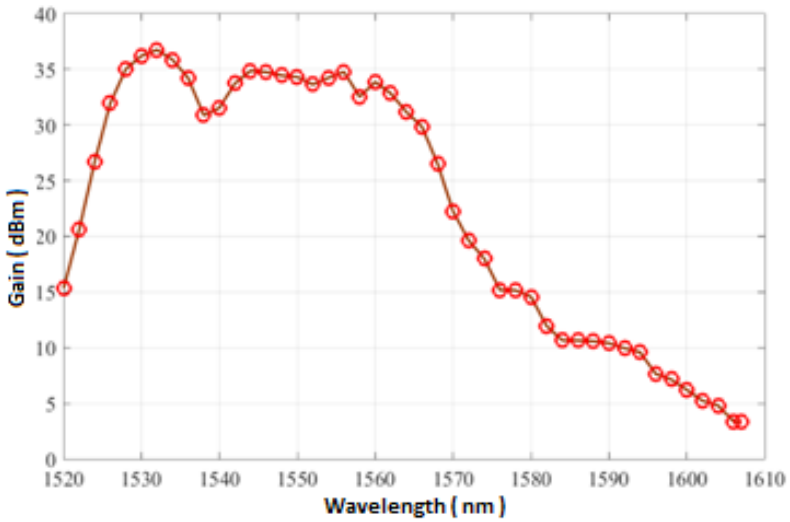

Figure 2. Gain spectrum of EDFA designed with 6 m EDF.

In the second experiment, passively Q switched EDFRL configuration has been set up as seen in Fig.1 using a GaAs based microchip saturable absorber. In Table 1, the optical output power, repetition rate and pulse width values obtained at the output of the Q switched wavelength tunable fiber ring laser designed across the entire spectrum are given. It should be noted that the output average power values measured in OSA were taken from one of the output ports of the 50%-50% splitter added to the assembly at the EDFRL output. It means that the power values given in Table 1 correspond to half the actual output power of the designed Q switched wavelength tunable EDFRL.

Table 1. The repetition rate, pulse width and output power of Q-switched wavelength tunable fiber ring laser.

Wavelength (nm)	Repetition Rate (kHz)	Pulse width (μs)	Output Peak Power (dBm)
1520	47.010	4.35	- 2.65
1530	51.516	4.274	- 2.63
1535	45.446	4.676	- 2.33
1540	38.459	4.982	- 1.74
1545	38.026	5.11	- 1.97
1550	39.435	5.334	- 1.58
1555	36.813	5.234	- 1.58
1560	33.928	5.554	- 1.54
1565	33.562	6.494	-2.03
1570	31.421	7.166	-1.53

JSR A
Journal of Scientific Reports

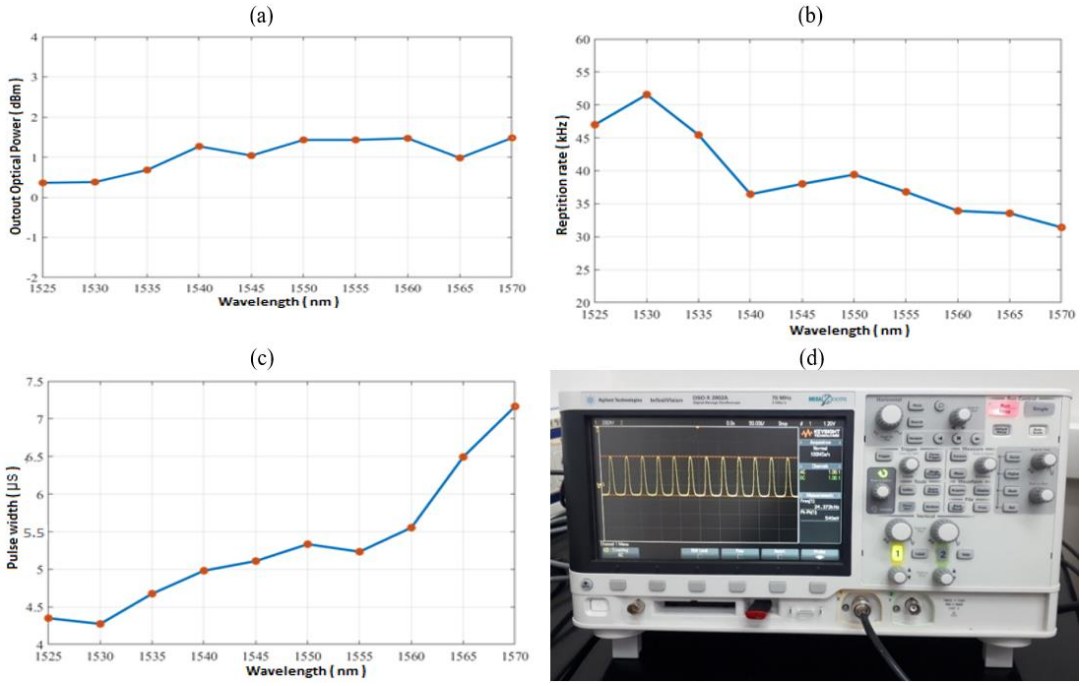

Figure 3. (a) Optical output power **(b)** Repetition rate and **(c)** Pulse width of the Q switched EDFRL as a function of tuning wavelength **(d)** A typical output waveform of the designed GaAs-SA based Q-switched wavelength tunable fiber laser.

With the Q-switched pulsed EDFRL design, highly stable pulses could be obtained for the lasing wavelength range of 1520-1570 nm having clearly measurable repetition rate, pulse width and output power values. The Optical output power, repetition rate and pulse width values measured through a 50 nm tunable wavelength range are given in Figure 3 (a), (b) and (c). The output average power measured in OSA at one port of the output splitter was changing between 0.65 dBm to 1.5 dBm depending on the lasing wavelength which correspond to the repetition rates varying between 31.42 kHz and 51.51 kHz and pulse widths varying between 4.35 µs and 7.16 µs.

JSR A
Journal of Scientific Reports

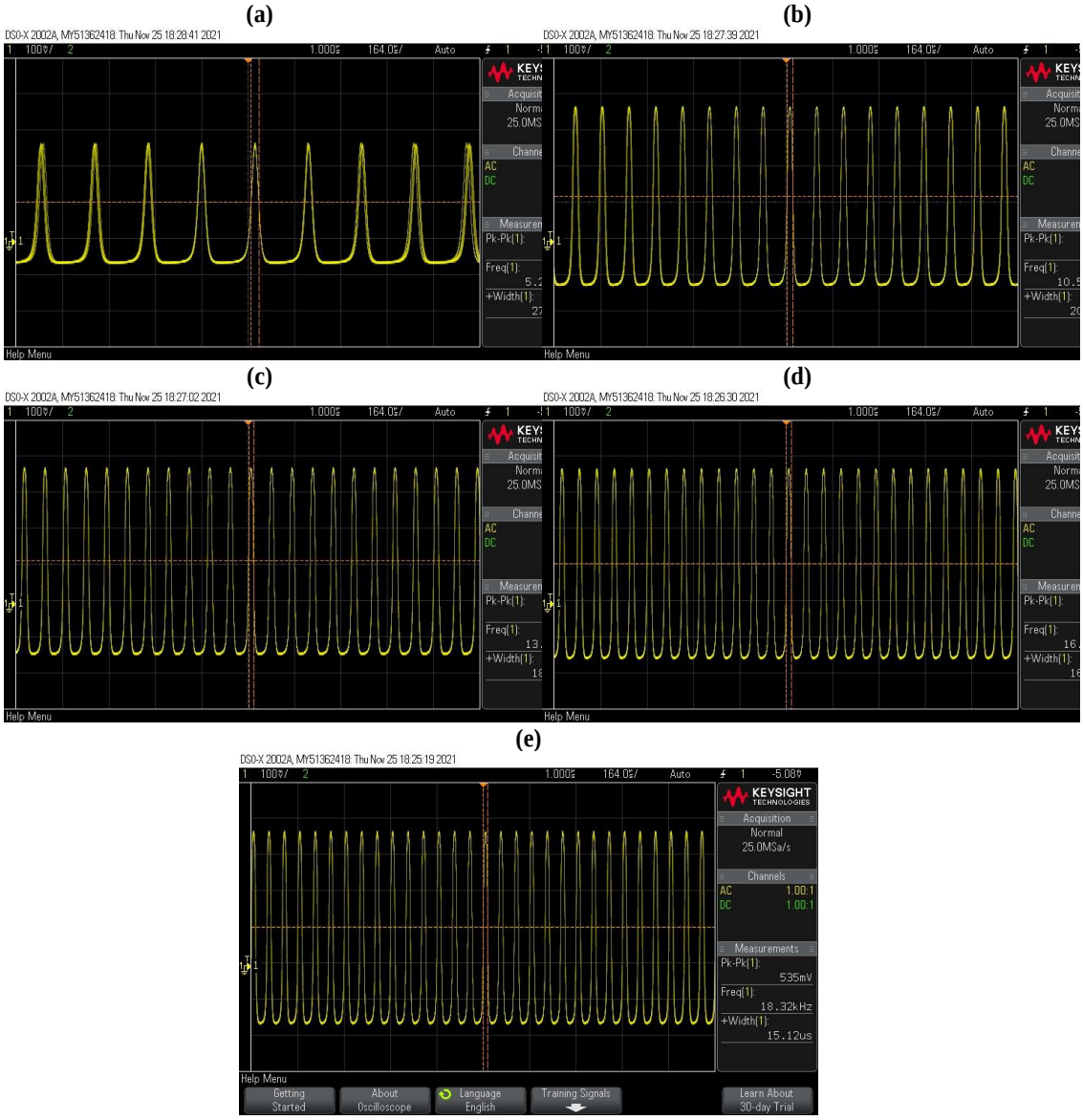

Figure 4. The Q-switched EDFRL output pulse trains at the lasing wavelength of 1567 nm obtained without using a OTBPF in the cavity at the following pump currents of **(a)** 60 mA, **(b)** 70 mA, **(c)** 80 mA, **(d)** 90 mA, **(e)** 100 mA.

A self-starting and stable Q-switched fiber laser operation using GaAs SA without OTBPF was achieved after the threshold pump currents of 60 mA. The lasing oscillation was centered at a

wavelength of 1567 nm. The Q-switched lasing operation remained stable as the pump laser currents were raised up to 100 mA. Fig.4 shows the increment of the repetition rate from 5.27 kHz to 18.32 kHz and the decreasement of the pulse with from 27.64 μs to 15.12 μs as the pump laser currents were increased from 60 mA to 100 mA.

4. CONCLUSION

In this study, highly stable Q-switched output pulses have been obtained in a bidirectionally pumped EDFRL configuration for a tunable wavelength range of 50 nm from 1520 nm to 1570 nm with an output average power of between +0.65 dBm and +1.53 dBm, the pulse width of 4.27 μs – 7.16 μs and the repetition rate of 51.51 kHz - 31.42 kHz for a moderate pumping level and non-optimized cavity losses. The Q switched output pulse trains were also obtained for different pumping levels at a natural lasing wavelength of 1567 nm in the cavity. The results show that Q-switching performance of wavelength tunable EDFRL design proposed can further be upgraded by optimizing the cavity length and losses. However, low damage threshold of GaAs based SA is serious limiting factor to be considered for high power applications. This kind of EDFRL Q switched pulse source can be widely used as a tunable laser source in DWDM optical communication systems operating in 1.55 μm region and for spectral response measurements in fiber optical sensor applications. In our future work, we will work on optimizing the cavity length and loss for a better Q-switching performance regarding wavelength tuning range, pulse width, repetition rate and output power.

ACKNOWLEDGEMENTS

This work was supported by Kütahya Dumlupınar University (Project No.DPU.2020-20).

REFERENCES

[1] El-Sherif, A.F. and King, T.A., (2003), High-energy, high-brightness Q-switched Tm^{3+}-doped fiber laser using an electro-optic modulator, Opt. Commun., 218(4),337-344.

[2] Li, W., Liu, H., Zhang, J., Long, H., Feng. S. and Mao, Q., (2016), Q-switched fiber laser based on an acousto-optic modulator with injection seeding technique, Appl. Opt., 55(17), 4584-4588.

[3] Wang, M., Chen, C., Huang, C., and Chen, H., (2014), Passively Q-switched Er-doped fiber laser using a semiconductor saturable absorber mirror, Optik (Stuttg)., 125(9), 2154–2156.

[4] J. J. Zayhowski, J.J., and Wilson, A.L., (2003), Pump-induced bleaching of the saturable absorber in short-pulse Nd:YAG/Cr/sup 4+/:YAG passively Q-switched microchip lasers, IEEE J. Quantum Electron., 39(12), 1588–1593.

[5] Zulkipli, N.F., Rosol, A.H.A., Sadik, S.A., Durak, F.E., Altuncu, A., Yasin, M. and Harun, S.W., (2021), Q-Switched Pulse Generation in a Bidirectionally Pumped EDFL Utilizing Lu_2O_3 as Saturable Absorber, Optoelectronics Letters, 17 (9), 529–533.

[6] Kasim, N., Al-Masoodi, A.H.H., Ahmad, F., Munajat, Y., Ahmad, H., and Harun, S.W., (2014), Q-switched ytterbium doped fiber laser using multi-walled carbon nanotubes saturable absorber, Chinese Opt. Lett.,12(3), 31403.

[7] Yu, Z., Song, Y., Tian, J., Dou, Z., Guoyu, H., Li, K., Li, H., and Zhang, X., (2014), High-Repetition-Rate Q-Switched Fiber Laser with High Quality Topological Insulator Bi_2Se_3 Film, Optics Express, 22(10), 11508–11515.

[8] Luo, Z.,Zhou, Z., Weng, J., Huang, G., Xu, H., Ye, C., and Cai, Z., (2010), Graphene-Based Passively Q-Switched Dual-Wavelength Erbium-Doped Fiber Laser. Optics Letters,35(21), 3709–3711.

[9] Chen, B., Zhang, X., Wu, K., Wang, H., Wang, J., and Chen, J., (2015), Q-switched fiber laser based on transition metal dichalcogenides MoS_2, $MoSe_2$, WS_2, and WSe_2, Opt. Express, 23(20), 26723–26737.

[10] Zhang, Q., Chang, J., Wang, Q., Wang, Z., Wang, F., and Qin, Z., (2018), Acousto-optic Q-switched fiber laser-based intra-cavity photoacoustic spectroscopy for trace gas detection, Sensors, 18(1), 42.

[11] Shi, W., Petersen, E., Moor, N., Chavez-Pirson, A., and Peyghambarian, N., (2011), All fiber-based single-frequency Q-switched laser pulses at 2 um for lidar and remote sensing applications, in Proc.SPIE, 2011, vol. 8164.

[12] Celen, S. , Özden, H. and Uyar, E. (2014), İterbiyum-katkili fiber lazerle Q-anahtarlamalı modda implant yüzeyi mikro-imalatı ve karekterizasyonu . Gazi University Journal of Science Part C: Design and Technology , 2 (2) , 197-202 .

[13] Ismail, M.A., Ahmad, F., Harun, S.W., Arof, H., and Ahmad, H., (2013), A Q-switched erbium-doped fiber laser with a graphene saturable absorber, Laser Phys. Lett.,10(2), 25102.

[14] Chen, Y., Zhao, C., Chen, S., Du, J., Tang, P., Jiang, G., Zhang, H., Wen, S., and Tang, D., (2013), Large Energy, Wavelength Widely Tunable, Topological Insulator Q-Switched Erbium-Doped Fiber Laser, IEEE Journal of Selected Topics in Quantum Electronics,20(5),315–322.

[15] Sadik, S. A., Durak, F. E., & Altuncu, A. (2020), Widely tunable erbium doped fiber ring laser based on loop and double-pass EDFA design. Optics & Laser Technology, 124, 105979.

Kütahya Dumlupınar University
Institute of Graduate Studies

Journal of Scientific
Reports-A
E-ISSN: 2687-6167
Number 51, December 2022

RESEARCH ARTICLE

PERFORMANCE of MULTIUSER V-BLAST WITH LIMITED FEEDBACK for USER SCHEDULING over NAKAGAMI-*m* FADING CHANNELS

Katherin AMELIA[1*], Serdar ÖZYURT[2], Mustafa NAMDAR[3]

[1*]Ankara Yıldırım Beyazit University, Faculty of Engineering and Natural Sciences, Department of Electrical and Electronics Engineering, Ankara, 195105120@ybu.edu.tr, ORCID: 0000-0002-9605-8789
[2]Ankara Yıldırım Beyazit University, Faculty of Engineering and Natural Sciences, Department of Electrical and Electronics Engineering, Ankara, sozyurt@ybu.edu.tr, ORCID: 0000-0002-9612-6227
[3]Kütahya Dumlupınar University, Faculty of Engineering, Department of Electrical and Electronics Engineering, Kütahya, mustafa.namdar@dpu.edu.tr, ORCID: 0000-0002-3522-4608

Receive Date:12.09.2022 *Accepted Date: 11.10.2022*

ABSTRACT

In this paper, the performance of a downlink multiuser zero-forcing (ZF) Vertical Bell Laboratories Layered Space-Time (V-BLAST) with an ordering scheme over Nakagami-*m* fading channels is presented. A system with two transmit antennas while each user is equipped with r ($r \geq 2$) receiver antennas is considered. In every time slot, the base station schedules a single user out of U users and communicates with it by adopting a limited feedback (FB) technique for user scheduling. One user is chosen based on a set of bits each sent from a distinct user to the transmitter. The channel considered in this investigation is the fading channel with Nakagami-*m* distribution which covers a wide range of multipath fading patterns. The adopted FB scheme requires a threshold value which is attained through a numerical optimization process. For a given shape parameter, the optimum threshold value approaches to zero as SNR increases. The results of the outage probability of the investigated systems with varying *m*-parameter value of Nakagami-*m* fading channels are presented and compared with the no FB method. It is shown that the studied FB approach on multiuser ZF V-BLAST indeed outperforms the no FB technique. The shape parameter value clearly affects the performance of the FB system, whereas it seems have no significant effect on the random user scheduling (no FB) method.

Keywords: *Zero-Forcing, V-BLAST, User Scheduling, Limited Feedback, Multiuser System, Nakagami-m Fading Channel*

1. INTRODUCTION

The transmission methods that rely on multiple antennas at both transmitter and receiver sides are reputable in significantly improving the channel capacity of wireless communication systems. Among of many techniques which have been suggested to employ the high spectral efficiency of multiple-input multiple-output (MIMO) channels, the Vertical Bell Laboratories Layered Space-Time (V-

BLAST) with zero-forcing (ZF) approach is capable of achieving high spectral efficiency. Moreover, it seems comparatively less complicated to implement. By using the V-BLAST technique, the input data streams are transmitted in parallel and simultaneously over the transmitting antennas without the requirement of channel state information (CSI) known at the transmitter side. The receiver applies sequential interference nulling and cancellation (SIC) processes to decode the received sub-streams, which are combined and overlapped by noise, one after one [1,2]. The SIC allows the symbol to be detected and decoded without inter symbol interference (ISI). The implementation of symbol detection and decoding at a specified SIC stage can be carried out by an ordering or non-ordering scheme. The ordering method is an approach to improve the drawback caused by the non-ordering scheme, i.e., error propagation. In fact that the detection error of the first symbol may incur more errors in the following symbol detections, the overall performance of the ZF V-BLAST with a non-ordering scheme is narrowed as the result. The ordering scheme based on the highest signal-to-noise ratio (SNR) level, offers a solution to mitigate this error propagation problem, i.e., the data sub-stream with the largest post-processing SNR is detected first [1].

In this paper, the multiuser ZF V-BLAST with ordering SIC scheme is combined with a feedback (FB) technique for user scheduling to improve performance. The FB technique that is exploited for user selection purposes practically lets every user to feed back the necessary information to the transmitter under the predetermined requirement. In general, the FB technique can be implemented by reporting the information in a scalar or limited form. Some studies exist regarding user scheduling in the multiuser scenario, such as opportunistic scheduling, threshold-based scheduling, and limited FB. The opportunistic scheduling technique implies the process based on the maximum SNR so that every user will send the information of its highest post-processing SNR to the transmitter [3-5]. While in the user selection that employs the threshold-based approach, one allows only the users satisfying the condition to report back their SNR values to the transmitter [6]. The threshold-based scheduling presents a solution for the disadvantage introduced by the opportunistic scheduling, i.e., the heavy FB load. However, the threshold-based scheduling also becomes not feasible as the number of users increases. Then, there is the combination between threshold-based scheduling and quantization of the FB values which has proposed a proper technique to improve the user selection process. This combination, which is also noted as the limited FB technique, enables users to feed back a bit 1 or 0 relying on compliance with the threshold requirement, then leads the reduction of the FB load [7]. The studies about the performance of multiuser V-BLAST with limited FB can be found in the papers [8-9]. The contributions by [8] assume Rayleigh channel fading condition through the work, whereas [9] utilizes transmit antenna selection and maximal-ratio combining (MRC) schemes at the transmitter and the receiver side, respectively. As for predetermining criteria to be implemented in the FB technique, various strategies can be applied for optimization purposes. Some studies have shown different approaches regarding the predetermining criteria for the FB requirement. For example, the study by [9] applies a threshold scheme to not only select a user but also choose the best transmit antenna for which the SNR at the scheduled user is maximized. The work in [10] employs several criteria for user scheduling of V-BLAST users.

The Nakagami-*m* distribution is regarded as one of the essential models because of its versatility in representing the fading envelope due to multipath fading in wireless communications [11]. The distribution in which the method of derivation and the fundamental characteristics were presented

initially based on field measurements is a model with two parameters, i.e., scale and shape parameter (or the fading parameter or *m*-parameter). This distribution, through its parameter *m* can be utilized to characterize fading channel conditions in the range from severe to moderate levels [12]; moreover also accommodates the Rayleigh distribution model as a particular case ($\boldsymbol{m = 1}$). Some studies have shown that the Nakagami-*m* distribution is proper for data signals received in urban radio multipath channels [13-14]. The Nakagami-*m* distribution is more suitable in land mobile and indoor propagation environments, so we are motivated to examine the limited FB concept by [10] over Nakagami-*m* fading channels. To the best of our knowledge, the performance of multiuser V-BLAST with ordering scheme and 1-bit FB over Nakagami-*m* fading channels has not yet been investigated in any literature.

The main points of the paper are summarized as follows. First, the average outage probability (AOP) of the investigated system at a certain number of *m*-parameter, SNR value, and *U* users is examined to a range value of threshold values. Consequently, the optimized threshold values will be attained for every *m*-parameter, SNR value, and *U* user of the studied systems. Furthermore, the AOP in a range of SNR values at a given *m*-parameter and *U* users is illustrated by applying the obtained threshold values from the threshold optimization process. Consequently, the gain of exploiting the limited FB scheme in V-BLAST for user scheduling over Nakagami-*m* fading channels is represented by comparing its error performance with no FB method.

The rest of this paper is structured in the following way. Section 2 describes the V-BLAST system model used in the investigation. Section 3 covers the simulation results of the studied system. Finally, the conclusion is given in Section 4. Throughout the paper, the operators $(.)^{\boldsymbol{H}}$ and $\|.\|$ represent the Hermitian transpose and Euclidean norm, respectively. Uppercase and lowercase bold letters denote the matrices and column vectors, respectively.

2. SYSTEM MODEL

We consider a MIMO downlink system that establishes communication between a base station equipped with two transmit antennas and *U* users, each with r ($r \geq 2$) antennas as depicted in Figure 1. The complete knowledge of CSI is assumed to be available only at the receivers. Each user is required to report back to the transmitter in a form of a single bit which correlates with its sub-channel gain. Following this, the transmitter receives a set of FB bits from users and then opportunistically chooses only one user to communicate with in every training slot. Later, in each communication sequence, the transmitter dispatches two autonomously encoded streams through its antennas in a synchronous and parallel way to the scheduled user. At the receiver side of the chosen user, detecting and decoding the streams processes are performed by utilizing the ZF V-BLAST with the ordering scheme technique.

The fading channel vector between the *s*th transmit antenna and the receiver antennas at the user u is denoted by $\mathbf{h}_s^u$ for $u \in \{1,2 \dots, U\}$ and $s \in \{1,2\}$. Hence, the *k*th entry of $\mathbf{h}_s^u$ represents the fading coefficient between the *s*th transmit antenna and the *k*th receive antenna at the user u. Nakagami-*m* fading scenario is considered in this study, and the random channel matrices for the users are assumed to be not correlated with each other. Each channel of any user remains fixed in the course of one

JSR A
Journal of Scientific Reports

transmission cycle and switches independently from one to another transmission process. The norms of entries of $\mathbf{h}_s^u$ are independent and identically distributed Nakagami-*m* random variables, each with a certain *m*-parameter ($m \geq 0.5$) and a scale parameter of unity. Furthermore, we assume that a capacity-achieving code applied on both sub-streams.

The transmitter decides one user out of *U* users based on the FB reported back from all users in a limited format. The limited FB utilized in this work as the FB scheme is a technique that allows users to send a single bit (bit 1 or 0) based on the decided standard. For this reason, this approach is also noted as the 1-bit FB technique. The *u*th user sends back bit 1 to the transmitter if its highest outcome of sub-channel gain on the first layer γ_{u1} is greater or equal to a threshold value γ_{th}, and bit 0 any other way. Let a set of users feed back bit 1 to the transmitter symbolized by B, and then transmitter performs the selection for user scheduling by observing the cardinality of B denoted as $\overline{\overline{\mathrm{B}}}$. If $\overline{\overline{\mathrm{B}}}$ is unity, the user in B is scheduled by the transmitter. In case B's number of elements exceeds one, the transmitter randomly selects and schedules one user from B. Otherwise (when B equals empty set), which means that all the users feed back bit 0, the transmitter chooses one user out of *U* users in a random fashion.

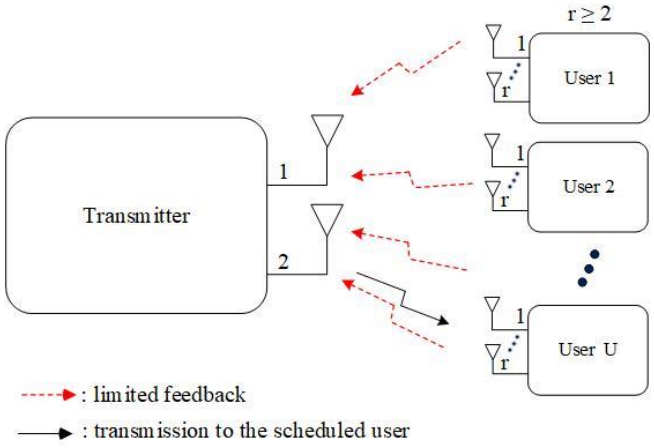

Figure 1. The system's block diagram.

Assume that u' ($u' \in \{1,2 \ldots, U\}$) represents the index of the scheduled user to communicate with the transmitter. Then, the received complex signal at the selected user is given by

$$\mathbf{y}^{u'} = \mathbf{h}_1^{u'} x_1 + \mathbf{h}_2^{u'} x_2 + \mathbf{n} \tag{1}$$

where x_s and $\mathbf{n}$ respectively denote the transmitted modulated symbol from the *s*th transmit antenna and the additive white Gaussian noise (AWGN) at the receiver. The ZF V-BLAST with an optimum ordering approach is applied to decode the symbols at the receiver. The decoding processes start with a sub-stream with the highest post-processing sub-channel gain, hence the outage probability is

minimized. First, the received signal is multiplied with a particular matrix obtained employing QR factorization, thereby the interference at a given sub-stream induced by other sub-streams is eliminated. Later, that specific sub-stream is decoded without any interference. Subsequently, the interference caused by the previously decoded sub-stream is subtracted from the total signal, and the other symbol is decoded. The first and second squared sub-channel gains produced by the ZF V-BLAST with the optimum ordering scheme are expressed as $\gamma_{u1} = \max\{\left((\mathbf{h}_1^{u\prime})^H \mathbf{P}_{\mathbf{h}_2^{u\prime}}^{\perp} \mathbf{h}_1^{u\prime}\right), \left((\mathbf{h}_2^{u\prime})^H \mathbf{P}_{\mathbf{h}_1^{u\prime}}^{\perp} \mathbf{h}_2^{u\prime}\right)$ and $\gamma_{u2} = \min\{\|\mathbf{h}_1^{u\prime}\|^2, \|\mathbf{h}_2^{u\prime}\|^2\}$, respectively [2]. Here, $\mathbf{P}_{\mathbf{h}_s^u}^{\perp}$ represents the projection matrix onto the null space of the vector $\mathbf{h}_s^u$. The result of $\arg\max\{\left((\mathbf{h}_1^{u\prime})^H \mathbf{P}_{\mathbf{h}_2^{u\prime}}^{\perp} \mathbf{h}_1^{u\prime}\right), \left((\mathbf{h}_2^{u\prime})^H \mathbf{P}_{\mathbf{h}_1^{u\prime}}^{\perp} \mathbf{h}_2^{u\prime}\right)\}$ indicates the index of the transmitted symbol which is best to be decoded first [2].

3. SIMULATION RESULTS

In this section, we present the numerical results based on the Monte Carlo simulations regarding the AOP. First, separately assuming three distinct values of the shape parameter, i.e., $m = 1$, $m = 2$, and $m = 5$, each scenario at a specific number of users is examined independently within a range of estimated threshold values and varying SNR. The threshold value γ_{th} is used by all the users to feed back either bit 1 or bit 0. For the optimization, we numerically evaluate AOP for a range of threshold values and the one minimizing AOP is adopted as γ_{th}. This procedure is followed for all the inspected scenarios. Following this, the proposed scheme of multiuser ZF V-BLAST is simulated using all the obtained γ_{th} corresponding to each SNR value. The comparison between the FB and the no FB technique with various fading parameter values is presented as well. The simulation is implemented under the condition of $t = r = 2$ for $U = 5$ and $U = 10$. In addition, each sub-channel is assumed to have a target spectral efficiency of $R = 2$ bits/s/Hz.

In this work, we utilize Nakagami-*m* distribution, whose probability density function is stated below.

$$f_{|\mathbf{h}_{s,r}|}(z) = \frac{2m^m z^{2m-1} \exp(-mz^2)}{\Gamma(m)} \tag{2}$$

for $z \geq 0$, where $\mathbf{h}_{s,r}$ denotes the multipath channel coefficients between transmit and receive antennas which are independent complex variables, *m* represents the fading figure or shape parameter, exp (.) denotes the exponential function, and $\Gamma(.)$ is the Gamma function. All multipath channel coefficients are assumed to have the same *m* value. Moreover, the average received power here is considered by $E\left\{\left|\mathbf{h}_{s,r}\right|^2\right\} = 1$, i.e., all the channel coefficients have identical average power.

As mentioned before, the optimization processes are performed to obtain the best threshold values for varying numbers of users, *m*-parameter, and SNR values such that AOP is minimized. Outage probability is defined as the probability that the attained (achievable) information rate is less than the required information rate. In such a case the receiver cannot decode the transmitted message signal and an outage occurs. The acquired γ_{th} with respect to SNR values for $U = 5$ and $U = 10$ are shown in

JSR A
Journal of Scientific Reports

Table 1 and 2, respectively. Figure 2 and Figure 3 respectively show the suitable values γ_{th} for $U = 5$ (with $m = 2$) and $U = 10$ (with $m = 5$) in terms of AOP. Based on the optimization results, it is shown that for every scenario of the m-parameter, the optimum threshold value γ_{th} reaches zero when SNR escalates.

The results of multiuser ZF V-BLAST with FB technique are shown in Figure 4 and Figure 5 for $U = 5$ and $U = 10$, respectively, by applying the attained optimal γ_{th} values (at which AOP is minimized), which correspond to a given shape parameter and SNR value. The comparisons with the random user scheduling ZF V-BLAST (no FB technique) can be observed as well from the graphs. The FB technique outperforms the random user scheduling technique in all shape parameters of Nakagami-m fading channels. Applying the limited FB has shown its advantage on the performance of multiuser ZF V-BLAST over Nakagami-m channels, i.e the acquired AOP performances of FB method are better than those of no FB, which share the same values of U, m-parameter and SNR. For $U = 5$, an AOP of 10^{-4} is reached by the FB method at SNR values around of 27.5 dB, 18 dB and 15 dB for $m = 1$, $m = 2$ and $m = 5$, respectively. On the other hand, the no FB method for all m-parameter values cannot reach an AOP of 10^{-4}, even though the SNR value already reaches 28 dB. In the scenario of $U = 10$, the 1-bit FB approach again surpasses the no FB technique in every m-parameter value. For an AOP of 10^{-4}, the attained SNR gains of FB technique are about 27, 18, and 12 dB for $m = 1$, $m = 2$ and $m = 5$, respectively. The graphs also exhibit that the performances for the no FB scheme are almost the same regardless of the shape parameter values. Conversely, the performances improve as the m-parameter increases for the FB method.

Table 1. Threshold values with respect to SNR values for $U = 5$.

m	Threshold values γ_{th}		
	SNR (*10 dB*)	SNR (*19 dB*)	SNR (*28 dB*)
1	1.1	0.5	0.4
	SNR (9 *dB*)	SNR (*14 dB*)	SNR (*19 dB*)
2	1	0.4	0.2
	SNR (10 *dB*)	SNR (*13 dB*)	SNR (*16 dB*)
5	0.6	0.4	0.2

Table 2. Threshold values with respect to SNR values for $U = 10$.

m	Threshold values γ_{th}		
	SNR (*10 dB*)	SNR (*19 dB*)	SNR (*28 dB*)
1	1.9	1	0.7
	SNR (9 *dB*)	SNR (*14 dB*)	SNR (*19 dB*)
2	1.3	1.2	0.6
	SNR (*8 dB*)	SNR (*10 dB*)	SNR (*12 dB*)

JSR A
Journal of Scientific Reports

5	1.2	0.6	0.5

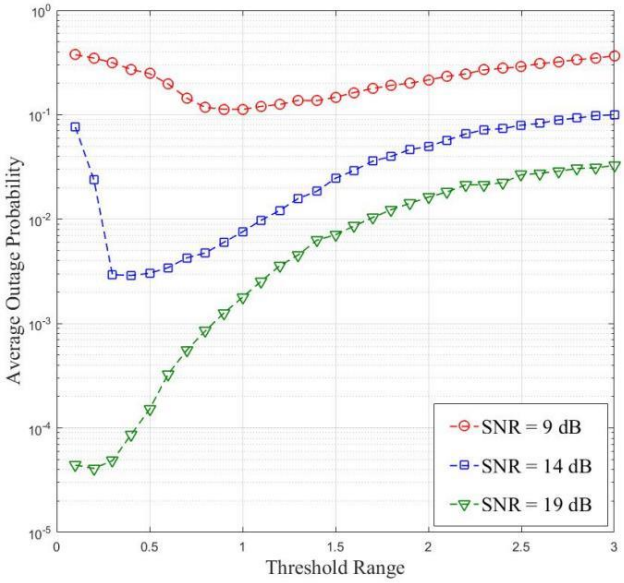

Figure 2. Average outage probability vs threshold range for $U = 5$ and $m = 2$ with varying SNR values.

JSR A
Journal of Scientific Reports

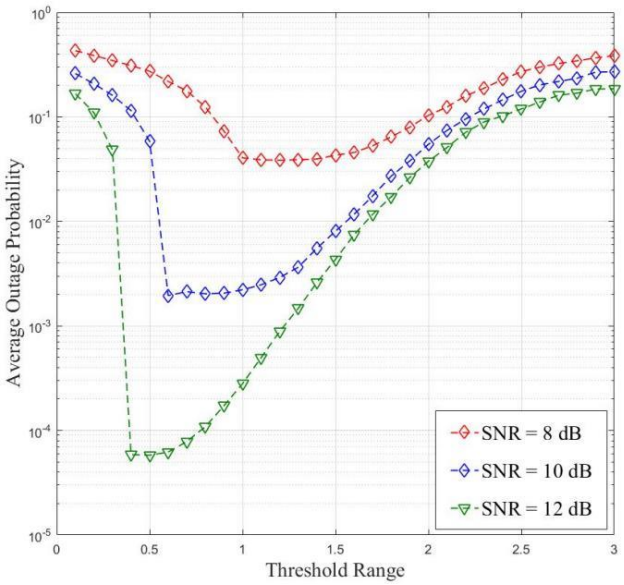

Figure 3. Average outage probability vs threshold range for U = 10 and m = 5 with varying SNR values.

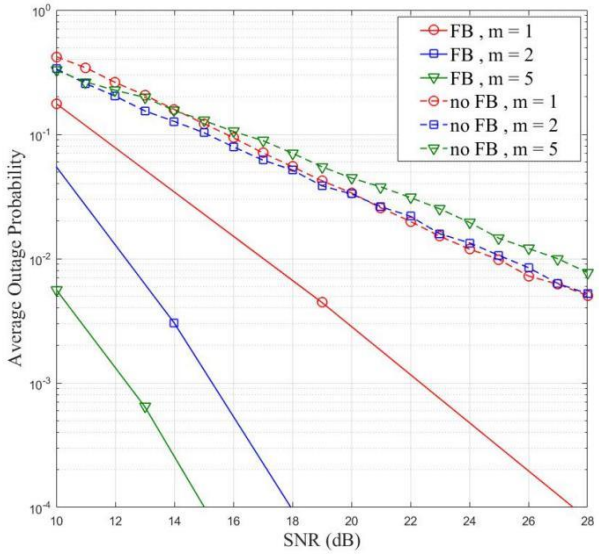

Figure 4. Average outage probability comparison between the limited FB and no FB (random user scheduling) of ZF V-BLAST for U = 5 with varying SNR values.

JSR A
Journal of Scientific Reports

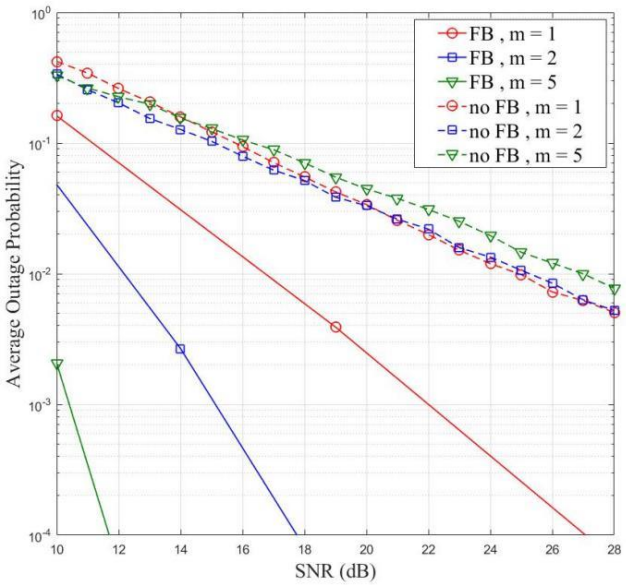

Figure 5. Average outage probability comparison between the limited FB and no FB (random user scheduling) of ZF V-BLAST for U = 10 with varying SNR values.

4. CONCLUSION

The performance of the ZF V-BLAST with the optimum ordering and limited FB method has been presented in a U-user downlink network system where the transmitter has two antennas and every user is equipped with r ($r \geq 2$) antennas. Each user reports back a single bit FB (either bit 1 or 0) regarding its sub-channel gain to the transmitter. In each training cycle, the transmitter only selects and schedules one user to communicate with based on the FB data. The user scheduling is carried out by applying a threshold value. The limited FB strategy is implemented in different scenarios, including the number of users, the fading parameter of Nakagami-m channels, the SNR values, and the threshold values. The numerical optimization process is implemented to obtain the optimum threshold values and the results show that as SNR increases, the attained threshold gets closer to zero value for every shape parameter. The simulation results of the investigated FB system on multiuser ZF V-BLAST have shown that the performance of the adopted limited FB method exceeds that of the no FB technique. Furthermore, for the multiuser ZF V-BLAST, the AOP outcomes of the random user scheduling (no FB) technique show almost similar results regardless of the value of the m-parameter while the FB scheme yields better performance as the shape parameter value gets higher.

ACKNOWLEDGEMENT

The authors acknowledge the support provided by Presidency for Turks Abroad and Related Communities (YTB).

REFERENCES

[1] Foschini, G.J., Golden, G.D., Valenzuela, R.A. and Wolniansky, P.W., (1999), Simplified processing for high spectral efficiency wireless communication employing multi-element arrays. IEEE Journal on Selected Areas in Communications, 17(11), 1841-1852.

[2] Loyka, S. and Gagnon, F., (2004), Performance analysis of the V-BLAST algorithm: an analytical approach. IEEE Transactions on Wireless Communications, 3(4), 1326-1337.

[3] Zhang, X., Lv, Z. and Wang, W., (2008), Performance analysis of multiuser diversity in MIMO systems with antenna selection. IEEE Transactions on Wireless Communications, 7(1), 15-21.

[4] Zhang, X., Chen, F., and Wang, W., (2007), Outage probability study of multiuser diversity in MIMO transmit antenna selection systems. IEEE Signal Processing Letters, 14(3), 161-164.

[5] Yu, X., Dang, X., Leung, S., Liu, Y. and Yin, X., (2014), Unified analysis of multiuser scheduling for downlink MIMO systems with imperfect CSI. IEEE Transactions on Wireless Communications, 13(3), 1344-1355.

[6] Gesbert, D. and Alouini, M.-S., (2004), How much feedback is multi-user diversity really worth?. 2004 IEEE International Conference on Communications (IEEE Cat. No.04CH37577), 234-238.

[7] Zhang, W. and Letaief, K.B., (2007), MIMO broadcast scheduling with limited feedback. IEEE Journal on Selected Areas in Communications, 25(7), 1457-1467.

[8] Amelia, K., Özyurt, S. and Namdar, M., (2022), Performance of multiuser zero-forcing V-BLAST under 1-bit feedback for user scheduling. 2. International Cappadocia Scientific Research Congress, 1617-1623.

[9] Özyurt, S. and Kucur, O., (2020), Performance of multiuser TAS/MRC with 1-bit feedback user scheduling over correlated fading channels. AEU - International Journal of Electronics and Communications, 121,153210, ISSN 1434-8411.

[10] Al-Ghadhban, S., (2014), Opportunistic round robin scheduling for V-BLAST systems over multiuser MIMO channels. J Wireless Com Network 2014, 128.

[11] Nakagami, N., (1960), The m-Distribution, a general formula for intensity distribution of rapid fading. Hoffman, W.G., Ed., Statistical Methods in Radio Wave Propagation, 3-35.

[12] Popovic, H., Stefanovic, D., Mitic, A., Stefanovic, I. and Stefanovic, D., (2007), Some statistical characteristics of Nakagami-m distribution. 2007 8th International Conference on Telecommunications in Modern Satellite, Cable and Broadcasting Services, 509-512.

[13] Turin, G.L., Clapp, F.D., Johnston, T.L., Fine, S.B. and Lavry, D., (1972), A statistical model of urban multipath propagation. IEEE Transactions on Vehicular Technology, 21(1), 1-9.

[14] Suzuki, H., (1977), A statistical model for urban radio propagation. IEEE Transactions on Communications, 25(7), 673-680.

[15] Reşat, M.A., Karakoç, M.C. and Özyurt, S., (2020), Enhancement of physical layer security in Alamouti OFDM systems over Nakagami-m fading channels. 2020 28th Signal Processing and Communications Applications Conference (SIU), 1-4.

Kütahya Dumlupınar University
Institute of Graduate Studies

Journal of Scientific
Reports-A
E-ISSN: 2687-6167
Number 51, December 2022

RESEARCH ARTICLE

LIGHTWEIGHT AGGREGATE PRODUCTION by RAPID SINTERING TERRA ROSSA-NaOH MIXTURES in MICROWAVE OVEN

Mehmet Uğur TOPRAK[1,*], Kübra ÇEKİL[2]

[1*]Kütahya Dumlupınar University, Engineering Faculty, Civil Engineering Department, mugur.toprak@dpu.edu.tr,
ORCID:0000-0001-5483-2871
[2]Kütahya Dumlupınar University, Engineering Faculty, Civil Engineering Department, kubracekil@hotmail.com,,
ORCID:0000-0002-9064-4293

Receive Date:30.09.2022 *Accepted Date: 08.11.2022*

ABSTRACT

In this study, the use of microwave ovens (MO) in the production of lightweight aggregates (LWA) with rapid sintering method was investigated. Sintering temperatures up to 1200 C° was obtained by using SiC coated microwave kiln in MO. LWA were produced by rapid sintering terra rossa (TR)-NaOH mixtures at MO. Alkali amount (2.5, 5 and 7.5% NaOH by weight of TR), drying type (no drying, drying in laboratory at 20 °C or in oven at 80 °C for one day) and sintering time (8, 12 and 18 min) on the physical, mechanical and microstructure of aggregates were investigated. The aggregate pellets dried in oven were stronger than those dried in the laboratory. Thus the sintering cracks diminished and the compressive strengths were enhanced for aggregates. The highest compressive strength (36.96 kg/cm^2) was obtained in aggregates using 2.5% NaOH by weight of TR, dried in oven and rapid sintered for 18 minutes. When more alkali (5% NaOH) was used, due to the increase in flux content; the aggregate shell formed earlier and had more time to expand up to 127%. Thus the unit weight (0.67 g/cm^3) and compressive strength (4.74 kg/cm^2) of the aggregate were decreased.

Keywords: *Rapid sintering, Microwave, Terra rossa, Lightweight aggregate, Compressive strength*

1. INTRODUCTION

Humans first kneaded and shaped the soil, which can remain intact later, in the Paleotic era, 35,000 years ago [1]. Terra rossa (TR) are reddish, bordeaux and brownish clay and silt-sized soils commonly found in the Mediterranean region. TR consists of clay minerals such as sericite, montmorillonite, illite, chloride, hydromica and silicon compounds, clay minerals rich in Fe2O3, clay minerals, albeit in small quantities, with a fine material content of more than 20%, containing less than 30% Al2O3 [2]. Soft and very fine-grained feldspar with a high amount of clay, aluminum and silica, with a large amount of fine grains, is called a sedimentary mineral formed by the decomposition of mica and other silicates. Clay makes it easier to shape the soil. It is of great importance that the type and amount of clay in the soil is suitable for lightweight expanded clay aggregate (LECA) production [3]. LECA can

JSR A
Journal of Scientific Reports

be produced by drying, heating and rapid sintering plastic clay having too low or no lime content in rotary kilns at 1100 to 1300 °C [4]. LECA were commonly used as lightweight filler material in geotechnical works and production of lightweight concrete [5].

At high sintering temperatures, the aggregate pellets become pyroplastic. In the meantime, the gas phase is formed from the combustion of organic materials, water vapor, reduction of iron oxides and decomposition of carbonates and sulfates. In the pyroplastic state, gases trying to escape inflates the closed pores of agregate. Thus increases up to 5-6 times in the volume of agregate can be observed [6, 7, 8, 9, 10,11]. Na_2O can significantly reduce the viscosity of the silicate melt by depolymerizing the silicate networks [12]. Ge et al. [13] observed that increasing the Na_2O contents reduced the viscosity of ceramic foams sintered.

Microwaves are defined as electromagnetic radiations with wavelengths ranging from 100 cm to 1 mm. Microwave ovens operate at frequencies in the range of 950 MHz and 2450 MHz. It became widespread with the use of radar in the second world war. Later, microwave ovens entered the interiors of homes and were used for tasks such as heating food. Microwaves stimulate molecules or ions [14]. It is stated that the sintering time of Nickel-Zinc ferrites has been reduced from 9 hours to 4 hours and less than 69% energy is used by microwave sintering.The sintering time of alumina decreased from 15-20 hours to 6 hours and 65% less energy was consumed by microwave sintering. The pure Al_2O_3 sample from room temperature to 1700°C using 60 GHz radiation, an intensity of 95.7% was achieved over a period of 6 hours.To achieve a density of 95.7% of the same type of samples, conventional sintering requires sintering at 1600 °C for 20 hours. In any case, microwaves have produced fine-grained structures than traditional sintering. As a result, the materials became denser, stronger and more durable. At the same time, they have undergone less deformation and breakage during production. Microwave technology has been shown to significantly shorten the sintering time. The microwave sintering method is most often used in the sintering of ceramics [15]. Silicon carbide (SiC) is high temperature resistant microwave-absorber. Besides it has good chemical stability and mechanical strength and it is readily available [16, 17]. Thus SiC coated microwave kiln was used in this study to reach high sintering temperatures.

A significant part of the area of Kütahya-Turkey was occupied by mountain terrains/high lands, which are meta-carbonate rocks (marbles). The most characteristic types of red soil over carbonate rocks are Terra Rossa. The TR can be suitable as raw material in the brick and roofing tile industry. The present study presents the results of a master thesis [18] that was motivated by a lack of data on the production of aggregates by rapid sintering of TR-NaOH mixtures at microwave oven. This paper aims to determine the contribution of alkali amout, drying type and rapid sintering time to the physical and mechanical properties of aggregates.

2. MATERIALS AND METHOD

Terra rossa (TR) collected from the village of Çöğürler in Kütahya/Turkey was ground by a ringed mill (Fig.1) to increase the surface area up to 2700 cm^2/g. The TR was mainly composed of SiO_2, and Al_2O_3 (Table 1). Aggregates were produced by i) mixing TR with technical grade NaOH (>99% purity obtained from Detsan Chemicals Company in Eskişehir/TURKEY) and 33% water by weight of

JSR A
Journal of Scientific Reports

TR+NaOH for 3 minutes and forming pellets by hand ii) drying them for one day or no drying iii) rapid sintering them at microwave oven.

Table 1. Oxide content of TR.

Oxide content	SiO_2	Al_2O_3	Na_2O	K_2O	TiO_2	Fe_2O_3	CaO	MgO	MnO	Cl	SO_3	*LOI
% mass	56.07	15.98	0.14	1.93	0.57	6.52	1.91	1.27	0.11	0.06	0.05	15.25

*LOI: Loss on ignition

A total of 27 series were produced. Variables were alkali amount (2.5, 5 and 7.5% by weight of TR), drying type (drying them at 20±2 °C in laboratory for one day: L or 80 °C in oven (Fig.1) for one day: O or no drying: N) and rapid sintering time (sintering them at microwave oven given in Fig.1 for 6, 12 or 18 mins). As an example series produced with 5% NaOH by weight of TR, dryed for one day at 20±2 °C in laboratory and rapid sintered in microwave oven (MO) for 18 mins was named as NH5-L18.

Household microwave with output power of 700 Watts and microwave frequency of 2450 Megahertz was used.), SiC coated microwave kiln given in Fig. 2 was used to absorb microwaves and reach high sintering temperatures. The temperatures of aggregate shell were determined as 840, 980 and 1200 °C with infrared thermometer after 6, 12 and 18 mins of sintering at highest power.

Figure 1. The photos of (a) ringed mill, (b) blaine device, (c) oven and (d) household microwave oven
Unit weight (UW) of the aggregates were calculated according to TS EN 1097-6 [19]. Fracture load of agregates were determined by one point loading device using aparatus given in Fig. 2 to spread the load uniformly. One point loading device was preferred for precise measurement of the little crushing loads. All the reported results are the means of three samples. The crushing strength (σ, kg/cm^2) for speherical aggregates are calculated by the equation 1 where: P: fracture load (kN), and X: the distance between loading points (mm) [20, 21]. SEM-EDX analyses on core and shell of the aggregates were conducted.

JSR A
Journal of Scientific Reports

σ =((2.8*1000*P) / (π*X²)) (Yıldırım & Özturan, 2013) (1)

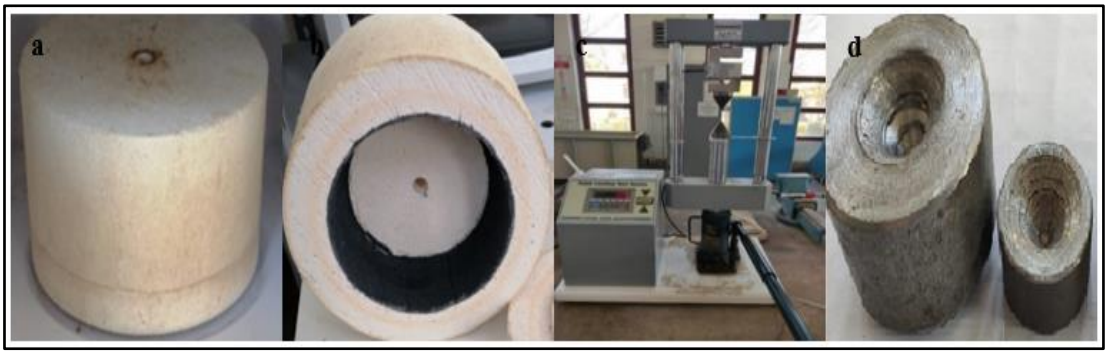

Figure 2. The photos of (a), microwave kiln (b), SiC coating inside the kiln (c) single point loading device (d) apparatus to spread the load uniformly

3. EXPERIMENTAL RESULTS

3.1. Evaluation of Aggregate Photos

The photos of aggregates with different NaOH amounts, drying types and sintering times were shown in Fig. 3-5. Sintering times of 6 minutes was inadequate and caused cracking on the outer shell of aggregates as seen in Fig. 3. Aggregates which were sintered without drying were too week and crushed during sintering. Increasing the amount of NaOH, cracks in the outer shell of aggregates were decreased. The surface of oven dried aggregates were smoother compared to others.

JSR A
Journal of Scientific Reports

Figure 3. The photos of (a) NH2.5-N6, (b) NH2.5-L6, (c) NH2.5-O6, (d) NH5-N6, (e) NH5-L6, (f) NH5-O6, (g) NH7.5-N6, (h)NH7.5-L6 (ı) NH7.5-O6.

As the MW sintering time increased sintering enhanced. There is a noticeable formation of glassy phase on surface of aggregate on series produced with 5 and 7.5% NaOH by weight of TR (Fig. 4). Noticeable amount of expansion were not seen for sintering of 12 mins.

JSR A
Journal of Scientific Reports

Figure 4. The photos of (a) NH2.5-N12, (b) NH2.5-L12, (c) NH2.5-O12, (d) NH5-N12, (e) NH5-L12, (f) NH5-O12, (g) NH7.5-N12, (h)NH7.5-L12 (ı) NH7.5-O12.

As a result of the visual examinations in Fig 5, the colour of aggregates got darker with increasing sintering time. After sintering the iron element in oxidation state II oxidised to state III could be responsible from darker colours of aggregates [22, 23]. Glassy phase enhanced in the aggregates sintered for 18 minutes.

JSR A
Journal of Scientific Reports

Figure 5. The photos of (a) NH2.5-N18, (b) NH2.5-L18, (c) NH2.5-O18, (d) NH5-N18, (e) NH5-L18, (f) NH5-O18, (g) NH7.5-N18, (h)NH7.5-L18 (ı) NH7.5-O18.

3.2. Evaluation of Physical and Mechanical Properties

The aggregates produced with 5% NaOH by weight of TR and 18 mins of sintering time showed the highest expansion rates. After rapid sintering in microwave oven (MO) shrinkage up to 31.4% (NH7.5-N6) and expansion up to 127% (NH5-L18) were observed in aggregates. NaOH accumulated on the aggregate shell by diffusion of alkali solution during drying. By the aid of fluxing alkalis, the shell formation accelerated. Since sintering time is constant for all aggregates, there was more time for expansion of aggregate pellets produced with more NaOH.

Drying at laboratory also supported the expansion of aggregate by holding more water in aggregate pellet. Escaping of the water vapour during sintering blowed up the aggregate. The lowest unit weight (0.67 gr/cm^3) was obtained for NH5-L18. The highest unit weight was 2.13 g/cm^3 for NH2.5-O18. Drying in oven at 80 °C excessively decreased the water content of aggregate pellets. Thus there were not enough water steam that will blow the aggregate during sintering.

JSR A
Journal of Scientific Reports

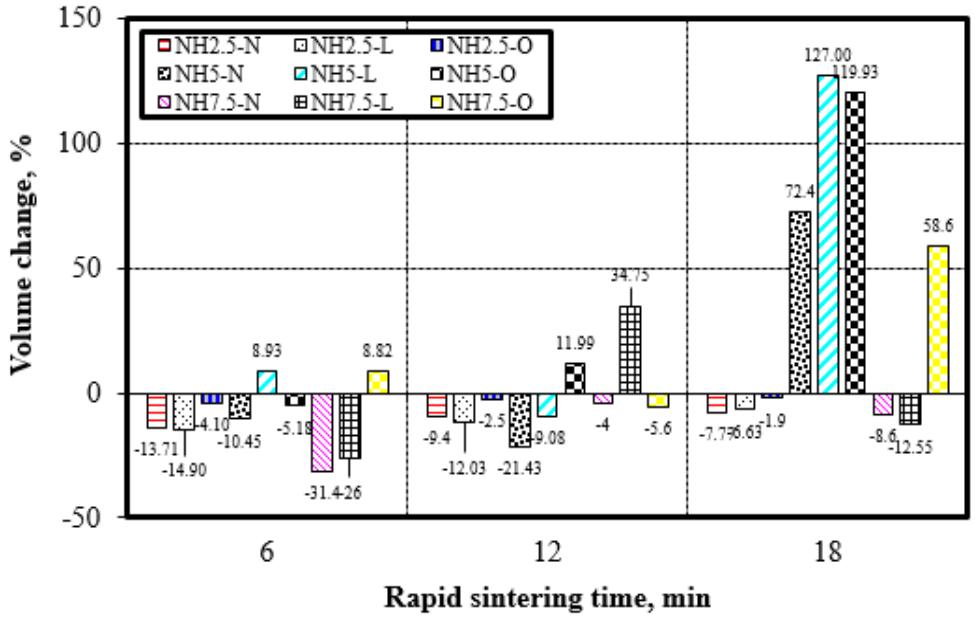

Figure 6. Volume change of the aggregates.

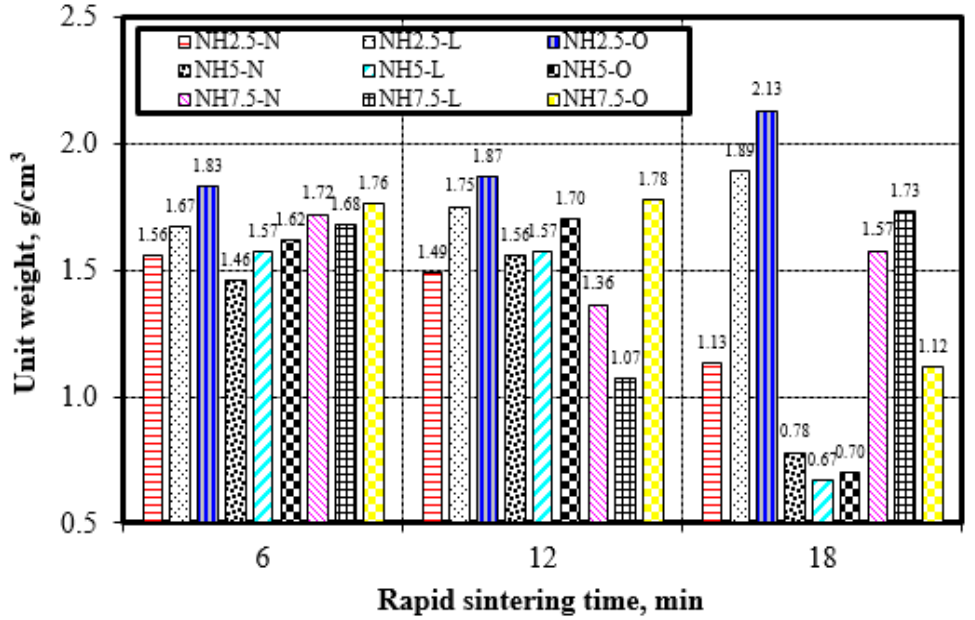

Figure 7. Unit weight of the aggregates.

JSR A
Journal of Scientific Reports

Drying process significantly affected the water absorption by weight (WA) of aggregates. The highest WA were obtained for aggregates that were not dryed before sintering. The lowest values were obtained for aggregates sintered for 18 mins. Thus drying before sintering decreased the WA.

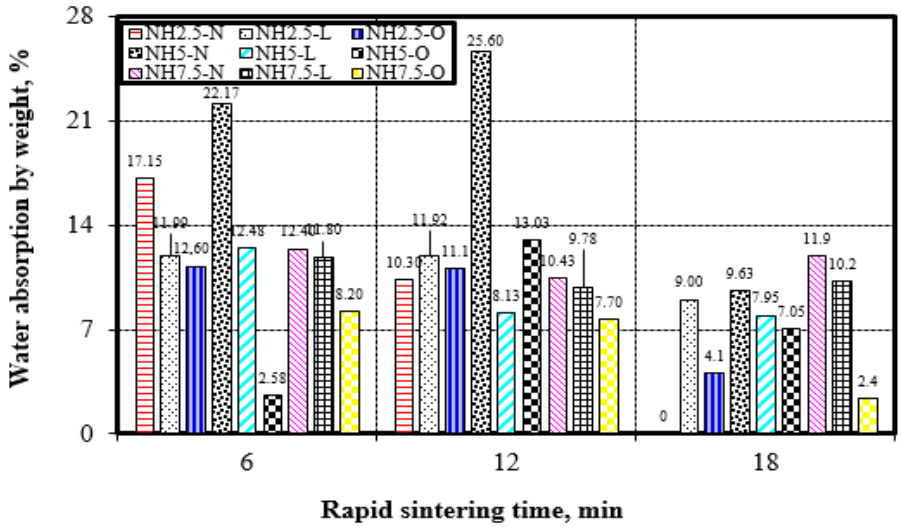

Figure 8. Water absorption of the aggregates.

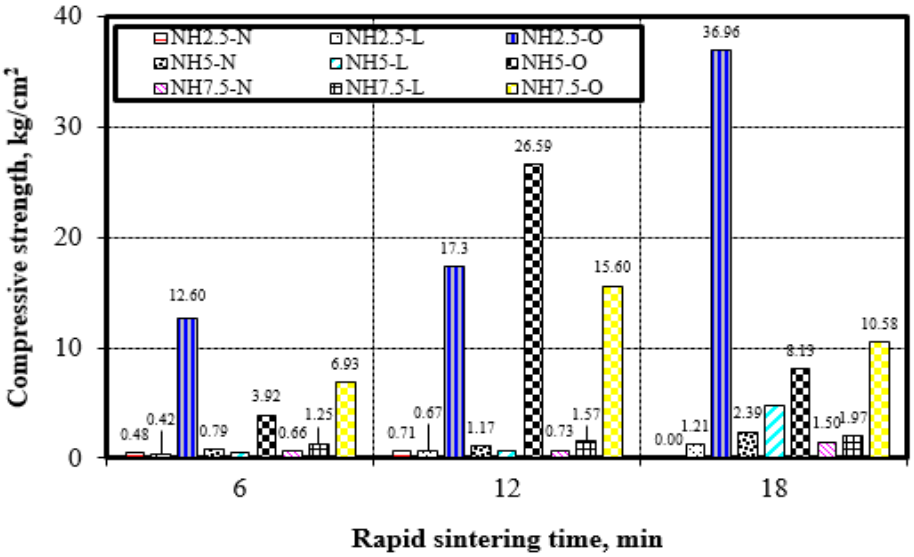

Figure 9. Compressive strength of the aggregates.

JSR A
Journal of Scientific Reports

The compressive strength of NH2.5-018 (36.96 kg/cm^2) is much higher than that of NH5-L18 (4.7 kg/cm^2). It is clearly seen from aggregate photos for sintering time of 18 mins (Fig.5) that the NH2.5-O18 forms a thicker and stronger shell than NH5-L18. This situation coincides with SEM analysis. It was revealed that aggregates can be produced by rapid sintering TR-NaOH mixtures in MO.

3.3. Evaluation of SEM-EDX Analysis

Most of the ceramics are transparent to microwaves at 2.45 GHz for low temperatures. Susceptors absorbing the microwaves and transferring the heat to the material were used for microwave sintering of ceramics. Until the critical temperature, susceptors heat the material from surface to core. Then the material starts to absorb the microwaves and participate to sintering process [24, 25]. Lyra et al. produced light weight aggregates (LWA) by microwave oven using silicon carbide as susceptor or electric oven for sintering red clay-sugarcane bagasse ash mixtures. They indicated with SEM observations that the pores were closed and homogeneously distributed when sintered with microwave oven. Lower water absorption and higher compressive strength values were obtained when compared with electric oven sintering [26]. A significant expansion was seen in NH5-L18 from the SEM images compared to NH2.5-O18. NH5-L18 expanded 127% by volume, while reducing the unit weight of aggregate to 0.67 g/cm^3. In NH5-L18, amount and diameter of pores were bigger. Low water absorption of NH2.5-O18 could be linked to it's lower porosity than NH5-L18.

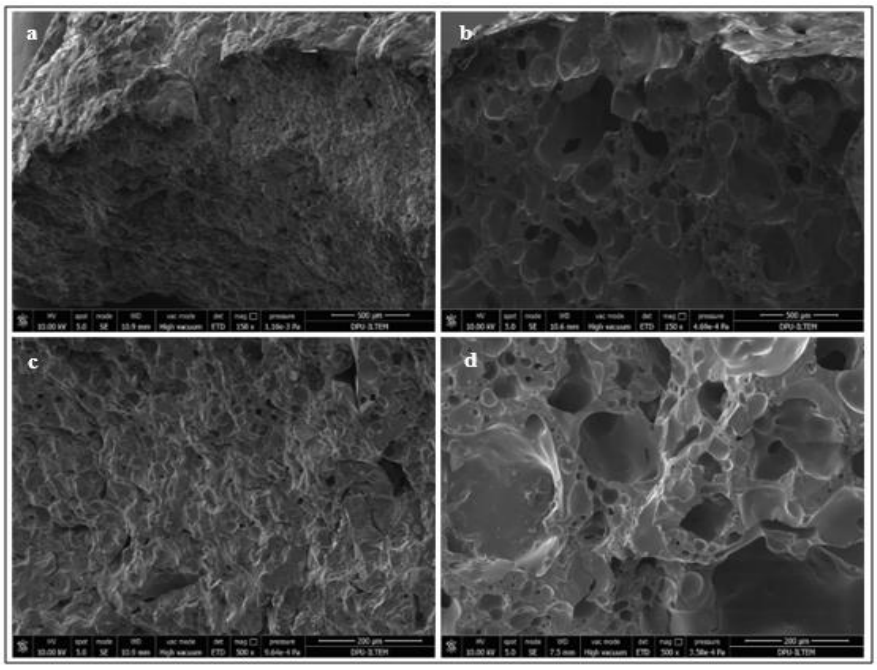

Figure10. SEM photo (150X) of aggregate shell (a) NH2.5-O18, (b) NH5-L18 and (500X) of aggregate core (c) NH2.5-O18, (d) NH5-L18.

JSR A
Journal of Scientific Reports

NH2.5-O18 have a homogeneous structure with small cracks and pores. It is seen in EDX data (full area 1) that the amount of alkali is significantly lower than NH5-L18 (selected area 2). NH5-L18 aggregate appears to contain quartz crystals in the glassy structure, indicated by a SiO_2 ratio of 93% (selected area 1). This structure was also seen as white grains in aggregate photos (Fig 3-5). NaOH accumulated on the aggregate shell by diffusion of alkali solution during drying. By the aid of fluxing alkalis, formation of the aggregate shell accelerated. Since sintering time is constant for all aggregates, there was more time for expansion of aggregate pellets produced with more NaOH. Drying at laboratory also supported the expansion of aggregate by holding more water in aggregate pellet.

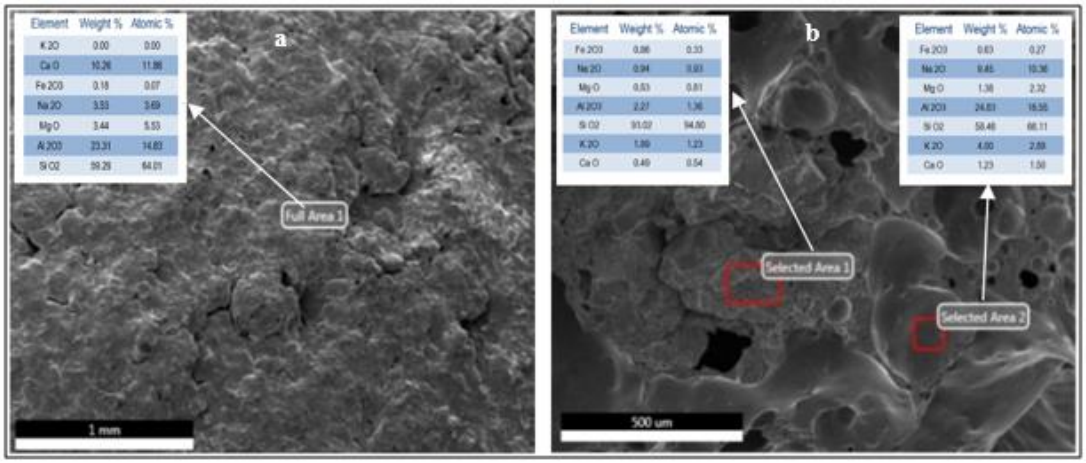

Figure 11. SEM-EDX analysis of (a) NH2.5-O18, (b) NH5-L18.

4. CONCLUSIONS

Lightweight expanded clay aggregates are produced by rapid sintering in tunnel kilns all over the world. This study revealed that lightweight aggregates can also be produced by rapid sintering in household microwave oven. Industrial microwave ovens can be used for commercial production and optimization of the process. Cost analyses should also be performed for commercial use. As the sintering time increased colours of the aggregates got darker. The rapid sintering time of 6 mins was very short to reach adequate sintering temperature for Terra rossa-NaOH mixtures. Aggregate pellets produced with more NaOH expanded more. Drying at laboratory also supported the expansion of aggregate by holding more water in aggregate pellet. The lowest unit weight (0.67 gr/cm^3) was obtained for NH5-L18. The highest unit weight was 2.13 g/cm^3 for NH2.5-O18. The aggregate pellets dried in oven were stronger than those dried in the laboratory. The highest compressive strength (36.9 kg/cm^2) was obtained for NH2.5-L18. For future studies, minerals containing higher alkali content can be effective raw materials for lightweight aggregate production.

ACKNOWLEDGMENT

The authors, acknowledge the Center for Advanced Technologies of Kütahya Dumlupınar University for their help in analysis. This research did not receive any specific grant from funding agencies.

REFERENCES

[1] Ceramic history., (2016, 10 February). Access Address: https://hititterra.com/seramik-tarihcesi.

[2] Cengiz, O. and Kuşçu, M., (2010), Usability of Anamas Mountains-Isparta terra rossa in brick-tile production (Unpublished Master Thesis). Süleyman Demirel University, Institute of Science and Technology, Isparta.

[3] Rice, P.M., (1987), Pottery analysis, Chicago: The University of Chicago Press.

[4] Rashad, A.M., (2018), Lightweight expanded clay aggregate as a building material-An overview, Construction and Building Materials, 170, 757-775.

[5] Roces, E., Menéndez, M.M, Galindo, J.G, Estaire J., (2021), Lightweight expanded clay aggregate properties based on laboratory testing, Construction and Building Materials, 313, 125486, https://doi.org/10.1016/j.conbuildmat.2021.125486.

[6] Rattanachan, S., Lorprayoon C., (2005) Korat clays as raw materials for lightweight aggregates. Sci. Asia., 31, 277-281. doi: 10.2306/scienceasia1513-1874.2005.31.277.

[7] Kowalenko, W., Mojsiejenko, J., Roszak, W., (1972), Artificial Lightweight Aggregate, Production and Application, Arkady; Warsaw, Poland, 120-283.

[8] Piasecki, J., (1992), Structure of Grains of Lightweight Expanded Clay Aggregate a Model Approach. Scientific Works of Szczecin University of Technology, Institute of Civil Engineering; Szczecin, Poland, 69-77.

[9] Osiecka, E., (2000) Selected Issues on the Technology of Mineral Construction Composite Materials. Warsaw University of Technology; Warsaw, Poland, 98-184.

[10] de'Gennaro R., Cappelletti, P., Cerri, G., de'Gennar, M., Dondi, M., Langella, A. (2004), Zeolitic tuffs as raw materials for lightweight aggregates. Appl. Clay Sci., 25, 71-81. doi: 10.1016/j.clay.2003.08.005.

[11] Latosińska, J, Żygadło, M, Czapik, P., (2021), The Influence of Sewage Sludge Content and Sintering Temperature on Selected Properties of Lightweight Expanded Clay Aggregate. Materials, 14-3363, 1-17. doi: 10.3390/ma14123363.

[12] Kang, J., Wang, J., Zhou, X., Yuan, J., Hou, Y., Qian, S., Li, S., Yue, Y., (2018), Effects of alkali metal oxides on crystallization behaviour and acid corrosion resistance of cordierite based glass-ceramics, J. Non-Cryst. Solids, 481, 184-190.

[13] Ge, X., Zhou, M., Wang, H., Chen, L., Li, X., & Chen, X., (2019), Effects of flux components on the properties and pore structure of ceramic foams produced from coal bottom ash, Ceramics International, 45-9, 12528-12534.

[14] Avcı, M., (2018, 25 May, Microwave, Access Address: https://www.foodelphi.com/mikrodalga-teknolojisi/.

[15] Nabi, G., (2018, 5 February), Microwave sintering method, Access Address: https://docplayer.biz.tr/109511016-Mikrodalga-sinterleme-yontemi.html.

[16] Li, Q., Ye, R., Jin, R., Chen, H., Xia, G., & Li, T., (2020), Experimental study on dielectric properties of SiC material and temperature distribution of rubber materials containing silicon carbide coated metal via microwave heating. IOP Conference Series: Materials Science and Engineering, 772(1), 012012. https://doi.org/10.1088/1757-899x/772/1/012012.

[17] Wu, R., Zhou, K., Yue, C. Y., Wei, J., & Pan, Y., (2015). Recent progress in synthesis, properties and potential applications of SiC nanomaterials. Progress in Materials Science, 72, 1-60. doi: 10.1016/j.pmatsci.2015.01.003.

[18] Çekil, K., (2022), Mikrodalga sinterleme ile agrega üretimi, Yüksek Lisans Tezi, Kütahya Dumlupınar Üniversitesi, Fen Bilimleri Enstitüsü, Kütahya.

[19] EN 1097-6, (2015), Tests for mechanical and physical properties of aggregates - Part 6: Determination of particle density and water absorption, Comite European de Normalisation.

[20] Kockal N.U, Özturan T. (2011) Characteristics of lightweight fly ash aggregates produced with different binders and heat treatments, Cement and Concrete Composites, Volume 33-1, 61-67. https://doi.org/10.1016/j.cemconcomp.2010.09.007.

[21] Hiramatsu, Y., & Oka, Y., (1966), Determination of the tensile strength of rock by a compression test of an irregular test piece. Int. Journal of Rock Mechanics and Mining Sciences & Geomechanics Abstracts, 3-2, 89-90. doi:10.1016/0148-9062(66)90002-7.

[22] De' Gennaro, R., Cappelletti, P., Cerri, G., de' Gennaro, M., Dondi, M., Guarini, G., Naimo, D., (2003), Influence of zeolites on the sintering and technological properties of porcelain stoneware tiles. Journal of the European Ceramic Society, 23-13, 2237-2245.

[23] Duvarcı, Ö.Ç., Akdeniz, Y., Özmıhçı, F., Ülkü, S., Balköse, D., Çiftçioğlu, M., (2007), Thermal behaviour of a zeolitic tuff, Ceramics International, 33-5, 795-801.

[24] Bhattacharya, M., Basak, T.A., (2016), Review on the susceptor assisted microwave processing of materials. Energy, 97, 306-38. https:// doi.org/10.1016/j.energy.2015.11.034.

[25] Lyra, G.P, Santos, V., Pallone, E.M.D.J.A., Herta Goldschmidt, A.K.R., De Santis, B.C., Adriano Rossignolo, J., (2021), Microwave hybrid fast sintering of red clay ceramics. Int. J. Appl. Ceram Technol., 18, 705-715. https://doi.org/10.1111/ijac.13676.

[26] Lyra, G.P., Santos, V., De Santis, B.C., Rivaben, R.R., Fisher, C., Pallone, E.M.D.J.A., Adriano Rossignolo, J., (2019), Reuse of sugarcane bagasse ash to produce a lightweight aggregate using microwave oven sintering, Construction and Building Materials, 222-20, 222-228. https://doi.org/10.1016/j.conbuildmat.2019.06.150.

Kütahya Dumlupınar University
Institute of Graduate Studies

Journal of Scientific
Reports-A
E-ISSN: 2687-6167
Number 51, December 2022

RESEARCH ARTICLE

A DEEP TRANSFER LEARNING FRAMEWORK for the STAGING of DIABETIC RETINOPATHY

Gökalp ÇINARER[1], Kazım KILIÇ[2], Tuba PARLAR[3,*]

[1]Bozok University, Department of Computer Engineering, Yozgat, gokalp.cinarer@yobu.edu.tr, ORCID:0000-0003-0818-6746
[2]Bozok University, Department of Computer Technologies, Yozgat, kazim.kilic@yobu.edu.tr, ORCID: 0000-0003-2168-1338
[3*]Mustafa Kemal University, Department of Computer Technologies, Hatay, tparlar@mku.edu.tr, ORCID:0000 0002 8004 6150

Receive Date:25.08.2022 *Accepted Date: 30.09.2022*

ABSTRACT

Diabetes is a highly prevalent and increasingly common health disorder, resulting in health complications such as vision loss. Diabetic retinopathy (DR) is the most common form of diabetes-caused eye disease. Early diagnosis and treatment are crucial to prevent vision loss. DR is a progressive disease composed of five stages. The accurate diagnosis of DR stages is highly important in guiding the treatment process. In this study, we propose a deep transfer learning framework for automatic detection of DR stages. We examine our proposed model by comparing different convolutional neural networks architectures: VGGNet19, DenseNet201, and ResNet152. Our results demonstrate better accuracy after applying transfer learning and hyper-parameter tuning to classify the fundus images. When the general test accuracy and the performance evaluations are compared, the DenseNet201 model is observed with the highest test accuracy of 82.7%. Among the classification algorithms, the highest AUC value is 94.1% obtained with RestNet152.

Keywords: *Convolutional neural networks, CNNs, Deep learning, Diabetic retinopathy, Transfer learning.*

1. INTRODUCTION

Diabetes is a major public health concern, estimated to affect around half a billion people worldwide [1]. It can lead to a variety of complications, such as heart attack, stroke, and vision loss. Among various types of eye diseases that occur due to diabetes, the most common type is diabetic retinopathy (DR). Changes in the vessels as a result of the disease's damage to the light-perceiving retina layer cause vision loss [2]. DR occurs in several stages. The early stage of DR is non-proliferative diabetic retinopathy (NPDR), being the first indicator of abnormal changes in the eye [3]. In this stage, there are three important levels: mild, moderate, and advanced. The veins start abnormally leaking out substances that cause fluid accumulation. Consequently, the nutrition of the retina begins to deteriorate, and if not treated, the disease will slowly continue to progress [4]. In the later stages, or the proliferative diabetic retinopathy (PDR) stage, new vessel formation along the retinal surface and disruptions in tissue nutrition are observed. The thinness of these new vessel formations causes

intraocular bleeding. With intense bleeding, retinal layer deterioration occurs, and vision loss becomes inevitable [5]. Therefore, accurate detection of DR stages is very vital for treatment. In the diagnosis of DR-induced diseases, devices such as optical coherence tomography (OCT), fundus fluorescein angiography (FFA), and eye ultrasonography (USG) are used. The use of artificial intelligence algorithms in medical image synthesis facilitates the interpretation of medical images and helps medical professionals in the treatment process by obtaining quantitative measurements from the images [6, 7].

There are many different studies for the detection of DR disease stage using retinal fundus images with machine learning methods in the literature [8-11]. Many recent studies have focused on the diagnosis of retinal diseases with deep learning algorithms [7, 12-15], such as the definition of retinal regions with hemorrhage using FFA images [16], determination and classification of retinal images [17], mathematical morphology and template matching assisted retinal hemorrhage detection [18]. In studies, it is seen that for images the preprocessing step is very important to remove the noise. In medical imaging, wavelet transformation has also been applied to fundus images with high-band filters. Rehman et al. [19] obtain an accuracy of 97.85% using the support vector machines algorithm with two classes. Jiang et al. [20] classify 8626 images using the CNNs model as DR and no DR with an accuracy of 75.70%. Gao et al. [21] study with four classes and resize the fundus images to 600x600 pixels and then divide them into 300x300 pixels. Then they transfer these parts to a single vector with four different InceptionNetV3 models. They achieve an accuracy of 88.72% in classifying DR stages in four classes.

Sarki et al. [15] use the ImageNet dataset as a transfer learning model. They have experimented with different CNNs models such as ResNet50, DenseNet, Xception, and VGGNet. Among these models, they obtain the highest accuracy of 86% using ResNet50. Wang et al. [14] examine a transfer learning model by comparing different CNNs models including AlexNet, VGG16, and InceptionNetV3 on the Kaggle dataset. They crop the images to different sizes for each model to classify them into five classes accurately. They obtain the highest accuracy of 63.2% using the InceptionNetV3 model. Another study [17] investigates performances of transfer learning by using three CNNs architectures, namely AlexNet, ResNet, GoogleNet, and VGG on the Kaggle dataset. They obtain the best classification accuracy of 95.68% with the VGG-s model. Sugeno et al. [7] use EfficientNet-B3 which is a transfer learning CNNs model on APTOS 2019 Kaggle dataset. They crop the images to 416x416 pixels. They compare their model EfficientNet-B3 against ResNet50 and VGG16 and obtain sensitivity and specificity values greater than 0.98. On the other hand, morphological procedures performed to clarify retinal blood vessels are widely used in different studies [33-36]. These processes positively increase the accuracy of DR detection. For this reason, morphological processes are applied to the fundus images to highlight the retinal blood vessels.

In this paper, we propose a new deep neural network architecture that is a deep transfer learning-based image detection and classification model to accurately diagnose the five stages of DR. For this purpose, experiments are conducted to classify in five stages: one stage of no DR and four levels of DR lesions. In the preprocessing step, color space transformation, noise removal, segmentation mask determination of the relevant region, and cropping from the mask coordinates are applied in the fundus images. For DR stage detection, cropped images are clarified by the contrast limited adaptive

histogram equalisation (CLAHE) method. DR stage is diagnosed more accurately using our proposed model. The contributions of the research to the literature are as follows:

- In the study, data augmentation is applied only to the training set, and the test set consists of independent data.
- Fundus images are classified at 5 different levels.
- CLAHE is used to highlight the eye vessels.
- Well-known CNN architectures are used for feature extraction, classification, and their performances are compared.
- The results obtained are presented in a table based on class.

This paper is organized as follows, in this section we introduce the study and summarise the previous studies. Section 2 explains the methods we used. Section 3 presents and discusses our experimental results. Finally, Section 4 provides our conclusions.

2. MATERIALS AND METHODS

2.1. Dataset

Different procedures can be performed for the detection of blood vessels on the retina, determination of the optic disc and macular region, staging of DR, and detection of lesions. In this study, the classification process of fundus images is run on the open-source Kaggle APTOS 2019 dataset, which has been used in many recent studies with deep learning models. This dataset is introduced by the Asia Pacific Tele-Ophthalmology Society [22]. DR is classified into five stages according to the disease state. In this dataset, these five stages of DR are defined as follows:

- normal: patients without diabetic retinopathy.
- mild non-proliferative retinopathy stage: mild swelling occurs in the blood vessels of the retina.
- moderate non-proliferative retinopathy stage: the blood vessels are swollen and complex and blood carrying capacity is low.
- severe non-proliferative retinopathy stage: the blood vessel is clogged and the blood circulation around the retina slows down.
- proliferative diabetic retinopathy stage: the blood vessels are more fragile, and the fluid of the eye is in gel consistency. Detachment formation is seen in the retina.

Fig. 1 presents the data distribution of images among the DR stages for the APTOS 2019 dataset. The image samples of DR stages can be shown in Fig. 2.

JSR A
Journal of Scientific Reports

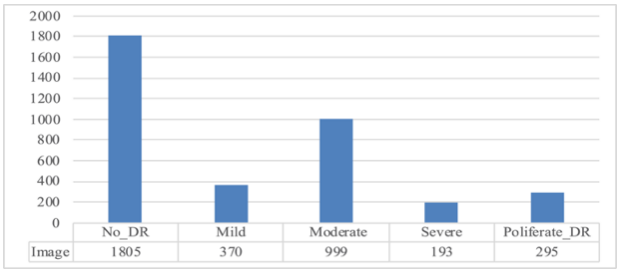

Figure 1. Distribution of images in the dataset according to their classes.

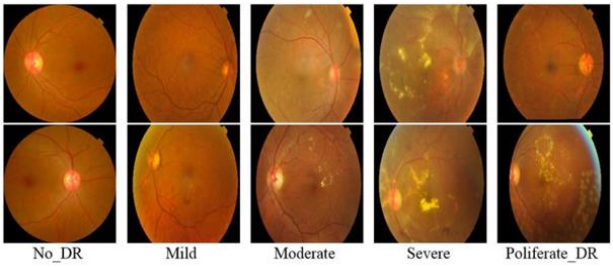

Figure 2. Image samples of DR lesion stages.

2.2. Model

We develop a computer-based system that analyses colored fundus images of the stages of DR and detects the stage of retinal lesions, considered as clinical signs of the disease. In the proposed system, gaussian smoothing is applied by converting fundus images to gray-level color space.

Then, the masks of the images are obtained with the threshold method. The contours of the unmasked images are extracted and cropping is applied to the images. In the final stage, well-known CNN architectures are used for feature extraction and classification. The detected lesions are classified using optimization techniques and deep learning algorithms. The structure of our proposed model is presented in Fig. 3.

JSR A
Journal of Scientific Reports

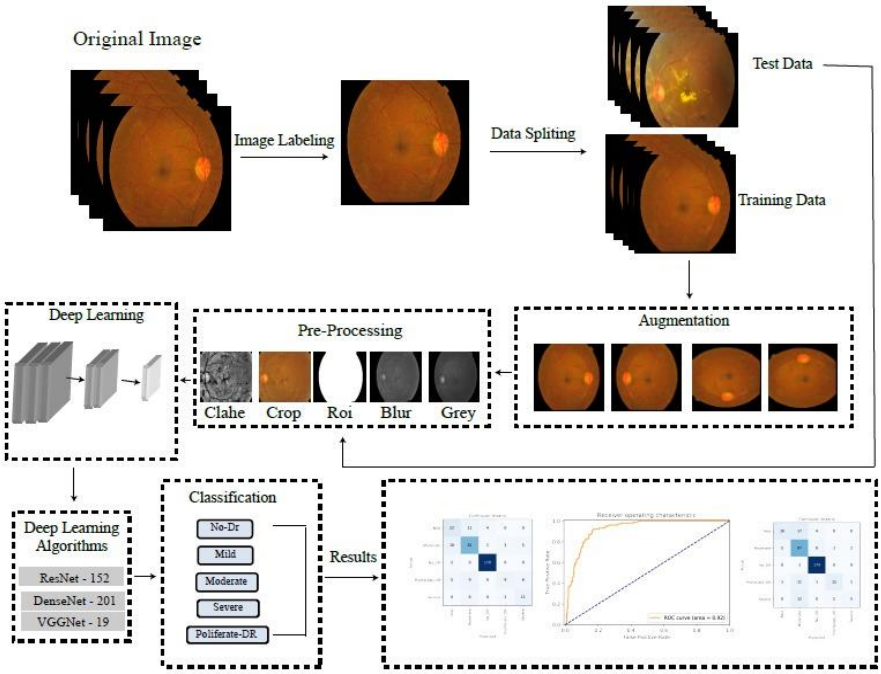

Figure 3. The structure of the proposed model.

2.3. Preprocessing

Preprocessing techniques have been applied to fundus images in the dataset to increase classification accuracy. As can be observed in Fig. 4, the pre-processing involves five steps. In the first step, the images are converted from RGB color space to grayscale. Then, a Gaussian smoothing filter is applied to the images to eliminate the noise from the images. The threshold used for the segmentation process of the Gaussian filter applied images. The mask of the fundus images is obtained with this procedure. By using the contour finding method on the masks, the matrix giving the boundaries in the 2-dimensional plane is extracted for cropping the images. From this matrix, endpoints on the x and y axis are determined, and a standard deviation value is added. Following this step, cropping is performed, and all the cropped images are rescaled to 224x224. The cropping step aims to enable CNNs architectures to focus on the bleeding regions in the fundus images during the feature extraction process. In the last step, the CLAHE method is applied to the cropped images. The purpose of this method is to improve the discrimination ability of the model by making the bleeding vessels in the fundus images apparent.

Fig. 4 shows the visualization of the images after performing the five preprocessing steps. Color fundus images compose groups of pixels with different brightness levels and the contrasts of the fundus image can be quite different. These differences significantly affect the performance of DR stage detection.

Contrast enhancement and image segmentation are important preprocessing steps for the fundus images. The CLAHE method is used to make vessels distinct by increasing the background contrast of

the fundus images. The number of sub-images and image boundaries affect the results of the CLAHE method [29]. Thus, the noise and contrast condensation barriers are removed and the problem of oversaturation in similar regions is prevented. As shown in Fig. 4b, the fundus images are converted from RGB colour to grayscale. In the second step, the Gaussian filter is applied to the grayscale fundus images to detect the boundaries (Fig. 4c). Also, a threshold value is applied to do segmentation to obtain the mask of the images. In the third step, the matrix that gives the boundaries is extracted using the contour findings method on the masks (Fig. 4d). In the fourth step, the cropping process is performed to classify the images effectively (Fig. 4e). In the last step, the CLAHE method is applied to better distinguish the stages of DR lesions and to improve the discrimination ability of the model (Fig. 4f).

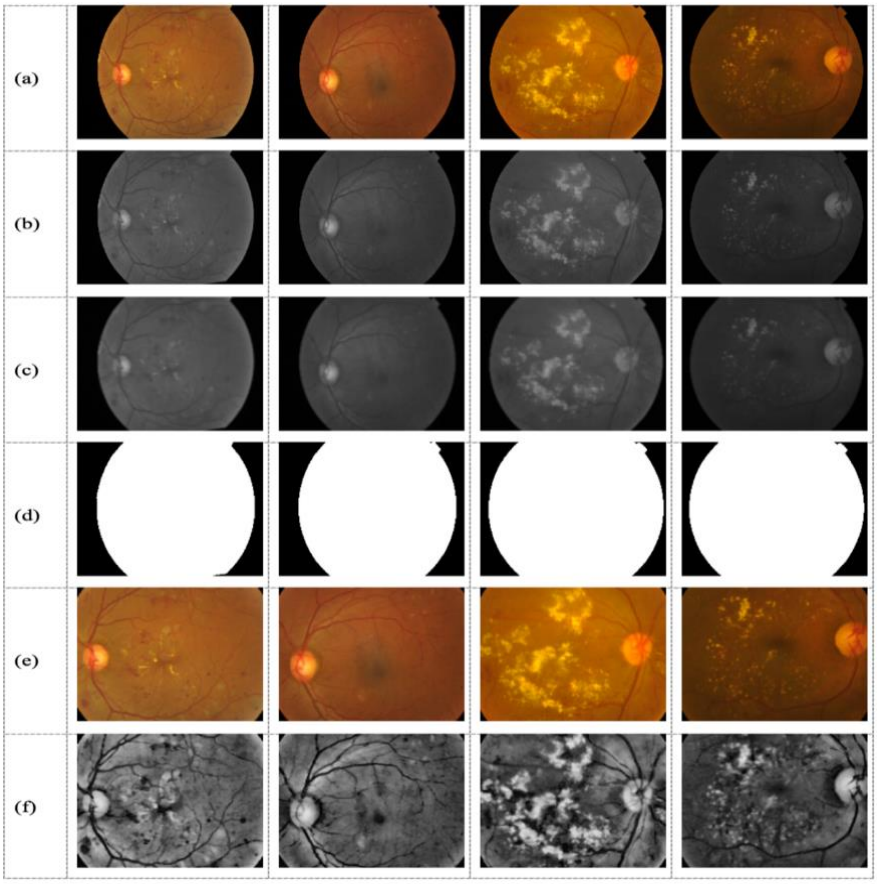

Figure 4. Preprocessing steps applied to fundus images (a) original image (b) grayscale image (c) Gaussian blur applied image (d) image mask (e) cropped image (f) CLAHE applied image.

Data augmentation is an important process that prevents overfitting and increases the performance of the deep learning model [23]. In recent studies that employ CNNs methods, the success of the network

depends largely on the amount of data, otherwise training the CNNs with fewer data creates some problems such as overfitting. Data augmentation techniques such as horizontal and vertical shift, brightness change, angular change, zoom, and horizontal and vertical rotation are applied to the fundus images, and then classification performance is improved. Transfer learning is known as a machine learning method for using to train a new model from a previously trained model. Some information such as features or weights is imported from the model that was trained on a larger dataset. We use a transfer learning approach to detect DR in the fundus images using the features of CNNs pre-trained on ImageNet [24] and train a new model on these features.

2.4. Convolutional Neural Networks Architecture Used

Deep Learning algorithms can be considered as the more complex form of artificial neural networks. The increasing abundance of data and accessing more relevant information from this data require optimization regarding the feature estimates. Artificial neural network-based systems can produce solutions to solve problems of image classification. Convolutional Neural Networks (CNNs) have become a model that solves the computational difficulties created by the connections between neurons and layers and the learned parameters experienced in the classical artificial neural network models [25].

The convolution layer is the first layer to process the image in CNNs algorithms. The number of filters and the filter size are hyper-parameters of the convolutional layer, and these are determined individually for each algorithm. In addition, by sharing the parameters, the number of parameters is reduced, and simpler decision limits can be learned. With this process, more accurate predictions can be made with less training data. The pooling layer is a sampling process that is implemented with some spatial invariance. After the convolutional layer, activation functions are determined for the pooling layer. Since linear activation functions are weaker in learning complex properties, nonlinear activation functions are generally preferred in the algorithms. The FC layer is usually the last layer of the CNNs architecture and can be used to optimize class scores. After extracting basic parameters with a 2x2 local image matrix, the low-dimensional images are transferred to the fully connected layer.

ResNet152[26], DenseNet201[27], and VGGNet19[28] architectures can use for feature extraction and classification steps to diagnose DR stage. The ResNet152 achieved a lower error value than the human vision error rate in the ImageNet competition in 2015. Although this architecture uses residual blocks with multiple layers to decrease the training error, it also solves the over-compliance problem of multi-layer networks. In residual blocks, input information from the convolution layer is added to the information after the activation process and transmitted to the next layer.

DenseNet201 was introduced because of attempts to deepen CNN architectures in 2016. Traditional CNN architectures pass the information from the convolution layer to the next layer with n connections. In DenseNet architecture, the information coming out of the convolution layer is sent as input to all layers after it and this process continues towards the last layer with $n(n+1)/2$ connections. DenseNet minimizes the vanishing-gradient problem and strengthens feature propagation. VGGNet19 was first introduced at the ImageNet competition in 2014. VGGNet architecture focuses on deepening the network rather than increasing its layers to improve performance. VGGNet19 architecture has sixteen convolutional and three fully connected layers. Convolution layers have a maximum pooling and ReLU activation function.

JSR A
Journal of Scientific Reports

3. EXPERIMENTS AND RESULTS

We examine our proposed model by comparing VGGNet19, DenseNet201, and ResNet152 CNN architectures on the Kaggle APTOS 2019 dataset for DR stage detection. The dataset is divided into 70% for training, 20% for validation, and 10% for testing. Data augmentation has been applied to increase the performance of the model and to prevent overfitting on the training set. It is applied only to the train data and not to validation and test sets. In this way, excessive learning and manipulation are prevented. All experiments are carried out on the K80 Tesla graphics card. Adam optimization algorithm is used for the optimization of CNN architectures, and ReLU activation is used in convolution layers. The batch size is determined as 64 and the epoch number as 50 in the experiments. Five performance evaluation metrics are used in the experiments: accuracy, area under the curve (AUC), precision, recall, and F-Score. The results of the experiments are shown in Table 1 for each CNNs model in these metrics.

Table 1. Classification Performances of CNNs architectures.

	Accuracy	**AUC**	**Precision**	**Recall**	**F-score**
ResNet152	0.824	0.941	0.820	0.820	0.820
DenseNet201	0.827	0.923	0.830	0.830	0.810
VGGNet19	0.824	0.938	0.810	0.810	0.810

In the experiments, 82.4% accuracy and 82% F-score value were obtained using the ResNet152 architecture. Using DenseNet201 architecture, 82.7% accuracy and 81% F-score value were found. The results of VGGNet19 architecture are seen as 82.4% accuracy and 81% F-score. Although DenseNet201 architecture obtained the best accuracy value, ResNet152 architecture found the best F-score value. However, the findings of the 3 architectures are close to each other. Table 2 shows the weighted average performance values of CNNs architectures for all classes in precision, recall, and F-score values. The ResNet152, DenseNet201, and VGGNet19 architectures predicted the No_DR class with an F-score of 97% and above. The best estimate for the Mild class was the ResNet152 architecture with an F-score of 58%.

Table 2. Comparative analysis of CNN architectures and DR classes.

	Class	**Precision**	**Recall**	**F-score**
ResNet152	Mild	0.56	0.59	0.58
	Moderate	0.76	0.81	0.78
	NoDR	0.97	0.99	0.98
	Severe	0.50	0.58	0.54
	PoliferateDR	0.64	0.31	0.42
DenseNet201	Mild	0.73	0.43	0.54
	Moderate	0.76	0.81	0.78
	NoDR	0.94	0.99	0.97
	Severe	0.71	0.26	0.38
	PoliferateDR	0.83	0.52	0.64
VGGNet19	Mild	0.59	0.46	0.52

JSR A
Journal of Scientific Reports

	Moderate	0.75	0.77	0.76
	NoDR	0.94	0.99	0.97
	Severe	0.67	0.74	0.70
	PoliferateDR	0.61	0.48	0.54

Fig. 5 presents the complexity matrix showing the predictions and real values obtained by the proposed CNNs model because of 50 epochs.

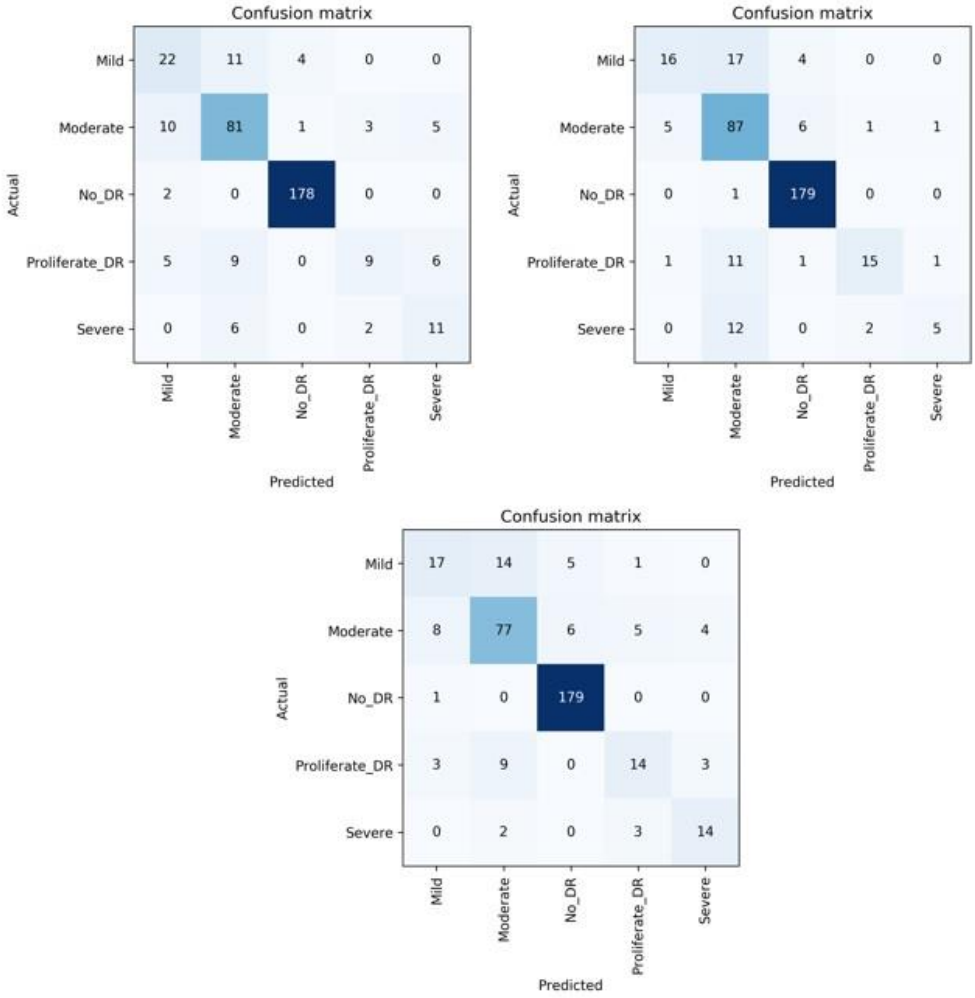

Figure 5. Confusion matrices, (Left Top) ResNet152, (Right Top) DenseNet201, (Bottom) VGGNet19.

JSR A
Journal of Scientific Reports

As can be observed, Fig. 6 presents the ROC curve showing the discrimination capability of classification models. The x-axis of the ROC curve gives the false-positive rate, and the y-axis gives the correct positive rate. The area under the curve shows the AUC score. AUC gives the classification model's ability to distinguish.

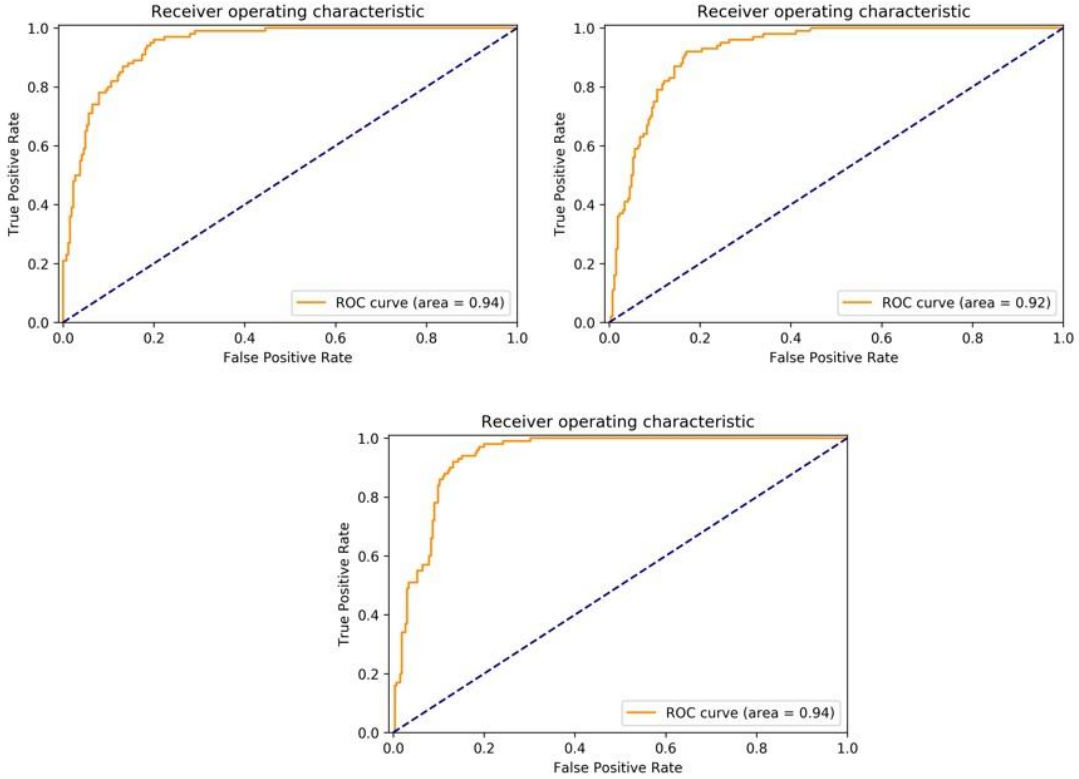

Figure 6. Roc Curves (Left), ResNet152 (Right), DenseNet201 (Bottom), VGGNet19.

Unlike other studies, we do not use the enhanced data in the test set. In this way, the effect of memorized images on learning is minimized. Khalifa et al. [30] achieve 80% accuracy with the SqueezeNet algorithm as a result of the data augmentation process they perform without considering this situation. Lam et al. [31] test their work with the deep learning model in which they apply the accuracy value in three classes; no DR, Mild and Severe. Transfer learning in the pre-trained GoogLeNet and AlexNet models in ImageNet, they find the highest test set accuracy as 74.5% in two classes, 68,8% in the three classes, and 57.2% in four classes. Pratt et al. [23] use CNNs to classify DR stages from fundus images and obtain 75% accuracy with five-fold cross-validation using 5000 images.

We obtain an accuracy of 82.7% using the DenseNet201 algorithm for the classification performance of DR stages. When the AUC values are examined, the ResNet152 algorithm gives the best result with 94.1%. The proposed model stands out with both its accuracy results and classification performance success. Most of the studies in the literature classify two classes as no DR and DR. Kumar et al. [32] find a test accuracy of 80.59% in their study using a mixed dataset for two classes. In this study, VGGNet19, DenseNet201, and ResNet152 algorithms classify the no DR images in four stages with accuracies of 94%, 94%, and 97%, respectively.

4. CONCLUSIONS

Diabetic retinopathy is an important disease that occurs due to diabetes mellitus. With this disease, deteriorations such as microaneurysms, hemorrhages, exudates and new vessel formation occur in the retina of the eye. The computer-aided system has been developed to assist specialist physicians in an effective diagnosis of the disease. The stages of DR lesions have been tried to be determined from color retinal images by deep learning algorithms. We examine our proposed model by comparing VGGNet19, DenseNet201, and ResNet152 CNN architectures on the Kaggle APTOS 2019 dataset for DR stage detection. When the overall test accuracy and performance metrics are examined, it seems the DenseNet201 model reaches the best test accuracy with 82.7%. The highest AUC value is obtained using the ResNet152 model with 94.1%. For future studies, the features of well-known CNN architectures can be combined and the ensemble learning method can be applied for classification. This can increase the accuracy of DR classes that are predicted particularly unsuccessfully.

ACKNOWLEDGMENT

This research received no specific grants from any funding agency.

REFERENCES

[1] Roglic, G. (2016), WHO global report on diabetes: a summary. International Journal of Noncommunicable Diseases, 1(1), 3.

[2] Lynch, S.K. and M.D. Abràmoff. (2017), Diabetic retinopathy is a neurodegenerative disorder. Vision research, 139, 101-107.

[3] Benson, W.E., Blodi, B.A., Boldt, H.C., Olsen, T.W., Regillo, C.D., Scott, I.U., et al. (2008), Prepared by the American Academy of Ophthalmology Retina/Vitreous Panel Members.

[4] Mohammadpoory, Z., Nasrolahzadeh, M., Mahmoodian N., and Haddadnia, J. (2019), Automatic identification of diabetic retinopathy stages by using fundus images and visibility graph method. Measurement, 140, 133-141.

[5] Biyani, R. and Patre, B. (2018), Algorithms for red lesion detection in diabetic retinopathy: a review. Biomedicine & Pharmacotherapy, 107, 681-688.

[6] Neffati, S., Ben Abdellafou, K., Taouali, O. and Bouzrara, K. (2020), Enhanced SVM–KPCA method for brain MR image classification. The Computer Journal, 63(3), 383-394.

[7] Sugeno, A., Ishikawa, Y., Ohshima, T. and Muramatsu, R. (2021), Simple methods for the lesion detection and severity grading of diabetic retinopathy by image processing and transfer learning. Computers in Biology and Medicine, 137, 104795.

[8] Bhardwaj, C., Jain, S. and Sood, M. (2021), Hierarchical severity grade classification of non-proliferative diabetic retinopathy. Journal of Ambient Intelligence and Humanized Computing, 12(2), 2649-2670.

[9] Shaban, M., Ogur, Z., Mahmoud, A., Switala, A., Shalaby, A., Abu Khalifeh, H., et al. (2020), A convolutional neural network for the screening and staging of diabetic retinopathy. Plos one, 15(6).

[10] De La Torre, J., Valls, A. and Puig, D. (2020), A deep learning interpretable classifier for diabetic retinopathy disease grading. Neurocomputing, 396, 465-476.

[11] Zhao, L., Ren, H., Zhang, J., Cao, Y., Wang, Y., Meng, D., et al. (2020), Diabetic retinopathy, classified using the lesion-aware deep learning system, predicts diabetic end-stage renal disease in Chinese patients. Endocrine Practice, 26(4), 429-443.

[12] Kermany, D.S., Goldbaum, M., Cai, W., Valentim, C.C., Liang, H., Baxter, S.L., et al. (2018), Identifying medical diagnoses and treatable diseases by image-based deep learning. Cell, 172(5), 1122-1131.

[13] Wang, Y. and Shan, S. (2018), Accurate disease detection quantification of iris based retinal images using random implication image classifier technique. Microprocessors and Microsystems, 80, 103350.

[14] Wang, X., Lu, Y., Wang, Y. and Chen., W. (2018), Diabetic retinopathy stage classification using convolutional neural networks. IEEE International Conference on Information Reuse and Integration (IRI).

[15] Sarki, R., Michalska, S., Ahmed, K., Wang, H. and Zhang, Y. (2019), Convolutional neural networks for mild diabetic retinopathy detection: an experimental study. bioRxiv, 763136.

[16] Xiao, D., Yu, S., Vignarajan, J., An, D., Tay-Kearney, M.-L. and Kanagasingam, Y. (2017), Retinal hemorrhage detection by rule-based and machine learning approach. 39th Annual International Conference of the IEEE Engineering in Medicine and Biology Society (EMBC).

[17] Wan, S., Liang, Y. and Zhang, Y. (2018), Deep convolutional neural networks for diabetic retinopathy detection by image classification. Computers & Electrical Engineering, 72, 274-282.

[18] Molina-Casado, J.M., Carmona, E.J. and García-Feijoó, J. (2017), Fast detection of the main anatomical structures in digital retinal images based on intra-and inter-structure relational knowledge. Computer methods and programs in biomedicine, 149, 55-68.

[19] Ur Rehman, M., Abbas, Z., Khan, S.H., and Ghani, S.H. (2018), Diabetic retinopathy fundus image classification using discrete wavelet transform. 2nd International Conference on Engineering Innovation.

[20] Jiang, Y., Wu, H. and Dong, J. (2017), Automatic screening of diabetic retinopathy images with convolution neural network based on caffe framework. Proceedings of the 1st International Conference on Medical and Health Informatics.

[21] Gao, Z., Li, J., Guo, J., Chen, Y., Yi, Z. and Zhong, J. (2018), Diagnosis of diabetic retinopathy using deep neural networks. IEEE Access, 7, 3360-3370.

[22] Asia Pacific Tele-Ophthalmology Society "APTOS". (2019), Accessed april 2022. [Online]. Available: https://www.kaggle.com/c/aptos2019-blindness-detection

[23] Pratt, H., Coenen, F., Broadbent, D.M., Harding, S.P. and Zheng, Y. (2016), Convolutional neural networks for diabetic retinopathy. Procedia computer science, 90, 200-205.

[24] Deng, J., Dong, W., Socher, R., Li, L.-J., Li K. and Fei-Fei, L. (2009), Imagenet: A large-scale hierarchical image database. IEEE conference on computer vision and pattern recognition.

[25] LeCun, Y., Bengio, Y. and Hinton, G. (2015), Deep learning. Nature, 521, 7553, 436-444.

[26] He, K., Zhang, X., Ren, S. and Sun, J. (2016), Deep residual learning for image recognition. Proceedings of the IEEE conference on computer vision and pattern recognition.

[27] Huang, G., Liu, Z., Van Der Maaten, L. and Weinberger, K.Q. (2017), Densely connected convolutional networks. Proceedings of the IEEE conference on computer vision and pattern recognition.

[28] Simonyan, K. and Zisserman, A. (2014), Very deep convolutional networks for large-scale image recognition. arXiv preprint, 1409-1556.

[29] Patil, S.B. and Patil, B. (2020), Retinal fundus image enhancement using adaptive CLAHE methods. Journal of Seybold Report, (1533), 9211.

[30] Khalifa, N.E.M., Loey, M., Taha, M.H.N. and Mohamed., H.N.E.T. (2019), Deep transfer learning models for medical diabetic retinopathy detection. Acta Informatica Medica, 27(5), 327.

[31] Lam, C. , Yi, D., Guo, M. and Lindsey, T. (2018), Automated detection of diabetic retinopathy using deep learning, AMIA summits on translational science proceedings, 147.

[32] Kumar, G., Chatterjee, S.K. and Chattopadhyay, C. (2020), Drdnet: Diagnosis of diabetic retinopathy using capsule network (Workshop Paper), IEEE Sixth International Conference on Multimedia Big Data (BigMM), 379-385.

[33] Lahmar, C., and Ali, I. (2022), Deep hybrid architectures for diabetic retinopathy classification. Computer Methods in Biomechanics and Biomedical Engineering: Imaging & Visualization, 1-19.

[34] Anoop, B.K. (2022), Binary classification of DR-diabetic retinopathy using CNN with fundus colour images. Materials Today: Proceedings 58, 212-216.

[35] Mungloo-Dilmohamud, Z., Heenaye-Mamode Khan, M., Jhumka, K., Beedassy, B.N., Mungloo, N.Z. and Peña-Reyes, C. (2022), Balancing data through data augmentation improves the generality of transfer learning for diabetic retinopathy classification. Applied Sciences 12(11), 5363.

Kütahya Dumlupınar University
Institute of Graduate Studies

Journal of Scientific
Reports-A
E-ISSN: 2687-6167
Number 51, December 2022

RESEARCH ARTICLE

EDUCATION of BRAIN FUNCTIONS with AUGMENTED REALITY for DISABLED PEOPLE

Yusuf UZUN[1,*], Hasibe Nur KILINÇ[2]

[1*]Necmettin Erbakan University, Faculty of Seydisehir Ahmet Cengiz Engineering, Department of Computer Engineering, Konya, yuzun@erbakan.edu.tr, ORCID: 0000-0002-7061-8784
[2]Necmettin Erbakan University, Faculty of Engineering, Department of Computer Engineering, Konya, hasibenurkilinc@gmail.com, ORCID: 0000-0003-1169-9315

Receive Date:15.06.2022 *Accepted Date: 19.11.2022*

ABSTRACT

In recent years, it has been possible to prepare very important studies in the field of education by using Augmented Reality technology. With this technology, video, graphics, sound and three-dimensional models are used in the environment of physical objects in the real world. Today, Augmented Reality technology is used in industry, education, medicine, logistics, industry, etc. are frequently used in the fields. Therefore, due to the development of applications in this field, technological devices have been enabled to communicate with their environment and acquire new information. In this study, an application has been developed to help disabled individuals understand the functions of their brain functions and to improve their learning abilities. In the application, the functions of brain functions are explained, thanks to the content activated with the help of a button that appears on the screen on any technological device. If a visually impaired person uses this application, brain functions are explained only with audio narration and animations. If a hearing-impaired individual uses it, brain functions are explained only with texts and animations. In this way, the learning abilities of the disabled are improved more easily and it is easier to understand the subjects.

Keywords: *Disabilities, Augmented Reality, Brain Dec, AR*

1. INTRODUCTION

Augmented Reality (AR) defines a function for using images, objects, locations, three-dimensional objects and videos created using computer hardware and software on a real world environment[1]. With Augmented Reality, video and images combined on real physical environments are decoded as part of the real world environment. Therefore, logistics, military, education, medicine, construction, health, etc. widely used in industries. The use of three-dimensional visual objects in AR studies attracts the attention of individuals with disabilities, enables them to participate more in training and motivates them to learn. It also offers a different perspective in the presentation of the subjects [1].

For AR, the first process to be created is the creation of videos, objects and images with application software that will be combined in real environments. These combined videos, objects, and images are often combined with three-dimensional objects [2].

The developed study was added to the dec application and combined with various location data, it was provided to work with real environments. It has also been made available for use with smartphones, tablets or technological devices so that the images created can be transferred to individuals with disabilities [2]. Thanks to the unique interaction feature provided by AR technologies, it is possible to gain significant advantages in developing some special abilities of the disabled that cannot be obtained with traditional studies [3]. The AR method helps people with disabilities learn about complex real-world issues. Astronomy, geography, medicine, biology, chemistry, physics, etc. It prepares a realistic understanding environment for the transfer of the subjects.

Thanks to the DEC application, it also improves the communication between the disabled individuals in an easy way by enabling them to perform the tasks they will perform on complex issues. It helps people with disabilities develop their imagination and creativity. AR can be used as a useful method for the learning or education of people with disabilities by improving their perception and interaction with this world in the real world.

In the second part of this study, there are details about AR. In the third chapter, information about the vuforia application used in this study is given. In the fourth chapter, the output samples and codes of the application developed for this study are given. In the fifth chapter, the conclusion part of this study is given and the results obtained from the application are explained.

2. MATERIAL and METHODS

2.1. Augmented Reality

Technologies used in AR studies also consist of optical and video-based technologies. The difference between these technologies is where the environment created by separating the virtual and real worlds is seen. The separation of the virtual and real world are the differences between virtual and real world environments. Scenes combined in video processes are deconstructed with the help of technological devices (mobile devices, tablets, computers, etc.), optics is a combination of studies and the integration of glasses with real environments is provided [2].

AR allows individuals with disabilities and educators to identify the knowledge and skills they have learned by combining their learning environments with the real worlds they live in[4].

AR applications are developed using one of three methods: marker-based, location-based and unsigned-based [5].

Marker-Based AR: It is created by placing virtual objects on images in real environments. It is the most used structure. Artoolkit, Vuforia, Wikitude, Layar etc. It is used with software development kits [5].

Location-Based AR: It is created to display the materials created in virtual environments using location or location information in real environments by being triggered at certain locations. It is more widely used in the tourism industry. ARtoolkit6 is used with Vuforia and Wikitude applications [5].

UnMarker-Based AR: It is used today with the help of new generation smart glasses. It involves the user in interacting with a real environment. Military, education, medicine, logistics, etc. It is used in many fields, especially in fields. ARKit, Vuforia, Wikitude, Vuforia, ARtoolkit6 etc. It is used with applications [5].

Hardware, software, marker and AR glasses are used in AR technologies, respectively. All work on hardware peripherals takes place with a computer infrastructure. Generally, high-performance technological devices are needed in terms of the speed of the work application for the creation and display of three-dimensional models in real environments. Hardware units that can be used for AR technology include Ipad, PC, Notebook etc. devices can be shown as an example [6]. In software peripherals, there is a need for an auxiliary surface that will decode the virtual and real environment together. Software companies offer these utilities as licensed software packages. Generally, a number of features are designed in the software of these companies to provide some convenience for AR. These usually consist of dec mobile application devices, modeling and markup tools, and web interface developers [5]. In marker peripherals, markers provide the spatial link between the real and virtual environment. While markers were created in 2-bit shapes when they were first applied, nowadays any real-life object can be displayed as a marker [6]. AR glasses allow the users of the application to decipher the virtual and real environment so that the data and images between the real and virtual environment can be used with each other [6]. AR technology has become a technology that can allow the use of mobile applications on textbooks [7]. Additions to the Unity program can be made by using different applications for modeling [8]. During the collection and analysis of information, one of the first goals of augmented reality is to highlight its specific features in the physical environment to provide a better understanding and to obtain intelligent and accessible interior images that can be achieved by applications in the physical environment [9].

2.2. Vuforia

In this study, which was developed with AR, in the first step, three-dimensional brain images and brain functions were created with the help of Unity program. These images were created with the 3DMAX program. The three-dimensional images added to the application were named Assets in the Unity program. Unity allows us to work with 3D images on the Asset Store page for free/paid. In this way, the images to be used were imported from this section and used easily. After creating our three-dimensional images, the parts that we will position on the page should be selected. Cameras, often called markers, were provided for these surfaces. When the cameras focus on these images, three-dimensional images and texts will be created on them. After selecting the markers, the Vuforia Sdk developer was chosen to use them in the work. The process image of the Vuforia Sdk developer was shown in Figure 1.

JSR A
Journal of Scientific Reports

Uzun, Y. and Kılınç, H. N., Journal of Scientific Reports-A, Number 51, 120-126, December 2022.

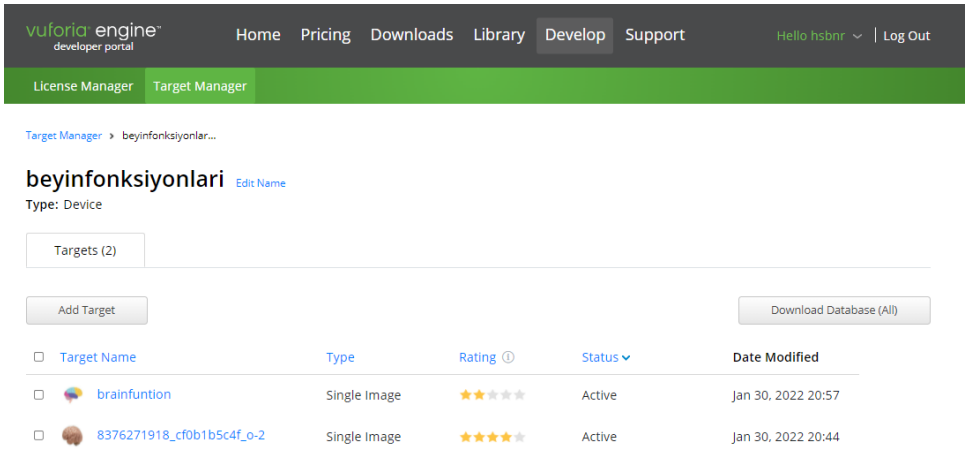

Figure 1. Vuforia database.

In order to create a database in Vuforia, a membership must be created on the web page in the first place. Then a key was created from the lower tab of the language key menu in the development section. The key provides the license key for the database portion of the AR application. A different key must be created for each application. The Vuforia object was also defined as a marker. For object images that received 5 stars in the evaluation of the object uploaded to Vuforia, it can be said that the tracking quality of the object is good. The more stars the marker receives, the higher the rate of evaluation of the marker.

3. EXPERIMENTAL WORK

Position and Marker Based AR was preferred in this study. While preparing this study, the widely used Vuforia SDK was used. Unity, Android Studio and Visual Studio were chosen as the development environment. Vuforia SDK was used with AR. Two buttons were placed on the home screen of this application, which was developed for disabled individuals. In the first button there are subtitled texts, animations and videos.

In the second button, brain functions are explained audibly. Both buttons used in the study have features such as 360 virtual tour rotation, enlargement and reduction with the visual created for brain functions in common. In this way, disabled individuals can see the important points they want to learn or comprehend for their brain functions from every angle. In this way, it was ensured that the attention of the disabled people was drawn more to the practice and it was aimed to improve their comprehension skills. C# codes for object enlargement, reduction and rotation written in Unity 3D application were shown in Figure 2.

JSR A
Journal of Scientific Reports


```
private void OnTrackingFound()
{
    Renderer[] rendererComponents = GetComponentsInChildren<Renderer>(true);
    Collider[] colliderComponents = GetComponentsInChildren<Collider>(true);
    foreach (Renderer component in rendererComponents)
    {
        component.enabled = true;
    }
    foreach (Collider component in colliderComponents)
    {
        component.enabled = true;
    }

    Debug.Log("Trackable " + mTrackableBehaviour.TrackableName + " found");
    if (mTrackableBehaviour.TrackableName == "2")
        TextTargetName.GetComponent<Text> ().text = "Limbik sistem ağrının d

}
```

Figure 2. Object zoom and rotate operations codes.

The screen output of the developed application was shown in Figure 3.

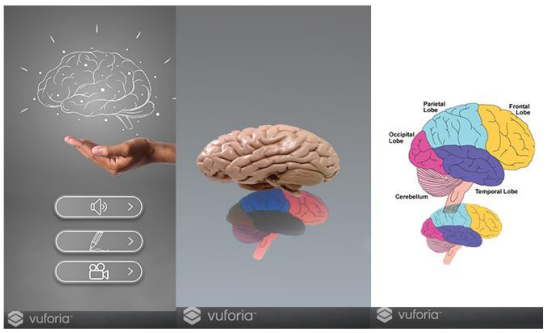

Figure 3. Application output (display of brain functions).

When the findings regarding the usefulness of this study, which was prepared for the training of brain functions for disabled individuals, were examined, it was determined that the disabled individuals could operate the application very easily and accurately by moving the markers. In addition, the easy usability, faster accessibility and use of this application with different technological devices have led to greater interest by disabled individuals and increased participation in the experimental study. Three-dimensional images, objects and information created by reading the points are planned to be more memorable by enlarging, reducing and rotating 360 degrees on these devices.

In the first button used in the application, brain functions and tasks were explained with sounds for the visually impaired. In the second button, the functions of the brain were explained in writing with the help of the cameras of technological devices for both hearing and other handicapped individuals. In the third button, animations and videos for all disabled individuals and brain functions were explained.

In the video in Figure 4, the brain functions of a hearing impaired individual using sign language were shown.

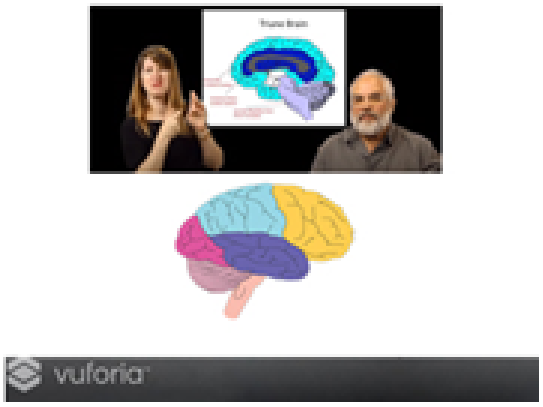

Figure 4. Video narration output for the hearing impaired.

4. CONCLUSIONS

This study has been prepared in order to facilitate the understanding and comprehension of educational information about brain functions for people with disabilities. In the application developed with AR technology, three-dimensional pictures of the brain and brain functions were mentioned and a more exploratory learning experience was offered to individuals with disabilities. Therefore, disabled individuals have experienced education in their own living environments by staying away from the risks of external environments with AR. It can also lead the development of more flexible practices according to the needs of disabled individuals and educators. This application will not only provide information or training, but also a better education will be provided to individuals with disabilities, with feedback on brain functions and course components, with the contributions of disabled individuals and trainers using this system. Today, when we take a break from face-to-face education due to Covid-19, such an application, especially in the field of education, helps people with disabilities to perceive their experiences and brain functions faster.

5. DISCUSSION

In this study, a more efficient and effective education environment has been prepared by using the AR method in applications for the education of the disabled. Since experimental and educational studies can be carried out on the real physical environment with AR technology, it is very easy to carry out their education with the disabled person in the environment they are in. One of the biggest shortcomings in this field is the lack of education materials and widespread use. It is thought that the prepared application can be an example for different researchers and can be developed. In future studies, it is planned to develop AR supported mobile applications in different fields.

ACKNOWLEDGMENT

This research received no specific grants from any funding agency in public, commercial or non-profit sectors.

REFERENCES

[1] Yolcu, M. B., Emre, Ş. and Celayir, S., (2018), Artırılmış gerçekliğin tıpta ve çocuk cerrahisinde kullanımı, Çoc. Cer. Derg., 32(3), 89-92.

[2] İçten, T. and Bal, G., (2017), Artırılmış gerçeklik teknolojisi üzerine yapılan akademik çalışmaların içerik analizi, Bilişim Teknolojiler Dergisi, 10(4), 401-415.

[3] Özdemir, M., (2017), Artırılmış gerçeklik teknolojisi ile öğrenmeye yönelik deneysel çalışmalar: Sistematik bir inceleme, Mersin Üniversitesi Eğitim Fakültesi Dergisi, 13(2), 609-632.

[4] Küçük, S., Kapakin, S. and Göktaş, Y., (2015), Tıp fakültesi öğrencilerinin mobil artırılmış gerçeklikle anatomi öğrenimine yönelik görüşleri, Yükseköğretim ve Bilim Dergisi, 3, 316-323.

[5] Akkuş, İ. and Özhan, U., (2017), Matematik ve geometri eğitiminde artırılmış gerçeklik uygulamaları, Inonu University Journal of the Graduate School of Education, 4(8), 19-31.

[6] Çakal, M.A. and Eymirli, E., (2012), Artırılmış gerçeklik teknolojisi, Kuzeydoğu Anadolu Kalkınma Ajansı, 1, 1-10.

[7] Çiloğlu, T., Yılmaz, Ö., Yılmaz, A. and Yılmaz, F. G., (2021), Eğitimde artırılmış gerçeklik konulu makalelerin incelenmesi, Ahmet Keleşoğlu Eğitim Fakültesi Dergisi, 3(2), 147-158.

[8] Chang, H., Binali, T., Liang J., Chiou, G., Cheng, K., Lee, S., and Tsai, C., (2022), Ten years of augmented reality in education: A meta-analysis of (quasi-) experimental studies to investigate the impact, Computer & Education, 191, 10641.

[9] Kok, D., Dushyanthen, S., Peters G., Sapkaroski, D., Barrett, M., Sim, J., and Eriksen, J.G., (2022), Virtual reality and augmented reality in radiation oncology education - A review and expert commentary, Technical Innovations & Patient Support in Radiation Oncology 24, 25-31.

Kütahya Dumlupınar University
Institute of Graduate Studies

Journal of Scientific
Reports-A
E-ISSN: 2687-6167
Number 51, December 2022

RESEARCH ARTICLE

SOLAR RADIATION FORECAST by USING MACHINE LEARNING METHOD for GAZIANTEP PROVINCE

Yusuf Alper KAPLAN[1], Emre BATUR[2], Gülizar Gizem TOLUN[3,*]

[1]Osmaniye Korkut Ata University, Faculty of Engineering, Energy Systems Engineering, Osmaniye, alperkaplan@osmaniye.edu.tr, ORCID: 0000-0003-1067-110X
[2]Osmaniye Korkut Ata University, Faculty of Engineering, Energy Systems Engineering, Osmaniye, emrebatur.esm@gmail.com, ORCID: 0000-0002-7538-7575
[3*]Osmaniye Korkut Ata University, Faculty of Engineering, Energy Systems Engineering, Osmaniye, gulizargizemunaldi@osmaniye.edu.tr, ORCID: 0000-0003-1876-9283

Receive Date:10.09.2022 *Accepted Date: 07.10.2022*

ABSTRACT

Renewable energy sources have become a popular topic all over the world in terms of cost, efficiency and environmental pollution. Solar energy is the most significant of the renewable energy sources. Solar energy, which was used only as heat and light energy in the past, is widely used in electrical energy production with the advancement of today's technology. Traditionally used photovoltaic cells are semiconductor materials that are produced in various chemical structures and convert the energy they receive from sunlight directly into electrical energy. The research and development of photovoltaic cells is moving forward at an accelerating pace. With this development process and relying on the today's technology, it is aimed to increase the efficiency of photovoltaic cells and to produce more electrical energy as a result of various trials. By analysing the energy production of photovoltaic cells, efficiency-enhancing situations are examined according to solar radiation values. In this study, a model was constructed using the regression approach, which is a method of machine learning. This model has been developed using the MATLAB program of the meteorological data of 2021 from Gaziantep. In addition, a variety of error analysis tests were utilized in order to evaluate the effectiveness of the model that was built. As a consequence, the model created using the linear regression method yields successful results in estimating solar radiation in Gaziantep province. This is demonstrated by the coefficient of determination (R^2) value of 0.98, the Mean Absolute Error (MAE) value of 0.023, the Root Mean Square Error (RMSE) value of 0.028, and the Mean Square Error (MSE) value of 0.0008.

Keywords: *Solar energy, Energy production, Photovoltaic cell, Cell efficiency, Machine learning*

1. INTRODUCTION

Depending on the development and progress of today's technology, energy consumption is increasing in all areas of life. In the current world order, energy needs are fulfilled with fossil-based resources

JSR A
Journal of Scientific Reports

such as coal, natural gas, and oil. However, fossil fuels are not energy sources that can be used in the long term due to their irreversible damage to the environment and their tendency to run out [1].

The intensity of solar energy before reaching the earth's atmosphere is approximately 1370 W/m², but the amount of solar energy reaching the earth's surface varies between 0-1100 W/m² due to the atmosphere [2]. A large part of this energy is used by plants. The remaining energy is converted into heat and is currently used in the formation of many atmospheric events. More specifically, Turkey has a high potential in terms of the efficiency level that can be obtained from solar energy. Figure 1 shows the regional solar radiation map of Turkey.

Figure 1. Total Solar Radiation Map of Turkey [3].

According to Turkey's solar energy potential map, the annual total sunshine duration is 2741 hours/year, and the annual total incoming solar energy is 1527.46 kWh/m^2-year. According to Table 1, the average daily sunshine duration in Turkey is 7.5 hours [4].

Table 1. Solar radiation and sunshine duration values of Gaziantep province.

Months	**Total Solar Energy per Day** (kWh/m^2-day)	**Total Solar Energy per Month** ($kWh/m^2-month$)	**Sunshine Duration per Day** ($hours/day$)	**Sunshine Duration per Month** ($hours/month$)
January	1,79	55,49	4,11	127,41
February	2,5	70	5,22	146,16
March	3,87	119,27	6,27	194,37
April	4,93	147,9	7,46	223,8
May	6,14	190,34	9,1	282,1
June	6,57	197,1	10,81	324,3
July	6,5	201,5	11,31	350,61
August	5,81	180,11	10,7	331,7
September	4,81	144,3	9,23	276,9
October	3,46	107,26	6,87	212,97

JSR A
Journal of Scientific Reports

November	2,14	64,2	5,15	154,5
December	1,59	49,29	3,75	116,25
Total	50,11	1527,46	89,98	2741,07
Average	4,18	127,29	7,50	228,42

Photovoltaic panels, which are used in the production of electricity from solar energy, provide production at different powers at different points of our country. Regional, seasonal, and environmental factors are at the forefront of these differences. This study forms the basis of examining the production of photovoltaic cells in different provinces and estimating the energy production in these provinces using a machine learning method called linear regression. Based on this estimation process, investors and institutions could be able to determine the feasibility of benefiting from solar energy, predict the amortization period, maximize energy production efficiency, and determine the best region to invest in. In the estimation part, the solar radiation data of Gaziantep province and the sunshine duration parameters were processed in the MATLAB environment and carried out by the linear regression method. In the MATLAB environment, the obtained data were estimated using the linear regression method. By means of these method, production values and error values were determined before the solar power plant was installed.

Kaplan used the moving least squares approach (MLSA) and the least squares method (LSM) to calculate the coefficients of the Weibull distribution function. In this study, the outcomes of the MLSA graph approach were compared against the results of the least squares method on a monthly and annual basis [5]. Atique et al. used auto-regressive integrated moving average (ARIMA) to model the time series with its seasonal variant and then compared the performance with support vector machine (SVM) and artificial neural network (ANN). The analysis revealed that SVM performed best, however it was proposed that the reasons behind ANN's low efficiency should be investigated [6]. Aksoy and Selbaş utilized machine learning methods to estimate energy values based on wind speed, temperature, and direction data acquired from a wind turbine. A mathematical equation was proposed by researchers who achieved 90% accuracy in their studies [7]. Abdelhafidi et al. developed a model based on global solar radiation estimation using temperature, cloud cover, insolation rate, evaporation, wind speed, sunshine duration, visibility, and global solar radiation data from 1986–2014 obtained from the Oran radiometric station in Algeria. A stepwise multiple linear regression analysis was performed to fit the meteorological variables to the global solar radiation data [8]. Nath et al. used two different machine learning approaches to estimate solar energy. In their study, they used Neural Network (NN) and long short-term memory (LSTM) and determined that NN performed better [9].

2. CALCULATION of SOLAR RADIATION

While calculating the solar radiation required for the energy production of photovoltaic systems, the monthly average solar radiation is used. The development of the Angstrom model was inspired by the meteorological, regional, astronomical, geographical, and geometric parameters of global solar radiation [10].

JSR A
Journal of Scientific Reports

$$\frac{H}{H_0} = a + b\left(\frac{S}{S_0}\right) \tag{1}$$

When this equation is examined in detail, H represents the monthly average daily global solar radiation of the determined region. S is the average daily sunshine duration of the monthly determined region, H_0 is the daily solar radiation value of the horizontal surface of the region, and S_0 is the astronomical day length. The specified a and b coefficients are the regression constants to be determined. The extraterrestrial solar radiation coming to the horizontal surface of the determined region is calculated by Equation 2 [11].

$$H_0 = \frac{24}{\pi} k \left[\cos(\phi)\cos(\delta)\sin(\omega_s) + \left(\frac{\pi}{180}\right)\sin(\phi)\sin(\delta)\omega_s\right] \tag{2}$$

In this equation, the value of k is the day of the year. δ is the sun declination angle, ∅ is the latitude angle of the region, and ωs is the average sunrise value for a certain month according to the angles of the region. Although Isc is expressed as solar constant, it is accepted as 1367 W/m^2 [11].

$$\omega_s = \cos^{-1}\left[-\tan(\delta)\tan(\phi)\right] \tag{3}$$

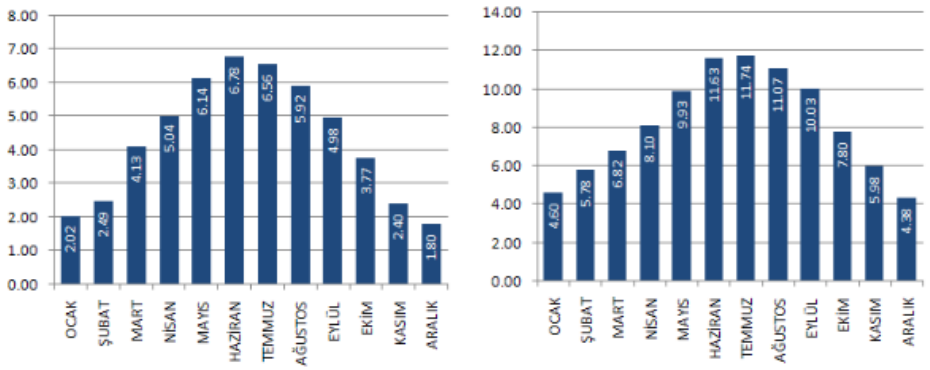

Gaziantep Global Solar Radiation Values ($kWh/m^2 - day$)

Gaziantep Sunshine Duration ($hours$)

Figure 2. Solar Radiation and Sunshine Duration of 2021 for Gaziantep Province [3].

Figure 2 illustrates the global solar radiation and sunshine duration of Gaziantep province, which is the region determined in this study.

JSR A
Journal of Scientific Reports

Table 2. Solar radiation and sunshine duration values of Gaziantep province.

Months	H	H_0	H/H_0	S	S_0	S/S_0
January	2020,000	4742,326	0,426	4,600	9,772	0,471
February	2490,000	6103,072	0,408	5,780	10,626	0,544
March	4130,000	7993,983	0,517	6,820	11,759	0,580
April	5040,000	9841,157	0,512	8,100	12,967	0,625
May	6140,000	11084,258	0,554	9,930	13,987	0,710
June	6780,000	11570,674	0,586	11,630	14,503	0,802
July	6560,000	11301,513	0,580	11,740	14,259	0,823
August	5920,000	10274,358	0,576	11,070	13,371	0,828
September	4980,000	8606,105	0,579	10,030	12,201	0,822
October	3770,000	6650,105	0,567	7,800	10,996	0,709
November	2400,000	5037,583	0,476	5,980	9,984	0,599
December	1800,000	4324,769	0,416	4,380	9,495	0,461

S_0 represents the astronomical day length obtained from the movement of the earth around the sun [11].

$$S_0 = \frac{2}{15}\omega_s \tag{4}$$

The sun declination angle δ is the angle that the sun rays coming to the earth make with the equatorial plane. This angle varies between -23.45˚ and +23.45˚ during the year. The value of n in the formula is the number of days of a year starting from January [12].

$$\delta = 23.45\sin\left(360\frac{n+284}{365}\right) \tag{5}$$

3. ESTIMATION PROCESS for GAZIANTEP PROVINCE

Gaziantep, which is located at the junction of the Mediterranean Region and the South-eastern Anatolia Region, is located between 36° 28' and 38° 01' east longitudes and 36° 38' and 37° 32' north latitudes [13]. Average global solar radiation H and mean sunshine duration S are shown in Figure 2. By obtaining H_0 and S_0 values, a and b coefficients were obtained by using the machine learning method.

The above-mentioned average solar radiation H, extra-atmospheric solar radiation H_0, average sunshine duration S, astronomical day length S_0, and the values of the H/H_0 and S/S_0 to be used when constructing the Angstrom model are given in Table 2. The datasets in Table 2 were processed in the MATLAB program, and the regression graphs and values were obtained by processing the 2021 average solar radiation data and sunshine duration data of Gaziantep province. The model was found

JSR A
Journal of Scientific Reports

by using the linear regression machine learning method over the MATLAB by using the average solar radiation value and average sunshine duration for Gaziantep province. In the model found, error analysis methods such as RMSE, MAE, MSE, and R^2 were applied, and the accuracy of the model was revealed as shown in Table 3.

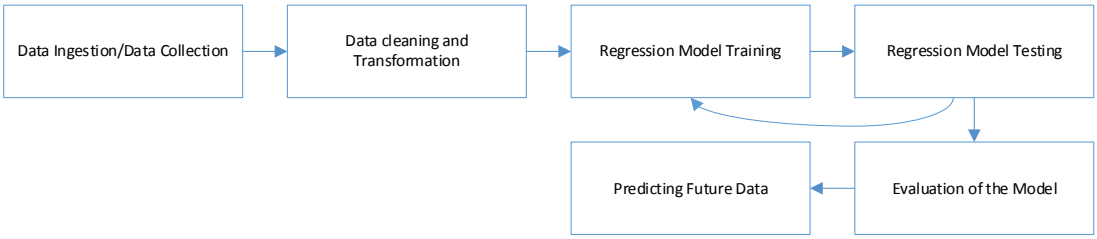

Figure 3. Flowchart of the Regression Process [14].

In this study, the linear regression model was utilized to forecast future values. Figure 3 illustrates a flow chart of the complete operation. The first data for the learning process is collected and processed in the data storage or data ingestion section. The dataset was collected from the Solar Potential Atlas (GEPA) [3]. The converted data is trained and tested on the Linear Regression Model in the Regression Model Training and Regression Model Testing sections. The training and testing process is repeated numerous times by modifying settings until the best accuracy is reached. In the evaluation model, regression metrics are measured. Future values can be predicted using the best model with satisfied metrics [14].

JSR A
Journal of Scientific Reports

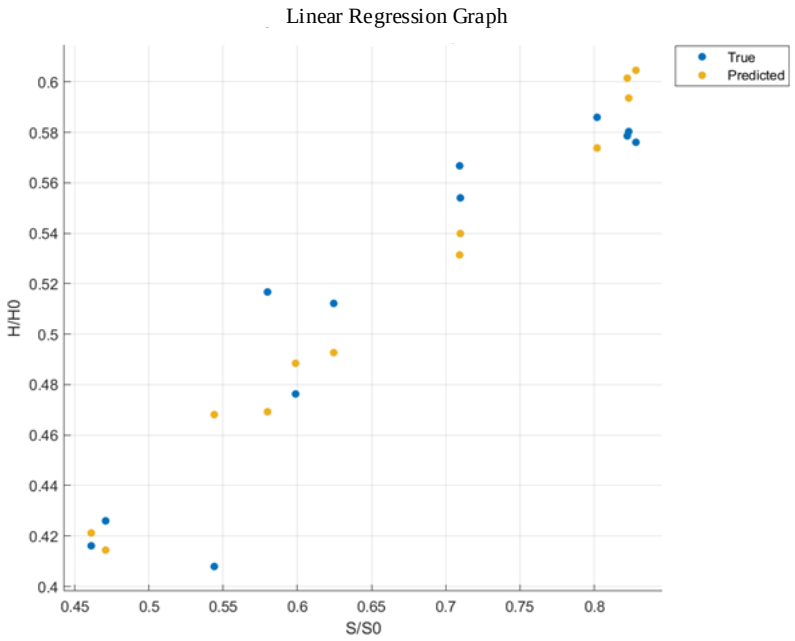

Figure 4. Linear Regression Graph.

Figure 4 shows the comparison of actual and estimated data on the graph. The model created is based on the data in this graph.

$$\frac{H}{H_0} = -0,1898 + 0,4918\left(\frac{S}{S_0}\right) \tag{6}$$

The model in Equation 6 is obtained to estimate the solar radiation for selected region. The linear model that emerges as a result of the linear regression method.

Table 3. Regression model and error parameters.

Regression Model	a	b	Model	MAE	RMSE	R^2	MSE
Linear Regression	-0,1898	0,4918	$y = 0,4918x - 0,1898$	0,023	0,028	0,98	0,0008

Four distinct statistical tests were used to evaluate the performance of the model constructed for the Gaziantep region. As demonstrated in Table 3, the created model performed accurately in terms of estimating solar radiation.

4. RESULTS and DISCUSSION

The increase in the need for energy used in the world day by day proves that the current energy is not at a sufficient level. Today, the increase in the cost of fossil fuels, which are the most widely used to satisfy the world's energy needs, and the irreversible damage to the environment have led humanity to seek alternative sources. Renewable energy sources have emerged as a result of this search, and solar energy is seen as the most popular among these sources.

The utilization of developing technology has increased due to the development of computer science and the emergence of new methods. The use of artificial intelligence, machine learning methods, and many different algorithms paves the way for the solar energy sector. In this study, it is aimed to create a new model by using linear regression from machine learning methods in the MATLAB program. Machine learning methods are one of the most efficient methods of estimation.

Machine learning algorithms have grown in popularity for estimating solar radiation. The linear regression method was chosen from among numerous machine learning algorithms due to its ease of use. However, different machine learning methods can also be used to predict solar radiation in the selected region for a higher accuracy and more precise estimation process. When the estimated experimental results analysis for Gaziantep province was examined, the results were obtained according to the MATLAB program, with the linear regression results as RMSE is 0.028, MAE is 0.023, MSE is 0.0008, and the coefficient of determination R^2 is evaluated as 0.98. When the results were analysed, it was seen that realistic results could be obtained when the linear regression method was tried for Gaziantep province. By comparing the similar studies in the literature, it is clearly observed that the developed model gives accurate results. In a conclusion, it is seen that each province-based region can be modelled by using the machine learning method in terms of solar radiation intensity, and sunshine duration. The linear regression model could be utilized in order to estimate solar radiation for various regions.

ACKNOWLEDGEMENT

The author declares that there are no conflict of interests.

REFERENCES

[1] Sayin, S., Koc, İ., (2011), Photovoltaic (PV) Systems used in active utilization of solar energy and usage methods in building, Selcuk University Journal of Engineering, Science and Technology, 26, 89-106.

[2] Sahan, M., Sahan, H., and Yegingil, I., (2014), Measuring annual total and ultraviolet (UV) solar energy data, Journal of Suleyman Demirel University Graduate School of Natural and Applied Sciences, 14, 10–16.

[3] (2022), Solar Energy Potential Atlas. [Online]. Available: https://gepa.enerji.gov.tr/Mycalculator/Default.Aspx

[4] Canka Kilic, F., (2015), Latest status in Turkey and production technologies, Engineer and Machine, 56, 28-40.

[5] Kaplan, A.G., (2022), A new approach based on moving least square method for calculating the Weibull coefficients, Environmental Progress & Sustainable Energy, 41(4), e13934.

[6] Atique, S., Noureen, S., Roy, V., and Macfie, J., (2020), Time series forecasting of total daily solar energy generation: A comparative analysis between ARIMA and machine learning techniques, 2020 IEEE Green Technologies Conference, 1-3 April 2020, 175-180.

[7] Aksoy, B., and Selbas, R., (2019), Estimation of wind turbine energy production value by using machine learning algorithms and development of implementation program, Energy Sources Part A: Recovery, Utilization and Environmental Effects, 43, 692-704.

[8] Abdelhafidi, N., Bachari, N.I., and Abdelhafidi, Z., (2021), Estimation of solar radiation using stepwise multiple linear regression with principal component analysis in Algeria, Meteorology and Atmospheric Physics, 133, 205-216.

[9] Nath, N.C., Sae-Tang, W., and Pirak, C., (2020), Machine learning-based solar power energy forecasting, Journal of the Society of Automotive Engineers Malaysia, 4, 307-322.

[10] [Besharat, F., Dehghan, A.A., and Faghih, A.R., (2013), Empirical models for estimating global solar radiation: A review and case study, Renewable and Sustainable Energy Reviews, 21, 798-821.

[11] Kaplan, Y.A., Sarac, M.S., and Unaldi, G.G., (2022), Developing a new model in solar radiation estimation with genetic algorithm method, Environmental Progress & Sustainable Energy.

[12] Sahan, M., (2021), Global solar radiation forecast for Gaziantep, Antakya and Kahramanmaras using artificial neural networks and Angström-Prescott equations, Suleyman Demirel University Faculty of Arts and Science Journal of Science, 16, 368-384.

[13] Roger, A., and Ventre, M.J., (2003), Photovoltaic Systems Engineering, 2nd ed., CRC Press.

[14] Killada, P., (2017), Data analytics using regression models for health insurance market place data, MSc. Thesis in Engineering: Computer Science, The University of Toledo.

Kütahya Dumlupınar University
Institute of Graduate Studies

Journal of Scientific
Reports-A
E-ISSN: 2687-6167
Number 51, December 2022

RESEARCH ARTICLE

EVALUATION of GEOTECHNICAL BEHAVIOR of CLAY SOIL with CRUMB RUBBER ADDITION

Sadettin TOPÇU[1,*], Evren SEYREK[2]

[1*]Kütahya Dumlupınar University, Kütahya Vocational School of Technical Sciences, Department of Construction Technology, Kütahya, sadettin.topcu@dpu.edu.tr, ORCID: 0000-0003-1306-2502
[2]Kütahya Dumlupınar University, Faculty of Engineering, Department of Civil Engineering, Kütahya, evren.seyrek@dpu.edu.tr, ORCID: 0000-0003-4373-6723

Receive Date:30.09.2022 *Accepted Date: 24.10.2022*

ABSTRACT

The issue of investigating the usability of waste materials in many different applications of civil engineering has attracted the attention of researchers until today. The additive material used for stabiliser is waste material that causes positive effects on the environment, engineering and economy. Studies on the use of waste materials, especially in improving road and foundation filling materials, have recently attracted attention. In this study, compaction parameters, California Bearing Ratio (CBR) with the soaked and unsoaked condition and unconfined compressive strength values of soil-crumb rubber mixtures were evaluated. To investigate these effects, crumb rubber with various percentages (2.5%, 5.0%, 7.5%, 10.0% and 15.0%) was added to clay soil taken from Eskisehir city in Turkey. CBR and unconfined compressive test results show that a 5.0% crumb rubber level is optimum. For 5.0% additive level, soaked and unsoaked CBR values increased by approximately 18% and 25%, respectively. The highest increase was seen at same additive level as 8% compared to pure clay specimen for unconfined compressive strength.

Keywords: *Clay, Crumb rubber, CBR, Strength*

1. INTRODUCTION

Due to the rapid growth in vehicle production worldwide, approximately 1,5 billion tons of tires are wasted yearly [1]. About 3 million tons of tires are scrapped every year in Europe [2]. 180.000-200.000 tons of scrap tires are generated every year in Turkey [3]. Most waste tires are deposited in storage yards and landfills. Therefore, they occupy significant lands. In addition, many of them burn and cause toxic fumes (containing substances such as styrene, benzene, butadiene, CO, SO_2, etc.) to nature. These rubber-based wastes, which harm nature and human health, pose a significant problem.

Waste tires are used as a wedge in port structures, parking equipment in children's playgrounds, and fuel in power plants and cement factories [4]. There are three different specifications for waste tires to

JSR A
Journal of Scientific Reports

be used in the shredded form [5-7]. Besides Busic et al.[8] and Li et al. [9], there are also classifications based on the sizing suggested. In general, in these specifications and approaches, waste tire pieces are called chips, tire-derived aggregate, ground, crumb, fibre, granulate and powder rubber, depending on their size and shape. The performance of composite mixtures consisting of soil and waste tire depends on the type of soil and the size of the waste tire pieces.

Many types of research have been carried out in geotechnical engineering applications such as landfill, subgrade backfilling and retaining walls to obtain a benefit for the recycling of waste tires [10-13]. These materials, which are lightweight aggregates, can absorb vibrations while creating low stress in soil. Sandy soils are generally preferred for stabilization with the waste tire. The reason for this is the lack of cementing at the molecular level of the waste tire. Their interaction with the sand grains is also limited to friction, locking and filling the spaces between the grains. Use of waste rubber pieces on sand soils; compression and deformation [10,14,15], strength [15,16-18], dynamic properties [19-21], thermal properties [22,23], hydraulic properties [17,24] and microstructural properties [10,15,25]. In summary, waste rubber pieces mixed with sand reduce compressibility and vibrations, increase strength and hydraulic conductivity, and decrease thermal conductivity.

Studies carried out on clay soils were carried out under the headings of compression, strength, dynamic, thermal, hydraulic and microstructural characteristics like sand. Using different waste rubber particle diameter distributions, the variation of compaction parameters is also different. In general, the maximum dry density (M.D.D) and optimum moisture content (O.M.C) decrease depending on the size of the waste rubber [1,26,27]. Knowing the consolidation characteristics in determining the settlement behavior in fine-grained soils is necessary. There are also many studies on the consolidation characteristics of clay soil-waste rubber mixtures [28-30]. The effect of the waste rubber may also vary in the consolidation characteristics depending on the particle diameter distribution.

Strength parameters of soil-waste rubber mixtures in fine-grained soils are investigated by the Direct Shear Test [31,32], Triaxial Test [33-35], Unconfined Compressive Test [27,32,36-38] and California Bearing Ratio (CBR) Test) [26,27,35]. When these studies are evaluated in general, it can be said that waste rubber makes positive changes in the strength parameters of clay soils up to a certain percentage of contribution.

Clay-waste rubber mixture improves the seismic design parameters of slopes, embankments and retaining walls where it will be used as filling material. Waste rubber additive reduces the vibration of clay soils and provides high damping characteristics [19]. In waste rubber additives, clay soils' permeability coefficients and hydraulic conductivity are greatly reduced [36,39]. SEM analysis showed voids, gaps and micro-cavities at the crumb rubber-clay soil interfaces [27].

In this study, modification properties of soil-crumb rubber mixtures were assessed in term of compaction behavior, California Bearing Ratio (CBR) with the soaked and unsoaked condition and unconfined compressive strength. To investigate these effects, crumb rubber varying from 0.4 to 5.0 mm with various percentages (2.5%, 5.0%, 7.5%, 10.0% and 15.0%) was added to clay soil taken from Eskişehir city in Turkey.

JSR A
Journal of Scientific Reports

2. MATERIAL AND METHOD

2.1. Soil

The clay soil was taken from Eskisehir city in Turkey. The physical parameters including sieve and hydrometer test, water content, consistency limits and specific gravity values were obtained based on ASTM methods [40]. The particle size distribution of the clay soil is given in Figure 1. As seen in Figure 1, the soil contains 56% fines.

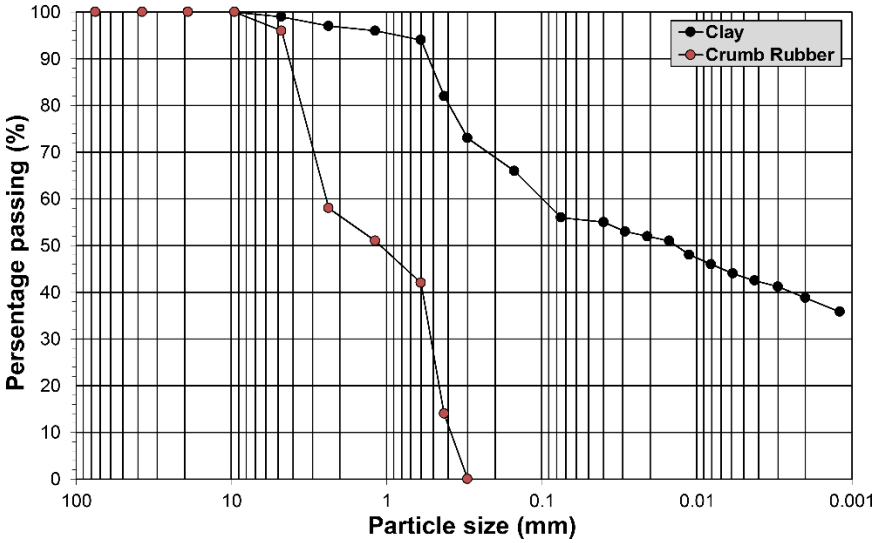

Figure 1. Particle size distribution of clay and crumb rubber.

The geotechnical features of the soil are summarised in Table 1. According to Table 1, the soil was classified as low plasticity (CL) clay under the Unified Soil Classification System (USCS). The clay soil sample with an activity value of 0.49 was described as inactive. The specific gravity of clay soil is 2.72. Liquidity limit value is calculated as a ratio of the difference between natural water content, plastic limit and liquid limit, and consistency is semi-solid. The compaction parameters maximum unit weight and optimum water content were determined with Standard Proctor Test [41] as 18.2 kN/m^3 and 14.2%, respectively.

Table 1. Geotechnical properties of clay soil.

Property	Clay
<4.75 mm (%)	99.0
<0.075 mm (%)	56.0
<0.002 mm (%)	38.8
Water content, w (%)	12.0

JSR A
Journal of Scientific Reports

Liquid Limit, LL (%)	34.0
Plastic Limit, PL (%)	15.0
Plasticity Index, PI (%)	19.0
Specific Gravity, G_s	2.72
Classification (USCS)	CL
Activity, A	0.49
γ_{dmax} (kN/m^3)	18.2
w_{opt} (%)	14.2

2.2. Crumb Rubber

The crumb rubber adopted as an additive in this investigation was gained from a private company in Istanbul, Turkey. The particle size distribution of crumb rubber is given in Figure 1. It can be seen that most of the particles ranged from 0.4 to 5.0 mm. Busic et al. [8] classified waste rubber with a size of between 0.425mm and 4.75mm as crumb rubber. Effective size (D_{10}), coefficient of uniformity and curvature was determined as 0.38 mm, 6.32 and 0.30, respectively. The gradation of crumb rubber is similar to poorly graded sand (SP) when evaluated based on the USCS classification system. The specific gravity value is 1.09 (Table 2). It is stated that specific values of crumb rubber are between 1.02 and 1.27 [2].

Table 2. Geotechnical properties of crumb rubber.

Property	**Crumb Rubber**
<4.75 mm (%)	96.0
<0.075 mm (%)	0.0
<0.002 mm (%)	0.0
D_{10} (mm)	0.38
D_{30} (mm)	0.52
D_{50} (mm)	1.05
D_{60} (mm)	2.4
Coefficient of uniformity, C_u	6.32
Coefficient of curvature, C_c	0.30
Specific Gravity, G_s	1.09

2.3. Experimental Program

In the literature, different studies are performed to research the impact of crumb rubber on the geotechnical engineering behavior of clay soils with different rubber content. Compaction and strength behavior of kaolin clay was investigated by Priyadarshee et al. [42] with different ratios of tire crumbles such as 1.0%, 2.0%, 5.0%, 10.0% and 20.0%. Yadav and Tiwari [27] used 2.5%, 5.0%, 7.5% and 10.0% rubber content to treat soft clay soil. Vijay [43] studied stress-strain and penetration characteristics of clay with crumb rubber addition varying from 10% to 50%. Li and Li [44] used three scrap tire crumbs contents,10.0%, 20.0% and 30.0%, to investigate the mechanical properties of

JSR A
Journal of Scientific Reports

mixtures. The most striking point in these studies is that the crumb rubber content is considered at different ratios. The results of these researches have shown that the selection of the most effective content of waste rubber material is closely related to the gradation of rubber material. For this reason, in this study, the crumb rubber material was added to clay soil in different amounts (2.5%, 5.0%, 7.5%, 10% and 15% of the dry soil weight).

The experimental studies carried out to determine compaction parameters, California Bearing Ratio (CBR%) and strength values of the clay soil-crumb rubber mixtures. According to Table 3, the designations used for clay soil are S and R for crumb rubber. For example, 5SR represents a mixture having 95% soil and 5% crumb rubber. Compaction Test, CBR Test and Unconfined Compressive Tests are performed for all of the selected mixture ratios.

Table 3. Experimental program.

Crumb Rubber (%)	Mixture Designation	Atterberg Limits	Compaction Test	CBR Test		Unconfined Compressive Test
				Soaked	Unsoaked	
0.0	0SR	☐	☐	☐	☐	☐
2.5	2.5SR		☐	☐	☐	☐
5.0	5SR		☐	☐	☐	☐
7.5	7.5SR		☐	☐	☐	☐
10.0	10SR		☐	☐	☐	☐
15.0	15SR		☐	☐	☐	☐

2.3.1. Preparation of clay soil-crumb rubber

Clay soil obtained from the field was dried for 24 hours in an oven, and then it was sieved from #4. Dry crumb rubbers were added to dry clay soil with different ratios (2.5%, 5.0%, 7.5%, 10.0% and 15.0%) and mixed (Figure 2). Special attention was paid to attaining a homogenous mixture during the mixture preparation stage. Proctor tests at the standard Proctor energy level were carried out on these prepared soil-crumb-rubber mixtures [41]. Maximum dry unit weight and optimum water content values of the mixtures were determined. CBR and unconfined compressive tests (UCT) were performed on the compacted samples having a optimum water content.

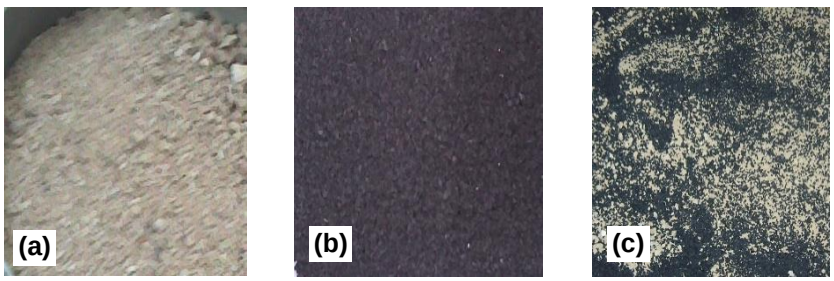

Figure 2. Test materials (a) clay soil (b) Crumb rubber (c) Clay-crumb rubber mixture.

JSR A
Journal of Scientific Reports

2.3.2. Compaction test

The water content and dry unit weight relationship are necessary for the geotechnical behavior of soil subjected to static and dynamic loading. The specimens were compacted in three layers and an energy degree of 600 kN-m/m3 was applied as suggested in ASTM D698–12 [41]. The dry crumb rubber and clay were mixed until obtaining a homogenous mixture before the compaction. A view of the compaction process for additive-free soil and soil with 5.0% crumb addition is given in Figure 3.

Figure 3. Compacted test materials (a) clay soil (b) Clay-crumb rubber mixture (%5 rubber).

2.3.3. California Bearing Ratio (CBR) test

CBR test results evaluate the subgrade strength of roads and pavements. The CBR test is performed to find a load-penetration relation by pushing a cylindrical piston with a cross-sectional area of 19.35 cm^2 into the ground at a certain speed. For any penetration value, CBR, defined as the ratio of the measured load to a standard load, is usually given for 2.5 mm and 5.0 mm penetration. In this study, CBR tests of pure clay and clay-rubber mixtures for unsoaked and soaked conditions as described in ASTM D1883-21[45]. The samples were prepared at each mixture's maximum dry unit weight and optimum water content. Mixtures were soaked in water for 96 h before testing for soaked conditions.

2.3.4. Unconfined compressive test

The unconfined compressive test is widely used for determining the undrained shear strength value. This test is preferred due to be practical, easy and rapid evaluation. Unconfined compression tests of soil-crumb rubber mixtures compacted according to their compaction characteristics were carried out according to standard [46]. The samples were prepared in a mold designed with a ratio of height/diameter is 2.

3. RESULTS and DISCUSSION

3.1. Results of Compaction Tests

Results of compaction tests for various additive levels are given in Table 4. It can be said that including the crumb rubber to clay soil causes to decrease the maximum unit weight and optimum moisture content. The maximum dry unit weight value of pure clay soil was 18.2 $kN/m^{3.}$ The same value decreased to 15.2 kN/m^3 with 15.0% crumb rubber addition. When the optimum water content

JSR A
Journal of Scientific Reports

was 14.2% for pure clay soil, the optimum water content decreased to 12.4% after the same amount of crumb rubber addition.

Table 4. Compaction characteristics of soil-crumb rubber mixtures.

Mixture Designation	γ_{dmax} (kN/m^3)	w_{opt} (%)
0SR	18.2	14.2
2.5SR	17.4	13.9
5SR	17.0	13.6
7.5SR	16.2	13.1
10SR	15.8	12.9
15SR	15.2	12.4

With 5% crumb rubber addition to clay soil, the maximum dry unit weight decreases by 7% of pure clay soil. The same value decreases by approximately 17% with 15% crumb rubber.

Figure 4 was prepared to see the general trend of the relationship between the optimum moisture content and maximum dry unit weight of the mixtures. This figure shows a decrease in maximum dry unit weight and optimum water content with an increment in the rubber content. The specific gravity value of crumb is 1.09. Since specific gravity value of crumb rubber is too low compared to pure clay soil, the specific gravity of the mixture reduces with the rise in the crumb rubber amount. A decrease in the maximum dry unit weight can be explained with this situation. In addition, Cabalar et al. [26] expressed that the decrease in optimum moisture content of the clay-rubber mixtures could be explained with rubber's lower water absorption capacity. These results are similar with the other researches in the literature [27,44].

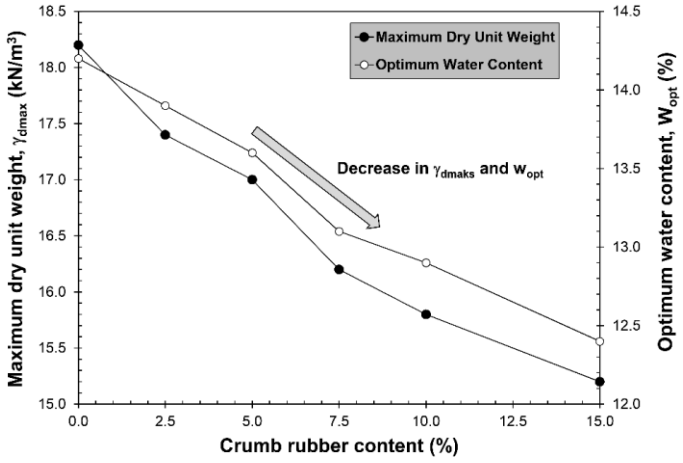

Figure 4. Compaction properties of clay-crumb rubber mixtures.

JSR A
Journal of Scientific Reports

3.2. Results of California Bearing Ratio (CBR) Tests

Results of the CBR test performed on clay soil stabilized using various percentages of crumb rubber are shown in Figures 5a for unsoaked conditions and 5b for soaked conditions.

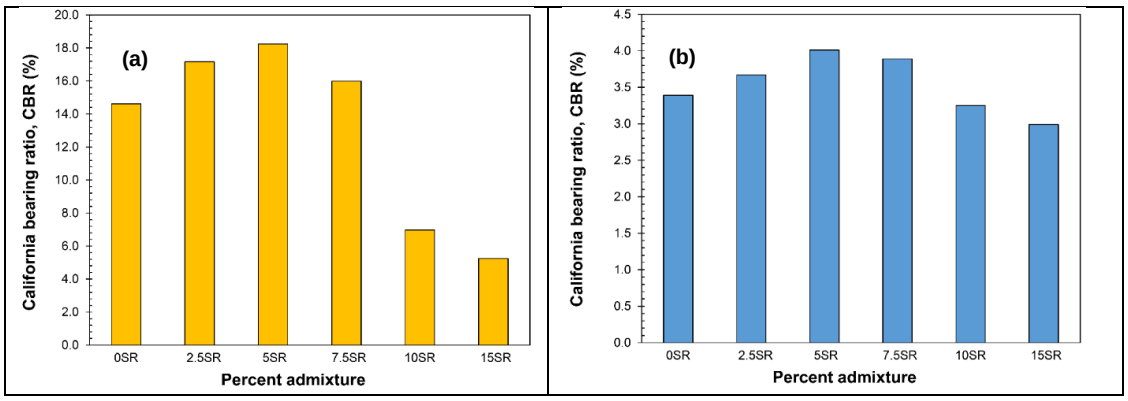

Figure 5. Variations of CBR value of pure clay and mixtures (a) soaked (b) unsoaked condition.

When both Figure 5a and Figure 5b are evaluated together, the CBR value of mixtures for the soaked condition is smaller than mixtures for the unsoaked condition. It should be noted that the CBR value of mixtures with 10.0% and 15.0% additive levels is much smaller than the CBR value of clay soil in a non-additive state for dry conditions. CBR value is 14.61% for specimen 0SR. The highest CBR value is 18.24%, corresponding to a 25% increase compared to specimen 0SR (Figure 5a).

CBR test results for soaked conditions show that the additive level giving the largest CBR value is 5.0% crumb rubber (Figure 5b). The CBR value for clay soil with 5.0% crumb rubber corresponds to approximately 1.18 times the CBR value of pure clay soil. Another remarkable point between Figure 5a and Figure 5b is that the CBR value for clay with 10.0% crumb rubber is very close to the CBR value of pure clay soil.

For both conditions, the CBR value increases to 5.0% crumb rubber and decreases. These results are in concord with other studies in the literature. According to Yadav and Tiwari, the reduction in CBR value with increasing the rubber content can be explained with the higher compressibility of rubber particles compared to soil particles [27].

3.3. Results of Unconfined Compressive Tests

Unconfined compressive strength (UCS) values for different proportions of Clay–crumb rubber mixtures compacted according to their compaction characteristics are given in Figure 6 as the UCS value of the treated soil to the UCS value of the untreated soil. UCS value of pure clay soil is determined as 140.1 kPa.

UCS values are 145.2 kPa and 151.2 kPa for 2.5% and 5.0% crumb rubber addition, respectively. Minimum UCS value is observed in clay soil with 15.0% crumb rubber additives as 119.6 kPa. The

JSR A
Journal of Scientific Reports

UCS value of the mixtures with a rubber ratio between 2.5% and 15% to the UCS value of the pure clay soil varies between 0.85 and 1.03. The highest rate value is seen at the 5.0% additive level.

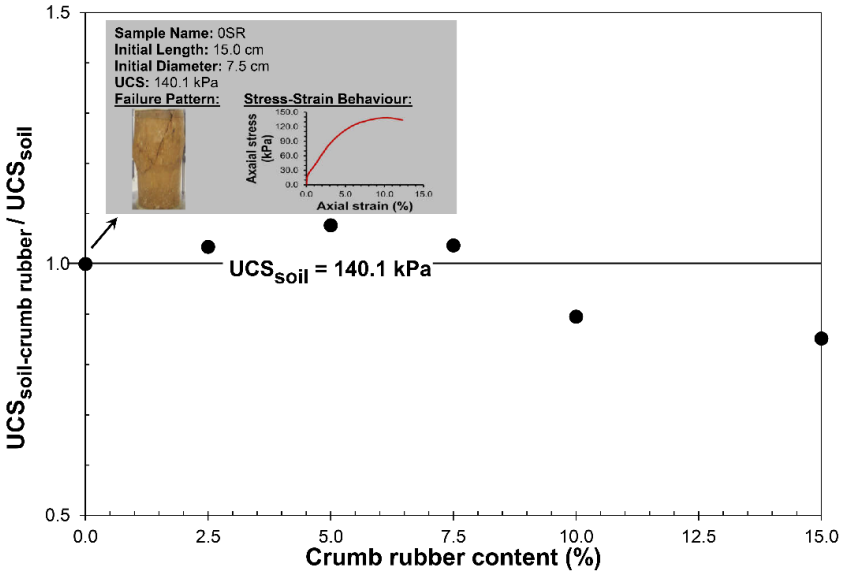

Figure 6. Effect of crumb rubber contents on unconfined compressive strength (UCS) of mixtures.

According to Figure 6, UCS value of mixtures increases with the crumb rubber content by up to 5%. Ajmera et al. [38] stated that this behavior could be related to the increase in the dry unit weight of the mixtures with crumb rubber addition until the threshold content. According to a different perspective by Kim and Kang [47], the friction and bonding loss between crumb rubber and clay particles could reduce unconfined compressive strength.

4. CONCLUSIONS

This study was carried out to investigate the influence of crumb rubber sizes varying from 0.4 to 5.0 mm on the compaction and strength behavior of clay soil taken from Eskisehir city in Turkey. Compaction, CBR and UCT experiments were performed on clay soil with different crumb rubber contents (2.5%, 5.0%, 7.5%, 10.0% and 15.0%), and the following results have been reached:

- Including the crumb rubber in clay soil reductions the maximum unit weight and optimum moisture content of the mixtures with all different additive ratios. It is thought that the lower water absorption capability of rubber causes to this behavior.
- For unsoaked and soaked conditions, CBR values increase to 5.0% crumb rubber and starts to decrease after this threshold value. This decrease in CBR values on increasing the rubber content may be ascribed to the higher compressibility of rubber particles.

- Addition of crumb rubber to the clay soil results in an initial increase in the UCS followed by a reduction in the unconfined compressive strength (UCS) after a peak value is achieved. The UCS value peak occurs when 5.0% crumb rubber is used. Therefore, 5.0% crumb rubber content can be accepted as optimum strength for this study.
- It should be noted that the results obtained within the scope of this study are not independent of rubber size.
- Experimental findings demonstrate that optimum crumb rubber content is 5.0% for effective solution. In this way, the unfavorable effects of this waste material on the environment will be reduced and contribute to the economy.

ACKNOWLEDGEMENT

The authors declare that there is no conflict of interest in the course of this study.

REFERENCES

[1] Yadav, J.S., Tiwari, S.K., (2016), Effect of inclusion of crumb rubber on the unconfined compressive strength and wet-dry durability of cement stabilized clayey soil, J Build Mater Struct, 3:68–84.

[2] Edinçliler, A., (2010), Atık lastiklerin geoteknik uygulamalarda hafif malzeme olarak kullanılması, Dördüncü Ulusal Geosentetikler Konferansı, İstanbul, Türkiye, 58-68.

[3] URL-1, Lastik Sanayicileri Derneği, https://www.lasder.org.tr/, Erişim 26.09.2022.

[4] Karabörk, F., Akdemir, A., (2013), Atık Taşıt Lastiklerinin Parçalanması ve Lastik Tozunun Karakterizasyonu, Erciyes Üniversitesi Fen Bilimleri Enstitüsü Fen Bilimleri Dergisi, 29(1): 29-40.

[5] ASTM D6270-08, (2008), Standard practice for use of scrap tires in civil engineering applications. West Conshohocken, Pa: ASTM standard D6270-08. ASTM International.

[6] ASTM D5681-18, (2018), Standard Terminology for waste and waste management. West Conshohocken, Pa: ASTM standard D5681-18. ASTM International.

[7] CEN Workshop agreement (CWA) 14243-2002. CWA; 2002.

[8] Busic, R, Milicevic, I., Sipos T. and Strukar, K., (2018), Recycled rubber as an aggregate replacement in self-compacting concrete—literature overview, Materials, 11:1729.

[9] Li, B., Huang, M. and Zeng, X., (2016), Dynamic behavior and liquefaction analysis of recycled-rubber sand mixture, J Mater Civ Eng, 28:04016122.

JSR A
Journal of Scientific Reports

[10] Liu, L., Cai, G. and Liu, S., (2018), Compression properties and micro-mechanisms of rubber-sand particle mixtures considering grain breakage, Construct Build Mater, 187: 1061–1072.

[11] Morales, E., Filiatrault A. and Aref, A., (2018), Seismic floor isolation using recycled tires for essential buildings in developing countries, Bull Earthq Eng, 16:6299–6333.

[12] Neaz Sheikh, M,, Mashiri, M., Vinod, J. and Tsang, H-H., (2012), Shear and compressibility behavior of sand–tire crumb mixtures, J Mater Civ Eng, 25:1366–1374.

[13] Tafreshi, S.M., Mehrjardi, G.T. and Dawson, A.R., (2012), Buried pipes in rubber-soil backfilled trenches under cyclic loading, J Geotech Eng, 138:1346–1356.

[14] Guo, Y., Morgan, J.K., (2006), The frictional and micromechanical effects of grain comminution in fault gouge from distinct element simulations, J Geophys Res Solid Earth,111.

[15] Zhang, T., Cai, G. and Duan, W., (2018), Strength and microstructure characteristics of the recycled rubber tire-sand mixtures as lightweight backfill, Environ Sci Pollut Res, 25:3872–3883.

[16] Ahmed, I., (1993), Laboratory study on properties of rubber-soils.

[17] Edil, T.B., Bosscher, P.J., (1994), Engineering properties of tire chips and soil mixtures, Geotech Test J, 17:453–464.

[18] Foose, G.J, Benson, C.H. and Bosscher P.J., (1996), Sand reinforced with shredded waste tires, J Geotech Eng-ASCE, 122:760–767.

[19] Feng, Z-Y, Sutter, K.G., (2000), Dynamic properties of granulated rubber/sand mixtures, Geotech Test J, 23:338–344.

[20] Zornberg, J.G., Cabral, A.R. and Viratjandr, C., (2004), Behavior of tire shred-sand mixtures, Can Geotech J, 41:227–241.

[21] Senetakis, K., Anastasiadis, A. and Pitilakis, K., (2012), Dynamic properties of dry sand/rubber (SRM) and gravel/rubber (GRM) mixtures in a wide range of shearing strain amplitudes, Soil Dynam. Earthq. Eng., 33:38–53.

[22] Mounanga, P., Gbongbon, W., Poullain, P. and Turcry, P., (2008), Proportioning and characterization of lightweight concrete mixtures made with rigid polyurethane foam wastes, Cement Concr Compos, 30:806–814.

[23] Corinaldesi, V., Mazzoli, A. and Moriconi, G., (2011), Mechanical behavior and thermal conductivity of mortars containing waste rubber particles, Mater Des, 32: 1646–1650.

[24] Edil, T.B., Bosscher, P.J., (1992), Development of engineering of Criteria for shred waste tires in highway applications final report.

[25] Perez, J.L., Kwok, C. and Senetakis, K., (2017), Micromechanical analyses of the effect of rubber size and content on sand-rubber mixtures at the critical state, Geotext Geomembranes, 45:81–97.

[26] Cabalar, A.F., Karabash, Z. and Mustafa, W.S., (2014), Stabilising a clay using tyre buffings and lime. Road Mater. Pavement Des., 15, 872–891.

[27] Yadav., J., Tiwari, S., (2017), The impact of end-of-life tires on the mechanical properties of fine-grained soil: a review, Environ Dev Sustain,1–84.

[28] Cokca, E., Yilmaz, Z., (2004), Use of rubber and bentonite added fly ash as a liner material, Waste Manag, 24:153–164.

[29] Seda, J.H., Lee, J.C., Carraro, J.A.H., (2007), Beneficial use of waste tire rubber for swelling potential mitigation in expansive soils, ASCE Geotechnical Special Publication 172, 1–9.

[30] Srivastava, A., Pandey, S. and Rana, J., (2014), Use of shredded tyre waste in improving the geotechnical properties of expansive black cotton soil, Geomechanics Geoengin, 9:303–311.

[31] Tatlisoz, N., Benson, C.H. and Edil, T.B., (1997), Effect of fines on mechanical properties of soil- tire chip mixtures, Testing Soil Mixed with wWaste or Recycled Materials, ASTM International.

[32] Akbulut, S., Arasan, S., Kalkan, E., (2007), Modification of clayey soils using scrap tire rubber and synthetic fibers, Appl Clay Sci, 38:23–32.

[33] Ozkul, Z.H., Baykal, G., (2007), Shear behavior of compacted rubber fiber-clay composite in drained and undrained loading, J Geotech Geoenviron, 133:767–781.

[34] Asadzadeh, M., Ersizad, A., (2013), Effect of tire-chips on geotechnical properties of clayey soil, In: International Symposium on Advances in Science and Technology, p. 117–20.

[35] Tajdini, M., Nabizadeh, A., Taherkhani, H. and Zartaj, H., (2017), Effect of added waste rubber on the properties and failure mode of kaolinite clay, Int J Civ Eng, 15:949–958.

[36] Al-Tabbaa, A., Aravinthan, T., (1998), Natural clay-shredded tire mixtures as landfill barrier materials, Waste Manag, 18:9–16.

[37] Signes, C.H., Garzon-Roca, J., Fernandez, P.M., de la Torre, M.E.G. and Franco, R.I., (2016), Swelling potential reduction of Spanish argillaceous marlstone Facies Tap soil through the addition of crumb rubber particles from scrap tyres, Appl Clay Sci,132: 768–773.

[38] Ajmera, B., Tiwari, B., Koirala, J. and Obaid, Z., (2017), Compaction Characteristics, Unconfined Compressive Strengths, and Coefficients of Permeability of FineGrained Soils Mixed with Crumb-Rubber Tire, Journal of Materials in Civil Engineering, 29 (9), 1-10.

[39] Al-Tabbaa, A., Blackwell, O., Porter, S., (1997), An investigation into the geotechnical properties of soil-tyre mixtures, Environ Technol, 18:855–860.

[40] ASTM, (1994), Annual Book of ASTM Standards, Soil and Rock. American Society for Testing and Materials, 04.08.

[41] ASTM D698–12, (2021), Standard Test Methods for Laboratory Compaction Characteristics of Soil Using Standard Effort (12,400 ft-lbf/ft3 (600 kN-m/m3)), ASTM International, West Conshohocken, PA USA.

[42] Priyadarshee, A., Gupta, D., Kumar, V. and Sharma, V., (2015), Comparative study on performance of tire crumbles with fly ash and kaolin clay, International Journal of Geosynthetics and Ground Engineering, 1:38, 7p.

[43] Vijay, S., (2018), Stress-strain and penetration characteristics of clay modified with crumb rubber, Revista Facultad de Ingenieria, vol. 27 (49), 65-75.

[44] Li, S., Li, D., (2018), Mechanical properties of scrap tire crumbs-clayey soil mixtures determined by laboratory tests, Advances in Materials Science and Engineering, Article ID 1742676, 10 pages.

[45] ASTM D1883-21, (2021), Standard Test Method for CBR (California Bearing Ratio) of Laboratory-Compacted Soils, ASTM International: Philadelphia, PA, USA.

[46] ASTM, D2166-13/D2166M-16, (2016), Standard Test Method for Unconfined Compressive Strength of Cohesive Soil, ASTM International, West Conshohocken, PA USA.

[47] Kim, Y.T., Kang, H.S., (2013), Effects of rubber and bottom ash inclusion on geotechnical characteristics of composite geomaterial. Marine Georesources and Geotechnology, 31(1), 71–85.

Kütahya Dumlupınar University
Institute of Graduate Studies

Journal of Scientific
Reports-A
E-ISSN: 2687-6167
Number 51, December 2022

RESEARCH ARTICLE

AUTONOMOUS GUIDANCE SYSTEM for UAVs with IMAGE PROCESSING TECHNIQUES

Salih TEKIN[1], Murat GOK[2], Mustafa NAMDAR[3,*], Arif BASGUMUS[4]

[1]Kütahya Dumlupınar University, Department of Elektrical-Electronical Engineering, Kütahya, salih.tekin@ogr.dpu.edu.tr, ORCID: 0000-0003-3281-9822
[2]Kütahya Dumlupınar University, Department of Elektrical-Electronical Engineering, Kütahya, murat.gok0@ogr.dpu.edu.tr, ORCID: 0000-0001-7010-2377
[3]Kütahya Dumlupınar University, Department of Elektrical-Electronical Engineering, Kütahya, mustafa.namdar@dpu.edu.tr, ORCID: 0000-0002-3522-
[4]Bursa Uludağ University, Department of Elektrical-Electronical Engineering, Bursa, basgumus@uludag.edu.tr, ORCID: 0000-0002-0611-3220

Receive Date:10.10.2022 *Accepted Date: 15.11.2022*

ABSTRACT

In this study, object detection is carried out by the image processing techniques of the images captured by the camera of the UAV in an autonomous flight route. After the desired object is detected, an algorithm is designed to land near this object by autonomous guidance of the UAV. In order to ensure the functioning of the algorithm, a UAV control system including ground station software has been designed. In addition, a deep learning-based human recognition system is tested in the algorithm in order to reduce the risk of accidents that may arise from UAV crashes. Image processing techniques were applied to the images taken by the UAV with the designed system and object detection was achieved successfully. 3 different objects to be detected were determined and the processes were repeated for each object. The deep learning-based human recognition process designed in this study has been tested in terms of recognition accuracy by using different models.

Keywords: *Deep learning, Image processing, HSV, UAV, Human recognition*

1. INRODUCTION

Unmanned Aerial Vehicles (UAV) have become an essential part of the technology world. UAVs, whose usage areas are increasing, also participate in object detection processes. When the UAV is controlled by humans to perform these tasks, incidents such as accidents, disintegration, and damage to the environment and living things may occur. In this case, there is a need to minimize the problems that may arise as a result of human intervention during flight guidance and control in a UAV that is planned to be used for object detection.

JSR A
Journal of Scientific Reports

Significant advances have been realized in the use of UAVs [1-3]. Object detection, which is one of the subjects of computer vision, is an area on which many studies have been carried out recently [4, 5]. When the literature is examined, it is seen that object tracking is done with UAVs by using image processing techniques [6]. Applications of image processing techniques on UAVs are examined in [7-9]. Autonomous control has an important place among UAV applications. In [10-12], autonomous guidance systems for UAVs were evaluated. In addition, deep learning-based applications and artificial intelligence have started to be applied frequently on UAVs in recent years with their increasing popularity [13, 14].

In this study, object detection is realized by using image processing techniques. Regarding the visual and numerical data obtained, the autonomous guidance of the UAV is ensured. As a first step, the images captured by the UAV's camera were detected with the help of various filters and arrangements, and the object with the desired properties was determined. After the object was detected, the necessary algorithm was designed to land next to this object and the parameters that allow the UAV to be controlled autonomously were obtained. A deep learning-based human recognition system is included in the system design so that the UAV does not harm people during landing. As a result of these processes, the main contributions of this study are given as follows:

- The object detection and routing task is carried out autonomously without human control.
- With the benefit of being autonomous, it saves processing time, cost, and labor.
- In addition, human-induced accidents and possible risks are also reduced.
- Besides, since the properties of the object to be detected can be changed in the designed system, it provides flexibility to the user.

In the second part of the study, the system model is explained in detail. In this section, image processing steps used for UAV control systems and object detection are presented. In the third chapter, the results of the image processing techniques and the human recognition system, and artificial intelligence improvements on the system design are presented. In the last section, the obtained results are interpreted.

2. SYSTEM MODEL

In this study, firstly, the control system of the UAV was designed. Then, image processing techniques were applied to the data coming from the camera. At the end of the image processing steps, the object was detected and an algorithm was created that allows the UAV to land next to the object.

In the designed algorithm, firstly, it is expected that the user enters the physical properties of the object to be detected into the UAV control computer. Then, the departure and fixed flight information are transmitted to the UAV within the route defined with the ground station software. Then, the images taken from the UAV camera are processed simultaneously with the fixed flight and scan the object that the user wants to be detected. The UAV continues its stable flight until the object is detected. After the detection process, artificial intelligence-assisted image processing techniques are used. If there is no risk of an accident in the landing zone and no person can be detected, the UAV makes a landing near the object with the ground station software commands.

JSR A
Journal of Scientific Reports

2.1. UAV Control System

Ground station software is needed to enable the UAV to move automatically. In this study, Mission Planner with open-source code was used as ground station software. The program's support for Ardupilot and its wide and clear user interface were the main factors in its selection. In addition, tracking altitude changes, speed, GPS (Global Positioning System) position, the current supplied by the battery, and amount of usage during a flight are the features that make Mission Planner stand out. The analysis of the data received during the flight is provided, and optimization processes are carried out over the algorithm written using Python and the drone kit library. Thanks to the flight plan recording feature, possible errors are solved and diversity is offered with different map supports, especially Google Maps. Mission Planner has multiple flight modes. Among these flight modes, the most optimal one can be set.

Figure 1. A flight route set in the Mission Planner application on the DPU campus.

In addition, the problem that may occur during autonomous flight can be intervened through the program. In addition, a possible accident can be prevented with the Failsafe mode.

In the UAV control system, a flight route should be selected for the desired mission and scanning area. In this study, a flight route was determined on the campus of Kutahya Dumlupınar University (DPU), as seen in Fig. 1. This system, which provides control of the UAV whose flight route is determined, also makes the necessary interventions (landing, take-off, fixed flight, etc.) in its movements within its route.

JSR A
Journal of Scientific Reports

2.2. Image Processing Techniques

In line with a specific mission, UAVs may need to perform various tasks such as detecting an object and determining its location of the object. The image processing techniques used in the system designed to perform these operations with a high success rate were examined in two groups. The data obtained by the image processing techniques used in the algorithm is transmitted to the UAV control unit, and the UAV is directed autonomously. The system, designed using the Python software language, uses the open-source OpenCV library. The designed algorithm is embedded in the Nvidia Jetson Nano microcontroller board. This microcontroller performs image processing and deep learning techniques in line with the desired task. The obtained data is transferred to the basic units of the UAV (flight control card, ESC, engine, battery).

2.2.1. Image processing steps used for object detection

The first step of image processing is the application of the Gaussian function to the image in Figure 2 taken from the UAV camera. The picture smoothing effect of this function blurs an image similar to an average filter, and this degree of correction is determined by the Gaussian standard deviation [15]. First, the weighted average per selected kernel (9x9 matrices with pre-valued values) is obtained. The weight increases as it gets closer to the center pixel value. This makes a better correction than other filtering operations such as the average filter [7].

Figure 2. Object image taken from 5m height with UAV camera.

The next step is to change the color space. Processing the image in RGB (Red-Green-Blue) color space is very difficult and slow. In order to change the color intensity of an image, firstly, after reading the red, green, and blue color intensities from the image, changes can be made to it. Faster and easier processing can be done by using a different color space for the intensity and color formats of the image. In this way, the image can be processed faster and the operation of the algorithm can be

JSR A
Journal of Scientific Reports

accelerated and the processing time can be reduced. The color space used in this direction is defined as HSV (Hue Saturation Value), hue, saturation, and brightness. Obtaining HSV values from RGB values is provided by the following equations.

$$h = \begin{cases} 0°, & if max = min \\ 60° \times \frac{g-b}{max-min} + 0°, & if max = r \; and \; g \geq b \\ 60° \times \frac{g-b}{max-min} + 360°, & if max = r \; and \; g < b \\ 60° \times \frac{b-r}{max-min} + 120°, & if max = g \\ 60° \times \frac{r-g}{max-min} + 240°, & if max = b \end{cases} \quad (1)$$

$$s = \begin{cases} 0, & if max = 0 \\ \frac{max-min}{max} = 1 - \frac{min}{max}, & otherwise \end{cases} \quad (2)$$

$$v = max \quad (3)$$

H (hue) is the basic property of color and it is hue. It changes from 0° to 360° depending on its position on the standard color wheel. The higher the S (saturation) value, the more saturated the color is, and it ranges from [0 to 100%]. V (value) is called luminance or brightness and ranges from % 0 to 100.

In this study, the conversion process from RGB to HSV is performed and the desired color range is selected. The process was carried out for the objects in 3 different colors in Fig. 2. In order to test the stable operability of the system, objects with 3 different color ranges were used.

The UAV can make real-time changes between the colors in the received image. Thus, the user can select the object to be detected without any restrictions. In the algorithm, the absence of color limitation of the object to be detected provides easiness to the users. However, the color range and the background of the object must be distinctive. If the ground and object colors are the same, instabilities may occur in the object detection process. Excessively bright glass, snow, metal, etc. that may be on the ground surfaces can adversely affect the system stability. The most suitable solution against such situations is the appropriate selection of the color detection range and the color of the object.

After switching to HSV values, the image in Fig. 3 is masked. The UAV can make real-time changes between the colors in the received image. Thus, it enables the selection of the desired object to be detected.

The lower and upper limits of the determined color in the HSV color space are determined. Since the determined colors are in two different ranges in the HSV color space, filtering is done in both ranges and the color is determined according to the data obtained. The color to be determined here can be changed optionally and according to the range in the HSV space. The image of the object whose color is determined after masking is shown in Fig. 4.

JSR A
Journal of Scientific Reports

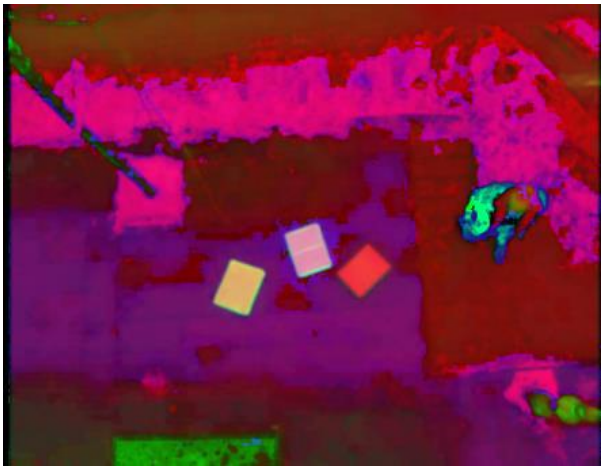

Figure 3. Image converted from RGB values to HSV values.

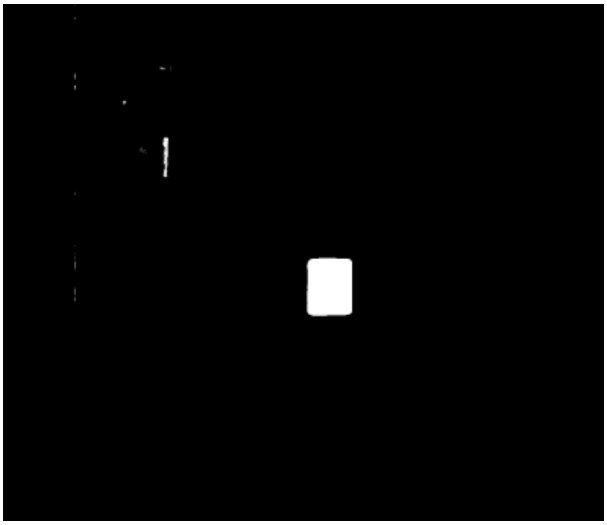

Figure 4. The image formed after masking.

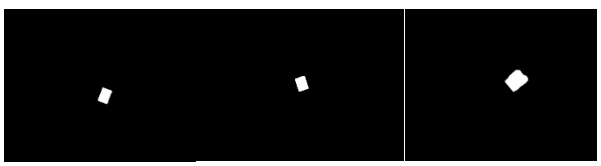

Figure 5. Applying Erosion and Dilation to the images formed after masking.

JSR A
Journal of Scientific Reports

The next step after masking is to create a contour. The concept expressed as a contour in image processing is a closed curve that connects all the continuous points that color or intensity has. Contour detection is an approach used for shape analysis, object detection, and recognition. When the contour operation is performed, there are points where the determined color intensity changes significantly. After subtracting all the contours from the binary image, the area, circumference, and circularity of the contours are calculated. The contour is removed if its circumference or circularity is less than the given threshold. Circularity is a characteristic parameter that indicates the complexity of the region shape and is calculated with the area and perimeter of the region as equations. In the contour subtraction equation below, A is the area and P is the perimeter.

$$e = \frac{4\pi \times A}{P^2} \tag{4}$$

Erosion and Dilation filters were used to remove most of the noises around the masking in Fig. 4 as in Fig. 5. With Erosion, etching is applied to the image. According to the parameters, the pixels in the specified area are abraded and the distorted image (noise) is cleaned. With the dilation process, the borders of the image given as input are expanded within the given area. Thanks to this enlargement, it is seen that the pixel groups get bigger and the spaces between the pixels get smaller.

Figure 6. Indication of the center of gravity of the detected object.

2.2.2. Functions created for tracking the detected object

In order for the algorithm to work without problems, it is first checked whether the calculated contour exists. It is possible that the factors that cause the contour not to appear are the factors such as excessive sunlight, a reflection of the light from the snow hitting the camera, and insufficient light on the object to be detected. For this reason, if no object can be detected in the algorithm, a notification is sent to the control unit of the UAV, the altitude distance is reduced at 1-meter intervals and descent is provided up to 5 meters. If no object has been detected yet, the UAV continues on the route automatically set by the Mission planner. In the scenario where the object is detected, the image moment of the detected contour is taken. Image moment is the weighted average of image pixel densities, which gives properties such as the image's radius, centroid, etc. Finally, this calculated center is designated as a point and followed up to that point.

JSR A
Journal of Scientific Reports

Detection of 3 different colored objects was detected as seen in Fig. 6. The centers of gravity of the detected objects were determined [13]. The image is divided into 9 in order to follow the object whose center of gravity is detected. It is ensured that the object is located in the middle of the image divided into 9 (5th region) and that it can continue its flight in that region with determination. As seen in Fig. 6, this algorithm evaluates the image position of the object after the object is detected and in case it is not in the center, it gives the flight command to the UAV in order to keep the image of the object in the 5th region. When the object remains stationary in the middle, the deep learning-based human recognition algorithm described in the 3rd section is activated and it is checked whether there are people in the area where it will land. If there is no person in the image, the UAV control system is directed so that the UAV can land at intervals of 1 meter to 10 meters.

3. TEST RESULTS

In order for the UAV to land safely on the ground, it is necessary to conduct environmental control. As a result of processing the images taken by the camera on the UAV, it is examined whether there is a human in the image. In the absence of a human, a landing command is given to the UAV flight control system. In the case of a human, it remains stationary in the air. A deep learning-based human recognition algorithm has been designed to perform these operations.

For object detection and recognition, the YoloV4-Tiny model of the YoloV4 module, which is a deep learning architecture, which is frequently used in the literature, was used. The YoloV4-Tiny model uses the Darknet architecture to classify the types of objects. The Google colab platform, which offers ready-made programs such as NumPy, pandas, and matplotlib for machine learning, GPU, CUDA, CUDNN, Python, and data analysis, has been used. First, the cloning and installation processes of the Darknet architecture were performed on the platform. Here, the OpenCV and matplotlib libraries are installed.
Images recorded by the UAV camera were used for the object to be recognized. For the training, 1200 photographs out of 1600 photographs were used. The photographs were labeled in Yolo format using the LabelImg program and files in .txt format were created. In these text files, there are 5 numerical data including the class of the selected object in the photo, x value, y value, height, and width. 960 of the images were transferred to the training file and 240 to the test file. The train and test files, which contain the photos and the information of the object to be detected, have been converted to .txt format. Then, the deep learning layers used for YoloV3, a pre-trained convolution layer, were downloaded to Google Colab [16, 17].

In this study, training was applied to 216256 images. As seen in Table 1, the lowest success rate is 84%, and the average success rate is 93%. Human recognition accuracy rates on various photographs are shown in Fig. 7. Finally, the models trained in Google Colab were run in real-time via the PyCharm module with the necessary config, last weight files, and the Anaconda program.

Table 1. Detection rates of deep learning-based human recognition system in various images.

	Number of People	Minimum Human Detection Rate	Average Human Detection Rate

JSR A
Journal of Scientific Reports

Fig. 7	3	%99	%99
Fig. 8	4	%84	%95
Image A	4	%87	%89
Image B	5	%88	%92
Image C	2	%91	%93

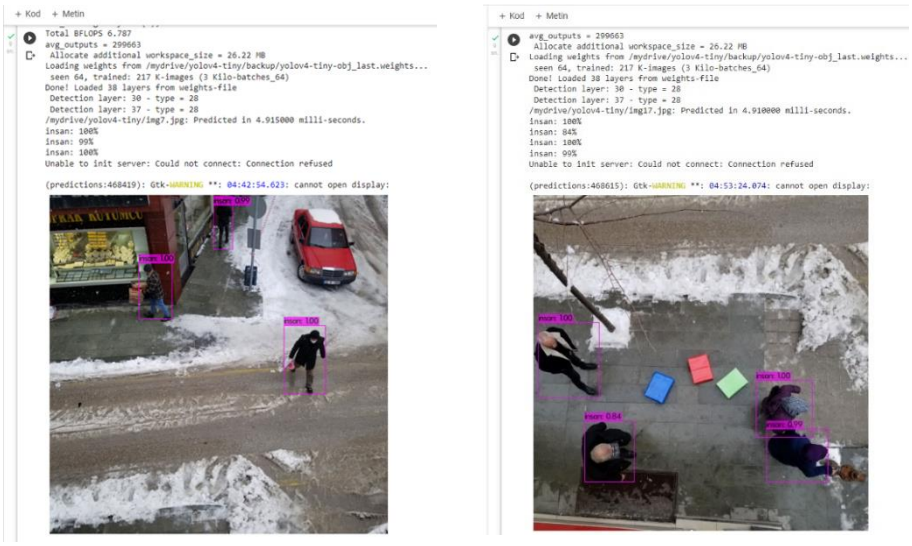

Figure 7. Application of deep learning-based human detection to UAV imagery.

4. CONCLUSION

In this study, object detection was performed by applying image processing steps on the data received from the camera of the UAV moving in a certain flight route. An algorithm has been designed so that the UAV can land at the location of the detected object. Moreover, a deep learning-based human recognition system that can be applied to UAV camera images has been realized. As a result, the autonomous guidance system algorithm design for UAVs with image processing techniques has been successfully applied. It is considered that being autonomous has the advantage of reducing processing time, expenses, and manpower. Furthermore, human-caused failures and potential risks are decreased. Finally, it gives the user flexibility because the designed system allows for changes to the attributes of the object to be detected.

ACKNOWLEDGMENT

This study was supported within the scope of the TUBITAK 2209-A university students' research projects support program with the application number 1919B012102370.

REFERENCES

[1] Ilhan, I., (2013), Development of image processing based intelligent control algorithms for quadrotors, Firat University, Institute of Nat. and Appl. Sci., MSc. Thesis.

[2] Akyuz, S., (2013), Quad-rotor unmanned aerial vehicle (Quadrotor) design and simulation with pd and fuzzy controller, Ege University, Institute of Nat. and Appl. Sci., MSc. Thesis.

[3] Aksoy, B., Korucu, K., Çalışkan, Ö., Osmanbey, Ş., and Halis, H. D., (2021), İnsansız Hava Aracı ile Görüntü İşleme ve Yapay Zekâ Teknikleri Kullanılarak Yangın Tespiti: Örnek Bir Uygulama, Düzce Üniversitesi Bilim ve Teknoloji Dergisi, 112-122.

[4] Kar, Y.E, Basgumus, A. and Namdar, M., (2021), Machine Learning Assisted Autonomous Vehicle Design and Control, IEEE 5th Int. Symposium on Multidisciplinary Studies and Innovative Technologies, 462-466.

[5] Kar, Y.E, Basgumus, A. and Namdar, M., (2021), Machine Learning and Image Processing Based Autonomous Vehicle Design, IEEE 29th Signal Processing and Comm. Applications Conf., 1-4.

[6] Ceylan, A., (2018), Visual-based object tracking with four-rotor aerial vehicle, Firat University, Institute of Nat. and Appl. Sci., MSc. Thesis.

[7] Soyhan, I., Gurel, S. and Tekin, S.A., (2021), Yapay Zeka Tabanlı Görüntü İşleme Tekniklerinin İnsansız Hava Araçları Üzerinde Uygulamaları, Avrupa Bilim ve Teknoloji Dergisi, 24, 469-473.

[8] Ozkan, Z., Bayhan, E., Namdar, M. and Basgumus, A., (2021), Object Detection and Recognition of Unmanned Aerial Vehicles Using Raspberry Pi Platform, IEEE 5th International Symposium on Multidisciplinary Studies and Innovative Technologies, 467-472.

[9] Bayhan, E., Ozkan, Z., Namdar, M. and Basgumus, A., (2021), Deep Learning Based Object Detection and Recognition of Unmanned Aerial Vehicles, IEEE 3rd Int. Congress on Human-Computer Interaction, Optimization and Robotic Applications, 1-5.

[10] Koc, M., (2020), Derin ogrenme kullanarak iha ile hareketli bir hedefin otonom olarak yakalanmasi, Istanbul Sabahattin Zaim University, Institute of Nat. and Appl. Sci., MSc. Thesis.

[11] Ekmen, M. İ., Aydoğdu, Ö., (2020), İnsansız Hava Araçları İçin Görüntü İşleme Tabanlı Otonom İniş. Avrupa Bilim ve Teknoloji Dergisi, 297-303.

[12] Sivritaş Ş, Tekin A. (2022), Autonomous 3D Target Tracking via UAV. Balkan Journal of Electrical and Computer Engineering, 10(1), 1 - 9.

[13] Toraman S., (2018), Pedestrian Detection with Deep Learning from Unmanned Aerial Imagery, Journal of Aviation, 2(2), 64-69.

[14] Bayhan, E., Deligoz, C.B., Seymen, F., Namdar, M. and Basgumus, A., (2022), Unimpeded Walking with Deep Learning, IEEE 30th Signal Processing and Comm. Applications Conf., 1-4.

[15] Arndt, C., (1996), An introduction to systematic sensitivity analysis via Gaussian quadrature, Technical Report.

[16] Redmon J. and Farhadi, A., (2018), Yolov3: An incremental improvement, arXiv preprint arXiv:1804.02767.

[17] Shopa, P., Sumitha, N. and Patra, P.S.K., (2014), Traffic sign detection and recognition using OpenCV, IEEE Int. Conference on Information Communication and Embedded Systems, 1-6.

Kütahya Dumlupınar University
Institute of Graduate Studies

Journal of Scientific
Reports-A
E-ISSN: 2687-6167
Number 51, December 2022

RESEARCH ARTICLE

COMPUTATIONAL and TEORIC INVESTIGATION of the EFFECTS of FINNED TRICKLEVENT SYSTEM on BUILDING ENERGY SAVINGS

Kemal Furkan SÖKMEN[1]*, Burhan ERGÜNER[2], İlknur AKIN[3]

[1*]Bursa Technical University, Eng. and Natural Sciences Faculty, Department of Mechanical Engineering, Bursa, furkan.sokmen@btu.edu.tr, ORCID: 0000-0001-8647-4861
[2]Metal ve Yapı Sistemleri Tic ve A.Ş, 34805, İstanbul, burhan.erguner@metalyapi.com,, ORCID: 0000-0003-1159-1662,
[3]Metal ve Yapı Sistemleri Tic ve A.Ş, 34805, İstanbul, ilknur.akin@metalyapi.com, ORCID: 0000-0001-9078-5398

Receive Date:11.10.2022 *Accepted Date: 15.11.2022*

ABSTRACT

In our study, the effects of the finned Tricklevent passive air condition system on building energy savings were investigated. The system has been patented internationally with the patent number 2013/08326. A 14 m^2 sample prototype office room was built for the study. Numerical studies were performed with FloEFD software. Theoretical calculations and numerical work values confirmed each other. In the analyses, independence from mesh was studied. The solar load is defined as 1009 W/m^2. Office exterior windows are designed with a thickness of 6 mm and an air gap of 16 mm. In the study, it was determined that there was a fresh air inlet at a volumetric flow rate of 0.024 m^3/s in the prototype office. It has been determined that the finned Tricklevent system cools the hot air coming from the outside environment and takes it in with a temperature drop of 5-6 ^{o}C. When the system is operated at the same time as the air conditioner, the air conditioner set temperature can be adjusted to higher temperatures, saving 28 kWh/m^2 of energy and reducing the carbon footprint by 15.4 kg/m^2. With the sequential operation of the system with the air conditioner, 21 kWh/m^2 of energy was saved in a 3-hour period, while a carbon footprint of 11.5 kg/m^2 was reduced.

Keywords: *Heat transfer, passive ventilation, energy, zero building, energy saving, carbon foot print,*

1. INTRODUCTION

As a result of population growth, high demands for building construction have arisen and the number of high-rise buildings has increased. As a result of the increase in building and building heights, the heating and cooling needs of the houses have increased. As a result, energy is needed to cool and heat buildings. Housing and office heating and cooling increased to 6.7% of the world's total energy consumption [1]. According to the 2008 World Business Council for Sustainable Development

JSR A
Journal of Scientific Reports

(WBCSD) report, 40% of the energy produced in the world is consumed to provide thermal comfort in buildings [2]. The carbon emission and energy consumption of a house cooled with an air conditioner for ambient comfort are 67% and 66%, respectively. These rates are higher than in a naturally ventilated home. Scientific studies have shown that passive cooling systems can reduce the energy spent for thermal comfort conditions by 2.35%. Passive cooling is to ensure the comfort of the environment by making use of the natural air flow. Passive cooling is a method that directs architecture to create comfortable indoor conditions naturally [3]. In order to minimize the rising energy need in buildings, the energy performance of the buildings has been examined. Official decisions have begun to be taken to construct zero-energy buildings for energy saving [4-6]. Double skin facades (DSF) have become frequently used in architecture to save energy and support passive ventilation of the building. Building facades can reduce the energy consumption of the HVAC system if well designed. Well-designed façades can absorb some of the solar radiation in winter, while preventing overheating during hot periods [7]. Double-skinned facades are generally structures consisting of two transparent surfaces with air between them [8]. Facade in buildings; It is a part of the building structure that acts as a kind of filter and sheath for the building, which keeps the outdoor conditions outside the building, protects the building from various external effects, and also adds aesthetics to the building. Some factors affecting the design and construction of the facade are listed as the height of the building, the environment, and the purpose of use of the building [9]. There are several different types of DSF that provide ambient ventilation. These are grouped under the box window façade, the shaft box façade, the corridor façade, and the multi-level façade [10-12]. DSF can operate under different forms of ventilation (Fig. 1a–c) or connected to the building ventilation system with adjustable flaps (Fig. 1d) can work [13].

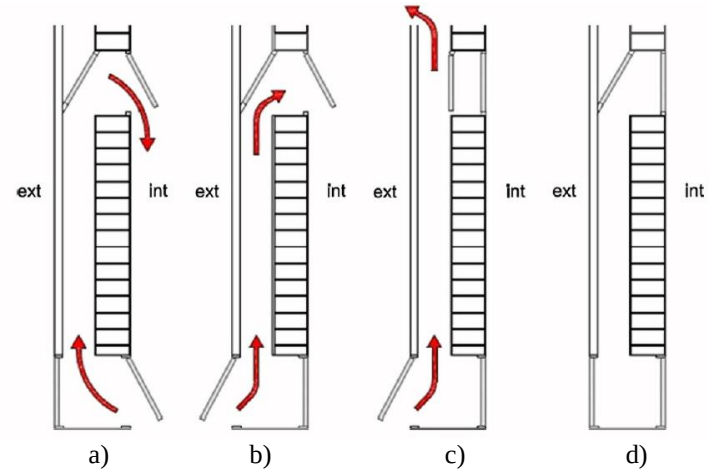

Figure. 1. Different operational modes of a ventilated DSF [2].

In another study, in the façade system designed for cold seasons, outside air is taken into the indoor environment as in Figure 2.a, while indoor air conditioned by air conditioner in hot seasons is filled between the façade as in Figure 2.b, working towards providing interior comfort [14].

JSR A
Journal of Scientific Reports

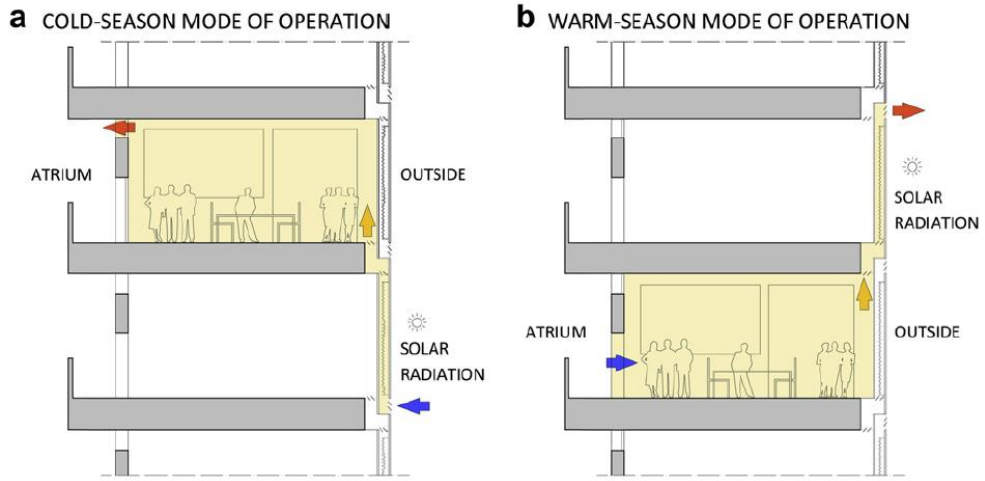

Figure. 2. a) Cold-season and b) warm-season modes of operation of a basic double-skin facade system [14].

Influential design parameters for DSF are cavity thickness, glass materials, glass coating, shading condition, cavity openings. Most of the energy lost in buildings comes from windows. The material, transparency and reflective properties of the glass used in facade systems prevent overheating in summer and minimize heat loss in winter. Therefore, the selection of suitable windows with the necessary characteristics is important [15]. The thermal performance of double-skinned facades has been examined in studies and it has been reached that it reduces the effects of radiation. As a result of the study, it was revealed that double-skinned facades have an effect on radiation in summer and insulation in winter [16]. Double-layer facade systems have been examined with the CFD method and it has been revealed that such systems cause reductions in building energy consumption [17].

An exemplary double skin façade (DSF) system has been examined. As a new approach, the facade where the PV system is placed showed the best performance [18]. In another study, heat transfer in double-skinned facades was investigated. Its performance was investigated with various glass systems [19]. In particular, the effects of shading on the windows on thermal comfort have been revealed. The use of Aluminum blinds in double-walled systems was investigated with CFD and examined in terms of heat transfer [20]. In another study conducted in Singapore, a double glazing facade was compared with a single glass facade in buildings with high humidity and sun load. CFD application was made in the study. It has been determined that double glass facades contribute to building energy savings. In another study, single layer and double-glazing application was examined with another software. According to the results obtained in the study, double glazing is recommended for energy saving and indoor thermal comfort. In another study conducted with a passive ventilation system, double glazing was supported by passive ventilation in accordance with the literature. It has been demonstrated that 16% savings are achieved in the mechanical ventilation system energy that provides indoor thermal comfort. [21].

JSR A
Journal of Scientific Reports

Zero energy buildings are attracting a lot of attention internationally to reduce energy consumption in buildings, save on energy bills and protect the environment at the same time [23]. It has been determined that people spend an average of 90% of their lives indoors, therefore the use of HVAC systems and the associated energy consumption increase [24]. The expected performance from double-skinned facades is to reduce the effects of air temperature, to meet the need for thermal comfort and to reduce energy consumption. Expected features from building facade systems are increasing [14].

In the studies in the literature, it has been determined that while providing air circulation in the double facade system, energy saving is achieved with passive ventilation. However, in these systems, there is no situation to reduce the outside air temperature. In our study, the mechanical and numerical analysis of the fin structured version of the passive ventilation system, which takes up very little space on the facade, takes the outside air from the facade and reduces the temperature to the indoor environment, and its effects on energy saving. The difference of our study from other studies is the patented passive ventilation system that provides energy saving by reducing the air conditioner operating time and power while providing indoor thermal comfort. The efficiency of the system with the finned design of the Innovative Passive Ventilation system (Tricklevent) , which brings an innovative approach to facade systems, has been examined. The effects of using fin material of materials with thermal capacity and high thermal conductivity on the efficiency of the system were investigated. Again, different from the literature, the contribution of the energy-saving system to the carbon footprint has been examined.

2. MATERIALS AND METHOD

2.1. Working Principle of Tricklevent Passive Ventilating System

The tricklevent system, which is in question in the study, can reduce the temperature of the outdoor air with the help of a fin and take it to the indoor environment. In addition, the Tricklevent system also performs the task of providing air circulation, as in the literature studies. The working principle of the Tricklevent passive ventilation system is as follows. First of all, the room is conditioned with air conditioning. When the interior volume becomes stable at the set temperature, the tricklevent system made of Al material comes to the indoor temperature. After the air conditioner is turned off, natural ventilation of the system from the outside is started. The air coming from outside at a higher altitude cools in the cold finned system and enters the interior volume in a cooled state. In this way, the temperature of the air entering the interior volume for a certain period of time is reduced and the use of air conditioners is reduced. At the same time, the system can be operated in parallel with the air conditioner. The air conditioning setting temperature is set above the normal temperature, and the Tricklevent system is kept open all the time. The hot air coming from the outside will constantly reduce the temperature in the system and ventilate the indoor environment. The working schematic of the Tricklevent system is given in Figure 3.

JSR A
Journal of Scientific Reports

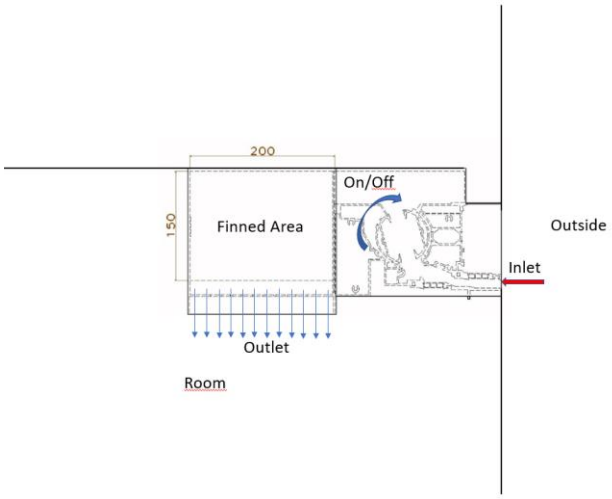

Figure 3. Working diagram of the Tricklevent system.

2.2. Geometry

The isometric view of the Tricklevent system, which changes the circulation air temperature developed in our study, is given in Fig. 4. System design was made in Catia V5 R19 software. A fin design has been made to reduce the temperature of the outside air in the system (Fig. 5).

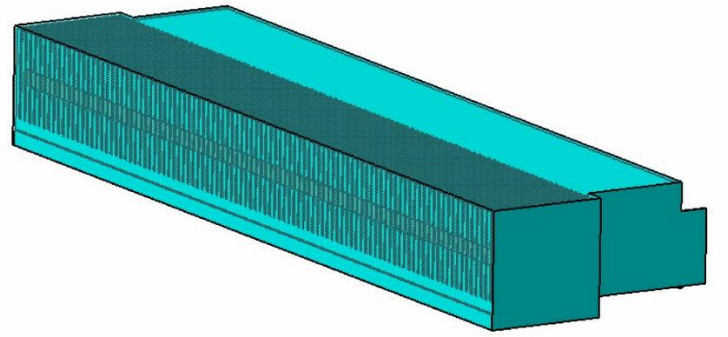

Figure 4. The isometric view of the Tricklevent system.

Fin thickness is designed as 5 mm, spacing between fins is designed as 10 mm.

JSR A
Journal of Scientific Reports

Figure.5. Fin system dimensions used in the system

2.3. Computational and Theoretical Work

For numerical analysis, first of all, the Tricklevent system is a data obtained through tests in which a maximum of 50 m^3/h air can be taken at a pressure difference of 1 Pa from the facade of the building (Fig.6). The measurement of the flow entering the system was obtained by calculating the velocity measurement taken from the entrance of the triclevent system on the prototype room. During the test phase, the amount of flow depending on the pressure difference was determined in the calculations made over the external air dynamic pressure. The external air temperature was measured using a Thermocouple from the location indicated by the circular sign in Fig.6. The outside air enters the interior volume through the sections depicted in Fig.6 with the red rectangular shape. Table.1 shows the measurement range and error rate of the thermocouples used in the measurements. Testo brand Telescopic 3-Function Air Velocity Probe was used for air velocity measurements. Velocity probe features are also given in Table 1.

Table 1. Probes' properties.

Probes	**Measurement Range**	**Error Rate**
Standard (K-type)	100℃ /+400℃	-/+0.1℃
Testo Telescopic	0-20 m/s	-/+0.1m/s

JSR A
Journal of Scientific Reports

Figure.6. Prototype office room.

In this study, for a sample office with a height of 10 m, the air velocity is 1.508 m/s and the pressure difference is 1.714 Pa, calculated from Eq. 1 and 2. The velocity value obtained in the tests are respectively 1,49 m/s.

$$V(z) = V(Z_R)\frac{In(\frac{Z}{Z_0})}{In(\frac{Z_R}{Z_0})} \quad (1)$$

$$P = \frac{1}{2}\,\rho\,{V_z}^2 \quad (2)$$

The Tricklevent system takes the outside air into the indoor environment due to the dynamic pressure caused by the speed of the air. According to the calculated pressure difference, the inlet flow rate of the outside air to the Tricklevent system was calculated as 0.024 m^3/s. As seen in Fig. 7, the area where the air enters was determined as 0.016 m^2.

JSR A
Journal of Scientific Reports

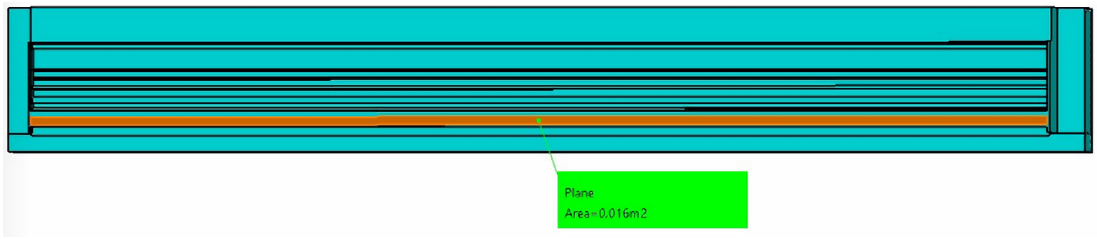

Figure 7. Tricklevent air intake area area.

The velocity value calculated with Equation.3 was calculated as 1.5 m/s in order to verify the air entry velocity into the system.

$$\dot{m} = \rho . V . A \tag{3}$$

The Re number in the first entry zone of the outside air into the system was calculated as 2296 (Eq.4). This data revealed that the flow characteristic in the entrance region of the system is laminar.

$$Re = \frac{\rho V D_h}{\mu} \tag{4}$$

D; hydraulic diameter is calculated by Equation (5).

$$D_h = 4 * A / P_s \tag{5}$$

The air entering the system is 32 °C ambient air. The initial temperature of the Tricklevent system and fins was accepted as 24 °C equal to the indoor air. The average temperature value of the exit temperature of the air from the system and the entrance to the indoor environment was accepted as 28 °C. The μ (Dynamic viscosity) value expressed in Eq. 2 in the calculation of Re number is taken from the tables for 28 °C. μ is taken as 1.867×10^{-5} kg/m.s.

The air inlet velocity to the system obtained in the computational study was taken as both a validation for the study and the basic parameter for the element number independence study. Table 1 shows the air inlet velocity data confirming the element number independence study and Fig. 8 confirming the numerical study with computational work. Mesh number is determined 2578585 in this study according to Table 2.

Table 2. Mesh independence study.

No	Fluid Element	Solid Element	Total Element	Results (Velocity inlet air, m/s)
1	632586	723589	1356175	1,454
2	1002548	958642	1961190	1,486
3	1321598	1256987	2578585	1,505

JSR A
Journal of Scientific Reports

4	1575896	1421589	2997485	1,506

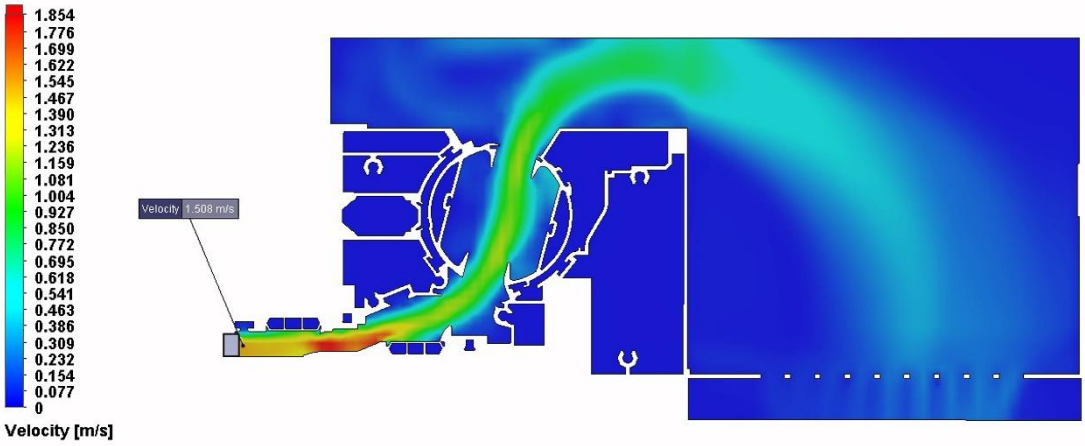

Figure.8. Tricklevent air inlet zone velocity result.

After the velocity data in the inlet region was verified numerically, the flow characteristics of the air in the inlet region between the fins were examined again. This review is based on the result obtained from the numerical study and given in Figure 6. The speed of the air entering the fin area was determined as 0.659 m/s and the Re number was calculated as 6298. The flow characteristic between the fins was determined as turbulent flow. FloEFD script was used in the analysis. The software determines the flow characteristic by determining the Re number in the analysis steps and continues the calculations according to the result. In regions where the flow is turbulent, the k-Ɛ turbulence model is used. In the analysis for sample office room 1009 W/m^2 of the solar load was taken. The facade system is defined as 6 mm thick double glazing.

The variation of air temperature with altitude was taken into account in the analysis. With the help of Eq. 6, the temperature drop according to the building height is defined in the analysis. It has been revealed from a study in the literature that the change in air temperature with altitude varies depending on equation 6. In the study, it was stated that the temperature decreased according to the height difference and the higher floors encountered lower temperatures. This data has been a result supporting our study [25].

$$\frac{dT}{dx} = -\frac{0{,}0066\,°C}{m} \tag{6}$$

The fin system is calculated by assuming a fin with a constant surface temperature. Nu number was found with the help of Eq. 7.

JSR A
Journal of Scientific Reports

$$Nu = \frac{hS}{k} = \left[\left[\frac{576}{(Ra_s.S/L)^2}\right] + \left[\frac{2{,}873}{(Ra_s.S/L)^2}\right]\right]^{-1/2} \quad (7)$$

The heat transfer coefficient between the designed fins is calculated as h_{mid}= 12 W/m^{2}K.

3. RESULTS AND DISCUSSIONS

When the results obtained in the numerical and numerical examination of the Trickle Vent passive ventilation system are examined, the data obtained are as follows. According to the numerical analysis results, it has been determined that in the Tricklevent system, the heat transfer area can be increased with the fin design and the outdoor air can be taken in by reducing the indoor temperature. It was observed that in the tests the temperature of the air entering the Tricklevent system decreased to 29.01 °C until it entered the fins and decreased to approximately 25.5 °C at the exit of the fins (Fig. 9 a). This shows that a temperature drop of about 7 °C is achieved. The comparative values of the analyzes and tests are given in Table 3. According to these data, it was determined that the result of tests and analyzes were compatible. The comparison of velocity values, as well as temperature values, is given in Table 4. It has been determined that the velocity values are compatible in terms of test and analysis, just like the temperature data.

Table 3. Temperature comparison of test and analysis results.

Test Results	**Test Results (^{o}C)**	**Analysis Results (^{o}C)**
Temperature (entrance of fins)	29,01	29,12
Temperature (outlet fins)	25,5	25,10

Table 4. Velocity comparison of test and analysis results.

Test Results	**Test Results (m/s)**	**Analysis Results (m/s)**
Velocity (entrance of fins)	0,65	0,662
Velocity (outlet fins)	0,15	0,101

In Figure 9 b, the velocity values of the air entering the system are taken randomly over the air flow profile. It has been determined that the entrance speed of the cooled air into the interior does not disturb the thermal comfort and enters the room with a speed below 5 m/s. The temperature distribution data taken over the curve in Fig. 9 c are given graphically in Fig 10.

JSR A
Journal of Scientific Reports

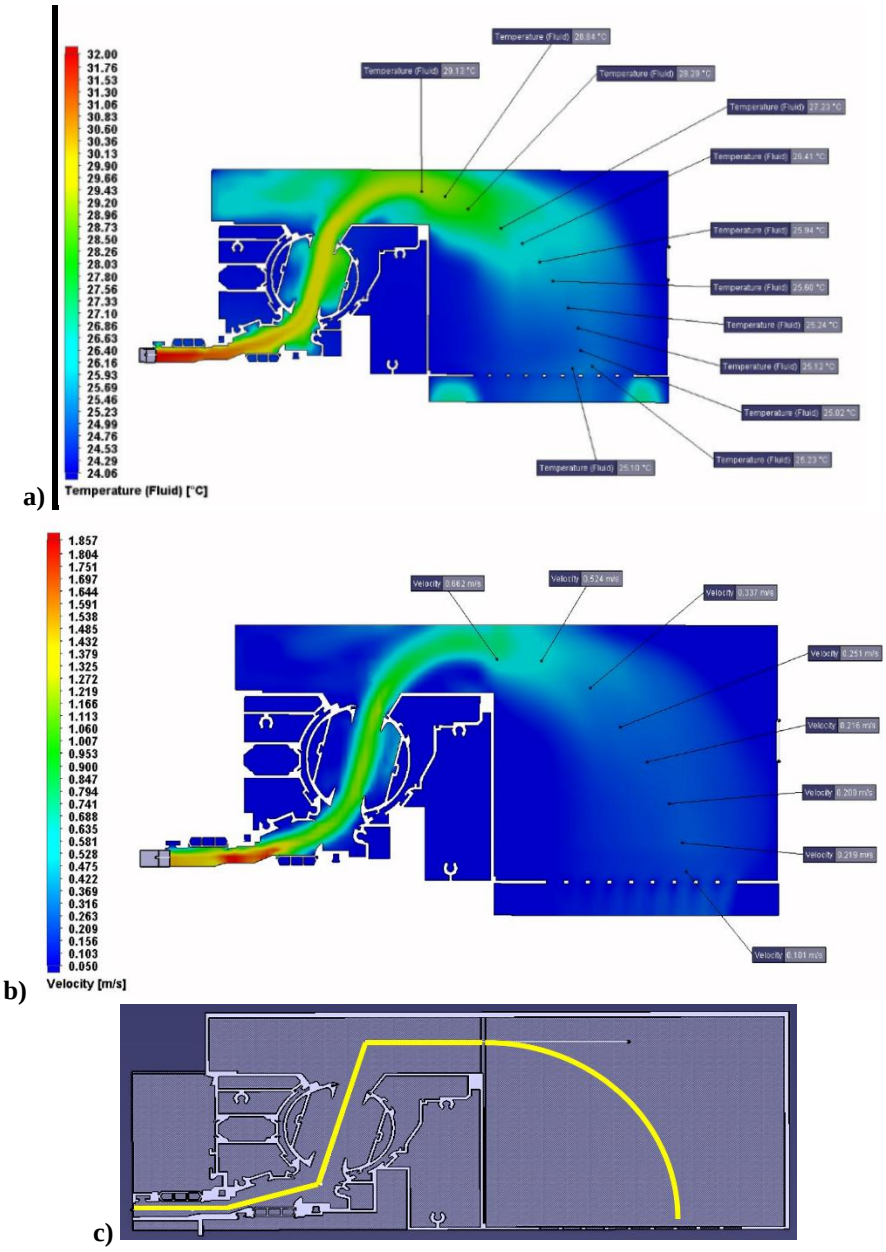

Figure 9. Within the Tricklevent system a) Temperature distribution b) Velocity distribution c) Temperature data curve.

JSR A
Journal of Scientific Reports

Figure 10 shows the comparison of the Tricklevent system with and without heatsink. As can be seen in Fig. 10, the temperature drop in the finned area is higher than in the finless area.

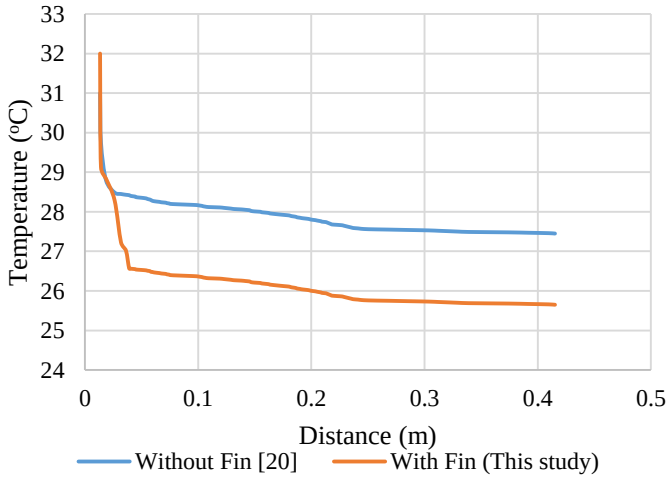

Figure 10. Temperature drop comparison chart in Tricklevent system with and without fins.

With the fin design, the heat transfer area has been increased and the target of further reduction in air temperature has been achieved. This result is theoretically expected. Studies are continuing to optimize the fin thickness and spacing design and to obtain the most efficient heat transfer. The graph of the heat transfer coefficient on the curve swept by the air inside the fin is given in Fig. 11 a. The heat transfer coefficient graph given in Fig. 11 a is taken over the curve shown in Figure 11 b. This graph shows the local heat convection coefficients along the curve. The value obtained by the calculation method is the average value of heat convection coefficients is 12 W/m^{2}K. The average value of the heat transfer coefficient obtained from the analysis was determined as 11.33 W/m^{2}K. It is thought that the reason for the difference between the two values may be that the fin surface area is not completely swept with hot air on the path followed by the air, and the curve seen in Fig. 11 b, on which the graph is based, cannot fully represent the path followed by the air. In addition to these comments, an error of 6% in the analysis value is considered to be an acceptable error.

JSR A
Journal of Scientific Reports

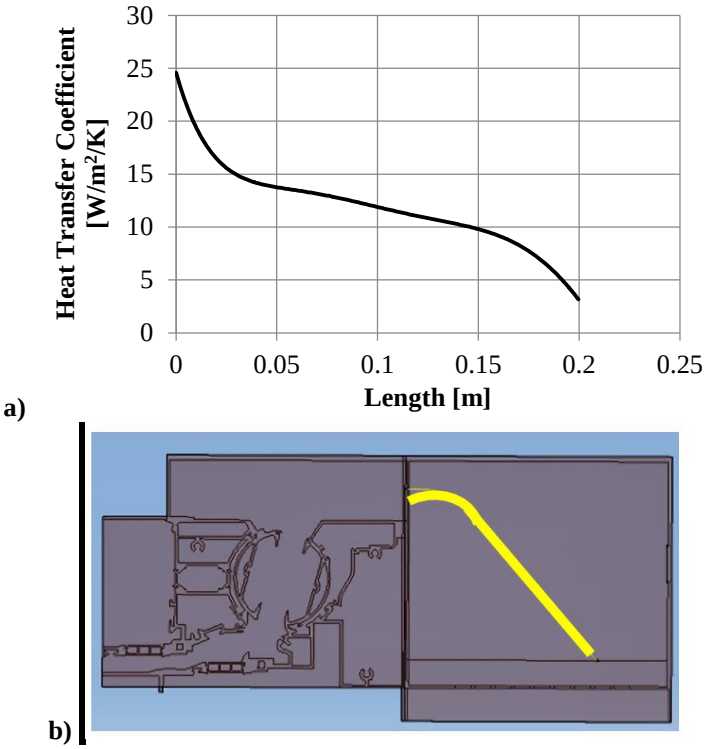

Figure 11. a) Variation graph of heat convection coefficient, b) the curve from which the graph is drawn.

Another result obtained in the study is the effects of the triclevent system on the temperature distribution in the interior volume. In the literature study, when the temperature distribution in the same sample office room in the Triclevent system without fins is compared with the temperature distribution at 1.75 m height, it has been determined that the room conditions become better with the finned structure. It can be seen in Figure 12 that the indoor temperature varies between 30-36 ^{o}C during operation without blades and when the system is closed. When the finless system is turned on, it can be seen from Figure 12 that the temperature distribution varies between 27-32 ^{o}C at height of 1.75 m. In the open state of the finned Tricklevent system, it was determined that the temperatures remained in the range of 25,5-29 ^{o}C at an altitude of 1.75 m. This clearly shows that the finned system is more effective (Fig. 12).

JSR A
Journal of Scientific Reports

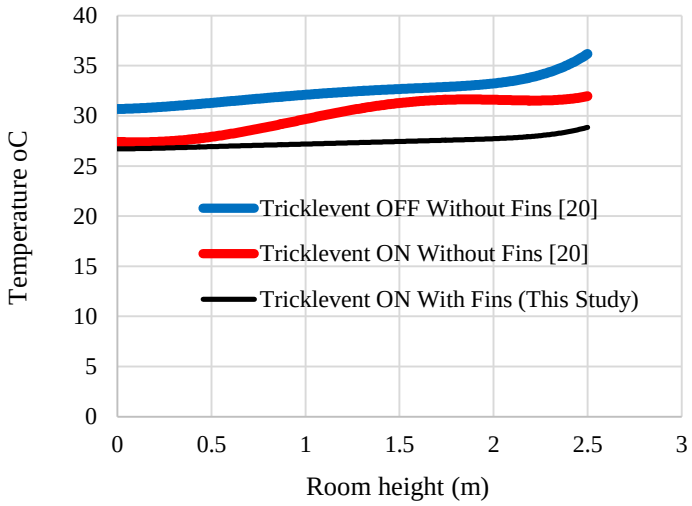

Figure.12. Example office room temperature change graph of 1.75.

As can be seen in Figure 13, Tricklevent system with fin structure can keep the temperature distribution in the room at lower temperatures than the system without fin structure. In the images given in Figure 13 a and b in comparison with the literature, it is seen that the temperature of the trickle vent system without blades is 32 ^{o}C at an altitude of 1.75 m as a result of the analysis.

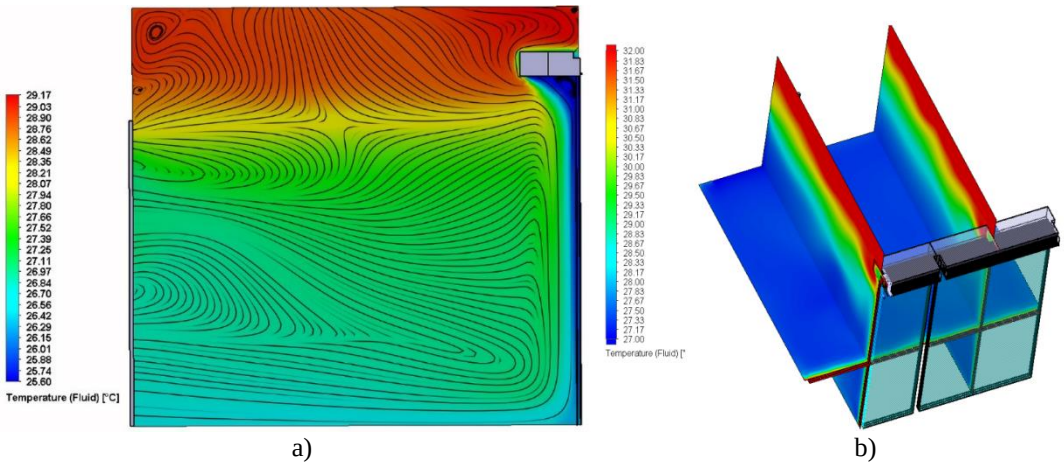

a) b)

Figure 13. a) Example office room temperature change graph of 1.75 m b) Example office temperature distribution sections [21].

JSR A
Journal of Scientific Reports

4. CONCLUSION

It has been determined that the system reduces the temperature of the air coming from the outside environment and provides the appropriate temperature value to provide thermal comfort to the indoor environment. The hot air taken from the outside air increases the temperature of the fins made of Al material over time. However, turning off the air conditioner during this time is the main parameter that will save energy. According to the data we obtained in our study. It is a great advantage in terms of heat transfer that the Tricklevent system is made of Al material, is not exposed to solar radiation, and quickly reaches the temperature of the air conditioned indoors according to the Al material properties. According to the literature studies, it was stated that every 1 ^{o}C increase in the air conditioner setting saves 3-6% in electricity consumption. [22]. According to the studies of ACEEE (American Council on Energy Efficiency Economics), the factors affecting the electricity consumption of the air conditioner are listed as: Indoor air temperature, Outdoor temperature, Heat insulation of the room and temperature setting of the air conditioner. Energy saving in air conditioners depends on the thermostat setting and indirectly on the compressor operating time. Since setting the thermostat to 18 ^{o}C and setting it to 25 ^{o}C will directly affect the compressor operating time, it is clear that less energy will be spent at high temperature settings. Another study revealed the energy cost per m^2 for each 1 °C reduction [10]. In the study, he reported that there is 1 kWh/m^2 energy saving for each ΔT= 1 ^{o}C temperature drop in the air conditioner setting. This means 14 kWh energy savings for a 14 m^2 sample office. Setting the air conditioner to higher temperatures such as 25-26 ^{o}C instead of setting it to 23 ^{o}C in hot summer months will cause the air conditioner compressor to consume less energy.

An A+ class air conditioner operating 3 hours a day for a month consumes an average of 97 kWh, while A++ air conditioner consumes 81 kWh and A+++ air conditioner consumes an average of 63 kWh. Energy companies draw attention to the fact that this difference will be reflected on the bills even more as the consumption increases depending on the usage period. An air conditioner operated 3 hours a day; It consumes 4 times more energy than an iron, 6 times more than a television, 4 times more than a computer, 8 times more than a dishwasher, and 3 times more than a refrigerator that works all day. Considering that air conditioning operation times are 6 hours for average workplaces, it is clear that the costs will double.

The Tricklevent system has 2 different ways of working. The first mode of operation is parallel operation with the air conditioner. While the air conditioner keeps the interior volume at a certain temperature, the fins cool the air coming from the outside at the indoor temperature and take it inside. In such a case, the air conditioner power is adjusted to higher temperatures and energy costs are reduced with the savings in compressor power. Working in parallel with the air conditioner the air passing through the fin structure enters the interior volume as 25.5 °C. The system took the air, which is 32-31 ^{o}C in the external environment, by cooling it into the interior volume. According to the literature, with a temperature drop of 5.5 ^{o}C, 70 kWh energy recovery was achieved. When the system is turned on at the same time as the air conditioner, 2 ^{o}C air conditioning power is gained by adjusting the indoor temperature to 25 ^{o}C instead of 23 ^{o}C. This data means 28 kWh savings per m^2. When the system is turned on after the ambient conditioning of the air conditioner, the Al material fins that reach the air conditioner setting temperature reduce the temperature of the air coming from the outside environment.

The second operation plan of the system is based on not operating the air conditioning system until the fin temperature, which is at the indoor temperature, reaches the outdoor air temperature after the air conditioner is turned off. In the computational analyzes made based on time, the temperature of the air coming from the outside environment reaches 31 ^{o}C after 19.6 minutes. This value means that the air conditioner does not operate for 20 minutes in a 1 hour period. This data provides an energy saving of 21 kWh by reducing the 3-hour air conditioner operating time by 30% in the energy consumed. In the studies in the literature, the effects of providing the integrated operation of the HVAC system and the facade system with the automation system on energy saving have been examined. It is stated that with the automation system, around 70% energy savings are achieved [25]. Our work continues with the optimization of the number and spacing of the blades as well as the automation system studies.

According to the data of the Ministry of Environment, Urbanization and Climate Change, 0.55 kg of CO2 is emitted for 1 kWh of electrical energy. When the system is turned on at the same time as the air conditioner, the carbon footprint of 15.4 kg per m^2 will be removed with the reduction in the air conditioning set temperature and the savings in air conditioning power. For the 14 m^2 office room designed in our study, this rate means that 215.6 kg of carbon is not released into nature. With the sequential operation of the system with the air conditioner, the carbon footprint of 11.55 kg will be erased from the nature in a 3-hour period with a 30% savings of approximately 21 kWh. It is calculated that 23 kg of carbon footprint reduction will be achieved in the carbon footprint during the six-hour air conditioning period.

With the addition of fins, the heat transfer surface area has been increased and the amount of energy saving has been increased compared to our previous study. Today, when energy problems are experienced, the development of the Tricklevent system and the integration of different modules into the system provide great savings in building energy use.

ACKNOWLEDGEMENT

This study was produced within the scope of the Panel Facade Project that Conditions the Outside Air and takes it inside within the scope of Tübitak 1501 Project. We would like to thank Tübitak for the support given to our project.

REFERENCES

[1] Agrawal, P.C. (1989). A review of passive systems for natural heating and cooling of buildings. Solar Wind Technology, 6 (5) 557–567.

[2] Khedari, J., Waewsak, J., Thepa, S., Hirunlabh, Field, J. (2000). Investigation of night radi-ation cooling under tropical climate. Renewable Energy, 20 (2) 183–193.

[3] Stec, W.J., Van Paassen, AHC. (2005). Symbiosis of the double-skin facade with the HVAC system. Energy and Buildings, 37:461–9.

[4] Directive2010/31/euoftheEuropeanparliamentandofthecouncilof19 May 2010on the energy performance of buildings;2010.Availablefrom: /http://www.epbd-ca.euS.

[5] Cabezal, F., Castell, A., Medrano, M., Martorel, P., Fernandez, G. (2010). Experimental study on the performance of insulation materials in Mediterranean construction. Energy and Buildings, 42:630–6.

[6] Shameri, MA., Alghoul, MA., Sopian, K., Fauzi, M., Zain, M., Elayeb, O. (2011). Perspectives of double skin facade system in buildings and energy saving. Renewableand Sustainable Energy Reviews, 15:1468–75.

[7] Saelens, D. (2002). Energy performance assessments of single storey multiple-skin facades. Belgium: Katholieke Universiteit Leuven; PhD Thesis.

[8] Pasquay, T. (2004). Natural ventilation in high-rise building with double facade, saving or waste of energy. Energy and Buildings, Volume 36, Issue 4, Pages 381-389.

[9] Wang, P.C. (2008). Natural ventilation in double-skin facade design for Office buildings in hot and humid climate. PhD Thesis, University of New South Wales, Australia, December.

[10] Faggembauu, D.H. (2006). Fluid-dynamics in double and single skin facades. PhD Thesis. Universitat Politecnicade Catalunya, Spain, December.

[11] Poirazis,. H. (2004). Double skin facades for Office buildings. Report EBD-R-04/3.Lund University.

[12] Ding, W., Hasemi, Y., Yamada,T. (2005). Natural ventilation performance of a double skin facade with a solar chimney. Energy and Buildings, 37:411–8.

[13] Shameri, MA., Alghoul, MA., Sopian, K., Zain, MFM., Elayeb, O. (2011). Perspectives of double skin façade systems in buildings and energy saving. Renewable Sustain Energy, 15:1468–75.

[14] Mingotti, N., Chenvidyakarn, T.,Woods,A.W. (2011). The fluid mechanics of the natural ventilation of a narrow-cavity double-skin façade. Building and Environment, 46 807-823

[15] Wahhad, A.M., Adam, N.M., and Sapuan, S.M. (2015). Comparison of numerical simulation and experimental study on indoor air quality of air-conditioned office building in a desert climate. International Journal of Automotive and Mechanical Engineering (IJAME), ISSN: 2229-8649 Volume 12, pp. 3109-3124.

[16] Manz, H., Th, Frank. (2005). Thermal simulation of buildings with double-skin facades. Energy and Buildings, 2005;37:1114–21.

JSR A
Journal of Scientific Reports

[17] Gratia, E., Herde, A.D. (2004). Natural ventilation in a double-skin façade. Energy and Buildings, 36 137–146.

[18] Sharda, A. and Kumar, S. (2014). Heat Transfer through Glazing Systems with Inter-Pane Shading Devices. Energy Technology & Policy Journal, volume1, pp. 23– 34.

[19] Marjanovic, L., Cook, M., Hanby, V., and Rees, S. (2005). CFD Modeling of Convective Heat Transfer From A Window With Adjacent VENETIAN Blinds. Ninth International IBPSA Conference Montréal, Canada August 15-18.

[20] Urbikain, M. K., and Sala, J.M. (2012). Heat transfer through a double-glazed unit with an internal louvered blind. International Journal of Heat and Mass Transfer volume 55, pp. 1226-304.

[21] Sökmen, K.F., Ergüner, B., .Akın, İ. (2022). Tricklevent Yenilikçi Pasif Cephe Havalandırma Sisteminin Isıl Konfor ve Enerji Tasarrufu Açısından İncelenmesi. Avrupa Bilim ve Teknoloji Dergisi, Sayı 37, 170-178.

[22] Amai, H., Tanabe, S., Akimoto, T., and Genma., T. (2007). Thermal sensation and comfort with different task conditioning systems. Building and Environment, 42(12): 3926 – 3932.

[23] Lynch, P. (2015). How energy modelling wil impact the design process ArchDaily. Retrieved December 15. from http://www.archdaily.com/778309/how-energy-modellling-will-impact-the-design-process.

[24] Hensen, J., and Clarke, J. (2015). Integrated simulation for HVAC Performance prediction: state-of- the-art illustration. International Conference of Sustainable Building 2000, pp.1-3.

[25] Stec, W., and Van Paasen, A. (2004). Symbiosis of the double skin façade with the HVAC system. Energy buildings 37(200).

NOMENCLATURE

A	cross-section
D_h	hydraulic diameter
k	heat conduction coefficient
L	length
$\dot{m}$	mass flow
Nu	Nusselt number
V	velocity
P	pressure
P_s	perimeter
Ra	Rayleigh number

Re	Reynolds number
T	temperature
Greek symbols	
ρ	density, kg m^{-3}
μ	dynamic viscosity
Abbreviations	
WBCSD	World Business Council for Sustainable Development
DSF	Double skin facades
HVAC	Heating, ventilation, and air conditioning
CFD	Computational fluid dynamics

Kütahya Dumlupınar University
Institute of Graduate Studies

Journal of Scientific
Reports-A
E-ISSN: 2687-6167
Number 51, December 2022

RESEARCH ARTICLE

INVESTIGATION of the EFFECTS of PREPARED PVA/NANO LA_2O_3 MIXTURE on ALIZARIN DYE REMOVAL: KINETIC, ISOTHERM and THERMODYNAMIC STUDIES

Mehmet Semih BİNGÖL[1,*]

[1*]Atatürk Üniversitesi, DAYTAM, Erzurum, semih.bingol@atauni.edu.tr , ORCID: 0000-0002-4616-7143

Receive Date:13.10.2022 *Accepted Date: 15.11.2022*

ABSTRACT

With the increasing industrialization, the use of dyestuffs increases. This increasing use causes serious dangers to the environment as waste. For this reason, studies on the removal of dyestuffs have increased. In this study, an adsorbent was prepared by adding nano-sized Lanthanum Oxide (La_2O_3) to Polyvinyl Alcohol for Alizarin Red S removal. The chemical structures of this adsorbent were confirmed by FT-IR analysis. The effects of adsorbent masses, pH, contact time on Alizarin Red S removal were investigated in adsorption studies. Accordingly, the highest 94.5% removal was achieved in 1 gram adsorbent mass, pH 7, 60 minutes. In addition, thermodynamic, isotherm and kinetic studies were carried out in the study. In isotherm studies, it was determined that the most suitable model was Freundlich and the qmax value was found to be 5.06 mg/g. However, the pseudo second order kinetic model was found to be suitable.

Keywords: *Polyvinyl Alcohol, Lantanium Oxide, Alizarin, Adsorption*

1. INTRODUCTION

Dyes are used to color products in a variety of industries, including the textile, pharmaceutical, chemical, and petrochemical industries. These industries discharge a lot of toxic, colored wastewater into bodies of water. Resistant wastewater, particularly textile dyes and derivatives, contains physiologically resistant chemicals that are difficult to decrease or destroy using standard methods such as biological oxidative pathways. Colored organic compounds produce a coating on the water's surface, keeping deep sunlight out of bodies of water. As a result, adequate light cannot be delivered for water flora and fauna's photosynthetic processes. As a result, the dye reduces the total oxygen required to maintain the chemical oxidation of the biological entities in need of chemical oxygen and biological oxygen. On the paint market, 700000 tons are manufactured annually, and 10% of these totals are industrially processed and released into the environment [1].

Anthraquinone dye group member Alizarin Red S (ARS) is a long-lasting anionic dye. In the textile industries, it is frequently used as a coloring agent. Additionally, this dye is used to stain biological material including small invertebrate embryos and the calcified bones of vertebrate species. Due to its

chemical stability and lack of biodegradability, ARS cannot be fully mineralized using standard refining techniques. Due to its great thermal, optical, and physicochemical stability, it resists deterioration. As a result, numerous studies have concentrated on creating quick, easy, and effective procedures for their secure removal [2].

For the overall removal of dyes, numerous methods have been tried. The most widely employed of these are physical ways like adsorption, biological methods, and chemical methods. One of these investigations, which is also economical and efficient, is adsorption. Various adsorbent compounds were utilized. Ion exchange resins, silica, clay, synthetic and natural polymers, composite adsorbents, and biomass are examples of adsorbents. Synthetic polymers have received extra attention since they have several unique features. Poly(vinyl alcohol, or PVA), which has recently caught the interest of researchers among the various synthetic polymers, is notable for its compatibility, non-toxicity, biodegradability, availability, low cost, and good film formation[3].

Therefore, in this study, PVA was used for the removal of alizarin red s dye in water. To make PVA functional, specially prepared nano-sized La2O3 is doped. Adsorption studies were carried out with the help of this prepared adsorbent. The effectiveness of the adsorbent was determined by kinetic, thermodynamic and isotherm studies.

2. MATERIAL AND METHOD

2.1. Materials

Polyvinyl Alcohol and glutaraldhyde were commercially purchased from Merck, La_2O_3 nanography.

2.2. Preparation of Adsorbent

We employed an immersion sonicator to perform mechanical delamination (75W). La_2O_3 was sonicated in DMF for 12 hours to achieve this. The finished product was then collected by allowing the solution to evaporate under normal conditions. The precipitated materials were then dried at 40°C after being centrifuged five times with distilled water. The synthesized nano La_2O_3 was shown to be nano in size via TEM analysis. In addition, XRD analysis was performed to understand the crystal structure of the prepared n-La particles.

At 90^0C with stirring, 5 grams of PVA were dissolved in 100 mL of distilled water. 0.25 grams of nano La_2O_3 (nLa) were then added after it had been cooled to room temperature. This mixture was held on a magnetic stirrer for three hours after being sonicated for one hour. The solution was then adjusted with 1M HCl to pH 2-3. 3 mL of glutaraldehyde was then added and combined. After that, it was put in glass bottles and stored at –12 °C for three days. It was taken out of the cooler and given a distilled water wash. The obtained adsorbent's chemical structures were verified by FT-IR analysis after it had dried.

2.3. Adsorption Studies

To study Alizarin Red S adsorption in produced adsorbents, a number of batch studies using various experimental parameters were conducted. These parameters include the amount of dye present (10, 25, 50, or 100 mg/L), the pH range (2–12), and the mass of the adsorbent (PVA-nLa) (0.1–2.0 g).

JSR A
Journal of Scientific Reports

To diluted the determined concentrations, a stock solution of Alizarin Red S at 1000 mg/L was prepared. Adsorption was performed using the IKA KS 3000i Control model shaker by adding the amount of adsorbents to 50 ml of Alizarin Red S (ARS) solution and shaking it at 150 rpm for the predetermined period of time. The pH of the ARS solution was changed to the required level using 0.1 M NaOH and 0.1 M HCl solutions. To remove the adsorbents from the solution after the adsorption procedure, it was centrifuged at 5000 rpm for 30 min. The adsorbents were taken out after centrifugation, and the solution's ARS concentration was calculated. The remaining dye concentration in the solution was evaluated by colorimetry after centrifugation using a UV spectrophotometer (Shimadzu UV-3600 Plus) with a maximum wavelength of 421 nm. The calibration curve between the concentration and absorbance of the dye solution was plotted to obtain an absorbance-concentration profile. The formulae below were used to compute the amount of ARS that was removed as well as the adsorbent's capacity [4].

$$q_e = (c_0 - C_e) \times \frac{V}{W} \quad (1)$$

$$q_t = (c_0 - C_t) \times \frac{V}{W} \quad (2)$$

$$Giderim, \% = \frac{(C_0 - C_e)}{C_0} \times 100 \quad (3)$$

C_0, C_e, and C_t represent the initial ARS concentration, equilibrium concentration, concentration at time t, adsorption capacities qe and qt at equilibrium and t, V ARS solution volume, and W adsorbent mass.

2.4. Thermodynamic, Isotherm and Kinetic Studies

Adsorption experiments were conducted thermodynamically at 3 different temperatures (298, 308, 318 Kelvin). With the use of the findings from these investigations, the following equations were used to derive Gibss, Enthalpy, and Entropy.

$$K_c = \frac{q_e}{C_e} \quad (4)$$

$$\ln K_c = \frac{\Delta S^0}{R} - \frac{\Delta H^0}{RT} \quad (5)$$

$$\Delta G^0 = \Delta H^0 - T\Delta S^0 \quad (6)$$

The most popular way to depict the equilibrium state of an adsorption system is using the adsorption isotherm. The amount of substance adsorbed by the adsorbent and the equilibrium concentration are related by an adsorption isotherm, which exists at constant temperature. Studies on equilibrium isotherms were conducted at 25^0C, using 1g of adsorbent and various ARS concentrations at pH 7. Analysis of equilibrium adsorption values was done using the Freundlich and Langmuir isotherm models.

JSR A
Journal of Scientific Reports

The first theoretically determined adsorption isotherm is represented by the Langmuir isotherm equation. This equation serves as the foundation for the majority of the following proposed equations that fit a variety of experimental results, or they were created using the Langmuir method. As a result, both chemisorption theories and physical adsorption continue to rely on the Langmuir isotherm model. The Langmuir isotherm's mathematical equation is provided below [5].

$$\frac{C_e}{q_e} = \frac{1}{q_{max}K_c} + \frac{C_e}{q_{max}} \tag{7}$$

The Freundlich isotherm, another popular experimental equation that uses two parameters and is consistent with a wide range of experimental data, is comparable to the Langmuir isotherm [6]. Below is the Freundlich isotherm equation:

$$\ln q_e = \ln K_F + \left(\frac{1}{n}\right) \ln C_e \tag{8}$$

The effective adsorbate-adsorbent contact time can be calculated using adsorption kinetics. There are steps in the analysis of adsorption kinetics that have an impact on the rate of the adsorption process. In order to explore the ARS adsorption mechanism on adsorbent surfaces, two distinct kinetic models were applied. These models are pseudo first order (PF) and pseudo second order (PS) kinetic models, respectively [7].
The PF kinetic model was developed by Lagergren (1898). The PF kinetic model equation is given below:

$$Log(q_e - q_t) = \ln q_e - \frac{K_1 t}{2.303} \tag{9}$$

The PS model equation is given below:

$$\frac{t}{q_t} = \frac{1}{k_2 q_e^2} + \frac{t}{q_e} \tag{10}$$

3. RESULT AND DISCUSSION

3.1. nLa TEM Analysis

Bulk La_2O_3 and nano La_2O_3 samples were imaged with TEM device. It is seen in Figure 1a that there are bulk La_2O_3's over 1 micron, and in Figure b the n-La dimensions vary between 30-50 nm. In this study, it was observed that the bulk La_2O_3's were reduced to nano size as planned and dispersed in approximately equal sizes.

JSR A
Journal of Scientific Reports

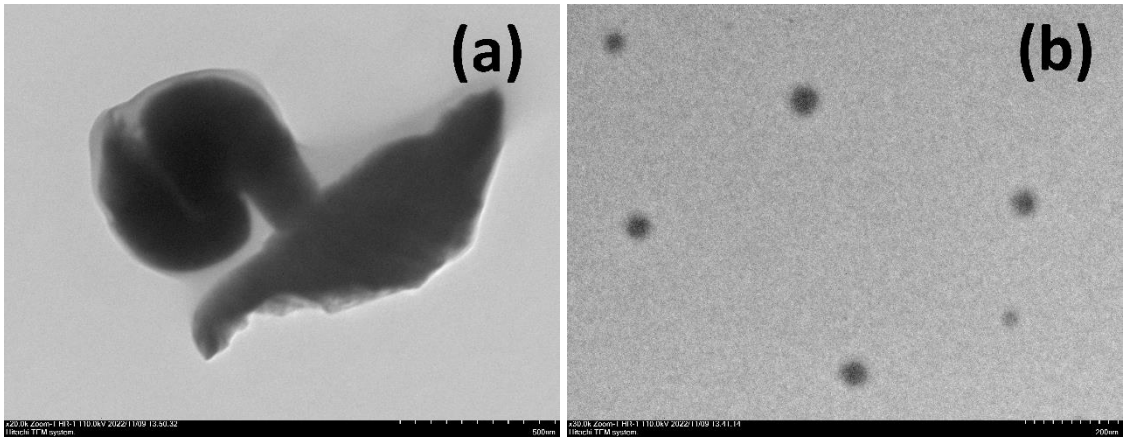

Figure 1. TEM images (a) bulk La_2O_3, (b) nano La_2O_3.

3.2. n-La XRD Analysis

Figure 2 shows the n-La XRD analysis. Accordingly, the peaks seen at 15, 28, 39, 48 and 55 were approximately the same as the xrd peaks of nano La_2O_3 materials prepared in several different studies[8,9]. It has been understood in the literature that n-La has a similar crystal structure to those prepared in the literature.

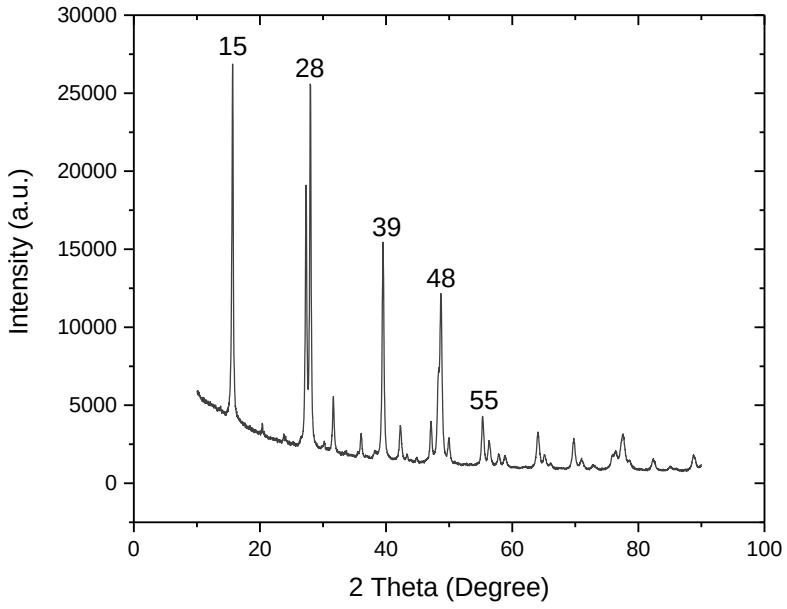

Figure 2. n-La XRD pattern.

JSR A
Journal of Scientific Reports

3.3. FT-IR Analysis

Figure 3 shows the FT-IR spectra of PVA, nano La_2O_3, and PVA-nLa. The main peaks of PVA were seen as 3283, 2907, 1700, 1418, 1321, 1086 and 834 cm^{-1} [10]. Nano La_2O_3 main peaks were found to be 3608, 1456 and 628 cm^{-1} [11]. When the PVA-nLa spectra were examined, it was understood that similar peaks appeared. The chemical groups corresponding to the peaks appearing in the FT-IR spectra are shown in Table 1.

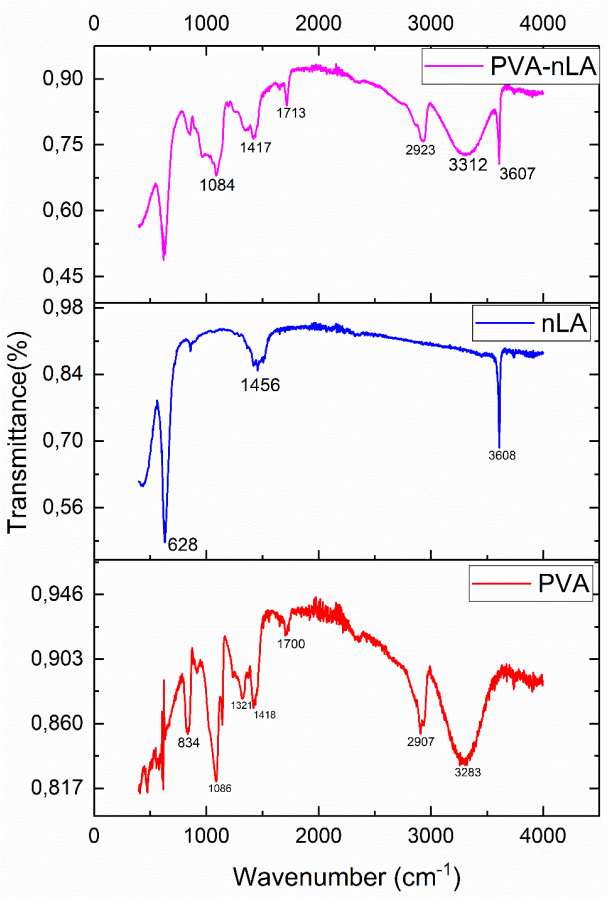

Figure 3. FT-IR spectrum.

Table 1. PVA and nLa_2O_3 FT-IR results.

Chemical Structure	Wavenumber (cm_{-1})
La_2O_3 OH stretching	3608
PVA-GA OH stretching	3283

JSR A
Journal of Scientific Reports

PVA-GA CH_2 asymmetric stretching	2907
PVA-GA C=O carbonyl stretching	1700
La_2O_3 CO_2 vibration	1456
PVA-GA CH_2 bending	1418
PVA-GA C-H deformation	1321
PVA-GA C-O stretching	1086
PVA-GA C-C stretching	834
La_2O_3 La-O-C stretching	628

3.4. Effect of Adsorbent Amount

First, the impact of adsorbent masses was assessed in the adsorption trials. As a result, the adsorption was completed in 120 minutes at 25 ^oC, pH 7, and 50 mg/l ARS concentration. According to Figure 4, the greatest amount of ARS that could be removed by adsorption was 94.04%. As seen in Figure 4, as the adsorbent mass is increased, the adsorption increased and remained constant after 1 gram, and the maximum ARS adsorption removal was determined as 94.04%.

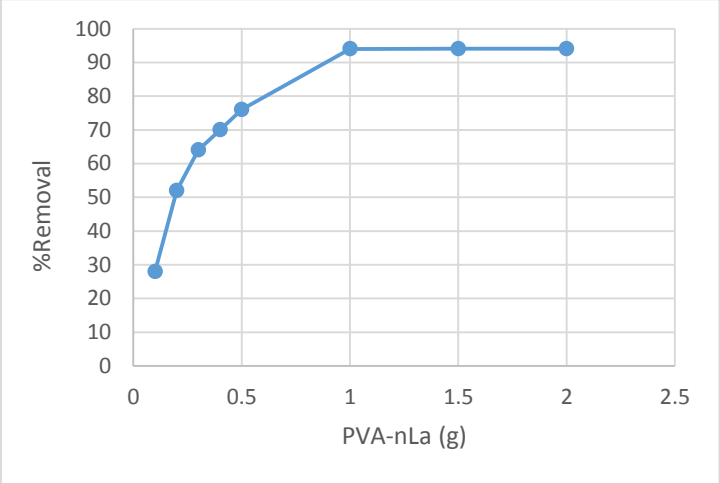

Figure 4. Effect of PVA-nLa amount on adsorption.

3.5. pH's Impact on ASR Removal

The effect of pH change on adsorption was investigated. The adsorption study was carried out at 25^oC, 1 gram of adsorbent, 50 mg/l ARS concentration and 120 min. As seen in Figure 5, the percentage of ARS removed increased until pH 7, but then remained steady. The maximum ARS removal rate was discovered to be 92.5% at pH 7.

JSR A
Journal of Scientific Reports

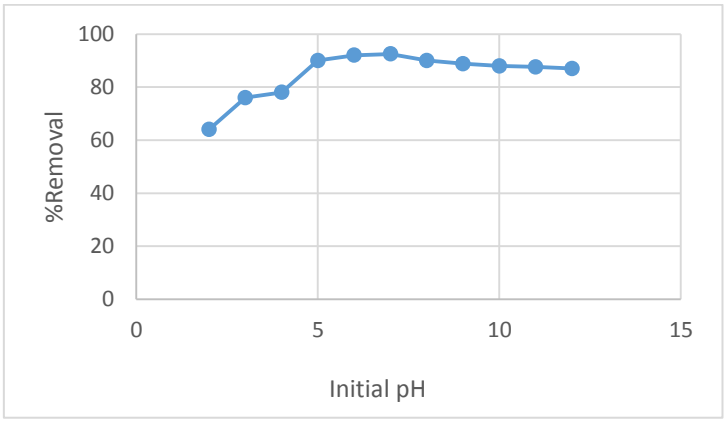

Figure 5. pH's impact on ASR removal.

3.6. Adsorption Effects of Time and Starting Concentrations

Figure 6 depicts the influence of time and initial concentration on adsorption. These tests were conducted out at a temperature of 25°C, with a gram of adsorbent and a pH of 7. As a result, highly quick adsorption was observed for up to 10 minutes. This is due to the adsorbent surface's active sites being filled. At a starting concentration of 10 ppm, the maximum ARS removal was reported to be 94.5%. At an initial concentration of 100 ppm, the greatest adsorption capacity was determined to be 4.6 mg/g.

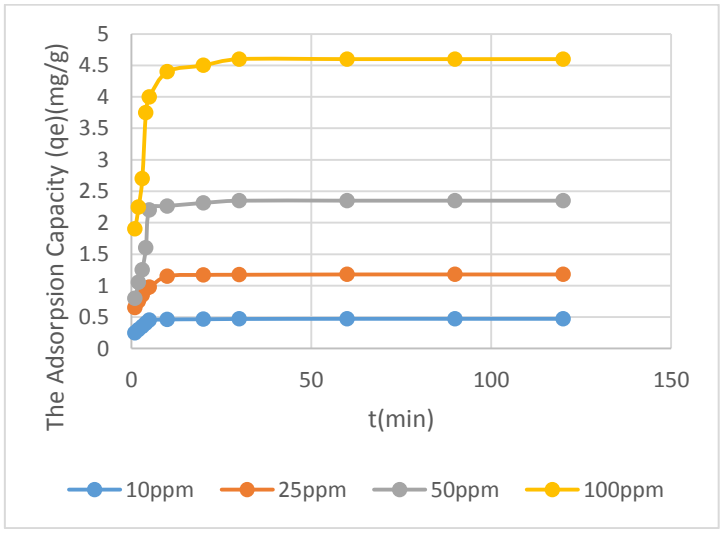

Figure 6. Adsorption effects of time and starting concentrations.

JSR A
Journal of Scientific Reports

3.7. Thermodynamic, Isotherm and Kinetic Study Results

Experiments were conducted out at 50 ppm ARS concentration for 60 minutes, pH 7, 1 gram adsorbent quantity to investigate the effect of temperature and thermodynamic investigations. Figure 7 shows that adsorption increased somewhat as temperature increased. Figure 7 was used to derive thermodynamic parameters. Table 2 displays the parameter results. At all temperatures, negative ΔG values (-4.05, -5.04, and -4.51 kJ/mol) suggest that the reaction is spontaneous. Physisorption is generally expressed by G values of -20< ΔG< 0 (kJ/mol). It was also discovered that G decreased with increasing temperature, indicating the possibility of adsorption at higher temperatures. Endothermic adsorption is shown by positive enthalpy (ΔH=2.8 kJ/mol). Positive entropy (ΔS = 0.023 kJ/mol) suggests greater randomness during solid-solution interface adsorption [12].

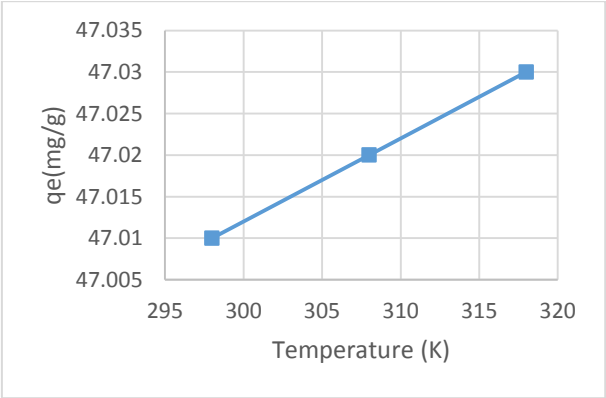

Figure 7. Effect of temprature on adsorption.

Table 2. Thermodynamic parameter values.

T (Kelvin)	ΔH (kJ/mol)	ΔS (kJ/mol)	ΔG (kJ/mol K)
298	2,80	0.023	-4,05
308	2,80	0.023	-5,04
318	2,80	0.023	-4,51

The values of the Langmuir and Freundlich model parameters for ARS adsorption by the produced adsorbent are shown in Table 3 and Figure 8. When these two models were compared, it became clear that the Freundlich model (R^2>0.999) provided a better fit than the Langmuir model (R^2=0.9324). He demonstrated that the adsorption mechanism was consistent with the Freundlich isotherm for this reason. This suggests that the energy and heterogeneity of the ARS adsorption surface are different [13].

JSR A
Journal of Scientific Reports

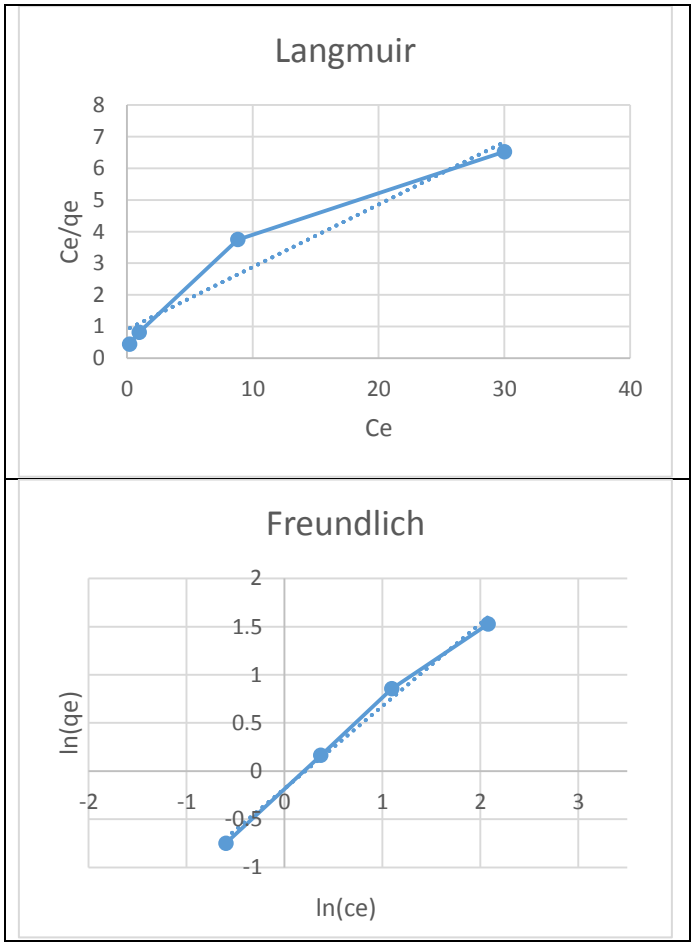

Figure 8. Langmuir and Freundlich plots.

Table 3. Isotherm parameter values.

Isotherm	**Parameters**	**Value**
Langmuir	R^2	0.9324
	q_{max}(mg/g)	5,06
	K_L	0,21
Freundlich	R^2	0.9934
	K_F (L/mg)	0,83
	n	1,16

JSR A
Journal of Scientific Reports

The experimentally collected data were used to apply the linear forms of the PF and PS velocity models in order to examine the adsorption control mechanism. Table 4 and Figure 9 contain the data and graphs for the kinetic parameter. Additionally, experimental results and R^2>0.999 demonstrated the compatibility of the PS. Improved and experimental kinetic velocity profiles further supported this. As a result, the rate-controlling step for this adsorbent is probably chemical adsorption[12]. In this study, which was tried for the first time in the literature; When the nano La_2O_3 doped PVA-based adsorbent was compared with many PVA-based studies in the literature, it was seen that similar results were obtained [14]. It has been seen that PVA-La_2O_3 adsorbents, which have never been tried in the literature, can be effective and La_2O_3 additive accelerates the adsorbtion much more than the literature [15]. For this reason, we think that this study can shed light on future studies.

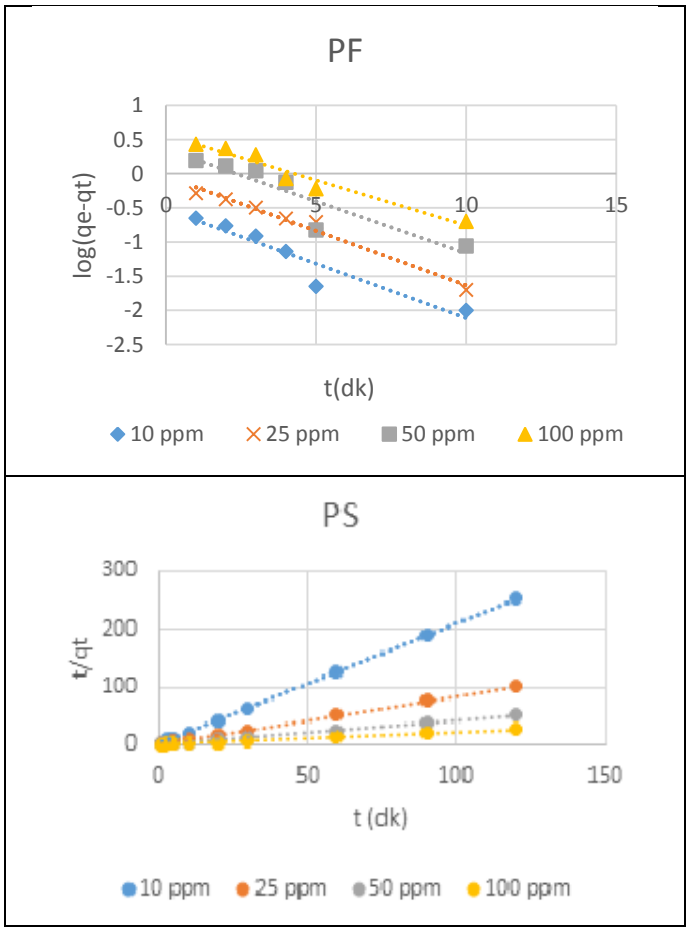

Figure 9. PFO and PSO kinetic model plots.

Table 4. Parameter values of PFO and PSO kinetic models.

		PF			PS		
Co (mg/l)	**q_{exp}(mg/g)**	**q_e (mg/g)**	**K_1**	**R^2**	**q_e (mg/g)**	**K_2**	**R^2**
10	0,47	0,59	0,3654	0.9036	0,476	3,13	0,9999
25	1,17	0,96	0,3668	0.9782	1,18	1,06	0,9999
50	2,35	1,429	0,3505	0,8379	2,39	0,288	0,9996
100	4,6	1,76	0,3056	0,9494	4,66	0,182	0.9998

4. CONCLUSION

As a result, La_2O_3 doped PVA was utilized for the first time in the literature to remove ARS. By using FT-IR analysis, the produced adsorbent's chemical structures were verified. Adsorption tests have shown that 1 g of adsorbent, pH 7, and 60 minutes of adsorption time are the best conditions. It was discovered that the Freundlich isotherm model was appropriate for this adsorption. The qmax value was also discovered to be 5.06 mg/g. The kinetic studies led to the conclusion that the PSO model was appropriate.

ACKNOWLEDGEMENT

I would like to thanks Eastern Anatolia High Technology Application and Research Center (DAYTAM) that provided for infrastructure support.

REFERENCES

[1] Al Naim, A.F.;El-Shamy, A.G. (2021). A new reusable adsorbent of polyvinyl alcohol/magnesium peroxide (PVA/MgO2) for highly selective adsorption and dye removal, Mater. Chem. Phys., 270, 124820.

[2] Roosta, M.;Ghaedi, M.;Mohammadi, M. (2014). Removal of Alizarin Red S by gold nanoparticles loaded on activated carbon combined with ultrasound device: Optimization by experimental design methodology, Powder Technol., 267, 134–144.

[3] Zhang, H.;Chen, H.;Azat, S.;Mansurov, Z.A.;Liu, X.;Wang, J.;Su, X.;Wu, R. (2018). Super adsorption capability of rhombic dodecahedral Ca-Al layered double oxides for Congo red removal, J. Alloys Compd., 768, 572–581.

[4] Bingöl, M.S. (2022). Effects of Prepared Gadolinium Oxide-Doped Chitosan/PVA Hydrogels on Congo Red Removal in Water, Water, Air, Soil Pollut., 233, 410.

[5] Langmuir, I. (1918). THE ADSORPTION OF GASES ON PLANE SURFACES OF GLASS, MICA AND PLATINUM., J. Am. Chem. Soc., 40, 1361–1403.

[6] Freundlich, H.M.F. (1906). Over the adsorption in solution, J. Phys. Chem, 57, 1100–1107.

[7] Lagergren, S.K. (1898). About the theory of so-called adsorption of soluble substances, Sven. Vetenskapsakad. Handingarl, 24, 1–39.

[8] Singh, A.;Palakollu, V.;Pandey, A.;Kanvah, S. (2016). Green Synthesis of 1, 4-Benzodiazipines over La2O3 and La(OH)3 Catalysts: Possibility of Langmuir-Hinshelwood adsorption, RSC Adv., 6(105), 103455-103462.

[9] Cheraghali, R.;Aghazadeh, M. (2016). A simple and facile electrochemical route to synthesis of metal hydroxides and oxides ultrafine nanoparticles (M=La, Gd, Ni and Co), Anal. Bioanal. Electrochem., 8, 64–77.

[10] Kharazmi, A.;Faraji, N.;Mat Hussin, R.;Saion, E.;Yunus, W.M.M.;Behzad, K. (2015). Structural, optical, opto-thermal and thermal properties of ZnS–PVA nanofluids synthesized through a radiolytic approach, Beilstein J. Nanotechnol., 6, 529–536.

[11] Sulaiman, N.;Yulizar, Y.;Apriandanu, D.O.B. (2018). Eco-friendly method for synthesis of La2O3 nanoparticles using Physalis angulata leaf extract, AIP Conf. Proc., 2023, 20105.

[12] Kavci, E. (2021). Malachite green adsorption onto modified pine cone: Isotherms, kinetics and thermodynamics mechanism, Chem. Eng. Commun., 208, 318–327.

[13] Kavci, E.;Erkmen, J.;Bingöl, M.S. (2021). Removal of methylene blue dye from aqueous solution using citric acid modified apricot stone, Chem. Eng. Commun., 1–16.

[14] Sabarish, R.;Unnikrishnan, G. (2018). Polyvinyl alcohol/carboxymethyl cellulose/ZSM-5 zeolite biocomposite membranes for dye adsorption applications, Carbohydr. Polym., 199, 129–140.

[15] Mok, C.F.;Ching, Y.C.;Muhamad, F.;Abu Osman, N.A.;Hai, N.D.;Che Hassan, C.R. (2020). Adsorption of dyes using poly (vinyl alcohol)(PVA) and PVA-based polymer composite adsorbents: a review, J. Polym. Environ., 28, 775–793.

Kütahya Dumlupınar University
Institute of Graduate Studies

Journal of Scientific
Reports-A
E-ISSN: 2687-6167
Number 51, December 2022

RESEARCH ARTICLE

PERFORMANCE ANALYSIS of DIFFERENT SOLAR TRACKING SYSTEMS for OFF-GRID PHOTOVOLTAIC POWER SYSTEM in BİLECİK, TURKEY USING PVSYST SOFTWARE

Hülya ÇINAROĞLU[1], Yasemin ÖNAL[2,*]

[1]Bilecik Şeyh Edebali University, Institute of Graduate Studies, Energy System Engineering Department, Bilecik, hly.plt.90@gmail.com, ORCID: 0000-0001-8775-1445
[2,*]Bilecik Şeyh Edebali University, Engineering Faculty, Electric and Electronics Department, Bilecik, yasemin.onal@bilecik.edu.tr, ORCID: 0000-0003-0173-0948

Receive Date:20.10.2022 *Accepted Date: 02.11.2022*

ABSTRACT

It is planned to install an off-grid photovoltaic system of 550Wp to meet the energy needs of the energy measurement laboratory at Bilecik Şeyh Edebali University in Bilecik, Turkey. In this study, the performance of different solar tracking systems in the off-grid photovoltaic system that will be installed in Bilecik, was compared. Monthly available solar energy, $E_{missing}$, y_a, y_r, y_f, P_r, l_a and l_s were compared in analysis of different solar tracking systems. The analyzed solar tracking systems are fixed tilted, seasonal tilted, horizontal axis, vertical axis and double axis. PVsyst 7.2 is widely used simulation software for analyzing the efficiency of photovoltaic systems and optimizing system design. Monthly average irradiation and panel temperature data used for analysis are obtained from PVsyst database. The minimum available energy and the maximum missing energy in the fixed tilted tracking with tilt angle of 40° and an azimuth angle of 0°, are 764.77 kWh/y and 93.36 kWh/y respectively. The maximum available solar energy and the minimum lost energy in the double axis tracking system are 1049.9 kWh/y and 57.03 kWh/y in July respectively. The highest average monthly performance ratio is 0.778 for the fixed axis system and the lowest is 0.558 for the double axis system. The results of this study show the performance analysis of the off-grid photovoltaic systems power generation, and can serve for the successful development of the photovoltaic system in real application situation.

Keywords: *Solar tracking systems, Off-grid PV system, PVsyst software, Performance analysis,*

1. INTRODUCTION

With climate changes in our world, problems of conventional energy sources and developments in technology, countries prefer clean and renewable energy sources [1,2]. Renewable energy sources have many advantages. These advantages: being ready in nature, being sustainable, helping to protect environment by reducing carbon dioxide emissions and reducing dependence on energy, which are

local resources. Renewable energy sources are hydrogen, geothermal, solar, wind and biomass [3]. After the energy crisis in the 70s, solar power technology has gained significant in worldwide market. It has been improving faster than other renewable energy sources in recent years. In addition, solar energy systems have started to become widespread around the world in order to reduce the amount of carbon released into the air too much [4].

Solar energy is clean energy and is abundant in our world. Photovoltaic (PV) panels, that convert the irradiation on them directly into direct current (DC) through cells, are system elements. Produced by a PV panels, the power value depends on the amount of irradiation falling on it. Since the position of solar changes throughout day, the PV panel must always be directed exactly towards the sun and adjusted to produce maximum possible power [5].

PV systems are classified as on-grid, off-grid or hybrid. For investments for only PV or hybrid PV systems, it is important to prepare feasibility studies in advance. Today, these studies and researches can be done by means of some computer programs. It is important for the power plant that is planned to be established in a region for the production data of the power plant and the cost of the installation, sizing of PV systems and accuracy of investment [6].

All over the world, different methods and simulation software programs are used for design of PV systems [7]. These simulation softwares are HOMER, RETScreen, SolarMAT, PVsol, PVGIS, SolarGIS and PVsyst [8]. PVsyst simulation software is available for on-grid connected or off-grid systems because selection parameters are suitable for the researches in studies and in literature. There are PV panels, inverters, batteries in many brands and models in the database, it is functional, economic analysis can be made, fast results and simulation data are close to reality and it is frequently used. Using numerous parameters; the final report that clearly shows estimated production data, loss values and the performance rate of the system in monthly, daily or hourly format is given to user. In addition to all these, with Meteonorm 8.0, which has a database in PVsyst, atmospheric data of the place where the PV system is desired can be produced synthetically [9].

The PVsyst software was originally developed in Geneva by Swedish scientist Andre Mermaid and his team. [10]. Mandelli et al. have done a study on the sizing methodology on the independent country electric power in Uganda, taking into account the cost and level of energy taken and lost [11]. Smiles et al. with PVsyst software made a technical and economic analysis of the situation of meeting the energy needs of the Bath Abbey building in the United Kingdom with roof-mounted PV systems [12]. Limem et al. evaluated the effectiveness of the 5.1 kW rooftop PV system installed in Kocaeli Technology Faculty building in Kocaeli climate conditions by using commonly used PVsyst software [13]. Jagadale et al. compared the two cases by placing the panels at 20° and different angles in a PV power plant with an installed power of 250 kW in Pure city of India with PVsyst [14]. Baqir et al. made a technical analysis of a PV power plant with an installed power of 700 kWp, which is planned to be built in Daikundi, Afghanistan with PVsyst [15]. Mohammed et al. selected the panels used in the PV plant with an installed power of 10 kW in Saudi Arabia using SolarGIS in CdTe, a-Si, c-Si, CSI technologies and determined the most efficient panel and made a technical and economic analysis of the plant [16]. Ghafoor et al. performed a technical and economic analysis for a single residential application of off-grid PV (OGPV) system in Faisalabad, Pakistan [17].

The performance analysis of PV power systems has been studied in several different countries by means of PVsyst or new methods. On the other hand, there is less studies in the literature on different solar tracking systems (STS) of OGPV systems in buildings. The performance of a 550Wp OGPV systems for a measurement laboratory planned to be established in Bilecik Seyh Edebali University for different STS is analyzed using PVsyst 7.2 simulation software in this study.

2. MATERIAL AND METHOD

2.1. Meteorogical Data of Bilecik

Bilecik city has three different climate types due to its location in the transition region, its proximity to water resources and its geographical location. In addition, the number of sunny days is quite high due to its latitude and longitude points. The region, where Bilecik Seyh Edebali University is located and this study was conducted, generally shows the climate characteristics of Central Anatolia Region. The city has an average of 2.190 hours of sunshine per year. With this advantage, Bilecik is among the provinces with high solar energy potential in Turkey [18].

In order to analyze the performance of the PV panel system, data such as solar irradiation and ambient temperature from the atmospheric data of the region are used. Before performing the simulation, meteorological data of the region should be taken from the database of program. Therefore, the region should be marked on the map in the geographic area management region in the PVsyst simulation software [19]. However, due to the project region is not available in Meteonorm 8.0., that is used to generate hourly synthetic data of the region with PVsyst 7.2, then the coordinate data of the region is introduced to simulation study [9].

Figure 1 shows the monthly average solar irradiation values, ambient temperature values, horizontal diffuse irradiation and global incident collector plane at tilt angle 40°, azimuth angle 0° and albedo 20% at the location of the PV system planned at Bilecik Seyh Edebali University.

JSR A
Journal of Scientific Reports

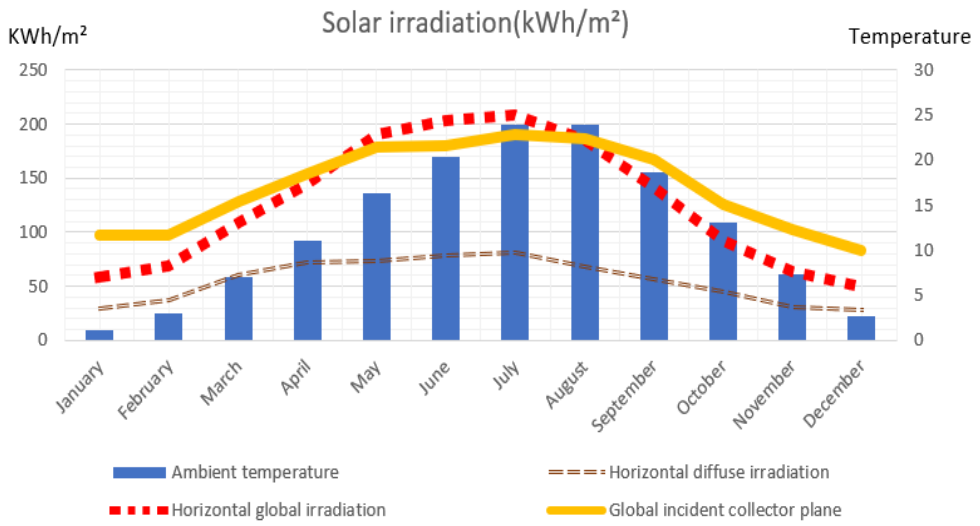

Figure 1. Monthly average solar irradiation and ambient temperature in Bilecik.

First of all, the monthly average horizontal global irradiance is between 50 kWh/m² in December and 208.5 kWh/m² in July. The monthly average horizontal irradiance is 29.7 kWh/m² in January and 81.2 kWh/m² in July. The monthly average global irradiance to the PV panel is 83.2 kWh/m² in December and 189.9 kWh/m² in July. The monthly average ambient temperature varies by 1.19 °C in January and 23.97 °C in July. Finally, the average ambient temperature is 12.41 °C throughout the year.

2.2. Parameters of PV Power System

The parameters used in the literature to analyze the performance of the PV system give a complete preliminary feasibility analysis of the PV system. These parameters are the efficiency of the PV system, the loss between the energy produced and the consumed, the system yields, the performance and the losses of the system at the full analysis report [20]. Daily, monthly and annual total AC energy values produced by the PV panel are obtained by using Eq. 1, Eq.2 and Eq. 3 for the desired time [21].

$$E_{(AC,d)} = \eta_{inv} \sum_{t=1}^{24} E_{(DC,t)} \quad (1)$$

$$E_{(AC,d)} = \eta_{inv} \sum_{t=1}^{24} E_{(DC,t)} \quad (2)$$

$$E_{(AC,y)} = \eta_{inv} \sum_{m=1}^{12} E_{(DC,m)} \quad (3)$$

Here, these values show that DC energy value is produced by for hourly $E_{(DC,t)}$, for daily $E_{(DC,d)}$, for monthly $E_{(DC,m)}$ and AC energy value is determined by for daily $E_{(AC,d)}$, for monthly $E_{(AC,m)}$, for annual $E_{(AC,y)}$ in addition N_d days, and η_{inv} the yield of the DC-AC inverter. Daily, monthly and

JSR A
Journal of Scientific Reports

annual energy and daily, monthly and annual energy values transferred to the user are used to calculate the daily, monthly and annual values of the lost energy consumed in the PV power system [4].

$$E_{(loss,d)} = E_{(load,d)} - E_{(user,d)} \quad (4)$$

$$E_{(loss,m)} = E_{(load,m)} - E_{(user,m)} \quad (5)$$

$$E_{(loss,y)} = E_{(load,y)} - E_{(user,y)} \quad (6)$$

The panel reference yield of the PV system is indicated by y_r. The panel producers have defined the efficiency of the panel in the standard test condition (STC) in the datasheet. It is calculated as the ratio of total irradiation to global irradiation. y_r is expressed numerically in kW/m² unit [22].

$$y_r = \frac{H_t}{G_0} \quad (7)$$

Here, H_t is the total horizontal irradiation in kW/m² and G_0 is the global irradiation in months/days kWh/Sq. The array yield of the PV system is indicated by y_a. It is obtained by dividing the power obtained at the PV panel output by the power of the PV panel. y_a is calculated using Eq. 8 [22].

$$y_a = \frac{E_{DC}}{P_0} \quad (8)$$

Here, E_{DC} shows the generated power value of the PV panel on a daily, monthly or yearly basis, and P_0 shows the nominal output power value of the PV panel in the STC.

$$E_{DC} = V_{DC} * I_{DC} * t \quad (9)$$

Here, V_{DC} and I_{DC} are the output voltage and the output current of the PV panel respectively, and t is the time in hours. The ratio of the AC energy output at the inverter output to the maximum power of the PV panel in the STC is defined by the final efficiency y_f. It is calculated on a daily, monthly or annual basis using Eq. 10.

$$y_f = \frac{E_{AC}}{P_P} \quad (10)$$

Here, E_{AC} is the daily, monthly or annual AC energy value at the inverter output of the PV system and P_P is the maximum power of the PV panel in STC.

Besides efficiency parameters, loss parameters also affect the performance of a PV power system. There are losses in all components used when designing a OGPV system. These loss parameters are panel capture losses, system losses and performance ratio.

JSR A
Journal of Scientific Reports

The PV system performance ratio is indicated by P_r and is defined as the ratio of the energy supplied to the grid to the nominal power specified in the PV catalog. The performance ratio gives information about all losses of energy converted from DC to AC. Therefore; The energy remaining after energy losses is expressed as a percentage [23].

$$P_r = \frac{y_f}{y_r} = \frac{E_{AC}}{Glob\_Irr} \tag{11}$$

Here, y_f is the panel final yield of the PV system and y_r is the panel reference efficiency. E_{grid} is AC injected energy into the grid and Glob_Irr is PV panel global irradiation.
System losses are expressed as l_c and are expressed as the difference between the panel reference efficiency of the PV system and the panel efficiency. The main components that make up this loss value are; the increase in PV panel temperature values, partial shading, the amount of dust accumulated on the panel, tracking errors and incompatibility between the PV panels are calculated using Eq. 12 [19].

$$l_c = y_r - y_a \tag{12}$$

Capture loss is obtained the difference between the panel yield of the PV system and the panel final yield. It is indicated by l_s. System loss value originates from the inverter and other devices used in the PV system and is calculated using Eq.13.

$$l_s = y_a - y_f \tag{13}$$

Using the equations given above, the relationships between performance evaluation parameters are given in Figure 2.

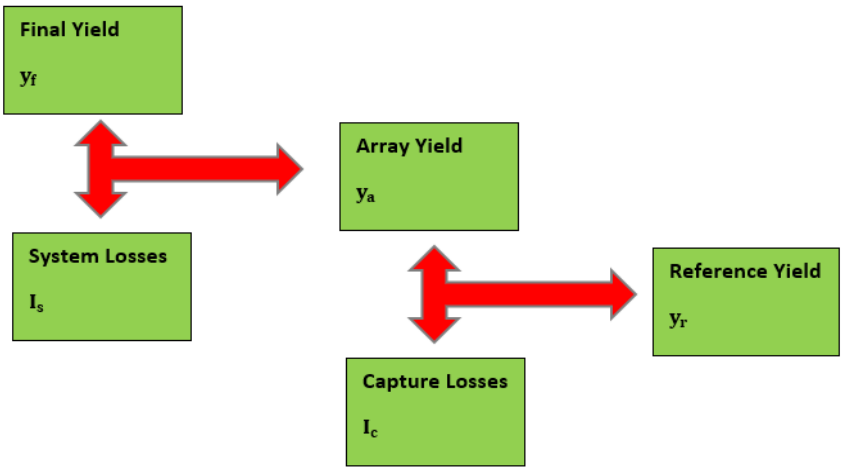

Figure 2. Performance evaluation parameters.

JSR A
Journal of Scientific Reports

2.3. Off-Grid PV (OGPV) System Components

OGPV systems are used in places that are far from the grid and require little energy. These systems are compared to systems that meet their energy from fossil sources, they are advantageous because of low operating, maintenance and cleaning costs [24].

The main components of OGPV systems consist of PV panels, battery pack, DC-AC inverter and charge controller, DC and AC load and connectors required for system integration. The model of OGPV system is shown in Figure 3.

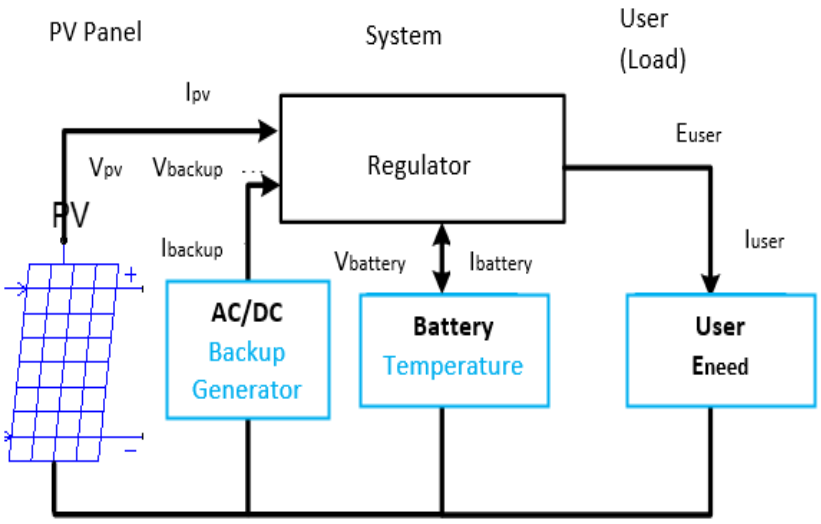

Figure 3. Model of OGPV system.

The PV panel converts the irradiation into electrical energy. The charge controller sets the desired current and voltage. When not all of the generated voltage is consumed, it is stored using the battery. When there is no or little irradiation, the voltage stored in the battery is used. Conventionally, it contains that battery charge controller and MPP tracking system for PV panels. DC-AC inverter converts DC-AC to drive AC system [25].

In this study; belonging to JINKO SOLAR company JKM275PP-60 model, 275Wp Si-poly 2 units PV panels were used. The selected panel has a weight of 19 kg, dimensions of 1.65 x 0.992 x 0.04 m and a surface area of 1.64 m². Table 1 shows the parameters of the PV panel using PVsyst simulation software STC at 1kW/m² irradiance and 25°C temperature. The open circuit voltage of the PV panel is 39.1V and the short circuit current 9.15A. The current in MPP is 8.61A and the voltage in MPP is 31.9V. In the simulation, 2 PV panels are connected in series and voltage 78.2V is obtained.

JSR A
Journal of Scientific Reports

Table 1. The parameters of PV panel.

Model	JKM275PP-60
Technology	Si-poly
Nominal Power	275 Wp
Dimension	1.65x0.992x0.04m
Surface Area	1.637 m²
Weight	19 Kg
Number of Cells N_s	60
Short Circuit Current I_{sc}	9.15 A
Open Circuit Voltage V_{oc}	39.1 V
Current in MPP I_{mpp}	8.61 A
Voltage in MPP V_{mpp}	31.9 V
Operating Temperature T_o	45 °C
Temperature Coefficient C_t	-0,39 %°A/C

In this study, belonging to TN POWER Company 1 unit TNG 12-200 model lead-acid battery was used. Lead acid batteries are frequently used in PV systems due to their low cost, high operating efficiency, fault free and long life. The parameters of the selected battery are presented in Table 2. The nominal voltage of the used battery is 12V and its rated capacity is 200Ah at C10. In addition, a 1000W, 12 V charge controller for MPP tracking system and battery charge with a maximum charge current of 16 A and a discharge current of 10 A was used. Since PV system is designed for 550 W, the DC-AC inverter is selected as 1kW according to the maximum power value.

2.4. Load Details

In this study, the electrical load representing the nominal consumption is acquired for the energy measurement laboratory. The power of an energy measurement laboratory is simulated from a OGPV system. Loads consist of LED, laptop, printer and fan. Load utilizations are assumed to be constant throughout the year. The daily energy consumption of the energy measurement laboratory is 2.094 kWp/day throughout the year. Table 3. shows the minimum daily electricity consumption required for the energy measurement laboratory.

Table 2. The parameters of Battery.

Model	TNG 12-200
Technology	Lead-Acid
Dimension	0.52x0.239x0.225 m
Weight	63.2 Kg
Internal Resistance	2.7 mΩ

JSR A
Journal of Scientific Reports

Nominal Voltage	12 V
Capacity	200 Ah
Coulomb Yield	%97
Number	1
Nu. of Autonomous Day	4 Day
Static life at 20 °C	5 Year

Table 3. Power consumption for the energy measurement laboratory.

Device	Power (kW)	Number	Average Daily Use	Daily Energy (Wh)
LED	15 W	5	6 Hour	450
Laptop	120 W	2	6 Hour	1440
Printer	30 W	1	2 Hour	60
Fan	2 W	10	6 Hour	120
Stand-by mode	1 W		24 Hour	24
Total daily energy				2094 Wh/day
Total monthly energy				62.82 kWh/month

3. FINDINGS and DISCUSSION

The simulation steps in this study are given as:1-The irradiation data of the region, where the power plant is located, are taken from the database of the program. The region is marked on the map in the geographical area management part of the simulation program [10]. The coordinate data (40.1933 °N, 29.9664 °E, altitude: 540 m) is manually introduced into the program.

2-The placing of the panels in the PV system has been done. In the study, the panel tilt angle is determined as 40°, the azimuth angle is 0° and the albedo value is determined as 20% for fixed angle system [26].

3-In the database of the program, there are electrical and mechanical data of system elements such as panels, inverters, batteries belonging to many companies. If the database of the program does not have system elements information, this information can be defined manually. PVsyst simulation software for the analyzed plant, the panel and battery in Table 1 and Table 2 are defined.

4-When all definitions which are essential for system design, done correctly, PVsyst program gives a warning that you are ready for the simulation. The report created as a result of the simulation includes system components, solar irradiation amount, product status and loss diagram.

Different STS are analyzed in the PVsyst program: fixed axis, seasonal axis, horizontal axis, vertical axis and double axis. The monthly usable available solar energy production values of different STS are given in figure 4. It can be seen from Figure 4 that the highest annual total available solar energy

JSR A
Journal of Scientific Reports

is 1049.9 kWh/y in the double axis STS, and the lowest 764.77kWh/y in the fixed axis STS with an inclination angle of 40° and azimuth angle of 0°.

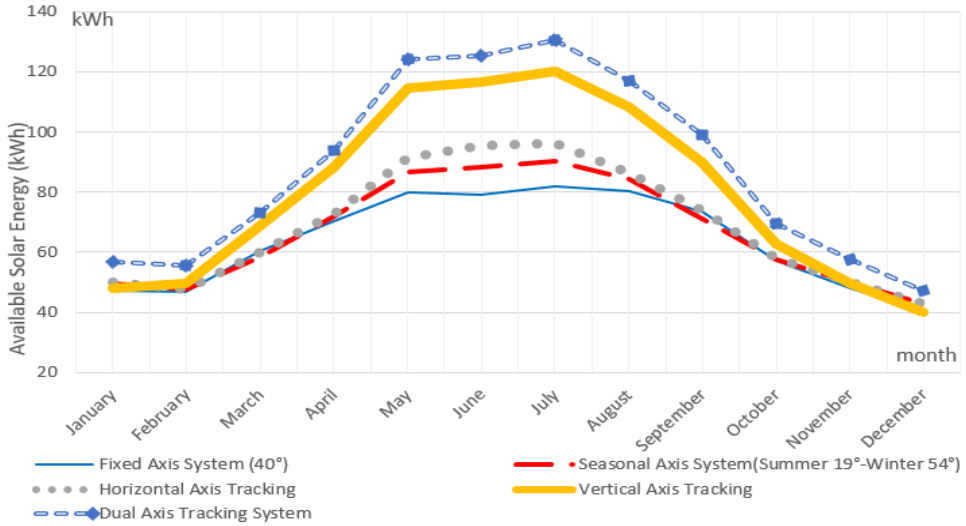

Figure 4. Monthly available solar energy obtained from different STS for OGPV system in Bilecik, Turkey

The monthly missing energy values of different STS are shown in figure 5. Figure 5 shows that the highest annual total missing energy value is in the fixed axis STS with 93.36 kWh, and the lowest in the double axis STS with 57.03 kWh. Missing energy increases mainly in December and January, when solar irradiation is lowest. In December and January, the minimum values of 20.39 kWh and 13.57 kWh are respectively in the double axis STS, while the maximum values are 27.78 kWh and 19 kWh in the fixed-axis STS respectively.

Figure 6 shows that monthly array yields of different STS are variable throughout the year. The highest array yield is 4.44 hours/day in the double axis STS in July. The lowest array yield is 2.47 hours/day in the vertical axis STS in December. Because the global irradiation and the PV temperature are higher in July and are lower in December. In general, array yield values increase in the summer months and decrease in the winter months in different STS.

JSR A
Journal of Scientific Reports

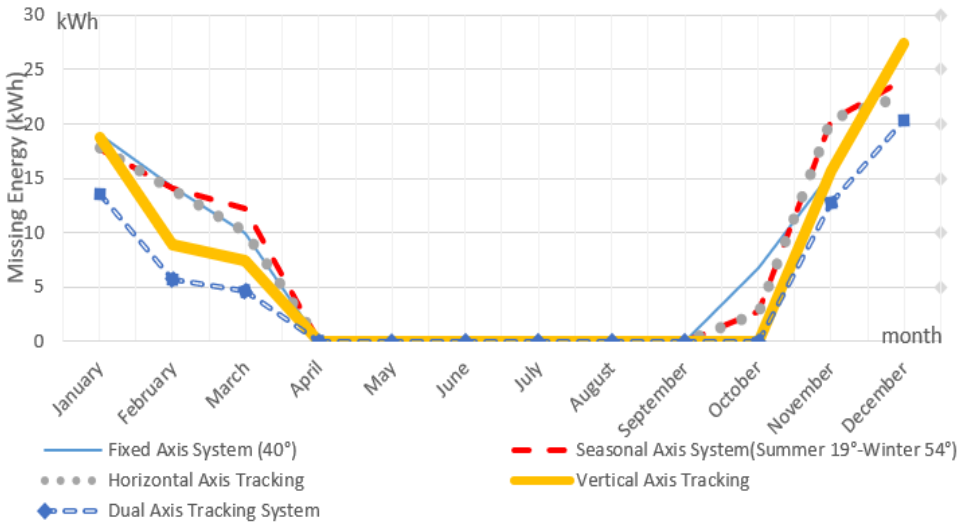

Figure 5. Monthly missing energy obtained from different STS for a OGPV system in Bilecik, Turkey

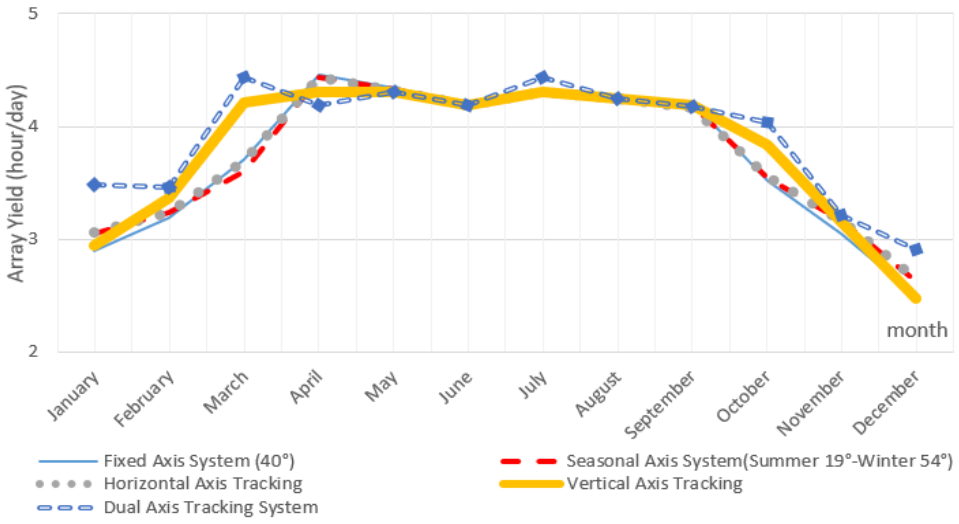

Figure 6. Monthly panel yield obtained from different STS for OGPV system in Bilecik, Turkey

The monthly final yield values of different STS are showed by Figure 7. It shows that monthly final yields are relatively stable, except for the winter months. Final yields are highest in between April and October with 3.81 hours/day. The reason for this situation is that especially the solar irradiation and

the number of sunny days is high. The system with the lowest final yield value is the fixed axis STS in December with 2.07 hours/day.

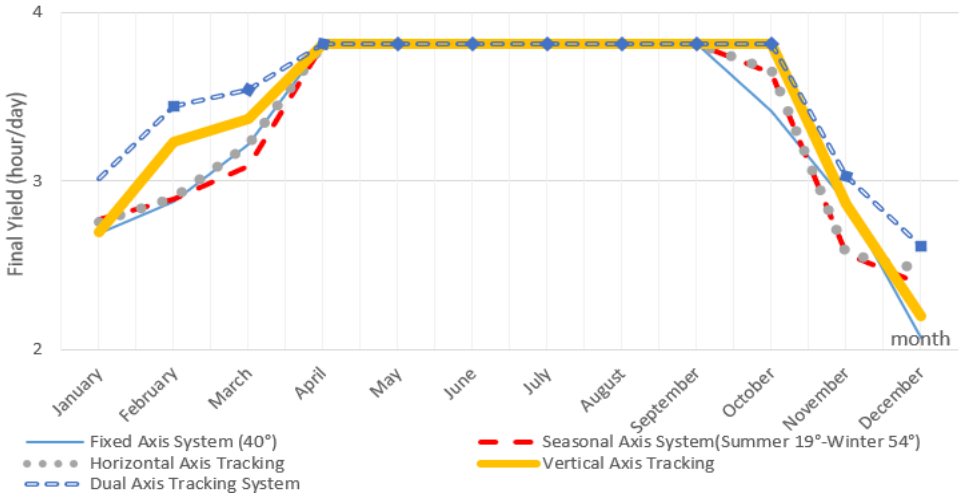

Figure 7. Monthly final yield from different STS for OGPV system in Bilecik, Turkey

The monthly yf values of different STS are showed by Figure 8. In July, the highest reference yield is 9.58 hours/day in the double axis STS and the lowest reference yield is 6.12 hours/day in the fixed axis STS.

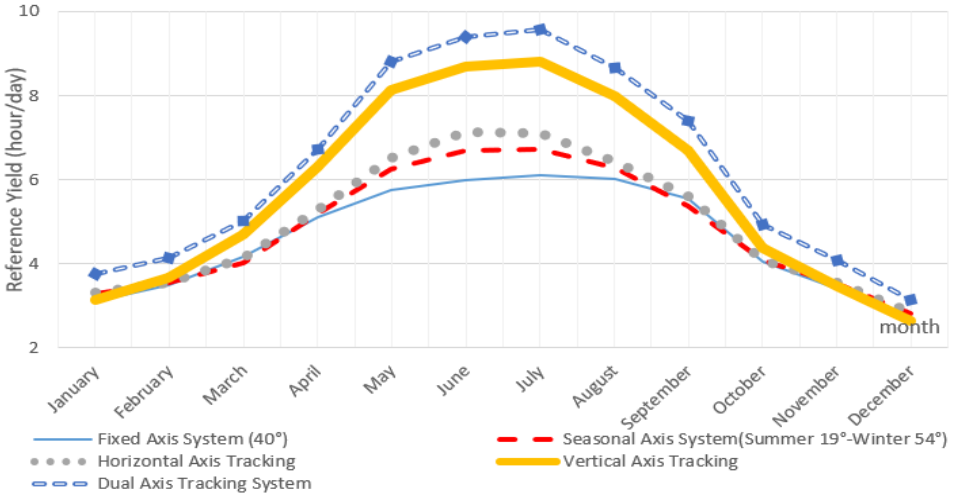

Figure 8. Monthly reference yield obtained from different STS for OGPV system in Bilecik, Turkey

JSR A
Journal of Scientific Reports

Figure 9 shows the P_r values of different STS. It is seen from Figure 9 that the highest average monthly P_r for the fixed axis STS is 0.778, while the lowest average monthly P_r for the double axis STS is 0.558. In general, the monthly P_r value for different STS increases in winter and decreases in summer. P_r value is affected by reasons that are PV panel temperature rise, inverter incompatibility and losses, shading, pollution factor.

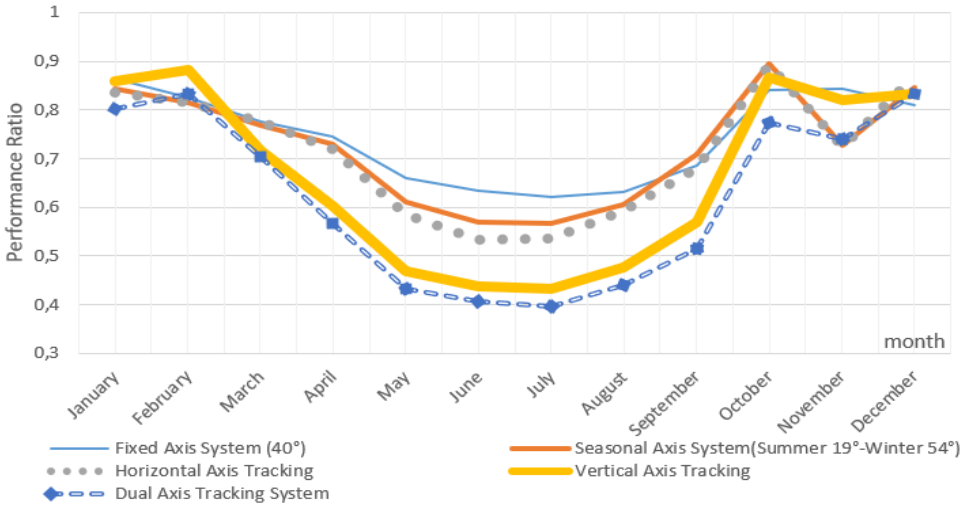

Figure 9. Monthly P_r from different STS for OGPV system in Bilecik, Turkey

The monthly la values of different STS are given in Figure 10. The highest average monthly la is 2.38 hours/day in the double axis STS. The lowest average monthly la is found 0.91 hours/day in the fixed axis STS. In the vertical axis STS, 4.51 h/day is obtained in la in July and 5.27 h/day was obtained in the double axis STS. It is observed that la was higher in the summer months in the obtained values. The highest monthly array losses in the other three tracking systems are 1.82, 2.49 and 2.93 hours/day, respectively. Because of the lowest global solar irradiation, the lowest la for all tracking systems is in January. Therefore, monthly la rises with increasing solar irradiation.

JSR A
Journal of Scientific Reports

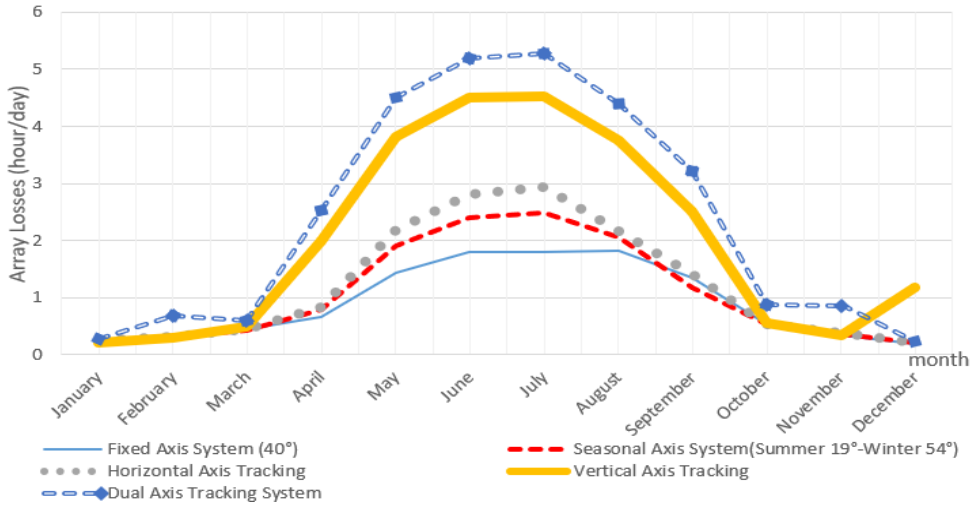

Figure 10. Monthly panel capture loss from different STS for OGPV system in Bilecik, Turkey

Figure 11 shows the monthly ls of different STS. From figure 11, it is seen that the highest monthly ls are 0.651 hours/day in April for the fixed axis STS, 0.621 hours/day in April for the seasonal axis STS, 0.636 hours/day in April for the horizontal axis STS, 0.842 hours/day in March for the vertical axis STS hours/day and 0.89 hours/day in March for the double axis STS. The lowest monthly ls were seen as 0.114 hours/day in October for the fixed axis STS, 0.103 hours/day in the seasonal axis STS, 0.101 hours/day in the horizontal axis STS and 0.03 hours/day in the vertical axis STS, and 0.016 hours/day in February in the double axis STS. Different types of field losses in off-grid photovoltaic systems all through the year are shown in Figure 12.

JSR A
Journal of Scientific Reports

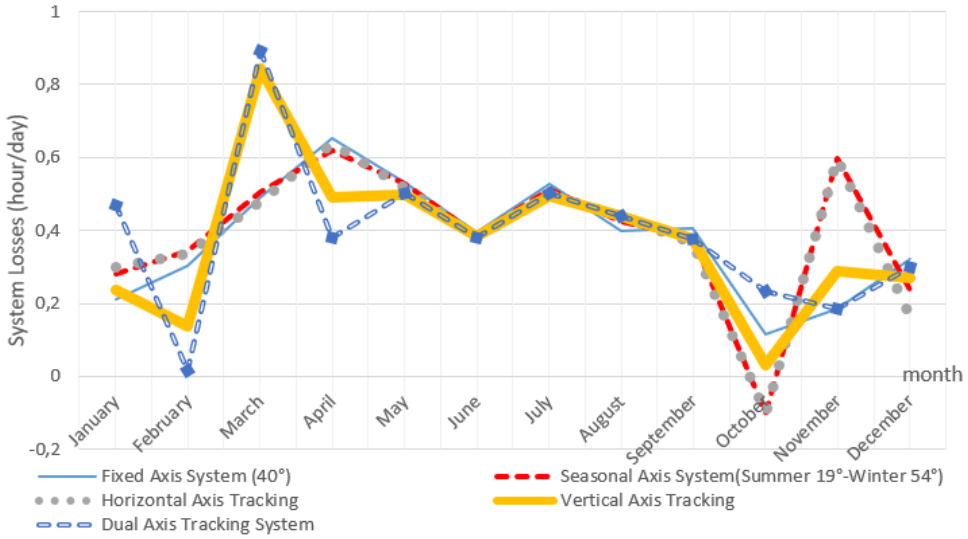

Figure 11. Monthly system loss from different STS for OGPV system in Bilecik, Turkey

4. RESULTS

In this study, the performance analysis of different STS for the 550Wp OGPV system planned for the energy measurement laboratory of Bilecik Seyh Edebali University was compared using the PVsyst 7.2 simulation program. The lowest annual total solar energy available is 764.77 kWh/y and the highest annual total loss energy is 93.36 kWh in the fixed axis STS with tilt angle of 40° and azimuth angle of 0°. However, there is only missing energy in December 27.78 kWh and January 19 kWh. The highest monthly average P_r was obtained in the fixed axis STS with 0.778 and the lowest average monthly l_a of 1.792 hours/day compared to other tracking systems. The highest annual total available solar energy is 1049.9kWh/y and the lowest annual total missing energy is 57.03 kWh in the double axis STS. At the same time, compared to other systems, the highest panel yield with 4.44 hours/day, the lowest monthly average P_r with 0.558 and the highest monthly average l_a with 5.27 hours/day were obtained from double axis STS. In this study, 137.28% more energy was produced per year and 61.08% less missing energy was obtained in the double axis STS compared to the fixed axis STS.
In addition, there are similarities between the different STS compared. The highest available energy for all systems obtained in summer, and the lowest in December. All of the missing energy takes place in December and January. y_r was obtained very close each other for all months and y_f was obtained very close to each other for the other months except December, January and February. Monthly P_r is high in October-February and low in June-July. Monthly l_a was higher in summer than all months, and l_a was lowest in January and December for the all MPPT system analyzed.

JSR A
Journal of Scientific Reports

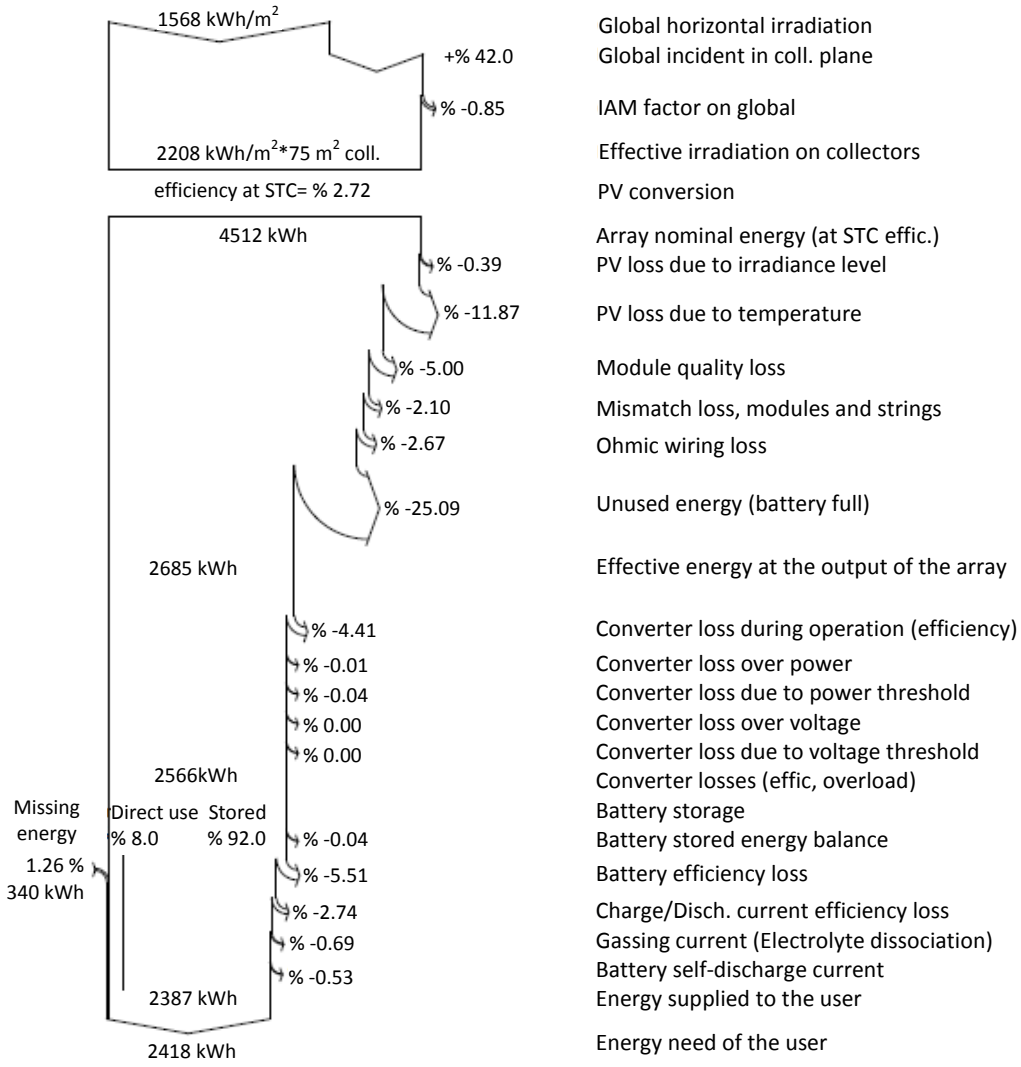

Figure 12. Energy loss diagram of the double axis STS for OGPV system in Bilecik, Turkey.

ACKNOWLEDGEMENT

The authors thank the Scientific Research Projects Coordinatorship of Bilecik Şeyh Edebali University for their support for the project titled Implementation of Photovoltaic Energy System with Solar Tracking in Bilecik Seyh Edebali University Central Campus, numbered 2020-01.BŞEÜ.03-07.

REFERENCES

[1] Dey, D. and Subudhi, B., (2020), Design, simulation and economic evaluation of 90 kW grid connected Photovoltaic system, Energy Reports, 6, 1778-1787. doi: 10.1016/j.egyr.2020.04.027

[2] Owusu, P. A. and Asumadu-Sarkodie, S., (2016), A review of renewable energy sources, sustainability issues and climate change mitigation, Cogent Engineering, 3(1), 1-14. doi: 10.1080/23311916.2016.1167990

[3] Akinsipe, O. C., Moya, D. and Kaparaju, P., (2021), Design and economic analysis of off-grid solar PV system in Jos-Nigeria, Journal of Cleaner Production, 287, 1-11. doi:10.1016/j.jclepro.2020.125055

[4] Li, C., Zhou, D., Yu, W., Wang, H., Zhu, D., Sun, M. and Li, G., (2017), Performance of off-grid residential solar photovoltaic power systems using five solar tracking modes in Kunming, China, International Journal of Hydrogen Energy, 42, 6502-6510. doi: 10.1016/j.ijhydene.2017.01.033

[5] Eldin, S. S., Abd-Elhady, M. S. and Kandil, H. A., (2016), Feasibility of solar tracking systems for PV panels in hot and cold regions, Renewable Energy, 85, 228-233. doi: 10.1016/j.renene.2015.06.051

[6] Kılcı, O. and Koklu, M., (2019), The importance of fixed and variable angle in solar power plants analysis, International Journal of Applied Mathematics Electronics and Computers, 7, 75-83. doi:10.18100/ijamec.653371

[7] Amrollahi, M. H. and Bathaee, S. M. T., (2017), Techno-economic optimization of hybrid photovoltaic/wind generation together with energy storage system in a stand-alone micro-grid subjected to demand response, Applied energy, 202, 66-77. doi: 10.1016/j.apenergy.2017.05.116

[8] Umar, N., Bora, B., Banerjee, C. and Panwar, B. S., (2018), Comparison of different PV power simulation softwares: case study on performance analysis of 1 MW grid-connected PV solar power plant. International Journal of Engineering Science Invention, 7, 11-24.

[9] Mermoud, A. and Wittmer, B., (2014), PVSYST user's manual, Switzerland, January.

[10] Kumar, R., Rajoria, C. S., Sharma, A. and Suhag, S., (2021), Design and simulation of standalone solar PV system using PVsyst Software: A case study. Materials Today: Proceedings, 46, 5322-5328. doi: doi.org/10.1016/j.csite.2019.100409

[11] Mandelli, S., Brivio, C., Colombo, E. and Merlo, M., (2016), A sizing methodology based on Levelized Cost of Supplied and Lost Energy for off-grid rural electrification systems, Renewable Energy, 89, 475-488. doi: 10.1016/j.renene.2015.12.032

[12] Smiles, M. J., Law, A. M., Urwick, A. N., Thomas, L., Irvine, L. A., Pilot, M. T. and Walker, A. B., (2022), Next steps in the footprint project: A feasibility study of installing solar panels on Bath Abbey, Energy Science & Engineering, 10, 892–902. doi:10.1002/ese3.1069

[13] Limem, F. and Sezen, S., (2021), Comparative Analysis of Different Photovoltaic Simulation Software: Case Study on Analyzing the Performance of a 5, 1 kWp Grid Connected Photovoltaic System, Avrupa Bilim ve Teknoloji Dergisi, 32, 816-826. doi: 10.31590/ejosat.1040126

[14] Jagadale, P. R., Choudhari, A. B. and Jadhav, S. S., (2021), Design and Simulation of Grid Connected Solar Si-Poly Photovoltaic Plant using PVsyst for Pune, Renewable Energy Research and Applications, 3(1), 41-49. doi: 10.22044/rera.2021.11057.1069

[15] Baqir, M. and Channi, H. K., (2022), Analysis and design of solar PV system using Pvsyst software, Materials Today: Proceedings, 48(5), 1332-1338. doi: 10.1016/j.matpr.2021.09.029

[16] Mohammed, A., Ghaithan, A., Al-Hanbali, A., Attia, A. M., Saleh, H. and Alsawafy, O., (2022), Performance evaluation and feasibility analysis of 10 kWp PV system for residential buildings in Saudi Arabia, Sustainable Energy Technologies and Assessments, 51, 1-14. doi:10.1016/j.seta.2021.101920

[17] Ghafoor, A. and Munir, A., (2015), Design and economics analysis of an off-grid PV system for household electrification, Renewable and Sustainable Energy Reviews, 42, 496-502. doi: 10.1016/j.rser.2014.10.012

[18] Sözen, A., Arcaklioğlu, E., Özalp, M. and Kanit, E. G., (2005), Solar-energy potential in Turkey. Applied Energy, 80(4), 367-381. doi: 10.1016/j.apenergy.2004.06.001

[19] Sharma, V., & Chandel, S. S. (2013). Performance analysis of a 190 kWp grid interactive solar photovoltaic power plant in India. *Energy*, 55, 476-485. doi: 10.1016/j.energy.2013.03.075

[20] Tripathi, B., Yadav, P., Rathod, S. and Kumar, M., (2014), Performance analysis and comparison of two silicon material based photovoltaic technologies under actual climatic conditions in Western India, Energy Conversion and Management, 80, 97-102. doi: 10.1016/j.enconman.2014.01.013

[21] Adaramola, M. S. and Vågnes, E. E., (2015), Preliminary assessment of a small-scale rooftop PV-grid tied in Norwegian climatic conditions, Energy Conversion and Management, 90, 458-465. doi: 10.1016/j.enconman.2014.11.028

[22] Kumar, N. M., Kumar, M. R., Rejoice, P. R. and Mathew, M., (2017), Performance analysis of 100 kWp grid connected Si-poly photovoltaic system using PVsyst simulation tool, Energy Procedia, 117, 180-189. doi: 10.1016/j.egypro.2017.05.121

[23] Okello, D., Van Dyk, E. E. and Vorster, F. J., (2015), Analysis of measured and simulated performance data of a 3.2 kWp grid-connected PV system in Port Elizabeth, South Africa, Energy conversion and management, 100, 10-15. doi: 10.1016/j.enconman.2015.04.064

[24] Qoaider, L. and Steinbrecht, D., (2010), Photovoltaic systems: A cost competitive option to supply energy to off-grid agricultural communities in arid region, Applied Energy, 87(2), 427-435. doi: 10.1016/j.apenergy.2009.06.012

[25] Singh, G. K., (2013), Solar power generation by PV (photovoltaic) technology: A review, Energy, 53, 1-13. doi: 10.1016/j.energy.2013.02.057

[26] Ozbay, H., Karafil, A., Onal, Y., Kesler, M. and Parmaksiz, H., (2017), The monitoring of monthly, seasonal and yearly optimum tilt angles by raspberry pi card for Bilecik city, Turkey, Energy Procedia, 113, 311-318. doi: 10.1016/j.egypro.2017.04.071

Kütahya Dumlupınar University
Institute of Graduate Studies

Journal of Scientific
Reports-A
E-ISSN: 2687-6167
Number 51, December 2022

RESEARCH ARTICLE

EVALUATION of OCCUPATIONAL HYGIENE MEASUREMENTS with REGARD to EMPLOYEES in a LIMESTONE QUARRY

Şahin YUVKA[1*], Orhan UYAR[2]

[1*]Kütahya Dumlupınar University, Faculty of Engineering, Department of Mining Engineering, Kütahya, sahin.yuvka@dpu.edu.tr, ORCID: 0000-0002-3219-2321
[2]Akşehir Municipality, Cleaning Affairs Directorate, Deputy Director of Cleaning Affairs, Akşehir/KONYA, orhan_uyar@hotmail.com, ORCID: 0000-0002-8885-1592

Receive Date:28.10.2022 *Accepted Date: 25.11.2022*

ABSTRACT

Although working environments have become safer with the developing technology, there are still negative effects on the health of employees. It is very important to detect these negative effects and take the necessary precautions. For this, occupational hygiene measurements should be made. Employees in the mining sector are exposed to physical and chemical risk factors depending on the type of work they do. Mining is a very dangerous business line where occupational diseases and occupational accidents occur. In this study, occupational hygiene measurements were made in a limestone quarry located in Sakarya region, physical and chemical risk factors that the working personnel are exposed to were investigated and evaluations were made in terms of occupational health and safety.

Keywords: *Dust, Illuminance, Limestone quarry, Physical and Chemical Factors, Noise, Vibration, Thermal Comfort*

1. INTRODUCTION

Working life contains different risk factors in itself. Many employees either die or become permanently disabled due to these risk factors. It is of great importance to evaluate these risk factors and to take the necessary precautions in workplace environment. When risk assessment is performed in workplaces, the physical and chemical risk factors in the working environment should also be taken into consideration. Evaluations should be made by performing ambient and personal exposure measurements to lay down the physical and chemical risk factors existence. The limit values determined by the legislation should be taken into consideration while evaluating the occupational hygiene measurements in the workplace. Necessary precautions must be taken to keep the measurement values in the working environment under the limit values determined in the legislation. Mining sector is one of the most dangerous business lines that occupational diseases and work accidents occur as a result of exposure to the physical and chemical risk factors. Therefore, ambient

measurements should be performed in terms of occupational health and safety and necessary measures must be taken due to the obtained results.

In a study relevant to the subject, Albayrak [1] carried out occupational safety ambient measurements at the Greton marble facility. In the selected facility, a risk assessment was performed by using the indoor measurement results obtained from measurements of noise, lighting, thermal comfort and dust. In the study onducted by Okşar [2], existing detrimental factors in a travertine quarry and factory were investigated. As a result of the measurements, values of environmental factors such as dust, noise, illuminance and thermal comfort were evaluated and suggestions were made to ensure that they do not affect the health of the employees. In the study carried out by Dolmaz [3], measurements of physical risk factors such as lighting, thermal comfort, noise, dust and vibration were performed in an exporter marble cutting and polishing facility and the results were interpreted by using L matrix and Fine Kinney risk analysis methods. In the study, it was determined that, luminous intensity was very low at night shift, there was a relative unfavourableness in the hot-cold balance of thermal comfort conditions, short-term noise values were far above near the ST machine, formation of dust was very low and forklift operator was exposed to very high vibration. In their study, Onder et al. [4] carried out measurements to determine the temperature and humidity increase in a fully mechanized underground mine in Türkiye and calculated the temperature and humidity changes in the mine air. In the study, they also analyzed the acceptability of climatic conditions according to EN ISO 7243:2017 by comparing them with the limit values given in the literature. Erol et al. [5] measured noise levels of some machines that operated in a mechanized underground mine. The lowest, highest, avarage and equivalent noise levels of machines and noise levels that the employees can be exposed to were calculated. The results obtained were evaluated pursuant to the noise regulation. In the assessment, it was determined that noise levels were over the exposure limit value (87 dBA) for the pneumatic perforator, over the exposure action value (85 dBA) for the shearer-loader, and between the lowest and the highest exposure action values (80-85 dBA) or under the lowest exposure action value (80 dBA) for other excavation and transportation vehicles. In another study, Doğan et al. [6] performed whole body vibration exposure measurements of drivers and operators working in various mining enterprises operating within the borders of Sivas province. The results obtained were evaluated pursuant to the national and international standards. In their study, Onder et al. [7] collected noise mesurement samples from three mining fields, including launder, opencast and underground mines between 2004 and 2007 in order to evaluate the equivalent noise levels from mining enterprises. The data obtained from measurement studies were evaluated by using one-way analysis of variance and Tukey's multiple comparison method. In another study by Erdem et al. [8], hand-arm vibration exposure measurements were performed for employees that work in various mining enterprises and evaluations were made pursuant to relevant regulations. The highest vibration value, equivalent vibration acceleration, total exposure score, hourly exposure score, vibration acceleration frequency, access time for exposure action value and access time for exposure limit value were calculated. In the study carried out by Şensöğüt [9], noise sources and levels encountered in mines, effects of noise on employees and suggestions to reduce these effects were given. A mine example in Türkiye was given in the study. In the study by Erol et al. [5], noise and vibration values that machine operators exposed to in an underground mine were measured and the results were evaluated within the scope of regulation. In the study, it was determined that the results were under limit values designated by regulation for all of the operators who use ear protectors. It was also determined that pneumatic

perforator operator was exposed to the highest noise and hand-arm vibration values. In the study, vibration values of machines were also measured as well as vibration exposure of operators. It was emphasized that the diversity of vibration values between crawler Jumbo and rubber wheeled Jumbo were changed due to the road roughness, engine vibrations and machine movements. In their study, Onder et al. [10] investigated dust related occupational diseases in open-pit lignite mine. Primarly, dust measurements were carried out and subsequently employees were gone through physical examinations. The data set obtained was categorized by considering the occupation, age, experience and dust exposure level of the employees. A hierarchical loglinear model was established to investigate the factors in the occurence of diseases while logistic regression analysis was performed to determine the possibility of worker exposure to dust. According to the logistic regression analysis, it was determined that the most risky occupation group was operators, followed by drivers, field personnel and technical personnel. It has been found that the probability of operators to get dust related occpuational diseases is approximately 2 times more than other occupation groups.

In this study, occupational hygiene measurements were performed in a limestone quarry located in Sakarya region, risk factors that employees were exposed to such as illuminance, thermal comfort, noise, dust and vibration were investigated and evaluations were carried out in terms of occupational health and safety.

2. WORK SITE

The work site located around Karakaya village in Pamukova district of Sakarya province. Site location map is given in Figure 1. The limestone quarry works in one shift and produces 2200 tons per day [11].

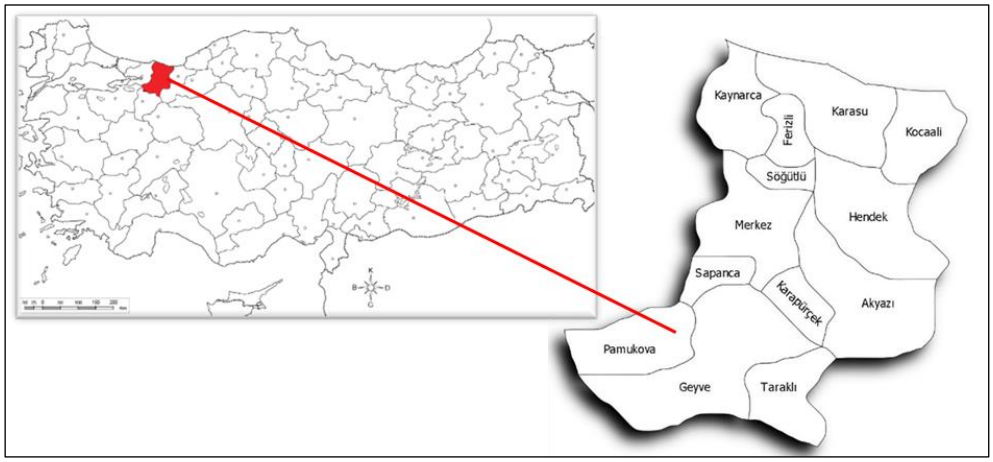

Figure 1. Site location map.

JSR A
Journal of Scientific Reports

3. MEASUREMENT PARAMETERS

3.1. Illuminance

Illuminance is the application of light to provide a clear visual perception of objects in an environment at intended standards. Depending on type of the work and size of the area that will be illuminated; one of the contrivances such as general lighting, local lighting with support of general lighting or only local lighting is used [1]. General lighting is the illuminance that needed to meet the demands between specific criteria in a whole volume. In addition to general lighting, significant emphasis, orientation or other luminous intensity may be needed. Lighting the local regions in these required sections is called local lighting. Local lighting is sometimes used to create the required luminous intensity in places where general lighting is not sufficient. Local lighting can sometimes be used to emphasize any object or to give an aesthetic appearance. Solutions should be generated to meet all expected requirements and settlement and usage area of objects should be specified uniformly to offer the most proper lighting solution in a volume. In order to offer the most suitable lighting solution in a volume, the layout and usage areas of the objects should be well determined and solutions should be produced to meet all the needs expected from them. With the purpose of meeting general requirements, local lighting should definitely be taken into consideration with general lighting [12]. While creating the most proper working environment in terms of illuminance, daylight should be utilized as much as possible. In cases where daylight is not sufficiently utilized, an artificial lighting system should be established. The use of daylight and artificial lighting systems together and in a balanced way is the most appropriate solution in terms of applicability [13]. Luminous intensity and its distribution in the space have a great impact on the employee's ability to perceive and perform a visual task quickly, safely and comfortably. As the lighting intensity increases, the finer details of the work are noticed. Studies have shown that high lighting intensity increases concentration and motivation, and as a result, employee performance increases. Since the level of making mistakes of the employee will decrease, there is a decrease in the work accidents caused by lighting in businesses with high lighting intensity. Workplaces should be adequately illuminated by daylight. If the daylight cannot be used adequately or in night works, appropriate and sufficient lighting is provided with artificial light. TS EN 12464-1: 2013 and TS EN 12464-1.2011: 2012 standards are taken as basis in the illumination of workplaces. Lighting systems in workplaces and passageways should be positioned in such a way that they do not pose a risk of accident. In case of failure of the lighting systems, an emergency lighting system, which is connected to a separate energy source, should be installed to provide sufficient lighting in places where there is a risk of accident [14]. Some values are recommended for the lighting of the workplaces in order to provide a suitable lighting that will not cause eyestrain, create dangerous situations and not disturb the employees. These values are; 80-170 lux for rough works, 130-350 lux for medium fine works, 350-700 lux for fine works and 700-1000 lux for very fine works [1]. It is known that artificial light is at an intensity of 200-300 lux in home environments, and 500 lux in well-lit workplaces. Required luminous intensity values in some areas and works in workplaces; corridor and storage areas are 100 lux, office work is 500 lux, surface preparation and painting is 750 lux, assembly, quality control and color control are 1000 lux [15]. The intensity of light emitted by daylight varies between 50000-100000 lux [16].

3.2. Thermal Comfort

Thermal comfort refers to the fact that most of the employees continue their physical and mental activities comfortably in their working environment in terms of certain climatic conditions such as temperature, humidity and air flow velocity. If the thermal comfort conditions are insufficient in the working environment, some problems and discomfort begin to be felt. As a result, there is a decrease in work efficiency [17]. Creating a suitable working environment is possible by considering factors such as light, hygiene, temperature, cleanliness, humidity, sound and vibration. Especially in winter and summer, works such as construction, machine assembly, piping, welding, which are done outside and often need to be completed in a limited time, bring important occupational health and safety risks [18]. Some measures that can be taken in the workplace can bring thermal comfort conditions to a better level. Since the ambient conditions of each business may be different, the measures to be taken will also be different. There are four factors that affect thermal comfort. These; temperature, humidity, velocity of air flow and thermal radiation. An increase or decrease in air temperature negatively affects the harmony of employees with their work. There is a high temperature problem in the industry in general. Excessive heat in the person causes fatigue and drowsiness. The human body keeps the central nervous system and internal organs at a constant temperature depending on the ambient temperature. The human body provides the necessary heat balance with the constant heat exchange with the external environment. The body temperature, which is usually 36,5 °C, is kept in balance by burning nutrients with oxygen in cold weather, and by sweating in hot weather. However, maintaining the body's heat balance in this way is limited [19]. It is essential that the thermal comfort conditions in the workplaces do not disturb the employees and do not adversely affect the physical and psychological conditions of the employees. It is ensured that the temperature of the working environment is suitable for the working style and the power consumed by the employees. Resting, waiting, changing rooms, showers and toilets, dining halls, canteens and first aid rooms are kept at a sufficient temperature according to their intended use. Vehicles used for heating and cooling are placed in such a way that they do not disturb the employee and do not pose a risk of accident, their maintenance and controls are carried out. TS EN ISO 7243 and TS EN ISO 7730 standards can be used to measure and evaluate thermal comfort conditions in workplaces. In case of continuous work in very hot or very cold environments and if this situation cannot be changed, measures should be taken to protect the employees from hot and cold [14]. The basic components of thermal comfort can be expressed as personal, environmental and external factors. While personal factors are expressed as metabolism level and thermal resistance of clothing, external factors can be expressed as nutritional status, age, gender, body shape and health of the employee. Environmental factors are air velocity, air temperature, relative humidity and mean radiant temperature [20].

According to the standards (TS EN ISO 7243 and TS EN ISO 7730), which will be taken as an example in determining and measuring thermal comfort, dissatisfaction is evaluated in two stages. One of these stages is PMV (Predicted Mean Vote) and PPD (Predicted Percentage of Dissatisfied) values obtained as a percentage to the determined PMV value correspond to the dissatisfaction values. In working environments where the temperature is high, the WBGT (Wet Bulb Globe Temperature) index specified in the TS EN ISO 7243 standard is calculated. The standard ISO 7243 provides limit values for the thermal environment according to WBGT, and limit values are determined based on metabolic rates for persons acclimatized and unacclimatized to heat [4]. The WBGT value is calculated by a measurement method that includes air temperature, humidity, air velocity and radiant

temperature values [21]. WBGT as the evaluation criterion of the thermal environment; It is an environmental thermal stress index associated with three different temperature indices. The WBGT index combines dry bulb temperature, wet bulb temperature under natural ventilation condition and black globe temperature [22]. The 3 sensors of the thermal comfort device are the nature wet-bulb temperature sensor (Tnw), the globe temperature sensor (Tg) and the dry air temperature (Ta) (dry-bulb temperature) sensor. These temperature values are used to determine the degree of heat stress that the person is exposed to in the working environment, to prevent heat damage and to determine how to reduce heat stress [21].

3.3. Noise

Noise is briefly defined as unwanted sound that undesirable and has a negative impact on people. Noise is a sound spectrum with an arbitrary structure [23]. This definition considers noise more as an event that reduces the feeling of comfort. However, the definition in occupational health is different. In the convention decision on noise and vibration published by the ILO in 1977 (no:148); There is a definition as "the term noise covers all sound which can result in hearing impairment or be harmful to health or otherwise dangerous"[24]. In other words, noise is an important environmental pollution consisting of unwanted sounds, which negatively affects people's hearing health and sense, disrupts their physiological and psychological balance and reduces work efficiency [25]. Noise is an environmental pollutant consisting of undesirable sounds with a random sloppy spectrum, which disrupts the hearing health of the workers and negatively affects the hearing sense, disrupts the balance of the organism physically and psychologically, causes reductions in working performance, changes the good characteristics of the environment by reducing or destroying the pleasantness and calmness [11]. Noise is an environmental pollution that negatively affects the hearing health of employees, disrupts the physiological and psychological balance of the person and reduces work efficiency [5]. Hearing loss is examined in two ways as temporary and permanent. Temporary hearing loss is the most common condition in the literature. Temporary loss of hearing sensitivity is defined as temporary threshold shift or listening fatigue. In cases where the level of exposure is high and the hearing system reaches its old features, it is mentioned that hearing loss becomes permanent if it is affected by noise again. Physiological effects of noise include stress, increase in blood pressure, changes in heart rate, circulatory disorders, acceleration of respiration, dilation of pupils, and tensions in the muscles. Psychological effects such as nervous breakdown, fear, discomfort, uneasiness, and fatigue are also observed [26]. In addition to reducing the working efficiency of the person, high noise levels also have effects such as inability to understand the sounds heard [5]. The regulation on the protection of employees from noise-related risks within the scope of Occupational Health and Safety No 6331 states the minimum requirements to be taken in order to protect employees from health and safety risks, especially hearing-related risks, that may occur as a result of exposure to noise. In this regulation, daily exposure level ($L_{EX,\ 8\ hours}$) [dB(A) re. 20 µPa] refers to the time-weighted average of all A-weighted noise exposure levels for an eight-hour working day, including the highest sound pressure and instantaneous pulsed noise, as defined in the TS 2607 ISO 1999 standard. The weekly noise exposure level ($L_{EX,\ 8\ hours}$) represents the time-weighted average of A-weighted daily noise exposure levels for a week consisting of five eight-hour working days, as defined in the TS 2607 ISO 1999 standard. In this regulation, the lowest exposure action value is ($L_{ex,8\ hours}$) is 80 dB(A), the highest exposure action value ($L_{ex,8\ hours}$) is 85 dB(A) and the exposure limit value is ($L_{ex,8\ hours}$) is 87 dB(A) [27]. According to the regulation, the effect of ear protectors is not taken into account in the

exposure action values. If the risks that may arise from exposure to noise cannot be prevented with the necessary precautions, the employer must keep the ear protection equipment ready for the use of the employees when the minimum exposure action values are exceeded. When the highest exposure action values are reached or exceeded, the employer ensures that the ear protection equipment is used by the employees and monitors this situation. The employer makes every effort to ensure the use of hearing protection equipment and checks the effectiveness of the personal protection measures taken in accordance with the regulation. The exposure of the employee cannot exceed the limit values in any way. In case the exposure limit values are exceeded despite taking all control measures as per the regulation, the employer immediately takes all necessary measures to reduce the exposure below the limit values. The employer determines the reasons for exceeding the limit values and reviews and rearranges the measures taken to prevent its recurrence.

3.4. Dust

Dust is a term used for solid particles of various sizes and is always in a mixture with air or another gas. Dust is formed by the separation of substances into small particles as a result of mechanical processes. These processes lead to the formation of dust in different sizes, from small particles that can hardly be seen even with a microscope, to large ones that can be seen with the naked eye. Dust is generally smaller than 1 mm in diameter, suspended in the air or precipitated over time [28]. The grain sizes of dust particles are generally below 300 µm. The size of the dust particles with low specific gravity can be up to 1 mm. The particle size of respirable dust is below 60 µm. Dusts that reach the alveoli through respiration and cause lung dust diseases called pneumoconiosis are called "fine dust". These dust particles are between 0,5-5,0 µm [29]. The smallest dust particles visible to the human eye are about 50 µm [30]. Therefore, harmful dust suspended in the air cannot be visually detected. About 80% (by mass) of respirable dust in mine air is smaller than 1 µm and only 4% is greater than 4 µm. This ratio is almost the same for dust in the lungs of patients who died of pneumoconiosis [30]. The degree of damage suffered by those working in a dusty environment varies depending on the duration of work in the dusty environment, the composition of the dust, the amount of dust, the distribution of the dust particle size and the personal sensitivity to the dust [28]. The particle size distribution of the dust is an important factor. However, dust smaller than a certain size causes various dust diseases. Dust particles larger than 5 µm is captured by the respiratory organs and expelled over time. For this reason, the size of the dust that can penetrate the alveoli the most is important. The sizes known as respirable dust are between 0,2-0,5 µm, but in practice, dust particles below 5 µm are considered harmful [28]. Dust has an important place in the industry and mining sector in terms of occupational health and safety today. While dusty air harms the health of the workers, on the other hand, it decreases the work efficiency, increases the cost and affects the economy. In addition, powders that cause pneumoconiosis cause chronic lung tissue damage and respiratory function losses [31]. Occupational branches and workplaces where dust is most common are drilling, blasting, grinding, crushing works, mines, tunnel and road construction works, porcelain, brick, tile manufacturing, cement, marble and welding works, iron and steel, sandblasting, transportation and storage. The amount of dust allowed is determined in a way that does not harm the health of the worker in case of working 8 hours a day, 40 hours a week. These values are known as threshold limit value (TLV), maximum allowed concentration (MAK), or time-weighted average (TWA). According to the dust control regulation, the employer ensures that dust measurements are made at periodic intervals determined as a result of the risk assessment [32]. The measurement results should be evaluated by

JSR A
Journal of Scientific Reports

taking into account the occupational exposure limit values given in the regulation. Necessary studies should be carried out to reduce the dust density below the limit values by methods such as preventing dust formation in dusty workplaces, eliminating dust at the source without dispersing into the working environment or suppressing dust. Total dust is powders that affects the entire respiratory system, including respirable dust, 50% of which has an aerodynamic diameter below 80-100 microns. Respirable dust, on the other hand, is defined as amorphous or crystalline dust with an aerodynamic diameter of 0,1 to 5,0 microns, and fibrous dust with a diameter of less than 3 microns and a length of at least 3 times its diameter. The devices used in dust measurement work on two principles: gravimetric and particle counting. In the gravimetric method, the total dust in a certain amount of air is separated, weighed and calculated in mg/m^3. In order to prevent errors that may occur due to the coarse grain effect, particles smaller than 5 microns are initially separated and weighed. Another method is the particle counting method. In this method, the dust collected on a glass plate is separated and those smaller than 5 microns are counted. The result is calculated in $particle/cm^3$.

3.5. Vibration

The oscillating motion of an object under the influence of internal or external forces is defined as vibration. When touching a vibrating surface or object, the person feels this vibration. Vibration is transferred to the human body through the contacting vibrating surface. There are two types of exposure: hand-arm vibration from hand-held tools with a handle and whole-body vibration transmitted from the seat or surface on a motorized machine [33]. Exposure to whole-body vibration usually occurs when a person is in contact with a vibrating surface. Whole-body vibration is mechanical vibration that, when transmitted to the entire body, poses a risk to the health and safety of the worker, causing discomfort, particularly in the lumbar region, and trauma to the spine. Hand-arm vibration is mechanical vibration that, when transferred to the hand-arm system of the person, poses a risk to the health and safety of the worker, and especially causes vascular, bone, joint, nerve and muscle disorders [34]. Vibration is described by its magnitude and frequency. The vibration magnitude is expressed in terms of vibration displacement (m), vibration velocity (m/s) or vibration acceleration (m/s^2) [35]. The magnitude of the vibration, the average value of the acceleration of the motion, is usually given as the square root of the sum of the squares of the frequency-weighted acceleration values (RMS) [32]. A frequency-weighted RMS average acceleration is measured from each vibration axis. This is expressed as a_{hw}. The value used to evaluate the exposure is the total vibration value combining the a_{hw} values in the X, Y and Z axes [35]. Calculation of a_{hw} value is given in Eq. 1.

$$a_{hw} = \sqrt{a_{hwa}^2 + a_{hwy}^2 + a_{hwz}^2} \quad (1)$$

Evaluation of the exposure level in hand-arm vibration is based on the calculation of the daily exposure value A(8) normalized to an eight-hour reference period, expressed as the square root of the sum of the squares of the frequency-weighted acceleration values (RMS) (total value) and it is made according to the standards and the most up to date versions of these standards which are TS EN ISO 5349-1 "Mechanical Vibration – Measurement and Evaluation of Hand-Transmitted Vibration Exposure of Persons-Part 1: General Rules" and TS EN ISO 5349-2 "Mechanical Vibration – Measurement and Evaluation of Hand-To-Body Vibration Exposure of Persons – Part 2: Practical

JSR A
Journal of Scientific Reports

Guide for Measuring in the Workplaces" [34]. Exposure action and limit values for vibration are given in the Regulation on the Protection of Employees from Risks Related to Vibration. The daily exposure limit value for hand-arm vibration is 5 m/s^2 and the exposure action value is 2,5 m/s^2 for an 8-hour working period. Evaluation of the exposure level in whole body vibration, calculated as the highest (RMS) value defined in terms of continuous acceleration equivalent in an eight-hour period A(8) based on the calculation of the daily exposure value and it is made according to the standards and the most up to date versions of these standards which are TS EN 1032+A1:2011 "Mechanical Vibration – Testing of Moving Machines for the Determination of Vibration Emission Value" and TS ISO 2631-1 "Mechanical Vibration and Shock-Whole Body Vibration Exposure Assessment – Part 1: General Guidelines". For whole body vibration, the daily exposure limit value for 8 hours of work is 1,15 m/s^2 and the exposure action value is 0,5 m/s^2. Vibration damage depends on various factors such as individual susceptibility, severity of vibration, frequency of exposure, duration (years), insulation level, grip strength, body part affected by the resource and maintenance of tools used [36]. Hand-arm vibration can cause narrowing of the vessels, decrease in blood flow, loss of vascular flexibility, as well as disorders in nerves, muscles, bones and joints. Findings such as tingling, numbness, pain and whitening in the hand and arm, cramps in the shoulder and loss of strength in the wrist are grouped under the name of "Hand-Arm Vibration Syndrome" [35]. Although the frequency range in hand-arm vibration varies between 5-1500 Hz, it usually occurs between 125-300 Hz. The effect of whole body vibration is greater at the end of the 0,5 Hz – 100 Hz range [6]. Vibration exposure is expressed as the average of the exposure measured in m/s^2 over a given period of time (usually 8 hours). Whole-body vibration is shaking or jolting of the human body through a supporting surface (usually a seat or the floor), for example when driving or riding on a vehicle along an unmade road, operating earth-moving machines or standing on a structure attached to a large, powerful, fixed machine which is impacting or vibrating [37]. Whole body vibration can cause discomfort especially in the lumbar region and trauma to the spine.

4. OCCUPATIONAL HYGIENE MEASUREMENTS

4.1.Illuminance

In the lighting measurements, care was taken not to create an angle that would affect the measurements of device in a different direction during the measurement. Lighting measurements were made with the Extech-SDL-400 model device at 5 points, including the dining hall, kitchen, storehouse, bureau and main control room. In Table 1, the places and ambient conditions where the lighting measurements were made are given. In Table 2, the lighting measurements for the dining hall, kitchen, storehouse, bureau and main control room are given.

Table 1. Lighting measurement parameters [11].

No	Measurement location	Ambient Conditions			
		Temperature (°C)	Humidity (%Rh)	Air flow velocity (m/s)	Air pressure (kPa)
A-01	Dining Hall	24,2	48,9	0,1	90,70
A-02	Kitchen	24,6	48,7	0,1	90,70

A-03	Storehouse	24,6	48,2	0,1	90,70
A-04	Bureau	24,3	48,1	0,1	90,70
A-05	Main Control Room	24.9	48.7	0.1	90.70

Table 2. Lighting measurements [11].

No	Measurement location	Measurement (Lux)	Result	Limit Value (Lux)	Assessment
A-01	Dining Hall	1009		200	Appropriate
A-02	Kitchen	304		500	Not Applicable
A-03	Storehouse	750		200	Appropriate
A-04	Bureau	2352		500	Appropriate
A-05	Main Control Room	3252		500	Appropriate

4.2. Thermal Comfort

The wet-bulb globe temperature change, called WBGT, which is one of the general principles related to thermal comfort measurements, is all of the experimental changes that show the heat stress on which the worker is affected. It is a method that allows an effective diagnosis and measuring the heat stress that the employee is affected by in hot environments. The WBGT index is based on the work of the employee between a certain period and is the effect of the heat generated on the employee during this work on an average employee. This index usually combines two combined parameter measures, nature wet-bulb temperature (tnw) and globe temperature (tg), and in some cases it combines air temperature (ta) (dry bulb temperature) which is a basic parameter measure. The metabolic rate can be approximated by measuring the oxygen consumed by the worker, or from reference tables. Due to the nature of the WBGT change, it will be sufficient to estimate the metabolic rate according to the reference table. Work/rest cycles for unacclimated and acclimated individuals are determined by estimating the reference values in the reference value chart of WBGT and WBGT heat stress index according to the specified standard. Reference values of WBGT are given in Table 3.

Table 3. Reference values of WBGT [22].

Metabolism level	Metabolism rate (M) (W·m-2)	Reference values of WBGT(°C)			
		Good heat acclimation		Bad heat acclimation	
0	M<117	33		32	
1	117<M<234	30		29	
2	234<M<360	28		26	
		Can't feel the air flow	Feel the air flow	Can't feel the air flow	Feel the air flow
3	360<M<468	25	26	22	23
4	M>468	23	25	18	20

In the thermal comfort measurements of the personnel working at the measurement point, metabolic rates and clothes of the employees were determined according to the work they did and included in the calculations. Thermal comfort measurements were made with a Delta ohm-HD 32.3 model device. Thermal comfort measurement locations, pre-measurement determinations and outdoor conditions are given in Table 4, and thermal comfort measurement results are given in Table 5.

Table 4. Thermal comfort measurement locations, pre-measurement determinations and outdoor conditions. [11].

No	Measurement location	Outdoor conditions				Pre-measurement determinations			
		Temp. (°C)	Humidity (%Rh)	Air flow velocity (m/s)	Air press. (kPa)	Clothes	Clo Value	Activity for Met. ratio	Met. Value
A-01	Dining Hall	24,5	48,7	0,1	90,70	Pants T shirt Shoe Sock	1	Standing Work	1,20

Table 5. Thermal comfort measurement results [11].

Measurement Point	Measurement Location	Parameters				WBGT	
		WBGT	T_g	T_{nw}	T_a	Reference Value Acclimated Person	Reference Value Unacclimated Person
TK-01/ Standing Work	Dining Hall	28,60	26,89	26,55	26,64	30 °C	29 °C

4.3. Noise

Noise measurements were carried out as workplace environment measurements and personal noise exposure. Care was taken not to make any noise that would affect the measurement during the measurement. The device was calibrated before each measurement. While Svantek-Svan971 model device was used for ambient noise measurements, Svantek SV104 model was used for personal exposure measurements. Information about ambient conditions in personal noise exposure and ambient noise measurements is given in Table 6. The measurement results of personal noise exposure are given in Table 7, and the results of ambient noise measurements are given in Table 8.

Measurements of personal noise exposure were carried out on 4 employees, including loader operator, truck driver, greaser and crusher operator, with an 8 hour exposure Svantek SV104 model noise dosimeter. Measurements related to personal noise exposure are given in Table 4.7.

JSR A
Journal of Scientific Reports

Ambient noise measurements were carried out at the main control room, dining hall and bureau. Measurements of ambient noise are given in Table 4.8. Ambient noise measurements were made taking into account some principles. If the residual noise level is lower than the measured sound pressure level in a value of 10 dB or more, no correction is made. The measured value is valid for the source under test. If the residual noise level is lower than the measured sound pressure level in a value of 3 dB or less, no correction is allowed. In this case, the measurement uncertainty is high. If the residual noise level is lower than the measured sound pressure level in a value between 3 to 10 dB, the corrected sound pressure level is used. The corrected sound pressure level can be calculated with the formula: $Lcorr = 10\,Log(10^{Lmeas/10}\text{-}10^{Lresid/10})$ In this formula, Lcorr indicates the corrected sound pressure level, L_{meas} indicates the measured sound pressure level, and L_{resid} indicates the residual noise level.

Table 6. Ambient conditions in ambient noise and personal noise exposure measurements [11].

No	Measurement Location/Person	Ambient Conditions			
		Temperature (°C)	Humidity (%Rh)	Air flow velocity (m/s)	Air pressure (kPa)
KG-01	Loader Operator	24,1	48,9	0,1	90,70
KG-02	Truck	24,9	48,7	0,1	90,70
KG-03	Greaser	24,5	48,2	0,1	90,70
KG-03	Crusher Operator	24,6	48,1	0,1	90,70
OG-01	Main Control Room (1.Measurement)	24,2	48,9	0,1	90,70
OG-02	Main Control Room (2.Measurement)	24,6	48,7	0,1	90,70
OG-03	Main Control Room (3.Measurement)	24,6	48,2	0,1	90,70
OG-04	Bureau (1. Measurement)	24,3	48,1	0,1	90,70
OG-05	Bureau (2. Measurement)	24,9	48,7	0,1	90,70
OG-06	Bureau (3. Measurement)	24,5	48,9	0,1	90,70
OG-07	Dining Hall (1. Measurement)	24,6	48,7	0,4	90,70
OG-07	Dining Hall (2. Measurement)	24,6	48,7	0,3	90,70
OG-08	Dining Hall (3. Measurement)	24,5	48,9	0,5	90,70

Table 7. Personal noise exposure measurements [11].

No	Measurement Location/Person	Measurement (dB(A)
		Lex,8h
KG-01	Loader Operator	77,2
KG-02	Truck	80,8
KG-03	Greaser	85
KG-04	Crusher Operator	74,6

JSR A
Journal of Scientific Reports

Table 8. Ambient noise measurement results [11].

Measurement No	Measurement Location	Measured(dB(A))				Corrected(dB(A))
		L_{min}	L_{max}	L_{meas}	L_{resid}	Lcorr
OG-01	Main Control Room 1. Measurement	61,8	106,8	86,8	65,7	86,5
OG-02	Main Control Room 2. Measurement	69,7	106,6	83,4	65,7	83,4
OG-03	Main Control Room 3. Measurement	55,4	101,2	86,2	65,7	86,2
OG-04	Bureau 1. Measurement	62,5	97,1	76,3	64,4	76,3
OG-05	Bureau 2. Measurement	61,8	79,2	71,5	64,4	70,5
OG-06	Bureau 3. Measurement	54,6	91,6	72,6	64,4	71,8
OG-07	Dining Hall 1. Measurement	54,9	81,0	65,6	61,6	63,3
OG-08	Dining Hall 2. Measurement	55,0	87,0	68,9	61,6	68,0
OG-09	Dining Hall 3. Measurement	54,5	96,5	68,1	61,6	66,9

4.4. Dust

A.P.Buck Lp-5 Libra Plus dust sampler was used to determine the dust and dust exposure in the working environment by gravimetric method. Total dust and respirable dust measurements are made differently. Respirable dust is based on dust particles smaller than 5 microns, while dust particles smaller than 80-100 microns in diameter are taken as the basis for total dust. Respirable dust can reach the alveoli and cause lung diseases called pneumoconiosis. Ambient conditions for dust measurements are given in Table 9.

In Table 10, occupational dust exposure limit values of some substances are given according to the Dust Control Regulation. In this regulation, in order to prevent the risks that may arise from dust in the workplaces, the procedures and principles are determined regarding the precautions to be taken in order to control dust in terms of occupational health and safety and to ensure that the workers in these works are protected from the effects of dust. In Table 11, the results of personal respirable dust concentration measurements made in the limestone quarry and the total measurement results are given.

Table 9. Ambient conditions in dust measurements [11].

No	Measurement location/person	Ambient conditions			
		Temperature (°C)	Humidity (%Rh)	Air flow velocity (m/s)	Air pressure (kPa)
KST-01	Loader Operator	24,2	48,9	0,1	90,70
KST-02	Truck	24,6	48,7	0,1	90,70
KST-03	Greaser	24,6	48,2	0,1	90,70

KST-04	Crusher Operator	24,3	48,1	0,1	90,70
FÖ-01	Crusher	24,9	48,7	0,1	90,70
FÖ-02	Filling Field / Stone Loading	24,5	48,9	0,1	90,70
FÖ-03	Dining Hall	24,6	48,7	0,4	90,70
FÖ-04	Compressor Room	24,6	48,7	0,3	90,70
FÖ-05	Control Room	24,5	48,9	0,5	90,70

Table 10. Occupational dust exposure limit values of some substances according to the Dust Control Regulation [32].

Material Name	**Total Dust Amount TWA/ZAODA (mg/m^3)**	**Respirable Dust Amount TWA/ZAOD (mg/m^3)**
Calcium Carbonate (Marble)	15	5
Calcium Carbonate (Limestone)	15	5
Calcium Hydroxide	15	5
Calcium Silicate	15	5
Calcium Sulphate	15	5
Magnesite	15	5

Table 11. Personal respirable dust concentration and total measurement results [11].

No	**Measurement Location/Person**	**Measurement Value (mg/m^3)**	**Limit Value (mg/m^3)**
KST-01	Loader Operator	0,258	5
KST-02	Truck	0,208	5
KST-03	Greaser	0,350	5
KST-04	Crusher Operator	0,567	5
FÖ-01	Crusher	0,958	15
FÖ-02	Filling Field / Stone Loading	2,833	15
FÖ-03	Dining Hall	1,333	15
FÖ-04	Compressor Room	2	15
FÖ-05	Control Room	1	15

4.5. Vibration

In the study, vibration measurements were made with Svantek SV38 and SVANTEK SVAN SV-106 Model devices. Hand-arm and whole body vibrations of the jaw crusher operator, truck driver and loader operator were measured. The ambient conditions of vibration measurements are given in Table 12. Hand-arm and whole body vibration values are given in Table 13.

Table 12. Ambient conditions of vibration measurements [11].

No	**Measurement**	**Ambient conditions**

	location/person	Temperature (°C)	Humidity (%Rh)	Air flow velocity (m/s)	Air pressure (kPa)
TT-01	Jaw Crusher Operator	24.5	48.9	0.1	90.70
TT-02	Truck Driver	24.6	48.7	0.3	90.70
TT-03	Loader Operator	24.5	48.9	0.5	90.70

Table 13. Hand-arm vibration and whole body vibration measurement results [11].

No	**Measurement**		**Measurement Results**				**Assessment**	
	Location/person	**Type****	a_{hwx} (m/s^2)	a_{hwy} (m/s^2)	a_{hwz} (m/s^2)	a_{hw} (8h)* (m/s^2)	Daily Exposure Limit Value (8h) (m/s^2)	Daily Exposure Action Value (8h) (m/s^2)
TT-01	Jaw Crusher Operator	HAV	0.205	0.249	0.198	0.384	5	2,5
TT-02	Truck Driver	HAV	0.001	0.001	0.001	0.006	5	2,5
TT-03	Loader Operator	HAV	0.0003	0.000261	0.000286	0.00049	5	2,5
TT-01	Jaw Crusher Operator	WBV	0.119	0.113	0.270	0.270	1,15	0,5
TT-02	Truck Driver	WBV	0.216	0.172	0.280	0.303	1,15	0,5
TT-03	Loader Operator	WBV	0.215	0.386	0.269	0.541	1,15	0,5

∗ Evaluated according to exposure times. ** Hand-Arm Vibration (HAV), Whole Body Vibration (WBV)

5. RESULTS and SUGGESTIONS

According to article 10 of the Occupational Health and Safety Law No. 6331, the employer is obliged to ensure that the necessary controls, measurements, examinations and researches are carried out in order to determine the risks which the employees are exposed to in terms of occupational health and safety. Noise, vibration, dust, insufficient or excessive lighting and thermal temperatures in the working environment can cause temporary health problems and occupational diseases in employees. In order to prevent these health problems and occupational diseases, the degree of physical and chemical risks in the working environment should be measured. Measures to be taken against these risks can be revealed more easily as a result of these measurements. According to the lighting measurement results in the facility where the study was conducted, considering the values specified in the regulations and standards, the value of lighting measurement made in the kitchen section was 304

lux. Considering that the limit value should be 500 lux, some precautions should be taken in the kitchen section. Local illuminators can be placed in the kitchen section. Instead of the few yellow bulbs in the kitchen, white bulbs close to daylight can be used. Light sources with uniform illumination can be used which have the same level of illumination throughout the work surface and at sufficient distance intervals. It is essential that thermal comfort conditions are in a way that does not disturb the employee in the working environment and does not adversely affect their physical and psychological conditions. The working environment should be suitable for the way of working and the effort spent by the employees. According to the thermal comfort measurement results made at the facility, there are no parts that do not meet the recommended values of 29°C. Only in the standing study in the kitchen, the value is 28,6°C. This is a factor due to both the temperature of the stove and the steam of the food. In this part, a more ideal temperature can be reached with a suitable ventilation. Based on the minimum exposure action value of ($L_{ex,8\ hours}$) 80 dB(A), the highest exposure action value of ($L_{ex,8\ hours}$) 85 dB(A) and the exposure limit value of ($L_{ex,8\ hours}$) 87 dB(A) specified in the regulation on the protection of workers from noise-related risks, ambient noise was measured as 86,5 and 86,2 dB(A) in the measurements made in the crusher main control section. The highest exposure action value of 85 dB(A) was exceeded. Covering the crusher with materials that will provide sound insulation in the crusher plant will reduce the noise rate. For personnel working in the main control room, exposure can be prevented by covering around of the control room with sound insulation material and also by ensuring that the personnel use earplugs. The dust measurement results were evaluated according to the limit values specified in the Dust Control Regulation, which was published in the Official Gazette of the Republic of Türkiye dated 05.11.2013 and numbered 28812. According to the measurement results of Respirable and Total Dust Exposure of Persons at the facility, the limit values specified in the regulation were not exceeded. The hand-arm and whole body vibration measurement results were evaluated according to the Regulation on the Protection of Employees from Risks Related to Vibration. In this regulation, the exposure limit value for hand-arm vibration is 5m/s² for 8 hours of operation and the exposure action value is 2,5m/s². In the same regulation, for whole body vibration, the exposure limit value is given as 1,15 m/s² during the 8-hour working period and the daily exposure action value is 0,5 m/s². Considering the vibration acceleration parameter (A(8)) in the measurements made, the 8-hour whole body vibration value of the loader operator is 0,541 m/s². In 8 hours of operation, the daily exposure action value of 0,5 m/s² for whole body vibration was exceeded. In order to minimize the vibration exposure of the operators and increase the working efficiency, vehicle driving training should be given, periodic maintenance of the vehicles should be done and the vibration caused by the work machine should be reduced.

ACKNOWLEDGMENT

This paper is based on the data from the master thesis named “Assessment of work hygiene measurements in terms of employees in a limestone quarry.

REFERENCES

[1] Albayrak O. (2014). Greton Mermer Tesisinde İş Güvenliği Ortam Ölçümlerinin Risk Değerlendirmesi. Süleyman Demirel Üniversitesi, Fen Bilimleri Enstitüsü, Maden Mühendisliği Anabilim dalı Yüksek Lisans Tezi.

[2] Okşar, A. (2018). Örnek Bir Traverten İşletmesinde İş Sağlığı ve Güvenliği Açısından Ergonomik Şartların İncelenmesi. Afyon Kocatepe Üniversitesi, Fen Bilimleri Enstitüsü Yüksek Lisans Tezi.

[3] Dolmaz, O. (2018). Psychrometric Analysis of a Fully MeWchanized Underground Coal Mine and Establishment of Acceptable Climate Conditions. Journal of Mining Science, Vol.57, No.5, ISSN 1062-7391.

[4] Onder, M., Kursunoglu, N. ve Onder, S. (2021). Psychrometric Analysis of a Fully Mechanized Underground Coal Mine and Establishment of Acceptable Climate Conditions. Journal of Mining Science, Vol.57, No.5, ISSN 1062-7391.

[5] Erol, İ. ve Su, O. (2015). Mekanize Bir Yeraltı Maden İşletmesinde Gürültü Seviyelerinin İncelenmesi. Çukurova Üniversitesi Mühendislik Mimarlık Fakültesi Dergisi, 30(2), s191-200.

[6] Doğan, T., Erdem, B. ve Duran, Z. (2015). Tüm Vücut Titreşiminin Operatör ve Sürücüler Üzerindeki Etkileri: Ölçümü ve Değerlendirilmesi. Madencilik, Cilt 54, Sayı 3-4, s25-39.

[7] Onder, S. ve Onder M. (2017). Statistical Investigation of The Noise Levels in Coal Mining Industry. The Journal of Engineering and Architecture Faculty of Eskisehir Osmangazi University 26 (1), 30-35.

[8] Erdem, B., Doğan, T., Duran, Z. ve Özgen, Z. (2016). Maden İşyerlerinde Kullanılan Bazı İş Araçlarından Kaynaklanan El-Kol Titreşim Maruziyetinin Ölçümü ve Değerlendirilmesi. Madencilik, Cilt 55, Sayı 2, s23-44.

[9] Sensogut, C. (2007). Occupational Noise in Mines and Its Control – A Case Study. Polish J. of Environ. Stud. Vol. 16, No. 6, s939-942.

[10] Onder, M., Iroz, B.D. ve Onder, S. (2021). Using categorical data analyses in determination of dust-related occupational diseases in mining. International Journal of Occupational Safety and Ergonomics (JOSE),Vol. 27, No. 1, 112–120.

[11] Uyar, O. (2019). Bir Kalker Ocağında İş Hijyen Ölçümlerinin Çalışanlar Açısından Değerlendirilmesi. Kütahya Dumlupınar Üniversitesi, Fen Bilimleri Enstitüsü, Maden Mühendisliği Anabilimdalı, Yüksek Lisans Tezi. s2-57.

[12] Camkurt, M. Z. (2007). İşyeri Çalışma Sistemi ve İşyeri Fiziksel Faktörlerinin İş Kazaları Üzerindeki Etkisi. TÜHİS İş Hukuku ve İktisat Dergisi, 20(6), 21(1), s93-96.

[13] Aydın F. (Ed.). (2014). İş Sağlığı ve Güvenliği Uygulamaları Rehberi. Çalışma ve Sosyal Güvenlik Bakanlığı, Yayın No: 09, s.17, Ankara.

[14] İşyeri Bina ve Eklentilerinde Alınacak Sağlık ve Güvenlik Önlemlerine İlişkin Yönetmelik. (2013). Resmî Gazete Tarihi: 17.07.2013. Resmî Gazete Sayısı: 28710.

[15] Çınar, İ. ve Şensöğüt, C. (2017). Yeraltı Maden Ocaklarında Aydınlatma Koşullarının Belirlenmesi. Çukurova Üniversitesi Mühendislik Mimarlık Fakültesi Dergisi, 32 (2), ss 77-83. Haziran 2017.

[16] Demir, Z. (2018). İş Sağlığı ve Güvenliği Aydınlatma Yönetmeliği Bakımından Eğitim-Öğretim Kurumlarındaki Gece Öğretiminin Bir Durum Çalışmasıyla Değerlendirilmesi. Mersin Üni. Fen Bilimleri Ens., İş Sağlığı ve Güvenliği Anabilimdalı, Yüksek Lisans Tezi, s16.

[17] Phesant, S. (1991). Ergonomics. Work and Health. Mac Millian Press, s.27-35, Australia.

[18] Akkaya, C. (2001). Maden Sektöründe Risk Faktörleri. Türk Tabipleri Birliği Mesleki Sağlık ve Güvenlik Dergisi, 1(5):38-41.

[19] Akal, Z. (1991). İş etüdü, M.P.M. Yayınları, Yayın No: 29, 4.Basım, s.67, Ankara.

[20] Arıtan,A.E., Şensöğüt, C. ve Tümer, M. (2017). Doğaltaş İşleme Tesisinde Termal Konfor Analizi. MCBÜ Soma Meslek Yüksekokulu Teknik Bilimler Dergisi, Sayı:23, Cilt:I.

[21] Öz, İ.O., Korcan, S.E. ve Bulduk, İ. (2018). Tekstil Sektöründe Termal Konfor Ölçümleri ve Alınacak Önlemlerin Değerlendirilmesi. Uşak Üniversitesi Fen ve Doğa Bilimleri Dergisi, s21-34.

[22] Linhua Z., Linfang Z., Ming J. and Jiying L. (2017). Numerical Study of Outdoor Thermal Environment in a University Campus in Summer. 10th International Symposium on Heating, Ventilation and Air Conditioning, ISHVAC2017, pp 4052, 19- 22 October, Jinan, China

[23] Çetin, O. (2000). OAL'de Gürültüye Bağlı İşitme Kayıplarının İncelenmesi. Bilimsel Madencilik Dergisi, 39 (4), s39-45.

[24] International Labour Office. (1997). Report Form for the working environment (Air Pollution, Noise and Vibration), No:148, Geneva.

[25] Ediz, İ.G., Beyhan, S., Akçakoca, H. ve Sarı E. (2002). Madencilikte Gürültüye Bağlı İşitme Kayıplarının İncelenmesi. Türkiye 13. Kömür Kongresi Bildiriler Kitabı, 29-31 Mayıs, Zonguldak, Türkiye.

[26] Şensöğüt, C. ve Eralp, H. (1998). Ömerler Yeraltı Ocağındaki Gürültü Ölçümleri ve Öneriler, Türkiye 11. Madencilik Kongresi Bildiriler Kitabı, s43-51, Bartın.

[27] Çalışanların Gürültü ile İlgili Risklerden Korunmalarına Dair Yönetmelik. (2013). Resmî Gazete Tarihi: 28.07.2013. Resmî Gazete Sayısı: 28721.

[28] Güyagüler, T. ve Durucan Ş. (1985). Ocak Tozları, Yeraltı Kömür Madenciliğinde Çevre Sorunları ve Kontrol Yöntemleri. Seminer El Kitabı, s55-58.

[29] Baysal, F. (1979). "İşyerlerinde Toz Sorunu, Türkiye Madencilik Bilimsel Teknik 6.Kongresi, s85-88.

[30] Cronje G.P., Vuuren, P.J.J. and Rawlins C.A. (1997). Respirable dust in the take airways of a coal mine. Journal of the Mine Ventilation Society of South Africa , January, p11-14.

[31] Ediz, İ. G., Yuvka, Ş., Beyhan, S. ve Çolpan, R. (2001). GLİ Tunçbilek-Ömerler Bölgesinde Mekanize Üretimde Toz Sorunu. Türkiye 17 Uluslararası Madencilik Kongresi ve Sergisi, s169-174.

[32] Tozla Mücadele Yönetmeliği. (2013). Resmî Gazete Tarihi: 05.11.2013. Resmî Gazete Sayısı: 28812.

[33] Zeyrek, S. (2009). Titreşim. İş Sağlığı ve Güvenliği Uzmanlık Tezi, Çalışma ve Sosyal Güvenlik Bakanlığı Genel Müdürlüğü, Ankara.

[34] Çalışanların Titreşimle İlgili Risklerden Korunmalarına Dair Yönetmelik. (2013). Resmî Gazete Tarihi: 22.08.2013. Resmî Gazete Sayısı: 28743

[35] Erdem, B., Dogan, T., Duran Z. ve Ozgen, Z. (2016). Maden İşyerlerinde Kullanılan bazı iş araçlarından kaynaklanan El-Kol Titreşim Maruziyetinin Ölçümü ve Değerlendirlmesi. Madencilik Dergisi, Cilt 55, Sayı 2, s23-44.

[36] Boğa, B. (2014). Açık Ocak Yöntemi İle Çalışılan Bir Madende Ergonomik Risklerin Anket Yoluyla Değerlendirilmesi. İş Sağlığı ve Güvenliği Uzmanlık Tezi/Araştırma, Çalışma ve Sosyal Güvenlik Bakanlığı Genel Müdürlüğü, Ankara.

[37] Health and Safety Executive (HSE). (2005). Control the risks from whole-body vibration, Advice for employers on the Control of Vibration at Work.

Kütahya Dumlupınar University
Institute of Graduate Studies

Journal of Scientific
Reports-A
E-ISSN: 2687-6167
Number 51, December 2022

RESEARCH ARTICLE

DEVELOPMENT NEW MODEL for FORECASTING SOLAR RADIATION by USING RATIONAL APPROACH

Ayşe Gül KAPLAN[1*]

[*1]Osmaniye Korkut Ata University, Faculty of Arts and Sciences, Department of Mathematics, 80000, Osmaniye, aysegulkaplan@osmaniye.edu.tr, , ORCID: 0000-0002-3131-9079

Receive Date:30.10.2022 *Accepted Date: 24.11.2022*

ABSTRACT

In this study, solar energy potential of south region of Turkey was assessed statistically by using the Solar Energy Potential Map of Turkey data for one year. A new model was developed by using rational approach for global solar radiation (SR) estimation. Calculations was performed in Matlab program. To demonstrate the efficiency of new model the four different statistical indicators were used. The obtained results reveal that the new proposed model give very appropriate results for SR estimation for mentioned region.

Keywords: *Solar energy, Solar radiation, Rational approach, Statistical indicators.*

1. INTRODUCTION

The globalizing energy need and the updating of the world population cause the demand for new energy sources to increase continuously. The increase in the need for energy used in the world day by day proves that the energy used is not at a sufficient level. Fossil fuels used today, etc. With the increasing population and technological developments around the world, the need for energy is constantly increasing due to the use of many technological devices. In order to meet this increasing need for electrical energy, renewable energy sources should be used more effectively [1]. Both the use of other non-renewable energy sources and the increase in their costs at the point of production have led the world community to seek new sources that can provide more efficient energy. Renewable energy sources, on the other hand, have been seen as a solution point for this search and their use has increased day by day. It has been observed in the projects carried out today that renewable energy sources can produce high-efficiency energy thanks to the right system and engineering service. Solar energy, which is the most important of renewable energy sources, has started to appear in every aspect of our lives. When we look at fossil fuels and the progress of our world today, solar energy emerges as a solution option against the negative environmental conditions created by climate changes. Developed countries are constantly supporting this source in order for solar energy to potentially reach the most efficient production values. At this point, our country has shown how important this energy

JSR A
Journal of Scientific Reports

is to every individual of the society by providing the right investments and incentives. When the global solar radiation values are examined at the point of production of solar energy, our country has a very strong potential in this regard. Today, the need for energy is constantly increasing due to the increasing population and developing technology. All countries around the world have sought new energy sources in order to meet their energy needs. Due to the fact that fossil fuel resources are too limited to meet the need in the near future, as well as environmental problems in the form of greenhouse effect as a result of air pollution and acid rain, renewable energy sources are met with increasing interest all over the world and are seen as an important alternative in meeting energy needs. The amount of energy consumption is one of the most important parameters that show the technological and economic development level of countries [2]. Solar energy (SE), which is one of the renewable energy sources, is an important alternative to fossil fuels thanks to the rapidly developing technology as well as being a clean source in terms of environment. Many solar applications require accurate information on solar availability and sufficiency in operating areas. However, long-term SR intensity measurements can only be made in certain locations. For places where no measured meteorological data is available, a practical method is to develop forecast models using empirically accepted correlations using data measured at some selected location. By using these correlations, desired models from meteorological, seasonal and geographical parameters such as latitude, sunshine duration, temperature can be developed with different methods and approaches. These developed methods can be used successfully in SR intensity estimation [3, 4, 5]. The solar map of Turkey is shown in Figure 1. For this study, the city of Gaziantep was chosen. The chosen area was within the spectrum of favourable provinces in terms of SE potential because to its geographic proximity to Turkey's South Coast. The fact that the global radiation and sunshine duration are located above the Turkey average has potential utility. Figure 1 details the SE potential of the location chosen for this investigation. The selected region is a SE-efficient region, as can be seen from the detailed figure.

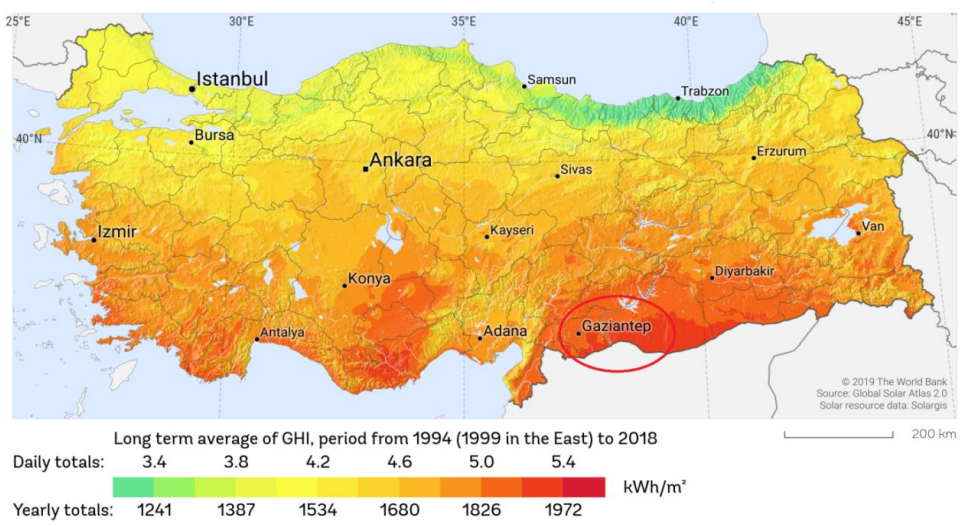

Figure 1. Solar map of Turkey (kW h/m^2 year) [6].

JSR A
Journal of Scientific Reports

In this study, new model was developed by using rational approach for estimating SR. The Matlab software was used to perform the calculations. They were looked at in various statistical tests to demonstrate the efficacy of the developed model. The obtained results shown that the developed model is effective and trustworthy. The average SR values of the region selected for this study and the average sunshine duration of the region are shown in Figure 2.

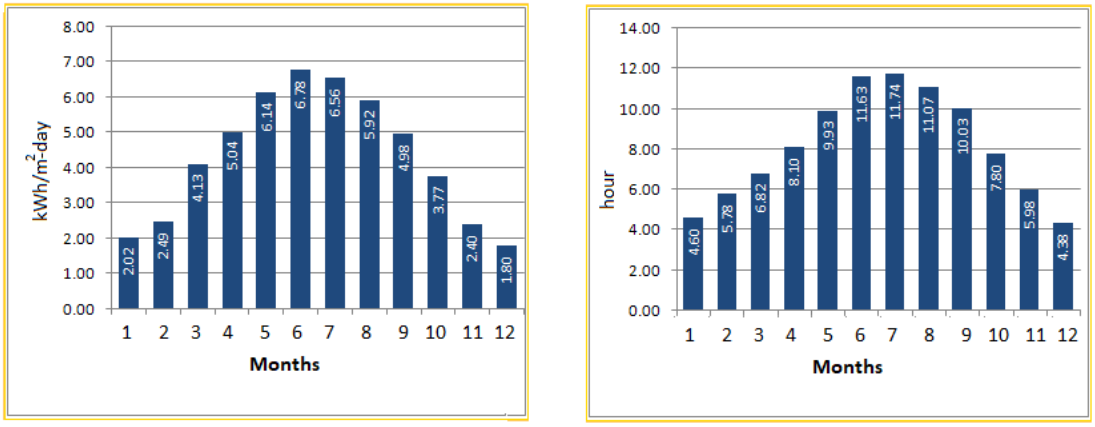

a-) b-)

Figure 2. SR and sunshine duration for selected region [6].

There are many studies in the literature on developing SR estimation models using different algorithms and approaches. Zang et al. [7] developed a total of 14 year-based diurnal models using data collected between 1994 and 2015 at 35 meteorological sites across six different climate areas of China to estimate the daily global SR. The comparison results demonstrated the new models' outstanding climatic adaptation and forecast accuracy. Husain and Khan [8] developed six machine learning models, including random forest, k-nearest neighbors, Gaussian process regression, support vector machine, multilayer detection, and XGBoost for GSR prediction using simply air temperature as input for several climate zones in India. The effectiveness of machine learning models was also contrasted using a few well-known experimental models. Feng et al. [9] compared different ML and empirical models for estimating global SR using only air temperature as input. The findings demonstrated that when compared to current ML and empirical models, the hybrid mind evolutionary algorithm and neural network model offered improved predictions. Almorox et al. [10] claimed that numerous values for the solar constant (SC) and total solar irradiance (TSI) had been provided and used in the literature. They stressed the crucial role that the TSI value has in engineering and academic studies of energy. They conducted a review to look at the ideas of TSE and SC in this study. . The impact of three distinct TSI values for various places was examined using the angstrom-prescott (a-p) equation to forecast global radiation over Spain.

JSR A
Journal of Scientific Reports

2. MATERIAL and METHOD

2.1. Rational Polynomials

In approximation theory, besides the problems in which linear parameters come into play, it is possible for the parameters to appear in a non-linear way. It is very difficult to develop a theory for such problems. General theories can be given under very limited conditions. These theories have certain features of polynomial approximations. Rational approaches are examples of these. Ratios of polynomials are what are known as "rational models," and they are given by [11]

$$y = \frac{\sum_{i=1}^{n+1} p_1 x^{n+1-i}}{x^m + \sum_{i=1}^{m} q_i x^{m-1}} \tag{1}$$

where n is the degree of the polynomial in the numerator and $0 \leq n \leq 5$, and m is the degree of the polynomial in the denominator and $1 \leq m \leq 5$. x^m 's coefficient is always 1. When the polynomial degrees are the same, the numerator and denominator are unique because of this.

The degree of the numerator and the degree of the denominator are used here to describe rationals. As an illustration, the rational equation given by

$$y = \frac{p_1 x^2 + p_2 x + p_3}{x^3 + q_1 x^2 + q_2 x + q_3} \tag{2}$$

Rationals are frequently employed when a straightforward empirical model is required, much like polynomials. Rationals' key benefit is its adaptability to data with complex structures. The biggest drawback is that when the denominator is close to zero, they become unstable.

2.2. Rational Models

In this section, the data set used in the article study explained and the method used is examined in detail. Insolation time is easily and reliably measured and data is widely available. With the correlation obtained based on these measured values, monthly average total daily solar radiation can be estimated. The sunshine time is measured easily and reliably and its data is widely available. Based on these measured values, the mean daily average daily SR can be estimated by the correlation obtained. Statistical models for estimating the monthly mean daily Diffuse SR are given based on measured sunshine duration, Global SR, and calculated pre-atmospheric SR. The most commonly used of these models is Angström-type equations. The equation of rational approach is expressed for $n = 1, m = 1$ and $n = 1, m = 2$ as follows, respectively [11, 12, 13]:

$$\frac{H}{H_0} = \frac{p_1 \frac{S}{S_0} + p_2}{\frac{S}{S_0} + q_1} \tag{3}$$

$$\frac{H}{H_0} = \frac{p_1 \frac{S}{S_0} + p_2}{\left(\frac{S}{S_0}\right)^2 + q_1 \frac{S}{S_0} + q_2} \tag{4}$$

JSR A
Journal of Scientific Reports

Here $p_i$and q_i, $i = 1,2$ values are constants calculated in Matlab program.

In this context, firstly, the radiation data used in the study is presented, and the details of extraterrestrial radiation and sunshine duration calculations are explained. The general formula of the model equations based on the sunshine duration is Eq. 5: the monthly average daily total solar radiation H, the monthly average extra-atmospheric solar radiation Ho, the sunshine duration S, the maximum possible monthly average daily sunshine duration S_0. In order to calculate the H_0 value, declination and hour angles must be calculated first. The declination angle is the angle between the plane on which the earth rotates around the sun and the equatorial axis. Various forecasting models have been developed in Turkey and many parts of the world to find the monthly average daily total solar radiation. Many of these developed models have been specific to a certain location since they contain the parameters of the region to be calculated.

Day length in hours 'S_o' changes according to different time periods in the year related to hour angle 'ω_s' [5]

$$H_0 = \frac{24}{\pi} I_{sc} \left(1 + 0{,}033cos\frac{360n}{365}\right)\left(cos\emptyset cos\delta sinw_s + \frac{\pi w_s}{180} sin\emptyset sin\delta\right) \quad (5)$$

where $\emptyset$ the latitude of the site, δ the solar declination hour angle, I_{sc} is the solar constant 1353 W/m^2 and n the number of days of the year [14, 15, 16].

$$\delta = 23{,}45sin\left[\frac{360(n+284)}{365}\right] \quad (6)$$

$$S_0 = \left(\frac{2}{15}\right) arccos(-tan\delta tan\emptyset) \quad (7)$$

2.3. Statistical Error Tests

In general, they are the methods that are used to analyze the radiation coming from the sun statistically and to subject it to error tests in the literature, and which are used to reveal the errors of these models. These methods are given below [2, 3, 17].

2.3.1. The sum of squared error (SSE)

$$SSE=\sum_{i=1}^{n}(m_i - c_i)^2 \quad (8)$$

2.3.2. The analysis of variance (R^2)

$$R^2=\frac{\sum_{i=1}^{n}(c_i-c_a)\times(m_i-m_a)}{\sqrt{[\sum_{i=1}^{n}(c_i-c_a)]\times[\sum_{i=1}^{n}(m_i-m_a)^2]}} \quad (9)$$

2.3.3. The adjusted analysis of variance (R^2_{adj})

$$R^2_{adj}=1-\left[\frac{(1-R^2)x(n-a)}{n-a-1}\right] \quad (10)$$

JSR A
Journal of Scientific Reports

2.3.4. The root mean square error

$$\text{RMSE}=\sqrt{\frac{1}{n}\sum_{i=1}^{n}(m_i - c_i)^2} \tag{11}$$

Error analysis methods are used to determine the error difference between the estimation result and the real result of the models found as a result of the rational approach. The specified error analysis method formulas are used to control more than one error analysis result of the model by giving different results. The R^2 equation used for error analysis is between 0 and 1 value. The fact that the value obtained as a result of the coefficient of determination is close to 1 indicates the accuracy of the model found as a result of machine learning to the real value. In other error tests, if the result is close to zero, it means that it performs better.

3. RESULTS

In this section, detailed expressions of the developed models are given. The graph of the model developed for $n = 1$, $m = 1$ is shown in Figure 3, and the graph of the model developed for $n = 1$, $m = 2$ is shown in Figure 4, respectively. Four different statistical error tests were used to evaluate the performance of the developed models. These statistical test results are given in Table 1 for both models.

The rational model equation for $n = 1, m = 1$ was developed as;

$$\textbf{Model 1: } \frac{H}{H_0} = \frac{0.9435\frac{S}{S_0} - 0.1369}{\frac{S}{S_0} + 0.2688} \tag{12}$$

The rational model equation for $n = 1, m = 2$ was developed as;

$$\textbf{Model2: } \frac{H}{H_0} = \frac{-0.2975\frac{S}{S_0} + 0.2824}{\left(\frac{S}{S_0}\right)^2 - 2.083\frac{S}{S_0} + 1.102} \tag{13}$$

JSR A
Journal of Scientific Reports

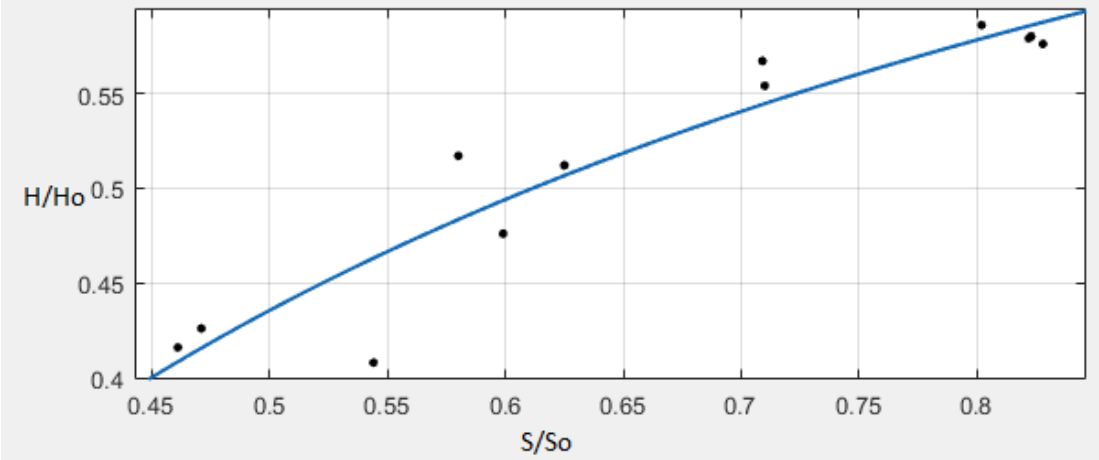

Figure 3. The graph of developed model by using rational polynomial for $n = 1,\ m = 1$.

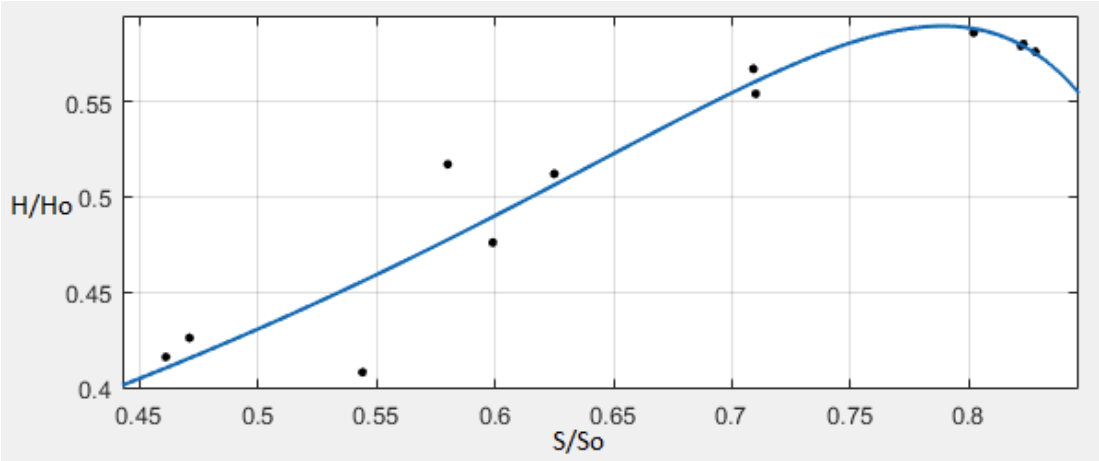

Figure 4. The graph of developed model by using rational polynomial for $n = 1,\ m = 2$.

Table 1. The statistical test results of the rational models.

Models	**Statistical Error Tests**			
	SSE	R^2	R^2_{adj}	**RMSE**
Model 1	0.00553	0.8936	0.87	0.0279
Model 2	0.00429	0.9174	0.8865	0.0232

In this study, the performances of the two models developed using the Rational approach were examined using different statistical tests. SSE statistics test results in both models were very close to the zero value. These results are an important indicator that the developed models give values very close to the real values. When the estimation results in terms of R^2 are examined, it is seen that the developed two models exhibit successful results. The R^2 values of the algorithms in the study vary between % 89.36 and % 91.74 according to different degrees. Considering the results of all developed models are examined in terms of R^2_{adj}, it is seen that the result of model 1and model 2 are 0.87 and 0.88, respectively. When all the results are evaluated in terms of the RMSE test, it is seen that these test results 0.0279 and 0.0232 for two models. Therefore, the prediction success of all algorithms was evaluated as "good" in terms of this metric. When the results are examined in general, it can be said that both methods developed are very successful in solar radiation estimation. However, according to the results obtained, it was seen that model 2 performed better than model 1.

4. CONCLUSIONS

In this study, a new model are developed to estimate the SR value using rational approach in the matlab program. In order to develop new model, a region with high SE potential was selected. The results were analyzed in different statistical error analysis tests. It can be seen from the obtained results that the developed model is quite effective. It is possible to obtain advanced versions of these models by using genetic algorithm, fuzzy logic and artificial intelligence to make predictions and create new models with a rational approach. With these models, optimum levels of results can be obtained and these results can be systematically improved and a great contribution can be made to the SE production sector. It is known that the solar power plant to be installed will provide great convenience before the investment is made. These models, which form the basic structure of online applications used for energy production globally, are open for continuous self-development and adapting to all kinds of innovative projects. Rational approach, thanks to some methods used in the photovoltaic sector today, SR intensity, sunshine duration, etc. It is a method that can be used in the solution of photovoltaic formulations and is constantly evolving thanks to the artificial intelligence logic with a high level of learning feature. As a result, with the rational approach, a prediction model can be developed for each province-based region by using SR intensity and sunshine duration, and it is seen that realistic data estimation is possible in SE production by using these models. The most important and distinctive feature of this study is that an SR prediction model has not been developed using a rational approach before. In this study, two new models were developed using different degrees of rational approaches. For this reason, it is expected that this study will make very important contributions to the literature. This study can provide an important motivation for future academic studies on SR estimation with a rational approach.

ACKNOWLEDGEMENT

This research received no specific grants from any funding agency in public, commercial or non-profit sectors.

JSR A
Journal of Scientific Reports

Kaplan, A. G., Journal of Scientific Reports-A, Number 51, 230-239, December 2022.

REFERENCES

[1] Yiğit, E., Özkaya, U., Öztürk, Ş., Singh, D., and Gritli, H. (2021). Automatic detection of power quality disturbance using convolutional neural network structure with gated recurrent unit. Mobile Information Systems, 2021, Article ID 7917500, 11 pages.

[2] Kaplan, A. G., and Kaplan, Y. A., (2020). Developing of the new models in solar radiation estimation with curve fitting based on moving least-squares approximation. Renewable Energy, 146, 2462-2471.

[3] Kaplan, Y. A., (2018). A new model for predicting the global solar radiation. Environmental Progress & Sustainable Energy, 37, 870-880.

[4] Zhou, Y., Liu, Y., Wang, D., Liu, X., and Wang, Y. (2021). A review on global solar radiation prediction with machine learning models in a comprehensive perspective. Energy Conversion and Management, 235, 113960.

[5] Mustafa, J., Alqaed, S., Almehmadi, F. A., and Jamil, B. (2022). Development and comparison of parametric models to predict global solar radiation: a case study for the southern region of Saudi Arabia. Journal of Thermal Analysis and Calorimetry, 147, 9559–9589.

[6] Solar Energy Maps of Turkey, https://gepa.enerji.gov.tr/MyCalculator/, (acces date: December 2022)

[7] Zang, H., Cheng, L., Ding, T., Cheung, K. W., Wang, M., Wei, Z., and Sun, G. (2019). Estimation and validation of daily global solar radiation by day of the year-based models for different climates in China. Renewable Energy, 135, 984-1003.

[8] Husain, S., and Khan, U. A. (2022). Development of machine learning models based on air temperature for estimation of global solar radiation in India. Environmental Progress & Sustainable Energy, 41(4), e13782.

[9] Feng, Y., Gong, D., Zhang, Q., Jiang, S., Zhao, L., and Cui, N. (2019). Evaluation of temperature-based machine learning and empirical models for predicting daily global solar radiation. Energy Conversion and Management, 198, 111780.

[10] Almorox, J., Voyant, C., Bailek, N., Kuriqi, A., and Arnaldo, J. A. (2021). Total solar irradiance's effect on the performance of empirical models for estimating global solar radiation: An empirical-based review. Energy, 236, 121486.

[11] MathWorks Help Center, https://ch.mathworks.com/help/curvefit/rational.html.

[12] Bamisile, O., Oluwasanmi, A., Ejiyi, C., Yimen, N., Obiora, S., and Huang, Q. (2022). Comparison of machine learning and deep learning algorithms for hourly global/diffuse solar radiation predictions. International Journal of Energy Research, 46, 10052-10073.

[13] Karaman, O. A., Agır, T. T., and Arsel, I. (2021). Estimation of solar radiation using modern methods. Alexandria Engineering Journal, 60, 2447-2455.

[14] Makade, R. G., Chakrabarti, S., and Jamil, B. (2021). Development of global solar radiation models: A comprehensive review and statistical analysis for Indian regions. Journal of Cleaner Production, 293, 126208.

[15] Oztürk, M., Ozek, N., and Berkama, B. (2012). Comparison of Some Existing Models for Estimating Monthly Average Daily Global Solar Radiation for Isparta. Pamukkale University Journal of Engineering Sciences, 18, 13-27.

[16] Khorasanizadeh, H., Mohammadi, K., and Mostafaeipour, A. (2014). Establishing a diffuse solar radiation model for determining the optimum tilt angle of solar surfaces in Tabass, Iran. Energy Conversion and Management, 78, 805-814.

[17] Akossou, A. Y. J., and Palm, R. (2013). Impact of data structure on the estimators R-square and adjusted R-square in linear regression. International Journal of Mathematics and Computation, 20, 84-93.

Kütahya Dumlupınar University
Institute of Graduate Studies

Journal of Scientific
Reports-A
E-ISSN: 2687-6167
Number 51, December 2022

RESEARCH ARTICLE

EVALUATION of the RELATIONSHIP BETWEEN EEG BAND POWERS and COGNITIVE TASKS

Evin ŞAHİN SADIK[1]*, Hamdi Melih SARAOĞLU[2], Sibel CANBAZ KABAY[3], Cahit KESKİNKILIÇ[4],

[1*]Kütahya Dumlupınar University, Engineering Faculty, Electrical-Electronics Engineering Department, Kütahya, evin.sahin@dpu.edu.tr, ORCID: 0000-0002-2212-4210
[2]Kütahya Dumlupınar University, Engineering Faculty, Electrical-Electronics Engineering Department, Kütahya, hmelih.saraoglu@dpu.edu.tr, ORCID: 0000-0002-5075-9504
[3]Kütahya Health Sciences University, Medicine Faculty, Department of Neurology, Kütahya, sibel.canbazkabay@ksbu.edu.tr, ORCID: 0000-0003-4808-2191
[4]İstanbul Gedik University, Faculty of Economics, Administrative and Social Sciences, Department of Psychology, Istanbul, ckesinkilic@gmail.com, ORCID: 0000-0003-3799-4427

Receive Date:18.08.2022 *Accepted Date: 02.11.2022*

ABSTRACT

To examine our brain's responses to different cognitive activities, the brain signals of 30 volunteers were evaluated in terms of verbal memory, visual memory, verbal attention, visual attention and mental processing speed cognitive activities by using Electroencephalogram (EEG) signals. The correlation between cognitive activities and EEG signals was analyzed by examining the EEG signals recorded during the resting state of the volunteers and during five different cognitive activities (Öktem Verbal memory test, Wechsler Memory Scale (WMS) visual memory subtest, Digit span test, Corsi block test and Stroop test). The spectral features of four EEG subbands (delta, theta, beta and alpha) were extracted from the EEG signals at rest and from the EEG signals during each cognitive activity using the Welch method. When the extracted features were evaluated statistically using the ANOVA test, it was observed that there were changes in the EEG bands of the volunteers who passed from the resting state to the test state. It was observed that the relative beta values of the volunteers' EEG signals decreased in the Öktem verbal memory processes test and Digit span test, while the relative alpha values decreased during the visual memory, Corsi block and Stroop tests.

Keywords: *ANOVA, Cognitive tasks, EEG band power, Relative alpha, Relative beta.*

1. INTRODUCTION

Although there are older studies on measuring electrical activities in the human brain, Berger's work on measuring the brain's electrical signals in the human skull [1] is accepted as the beginning of EEG studies. EEG signals have a frequency band in the range of 0.5 – 100 Hz in the low-frequency region. However, as a result of research, it has been seen that different brain activities and physical conditions

JSR A
Journal of Scientific Reports

affect different subbands in this wide frequency band, and different names have been given to distinguish these subbands from each other. These subbands are called delta (δ), theta (θ), alpha (α), beta (β), and gamma (γ) [2]. These frequency bands are associated with different brain processes [3]–[6].

The spectral power densities of EEG subbands may differ in different task situations. When the studies in the literature were evaluated, it was seen that the EEG signals during mental tasks were evaluated using different experimental paradigms. One of the commonly used mental tasks is the n-back paradigm. The N-back paradigm is widely used in EEG and working memory, fatigue and mental workload studies [7]–[9]. In some of the studies, mental tasks were evaluated with the amplitudes of the EEG subbands. In a study done [10], To observe the difference between short-term memory and working memory, EEG signals were recorded while applying the Corsi block test [11] to 18 healthy young male volunteers, beta and gamma band powers were observed to be lower. It has been seen from the literature that there are changes in different EEG band powers during various tasks. In one of the first studies in which mental arithmetic tasks were applied, it was observed that the theta band strengths increased while the alpha band powers decreased while the volunteers were performing the tasks [12]. In another study on mental arithmetic tasks, it was stated that theta and alpha band strengths changed during number processing tasks [13]. Some recent studies suggest that theta and alpha bands are responsible for mental arithmetic tasks and change during these tasks [14], [15]. Another study examining the difficulty of tasks during mental arithmetic tasks said that theta and alpha bands are associated with numerical task processes [16]. Low beta activity is indicative of successful memory encoding, and decreases in beta power are seen in memory-related tasks [17], [18]. Decreases in alpha and beta powers are seen in cognitive and estimation tasks [19]–[21].

When all these studies were evaluated, it was seen that the verbal, visual or numerical cognition of the volunteers was evaluated by applying one-way tests. In this study, the cognitive activities of volunteers were evaluated with versatile tests and experimental studies. It is presented as a contribution to the literature that the decrease in the relative beta band is associated with verbal and numerical retention and recall tasks, and the decrease in the relative alpha band is associated with cognitive tasks with visual content.

This paper is organized as follows: in the second part of the study, participants, mental tasks, data collection and preprocessing steps are mentioned under the title of materials and methods. In the third part, the evaluation of the results is given. In the fourth chapter, the conclusion sections are presented.

2. MATERIAL and METHOD

2.1. Participants

The 30 volunteers participating in the study are healthy individuals. All volunteers signed an informed consent form. In addition, the ethics committee approval of the study was obtained from the Clinical Research Ethics Committee of Kütahya Health Sciences University.

JSR A
Journal of Scientific Reports

2.2. Experimental Paradigm

The EEG signals recorded in this study were evaluated in two parts resting state and cognitive test moments. First, each volunteer's EEG signals at rest were recorded. Then, five different cognitive tests measuring the verbal memory, visual memory, verbal attention, visual attention and reaction time abilities of the volunteers were applied to the volunteers and the EEG signals during the tests were recorded. The experimental paradigm is as given in Figure 1. Tests applied: Öktem verbal memory processes test, WMS-R visual memory subtest, Digit span test, Corsi block test and Stroop test.

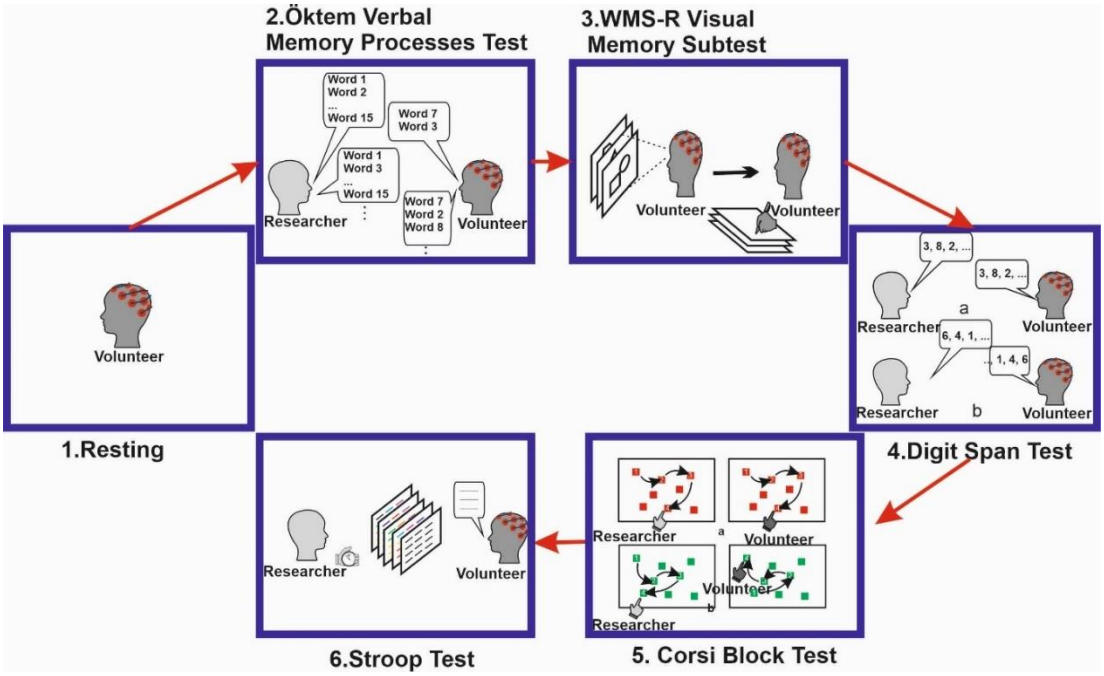

Figure 1. Experimental paradigm.

Resting state: During the resting, the volunteers were given commands such as eye-open, eye-close and eye-open, respectively, and then the EEG signals of the volunteers were recorded while their eyes were open.

Öktem verbal memory processes test: It is a word test that measures the verbal memory and learning abilities of volunteers [22], [23]. Volunteers are asked to repeat the words they have in mind without any order. Each volunteer performed this test in 10 trials.

Wechsler Memory Scale Revised (WMS-R) visual memory subtest: It is a visual memory test that measures the visual memory and learning abilities of volunteers [24]. Three different pictures are shown to the volunteers in sequence for a certain period and after each picture is turned off, the

JSR A
Journal of Scientific Reports

volunteers are asked to draw the pictures. This test was repeated 3 times as each volunteer was shown three different pictures.

Digit span test: The test shows the efficiency and capacity of attention and concentration to repeat numbers forward, consisting of two stages. Saying numbers backward is an execution task that depends on working memory [25], [26]. The test consists of repeating the number sequences read to the volunteers in the same order after the researcher and saying the numbers from the end to the beginning, retention numbers. Since there were 9 different number sequences forward and 8 different number sequences backward within the scope of this test, the volunteers performed this test in 9 trials forward and 8 trials backward.

Corsi block test: It is a two-stage visual attention test consisting of touching the squares shown to the volunteers in the same order after the researcher and handling the squares that the researcher touched from the end to the beginning, retention the frames that the researcher touched [11]. The step of touching forward squares of the test is evaluated as visuospatial memory space. Tapping the memorized frames from top to bottom measures working memory capacity. As there were both eight forward patterns and eight backward patterns within the scope of this test, the volunteers followed and applied these patterns in 8 forward trials and 8 backward trials.

Stroop test: During this test, which measures the mental processing speed of the volunteers, the volunteers are asked to quickly read five cards or say the colors of what is written on the cards [27], [28]. Since each volunteer read five different cards, each volunteer applied this test in 5 trials.

2.3. Data Acquisition and Preprocessing

EEG signals of 30 volunteers were recorded with a 16-channel Nihon Kohden EEG device. The device takes 500 samples per second.The block diagram showing the working stages is given in Figure 2. The study consists of the steps of separately collecting EEG data at rest and cognitive test moments, filtering the collected data, extracting spectral features from the data, and comparing the EEG features at rest/test states using statistical analysis.

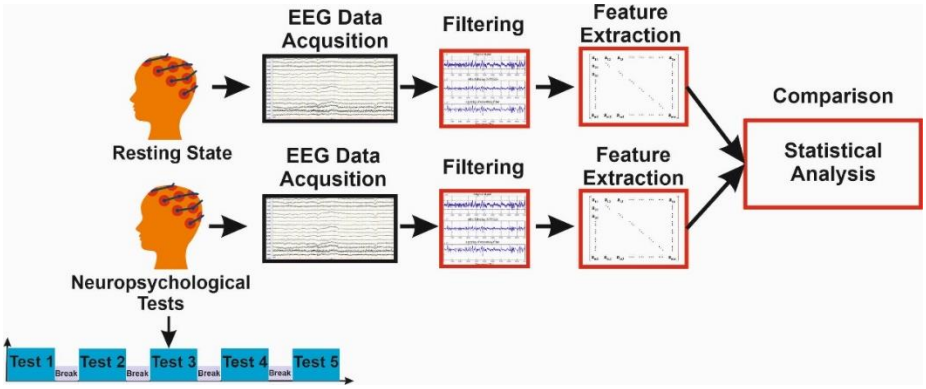

Figure 2. Experimental paradigm.

JSR A
Journal of Scientific Reports

The data collection step consists of two parts. In the first part, EEG signals were recorded while the volunteers were at rest and their eyes were open. In the second part, EEG signals were recorded while the volunteers were performing five different cognitive tasks. The application of cognitive tasks to volunteers was explained in the experimental paradigm section. Data were separated according to rest and cognitive test moments. Each EEG data was marked to which state it belongs and these data were separated according to the signs.

In the filtering phase, the independent component analysis (ICA) method [29], [30] and 50 Hz notch filter [31] were applied to EEG data. Thus, the signal was freed from the eye artifacts and 50 Hz mains frequency.

In feature extraction, the spectral features of the EEG subbands were extracted using the Welch [32], [33] method of the EEG signal. Detailed information about the extraction of features was explained in the section extraction of spectral features.
Finally, in the comparison step, the features at rest and cognitive test time were statistically evaluated with the One Way ANOVA test. Here, the most significant features were determined for each test and their status when they passed the test state without resting was evaluated.

2.4. Extraction of Spectral Features

Within the scope of the study, spectral power densities for delta, theta, beta and alpha subbands were extracted from the EEG signals in the resting state and when the volunteers performed cognitive tests, using the Welch method and the relative powers were calculated for each subband. In Eq. 1, the periodograms of the input function particles divided into time slots are calculated with the appropriate window function.

$$P_i(f) = \frac{1}{M}\frac{1}{H}\left[\sum_{n=0}^{M-1} w[n]x_i[n]e^{-j2\pi fn}\right]^2 \tag{1}$$

Shown as $x_i[n]$ in the equation, i. is the periodogram of the piece. w[n] is the selected window function in the equation. M is the length of the particles and should be equal for each. H is the normalized window function and can be calculated in Eq. 2.

$$H = \frac{1}{M}\sum_{n=0}^{M-1} w[n]^2 \tag{2}$$

By taking the average of the periodograms of the obtained particles, the power spectral density is obtained by the Welch method as in Eq. 3.

$$P_{welch}(f) = \frac{1}{S}\sum_{i=1}^{S} P_i(f) \tag{3}$$

JSR A
Journal of Scientific Reports

In Eq. 4, the equation for calculating the power spectral densities of each subband with the Welch method is given.

$$(f)=\frac{1}{S}\sum_{i=1}^{S}P_i(f)\;;\quad f=\begin{cases}0.4Hz<f<4Hz\;, Delta\,band\\ 4Hz<f<8Hz\quad, Theta\,band\\ 8Hz<f<12Hz\quad, Alpha\,band\\ 12Hz<f<30Hz\,, Beta\,band\end{cases} \tag{4}$$

In Eq. 5, the equation for the calculation of the relative power spectral densities for each subband with the Welch method is given.

$$P_{relative}=\frac{P_{subband}}{P_{toplam}} \tag{5}$$

These features were extracted separately from the volunteers' resting state EEG signals and from the EEG signals recorded during the five cognitive tests.

3. EVALUATION of RESULTS

In the evaluation phase, the spectral features of the resting state and the test moment were analyzed with the One Way ANOVA test. F and p values were evaluated for each test and are given in Table 1.

Table 1. F and p-value for each test as a result of the evaluation of the subbands with the ANOVA test to determine the correlation between the resting moment and the test moments from the EEG subbands.

		Öktem-SBST	**WMS-R Visual Memory Sub Test**	**Digit Span Test**	**Corsi Block Test**	**Stroop Test**
Relative Delta	**F**	20.408	1.510	127.948	31.290	36.461
	p	$7x10^{-6}$	$2.19x10^{-1}$	$1.72e^{-28}$	$2.65e^{-8}$	$2.21e^{-9}$
Relative Theta	**F**	0.862	7.061	1.465	2.171	0.471
	p	$3.53x10^{-1}$	$8.01x10^{-3}$	$2.26x10^{-1}$	$1.41x10^{-1}$	$4.93x10^{-1}$
Relative Beta	**F**	**83.854**	7.380	**230.723**	97.307	45.943
	p	**$3.06e^{-19}$**	$6.72x10^{-3}$	**$1.77e^{-48}$**	$2.91e^{-22}$	$2.11e^{-11}$
Relative Alpha	**F**	7.592	**68.116**	144.916	**125.152**	**75.622**
	p	$5.92x10^{-3}$	**$4.97e^{-16}$**	$6.95e^{-32}$	**$6.27e^{-28}$**	**$1.44e^{-17}$**

When Table 1 was examined, it was seen that the most significant F and p-values obtained as a result of the ANOVA test for the Öktem Verbal memory processes test were in the relative beta feature. As shown in Figure 3, the relative beta value of the volunteers in the resting state was higher than that of the volunteers who performed the Öktem verbal memory processes test. It is known that beta power

JSR A
Journal of Scientific Reports

decreases as the difficulty of the task increases [34]. During the Öktem verbal memory processes test, the volunteers tried to retain and say them by recalling them.

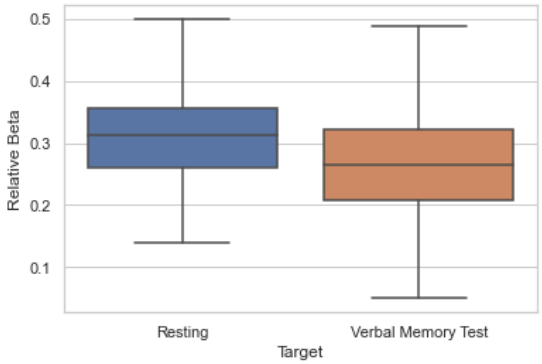

Figure 3. Box plot showing the relative beta subband power of the resting state and Öktem-Verbal Memory Processes Test.

When the ANOVA test results for the WMS-R visual memory subtest were analyzed from Table 1, it was seen that the most significant F and p-values were in the relative alpha feature. As given in Figure 4, the relative alpha value of the volunteers in the resting state was higher than that of the volunteers who performed the WMS-R visual memory subtest. A decrease in alpha band power is observed with an increase in mental workload, especially during visual tasks [35], [36]. In this study, the relative alpha power decreased compared to the resting state during the visual memory task.

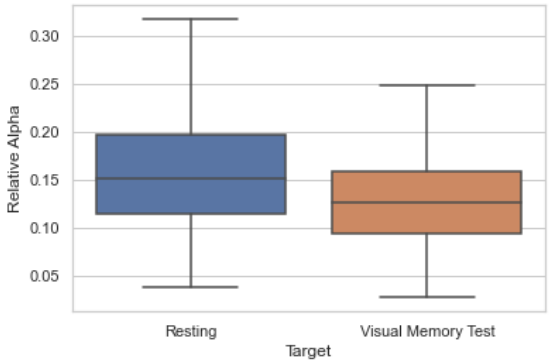

Figure 4. Box plot showing the relative alpha subband powers of the resting state and WMS-R Visual Memory Test.

JSR A
Journal of Scientific Reports

When the ANOVA test results for the digit span test were analyzed from Table 1, it was seen that the most significant F and p-values obtained were in the relative beta feature. As shown in Figure 5, the volunteers' relative beta value in the resting state was higher than the relative beta value when performing the Digit span test. The volunteers performed retention and recall in the Digit span test, as in the Öktem verbal memory processes test.

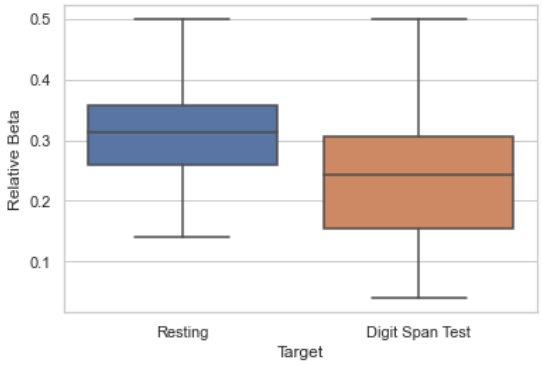

Figure 5. Box plot showing the relative beta subband power of the resting state and Digit Span Test.

During the Corsi block test, the volunteers followed the blocks visually and performed the same procedure. When the ANOVA test results for the Corsi block test were analyzed from Table 1, it was seen that the most significant F and p-values obtained were in the Relative alpha feature. As shown in Figure 4, the relative alpha value of the volunteers in the resting state was higher than that of the volunteers who performed the Corsi block test.

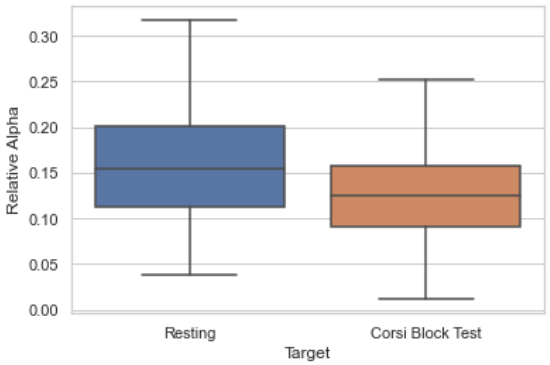

Figure 6. Boxplot showing the relative alpha subband powers of the resting and Corsi Block test.

When the ANOVA test results for the Stroop test were analyzed from Table 1, it was seen that the most significant F and p-values obtained were in the relative alpha feature. As shown in Figure 7, the

JSR A
Journal of Scientific Reports

relative alpha value of the volunteers at resting state was higher than that of the volunteers who performed the Stroop test. Changes in the alpha band are associated with attentional processes and inhibition of irrelevant information [37], [38]. In addition, there is a procedure in which visual abilities are measured, as in the Corsi block test and WMS-R Visual Memory subtest.

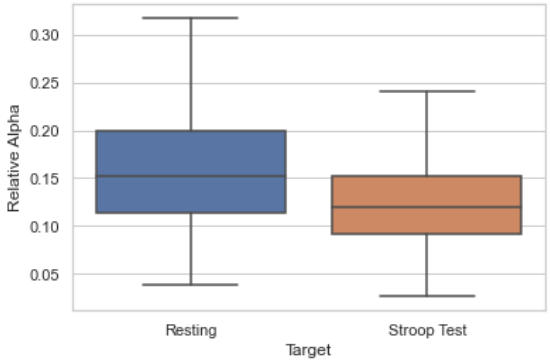

Figure 7. Box plot showing the relative alpha subband power of the resting state and Stroop Test.

4. CONCLUSION

Within the scope of the study, the EEG signals recorded during the resting state of 30 volunteers and while applying five cognitive tests were examined. Signal preprocessing was applied to EEG data. The spectral features of the EEG subbands were extracted from the recorded EEG signals using the Welch method, and these spectral features were evaluated statistically. As a result of the relationship between the cognitive test states and the resting states evaluated with the ANOVA test, the volunteers who switched from the resting state to the cognitive test state made a mental effort and the mental workload of the volunteers increased. The most significant spectral feature for each test was found with the help of ANOVA test. While the Öktem verbal memory processes test and the digit span test included retention and verbal recall tasks only, the relative beta power of the volunteers who performed this test decreased. Volunteers performed tasks with visual content during the WMS-R visual memory test, Corsi block test, and Stroop test, and their relative alpha power decreased compared to the resting state. In this study, it was observed that there were changes in different EEG bands during different cognitive tasks.

In different task situations, the difficulty and duration of the task are the factors affecting the task's success. The limits of the study are limited to the experimental group. In future studies, the experiments can be repeated by increasing the experimental group. In addition, the effects of cognitive tasks on sick individuals can be examined from EEG signals by working on individuals with impaired cognition. Furthermore, standardized different tasks can be determined, the examination can be carried out. System performance can be evaluated with novel performance metrics such as the current polygon area metric.

ACKNOWLEDGEMENT

This study was supported by the Scientific Research Projects of Kütahya Dumlupınar University within the scope of the project numbered 2020/26. Also, it was conducted by researchers at Kütahya Dumlupınar University Neurotechnology Education Application and Research Center.

REFERENCES

[1] Berger, H., (1929), "Über das elektroenkephalogramm des menschen," Arch. Psychiatr. Nervenkr., vol. 87, no. 1, pp. 527–570.

[2] Eroğlu, K.,(2020), Duygusal Görüntülerin Lüminans Düzeylerinin EEG Üzerindeki Etkisi, Doktora Tezi, Karadeniz Teknik Üniversitesi Fen Bilimleri Enstitüsü, Trabzon, 204s.

[3] Amzica, F., and Steriade, M., (1998), "Electrophysiological correlates of sleep delta waves,"

[4] Electroencephalogr. Clin. Neurophysiol., vol. 107, no. 2, pp. 69–83.

[5] Schacter, D. L.,(1977), "EEG theta waves and psychological phenomena: A review and analysis," Biol. Psychol., vol. 5, no. 1, pp. 47–82.

[6] Toscani, M., Marzi, T., Righi, S., Viggiano, M. P., and Baldassi, S., (2010), "Alpha waves: a neural signature of visual suppression," Exp. brain Res., vol. 207, no. 3, pp. 213–219.

[7] Dustman, R. E., Boswell, R. S., and Porter, P. B., (1962), "Beta brain waves as an index of alertness," Science (80-.)., vol. 137, no. 3529, pp. 533–534.

[8] Shigihara, Y., Tanaka, M., Ishii, A., Tajima, S., Kanai, E., Funakura, M., and Watanabe, Y., (2013), "Two different types of mental fatigue produce different styles of task performance," Neurol. Psychiatry Brain Res., vol. 19, no. 1, pp. 5–11, 2013.

[9] Jiao, X., Bai, J., Chen, S., and Li, Q., (2012), "Research on mental fatigue based on entropy changes in space environment," in 2012 IEEE International Conference on Virtual Environments Human-Computer Interfaces and Measurement Systems (VECIMS) Proceedings, pp. 74–77.

[10] He, D., Donmez, B., Liu, C. C., and Plataniotis, K. N., (2019), "High cognitive load assessment in drivers through wireless electroencephalography and the validation of a modified N-back task," IEEE Trans. Human-Machine Syst., vol. 49, no. 4, pp. 362–371.

[11] Guevara, M. A., Paniagua, E. I., Gonzalez, M. H., Carrillo, I. K. S., Sepulveda, M. L. A., Orozco, J.C.H., and Gutierrez, C. A., (2018), "EEG activity during the spatial span task in young men: Differences between short-term and working memory," Brain Res., vol. 1683, pp. 86–94.

[12] Corsi, P. M., (1972), Human memory and the medial temporal region of the brain (Doctoral dissertation, McGill University).

[13] Harmony, T., Fernandez, T., Silva, J., Bosch, J., Valdes, P., Fernandez-Bouzas, A., Galan, L., Aubert, E., and Rodriguez, D., (1999), "Do specific EEG frequencies indicate different processes during mental calculation?," *Neurosci. Lett.*, vol. 266, no. 1, pp. 25–28.

[14] Moeller, K., Wood, G., Doppelmayr, M., and Nuerk, H.-C., (2010), "Oscillatory EEG correlates of an implicit activation of multiplication facts in the number bisection task," *Brain Res.*, vol. 1320, pp. 85–94.

[15] Gärtner, M., Grimm, S., and Bajbouj, M., (2015), "Frontal midline theta oscillations during mental arithmetic: effects of stress," *Front. Behav. Neurosci.*, p. 96.

[16] Spüler, M., Walter, C., Rosenstiel, W., Gerjets, P., Moeller, K., and Klein, E., (2016), "EEG-based prediction of cognitive workload induced by arithmetic: a step towards online adaptation in numerical learning," *Zdm*, vol. 48, no. 3, pp. 267–278.

[17] Chin, Z. Y., Zhang, X., Wang, C., and Ang, K. K., (2018), "EEG-based discrimination of different cognitive workload levels from mental arithmetic," in *2018 40th Annual International Conference of the IEEE Engineering in Medicine and Biology Society (EMBC)*, pp. 1984–1987.

[18] Hanslmayr, S., Volberg, G., Wimber, M., Raabe, M., Greenlee, M. W., and Bäuml, K.-H. T., (2011), "The relationship between brain oscillations and BOLD signal during memory formation: a combined EEG–fMRI study," *J. Neurosci.*, vol. 31, no. 44, pp. 15674–15680.

[19] Scholz, S., Schneider, S. L., and Rose, M., (2017), "Differential effects of ongoing EEG beta and theta power on memory formation," *PLoS One*, vol. 12, no. 2, p. e0171913.

[20] León-Cabrera, P., Piai, V., Morís, J., and Rodríguez-Fornells, A., (2022), "Alpha power decreases associated with prediction in written and spoken sentence comprehension," *Neuropsychologia*, p. 108286.

[21] Prystauka, Y., and Lewis, A. G., (2019), "The power of neural oscillations to inform sentence comprehension: A linguistic perspective," *Lang. Linguist. Compass*, vol. 13, no. 9, p. e12347.

[22] Molinaro, N., Monsalve, I. F., and Lizarazu, M., (2016), "Is there a common oscillatory brain mechanism for producing and predicting language?," *Lang. Cogn. Neurosci.*, vol. 31, no. 1, pp. 145–158.

[23] Öktem, Ö., (1994), "Nöropsikolojik testler ve nöropsikolojik değerlendirme," Türk Psikol. Derg., vol. 9, no. 33, pp. 33–44

[24] Tanör, Ö. Ö., (2011) "Öktem sözel bellek süreçleri testi.(Öktem-SBST) el kitabı." Türk

Psikologlar Derneği.

[25] Wechsler, D. (1987). The Wechsler Memory Scale—Revised. Advances in Psychological Assessment. Advances in Psychological Assessment, içinde (s. 65-99), Boston, MA.

[26] Karakaş, S., and Yalın, A., (1995), "Görsel işitsel sayı dizileri testi B formunun 13-54 yaş grubu üzerindeki standardizasyon çalışması," Türk Psikol. Derg., vol. 10, no. 34, pp. 20–31.

[27] Osmanlıoğlu, U. M. ve Özgüzel, M. (1985). Hafıza bozukluğu gösteren çeşitli tanı gruplarındaki hastaların Wechsler Hafıza Ölçeği ile tetkiki. XXI. Psikiyatri ve Nörolojik Bilimler Kongresi Kitabı, içinde. Adana: Çukurova Üniversitesi Yayını.

[28] Jensen, A. R., and Rohwer Jr, W. D., (1966), "The Stroop color-word test: a review," Acta Psychol. (Amst)., vol. 25, pp. 36–93.

[29] Karakaş, S., Erdoğan, E., Soysal, A. Ş., Ulusoy, T., Ulusoy, İ., and Alkan, S., (1999), "Stroop Testi TBAG Formu : Türk Kültürüne Standardizasyon Çalışmaları ," Türk Psikiyatr. Derg., vol. 2, pp. 75–88.

[30] Stone, J. V, (2002), "Independent component analysis: an introduction," Trends Cogn. Sci., vol. 6, no. 2, pp. 59–64.

[31] Vigârio, R., Särelä, J., Jousmäki, V., Hämäläinen, M., and Oja, E., (2000), "Independent component approach to the analysis of EEG and MEG recordings," IEEE Trans. Biomed. Eng., vol. 47, no. 5, pp. 589–593.

[32] Jayant, H. K., Rana, K. P. S., Kumar, V., Nair, S. S., and Mishra, P., (2016), "Efficient IIR notch filter design using Minimax optimization for 50Hz noise suppression in ECG," Proc. 2015 Int. Conf. Signal Process. Comput. Control. ISPCC 2015, pp. 290–295.

[33] Welch, P. D., (1967), "The Use of Fast Fourier Transform for the Estimation of Power Spectra: A Method Based on Time Averaging Over Short, Modified Periodograms," IEEE Trans. Audio Electroacoust., vol. 15, no. 2, pp. 70–73.

[34] Villwock S., and Pacas, M., (2008), "Application of the Welch-method for the identification of two-and three-mass-systems," IEEE Trans. Ind. Electron., vol. 55, no. 1, pp. 457–466.

[35] Dimitrakopoulos, G. N., Kakkos, I., Dai, Z., Lim, J., deSouza, J.J., Bezerianos, and A.,Sun, Y., (2017) "Task-independent mental workload classification based upon common multiband EEG cortical connectivity," IEEE Trans. Neural Syst. Rehabil. Eng., vol. 25, no. 11, pp. 1940–1949, 2017.

[36] Fink, A., Grabner, R. H., Neuper, C., and Neubauer, A. C., (2005), "EEG alpha band dissociation with increasing task demands," Cogn. brain Res., vol. 24, no. 2, pp. 252–259.

[37] Stipacek, A., Grabner, R. H., Neuper, C., Fink, A., and Neubauer, A. C., (2003), "Sensitivity of human EEG alpha band desynchronization to different working memory components and increasing levels of memory load," Neurosci. Lett., vol. 353, no. 3, pp. 193–196.

[38] Foxe, J. J., and Snyder, A. C., (2011), "The role of alpha-band brain oscillations as a sensory suppression mechanism during selective attention," Front. Psychol., vol. 2, p. 154.

[39] Payne, L., Guillory, S., and Sekuler, R., (2013) "Attention-modulated alpha-band oscillations protect against intrusion of irrelevant information," J. Cogn. Neurosci., vol. 25, no. 9, pp. 1463–1476.

Kütahya Dumlupınar University
Institute of Graduate Studies

Journal of Scientific
Reports-A
E-ISSN: 2687-6167
Number 51, December 2022

RESEARCH ARTICLE

NEW DATA for SPHECIDAE (HYMENOPTERA: APOIDEA) FAUNA of TÜRKİYE

İlyas CAN[1,*]

[1*]Tokat Gaziosmanpaşa University, Faculty of Arts and Sciences, Department of Biology, Tokat, ilyascan41@gmail.com, ORCID: 0000-0003-3013-6614

Receive Date:14.06.2022 *Accepted Date: 08.11.2022*

ABSTRACT

This study is based upon material from subfamilies Ammophilinae, Sceliphrinae, and Sphecinae of the family Sphecidae collected from different localities of Türkiye between 2000 and 2021. A total of 27 species belonging to nine genera of three subfamilies have been presented. New provincial and regional records for some species have been given.

Keywords: *Sphecidae, fauna, locality records, solitary wasp, Türkiye*

1. INTRODUCTION

The Sphecidae family, which is in the Apocrita suborder and the Aculeata group, generally includes medium to large sized solitary wasps. The family comprises about 810 species belonging to five subfamilies in all zoogeographical regions of the world [1]. Most of the species belonging to this family are important to ecosystems for two reasons. Firstly, they control insect and spider populations by hunting them in order to gather food for their larvae and secondly, they contribute to the pollination of flowering plants as they feed on nectar [2].

In Türkiye; over the last decade, a number of studies have been conducted on the biodiversity of this family, including new and important findings [2-10]. According to recent contributions, the family Sphecidae contains 79 species and subspecies in Türkiye [2, 11]. But Sphecidae fauna of Türkiye is still incomplete, because most probably, so many species remain unknown. It is expected that the species number of Sphecidae will increase with future studies due to geographical location of Türkiye, its habitat and climate diversity.

We aimed in this study to contribute to the distribution knowledge of Sphecidae fauna in Türkiye.

2. MATERIALS and METHODS

The samples of Sphecidae were collected from different localities of Türkiye between 2000 and 2021.

JSR A
Journal of Scientific Reports

Totally 239 specimens for this study were collected using insect net from different localities (Fig. 1). The materials are deposited in the Entomological Research Laboratory, Faculty of Arts and Sciences, Gaziosmanpaşa University, Tokat, Türkiye. Provincial distributions were evaluated according to Can and Gülmez [2].

Figure 1. Türkiye map showing the provinces where the samples were collected.

3. RESULTS and DISCUSSION

In this study 27 species of nine genera belong to three subfamilies of Sphecidaee were given (11 species of three genera in the subfamily Ammophilinae; 6 species of two genera in the subfamily Sceliphrinae; 10 species of four genera in the subfamily Sphecinae).

Family Sphecidae (Latreille, 1802)

Subfamily Ammophilinae André, 1886

Genus *Ammophila* W. Kirby, 1798

***Ammophila heydeni* Dahlbom, 1845**

Material examined (17 ♀♀, **23** ♂♂**): AMASYA:** Central district, 555 m, 07.VII.2013, ♀, 3 ♂♂; Taşova, Dereköy, 255 m, 01.V.2013, 2 ♂♂; **ÇANKIRI:** Çerkeş, 1000 m, 26.VI.2001, ♂; **DENİZLİ:** Honaz, 800 m, 24.VI.2010, ♂; **ESKİŞEHİR:** Eskişehir-Ankara road, 930 m, 23.VI.2014, ♀; **KARS:** Central district, 1850 m, 09.IX.2009, ♂; **KOCAELİ:** Gölcük, İhsaniye, 100 m, 16.VI.2020, ♂; **TOKAT:** Central district, 680 m, 30.IX.2012, 9 ♀♀, 6 ♂♂; 07.X.2012, 6 ♀♀, 5 ♂♂; Central district,

JSR A
Journal of Scientific Reports

Geyras, 750 m, 06.VII.2013, ♂; Central district, Kömeç, 580 m, 06.V.2013, ♂; Niksar, Çamiçi, 1350 m, 21.VI.2013, ♂.

Distribution in Türkiye: It is widespread in all geographical regions.

Remark: New record for fauna of Denizli, Eskişehir and Kocaeli provinces.

***Ammophila hungarica* Mocsáry, 1883**

Material examined (3 ♂♂): TOKAT: Almus, 940 m, 07.VII.2011, ♂; 08.V.2012, ♂; Central district, 660 m, 01.V.2012, ♂.

Distribution in Türkiye: It is widespread in all geographical regions [2].

Remark: New record for fauna of Tokat province.

***Ammophila pubescens* Curtis, 1836**

Material examined (1 ♂): KIRŞEHIR: Çiçekdağı, 1050 m, 20.VII.2000, ♂.

Distribution in Türkiye: It spreads in Eastern and Central Anatolia regions [2].

Remark: New record for fauna of Kırşehir province.

***Ammophila sabulosa* (Linnaeus, 1758)**

Material examined (11 ♀♀, 40 ♂♂): AMASYA: Central district, 554 m, 07.VII.2013, 7 ♂♂; Central district, Ziyaret, 1050 m, 07.VII.2013, ♂; **ÇANKIRI:** Central district, 800 m, 30.VII.2000, 2 ♂♂; Çerkeş, 1000 m, 26.VI.2001, ♂; Ilgaz, Yenice, 1160 m, 30.VII.2000, ♂; **IĞDIR:** Kağızman, Kötek, 1400 m, 04.IX.2009, ♂; **KIRŞEHİR:** Çiçekdağı, 1050 m, 20.VII.2000, ♀, 4 ♂♂; **TOKAT:** Almus, 940 m, 14.V.2013, 7 ♂♂; Central district, 900 m, 15.IX.2012, ♀; Central district, Pınarlı, 760 m, 24.VIII.2013, 5 ♀♀, 6 ♂♂; Erbaa, 250 m, 25.IX.2012, ♀; Niksar, Akıncı, 765 m, 13.V.2014, 4 ♂♂; Niksar, Canpolat, 1095 m, 24.VI.2013, ♀; Niksar, Çamiçi, 1350 m, 21.VI.2013, ♀, 5 ♂♂; Niksar, Gökdere, 800 m, 04.VII.2013, ♂; Pazar, Akdağ, 1560 m, 16.IX.2012, ♀.

Distribution in Türkiye: It is widespread in all geographical regions [2].

Remark: New record for fauna of Kırşehir province.

***Ammophila terminata* F. Smith, 1856**

Material examined (1 ♀): SİVAS: İmranlı, 1830 m, 20.VII.2020, ♀.

JSR A
Journal of Scientific Reports

Distribution in Türkiye: It is distributed in all geographical regions except for Southeastern Anatolia region [2].

Remark: New record for fauna of Sivas province.

Genus *Hoplammophila* de Beaumont 1960

***Hoplammophila armata* (Illiger, 1807)**

Material examined (1 ♀, 3 ♂♂): TOKAT: Central district, Pınarlı, 760 m, 24.VIII.2013, ♀; 05.VIII.2015, 3 ♂♂.

Distribution in Türkiye: It is distributed in Eastern Anatolia, Central Anatolia and Black Sea regions [2].

Genus *Podalonia* Fernald, 1927

***Podalonia affinis* (Kirby, 1798)**

Material examined (5 ♀♀, 5 ♂♂): KARS: Central district, 1850 m, 25.VI.2006, ♀; 10.VIII.2006, ♂; 16.VII.2008, ♂; 25.VIII.2007, ♂; 30.VIII.2009, ♀, ♂; Central district, 2100 m, 26.VIII.2009, ♀; Central district, University campus, 1750 m, 05.VII.2009, 2 ♀♀; **TOKAT:** Nifkar, Efkerit valley, 350 m, 21.VI.2013, ♂.

Distribution in Türkiye: It is distributed in all geographical regions except for Aegean and Southeastern Anatolia regions [2].

***Podalonia fera* (Lepeletier de Saint Fargeau, 1845)**

Material examined (3 ♀♀): KIRŞEHİR: Çiçekdağı, 1400 m, 20.VII.2000, ♀; **TOKAT:** Central district, 680 m, 28.VII.2014, ♀; Central district, University campus, 620 m, 05.X.2012, ♀.

Distribution in Türkiye: It is widespread in all geographical regions [2, 10].

Remark: New record for fauna of Kırşehir province.

***Podalonia hirsuta* (Scopoli, 1763)**

Material examined (3 ♀♀, 2 ♂♂): KARS: Central district, 1850 m, 25.VI.2006, ♀; **TOKAT:** Erbaa, Karayaka, 250 m, 12.VII.2015, ♀; Niksar, Çamiçi, 900 m, 21.VI.2013, ♀, 2 ♂♂.

Distribution in Türkiye: It is widespread in all geographical regions [2].
***Podalonia luffii* (Saunders, 1903)**

JSR A
Journal of Scientific Reports

Material examined (7 ♂♂): KARS: Central district, 1850 m, 25.VI.2006, 3 ♂♂; 10.VIII.2006, ♂; 25.VIII.2007, ♂; 16.VII.2008, 2 ♂♂.

Distribution in Türkiye: It shows limited distribution in Central and Eastern Anatolia [2, 10].

Remark: New record for fauna of Kars province.

***Podalonia tydei tydei* (Le Guillou, 1841)**

Material examined (3 ♀♀, 3 ♂♂): SİVAS: Suşehri, 975 m, 18.VII.2017, ♀; **TOKAT:** Central district, 680 m, 30.IX.2012, 2 ♀♀; Central district, Kömeç, 580 m, 06.V.2013, 3 ♂♂.

Distribution in Türkiye: It is widespread in all geographical regions [2].

Subfamily Sceliphrinae Ashmead, 1899

Genus *Chalybion* Dahlbom, 1843

***Chalybion flebile* (Lepeletier de Saint Fargeau, 1845)**

Material examined (1 ♀, 3 ♂♂): SİVAS: Koyulhisar, 1150 m, 13.VII.2017, 2 ♂♂; **TOKAT:** Central district, University campus, 680 m, 20.V.2016, ♀; Erbaa, Tepekışla, 230 m, 03.VI.2017, ♂.

Distribution in Türkiye: It is widespread in all geographical regions [2].

***Chalybion omissum* (Kohl, 1889)**

Material examined (4 ♀♀, 1 ♂): DENİZLİ: Honaz, 800 m, 24.VI.2010, ♂; **TOKAT:** Central district, University campus, 660 m, 11.VII.2011 ♀; 12.VI.2012, 2 ♀♀; 19.VI.2014, ♀.

Distribution in Türkiye: It is distributed in all geographical regions except for Black Sea region [2].

Remark: New record for fauna of Tokat province.

Genus *Sceliphron* Klug, 1801

***Sceliphron curvatum* (Smith, 1870)**

Material examined (1 ♀): KOCAELİ: Gölcük, İhsaniye, 100 m, 16.VI.2020, ♀.

Distribution in Türkiye: It spreads in Black Sea, Eastern Anatolia and Marrmara regions [2].

***Sceliphron destillatorium* (Illiger, 1807)**

JSR A
Journal of Scientific Reports

Material examined (3 ♂♂): ESKİŞEHİR: Osmangazi University campus, 830 m, 25.VI.2014, 2 ♂♂; **KARS:** Central district, 2000 m, 16.VIII.2009, ♂.

Distribution in Türkiye: It is widespread in all geographical regions [2].

***Sceliphron funestum* Kohl, 1918**

Material examined (3 ♀♀): ANTALYA: Kalkan, 450 m, 22.VII.2021, ♀; **MUĞLA:** Seydikemer, 775 m, 20.VII.2021, 2 ♀♀.

Distribution in Türkiye: It spreads in Aegean, Mediterrenian, Central and Southeastern Anatolia regions. For provincial distribution, see Can and Gülmez [2].

***Sceliphron spirifex* (Linnaeus, 1758)**

Material examined (2 ♀♀): ANTALYA: Kalkan, 450 m, 20.VII.2021, ♀: **KARS:** Central district, 1850 m, 10.VI.2007, ♀.

Distribution in Türkiye: It is distributed in all geographical regions except for Eastern Anatolia region [2].

Remark: New record for fauna of Kars province.

Subfamily Sphecinae Latreille, 1802

Genus *Isodontia* Patton, 1880

***Isodontia splendidula* (Costa, 1858)**

Material examined (1 ♀, 4 ♂♂): TOKAT: Central district, University campus, 10.VII.2013, 3 ♂♂; 19.VI.2014, ♂; Erbaa, Karayaka, 250 m, 12.VII.2014, ♀.

Distribution in Türkiye: It is distributed in all geographical regions except for Southern Anatolia region [2].

Genus *Palmodes* Kohl, 1890

***Palmodes occitanicus* (Le Peletier & Serville, 1828)**

Material examined (3 ♀♀, 1 ♂): AMASYA: Central district, Ziyaret, 1050 m, 07.VII.2013, ♀; **ESKİŞEHİR:** Osmangazi University campus, 830 m, 25.VI.2014, ♂; **TOKAT:** Central district, 680 m, 15.VII.2014, 2 ♀♀.

Distribution in Türkiye: It is widespread in all geographical regions [2].

JSR A
Journal of Scientific Reports

Remark: New record for fauna of Amasya and Eskişehir provinces.

***Palmodes strigulosus* (Costa, 1861)**

Material examined (1 ♀): ÇANKIRI: Central district, 700 m, 29.VII.2000, ♀.

Distribution in Türkiye: It is widespread in all geographical regions [2].

Remark: New record for fauna of Çankırı province.

Genus *Prionyx* Vander Linden, 1827

***Prionyx kirbii* (Vander Linden, 1827)**

Material examined (7 ♀♀, 5 ♂♂): AMASYA: Taşova, Güngörmüş, 350 m, 31.VIII.2014, ♀; **ÇANKIRI:** Central district, 800 m, 29.VII.2000, ♀, ♂; **KARS:** Central district, 1850 m, 10.VI.2007, 3 ♂♂; **TOKAT:** Central district, 680 m, 07.X.2012, ♀; Central district, Pınarlı, 755 m, 24.VIII.2013, 2 ♀♀; 26.VIII.2013, ♀; 30.VIII.2013, ♀, ♂; Central District, University campus, 670 m, 15.VII.2013, ♀.

Distribution in Türkiye: It is distributed in all geographical regions except for Southern Anatolia region [2].

***Prionyx lividocinctus* (Costa, 1861)**

Material examined (2 ♂♂): TOKAT: Central district, 700 m, 15.VII.2015, 2 ♂♂.

Distribution in Türkiye: It is widespread in all geographical regions [2].

Remark: New record for fauna of Tokat province.

***Prionyx nudatus* (Kohl, 1885)**

Material examined (3 ♀♀, 5 ♂♂): AMASYA: Taşova, Boraboy, 970 m, 05.IX.2015, ♂; **ÇANKIRI:** Çerkeş, 1000 m, 26.VI.2001, ♀, ♂; **KARS:** Central district, 1850 m, 10.VI.2007, ♂; 15.VIII.2008, ♀; **TOKAT:** Central district, 700 m, 15.VII.2015, 2 ♂♂; Reşadiye, Zinav, 970 m, 17.VIII.2014, ♀.

Distribution in Türkiye: It is distributed in all geographical regions except for Aegean region [2].

***Prionyx songaricus* (Eversmann, 1849)**

Material examined (1 ♂): KARS: Central district, 1850 m, 10.VI.2007, ♂.

JSR A
Journal of Scientific Reports

Distribution in Türkiye: It is distributed in all geographical regions except for Black Sea and Marmara regions [2].

Remark: New record for fauna of Kars province.

Genus *Sphex* Linnaeus, 1758

***Sphex flavipennis* Fabricius, 1793**

Material examined (8 ♀♀, 36 ♂♂): AMASYA: Central district, 555 m, 07.VII.2013, 3 ♂♂; Taşova, Gökpınar, 730 m, 04.VII.2015, 2 ♀♀; **DENİZLİ:** Honaz, 800 m, 24.VI.2010, ♀, 4 ♂♂; **SİVAS:** Koyulhisar, 700 m, 27.VI.2015, ♀; **TOKAT:** Central district, 28.VI.2014, 680 m, ♂; Central district, Taşlıçiftlik, 700 m, 10.VII.2013, 14 ♂♂; Central district, Pınarlı, 750 m, 26.VIII.2013, 4 ♂♂; Erbaa, Karayaka, 350 m, 12.VII.2014, ♂; Erbaa, Tepekışla, 230 m, 18.VII.2015, 2 ♀♀, 2 ♂♂; Niksar, Efkerit Valley, 350 m, 21.VI.2013, 2 ♂♂; Niksar, Gökdere, 800 m, 04.VII.2013, ♂; Niksar, Köklüce, 400 m, 04.IV.2015, 2 ♀♀, 3 ♂♂; Reşadiye, Karlıyayla, 1200 m, 28.VII.2017, ♂.

Distribution in Türkiye: It is widespread in all geographical regions [2].

***Sphex funerarius* Gussakovskij, 1934**

Material examined (3 ♀♀, 4 ♂♂): AMASYA: Central district, Sarılar, 1120 m, 01.VII.2013, ♀; **ESKİŞEHİR:** Osmangazi University campus, 830 m, 25.VI.2014, 2 ♂♂; **SİVAS:** Koyulhisar, 1150 m, 13.VII.2017, ♂; **TOKAT:** Erbaa, Tepekışla, 230 m, 03.VI.2017, ♂; Niksar, Köklüce, 400 m, 04.IV.2015, 2 ♀♀.

Distribution in Türkiye: It is distributed in all geographical regions except for Southern Anatolia region [2].

Remark: New record for fauna of Amasya province.

***Sphex pruinosus* Germar, 1817**

Material examined (2 ♀♀, 4 ♂♂): SİVAS: Koyulhisar, 1150 m, 22.VI.2016, ♀; 13.VII.2017, ♂; **TOKAT:** Erbaa, Karayaka, 350 m, 12.VII.2014, ♂; Reşadiye, Karlıyayla, 1200 m, 28.VII.2017, ♀, 2 ♂♂.

Distribution in Türkiye: It is distributed in all geographical regions except for Southern Anatolia region [2].

1. CONCLUSIONS

According to Can & Gülmez [2, 11], the number of Sphecid species occurring in Türkiye is 79. A total of 27 species and material belonging to Sphecidae was presented in this study.

According to this study, *Ammophila heydeni* is recorded for the first time from three provinces: Denizli, Eskişehir and Kocaeli. Also, *Palmodes occitanicus* is newly reported from Amasya and Eskişehir provinces. Tokat province has the highest number of new records with 4 species (*Ammophila hungarica*, *Ammophila pubescens*, *Chalybion omissum* and *Prionyx lividocinctus*) followed by Kars province with 3 species (*Podalonia luffi*, *Prionyx songaricus*, and *Sceliphron spirifex*) and Kırşehir province with 2 species (*Ammophila sabulosa* and *Podalonia fera*). *Sphex funerarius*, *Palmodes strigulosus* and *Ammophila terminata* are new records for Amasya, Çankırı and Sivas provinces respectively.

Our knowledge of sphecid wasps in some parts of Türkiye is still limited. Further faunal investigations are necessary to draw a complete list of Sphecidae species of the country.

ACKNOWLEGMENTS

I would like to thank my colleagues who contributed to the collection of samples. I also thank the anonymous reviewers for all their valuable comments and suggestions which helped me to improve the quality of the manuscript.

REFERENCES

[1] Pulawski, W. J., (2022), Catalog of Sphecidae sensu lato. California Academy of Sciences. (Web page: https://www.calacademy.org/scientists/projects/catalog-of-sphecidae) (Date accessed: June 2022).

[2] Can, İ. and Gülmez, Y., (2021), A faunistic study on the family Sphecidae (Hymenoptera) in the Upper Kelkit Valley with two new records and a checklist for Turkey, Turkish Journal of Entomology, 45(3), 305-322.

[3] Can, İ. and Gülmez, Y., (2019), A new record for the Turkish Sphecidae fauna: *Prionyx radoszkowskyi* (Hymenoptera: Sphecidae), Entomological News, 128(4), 346-350.

[4] Dollfuss, H., (2013a), Revision of the wasps genus *Ammophila* Kirby, 1798 (Hymenoptera: Apoidea: Sphecidae) of the Palearctic region and India, Linzer Biologische Beiträge, 45(1), 383-564.

[5] Dollfuss, H., (2013b), The Ammophilini wasps of the " Biologiezentrum Linz "-Collection in Linz, Austria (part 2) including the genera *Ammophila* Kirby and *Podalonia* Fernald (Hymenoptera, Apoidea, Sphecidae), and description of the hitherto unknown male of *Podalonia erythropus* (F. Smith, 1856), Linzer Biologische Beitrage, 45(1), 565-591.

[6] Dollfuss, H., (2015), The Ammophilini wasps of the "Biologiezentrum Linz"- Collection in Linz, Austria (part 3) including the genera *Ammophila* Kirby, *Eremnophila* Menke, *Eremochares*

JSR A
Journal of Scientific Reports

Gribodo, *Hoplammophila* de Beaumont and *Podalonia* Fernald (Hymenoptera, Apoidea, Sphecidae), Linzer Biologische Beitrage, 47(1), 413-439.

[7] Dollfuss, H., (2016), The Chloriontinae, Sceliphrinae and Sphecinae wasps of the "Biologiezentrum Linz"-Collection in Linz, Austria including the Genera *Chalybion* Dahlbom, *Chlorion* Latreille, *Dynatus* Lepeletier de Saint Fargeau, *Penepodium* Menke, *Podium* Fabricius, Sceliphron Klug, *Stangeella* Menke and *Trigonopsis* Perty (Hymenoptera, Apoidea, Sphecidae) and description of the new species *Chalybion ohli* from Madagascar, Linzer Biologische Beiträge, 48(2), 1149-1185.

[8] Gülmez, Y. and Can, İ., (2015), First record of *Sceliphron (Hensenia) curvatum* (Hymenoptera: Sphecidae) from Turkey with notes on its morphology and biology, North-Western Journal of Zoology, 11(1), 174-177.

[9] Yıldırım, E., Ljubomirov, T., Özbek, H. and Yüksel, M., (2016), New data on Spheciformes fauna (Hymenoptera: Ampulicidae, Sphecidae, Crabronidae) of Turkey, Journal of Insect Biodiversity, 4(3), 1-51.

[10] Kaplan, E. and Yıldırım, E., (2022) The Current Knowledge of Turkey Sphecidae and Mutillidae (Hymenoptera: Aculeata) Fauna, Uluslararası Tarım ve Yaban Hayatı Bilimleri Dergisi 8(1), 53-64.

[11] Kaplan, E. and Yıldırım, E., (2022), The Checklist of Spheciformes (Hymenoptera: Apoidea) in Turkey, Munis Entomology & Zoology, 17 (Supplement), 1779-1791.

Kütahya Dumlupınar University
Institute of Graduate Studies

Journal of Scientific
Reports-A
E-ISSN: 2687-6167
Number 51, December 2022

RESEARCH ARTICLE

COMPARISON of ANALYTICAL and FINITE ELEMENT SOLUTIONS of LOW VELOCITY IMPACT PROBLEM for SIMPLY SUPPORTED BEAM

Yaşar ERBAŞ[1], Bahadır ALYAVUZ[2,*]

[1]Bartın University, Faculty of Engineering, Architecture and Design, Department of Civil Engineering, Bartın, yerbas@bartin.edu.tr, ORCID: 0000-0002-3475-9678
[2]Gazi University, Faculty of Engineering, Department of Civil Engineering, Ankara, balyavuz@gazi.edu.tr, ORCID: 0000-0003-4643-4368

Receive Date:26.07.2022 *Accepted Date: 09.11.2022*

ABSTRACT

The aim of this study is to compare the results obtained from analytical and finite element solutions of low velocity transverse impact problem of a sphere onto simply supported beam. Twelve models with various mass ratios were created by keeping the beam dimensions constant and changing the sphere radius. The effect of the element size in the finite element solution was analyzed with five separate meshes whose element size gradually decreases at the impact point. In the solutions, the deflections of the beam and the displacement of the sphere at the impact point were taken into account. To check the validity of the model, a comparison with an experimental study in the literature was also made. Comparisons show that the deflections obtained from the analytical solution are compatible with the finite element solution within the period of repetitive or continuous contact between the sphere and beam. Particularly, as the mass ratio defined for beam and sphere gets smaller, maximum deflection values obtained from analytical and finite elements become closer. For the cases including sub-impact, after the sphere leaves the beam there exist differences in the results mainly because of the sub-impacts.

Keywords: *Low velocity transverse impact, Analytical solution, Finite element analysis.*

1. INTRODUCTION

Research on the impact problem of beam-type structures helps to understand the behavior of this structural element and to make designs that consider dynamic effects. One of the fundamental problems frequently addressed is the impact of a spherical object in the transverse direction. An early work was done by Cox to find the deflection of a beam impacted by a ball in transverse direction [1]. The problem was considered by Timoshenko [2] in more detail with a theoretical work after the development of local contact deformations theory by Hertz [3].

JSR A
Journal of Scientific Reports

A simple approach for an analytical solution to the problem considers the beam as a massless spring. It is indicated that significant difference between the results obtained with this approach and the experimental results were due to the absence inertial effects of the beam [4]. A procedure that considers the mass of the beam is a completely inelastic impact approach that takes into account that a fraction of the beam mass and the sphere have a common velocity immediately after the impact [4, 5]. In this case, the energy equations are written considering the mass of beam. In case the beam vibrations were considered, the time-varying impact force can be expressed as a nonlinear integral equation by considering displacements and Hertz contact law at the point of impact. This integral equation can be solved by various approximate methods to calculate the maximum contact force and contact duration in case of transverse impact on beam and plate type structures [6]. In these calculations, the operations are time consuming and the integral equation to calculate the impact force can be solved by simplification provided that the beam support type is not effective on the formation of the maximum impact load [7]. An adequate and fast approximate solution for determining the beam deflections as a function of time is the analytical approach that takes into account the free vibrations of the elastic beam where the contact force not need to be calculated [4]. This approach is summarized in the next section.

In addition to analytical methods, two or three-dimensional finite element (FE) models of structural elements are frequently used to investigate the impact behavior in more complex cases including concrete [8], reinforced concrete [9-12], composite [13, 14] beams and slabs. The formation of the impact requires determining partial or complete contact state of the two impacting bodies and their separation over time so that the problem is considered primarily as the contact-impact problem [15-17]. ABAQUS [18], a comprehensive and general-purpose finite element software, is one of the tools that enables such computational simulations for several decades [19-24].

The following studies can be included to evaluate relevant studies on the low velocity impact of a sphere striker on a flexible beam. Considering the impact duration, Pashah et al. proposed a simplified half space approximation to estimate this for elastic and elastic-plastic simply supported beams, and performed 3d finite element analysis in ABAQUS in order to consider the structural effects [25]. They also presented a spring-mass model to take into account the structural response in the simplified analytical approach and indicated the range at which it produced good results based on a period ratio. To obtain a faster solution compared to finite element analysis, Zhang et al. [26] proposed a hybrid numerical-analytical approach for a simply supported elastic-perfectly plastic beam. Among the works which interested in the path of the sphere after the impact, Seifried [27] conducted experimental and numerical research on aluminum beams and noted a chaotic behavior for the coefficient of restitution due to the sub-impacts. The sub-impact phenomenon, repeated contacts between striker and beam after initial contact, was initially mentioned by Timoshenko [2] and Arnold [28]. This was later investigated widely by Qi and Yin using steel beams, and they stated that these repeated contacts were affected by local deformations and global vibrations of the beam [29]. In addition, using LS-DYNA [30], they numerically simulated their experimental work and highlighted factors affecting the duration of repeated impacts and the conditions of the sub-impact formation [31].

JSR A
Journal of Scientific Reports

In the following sections, the analytical formulation given by Goldsmith [4] for the beam deflections that occurred after the initial contact is summarized, the ABAQUS model for the finite element solution is explained and the results obtained from these two solutions are compared respectively.

2. ANALYTICAL a FINITE ELEMENT SOLUTIONS

If the mass of the beam is not negligible compared to the mass of the impacting object, the calculation should be made by taking into account the vibration and local deformation occurring in the beam [32]. Such an elastic impact problem has a more complex solution than the non-elastic impact problem where the beam mass can be neglected. Goldsmith [4], expressed the beam deflections as a series expression, starting from the governing differential equation of the forced vibration problem of the beam. Here, for a transverse impact of a rigid sphere of mass m_2 onto a simply supported beam of length L and mass m_1 with a velocity of v_2 as shown in Fig. 1, the formulation of the equation of the deflections of the beam will be summarized [4]. The analytical model assumes a uniform Euler-Bernoulli beam and a sphere which is attached to the beam after the impact. Impact force is replaced by an initial condition for velocity immediately after the impact. In the analytical and finite element solutions, it is considered that the behavior is linearly elastic and the material is homogeneous and isotropic. No damping is taken into account unless it is specified as in section 2.3.

When one-dimensional transverse impact problem is to be solved based on the beam vibration problem, a solution can be obtained from the following forced vibration differential equation.

$$EI\frac{\partial^4 w}{\partial x^4} + \rho A\frac{\partial^2 w}{\partial t^2} = F\# \tag{1}$$

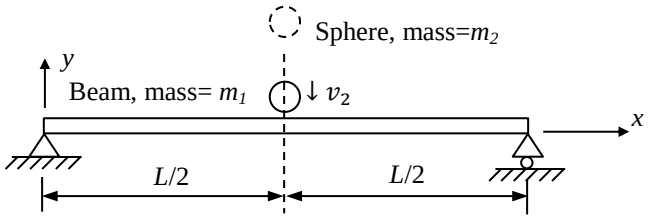

Figure 1. Properties of beam and sphere for transverse central impact.

where, w is the displacement of the beam in the transverse direction, F is a time-dependent force per unit length exerted by the sphere on the beam at contact point. Goldsmith [4] wrote the displacement of the beam as a series summation of the product of two position-dependent and time-dependent discrete functions in the analytical solution that considers vibration as follows,

$$w = \sum_{i=1}^{\infty} X_i(x)q_i(t)\ \# \tag{2}$$

This displacement function must satisfy the differential equation given in Eq. 1. At this point, Goldsmith [4] re-expressed the kinetic and potential energy functions of the beam using the

JSR A
Journal of Scientific Reports

displacement in Eq. 2, and by writing these energy functions into the Lagrangian equation of motion, defined a function for $q_i(t)$.

This function, and therefore the displacement function, involves an unknown forcing function that occurs on the beam at the impact, which changes with time and must be calculated to fully express the displacement. In order to calculate this forcing function, an equation can be written by considering the displacement of the striker and the deflection of the beam at the impact point are equal. But, it is stated that this equation does not have a solution in a closed form and must be solved by a computational method.

Instead of solving the forced vibration problem to obtain an approximate analytical solution of the displacement function, Goldsmith [4] proposed a solution of the beam's free vibration associated with the impulse replaced by a suitable boundary condition. The transverse free vibration equation can be written by setting the forcing function *F* in Eq. 1 equal to zero. Writing Eq. 2 into the transverse free vibration equation yields,

$$EI\sum_{i=1}^{\infty} q_i \frac{\partial^4 X_i}{\partial x^4} + \rho A \sum_{i=1}^{\infty} X_i \frac{\partial^2 q_i}{\partial t^2} = 0\# \tag{3}$$

Each term in the series summation must be equal to zero in order to satisfy the above equation, as follows,

$$a^4 q_i \frac{\partial^4 X_i}{\partial x^4} + X_i \frac{\partial^2 q_i}{\partial t^2} = 0\# \tag{4}$$

where $a^4 \equiv \frac{EI}{\rho A}$. This partial differential equation can be solved by considering,

$$\frac{1}{X_i}\frac{\partial^4 X_i}{\partial x^4} = -\frac{1}{a^4 q_i}\frac{\partial^2 q_i}{\partial t^2} = \xi_i^4\# \tag{5}$$

where ξ_i is an arbitrary constant and there are two separate differential equations. Solving these two differential equations for X_i and q_i, and by writing these two solutions into Eq. 2 yields,

$$w = \sum_{i=1}^{\infty}(A_i sin\xi_i x + B_i cos\xi_i x + C_i sinh\xi_i x + D_i cosh\xi_i x)(E_i sin\omega_i t + F_i cos\omega_i t)\ \# \tag{6}$$

where A_i, B_i, C_i, and D_i are constants to be determined from boundary conditions and E_i, and F_i are constants to be determined from initial conditions. For a simply supported beam, the boundary conditions are given by,

$$w\langle 0,t\rangle = 0;\ \ \frac{\partial^2 w}{\partial x^2}\langle 0,t\rangle = 0;\ \ \frac{\partial w}{\partial x}\langle \frac{L}{2},t\rangle = 0;\ \ EI\frac{\partial^3 w}{\partial x^3}\langle \frac{L}{2},t\rangle = \frac{1}{2}m_2\frac{\partial^3 w}{\partial t^3}\langle \frac{L}{2},t\rangle\ \# \tag{7}$$

JSR A
Journal of Scientific Reports

where displacement, moment at the supports and slope at the mid-span are equal to zero, and shear at the contact point is equal the reversed effective force of the striker. Substitution of first three conditions into Eq.6 with $w\langle x,0\rangle = 0$ yields the displacement function as,

$$w(x,t) = \sum_{i=1}^{\infty} \frac{1}{a^2\xi_i^2} G_i X_i sin\xi_i^2 a^2 t \,\# \tag{8}$$

where $G_i = a^2\xi_i^2 E_i A_i \cos\frac{1}{2}\xi_i L$ is constant, and $X_i = \frac{sin\xi_i x}{\cos\frac{1}{2}\xi_i L} - \frac{sinh\xi_i x}{\cosh\frac{1}{2}\xi_i L}$ is a function of x. Substitution Eq. 8 into the last condition in Eq.7 yields the following characteristic equation,

$$\phi_i(tan\phi_i - tanh\phi_i) = 2M\# \tag{9}$$

where $\phi_i = \frac{1}{2}\xi_i L$ and $M = \frac{m_1}{m_2}$. Solution of this equation gives ϕ_i or its equivalent ξ_i.

In order to determine the unknown constant G_i, the displacement function needs be converted to include the impactor's speed at the time of impact. If the impactor transfers its velocity entirely to the infinitesimal part of the beam at the contact point, momentum of the impactor just before the impact, m_2v_2, should be equal to the sum of the momentum of this part of the beam and the momentum of impactor just after the impact. At $t = 0$, this momentum equality is written as,

$$\int \frac{\partial w}{\partial t}_{(x,t=0)} d\overline{Q} = m_2 v_2 \,\# \tag{10}$$

where $\overline{Q}$ represents total mass of beam and impactor. The left hand side of this equation can also be written in terms of beam mass and impactor mass as,

$$2\int_{x=0}^{x=\frac{L}{2}} \frac{\partial w}{\partial t}\left(\frac{m_1}{L}dx\right) + \frac{\partial w}{\partial t} m_2 \# \tag{11}$$

Taking time derivative of Eq. 8 at $t = 0$ yields,

$$\frac{\partial w}{\partial t} = \sum_{i=1}^{\infty} G_i X_i = \psi \,\# \tag{12}$$

where ψ is velocity of the beam just after the impact as a function of *x*. By multiplying both sides of the above equation with X_j,

$$\sum_{i=1}^{\infty} G_i X_i X_j = \psi X_j \# \tag{13}$$

If Eq. 13 multiplied by m_2 and evaluated at $x = \frac{L}{2}$ is added to the integral of Eq. 13 with respect to the beam mass $dm_1 = \left(\frac{m_1}{L}\right)dx$, the following equation is obtained.

JSR A
Journal of Scientific Reports

$$\sum_{i=1}^{\infty} G_i \left(\frac{2m_1}{L} \int_{x=0}^{x=\frac{L}{2}} X_i \langle x \rangle X_j \langle x \rangle dx \; + X_i \left\langle \frac{L}{2} \right\rangle X_j \left\langle \frac{L}{2} \right\rangle m_2 \right) = \frac{2m_1}{L} \int_{x=0}^{x=\frac{L}{2}} \psi \langle x \rangle X_j \langle x \rangle dx \; + \psi \left\langle \frac{L}{2} \right\rangle X_j \left\langle \frac{L}{2} \right\rangle m_2 \# \quad (14)$$

Integration at left hand side of above equation vanishes when $i \neq j$ which yields G_i as,

$$G_i = \frac{\frac{2m_1}{L} \int_{x=0}^{x=\frac{L}{2}} X_i \psi \langle x \rangle dx + m_2 X_i \langle \frac{L}{2} \rangle \psi \langle \frac{L}{2} \rangle}{\frac{2m_1}{L} \int_{x=0}^{x=\frac{L}{2}} X_i^2 dx + m_2 X_i^2 \langle \frac{L}{2} \rangle} \# \quad (15)$$

As assumed earlier that the impactor transfers its velocity entirely to the infinitesimal part of the beam at the contact point, we may write $\frac{\partial w}{\partial t} = 0$ for $t = 0, x \neq \frac{L}{2}$ and $\frac{\partial w}{\partial t} = v_2$ for $t = 0, x = \frac{L}{2}$ and G_i becomes

$$G_i = \frac{m_2 X_i \langle \frac{L}{2} \rangle v_2}{\frac{2m_1}{L} \int_{x=0}^{x=\frac{L}{2}} X_i^2 dx + m_2 X_i^2 \langle \frac{L}{2} \rangle} = \frac{4v_2}{\phi_i \left(\frac{1}{cos^2 \phi_i} - \frac{1}{\cosh^2 \phi_i} \right) + \frac{2 m_1}{\phi_i m_2}} \# \quad (16)$$

By writing the above equation in Eq. 8 the approximate beam displacement function can be written as follows,

$$w = \frac{L^2 v_2}{a^2} \sum_{i=1}^{\infty} \frac{1}{{\phi_i}^3} \frac{\frac{sin \frac{2\phi_i x}{L}}{cos \phi_i} - \frac{sinh \frac{2\phi_i x}{L}}{cosh \phi_i}}{\frac{1}{cos^2 \phi_i} - \frac{1}{cosh^2 \phi_i} + \frac{2 m_1}{{\phi_i}^2 m_2}} sin \frac{4{\phi_i}^2 a^2 t}{L^2} \# \quad (17)$$

It should be noted that this approximate analytical solution is based on the classical beam theory and neglects the rotational inertia and shear effects.

2.1. The Finite Element Analysis

The following beam geometry and material properties were used to compare the displacements in transverse direction obtained from the analytical solution and finite element model. The beam has a square cross section with the dimensions of 0.01m x 0.01m, and its length is 0.4 m. Mass of the beam is m_1 = 0.314 kg. The beam and striking sphere have the same material properties such that the density is 7850 kg/m^3, the modulus of elasticity is 200 GPa and Poisson's ratio is 0.3. Analysis were carried out for different striker sizes. The velocity of the striker just before the impact is v_2 = 4.63 m/s downward for each case.

Models used in the finite element analysis were created in ABAQUS/Explicit software. Using the symmetry, a quarter geometry was modeled as shown in Fig. 2. Roller support condition was created on the bottom left edge of the beam along *z*-axis. The symmetry boundary conditions were applied on two vertical mid-sections of the beam and the sphere. The sphere was constrained to strike at the midspan and to move along transverse direction (*y*-direction) during the impact.

JSR A
Journal of Scientific Reports

The finite element used in the analysis is C3D8R, which is a linear brick element with reduced integration. This finite element, unlike C3D8, has one integration point and eliminates the possibility of occurrence of locking. The shear locking is a problem for which there exists the formation of shear stresses that should not normally occur, and the elements tend to be too stiff under bending. Similarly, for the volume locking the finite elements behave too stiff during the incompressible or almost incompressible material behavior [18].

General contact algorithm with defaults was used for defining the interaction between beam and sphere. Beam and striking sphere were meshed with the same type of elements. Contact interaction property along the normal direction was hard contact allowing separation after contact. Tangential behavior was implemented as rough friction formulation with no slip on the contacting surfaces.

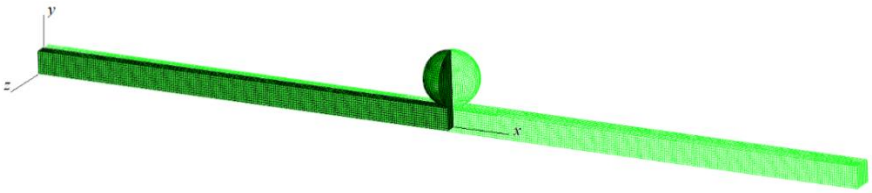

Figure 2. The geometry of quarter model for the beam and striker.

Table 1. The name of models used in the finite element analysis and their properties.

Model	R-50	R-75	R-100	R-125	R-150	R-175	R-200	R-300	R-400
Radius of striker (mm)	5	7.5	10	12.5	15	17.5	20	30	40
Mass ratio, M (m_1/m_2)	76.394	22.635	9.5493	4.8892	2.8294	1.7818	1.1937	0.3537	0.1492

A number of models with different mass ratios were considered, as given in Table 1. The beam dimensions were held constant while changing the radius of striker between the models. These models are shown in Fig. 3. An explicit dynamic analysis was performed in the solution. Time integration with explicit central finite differences can be performed effectively using small time increments. The finite elements solution has been obtained for a period of 16 ms starting from the initial contact which is sufficient to observe the vibrations and the sub-impacts.

Numerical calculations were carried out on a computer with 128GB of ram and 2.2 GHz 32 cores 64 threads dual CPU.

JSR A
Journal of Scientific Reports

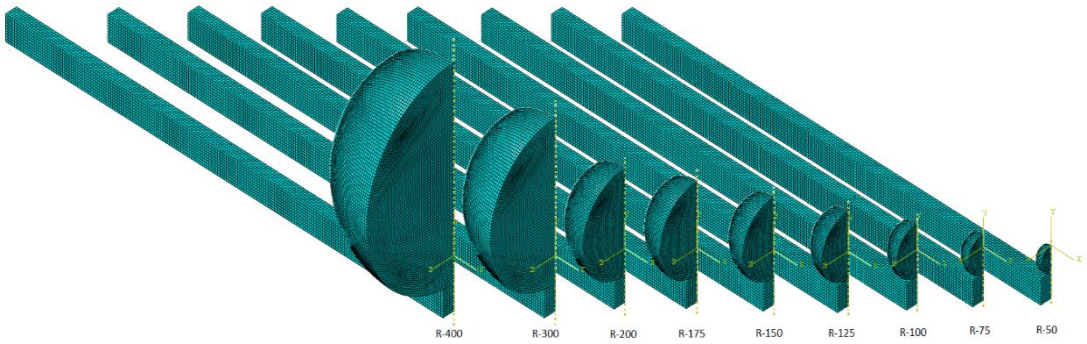

Figure 3. Models considered for the transverse impact between simply supported beam and sphere.

2.2. Mesh Size Analysis

A number of mesh distributions with different element sizes were considered. These mesh distributions are shown in Fig. 4. For each mesh from (a) to (e) in Fig. 4, the smallest element size formed at the impact point is 1 mm, 0.8 mm, 0.5 mm, 0.5 mm and 0.2 mm, respectively. Most of these have uniform element distribution. However, having smaller elements in the mesh, which decreases the "stable time increment" value, with the increase in number of elements prolongs the solution time significantly. Therefore, in order to reduce run time as much as possible, a non-uniform distribution was used for mesh (e). Total number of elements for each mesh is shown in Table 2. The CPU times of the solution range from 100 seconds to 9 hours.

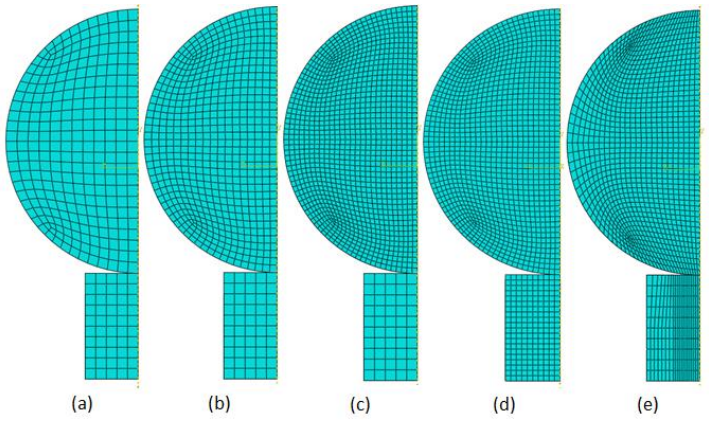

Figure 4. The finite element mesh distributions used for mesh size analysis.

In order to see the effect of element size on the solution, initially, the displacements obtained during the first contact were examined on the model R-125. The initial contact occurs within approximately 0.3 ms. As seen in Fig. 5 (a), the meshes from (a) to (d), present an element penetration occurred at certain amount. The sphere displacements indicated with the dashed lines are below the beam

JSR A
Journal of Scientific Reports

displacements indicated with a solid line, these are the regions where the sphere and beam elements are penetrated at the contact point. Maximum penetration occurred for mesh (a) among these mesh types and this penetration is 0.024 mm occurred at 0.03 ms. During the initial contact, it is observed that element penetration at the contact point is quite small for mesh (e) as shown in Fig. 5 (b) which is 0.002 mm occurred at 0.03 ms.

Table 2. Total number of elements for each mesh.

Radius (mm)	Mesh (a)	Mesh (b)	Mesh (c)	Mesh (d)	Mesh (e)
5	10224	10550	11792	81792	12082
7.5	10744	11792	16048	86048	13434
10	13480	14466	25040	95040	22602
12.5	13480	20192	39120	109120	37090
15	16048	22750	60016	130016	37262
17.5	23568	28496	89072	159072	52228
20	30376	39120	127632	197632	128082
30	60016	109720	389948	459948	390450
40	127632	238640	914932	984932	915222

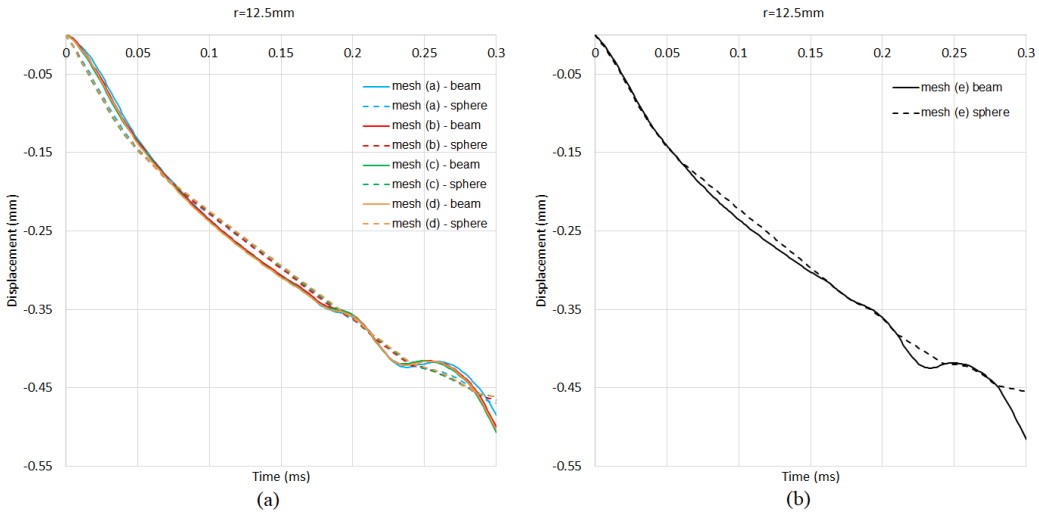

Figure 5. Displacements of the beam and striker during initial contact.

The beam deflections at the impact point and sphere displacements obtained from these meshes after the first contact are shown in Fig. 6. For the models without sub-impacts such as R-50 and R-75, the change in mesh size does not have a significant effect on the displacements of the impact point. For

JSR A
Journal of Scientific Reports

other models, deflections obtained from each mesh are quite similar until the sub-impact. After the sub-impact, an apparent difference is observed in the beam deflections depending on the time of occurrence of the sub-impact between beam and sphere. During the initial contact the mesh size has a slight effect on the contact penetration and the displacements but small changes create a considerable effect on the velocity of the sphere and the time of occurrence of the sub-impact.

2.3. Verification with the Experimental Study

In order to check the validity of the finite element model, a comparison was made with the results of the experimental study of Qi and Yin [29]. The geometric and mechanical properties used for the beam discussed in this section are the same as those used in the experimental study. As in the other numerical analyzes used in this study, the support conditions were chosen as simply supported and numerical analysis was performed using the quarter model. The finite element mesh used in numerical analysis is the mesh specified as mesh (e). Deflections for this problem are also computed using the analytical method and shown in Fig. 7.

The beam has the dimensions of b x h = 60 x 27.8 mm^2 and length of 780 mm. The density of the beam material is 7800 kg/m^3, the modulus of elasticity is 206 GPa and Poisson's ratio is 0.3. Mass of the beam is 10.213 kg. The striking sphere of 35 mm radius has a material density of 7800 kg/m3, the modulus of elasticity is 208 GPa and Poisson's ratio is 0.33. Mass of the striker is 1.4008 kg. The mass ratio M is 7.29.

When the results of the finite element analysis are examined it is seen that the finite element model gives quite similar displacement values for the first two peaks in the displacement-time curve, although there were differences in the contact times of the sphere with the beam as shown in Fig. 7 (a). If the time-displacement graphs of the experimental study are examined, the damping of the beam displacements is clearly observed. At this point, it is possible to obtain results closer to the experimental results by introducing the damping in the finite element model. Accordingly, damping has been defined and the displacement values obtained are shown in Fig. 7 (b).

JSR A
Journal of Scientific Reports

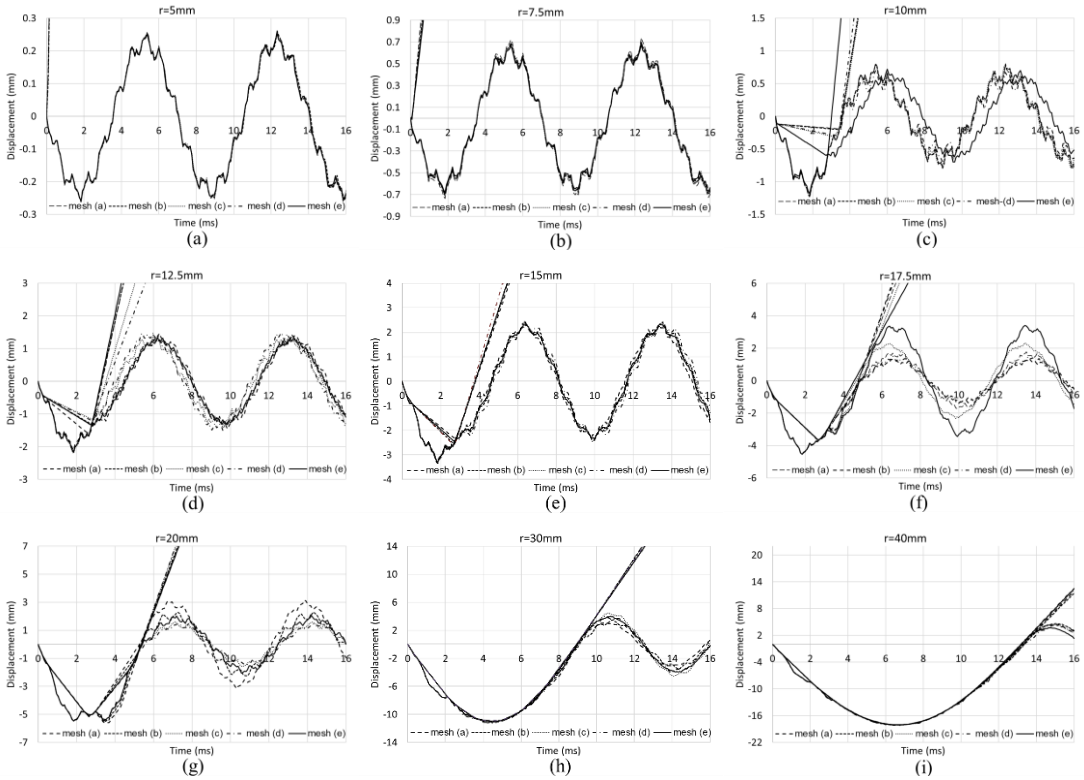

Figure 6. Displacements obtained by the mesh size analysis a) r=5mm, b) r=7.5mm, c) r=10mm, d) r=12.5mm, e) r=15mm, f) r=17.5mm, g) r=20mm, h) r=30mm, i) r=40mm.

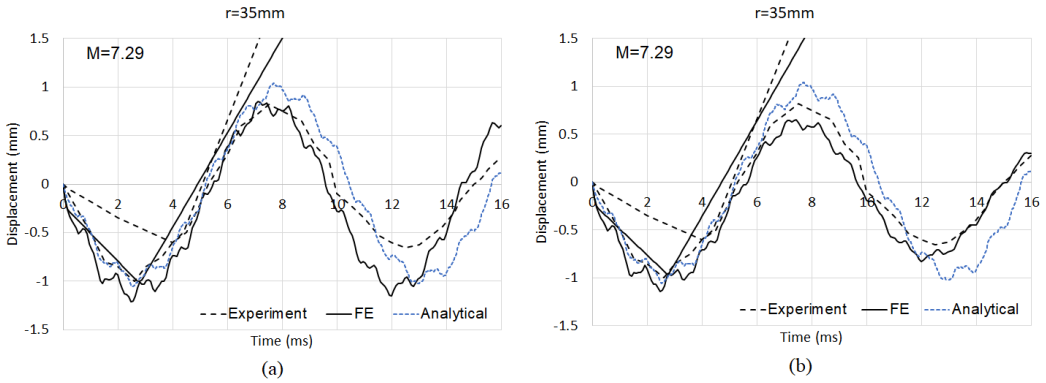

Figure 7. Displacements of the beam and striker a) without damping, b) with damping.

JSR A
Journal of Scientific Reports

2.4. Comparison Between the Analytical Solution and Finite Elements

First seven terms of the series in Eq. 17 were used to determine the deflections of the beam at contact point in the analytical solution. The ϕ_i terms obtained from solution of the Eq. 9 are given in Table 3. In the finite element solution, smallest element sized mesh (e) was used. Comparison of the displacements are shown in Fig. 8.

Period of motion, as the duration between two crests in displacement – time graphs, observed for the analytical and finite element solutions are quite similar in the model with largest mass ratio, but there exists a difference in vibration amplitudes. In models where sub-impact occurs, it is observed that the analytical solution and finite element solution are quite compatible until the sub-impact. The maximum amplitude value after the sub-impact is smaller in finite element solution compared to analytical solution. In models where the mass ratio is very small and the radius of the impacting sphere is large, sub-impacts turn into continuous contact and deflections obtained from the analytical solution and the finite element solution during this stage are very close. For these models as well, after the contact ends, there exists a difference between the amplitude values calculated in the analytical solution and in the finite element solution. The analytical and finite element solutions are more compatible during the time when sphere and beam are in contact.

Table 3. The values of ϕ_i based on mass ratio.

Radius of striker (mm)	Mass of striker (kg)	$\frac{m_1}{m_2}$ ratio	ϕ_1	ϕ_2	ϕ_3	ϕ_4	ϕ_5	ϕ_6	ϕ_7
5	0.00411	76.394	1.5606	4.6827	7.8054	10.929	14.053	17.178	20.304
7.5	0.01387	22.635	1.5379	4.6201	7.7095	10.805	13.906	17.012	20.122
9	0.02397	13.099	1.5159	4.5651	7.6321	10.713	13.805	16.905	20.012
9.35	0.02688	11.6825	1.5098	4.5508	7.6130	10.691	13.782	16.882	19.988
9.6	0.02909	10.7934	1.5053	4.5403	7.5993	10.676	13.766	16.865	19.972
10	0.03288	9.5493	1.4977	4.5232	7.5772	10.652	13.741	16.840	19.948
12.5	0.06422	4.8892	1.4413	4.4110	7.4460	10.517	13.610	16.716	19.830
15	0.1110	2.8294	1.3734	4.3045	7.3400	10.421	13.521	16.638	19.760
17.5	0.1762	1.7818	1.3000	4.2157	7.2631	10.356	13.468	16.590	19.718
20	0.2631	1.1937	1.2264	4.1468	7.2097	10.314	13.433	16.560	19.692
30	0.8878	0.3537	0.9754	4.0076	7.1159	10.244	13.378	16.514	19.653
40	2.104	0.1492	0.8038	3.9629	7.0892	10.224	13.363	16.502	19.643

JSR A
Journal of Scientific Reports

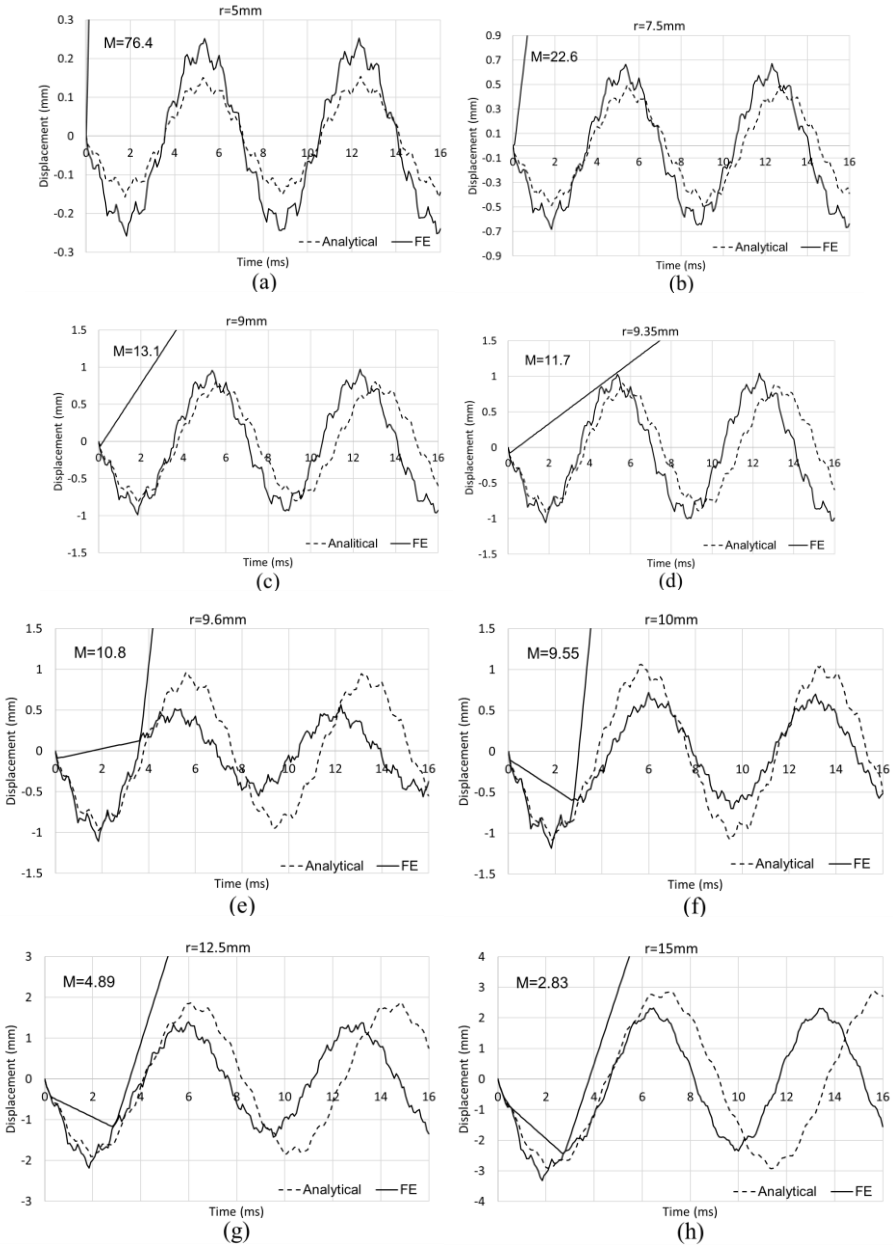

Figure 8. Displacements obtained from analytical solution and finite element solution a) M=76.4 b) M=22.6, c) M=13.1, d) M=11.7, e) M=10.8, f) M=9.55, g) M=4.89, h) M=2.83, i) M=1.78, j) M=1.19, k) M=0.35, l) M=0.15.

JSR A
Journal of Scientific Reports

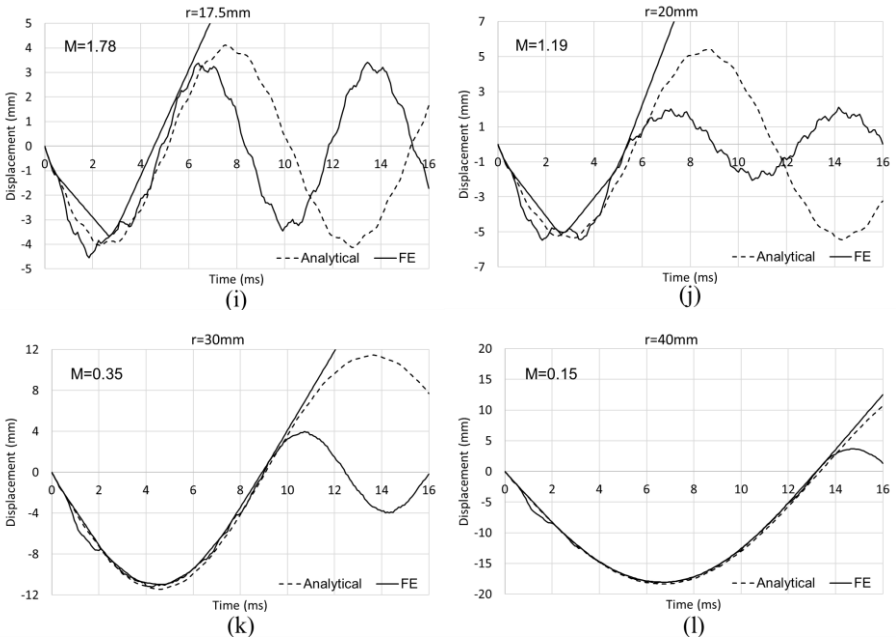

Figure 8. (Cont.) Displacements obtained from analytical solution and finite element solution a) M=76.4 b) M=22.6, c) M=13.1, d) M=11.7, e) M=10.8, f) M=9.55, g) M=4.89, h) M=2.83, i) M=1.78, j) M=1.19, k) M=0.35, l) M=0.15.

2.5. Effect of Sub-impact

If the impacting sphere is small, the period of interaction is very small instant of time which results in a direct separation of beam and sphere. In case of large mass impact onto a slender beam, there exists substantial structural deformations and energy loss to structural vibrations [33]. As the mass ratio decreases, the velocity of the sphere after the initial contact decreases. This results in secondary contacts that occur as the beam continues its motion. From the finite element analysis, it has been observed that sub-impacts occur when the mass ratio is less than 11.6 as shown in Fig. 9. As the mass ratio approaches to 1 the number of sub-impacts increases as shown in Fig. 8 (i) and Fig. 8 (j). As the ratio decreases further repetitive contacts give way to a state of continuous contact as shown in Fig. 8 (k) and Fig. 8 (l) until the sphere leaves the beam.

If a case is created by forcing the sphere to move upward, a finite element analysis can be done without the effect of sub-impacts on the beam motion. This forcing was realized by applying an artificial upward displacement on the sphere after the first contact. The deflection of the impact point on the beam obtained from this analysis is shown in Fig. 10 with dashed lines for a sphere of 10 mm radius and a mass ratio of M = 9.55. In this case, the amplitude value is 1.16 mm. In the actual case, the displacement amplitude after the sub-impact is 0.72 mm. This corresponds to a 38% reduction in

JSR A
Journal of Scientific Reports

the amplitude. Sub-impact causes the point on the beam to displace less and the subsequent amplitude values to continue at

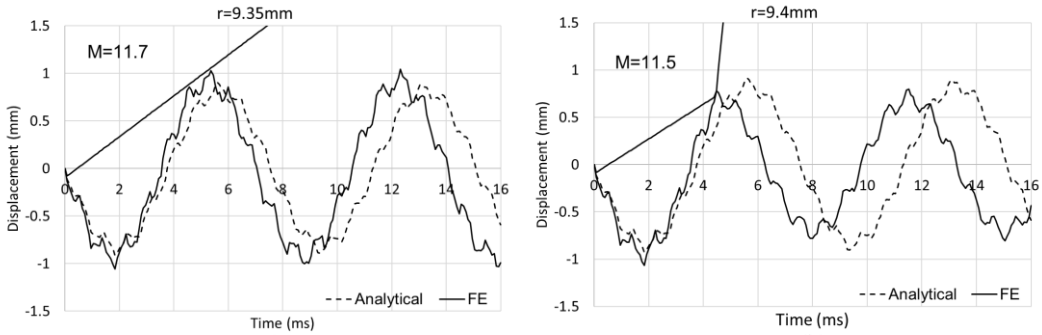

Figure 9. Displacements a) without sub-impact and b) with sub-impact.

this level. Furthermore, period of motion is around 7 ms for both cases. This value is quite close to the natural period, T_n, for the first free vibration mode of a simply supported beam when the mass is spread uniformly over its length. If one calculate the natural period using $T_n = \frac{2}{\pi}\sqrt{\frac{qL^4}{EI}}$ where q is mass per unit length [25], $T_n = 7ms$. The period value occurred around 7 ms in all finite element solutions.

The graph in Fig. 11 (a) shows variation of the maximum deflection of impact point on the beam after the initial contact, with the mass ratio, M. The analytical and finite element solutions yield similar maximum deflection values for the values of M close to 1 or less than 1. In this case, relatively large mass creates a single loading-unloading mechanism as mentioned in [34]. Maximum difference between the deflections obtained from the analytical and finite element solution is 39% which is observed for the largest mass ratio, that is for the smallest impactor mass. The analytical solution underestimates the deflection with respect to finite element solution for small sphere mass. It should be noted that the approximate displacement function is based on Euler-Bernoulli beam theory and it does not consider the actual contact force in the vibration equation. On the other hand, the finite element model is based on a 3d continuum element which does not have the assumptions of Euler-Bernoulli beam theory. Fig. 11 (b) shows the maximum upward deflection of the beam, i.e. the amplitude at the crest of the vibration, and reduction percent of the amplitude because of the sub-impact. The dashed line in the graph indicates the finite element results when the occurrence of sub-impacts is restricted.

JSR A
Journal of Scientific Reports

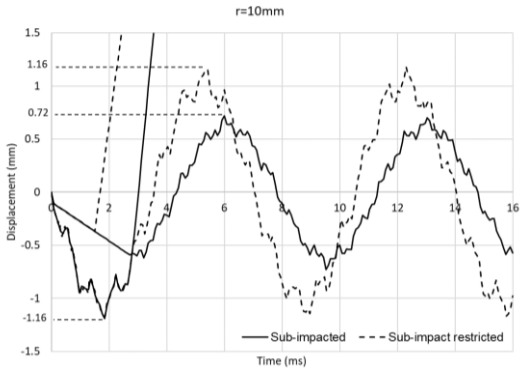

Figure 10. Decrease in the amplitude due to the sub-impact.

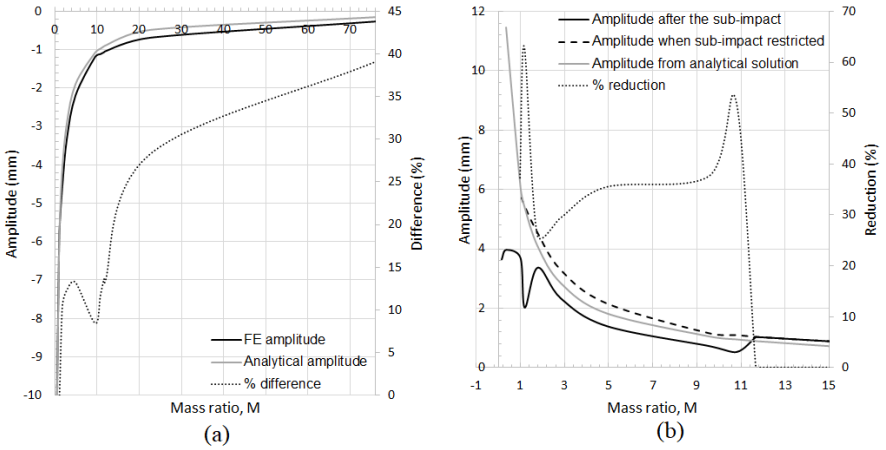

Figure 11. The maximum deflection of impact point (a), the amplitude at the crest of the vibration (b).

3. CONCLUSIONS

In this study, a comparison between the analytical solution and finite element solution was made for the transverse impact problem of a sphere to a simply supported beam. The deflection equation, given by Goldsmith [4], of an elastic beam impacted by a rigid sphere was considered in the analytical solution. Finite element solutions were obtained in ABAQUS for a number of models with different mass ratios and various mesh sizes. Deflections of the beam and displacement of the sphere were calculated at the contact point.

A mesh size analysis was carried out first with various mesh sizes. The deflections of the beam and the sub-impact effects were investigated. First seven term of the series were used in the analytical

JSR A
Journal of Scientific Reports

solution and the smallest element sized mesh was used in the finite element solutions. According to this;

1. Through the mesh size analysis, in models without sub-impacts such as R-50 and R-75 it is observed that, change in the mesh size has no significant effect on the calculated value of the beam deflection. For models with sub-impacts, the mesh size has also no significant effect on the beam deflections until the start of sub-impacts. Change in the mesh size results a slight change in the occurrence time of the sub-impacts. Therefore, amplitude of the vibration obtained from each mesh at the impact point also changes after the sub-impact process.
2. In the model with the largest mass ratio, the analytical solution and finite element solution yield similar vibration periods, but analytical solution underestimates the maximum deflection with respect to the finite element solution.
3. In models with sub-impacts, it is observed that the analytical solution and finite element solution are quite compatible until the sub-impact occurs. However, the finite element solution gives smaller amplitude values compared to the analytical solution after the sub-impact.
4. The sub-impacts are observed for the mass ratio less than a certain value. This value is M=11.6 for the models considered in this study.
5. In models with small mass ratio, sub-impacts turn into continuous contact and during this time period the analytical solution and the finite element solution are in very close agreement. After the contact period ends, a difference has arisen between the analytical solution and the finite element solution for the amplitude values calculated in these models.
6. As the mass ratio decreases, the maximum deflection value becomes more compatible for the analytical solution and the finite element solution. Maximum difference is 39% and the difference is less than 13% for the mass ratio values smaller than M=11.6.
7. As the mass ratio changes, the period of vibration obtained from the analytical solution changes, whereas the period of vibration remains the same in the finite element solution. For the largest mass ratio, the vibration period obtained from analytical solution and the finite element solution are quite close, but as the mass ratio decreases analytical solution gives larger vibration period values compared to finite element solution.

Because the impactor and beam are assumed to remain in contact, the analytical solution does not provide any information about the motion of impactor, the sub-impacts and effect of sub-impacts on displacements. Despite the assumptions made, this method yields maximum deflection values that correlate well with the finite elements especially for small mass ratio, i.e. for large-mass impact onto the beam. As the mass ratio decreases, bending becomes more significant and it prolongs the period of contact. For cases of large mass ratio, M, the period of interaction is very small instant of time so that the contact force has a very short range. Small mass impact is worth further studying. A solution including forcing function F can produce better results especially for small-mass impact.

ACKNOWLEDGMENT

The authors received no specific grant for the research, authorship, and/or publication of this article.

REFERENCES

[1] Cox, H., (1849), On impacts on elastic beams, Cambridge Philosophical Transactions, 9, 73-78.

[2] Timoshenko, S.P., (1913), Zur frage nach der wirkung eines stosses auf einen balken, Zeitschrift für Mathematik und Physik, 62(2), 198-209.

[3] Hertz, H., (1881), Über die berührung fester elastischer körper, Journal für die Reine und Angewandte Mathematik, 92, 156-171.

[4] Goldsmith, W., (2001), Impact the theory and physical behaviour of colliding solids, Dover Publications, New York.

[5] Gültop, T., Yılmaz, M.C., Alyavuz, B., (2015), An analytical investigation of rigid plastic beams under impact loading, Journal of the Faculty of Engineering and Architecture of Gazi University, 30(1), 87-94.

[6] Eringen, A.C., (1952), Transverse impact on beams and plates with arbitrary edge conditions, Naval Research Department Technical Report No 2.

[7] Schwieger, H., (1965), A simple calculation of the transverse impact on beams and its experimental verification, Experimental Mechanics, 5(11), 378-384.

[8] Yılmaz, M.C., Anıl, Ö., Alyavuz, B., Kantar, E., (2014), Load displacement behavior of concrete beam under monotonic static and low velocity impact load, International Journal of Civil Engineering Transaction A: Civil Engineering, 12(4), 88-503.

[9] Anıl, Ö., Kantar, E., Yılmaz, M.C., (2015), Low velocity impact behavior of rc slabs with different support types, Construction and Building Materials, 93, 1078-1088.

[10] Jin, L., Xu, J., Zhang, R., Du, X., (2017), Numerical study on the impact performances of reinforced concrete beams: a mesoscopic simulation method, Engineering Failure Analysis, 80, 141-163.

[11] Othman, H., Marzouk, H., (2017), Finite-element analysis of reinforced concrete plates subjected to repeated impact loads, Journal of Structural Engineering, 143(9), 04017120.

[12] Saatci, S., Vecchio, F.J., (2009), Nonlinear finite element modeling of reinforced concrete structures under impact loads, ACI Structural Journal, 106(5), 717-725.

[13] [Qiao, P., Yang, M., (2007), Impact analysis of fiber reinforced polymer honeycomb composite sandwich beams, Composites Part B: Engineering, 38(5-6), 739-750.

[14] Foo, C.C., Seah, L.K., Chai, G.B., (2008), Low-velocity impact failure of aluminum honeycomb sandwich panels, Composite Structures, 85(1), 20-28.

[15] Hughes, T.J., Taylor, R.L., Sackman, J.L., (1975), Finite element formulation and solution of contact-impact problems in continuum mechanics-IV Report No. UC SESM 76-4, Department of Civil Engineering University of California, Berkeley.

[16] Hughes, T.J.R., Taylor, R.L., Sackman, J.L., Curnier, A., Kanoknukulchai, W., (1976), A finite element method for a class of contact-impact problems, Computer Methods in Applied Mechanics and Engineering, 8(3), 249-276.

[17] [Belytschko, T., Liu, W.K., Moran, B., (2000), Nonlinear finite elements for continua and structures, Wiley, Chichester.

[18] ABAQUS Analysis User's Manual, (2011), Simulia.

[19] Yu, J., Jones, N., (1989), Numerical simulation of a clamped beam under impact loading, Computers and Structures, 32(2), 281-293.

[20] Yu, J., Jones, N., (1997), Numerical simulation of impact loaded steel beams and the failure criteria, International Journal of Solids and Structures, 34(30), 3977-4004.

[21] Li, Q.M., Jones, N., (2002), Response and failure of a double-shear beam subjected to mass impact, International Journal of Solids and Structures, 39(7), 1919-1947.

[22] Al-Thairy, H., Wang, Y.C., (2011), A numerical study of the behaviour and failure modes of axially compressed steel columns subjected to transverse impact, International Journal of Impact Engineering, 38(8-9), 732-744.

[23] Wang, R., Pei, C., (2013), Parametric analysis of dynamic response of hot-rolled h-shaped steel beam under lateral impact load, Gongcheng Lixue/Engineering Mechanics, 30(SUPPL.1), 258-262.

[24] Shi, S., Zhu, L., Yu, T.X., (2019), Dynamic modelling of elastic-plastic beams under impact, International Journal of Impact Engineering, 126, 1-10.

[25] Pashah, S., Massenzio, M., Jacquelin, E., (2008), Prediction of structural response for low velocity impact, International Journal of Impact Engineering, 35(2), 119-132.

[26] Zhang, L., Yin, X., Yang, J., Wang, H., Deng, Q., Yu, B. et al, (2018), Transient impact response analysis of an elastic-plastic beam, Applied Mathematical Modelling, 55, 616-636.

[27] Seifried, R., (2006), Multiple impacts of transversely struck aluminum beams, Proceedings in Applied Mathematics & Mechanics, 6, 333-334.

JSR A
Journal of Scientific Reports

[28] Arnold, R.N., (1937), Impact stresses in a freely supported beam, Proceedings of the Institution of Mechanical Engineers, 137(1), 217-281.

[29] Qi, X., Yin, X., (2016), Experimental studying multi-impact phenomena exhibited during the collision of a sphere onto a steel beam, Advances in Mechanical Engineering, 8(9), 1-16.

[30] LS-DYNA Theory Manual, (2006), Livermore Software Technology Corporation, Livermore.

[31] Qi, X., Yin, X., (2017), Sub-impacts of simply supported beam struck by steel sphere - Part II: Numerical simulations, Advances in Mechanical Engineering, 9(1), 1-11.

[32] Weaver, W., Timoshenko, S.P., Yong, D.H., (1990), Vibration problems in engineering, John Wiley & Sons, New York.

[33] Stronge, W. J., (2000), Impact mechanics, Cambridge University Press, Cambridge.

[34] Olsson, R., (2015), Analytical prediction of damage due to large mass impact on thin ply composites, Composites: Part A, 72, 184-191.

Kütahya Dumlupınar University
Institute of Graduate Studies

Journal of Scientific
Reports-A
E-ISSN: 2687-6167
Number 51, December 2022

RESEARCH ARTICLE

INVESTIGATION of the ADHESION PROPERTIES and STRENGTH of HOT MIX ASPHALT EXPOSED to SEA WATER

Mehmet SALTAN[1], Öznur KARADAĞ[2,*], Gizem KAÇAROĞLU[3]

[1]Süleyman Demirel University, Engineering Faculty, Department of Civil Engineering, Isparta, mehmetsaltan@sdu.edu.tr
ORCID: 0000-0001-6221-4918
[2*]Süleyman Demirel University, Engineering Faculty, Department of Civil Engineering, Isparta, oznurkaradag92@gmail.com
ORCID: 0000-0003-0755-5626
[3]Süleyman Demirel University, Engineering Faculty, Department of Civil Engineering, Isparta, gizemkacaroglu07@gmail.com
ORCID: 0000-0002-5734-7131

Receive Date:20.06.2022 *Accepted Date: 08.11.2022*

ABSTRACT

The presence of water on pavement causes loss of strength and moisture damage. Therefore, cracks and stripping occur on pavement over time. Pavements in the provinces on the Aegean and Mediterranean coasts are exposed to salty water as a result of overflow of sea due to atmospheric conditions in winter. For example, if wind blows towards the land, water level in sea rises and floods the land. In this study, effects of the Aegean and Mediterranean Sea waters which have different salinity rates on hot mix asphalt were investigated. Both stripping (Nicholson, California and Texas Boiling) and adhesion (Vialit) tests were carried out in order to evaluate the adhesion between aggregates and bitumen in samples which were exposed to Aegean and Mediterranean Sea waters which have different salinity rates. According to the test results, it was observed that the adhesion between aggregates and bitumen decreased with the increase in salinity. The unconditioned indirect tensile strengths of the hot mix asphalt exposed to pure water, Aegean Sea water and Mediterranean Sea water were determined as 798, 730 and 687 kPa respectively, while the conditioned indirect tensile strengths were determined as 725, 478 and 438 kPa. Also, the tensile strength ratios of hot mix asphalt conditioned with pure water, Aegean and Mediterranean Sea water were determined as %91, %68 and %60 respectively. The tensile strength ratios of the samples conditioned with the Aegean Sea and Mediterranean Sea waters have not met the specification limit value. It has been determined that Aegean and Mediterranean Sea waters which have different salinity rates damage to hot mix asphalt. Therefore, it is suggested that, certain features of pavements which built near the seaside should be improved. In literature, effect of solutions formed from the components of sea water on samples prepared in laboratory has been examined, but natural sea water has not been used on samples directly. This circumstance shows the originality of study.

Keywords: *Superpave, Sea water, Hot mix asphalt, Indirect tensile strength, Moisture susceptibility*

JSR A
Journal of Scientific Reports

1. INTRODUCTION

The presence of water on pavements causes loss of strength and moisture damages. Moisture damage which occurred in asphalt mixtures can be affected by many factors. These are properties of aggregates and bitumen, mixture design and construction (air void ratio, asphalt film thickness, permeability), environmental factors (temperature, life of pavement, freeze-thaw cycles), traffic conditions and the type and properties of materials added to the asphalt mixture [1]. The usage of anti-stripping additives is the most common method which is used to reduce moisture damage of asphalt mixtures. Nano materials (nano ZnO, nano TiO2) were used to increase the resistance to moisture damage of hot mix asphalt (HMA) [2-3]. Also, Surface Free Energy (SFE) method has been used to evaluate the adhesion formed between bituminous binder and aggregates which are coated with polyvinyl chloride in order to reduce moisture sensitivity of asphalt mixtures [4].

While the presence of water on the pavement is a problem on its own, freezing of this water due to atmospheric conditions creates bigger problems. Different anti-icing materials [5] and methods are used to prevent icing on the surface of pavement. The purpose of taking precautions like this is to reduce dangerous driving conditions and to melt the ice formed on the surface of pavement. Salt and calcium-acetate are widely used as de-icer materials. De-icing salts are caused various problems such as environmental pollution, early degradation of asphalt mixture and tire wear. De-icing salts are reduced the freezing temperature of liquids that cause significant hydraulic pressure in asphalt pores. The presence of anti-icing materials on the surface of pavement in the freeze-thaw cycle cause adverse effects on the pavement. It has been stated that in the case of presence of anti-icing chemicals and water flow on the pavement surface, the water flow increases the harmful effects of the chemicals and causes serious stripping during the freeze-thaw cycle [6]. In the winter months, sand-salt mixture is used to prevent freezing which occurs on the pavement. With the melting of the snow or ice, the salt water solution starts to damage to the pavement. Depending on the type and density of the salt, the damage caused by the salt to the pavement varies. For this reason, the effects of salt on the asphalt mixture have been investigated using three tidal waters with different chemical components. Chemical components in tidal waters alone have not caused excessive damage to the pavement. However, a combination and interaction of chemical compounds have had more damage to the pavement [7].

On Egyptian highways, because of the leakage of water between aggregates and bitumen, deteriorations such as stripping and ravelling are observed. Consequently, performance and service life of the pavement are reduced. Asphalt pavements in Egypt are often exposed to sea water and tap water. Therefore, asphalt mixtures prepared in the laboratory have been conditioned with both sea water and tap water, and the strengths and tensile strength ratios (TSR) of the mixtures were examined [8]. Since Bangladesh is a country surrounded by rivers, it may encounter natural disasters such as floods, hurricanes and tides. When these natural disasters occur, the pavement will be exposed mostly to salt water-containing sea waters. It has been known that pavements are affected by sea waters with different salt ratios. For this reason, the effects of salt on bituminous binder and HMA have been examined. It has been seen that, sea water also has indicated an effect exactly like de-icing salts or a sand-salt mixture. The limit value of salt has been determined for HMA samples. As the salt content of bitumen increases, the strength of the mixtures has decreased. For bituminous mixtures, the limit value of salt has been determined as 4%. It has been known that, salts are obtained from sea water or

JSR A
Journal of Scientific Reports

rock beds [9]. In order to increase the performance of asphalt mixtures exposed to sea water, low density polyethylene (LDPE) plastic waste was added in different ratios (1%, 2%, 3%, 4% and 5%) to mixtures. With the use of LDPE in the asphalt mixtures, it is aimed that reducing the waste materials and increasing of the performance of asphalt mixtures. In Marshall Test, it was explained that, even if exposure to sea water, asphalt mixtures containing LDPE improved some properties compared to reference asphalt mixtures [10]. The durability of asphalt mixtures due to tidal floods in the coastal areas are negatively affected. In order to increase the durability and life of asphalt mixtures which are exposed to tidal flood water, crumb rubber has been added to the asphalt mixtures. It has been stated that the skid resistance of asphalt mixtures containing crumb rubber increases [11].

Molten salts that affect the salinity of sea waters are chlorine, sodium, sulphates, magnesium, calcium, potassium bicarbonate and bromine, respectively. These known elements are found in sea waters. Recently, the salinity of sea water is determined with electrical conductivity measurement which is more practical and reliable [12]. Salt (sodium chloride, NACI) was added to the water by weight based on the amount of salt in the Cantabrian Sea (3.5%). Before preparing the asphalt mixtures, the aggregates to be used in the mixture were submerged in salt water. Different test results (Indirect Tensile Strength (ITS), Water Sensitivity (ITSR), Wheel Tracking Test and Cantabro Loss Particle Test) which are occurred on asphalt mixtures show that the properties of the asphalt mixtures adversely affected [13]. In the present study, the properties of asphalt mixtures (ITS, TSR) which were exposed to Aegean and Mediterranean Sea waters which has salinity of 23% and 38% respectively in our country, were investigated. In addition, the adhesion of mixtures (Nicholson and California Stripping, Vialit and Texas Boiling tests) conditioned with sea water which has different salinity ratios between aggregates and bitumen was evaluated.

2. MATERIALS and METHODS

2.1. Materials

2.1.1. Aggregates

The limestone aggregates were used in current study. Specific bulk gravity (TS EN 1097-6), water absorption, Los Angeles (ASTM C 131-03) and micro-deval abrasion tests (TS EN 1097-1) were performed on limestone aggregates. Test results of these tests can be seen in Table 1.

Table 1. Physical characteristics of aggregates.

Properties	**Coarse aggregates**	**Fine aggregates**	**Filler**
Specific gravity (g/cm^3)	2.701	2.606	2.501
Los Angeles wear loss (%)	18.48	-	-
Micro-Deval wear loss (%)	9.95	-	-

2.1.2. Bitumen

Bitumen which was used in current study has 50/70 penetration grade. Results of conventional tests which were applied on the bitumen are given in Table 2.

JSR A
Journal of Scientific Reports

Table 2. Characteristics of bitumen.

Test	50/70 Bitumen	Standard
Penetration (25˚C)	54	TS EN 1426
Softening point	49.8	TS EN 1427
Ductility (5cm/min)	>100	TS EN 13589
Specific gravity (g/cm^3)	1.021	TS EN 15326+A1

2.1.3. Aegean sea and mediterranean sea waters

Sea water may overflow to land due to atmospheric conditions (wind, rain, storm, tide, etc.) in the winter. This situation is also experienced in our provinces close to the Aegean Sea and Mediterranean Sea (Figure 1). In this study, the effects of sea waters with different salinity ratios on HMA was studied. In our country, salinity ratios of these sea waters are known as 23‰ and 38‰, respectively. Samples which prepared in the laboratory were exposed to Aegean Sea and Mediterranean Sea waters.

Figure 1. Flooding of sea water in İzmir and Antalya provinces.

2.2. Methods

2.2.1. Adhesion and stripping tests

The presence of water in the HMA causes a decrease in the adhesion between aggregates and bitumen. Over time, cracks and stripping occur in HMA. In this study, the effects of the Aegean Sea and Mediterranean Sea waters which have different salinity ratios on stripping behaviours and adhesion between aggregates and bitumen were investigated with the Nicholson and California Stripping, Vialit and Texas Boiling tests.

Stripping tests are implemented to determine the resistance of pavements to negative effects of water and traffic. According to this, Nicholson and California stripping tests was performed using both pure water and Aegean Sea and Mediterranean Sea waters.

Vialit is known as a test that performed to determination of the level of decreases in the adhesion between aggregates and bitumen with the effect of water. So, this method was also used to

JSR A
Journal of Scientific Reports

investigation of the effects of sea waters on adhesion properties of pavements in current study. In addition to Vialit, Texas Boiling test was also conducted to examine the effects of boiling action of water on the adhesion between aggregates and bitumen. 250 gr aggregate samples are prepared with the fractions of 8/11.2 mm. Loose asphalt mixture is obtained by adding bitumen up to 3% the weight of the prepared aggregate sample. Loose asphalt mixture which has temperature of 85-100 ℃ is added to 500 ml of boiling distilled water and it is allowed to boil for 10 minutes. After the test period is completed, the aggregates are placed on towel paper. Then, aggregates which covered with bitumen are determined observationally.

2.2.2. Superpave volumetric mix design

Superpave is a performance–based method which was developed for determining the properties of asphalt binders and aggregates, designing asphalt mixes and analysing pavement performance. This method includes tests which are taken into account the specifications of aggregate and asphalt binders to design the hot mix asphalt and analyse performance of HMA. It is commonly used for obtaining a well-performing mix. To obtain a well-performing mixture, in terms of Superpave process, selection of materials and volumetric proportioning of them are important. The four steps which are taken into consideration in testing and analysis process for Superpave method are;

- selection of materials (aggregate, binder, modifiers),
- selection of a design aggregate structure,
- selection of a design asphalt binder content,
- evaluation of moisture susceptibility of the design mixture.

The temperature values and traffic volume of region where the asphalt pavement will be constructed are also important in this method. To properly consider mix design, design ESALs of 20-years are always used. Voids in mineral aggregate (WMA) which is affected by both the aggregate gradation and the properties of aggregates, voids filled with asphalt (VFA) limit values and 4% air void are taken into consideration on calculation the optimum bitumen content (FHWA, 2000; FHWA, 2001).

2.2.3. Indirect tensile strength

The adhesion which is formed between aggregates and asphalt binder is known as a property that affects pavement performance. The presence of moisture between asphalt binder and aggregates causes loss of bonding and stripping. Therefore, Superpave volumetric mix design determines whether the mixture which is consisted of asphalt binder and aggregates is sensitive to moisture. Indirect tensile strength (ITS) test is used in determination of the moisture susceptibility of the unconditioned and conditioned mixtures in accordance with AASHTO T-283 standard. The mixtures which were prepared by considering optimum bitumen content are compacted with Superpave gyratory compactor.

The ITS values of cylindrical samples are determined with the Eq. 1 given below. Afterwards, for all samples, unconditioned (ITSdry), conditioned (ITSwet) values are saved and the Eq. 2 is used for the calculation of TSR values. The minimum limit for the TSR value is 80%. It means that mixtures with a value of less than 80% will exhibit a stripping problem after construction (FHWA, 2000).

JSR A
Journal of Scientific Reports

$$S_t = \frac{2P}{\pi t D} \quad (1)$$

Where St, tensile strength; P maximum load; t, sample thickness and D, sample diameter.

$$\text{TSR} = \frac{ITS_{wet}}{ITS_{dry}} \quad (2)$$

Where TSR, tensile strength ratio; ITSwet, average tensile strength of conditioned specimen; ITSdry, average tensile strength of unconditioned specimen.

3. RESULTS

3.1. Results of Adhesion and Stripping Tests

The Nicholson stripping test, the percentage of aggregates remaining without stripping in the samples exposed to pure water, Aegean and Mediterranean Sea waters was determined as 81, 78 and 3, respectively. In addition, the California stripping test the percentage of aggregates remaining without stripping in the samples exposed to pure water, Aegean and Mediterranean Sea waters was determined as 94, 92 and 86, respectively (Figure 2).

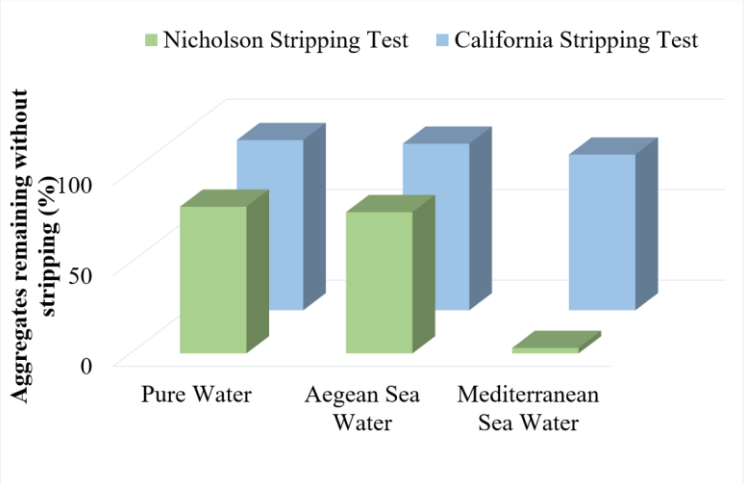

Figure 2. Results of Nicholson and California stripping tests.

In the Nicholson test, it was observed that almost all of aggregates exposed to Mediterranean Sea water were stripped (Figure 3). It can be seen that, number of aggregates remaining without stripping have not met the specification limit value of 60%. Mediterranean Sea water which has high salinity rate has reduced the adhesion between aggregates and bitumen. Measures against stripping (such as anti-stripping additives) should be taken in HMA which exposed to Mediterranean Sea water.

JSR A
Journal of Scientific Reports

Figure 3. Nicholson samples which conditioned with Mediterranean Sea.

As for the California stripping test, the percentage of aggregates remaining without stripping meets the specification limit value of 60%. Since Mediterranean Sea water has a higher salinity than Aegean Sea water, it has been observed that more aggregates were stripped. According to the obtained results, the salinity of sea water affects the adhesion between aggregates and bitumen. This result can be supported with a similar study which stated that waters with high acidity such as sea water negatively affect the adhesion between aggregates and bitumen because accelerate oxidation of asphalt [16]. Sea water affects the adhesion between aggregates and bitumen by facilitating the molecular migrations of bitumen components and weakening the agglomeration of asphaltene [17]. Thus, HMA which exposed to sea water must be resistant to stripping.

When the graph which is given in Figure 4 was examined, while the number of aggregates falling from the sample exposed to pure water was 3%, the number of aggregates falling from the samples exposed to Aegean and Mediterranean Sea waters which has different salinity ratios was determined as 4% and 6%, respectively. According to the obtained results, the adhesion between aggregates and bitumen was affected negatively in samples exposed to Aegean Sea and Mediterranean Sea waters which has different salinity ratios.

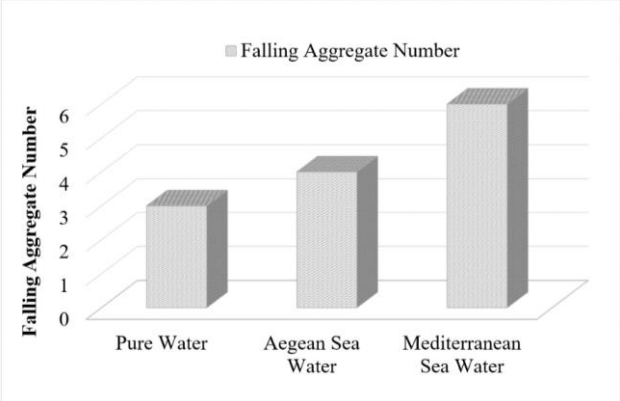

Figure 4. Vialit test results.

JSR A
Journal of Scientific Reports

In the Texas Boiling test, the number of aggregates covered with bitumen was 31% when conditioned with pure water, while the number of aggregates covered with bitumen was determined as 21% and 17%, respectively, when conditioned with Aegean and Mediterranean Sea waters (Figure 5). When the graph which is given in Figure 5 was examined, it was observed that sea waters which have different salinity ratios affect the adhesion between aggregates and bitumen. Since Mediterranean Sea water is saltier, the number of aggregates which covered with bitumen is the least. It has been observed that the adhesion between aggregates and bitumen decreases with increasing of salinity ratio in water. In addition, it can be seen that the results of the adhesion and stripping tests which performed in this study are consistent.

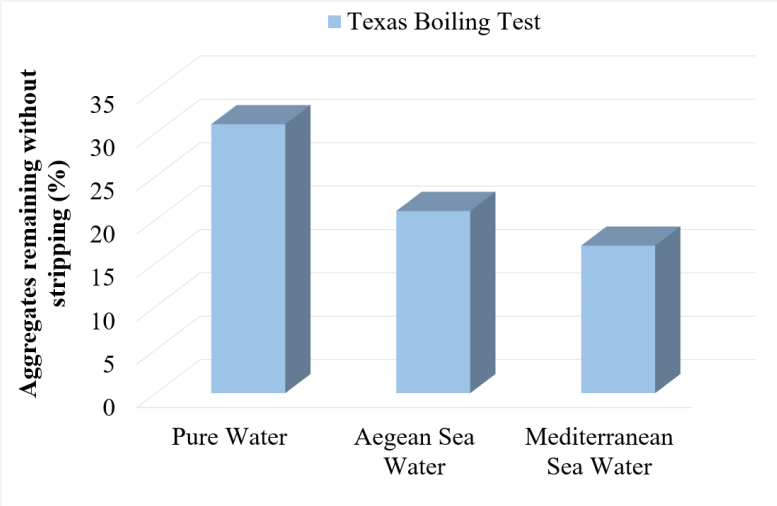

Figure 5. Texas boiling test results.

3.2. Optimum Bitumen Content

In order to determine the optimum bitumen content, mixtures were prepared by using bitumen at the rates of 4.5%, 5%, 5.5%, 6% and the compaction of them was provided with gyratory compactor. Initially, the bitumen content which corresponds to 4% air void was determined from the air void graph. Then, it was checked whether the determined bitumen content has provided the requirements of VMA and VFA. After these steps, the optimum content of bitumen for reference bitumen was determined as 5.20%. Obtained results are given in Figure 6.

JSR A
Journal of Scientific Reports

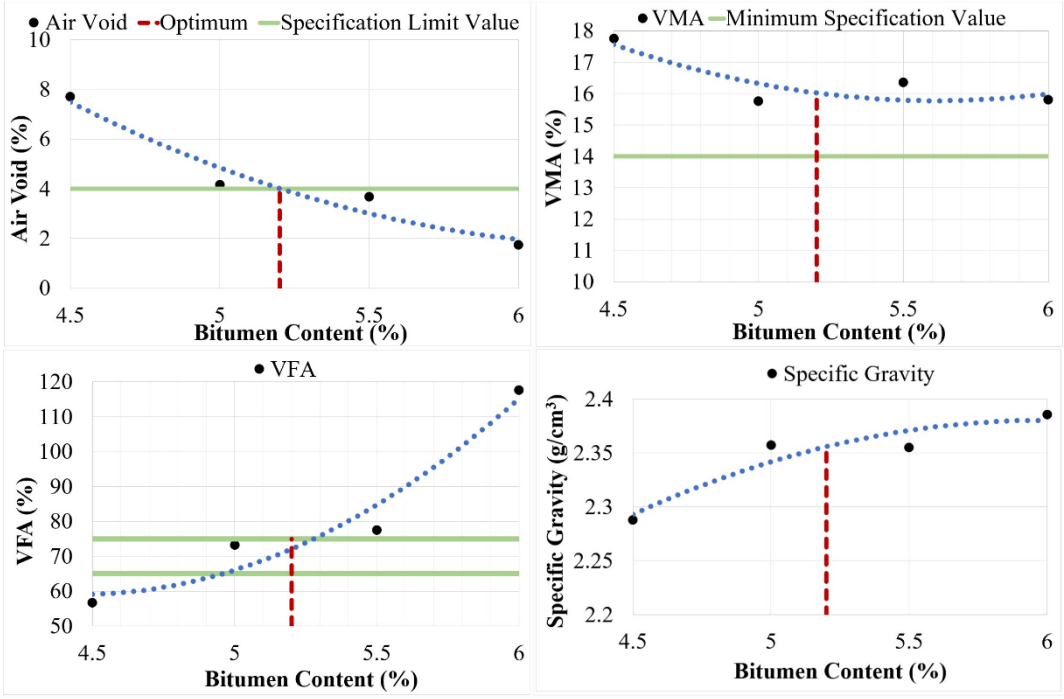

Figure 6. Graphs of reference bitumen.

3.3. Evaluation of Moisture Susceptibility

So as to evaluate the moisture susceptibility, ITS test was performed on the mixtures which were prepared by using determined optimum bitumen content. Unconditioned and conditioned ITS and TSR values were found for samples tested with Aegean Sea, Mediterranean Sea waters and pure water. The unconditioned indirect tensile strengths of the hot mix asphalt exposed to pure water, Aegean Sea water and Mediterranean Sea water were determined as 798, 730 and 687 kPa respectively, while the conditioned indirect tensile strengths were determined as 725, 478 and 438 kPa. Also, the tensile strength ratios of hot mix asphalt conditioned with pure water, Aegean and Mediterranean Sea water were determined as %91, %68 and %60 respectively (Figure 7-8).

JSR A
Journal of Scientific Reports

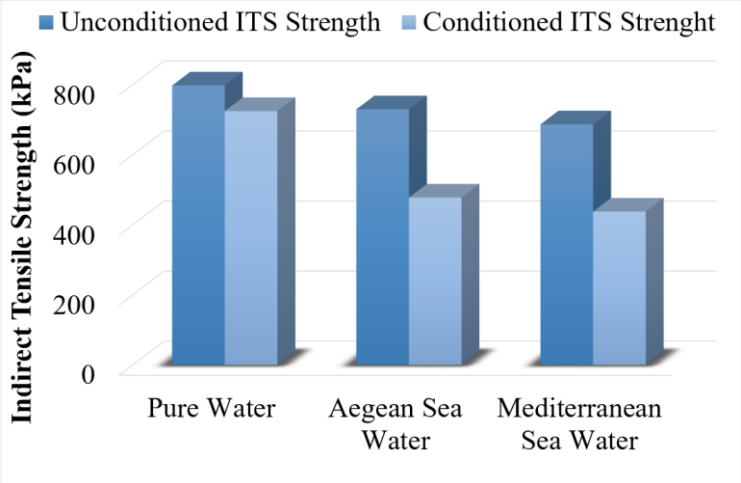

Figure 7. ITS results of samples.

When the graph given in Figure 7 is examined, it can be seen that the samples conditioned with pure water provides better strength than the samples which conditioned with Aegean Sea and Mediterranean Sea waters. In addition, the strength of the samples conditioned with Mediterranean Sea water which is saltier than Aegean Sea water is less. The salinity of sea water also affects the strength of the samples which were prepared by the Superpave method. This result can be supported with a similar study which stated that concrete samples exposed to the magnesium sulphate and sea water for certain periods decrease their strength [18]. In the light of the obtained results, it is observed that sea water reduces the stripping resistance and unconditioned and conditioned tensile strengths of HMA.

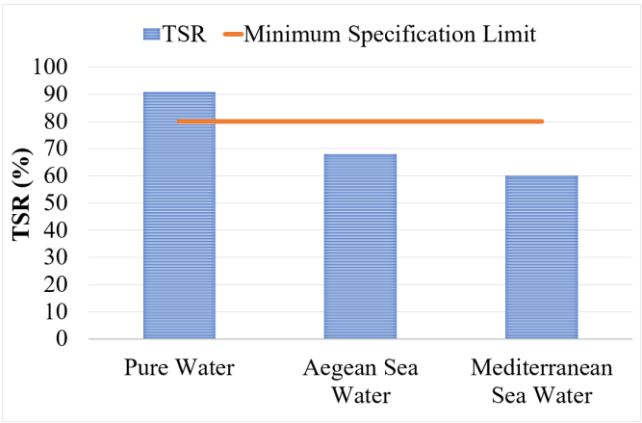

Figure 8. TSR results of samples.

JSR A
Journal of Scientific Reports

When Figure 8 was examined, it can be seen that the TSR values of the samples conditioned with the Aegean Sea and Mediterranean Sea waters have not met the specification limit value. Samples conditioned with sea waters increased moisture susceptibility compared to samples conditioned with pure water. The ITS values and moisture susceptibility of the samples conditioned with sea waters which have different salinity rates have decreased and increased, respectively. According to the obtained results, it can be said that sea water affects negatively the properties of HMA. Therefore, necessary measures should be taken to increase the stripping resistance and strength of the pavement that will be exposed to sea water.

In this study, it was exhibited that the stripping resistance, unconditioned and conditioned ITS values of HMA which conditioned with sea waters which have different salinity ratios have decreased. Also, according to tensile strength values, moisture susceptibility of samples exposed to sea waters have increased (Table 3).

Table 3. The results of hot mix asphalt exposed to sea water.

RESULTS OF HOT MIX ASPHALT EXPOSED TO SEA WATER							
Water Types	**Adhesion and Stripping Tests**				**Indirect Tensile Strength (ITS) Tests**		
	Nicholson Stripping	**California Stripping**	**Texas Boiling**	**Vialit Test**	**Unconditioned ITS (kPa)**	**Conditioned ITS (kPa)**	**TSR (%)**
	Aggregates remaining without stripping (%)			Falling aggregates number (%)			
Pure Water	81	94	32	3	798	725	91
Aegean Sea Water	78	92	21	4	730	478	68
Mediterranean Sea Water	3	86	17	6	687	438	60

4. CONCLUSION

The presence of water on the pavement decreases the adhesion between aggregates and bitumen, and correspondingly, cracks and stripping occur over time. Sea waters can overflow to land due to atmospheric conditions such as rain, wind, storm and tide etc. However, no study has been conducted on how the pavement is affected in the presence of sea water on it in our country. In this study, certain properties of HMA were investigated using natural Aegean Sea and Mediterranean Sea waters. The obtained results are as follows:

• Stripping tests were carried out to examine how the Aegean Sea and Mediterranean Sea waters with different salinity ratios affect the adhesion between aggregates and bitumen. The Nicholson stripping test, the percentage of aggregates remaining without stripping in the samples exposed to pure water,

Aegean and Mediterranean Sea waters was determined as 81, 78 and 3, respectively. It was observed that, aggregates exposed to Mediterranean Sea water which is saltier than Aegean Sea water were stripped approximately 100% in the Nicholson stripping test. In the California stripping test, it has seen that the percentage of aggregates remaining without stripping in the samples exposed to pure water, Aegean and Mediterranean Sea waters was determined as 94, 92 and 86, respectively. According to the obtained results, it can be said that, sea water has reduced adhesion between aggregates and bitumen.

• In the Vialit test, while the number of aggregates falling from the sample exposed to pure water was 3%, the number of aggregates falling from the samples exposed to Aegean and Mediterranean Sea waters which has different salinity ratios was determined as 4% and 6%, respectively. According to the obtained results, the adhesion between aggregates and bitumen was affected negatively in samples exposed to Aegean Sea and Mediterranean Sea water which has different salinity ratios. In the Texas Boiling test, it was observed that sea waters which have different salinity ratios affect the adhesion between aggregates and bitumen. Since Mediterranean Sea water is saltier, the number of aggregates which covered with bitumen is the least.

• The unconditioned indirect tensile strengths of the hot mix asphalt exposed to pure water, Aegean Sea water and Mediterranean Sea water were determined as 798, 730 and 687 kPa respectively, while the conditioned indirect tensile strengths were determined as 725, 478 and 438 kPa. According to the obtained results, samples conditioned with Mediterranean Sea water have put up less strength than samples conditioned with Aegean Sea water. The reason for this is that, the salinity of Mediterranean Sea water is higher than that of Aegean Sea water.

• The tensile strength ratios of hot mix asphalt conditioned with pure water, Aegean and Mediterranean Sea water were determined as %91, %68 and %60 respectively. The TSR values of the samples conditioned with the Aegean Sea and Mediterranean Sea waters have not met the specification limit value. Samples conditioned with sea waters increased moisture susceptibility compared to samples conditioned with pure water.

ACKNOWLEDGEMENT

This research received no financial supports from any funding agency in public, commercial or non-profit sectors.

REFERENCES

[1] Amini, B., Tehrani, S.S., (2014), Simultaneous effects of salted water and water flow on asphalt concrete pavement deterioratiob under freeze-thaw cycles, International Journal of Pavement Engineering, 15(5), 383-391.

[2] Azarhoosh, A., Moghaddas Nejad, F., Khodaii, A., (2018), Evaluation of the effect of nano-TiO_2 on the adhesion between aggregate and asphalt binder in hot mix asphalt, European Journal of Environmental and Civil Engineering, 22(8), 946-961.

[3] Behiry, A. E. A. E. M., (2013), Laboratory evaluation of resistance to moisture damage in asphalt mixtures, Ain Shams Engineering Journal, 4(3), 351-363.

[4] Can, M., Etemoğlu, A. B., Avcı, A., (2002), Atıf analizi: Deniz suyundan tatlı su eldesinin teknik ve ekonomik analizi [Citation analysis: Technical and economical analysis of desalination processes], Uludağ Üniversitesi Mühendislik-Mimarlık Fakültesi Dergisi, 7(1), 147-160.

[5] Hamedi, G. H., (2018), Effects of polymeric coating the aggregate surface on reducing moisture sensitivity of asphalt mixtures, International Journal of Civil Engineering, 16(9), 1097-1107.

[6] Hamedi, G. H., Nejad, F. M., Oveisi, K., (2016), Estimating the moisture damage of asphalt mixture modified with nano zinc oxide, Materials and Structures, 49(4), 1165-1174.

[7] Kakisina, E. M., Makmur, A., Salim, F. D., (2019), Influence of LDPE plastic waste on asphalt mixture soaked in sea water, IOP Conference Series: Earth and Environmental Science, 19-20, Johor, Malaysia.

[8] Li, F. and Wang, Z., (2012), Experiment on road performance of asphalt mixture with automatic long-term snowmelt agent, Journal of Highway and Transportation Research and Development (English Edition), 6(4), 11-17.

[9] Özen, H., (2011), Rutting evaluation of hydrated lime and SBS modified asphalt mixtures for laboratory and field compacted samples, Construction and Building Materials, 25(2), 756-765.

[10] Setiadji, B. H., Utomo, S., (2017), Effect of chemical compounds in tidal water on asphalt pavement mixture, International Journal of Pavement Research and Technology, 10(2), 122-130.

[11] Martina, N., Hasan, M. F. R., Setiawan, Y., Yanuarini, E., (2021), Analysis of the use of rubber waste to improve the performance of the asphalt concrete mixture against tidal floods, In IOP Conference Series: Earth and Environmental Science, 739 (1), 012005.

[12] Shahin, M., Khokon, Z. H., Sobhan, M. A., Ahmed, T. U., (2015), Salt tolerance limit of bituminous pavement, International Journal of Civil Engineering, 2(4), 1-7.

[13] Juli-Gandara, L., Vega-Zamanillo, A., Calzada-Perez, M. A., (2019), Sodium chloride effect in the mechanical properties of the bituminous mixtures, Cold Regions Science and Technology, 164, 102776.

[14] United States Department of Transportation Federal Highway Administration, (2000), Superpave Fundamentals Reference Manual, Washington, DC, USA.

[15] United States Department of Transportation Federal Highway Administration, (2001), Superpave Mixture Design Guide, Washington, DC, USA.

[16] Sugiyanto, G., Widarini, W., Indriyati, E. W., (2022), The effect of sea water immersion on buton asphalt (as-buton) mixture, Jurnal Teknologi, 84(1), 29-39.

[17] Long, Z., Tang, X., Ding, Y., Miljkovic, M., Khanal, A., Ma, W., You, L., Xu, F., (2022), Influence of sea salt on the interfacial adhesion of bitumen-aggregate systems by molecular dynamics simulation, Construction and Building Materials, 336, 124471.

[18] Kuyumcu, H. M., (2006), In concrete resist effects of sea water and with sulphate water, Master's thesis, Sakarya University.

Kütahya Dumlupınar University
Institute of Graduate Studies

Journal of Scientific
Reports-A
E-ISSN: 2687-6167
Number 51, December 2022

RESEARCH ARTICLE

AUTOMATIC INITIALIZATION of IMAGE CLUSTERING ALGORITHMS

Merve ARSLAN[1,*], Recep DEMİRCİ[2]

[1]Gazi University, Graduate School of Natural and Applied Sciences, Computer Engineering, Ankara, merve.arslan6@gazi.edu.tr, ORCID:0000-0002-2867-6198
[2]Gazi University, Technology Faculty, Computer Engineering, Ankara, rdemirci@gazi.edu.tr, ORCID:0000-0002-3278-0078

Receive Date:14.10.2022 *Accepted Date: 15.11.2022*

ABSTRACT

Clustering is partition of a data set into subsets where each item in assigned subset is similar and different from that of other subsets. K-means and fuzzy c-means (FCM) algorithms are frequently used for clustering of color image. On the other hand, randomly determination of initial cluster centers is one of the most important problems of both algorithms since results to be obtained vary according to initial values of cluster centers. Thus, obtaining different results at each run time reduces reliability of algorithms. One of a typical solution is that number of iterations is increased in order to obtain an accurate result. However, it increases computation cost. A novel solution for initial cluster centers has been proposed in this study where octree algorithm was used. Color images were initially quantized in certain numbers of color vectors depending on level of octree algorithm. Then, means of each quantized color vector set were obtained. The pixel numbers of each pre-subset were sorted and assigned as initial cluster centers. Consequently, cluster centers are selected automatically. As positions of quantized vectors in color space are fixed, a deterministic algorithm has been attained.

Keywords: *K-means, Fuzzy c-means, Octree, Color Quantization.*

1. INTRODUCTION

Image segmentation is considered the first stage of image processing area. It is defined as dividing an image into sub-regions, each of which contains meaningful features. Since it acts as a pre-processor in image processing studies, performing correct segmentation is very important for carrying out of further image analysis. K-means and fuzzy c-means approaches are frequently used to cluster images. Although both algorithms stated are highly preferred for color classification, their performance was insufficient in some cases. The random assignment of initial cluster centers of related algorithms and determination of number of clusters by user affect performances of algorithms. Since the initial cluster centers are randomly allocated, outputs of algorithms could be different for each run time. Thus, it is undesired properties of the algorithms.

JSR A
Journal of Scientific Reports

Arslan, M. and Demirci, R., Journal of Scientific Reports-A, Number 51, 297-316, December 2022.

Segmentation process is used in many areas such as health, traffic, industry, object recognition, and face recognition. For example, K-means algorithm is a frequently used segmentation algorithm in computer vision although it also has weaknesses. Determination of cluster number, K before algorithm starts is subjective as it depends on user judgment. K-means algorithm is extremely sensitive to initial conditions as it produces different results based on initial cluster centers [1].
Fuzzy c-means algorithm is also very sensitive to initial cluster centers and number of clusters. There is no generally accepted method for initializing the algorithm. Kim et al. proposed a dominant color-based approach. Idea behind the related solution is that dominant colors in image could not be belonging to the same cluster. So, if dominant colors in image is determined in advance, they could be assigned for initial centers [2]. Dörterler et al. dealt with the problem of randomly generating center values for K-means algorithm. It is combined with metaheuristic algorithms (DEA: differential evolution algorithm and HSA: harmony search algorithm) to increase performance of clustering success. For example, parameters used for diagnosis of heart disease were selected with metaheuristic algorithms. It is aimed to increase the clustering success of K-means algorithm [3].

Separation of revealing region in skin image for psoriasis diagnosis is an example of segmentation in field of health. In the study carried out by Juang and Wu, K-means algorithm was employed to complete diagnosis procedure for psoriasis disease [4]. Segmentation of brain MRI images with K-means algorithm for detection of tumors was realized. In the method proposed by Hrosik et al., the firefly algorithm was used to find optimal centroids. K-means algorithm and firefly algorithm was combined to improve performance of process [5]. In a study conducted by Nitta et al., peaks in histogram of grayscale image were detected and then assigned as initial cluster centers of K-means algorithm. Consequently, random assignment of initial values of cluster centers was partially prevented. Additionally, the suggested algorithm was tested with MR images [6].

A segmentation process was applied to fish images for disease detection and animal behavior. K-means algorithm was employed to accurately separate fish image from background. In a study conducted by Yao et al., number of peaks in histogram of gray level image was used as number of cluster. The first cluster centers were determined with Otsu thresholding method [7]. An automatic vehicle license plate recognition technique was recently developed for intelligent transportation systems where K-means algorithm was used for segmentation of license plate image. Accordingly, characters on license plates were recognized by using a convolutional neural network (CNN) [8].

An initialization method for fuzzy c-means algorithm was proposed by Tan et al. to select the first cluster center and determine the number of clusters. The proposed hierarchical approach consists of two levels. Firstly, partition module in which splitting technique is used to divide image into small homogeneous region is implemented. In the second stage, unification technique is applied, and merging procedure is completed to find the number of clusters and initial cluster centers. In merging procedure, Manhattan distance between two close clusters is calculated. An iterative operation is performed by comparing Manhattan distance with a predetermined threshold value [9].

Recently, noisy color images were segmented by means of fuzzy c-means algorithm. Initially, noise level was estimated and then eliminated. Finally, segmentation process was realized with fuzzy c-means algorithm and block matching [10]. Segmentation of gray-scale images can be reasonably

realized by using Otsu and Kapur threshold methods. However, since there are three channels such as red, green, and blue, it is a problem to unify results obtained from different channels. In the method proposed by Demirci et al., threshold values were calculated for each color channel. The color space is divided into small cubes. The remaining pixels in each cube are included in the same group. With the suggested method, color images are automatically classified into eight classes [11].

A study combining fuzzy c-means and color deconvolution method was carried out to increase segmentation outcome. The peaks in image histogram are determined. If the number of peaks is greater than two, layer segmentation based on fuzzy c-means is performed. If the number of peaks is two or less, color deconvolution method is applied. Therefore, peaks in histogram determine the method to be used. Moreover, mouse skin images were used to test the proposed algorithm [12]. In fact, image segmentation is a color quantization process. Aim of color quantization is to reduce the number of colors in an image by accumulating similar colors in the same cluster. Subsequently, methods used in color quantization are grouped under two headings: clustering and splitting [13]. On other hand, octree algorithm is one of the well-known color quantization techniques. Park and Kim have studied K-means algorithm and octree color quantization method. Different palettes with 8, 16, 32, 64, 128, or 256 colors were investigated [14].

Recently, an entropy-based technique for initialization of K-means algorithm has been proposed by Chowdhury et al. In the related study, partition coefficient, classification entropy, partition index, and separation index measures of data set were used to calculate number of clusters. Furthermore, performance of suggested algorithm depends on threshold value that is selected by user [15]. Also K-means algorithm initialization strategy proposed by Cao et al. is based on neighborhood concepts. Thus, two levels were defined as intra-cluster similarity and inter-cluster similarity. As all vectors in data set are processed, complexity of the scheme is $O(n^2)$ [16]. Performance analyzes of various K-means initialization techniques were completed by Çelebi et al. Eight popular initialization methods including Forgy's method, Jancey's method, and maximin have been compared. As a result, it was stated that Forgy's method, MacQueen's second method, and maximin method were slow in terms of convergence [17]. Segmentation procedures using Ham, Otsu, and Kapur thresholding algorithms were realized by Kılıçaslan et al. Unlike traditional methods, a segmentation process was implemented based on color space. In the related study, color ranges were initially determined by thresholding approaches, then color space was divided into 8 sub-cubes where each cube corresponds to a cluster [18].

In this study, a new method to automatically determine initial cluster centers of K-means and fuzzy c-means algorithms has been proposed. In the suggested procedure, color image to be segmented was initially quantized with octree algorithm and then means of each subset were obtained. Accordingly, one dimensional histogram of color image was attained by using pixel numbers assigned to particular subset. Once histogram data was sorted, the biggest subset was assigned as initial center of first cluster. Then, the process was repeated depending on desired cluster number of K-means and fuzzy c-means algorithms.

JSR A
Journal of Scientific Reports

Arslan, M. and Demirci, R., Journal of Scientific Reports-A, Number 51, 297-316, December 2022.

2. CLUSTERING ALGORITHMS

Clustering is an algorithm that involves partition process of given data points. Thus, clustering procedures are used to classify each data point into specific subgroups. Data points or vectors that are assigned to the same group should have similar features, while data vectors in different groups should have highly dissimilar features. On other hand, vector quantization is a lossy encoding method used for storing and transmitting data. Vector quantization is used to represent original data with fewer data points. It is desired to minimize data loss while quantizing. The similarity rate of the data around the same cluster center should be high, and the similarity rate between the data belonging to different cluster centers should be low [19]. Color image is a collection of pixels that are spatially distributed in plane. On the other hand, each pixel in image has three components that represent coordinates in RGB color space. Therefore, a color image is also data points or vectors in color space. When it is desired to quantize color images, a vector or data point clouds in RGB space are taken as input. At the end of clustering or color classification, a color image is represented with fewer colors [20]. When the size of color image increases, the computation cost of quantization process also grows.

2.1. K-means Algorithm

In digital environment, data set is basically colocation of vectors or data points in relevant space. Labeling of every data point under any of subsets could be defined as clustering. K-means algorithm, which is one of traditional approaches was developed by MacQueen in 1967 [21]. The goal of the algorithm is to minimize the objective function which is defined as follow:

$$J = \sum_{i=1}^{n} \sum_{j=1}^{K} \left\| x_i - c_j \right\|^2 \tag{1}$$

where n represents the number of data points or vectors, K is the number of clusters or subsets, x_i is data point or data vector, c_j is centroid of cluster. Furthermore, Euclidean distance between centroids of clusters and data points is calculated as:

$$d_{ij} = \left\| x_i - c_j \right\| \tag{2}$$

The number of clusters is determined by user and the centroid of cluster centers are initialized randomly. Mathematical target of K-means algorithm is to minimize the objective function defined in Eq.1. The specified goal is achieved by moving the centroids of clusters in related space as shown in Figure 1. Thus, positions of centroids of clusters are randomly initialized at the beginning and then the updated with proper algorithm. Consequently, fundamental steps of K-means algorithm are:

Step 1: Determine number of clusters (K),
Step 2: randomly select initial cluster centers,
Step 3: calculate Euclidean distances between centroids of clusters and all data points and classifies each point into the category of the nearest cluster center,
Step 4: recalculate the mean of each cluster as a new cluster center,

JSR A
Journal of Scientific Reports

Step 5: if there is no change in the cluster centers or the specified number of iterations is reached, terminate the algorithm; otherwise, it is repeated from step 3.

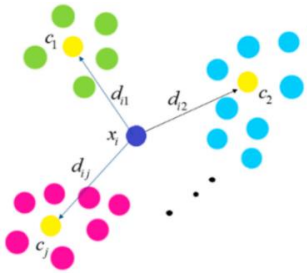

Figure 1. K-means algorithm.

2.2. Fuzzy C-means Algorithm

K-means is one of hard clustering algorithms since a data point is classified into only one of categories. Euclidean distance between a data point and the nearest cluster center is evaluated. The relationship between the particular data point and other classes is not considered. So, there is a kind of binary relation. On other hand, the data point to be classified may belong to more than one class in fuzzy c-means (FCM) algorithm which was established by Bezdek in 1981 [22]. The class to which the data point belongs is determined by membership degrees. Accordingly, the objective function of the FCM algorithm is defined as:

$$J = \sum_{i=1}^{n} \sum_{j=1}^{K} u_{ij}^{m} \left\| x_i - c_j \right\|^2 \tag{3}$$

where n represents the number of data points, K is the number of clusters, x_i is data points, c_j is centroid of cluster. The degree of membership between data point, $x_{i,}$ and cluster center, c_i calculated as:

$$u_{ij} = \frac{1}{\sum_{k=1}^{K} \left(\frac{x_i - c_j}{x_i - c_k} \right)^{\frac{2}{m-1}}} \tag{4}$$

where m is fuzziness index greater than 1. It is also chosen by user. In K-means algorithm, a data point belongs to only one cluster while in fuzzy c-means algorithm, the membership value is distributed for all classes. Accordingly, the sum of membership values of data point, x_i must be 1 as follows:

$$\sum_{i=1}^{K} u_{ij} = u_{i1} + u_{i1} + ... + u_{ij} = 1 \tag{5}$$

Furthermore, the cluster centers are updated by means of:

$$c_j = \frac{\sum_{i=1}^{n} u_{ij}^{m} x_i}{\sum_{i=1}^{n} u_{ij}^{m}} \tag{6}$$

Nevertheless, the fuzzy c-means algorithm has the same problems as the K-means algorithm since the centroids of clusters are randomly determined at the beginning. So, the performance of the algorithm depends on initial parameters.

2.3. Octree Algorithm

Octree algorithm was developed in 1988 [23]. It is one of the vector quantization methods in which the number of vectors representing data set is reduced to certain numbers. Color images that have three channels are collections of pixels scattered in spatial plane as shown in Figure 2(a). On the other hand, pixels in color image are also corresponding to a point in RGB color space. Accordingly, a color image shown in Figure 2(a) builds point clouds or data points as shown in Figure 2(b). Each channel in color image is coded with 8 bits memory area, color images may have 16,777,216 different colors. Since each channel range is limited with 255, pixels in color image take position in a 255x255x255 sized cube. Octree algorithm is based on a tree structure as shown in Figure 3. Cells are divided into 8 subsets at each level. Nodes in tree structure are numbered in Morton order [24] as shown in Figure 3 [25]. The simple principle of octree algorithm is based on slicing or partition of three-dimensional space into smaller cubes as shown in Figure 3. Each sub-cube holds different point clouds. The points which are included in a particular sub-cube are assigned to the same cluster or class. So, their labels will be the same as well. The octree algorithm is realized with different levels. If single level is used, 8 sub-cube or clusters is obtained. When second level is employed, each sub-cube is sliced again, and consequently, the whole space is partitioned into 64 clusters as shown in Figure 3. If third level is chosen, 512 subsets are obtained.

Color quantization is reduction in the number of colors in color image. As pixels in color image are presented by points or vectors in RGB color space, the octree algorithm could be easily used for clustering of color images. The cluster index is simply attained from red, green, and blue values of pixels as shown in Figure 4. Firstly, color values are converted to an 8-bit level. Then, the most significant bits of color channels (R: Red, G: Green, B: Blue) are combined at each level to form binary codes. The cluster index is achieved by using binary codes of each color component. If the most significant bits are used, a first-level quantization is performed. For example, if a pixel has 90,148 and 118 values for red, green, and blue channels, respectively, its cluster index becomes 2 as shown in Figure 4. On the other hand, when second level is preferred, its cluster index meets 10

JSR A
Journal of Scientific Reports

(2x5). Consequently, every pixel in color image is assigned into any of relevant sub-cube or relevant sub-set.

When Lena image given in Figure 2(a) is quantized octree algorithm by using first level, output shown in Figure 5(a) has been obtained. The total number of colors has been reduced into 8 as could be seen in Figure 5(b). Furthermore, cluster index of every pixel in image has been produced. So average of each clusters was assigned for every pixel in the same cluster. Subsequently, color reduction was achieved. Of course, information loss is indispensable. However, peak-signal-to noise level (PSNR) between original Lena image and quantized Lena image are 21.65, 21.85 and 24.35 for red, green, and blue channels, respectively. Moreover, the total number of pixels in image and the total number of pixels in every subset are known, one-dimensional color histogram of color Lena image has been obtained as shown in Figure 6. The horizontal axis represents cluster index whereas vertical axe indicates normalized pixel numbers of each cluster [26].

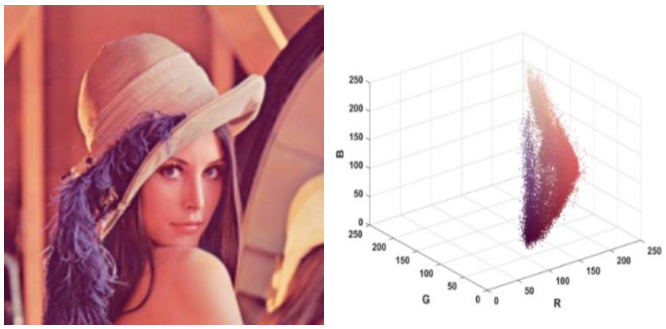

a) b)

Figure 2. Lena a) original b) distribution in RGB color space.

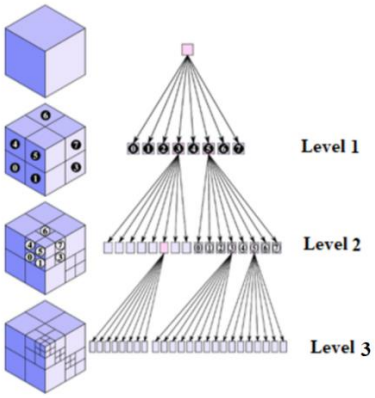

Figure 3. Octree algorithm [25].

JSR A
Journal of Scientific Reports

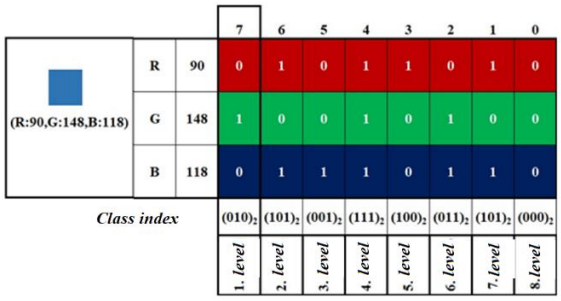

Figure 4. Octree algorithm for color quantization [26].

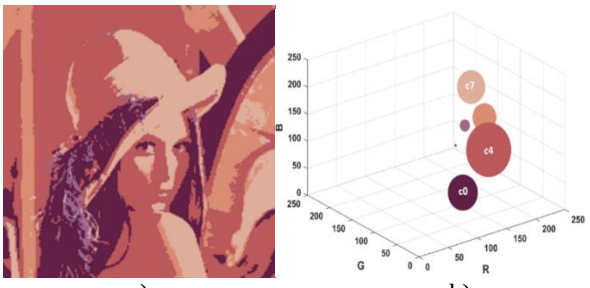

a) b)

Figure 5. Lena a) quantized with octree, level 1 b) quantized color distribution.

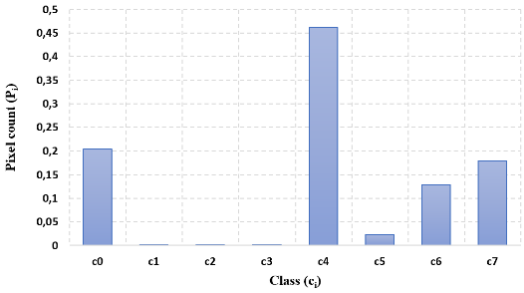

Figure 6. One-dimensional color histogram of quantized Lena.

2.4. Determination of Cluster Centers with Octree Algorithm

The purpose of K-means algorithm is to classify pixels in image. Mathematically, it is minimization process of the objective function given in Eq. 1. The number of data points, *n* in Eq. 1 corresponds to the number of pixels in image. Therefore, the computation cost of K-means algorithm increases with the size of images. Furthermore, since it is an iterative algorithm, in each iteration, all the pixels in image need to be processed again so that the objective function given in Eq. 1 converges to minimum. As the positions of centroids are updated in each iteration, they could be interpreted as moving

particles within RGB color space. Nevertheless, when the objective function is reached into minimum value, the positions of centroids are fixed. In other words, motion of centroids is stopped. If the centroids are located near to fixed or optimal positions, the iteration numbers or computation cost could be reduced.

The distribution of Lena image in RGB color space is shown in Figure 2(b) while its quantized version with octree algorithm is given in Figure 5(b). As first-level quantization is used, only eight balls with different spherical masses exist in Figure 5(b). Although diameters or masses are different, the centroid positions of each ball are fixed. Additionally, the numbers of balls represent the color vectors or cluster numbers obtained with octree algorithm.

The idea behind this study is based on employment of the color vectors or cluster centers obtained with octree algorithm for K-means algorithm and fuzzy c-means algorithms. The positions of quantized color vectors with octree algorithm could be set as initial positions of centroids of each algorithm. Consequently, the iteration numbers to reach minimum value of objective functions could be reduced. Thus, the computation cost is also reduced. It is logical that the positions of centroids which makes the minimum of the objective function must be somewhere within point clouds shown in Figure 2(b). On the hand, the positions of quantized color vectors with octree algorithm are already within point clouds shown in Figure 5(b). Therefore, it is reasonable that the quantized vectors could be set as initial centroids of K-means algorithm and fuzzy c-means algorithms.

Depending on level considered for octree algorithm, the number of cluster could be 8, 64, 512, and so on. If the number of cluster desired for K-means algorithm and fuzzy c-means algorithms are the same with that of octree algorithm, there would be no problem. However, if the cluster numbers are not the same, one dimensional color histogram given in Figure 6 help us to choose proper centroid. For example, cluster number for K-means algorithm or fuzzy c-means algorithms is set as 3 classes. Initially, one dimensional color histogram is sorted from the largest to minimum. Then the corresponding first three vectors or colors are assigned as centroids. It is clear that one dimensional color histogram holds the number of pixels assigned into related cluster. Also, diameters of globes in Figure 5(b) are proportional to number of pixels. Therefore, it means that some of pixels in image have already been labeled. Consequently, computation cost to reach minimum value of objective function is reduced. Consequently, flowcharts of suggested initialization strategy for K-means and fuzzy c-means algorithms are in Figure 7(a) and Figure 7(b), respectively.

Proposed method has eliminated the random assignment of initial cluster centers of K-means and fuzzy c-means algorithms. The octree algorithm use pixel values as shown in Figure 4. The developed algorithm does not require any threshold value. Once quantization process is completed without any recursive computation. Initialization of K-means algorithm and fuzzy c-means algorithms is realized. Since the number of pixels in color image is n, time complexity of proposed method is $O(n)$. On the other hand, time complexity of neighborhood concepts is $O(n^2)$ [16]. Thus it could be concluded that the developed algorithm is fast.

JSR A
Journal of Scientific Reports

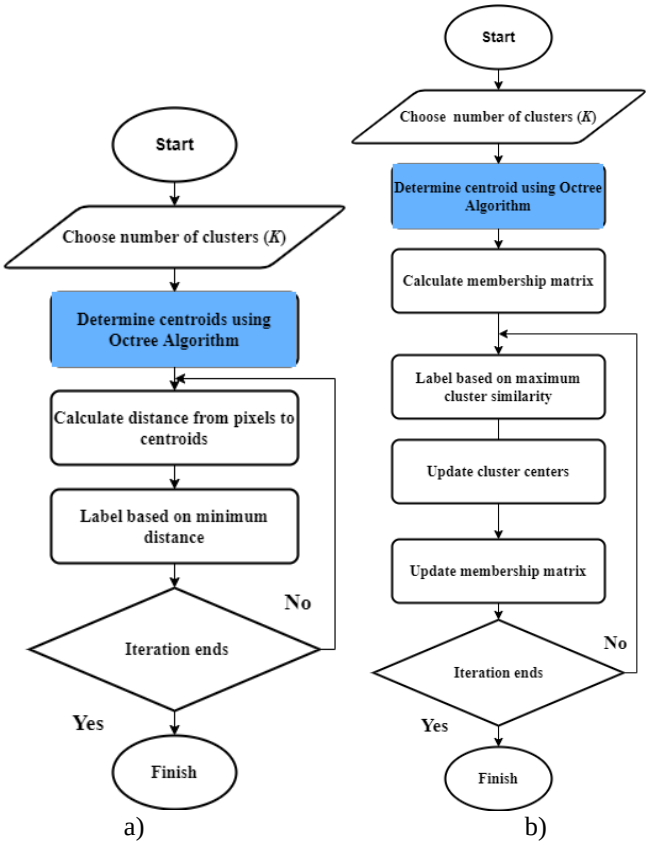

Figure 7. Octree-based initialization a) *K*-means b) fuzzy c-means.

3. EXPERIMENTAL RESULTS and DISCUSSIONS

A user interface was designed in visual C# environment to test the suggested algorithms. Lena image of 346x346 size and Landscape image of 256x192 size were used for experiments. The desired number of cluster for K-means and fuzzy c-means algorithms was chosen as three for Lena image. Hence, the first level octree algorithm would be enough to create centroids for K-means and fuzzy c-means algorithms since the number of quantized color vectors with octree will be eight. Experiments were realized with two concepts. In the first category, the centroid of K-means and fuzzy c-means algorithms were randomly initialized while they were automatically assigned with octree technique in second strategy. Figure 8(a) shows the output of K-means where the centroids: $C_0(233,45,244)$, $C_1(155,91,100)$, $C_2(22,219,2)$ were randomly selected. The means of pixels in each cluster are positioned in RGB color space as shown in Figure 8(b). Furthermore, the diameters of each globe in proportional with number of pixels in each class. The objective function converges to its minimum values at 6^{th} iteration as shown in Figure 8(c).

JSR A
Journal of Scientific Reports

Arslan, M. and Demirci, R., Journal of Scientific Reports-A, Number 51, 297-316, December 2022.

The color quantization of Lena image with first level octree algorithm was already given in Figure 5 where the size of balls in Figure 5(b) is proportional to number of pixels in related cluster. For example, cluster, c_4 is a larger set in terms of pixels count. So it is reasonable to assign it as the first centroid of K-means. With using similar approach, clusters, c_0 and c_7 were allocated for second and third centroids for K-means algorithm. Consequently, an automatic procedure has been obtained. As the outputs of the octree algorithm are fixed, the positions of centroids will also be stationary. Thus, the randomness has been avoided. Figure 9(a) shows the output of K-means algorithm initialized with octree algorithm where the centroids are C_0 *(187,89,92),* C_1*(99,32,70),* and C_2*(223,175,156).* The positions of centroids obtained with octree algorithm are shown in Figure 9(b). Moreover, variation of objective function is illustrated in Figure 9(c). It is obvious that the objective function converges to its minimum at third iteration. It is known that in each iteration, the whole image pixels are processed. When the size of image gets larger, the time consumed for each loop gets longer as well.

Figure 10(a) shows output of conventional fuzzy c-means algorithm where the centroids: C_0*(222,101,40),* C_1*(227,107,206),* and C_2*(161,223,125)* were randomly selected. Final positions of each cluster centers are shown in Figure 10(b) as balls. Furthermore, the objective function converges to its minimum value at 9^{th} iteration as shown in Figure 10(c). On the other hand, octree based Fuzzy c-means algorithm suggested in this study was also tested with Lena image. The centroid obtained with octree algorithm: C_0 *(187,89,92),* C_1*(99,32,70),* and C_2*(223,175,156)* were assigned as cluster centers for fuzzy c-means shown in Figure 7(b). Figure 11(a) shows output of fuzzy c-means algorithm initialized with octree algorithm while the final positions of color vectors are shown in Figure 11(b). It is obvious that the objective function converges to its minimum at second iteration as given in Figure 11(c). When the size of images to be clustered gets larger, computation cost becomes higher. Thus, it could be concluded that the overall performance of fuzzy c-means algorithm has been improved with octree algorithm.

Proposed algorithm was also tested with Landscape image shown in Figure 12(a). The desired number of cluster for K-means and fuzzy c-means algorithms was chosen as three. Since the number of quantized color vectors with octree algorithm is 8, the first level is suitable. Figure 13(a) shows the output with first level while quantized color vectors are given in Figure 13(b). The first three color vectors as shown in Figure 14, which have high frequencies, have been assigned as initial cluster centers. In experiments, initially random approach was tested. Figure 15(a) shows output of K-means algorithm where centroids: C_0*(154,125,156),* C_1*(108,54,55),* and C_2*(122,118,11)* were randomly selected while Figure 15(b) shows distribution in color space of image classified. Also, it could be seen that objective function in Figure 15(c) converges to minimum in 19^{th} iteration. Histogram of quantized Landscape image is shown in Figure 14 where color vectors: c_0, c_3, and c_1 were selected as cluster centers. Figure 16(a) shows the output of K-means algorithm initialized with octree algorithm where the centroids are C_0*(37,52,59),* C_1*(71,150,216),* and C_2*(30,112,179).* It is clear that objective function given in Figure 16(c) started to converge at 8^{th} iteration.

Additionally, Figure 17(a) shows output of conventional fuzzy c-means algorithm where centroids: C_0 *(242,230,154),* C_1*(95,243,27),* C_2*(182,151,62)* were randomly selected. Final positions of cluster centers are shown in Figure 17(b). The objective function begins to converge at iteration 11 as could be seen in Figure 17(c). Landscape image was also tested with the fuzzy c-means algorithm proposed

JSR A
Journal of Scientific Reports

in this study. Cluster centers obtained by octree algorithm: C_0 *(37,52,59),* C_1*(71,150,216),* and C_2*(30,112,179)* are assigned. The result obtained is given in Figure 18(a) and final positions of color vectors are displayed in Figure 18(b). Objective function converges at the 5th iteration as could be seen in Figure 18(c).

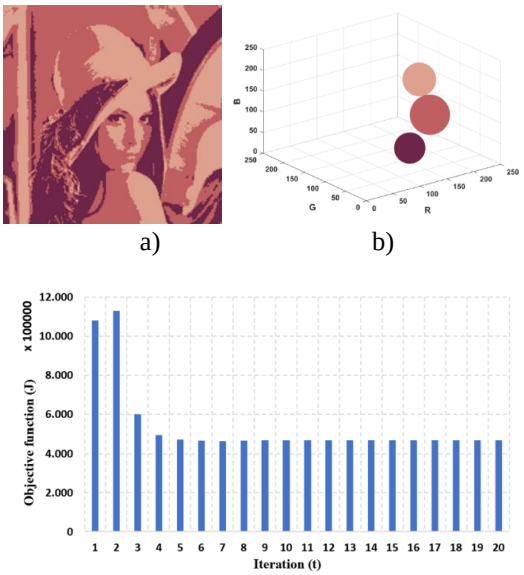

a) b)

c)

Figure 8. Lena: K-means (randomly initialized): C_0*(233,45,244),* C_1*(155,91,100),* C_2*(22,219,2)* a) clustered b) color distribution c) objective function.

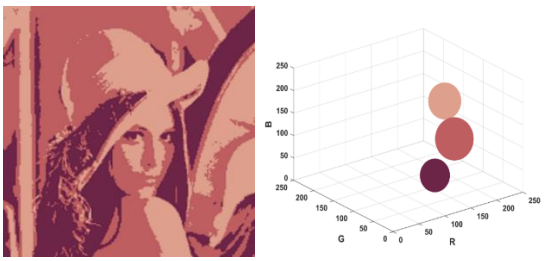

a) b)

JSR A
Journal of Scientific Reports

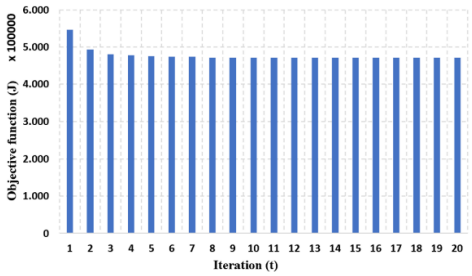

c)

Figure 9. Lena: K-means (octree-based): C_0 *(187,89,92),* C_1*(99,32,70),* C_2*(223,175,156)* a) clustered b) color distribution c) objective function.

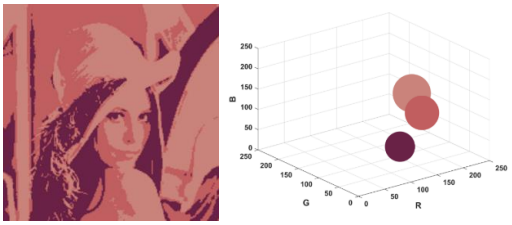

a) b)

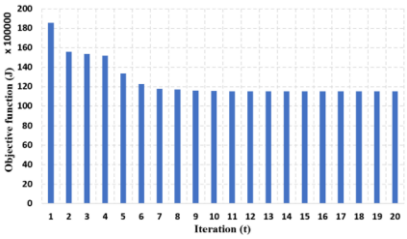

c)

Figure 10. Lena: Fuzzy c-means (randomly initialized): C_0*(222,101,40),* C_1*(227,107,206),* C_2*(161,223,125)* a) clustered b) color distribution c) objective function.

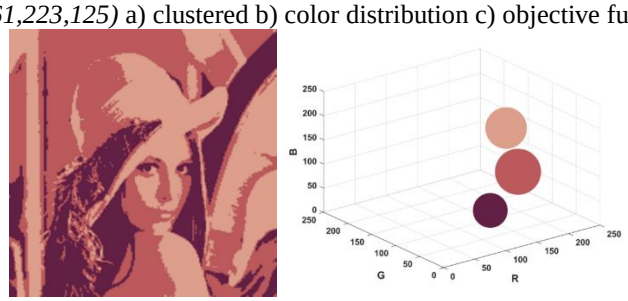

a) b)

JSR A
Journal of Scientific Reports

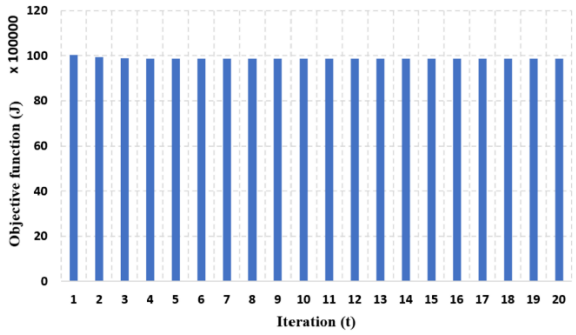

c)

Figure 11. Lena: Fuzzy c-means (octree-based): $C_0(187,89,92)$, $C_1(99,32,70)$, $C_2(223,175,156)$ a) clustered b) color distribution c) objective function.

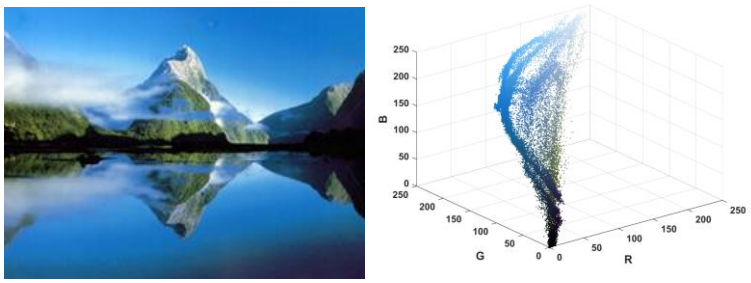

a) b)

Figure 12. Landscape a) original b) distribution in RGB color space.

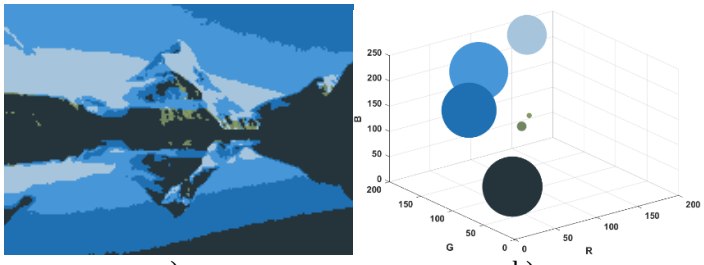

a) b)

Figure 13. Landscape a) quantized with octree, level 1 b) quantized color distribution.

JSR A
Journal of Scientific Reports

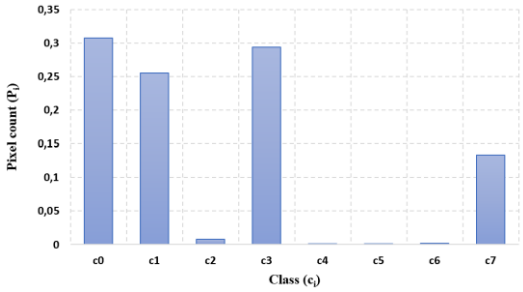

Figure 14. One-dimensional color histogram of quantized Landscape.

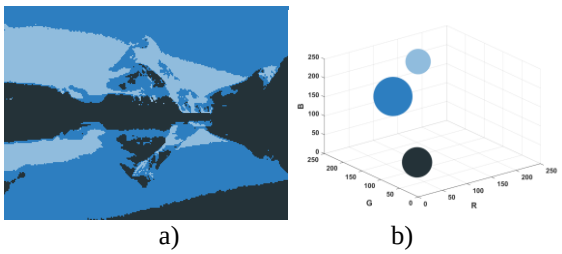

a) b)

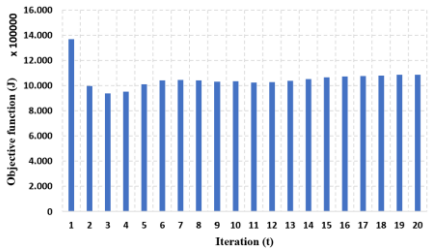

c)

Figure 15. Landscape: K-means (randomly initialized): $C_0(154,125,156)$, $C_1(108,54,55)$, $C_2(122,118,11)$ a) clustered b) color distribution c) objective function.

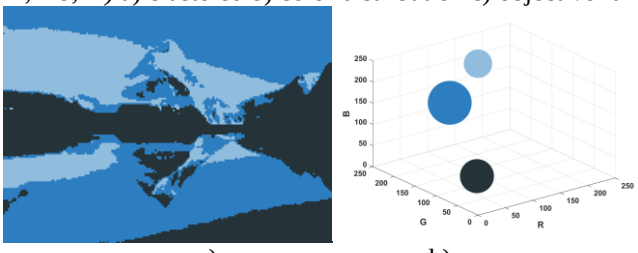

a) b)

JSR A
Journal of Scientific Reports

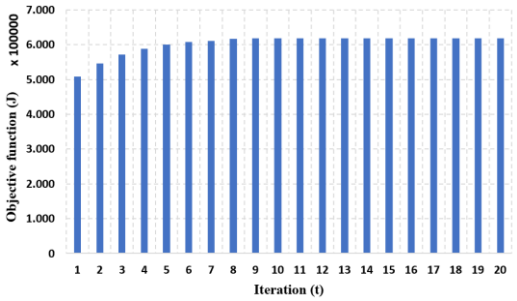

c)

Figure 16. Landscape: K-means (octree-based): *C_0(37,52,59), C_1(71,150,216), C_2(30,112,179)* a) clustered b) color distribution c) objective function.

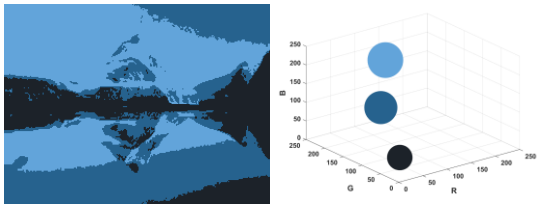

a) b)

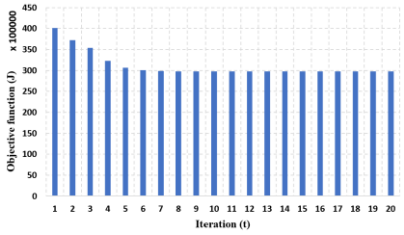

c)

Figure 17. Landscape: Fuzzy c-means (randomly initialized): *C_0 (242,230,154), C_1(95,243,27), C_2(182,151,62)* a) clustered b) color distribution c) objective function.

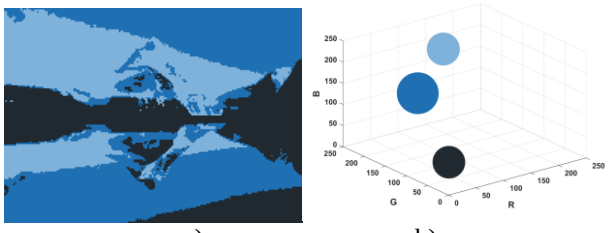

a) b)

JSR A
Journal of Scientific Reports

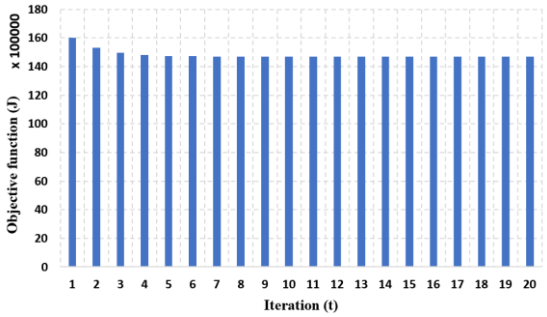

c)

Figure 18. Landscape: Fuzzy c-means (octree-based): C_0 *(37,52,59),* C_1*(71,150,216),* C_2*(30,112,179)* a) clustered b) color distribution c) objective function.

In computer science, data could be interpreted as collection of vectors. On the other hand, vector quantization is reduction of the number of vectors that represent any data set. Consequently, processing time and memory requirements are reduced. Thus, image clustering could also be considered color quantization. Therefore, it is desired that similarity between original image and quantized image is high. Table 1. and Table 2. show PSNR results for Lena and Landscape. According to tables, it is obvious that PSNR results obtained with octree-based approaches are better than those obtained with traditional techniques.

Table 1. PSNR results: Lena.

	K-means			Fuzzy c-means		
	R	G	B	R	G	B
Randomly	23.094	22.534	22.868	21.800	20.318	22.039
Octree-based	23.136	22.521	22.822	23.207	22.360	22.689

Table 2. PSNR results: Landscape.

	K-means			Fuzzy c-means		
	R	G	B	R	G	B
Randomly	19.117	19.908	17.948	16.410	19.866	17.714
Octree-based	19.348	20.144	18.420	18.469	20.006	18.267

4. CONCLUSION

Although they are frequently preferred for image segmentation process, results obtained from K-means and fuzzy c-means algorithms vary according to initial values of cluster centers. The related drawback is usually compensated by increasing the number of iterations. However, it causes serious computation cost. Automatic assignment of initial cluster centers helps to reduce computational cost. In this study, octree algorithm, also known as a color quantization technique, was employed to determine the initial centroids from K-means and fuzzy c-means procedures. Consequently, an

automatic assignment procedure for K-means and fuzzy c-means algorithms has been developed. The suggested algorithm has also been confirmed with experimental results.

ACKNOWLEDGMENT

The authors did not receive any financial support in the research and preparation of this article.

REFERENCES

[1] Isa, N. A. M., Salamah, S. A., and Ngah, U. K. (2009). Adaptive fuzzy moving k-means clustering algorithm for image segmentation. IEEE Transactions on Consumer Electronics, 55(4), 2145-2153.

[2] Kim, D. W., Lee, K. H., and Lee, D. (2004). A novel initialization scheme for the fuzzy c-means algorithm for color clustering. Pattern Recognition Letters, 25(2), 227-237.

[3] Dörterler, S., Dumlu, H., Özdemir, D., Temurtaş, H. (2022). Hybridization of k-means and meta-heuristics algorithms for heart disease diagnosis. New Trends in Engineering and Applied Natural Sciences (55-72. ss).

[4] Juang, L. H., and Wu, M. N. (2011). Psoriasis image identification using k-means clustering with morphological processing. Measurement, 44(5), 895-905.

[5] Hrosik, R. C., Tuba, E., Dolicanin, E., Jovanovic, R., and Tuba, M. (2019). Brain image segmentation based on firefly algorithm combined with k-means clustering. Studies Informatics and Control, 28(2), 167-176.

[6] Nitta, G. R., Sravani, T., Nitta, S., and Muthu, B. (2020). Dominant gray level-based k-means algorithm for MRI images. Health and Technology, 10(1), 281-287.

[7] Yao, H., Duan, Q., Li, D., and Wang, J. (2013). An improved k-means clustering algorithm for fish image segmentation. Mathematical and Computer Modelling, 58(3-4), 790-798.

[8] Pustokhina, I. V., Pustokhin, D. A., Rodrigues, J. J., Gupta, D., Khanna, A., Shankar, K., and Joshi, G. P. (2020). Automatic vehicle license plate recognition using optimal k-means with convolutional neural network for intelligent transportation systems. Ieee Access, 8, 92907-92917.

[9] Tan, K. S., Lim, W. H., and Isa, N. A. M. (2013). Novel initialization scheme for fuzzy c-means algorithm on color image segmentation. Applied Soft Computing, 13(4), 1832-1852.

[10] Gamino-Sánchez, F., Hernández-Gutiérrez, I. V., Rosales-Silva, A. J., Gallegos-Funes, F. J., Mújica-Vargas, D., Ramos-Díaz, E., and Kinani, J. M. V. (2018). Block-matching fuzzy c-means

clustering algorithm for segmentation of color images degraded with Gaussian noise. Engineering Applications of Artificial Intelligence, 73, 31-49.

[11] Demirci, R., Güvenç, U., and Kahraman, H. T. (2014). Görüntülerin renk uzayı yardımıyla ayrıştırılması. İleri Teknoloji Bilimleri Dergisi, 3(1), 1-8.

[12] Hussein, S. (2021). Automatic layer segmentation in H&E images of mice skin based on colour deconvolution and fuzzy c-mean clustering. Informatics in Medicine Unlocked, 25, 100692.

[13] Pérez-Delgado, M. L. (2019). The color quantization problem solved by swarm-based operations. Applied Intelligence, 49(7), 2482-2514.

[14] Park, H. J., and Kim, K. B. (2015). Improved k-means color quantization based on octree. Journal of The Korea Society of Computer and Information, 20(12), 9-14.

[15] Chowdhury, K., Chaudhuri, D., and Pal, A. K. (2021). An entropy-based initialization method of K-means clustering on the optimal number of clusters. Neural Computing and Applications, 33(12), 6965-6982.

[16] Cao, F., Liang, J., and Jiang, G. (2009). An initialization method for the K-Means algorithm using neighborhood model. Computers and Mathematics with Applications, 58(3), 474-483.

[17] Celebi, M. E., Kingravi, H. A., and Vela, P. A.(2013). A comparative study of efficient initialization methods for the K-means clustering algorithm. Expert System with Applications, 40(1), 200-210.

[18] Kılıçaslan, M., Tanyeri, U., İncetaş, M. O., Girgin, B. Y., and Demirci, R. (2017). Eşikleme Tekniklerinin Renk Uzayı Tabanlı Kümeleme Yönteminin Başarısına Etkisi. In 1st International Symposium on Multidisciplinary Studies and Innovative Technologies (ISMSIT 2017), Tokat, Türkiye (pp. 107-110).

[19] Dursunoğlu, N. (2006). Image compression using vector quantization, M.Sc. thesis, Yıldız Technical University, Graduate School of Science and Engineering, İstanbul, 4-7.

[20] Kalkan, M. B. (2019). Run-length encoding and segmentation based image compression, M.Sc. thesis, Gazi University, Graduate School of Natural and Applied Sciences, Ankara.

[21] MacQueen, J. (1967). Classification and analysis of multivariate observations. In 5th Berkeley Symposium Mathematical Statistics and Probability (pp. 281-297).

[22] Bezdek, J. C. (2013). Pattern recognition with fuzzy objective function algorithms. Springer Science and Business Media.

[23] Gervautz, M., and Purgathofer, W. (1988). A simple method for color quantization: Octree quantization. In New Trends in Computer Graphics (pp. 219-231). Springer, Berlin, Heidelberg.

[24] Morton, G. M. (1966). A computer oriented geodetic database and a new technique in file sequencing.

[25] Laurmaa, V., Picasso, M., and Steiner, G. (2016). An octree-based adaptive semi-Lagrangian VOF approach for simulating the displacement of free surfaces. Computers and Fluids, 131, 190-204.

[26] Kılıçaslan, M. (2020). Content based image retrieval by using color histogram, Ph.D. thesis, Gazi University, Graduate School of Natural and Applied Sciences, Ankara, 129s.

Kütahya Dumlupınar University
Institute of Graduate Studies

Journal of Scientific
Reports-A
E-ISSN: 2687-6167
Number 51, December 2022

RESEARCH ARTICLE

DETECTION of HFrEF and HFpEF USING PPG-DERIVED HRV with MACHINE LEARNING METHODS

Pınar ÖZEN KAVAS[1,*], Mehmet Recep BOZKURT[2]

[1*]Kütahya Dumlupınar University, Computer Enginering, Kütahya, pinar.ozen@dpu.edu.tr ORCID: 0000-0001-9884-2860
[2]Sakarya University, Electrical-Electronics Engineering, Sakarya, mbozkurt@sakarya.edu.tr ORCID: 0000-0003-0673-4454

Receive Date:17.10.2022 *Accepted Date: 21.11.2022*

ABSTRACT

Regarding heart failure (HF), reducing mortality and prolonging life is one of the main treatment goals. Many clinical studies define HF patients according to Left Ventricular Ejection Fraction (LVEF). Two different subtypes in patients with HF are: HF with preserved ejection fraction (HFpEF) and HF with reduced ejection fraction (HFrEF). Echocardiography is generally used to measure LVEF. This is a pricy device that requires an expert and there may be situations where attaining the device is restricted. There may be cases that treatment should be started without echocardiography. Economical and practical measurement and decision support systems are needed to solve such situations. In this study, an algorithm was improved to detect HFrEF and HFpEF by using solely heart rate variability (HRV) derived from photoplethysmography (PPG). PPG data were obtained from volunteers for 10s, digital filters were used to clean PPGs, and HRV derivation was made from cleaned PPG. Totally thirty-seven features were obtained. Consequently, features were selected, and classification that was realized with only 3 features extracted from HRV gave significant results. 10-fold cross validation was performed for evaluation. The classification performance parameters were: accuracy %98.33, sensitivity 0.967, specificity 1, AUC 0.983, F-measure 0.981 and Kappa 0.967. This study provided highly reliable non-random results for distinguishing between HFrEF and HFpEF. This system, which works with such high performance with traditional machine learning methods used in real-time systems, makes a significant contribution to the literature in terms of diagnosing HFrEF and HFpEF cases with a single signal.

Keywords: *Machine learning, Artificial intelligence, PPG-derived HRV, HFrEF, HFpEF, Classification.*

1. INTRODUCTION

Ejection fraction (EF) represents the pumping efficiency of the heart. It is related to the blood amount that is pumped from a ventricle with a heartbeat. It is the ratio of the pulse volume to the end-diastolic volume. The efficiency of ejecting to the circulation of systemic is Left Ventricular EF (LVEF), and the efficiency of ejecting to the circulation of pulmonary is the right ventricular EF. Echocardiography

is the gold standard to measure EF. LVEF is generally low in systolic HF. It is a significant determinant of the prognose of systolic HF. The heart rate may change (low or high) in a healthy person during the daily course, but reduced LVEF is evermore an indicator of HF [1].

Structural or functional disorganization resulting in the heart cannot supply enough oxygen to the tissues can be used for HF definition [2]. HF is described as a symptom complex that results from a structural or functional failure in the heart, and HF patients have signs like dyspnoea, ankle swelling, and fatigue and symptoms like apex beat shift, pulmonary crepitation, and elevated jugular vein pressure [3].

When systolic impairment rises, LVEF progressively reduces, end-systolic volumes generally rise. Many clinical studies define HF patients according to LVEF, so it is more significant than only an indication of HF.

At present attested treatments are efficient just in HFrEF or systolic HF. Furthermore, studies were also performed about HF patients of which LVEF is higher than 40-45% and have no other relating to the heart defects. LVEF was quite typical (generally higher than 50%) in some of them and no important decrease was seen in systolic function. Thus, to identify these patients, "HF with preserved EF (HFpEF)" term was improved [4].

In HFpEF patients, the underlying pathophysiological defect is considered to become LV diastolic dysfunction. So, for diagnosing HFpEF, LV diastolic dysfunction needs to be diagnosed. Any sole parameter of echocardiography is not adequately definitive and repeatable for defining LV diastolic disturbance. Thus, an exhaustive echocardiographic consultation with completely correlated bidimensional Doppler data is advised. Devices for Doppler ultrasound are pricy, and an expert is necessary for the echocardiographic consultation which is laborious. Since HFpEF might originate from structural and functional disturbances relating to the heart instead of only one malady presence, it is a sophisticated syndrome, even HF professionals have trouble making accurate diagnoses [5].

Physiological indicators like the amount of oxygen in the blood and cardiac outflow are widely measured using photoplethysmography (PPG). PPG is a well choice for health studies relating to the blood vessels and heart owing to the little dimension and cost-effectiveness. Moreover, researches demonstrate that this signal could be acquired regardless of calibration [6].

There were many studies using PPG, in most of which machine learning (ML) algorithms were used, on cardiovascular (CV) and heart diseases. Groups of CV diseased and healthy individuals were appreciated with a ML algorithm using synchronous ear and finger PPG signals [7]. Blood pressure prediction study was non-invasively made using PPG with ML and artificial intelligence (AI) methods [8].

For alternating to invasive techniques, studies have also been carried out using PPG. It was ascertained to indicate LV filling pressure in the course of the Valsalva maneuver [9]. The benefit of PPG in the course of the Valsalva Maneuver to specify whether HF patients admitted to the hospital for treatment were at risk was studied [10].

As PPG is measured easily, there are many studies on electronic devices, wearables, and smartphones. Using PPG, atrial fibrillation detection was made with a new algorithm using smartphones [11]. As PPG is easy to measure from wearables and smartphones, a study was made to detect diabetes using PPG [12]. A wristlet with PPG technology that could determine the heart rate and RR apertures with significant accuracy was studied [13].

An electronic device using PPG was improved for distinguishing congestive heart failure (CHF) patients and healthy persons [14]. A distinction between healthy and CHF patients was obtained using simultaneously collected ECG and PPG [15].

Studies on the HFrEF and HFpEF subtypes were also conducted. Neurophysiological differences of HF subtypes (HFrEF and HFpEF) in Nigeria were investigated. In the study, cognitive tests with universal validity were applied to both subtypes of patients. Echocardiographic and clinical correlation analysis with cognitive performance was made [16]. Using features such as comorbidity accumulation rates, frequency of hospitalization, and differences in the use of special care for both HF subtypes, it was determined that these subtypes showed different clinical comorbidities and disease progression patterns [17]. A study was performed to estimate HFrEF and HFpEF using features such as age, gender, body mass index, systolic blood pressure, antihypertensive therapy, and past myocardial infarction [18]. Using older age, history of diabetes and valvular disease, body mass index, smoking, and atrial fibrillation as features, risk prediction was made for HFpEF and HFrEF subtypes [19]. Different machine learning methods that predict HFrEF and HFpEF were compared using demographics such as gender, age, and features obtained by invasive methods such as hemoglobin, sodium, and glucose [20].

CHF contains the HFpEF and HFrEF cases. In the literature, studies on CHF are usually concerned about HF presence or absence. Features obtained by demographic, echocardiographic, or invasive methods were used in the binary classification studies of HFrEF and HFpEF. There is no study in the literature in which only the PPG signal is used. This study stands out in terms of distinguishing the cases of HFrEF and HFpEF with only the easily obtainable PPG signal. In this study, HFpEF and HFrEF distinction was made using PPG with machine learning methods.

Because HF patients have some similar symptoms as in chest diseases, such as fatigue, chest ache, and dyspnoea, particularly HFpEF cases (LVEF $\geq$ 50% as in healthy persons) may be steered to a pulmonologist. If the chest disease expert is cautious, B-type natriuretic peptide (BNP) and N-terminal proBNP (NT-proBNP) tests, which are blood tests, are done and the cases are defined as HFpEF. However, when solely chest disease tests are done and there is no abnormality, the HFpEF case may be overlooked. BNP and NT-proBNP are invasive and troublesome techniques. Furthermore, echocardiography is a pricy device, requires expert, and cases might be where attaining the device is restricted. Thus, for alternating to such states of affairs, economical and practical diagnosis technique was researched.

With this study, it is aimed to design a system that can diagnose HFpEF and HFrEF cases, which are difficult to diagnose even for experts and can be overlooked, with a single signal.

JSR A
Journal of Scientific Reports

In the literature, Heart Rate Variability (HRV) was used in studies about heart failure [21]. Albeit HRV was usually derived from ECG, HRVs derived from PPG were also used [22]. So, we thought that PPG-derived HRVs could be used for our study.

Statistical methods were used to analyze the difference between classes for investigating the usefulness of the HRV's features that could be utilized for the diagnosis algorithm in the absence of echocardiography, demographics, and other exhaustive tests.

The most distinguishing features were detected. The features were abated by selecting them, then studies about classification were achieved with ML algorithms. The best classifier results were acquired by Support Vector Machines (SVMs) technique.

2. MATERIALS and METHODS

Some of the data was acquired from the patients who came to the cardiology outpatient clinic of the Training and Research Hospital of Sakarya University and some of them were from the patients who were hospitalized in the cardiology service. The ethics committee report numbered 16214662/050.01.04/123 was acquired from the Dean's Office of Medicine Faculty of Sakarya University. Data collecting and data recording were performed with a Biopac MP36 device. Echocardiographic outcomes of volunteers that could be included in this research were evaluated by an expert cardiologist and the data were acquired. PPGs were obtained from the right signing fingers of sixty-one individuals (twenty-five years old or older) for 10 s. 200 Hz was the sampling frequency. PPG data from each volunteer were received during 10 s. PPGs from the same individuals at several time apertures were also employed. The dataset included 120 data, 60 of which were HFrEF, and 60 of which were HFpEF. Volunteers' demographic information was given in Table 1.

Table 1. Volunteers' Demographics.

Groups	Height (cm)	Weight (kg)	BMI (kg/m²)	Age (years)
Mean ± SD for females	67.2 ± 12.32	75.75 ± 10.93	172.6 ± 5.98	23.38 ± 2.94
Mean ± SD for males	72.18 ±12.81	69.09 ± 29.27	158.18 ± 6.03	27.56 ± 11.3
Mean ± SD for total	68.97 ±12.52	73.39 ± 19.28	167.48 ± 9.16	26.15 ± 7.01

2.1. Data Preprocessing

Figure 1 indicates the study's workflow diagram. This study was performed based on this flow and the outcomes were acquired. Following data acquisition, the data labelling was made by a specialist cardiologist. Firstly, the PPG signals were cleaned from artifacts and noise. The signal was filtered by Chebyshev Type II band-pass filter in the band of 0.25 – 100 Hz, stopband attenuation was stated as 60 dB. For the mains noise which is at 50 Hz, the signal was filtered by a notch filter in the interval of 49-51 Hz. Stopband attenuation was also 60 dB. As final, the signal was filtered with Moving Average Filter. Afterwards, from cleaned PPGs, HRVs were derived.

JSR A
Journal of Scientific Reports

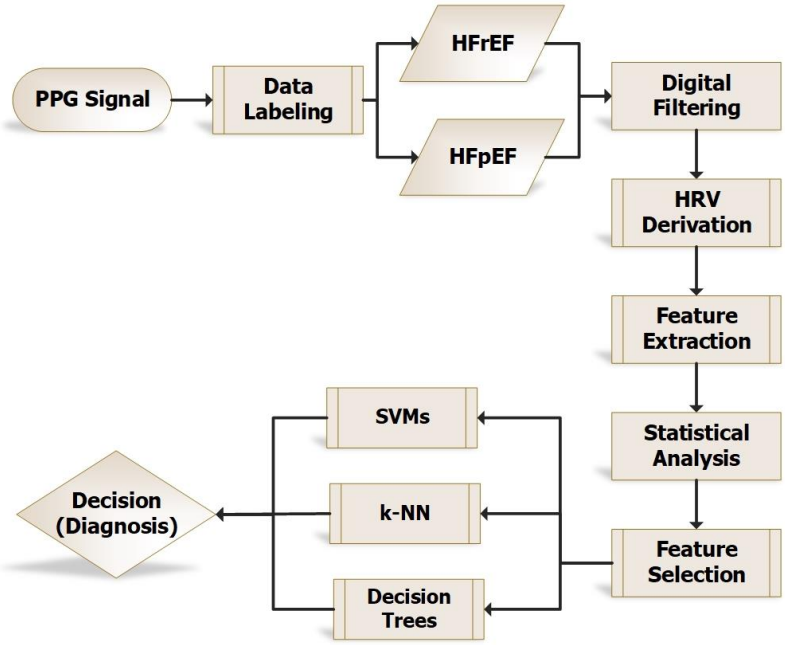

Figure 1. Work Flow of Study.

Sample PPGs of patients with HFrEF and HFpEF was presented in Figure 2. Further, Fast Fourier Transform was used to obtain the periodogram graph of signals and this graph was also presented in the figure. Whilst there was a similarity between the PPGs, they were distinguished in the periodogram. Hence, periodogram usage is advantageous for ML methods. After, features were extracted from HRVs. The features were statistically analyzed and they were selected. Eventually, we made classification studies with the features selected and we developed the diagnostic algorithm.

JSR A
Journal of Scientific Reports

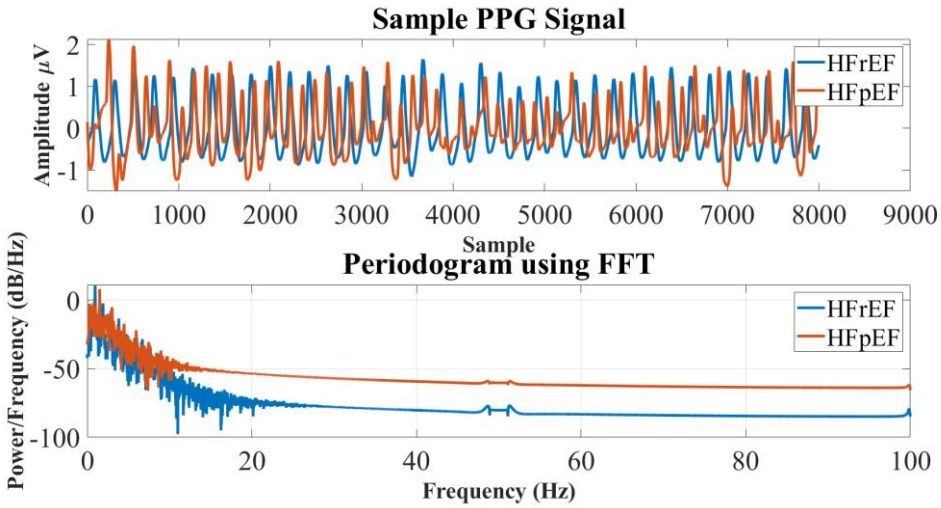

Figure 2. Periodogram Graph of PPGs.

2.2. HRV Features

Firstly, 21 features in the time domain were extracted from the HRVs. Table 2 shows these features [23]. In the 1st column the numbers given to the features, in the 2nd column the features' names and in the 3rd column the formulas of the features were given in Table 2. Furthermore, sixteen more features were also attached to the twenty-one features. Of the sixteen features were eight of which the output parameters of Burg's Method and eight of which the output parameters of the Yule-Walker Method. Each of these eight output parameters were four of which were the normalized autoregressive (AR) parameters equivalent to the fourth-order model, one of which was the predicted variance of the white noise input, and three of which were the reflection coefficients. The whole number of features extracted from HRV was 37. MATLAB was used to calculate features.

2.3. Statistical Analysis

The distribution of the HRV is not normal. For this reason, statistical analysis is made with non-parametric tests.

The Mann Whitney U test is performed to establish whether the two groups belong to the same population [24]. In this study, the Mann Whitney U test was performed to define which of the 37 extracted features were distinctive. Asymptotic Significances (p-values) of the features were given in Table 3. The features were also ranked in the table.

Table 2. Features Extracted From HRV at Time Domain.

Feature Number	Feature Name	Feature Equation

JSR A
Journal of Scientific Reports

1	Kurtosis	$x_{kur} = \frac{\sum_{i=1}^{n}(x_i - \bar{x})^4}{(\mathrm{n}-1)S^4}$
2	Skewness	$x_{ske} = \frac{\sum_{i=1}^{n}(x_i - \bar{x})^3}{(\mathrm{n}-1)S^3}$
3	* Interquartile range	$IQR = iqr(x)$
4	Geometric mean	$\mathrm{GeoM} = \sqrt[n]{x_1 + \cdots + x_n}$
5	Harmonic mean	$\mathrm{HarM} = n/(\frac{1}{x_1}+\cdots+\frac{1}{x_n})$
6	Hjort Parameters - Mobility	$M = S_1^2/S^2$
7	Hjort Parameters - Complexity	$\mathrm{C} = \sqrt{(S_2^2/S_1^2)^2 - (S_1^2/S^2)^2}$
8	Hjort Parameters - Activity	$A = S^2$
9	*Maximum	$x_{max} = max(x_i)$
10	Median	$\tilde{x} = \begin{cases} x_{\frac{n+1}{2}} & : x\ odd \\ \frac{1}{2}\left(x_{\frac{n}{2}} + x_{\frac{n}{2}+1}\right) & : x\ even \end{cases}$
11	*Mean Absolute Deviation	$MAD = mad(x)$
12	*Minimum	$x_{min} = min(x_i)$
13	*Central Moments	$CM = moment(x, 10)$
14	Mean	$\bar{x} = \frac{1}{n}\sum_{i=1}^{n} x_i$
15	Average curve length	$CL = \frac{1}{n}\sum_{i=2}^{n} \lvert x_i - x_{i-1} \rvert$
16	Standard Deviation	$S = \sqrt{\frac{1}{n}\sum_{i=1}^{n}(x_i - \bar{x})}$
17	Standard Error	$S_{\bar{x}} = S/\sqrt{n}$
18	Shape Factor	$SF = X_{rms}/\left(\frac{1}{n}\sum_{i=1}^{n}\sqrt{\lvert x_i \rvert}\right)$
19	*Singular Value Decomposition	$SVD = svd(x)$
20	*25% Trimmed Mean	$TM25 = trimmean(x, 25)$
21	*50% Trimmed Mean	$TM50 = trimmean(x, 50)$

* MATLAB was used to calculate the feature
$\bar{x}$: the distibution mean
n: the sample's observations number
S_1: the standard deviation of the signal's 1st derivative
S_2: the standard deviation of the signal's 2nd derivative
X_{rms}: Root Mean Square $X_{rms} = \sqrt{\frac{1}{n}\sum_{i=1}^{n}|x_i|^2}$

JSR A
Journal of Scientific Reports

Table 3. Mann-Whitney U Test Results.

Rank	Feature Number	R (Eta)	R^2	p value	Rank	Feature Number	R (Eta)	R^2	p value
1	**10**	0.4915	0.2415	0.0000	**20**	**11**	0.0354	0.0013	0.0223
2	**21**	0.4820	0.2323	0.0000	**21**	**34**	0.0137	0.0002	0.0054
3	**20**	0.4166	0.1736	0.0000	**22**	**26**	0.2383	0.0568	0.0739
4	**4**	0.4131	0.1707	0.0000	**23**	**6**	0.1889	0.0357	0.0500
5	**5**	0.4118	0.1696	0.0000	**24**	**30**	0.1689	0.0285	0.0739
6	**14**	0.3915	0.1533	0.0000	**25**	**37**	0.1605	0.0258	0.1749
7	**2**	0.3642	0.1327	0.0001	**26**	**32**	0.1000	0.0100	0.1667
8	**12**	0.3141	0.0987	0.0025	**27**	**36**	0.0954	0.0091	0.5655
9	**7**	0.2701	0.0729	0.0009	**28**	**24**	0.0938	0.0088	0.0925
10	**18**	0.2645	0.0700	0.0021	**29**	**31**	0.0749	0.0056	0.9102
11	**19**	0.2593	0.0672	0.0051	**30**	**27**	0.0689	0.0047	0.6688
12	**35**	0.2283	0.0521	0.0008	**31**	**3**	0.0639	0.0041	0.1488
13	**1**	0.2086	0.0435	0.0389	**32**	**22**	0.0563	0.0032	0.2784
14	**28**	0.1627	0.0265	0.0242	**33**	**33**	0.0448	0.0020	0.7628
15	**29**	0.1328	0.0176	0.0360	**34**	**25**	0.0278	0.0008	0.7950
16	**13**	0.1284	0.0165	0.0281	**35**	**9**	0.0238	0.0006	0.4264
17	**15**	0.1094	0.0120	0.0139	**36**	**23**	0.0235	0.0006	0.7708
18	**8**	0.1032	0.0106	0.0425	**37**	**17**	0.0106	0.0001	0.0748
19	**16**	0.0541	0.0029	0.0425					

According to Table 3, p-value is higher than 0.05 for the features 3, 6, 9, 17, 22, 23, 24, 25, 26, 27, 30, 31, 32, 33, 36, 37. That is, these 16 features are not distinctive for the two classes.

Classification with high accuracy was made with only three features as 10th, 20th, and 21st. These features were in the top three in the ranking.

2.4. Study of Classification

The dataset was arranged as a matrix. Rows were individuals and columns were features. After labeling, a label column was attached next to the feature columns as the last column. 10-fold cross validation was performed for evaluation. Performance values were calculated by comparing the pre-arranged label column and simulation results.

Inclusive of Support Vector Machines (SVMs), Decision Trees, and k-Nearest Neighbours (k-NN), three ML algorithms were applied.

Fine Gaussian SVM was applied. Kernel function was Gaussian, kernel scale was 0.35, and box constraint was 1. Fine Decision Trees was applied. Maximum number of splits was 100, and split criterion was Gini's diversity index. And for the fine k-NN, number of neighbors was 1, distance metric was Euclidean, and distance weight was equal.

As a result of classifications made with only 3 features of HRV as median, 25% trimmed mean and 50% trimmed mean, very high and reliable results were obtained.

For each classifier, performance parameters of classification were given in Table 4. SVMs classifier had the best results.

Table 4. Performance Parameters of Classification.

ML Algorithm	Accuracy (%)	Specificity	Sensitivity	AUC	F-Measure	Kappa
SVMs	98.33	1	0.9667	0.9833	0.9818	0.9667
k-NN	96.67	1	0.9333	0.9667	0.9618	0.9333
Decision Trees	95.83	0.9833	0.9333	0.9583	0.9561	0.9167

3. .RESULTS

A new algorithm was improved using only three features extracted from HRV for diagnosing HFrEF and HFpEF. At first, the number of extracted features was 37. But for real-time systems, extracting so many features was hard. So, to improve the performance, the amount of features was reduced. feature ranking for all features was given in the table of Mann Whitney-U Test results, amount of features was diminished to three for improving the classification efficiency, and used. These three features used for classification were in the top three in the ranking.

As a result of the algorithm, high accuracy was acquired using the 10th, 20th, and 21st features. The classification results were given in Table 4. These results, which were acquired only using three features, can be argued as a significant system performance for use in practice.

We mentioned HFrEF-HFpEF binary classification in the results section of our triple classification study with PPG [23] before. However, in the study, lower accuracy was achieved with more features extracted from both PPG and HRV. Since this binary classification with PPG has not been studied before in the literature, we continued to study this subject. In this study, high accuracy classification was performed with 3 features extracted from only HRV.

Classifiers' ROC curves were given in Figure 3. According to the figure, the sensitivities of SVMs and k-NN classifiers were very good, all classifiers were very close to ideal and gave good results.

The most generally made examination in cases with doubted HF is the echocardiogram. Since patients are mostly characterized with LVEF in many clinical studies, it is more important than being a manifestation of HF. LVEF is ordinarily identified by using the echocardiogram. Radionuclide angiography or radionuclide ventriculography (Multiple Gated Acquisition, MUGA) and Single Photon Emission Computerized Tomography (SPECT) are also employed seldomly. Those technical equipments are costly, each of them requires a specialist, and some of the techniques are invasive. Besides, conditions, in which reaching the devices is restricted, may ocur. On the contrary, PPG is not pricy, easy to get, and responds quickly. So, the applicability of the HFrEF - HFpEF distinction using HRV was studied for alternating to expensive devices.

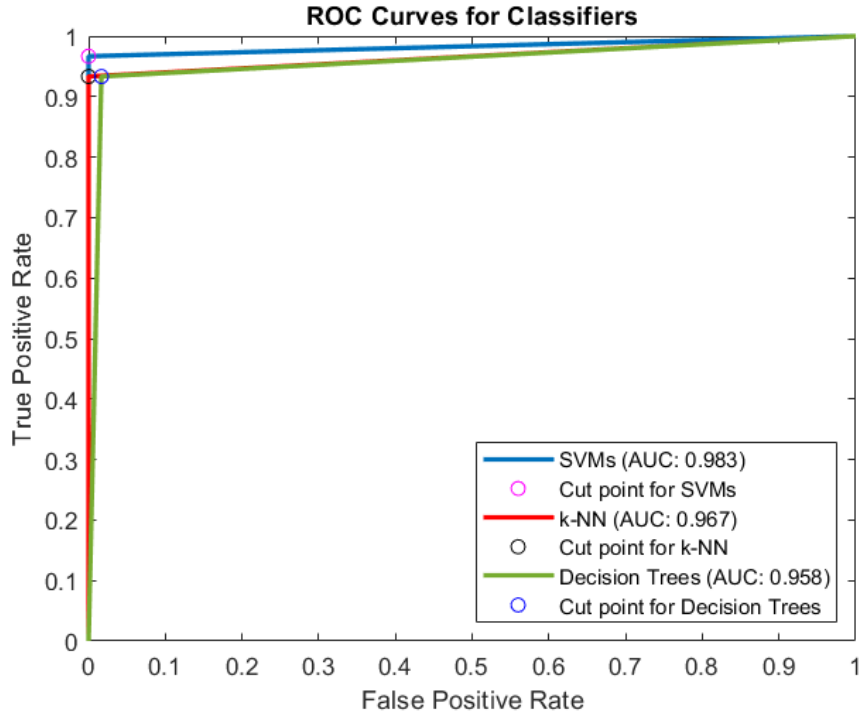

Figure 3. ROC curves for classifiers.

4. DISCUSSION

With this study, an algorithm for a system that supports the physician to diagnose, and didn't require a specialist was intended to use only PPG for two HF subtypes which could be overlooked and difficult to diagnose. The algorithm was developed with PPG, that could be readily obtained also with smartphones, to be inserted into appliances in the further.

The results of our study showed that three features ejected from PPG-derived HRV might be utilized in the diagnosing of HFpEF and HFrEF and would ensure significant outcomes. The way to diagnose HFpEF and HFrEF with only one signal is opened with easily obtained PPG signals.

Before echocardiography, expensive tests, and laborious blood tests, required for the diagnosis of HFpEF and HFrEF, PPG usage will abate the workload.

In our study, by signal processing and machine learning methods, it was deduced that PPG-derived HRV might be utilized in the diagnosis of HFpEF and HFrEF. Compared to other diagnostic methods, PPG measurement is easier. So, this system is also advantageous for patient comfort.

In the literature, HFrEF and HFpEF classification studies using PPG or PPG-derived HRV have not been previously performed. It is thought that our study will contribute to the literature with this aspect. In one of HF-related studies conducted in the current year, low HRV was shown to be associated with an increased incidence of coronary heart disease (CHD) and HF in a cohort of postmenopausal women [25]. In the study, a risk analysis was performed for HF, not a diagnostic study, using HRV derived from 12-lead ECG and demographic information such as age, race, body mass, etc. and information about treatments administered.. More features are used, which are obtained by more demanding methods in that study. So, the system we propose is more practical than that study.

The point that our study contributes to the literature is that HFpEF and HFrEF can be distinguished with a sole signal by using PPG. It is thought that it will pioneer to the next researches on the related subject. The used dataset wasn't very large. So, conventional machine learning methods were performed. Novel studies may be accomplished by applying more recent ML techniques with a bigger dataset.

ACKNOWLEDGEMENTS

The authors would like to thank Assist. Prof. İbrahim Kocayiğit and Assoc. Prof. Cahit Bilgin, from Sakarya University Faculty of Medicine, for their valuable contributions in data collection and labeling, and valuable referees who contributed to the development of the article with their evaluations. This study was supported by Sakarya University Scientific Research Projects Coordinatorship with the project numbered 2021-9-33-125.

REFERENCES

[1] Maceira, A.M., Prasad, S.K., Khan, M., Pennell, D.J. (2006). Normalized left ventricular systolic and diastolic function by steady state free precession cardiovascular magnetic resonance. Journal of Cardiovascular Magnetic Resonance, 8, 417–426.

[2] Dickstein, K., Cohen-Solal, A., Filippatos, G., McMurray, J.J.V., Ponikowski, P., ve Poole-Wilson, P.A. (2008). ESC Guidelines for the diagnosis and treatment of acute and chronic heart failure 2008‡. European Journal of Heart Failure, 10, 933–989.

[3] Remme, W.J., Swedberg, K. (2001). Guidelines for the diagnosis and treatment of chronic heart failure. European Heart Journal, 22, 1527–1560.

[4] Hogg, K., Swedberg, K., McMurray, J. (2004). Heart Failure with Preserved Left Ventricular Systolic Function: Epidemiology, Clinical Characteristics, and Prognosis. Journal of the American College of Cardiology, 43, 317–327.

[5] Ponikowski, P., Voors, A.A., Anker, S.D., Bueno, H., Cleland, J.G.F., ve Coats, A.J.S. (2016). 2016 ESC Guidelines for the diagnosis and treatment of acute and chronic heart failure: The Task Force for the diagnosis and treatment of acute and chronic heart failure of the European

Society of Cardiology (ESC)Developed with the special contribution of the Heart Failure Association (HFA) of the ESC. European Heart Journal, 37, 2129-2200.

[6] Nitzan, M., Noach, S., Tobal, E., Adar, Y., Miller, Y., ve Shalom, E. (2014). Calibration-free pulse oximetry based on two wavelengths in the infrared - A preliminary study. Sensors (Switzerland), 14, 7420–7434.

[7] Rubins, U., Grabovskis, A., Grube, J., Kukulis, I. (2008). Photoplethysmography Analysis of Artery Properties in Patients with Cardiovascular Diseases. International Federation for Medical and Biological Engineering Proceedings, 20, 319–322.

[8] El-Hajj, C., Kyriacou, P.A. (2020). A review of machine learning techniques in photoplethysmography for the non-invasive cuff-less measurement of blood pressure. Biomedical Signal Processing and Control, 58, 101870.

[9] Silber, H.A., Trost, J.C., Johnston, P.V., Lowell Maughan, W., Wang, N.Y., Kasper, E.K., vd. (2012). Finger photoplethysmography during the Valsalva maneuver reflects left ventricular filling pressure. American Journal of Physiology Heart and Circulatory Physiology, 302.

[10] Gilotra, N.A., Wanamaker, B.L., Rahim, H., Kunkel, K., Yenokyan, G., Schulman, S.P., vd. (2020). Usefulness of Noninvasively Measured Pulse Amplitude Changes During the Valsalva Maneuver to Identify Hospitalized Heart Failure Patients at Risk of 30-Day Heart Failure Events (from the PRESSURE-HF Study). American Journal of Cardiology, 125, 916–923.

[11] Schack, T., Safi Harb, Y., Muma, M., Zoubir, A.M. (2017). Computationally efficient algorithm for photoplethysmography-based atrial fibrillation detection using smartphones. Proceedings of the Annual International Conference of the IEEE Engineering in Medicine and Biology Society, 104–108.

[12] Avram, R., Tison, G., Kuhar, P., Marcus, G., Pletcher, M., Olgin, J.E., vd. (2019). PREDICTING DIABETES FROM PHOTOPLETHYSMOGRAPHY USING DEEP LEARNING. Journal of American Collage of Cardiology, 73, 16.

[13] Blok, S., Piek, M.A, Tulevski, I.I, Somsen, G.A, Winter, M.M. (2021). The accuracy of heartbeat detection using photoplethysmography technology in cardiac patients. Journal of Electrocardiology, 67, 148–157.

[14] Baldoumas, G., Peschos, D., Tatsis, G., Chronopoulos, S.K., Christofilakis, V., Kostarakis, P., vd. (2019). A Prototype Photoplethysmography Electronic Device that Distinguishes Congestive Heart Failure from Healthy Individuals by Applying Natural Time Analysis. Electronics, 8, 1288.

[15] Baldoumas, G., Peschos, D., Tatsis, G., Christofilakis, V., Chronopoulos, S.K., Kostarakis, P., vd. (2021) Remote sensing natural time analysis of heartbeat data by means of a portable

photoplethysmography device. International Journal of Remote Sensing, 42, 2292–2302.

[16] Adebayo, P.B., Akintunde, A.A., Adebayo, A.J., Asaolu, S.O., Audu, M., Ayodele, O.E. (2017). Comparison of Neuropsychological Patterns in Nigerians with different Heart Failure Phenotypes. Archives of Clinical Neuropsychology, 32, 280–288.

[17] Levinson, R.T., Vaitinidin, N.S., Farber-Eger, E., Roden, D.M., Lasko, T.A., Wells, Q.S., vd. (2021). Heart failure clinical care analysis uncovers risk reduction opportunities for preserved ejection fraction subtype. Scientific Reports 2021, 11(1), 1–9.

[18] Ho, J.E., Enserro, D., Brouwers, F.P., Kizer, J.R., Shah, S.J., Psaty, B.M., vd. (2016). Predicting Heart Failure With Preserved and Reduced Ejection Fraction: The International Collaboration on Heart Failure Subtypes. Circulation. Heart Failure, 9.

[19] Ho, J.E., Lyass, A., Lee, D.S., Vasan, R.S., Kannel, W.B., Larson, M.G., vd. (2013). Predictors of new-onset heart failure differences in preserved versus reduced ejection fraction. Circulation. Heart Failure, 6, 279–286.

[20] A Austin, P.C., Tu, J.V., Ho, J.E., Levy, D., Lee, D.S. (2013). Using methods from the data-mining and machine-learning literature for disease classification and prediction: a case study examining classification of heart failure subtypes. Journal of Clinical Epidemiology, 66 398–407.

[21] Işler, Y., Kuntalp, M. (2007). Combining classical HRV indices with wavelet entropy measures improves to performance in diagnosing congestive heart failure. Computers in Biology and Medicine, 37, 1502–1510.

[22] Bozkurt, M.R, Uçar, M.K., Bozkurt, F., Bilgin, C. (2020). Development of hybrid artificial intelligence based automatic sleep/awake detection. IET Science, 14(3), 353-366.

[23] Özen Kavas, P., Bozkurt, M.R., Kocayiğit, İ., Bilgin, C. (2023). Machine learning-based medical decision support system for diagnosing HFpEF and HFrEF using PPG. Biomedical Signal Processing and Control, 79, 104164.

[24] Nachar, N. (2008). The Mann-Whitney U: A Test for Assessing Whether Two Independent Samples Come from the Same Distribution. Tutorials in Quantitative Methods for Psychology, 4, 13–20.

[25] Baig, M., Moafi-Madani, M., Qureshi, R., Roberts, M.B., Allison, M., ve Manson, J.A.E. (2022). Heart rate variability and the risk of heart failure and its subtypes in post-menopausal women: The Women's Health Initiative study. PLoS One, 17(10), e0276585.

Kütahya Dumlupınar University
Institute of Graduate Studies

Journal of Scientific
Reports-A
E-ISSN: 2687-6167
Number 51, December 2022

RESEARCH ARTICLE

PREDICTION of WORKER MOTIVATION with ARTIFICIAL NEURAL NETWORKS and LINEAR MODELING

Akın ERDEMİR[1], Fatih SEYRAN[2*], Tuğrul BATIRER[3]

[1]Suleyman Demirel University Hospital, Isparta, akinerdemir@sdu.edu.tr, ORCID: 0000-0001-9884-6135
[2*]Ministry of Health General Directorate of Management Services, Ankara, fatihseyran@gmail.com, ORCID: 0000-0001-8546-11458
[3]Ministry of Health Sincan Oral and Dental Health Center, Ankara, tugrulbatirer@gmail.com, ORCID: 0000-0003-0453-159X

Receive Date:17.07.2022 *Accepted Date: 11.08.2022*

ABSTRACT

Organizational justice is a motivation tool that can produce positive results for the organization and employees in working life. The decrease in the perception of justice can cause moral disorders of the employees, may lead them to leave the organization and even to engage in negative behaviors towards the organization. This study was carried out to determine the effect of organizational justice perceived by employees on employee motivation and to predict organizational justice and motivation. The research was carried out with 294 participants working in public institutions serving in Isparta. Firstly, multiple regression analysis was conducted to test the effect of organizational justice on employee motivation. Within the scope of the study, linear modeling and artificial neural networks (ANN) models were also compared in order to contribute to the literature. Multiple regression analysis results showed that interactional and distributive justice had a significant and direct effect on motivation. In addition, it was determined that the highest predictive power was ANN (R^2 = 0.88) according to motivation models. As a result of the study, the predictability of the organizational justice phenomenon perceived by the employees and the motivation of the employee has emerged.

Keywords: *Artificial Neural Networks, Employee Motivation, Organizational Justice, Organizational Management*

1. INTRODUCTION

In general, individuals evaluate whether all events around them are fair and react differently when faced with injustice. One of the most important environments in which the idea of justice is evaluated is workplaces where people spend most of their time [1]. At the same time, one of the places where the existence of justice is questioned most is workplaces.

Organizational justice is the sum of transactions and practices among individuals that reveal how rewards and punishments are given to employees in the organization, how they are distributed and

JSR A
Journal of Scientific Reports

how these decisions are made [2,3]. In a broad sense, organizational justice is the perception of justice in the minds of employees regarding organizational practices In this context, employees are in search of justice on the axis of differentiation, cognition and externality [4].

Studies on organizational justice begin with Adams (1963)'s theory of equality. According to this theory, the achievements and satisfaction levels of the employees are related to the perceived equality or inequality in the workplace [5]. Equity theory includes the benefits of human resources to the organization and the gains they get from the organization [6]. According to the theory; equality is the employee's belief that he or she is treated fairly compared to other employees, while inequality is the employee's belief that he or she is not treated fairly compared to other employees. According to Adams (1963), the employees in the organization compare the gains they have achieved within the organization with the gains obtained by the employees working in different organizations and in the same position. As a result, they develop an attitude towards the managers of the organization and their work. This is about how the employee perceives the climate of justice within the organization [7].

Organizational justice is a motivational tool with valuable results for both the organization and the employees. The decrease in the perception of justice can lead to moral disorders in the employees and may push the employees to leave the organization and even to engage in negative behaviors related to the organization [8,9]. Positive results regarding its motivational effects in working life focused on informational justice as well as interpersonal justice. In this context, it is seen how important organizational justice is in order to ensure the processes of sustainable motivation in employees [4]. The decrease in the perception of justice can lead to moral disorders in the employees and may push the employees to leave the organization and even to engage in negative behaviors related to the organization Directing the effort of the members of the organization to achieve organizational goals and thus transforming them into performance is important in terms of organizational effectiveness and efficiency [10]. Therefore, managers who will control the process with the help of various incentive tools according to the personality traits of the members of the organization also play an important role in work motivation [11].

Studies in the literature to determine the motivation of employees have focused on causality. Especially in these studies conducted in recent years, many analyzes have been put forward on the main factors and relationships that affect employee motivation in general [12-16]. However, in an area where employee motivation is so important, it is necessary to go beyond the retrospective examination of causality and relational dimensions after this situation has arisen. In this context; in addition to the factors affecting employee motivation, a newer approach may be to predict the new situation that may arise as a result of these factors.

This research was conducted to predict the justice and motivation by determining the effect of organizational justice perceived by employees on employee motivation. In this context, it is of great importance to estimate the density of the concepts mentioned as a result of the findings to be obtained. Because planning made in this way can save time, effort and financial resources, especially for organizations.

JSR A
Journal of Scientific Reports

2. MATERIAL and METHOD

The population of the research consists of the employees of public institutions serving in Isparta. 350 volunteers to participate in the research were selected as a sample and the questionnaire was applied in the period of September-November 2019. 56 of them were not evaluated due to incomplete filling and 294 of the collected questionnaires were analysed. The organizational justice scale [17] developed by Colquitt (2001) and the motivation scale [18] developed by Özdaşlı and Akman (2012) were used in the research.

Three dimensions of organizational justice perception in the research; Perceptions of procedural justice, interactional justice and distributive justice are independent variables, employee motivation is the dependent variable of the research. While creating the variables, the data that will enter the analysis were obtained by taking the averages of the questions related to motivation (22 items), procedural justice (7 items), interactional justice (9 items) and distributive justice (4 items) based on the cumulative totals.

Normality tests were carried out to decide which analysis types to use within the scope of the research, and the relevant results are given in Table 1. According to Sposito et al., (1983), skewness and kurtosis values are between +3 and -3, indicating that the data are normally distributed [19]. Based on this information in the literature, the normal distribution of the data was determined for all subscales [20]. The findings were evaluated at the 95% confidence interval and at the 5% significance level.

Table 1. Normality test results.

Variables	**Skewness**	**Kurtosis**
Motivation	0,067	-0,992
Interpersonal justice	0,238	0,142
Procedural justice	0,714	0,745
Distributive justice	0,533	-0,094

3. RESULTS and DISCUSSION

3.1. Linear Modeling

In the first part of the study, multivariate regression analysis was performed to understand the effect of independent variables (organizational justice dimensions) on the dependent variable (employees' perception of motivation). In addition, it was evaluated whether there was a multicollinearity between the independent variables.

As seen in Table 2, VIF (variance inflation factor) values were found to be less than 10 and tolerance values greater than 0.10, and it was seen that there was no linear connection problem [21].

Table 2. Linear connection analysis results.

Variables	**Tolerance**	**VIF**

JSR A
Journal of Scientific Reports

Interpersonal justice	0,728	1,374
Procedural justice	0,784	1,276
Distributive justice	0,840	1,190

3.2. The Relationship Between Organizational Justice and Employee Motivation

As a result of the analysis, organizational justice with interactional, procedural and distributive origin explains 40% of the motivation perception of the employees.

ANOVA analysis (Table 3.) shows that at least one of our dependent variables has a significant effect on the dependent variable (p= 0.000).

Table 3. Results on employee motivation perceptions of interpersonal, procedural, and distributive organizational justice.

ANOVA	**F**	**Sig.**
Regression	15,932	0,000

The coefficients analysis we conducted to understand which independent variable has a significant effect on the motivation perception of the employees is given in Table 4. This table explains that the interactional justice and distributive justice dimensions have an effect on the motivation of the employees through linear models.

Table 4. Analysis of the coefficients of employee motivation perception of interpersonal, procedural and distributive organizational justice.

Variables	**B**	**T test**	**Sig.**
Constant	8,030	1,726	0,085
Interpersonal justice	1,423	9,361	0,000
Procedural justice	0,285	1,413	0,159
Distributive justice	1,092	3,517	0,001

3.3. Artificial Neural Networks Analysis

After the regression analysis, the modeling phase was started with artificial neural networks (ANN). ANN is a mathematical modeling method inspired by the functioning of the human brain. Learning process in artificial neural networks is carried out using examples. During learning, the user is given input and output information, and rules are set. These models are obtained with some computer software that exemplifies the principle of communication between neurons in human brain cells [22]. In order to determine the relationship between the variables, organizational justice with interactional, procedural and distributive origins was chosen as the input variable and the motivation variable as the output. Of the 294 data sets, 250 were randomly selected as training and 44 as test data sets.

In the literature, it is stated that the performance and accuracy of these networks will increase thanks to some normalization methods applied according to ANN data [23-26]. In this context, various normalization methods are used by researchers to solve problems, and the d_Min-Max method is

JSR A
Journal of Scientific Reports

mostly preferred (Equation 1). With d_Min-Max normalization, the data is scaled in the range of 0-1. In this way, the negative effects of extremely large and small data on the model are reduced [27-29].

$$x_{norm} = \frac{x_i - x_{min}}{x_{max} - x_{min}} \quad (1)$$

x_{norm}= Normalized data
x_i= Input value
x_{min}= The smallest number in the input set
x_{max}= The largest number in the input set

It has been observed that various ANN structures emerge as a result of some rules about learning according to the activation functions and the way neurons are connected to each other. It is understood that these basically mentioned structures are divided into 3 different classes. These; It can be summarized as feedforward neural networks, feedback neural networks and radial-based neural networks [23,24]. The feedforward ANN structure was used for the models created, and the Levenberg-Marquardt learning algorithm, which is one of the supervised learning algorithms, was preferred for the learning of the network. The Levenberg-Marquardt algorithm is the result of the speed of the Newton method and the robustness of the gradient decreasing method. This algorithm is the fastest among back propagation algorithms [25,26]. In practice, this learning algorithm was preferred because it is suitable for the type of problem and also because it is fast and has low learning errors [27]. The graphs of the artificial neural network model created with the training data are presented in Figure 1.

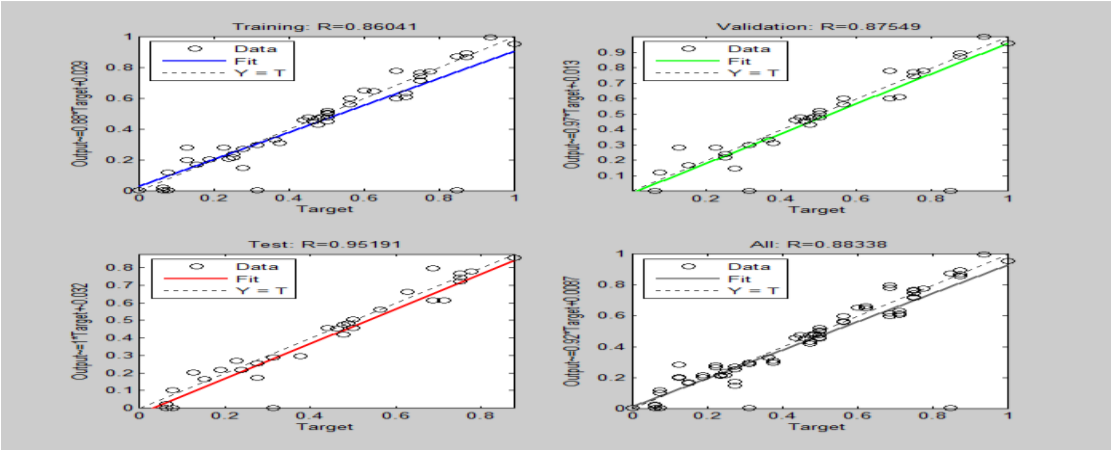

Figure 1. Neural network structure and training graph.

Considering the motivation estimation for the ANN model with the test data set, it is understood that the resulting predictive power of this model is remarkably high. (R^2 = 0.88). The relationship between actual and predicted motivation according to ANN is shown in Figure 2.

JSR A
Journal of Scientific Reports

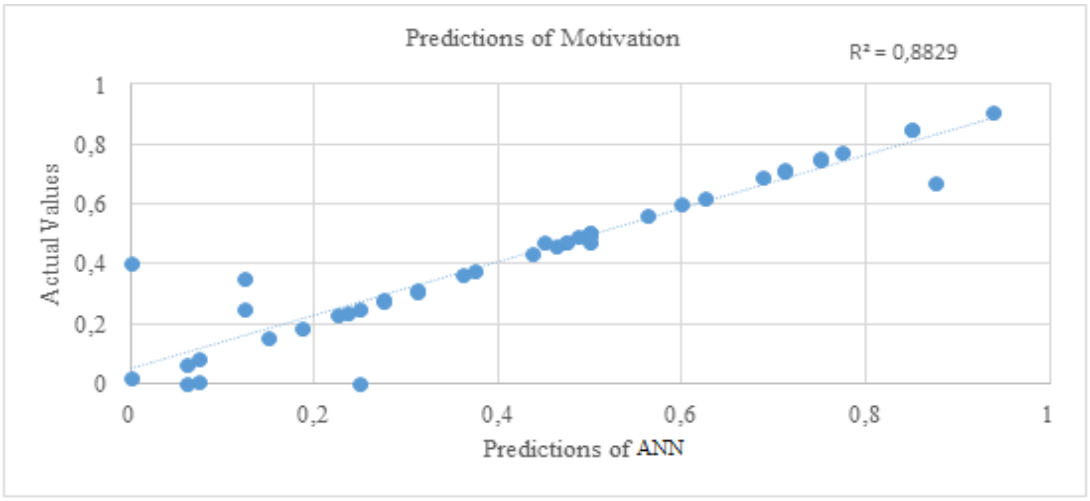

Figure 2. Actual and predicted motivation relationship according to ANN.

4. CONCLUSION

In this research, the effect of organizational justice perceived by employees on employee motivation was determined and focused on the predictability of justice and motivation.

The results of multiple regression analysis obtained in this study show that interactional and distributive justice have a significant and direct effect on employee motivation. According to this; employee motivation increases or decreases depending on the result of the perception of justice in the minds of employees regarding organizational practices. In addition, as a result of the analyzes made with the ANN model to predict the motivation of the employees, it was determined that the predictive power of this model was quite high ($R^2 = 0.88$). According to the results of the analysis, the fact that the predictive power of the ANN model is quite high and reliable is also important in terms of showing a more innovative approach for similar studies. It is understood that the findings obtained thanks to these new analysis methods contain more valuable results in terms of predictability.

Turunç and Tabak (2009) investigated the effects of organizational justice factors (procedural, distributive and interactional justice) on motivation, and in this context, the relationships between the variables were examined with the help of the structural equation model. As a result of the analysis, it was determined that interactional justice and distributive justice positively and significantly affect motivation in parallel with this study[28]. Karanika-Murray and Cox (2010) determined the applicability of neural networks as a result of their study to model the effect of job characteristics on employee health outcomes. According to the same study, linear approaches were found to be effective in this process [29]. According to Erenler-Tekmen et al. (2020) evaluated whether conflicts have an effect on workplace bullying using linear and fuzzy logic methods. As a result of the study in question, according to the results of multiple regression analysis; It has been determined that there is a

significant and direct effect of task and relationship conflict on the behavior of being exposed to workplace bullying. However, within the scope of the same research results, fuzzy logic qualitative comparison analysis (fsQCA) showed that only relationship-based conflict was effective on workplace bullying [30].

It can be said that the sense of justice in people is generally evaluated within the framework of a universal ethical understanding. Every person can demand justice both for himself and for his environment. Because we witness that individuals who think that their rights are violated from time to time in social life may experience conflict, get angry, upset or demoralized. However, individuals will want their rights not to be usurped not only in social life but also in business life. Almost every employee will want their job to be respected by their employers and colleagues. In this way, employees can feel more motivated. But let's consider the opposite. Can an employee who thinks he/she is not treated fairly be motivated in business life? In this context; we should focus on a predictability for the positive behaviors that are expected to emerge in working life.

In today's innovation world, predictability gains importance for the ever-changing business life. Thanks to artificial intelligence studies, possible risks are estimated especially in the service and production sectors and it is desired to prevent them. Moreover, in the light of feasibility and efficiency analyzes, an intense effort is made for the most effective results. In addition, intellectual capital, which is an inevitable resource for all sectors, maintains its importance. Considering all these, it would be appropriate to make predictions about the performance and productivity of the employees.

As a result of this estimation study made with linear modeling, the predictability of the organizational justice phenomenon perceived by the employees and the motivation of the employee has emerged. As a result; thanks to this research, the predictability of the organizational justice phenomenon perceived by the employees and the motivation of the employee has emerged.

As can be seen from this study; it can be said that the perception that employees are treated fairly has a triggering importance in terms of their own work motivation. Thanks to these estimates, when it is aimed to increase the motivation of the employees in the organizations, it can be recommended to make the employees feel that they are treated more fairly and to carry out organizational studies to increase this level. In addition, it may be recommended to diversify the size and scope of similar estimation studies for researchers working in this field.

ACKNOWLEDGEMENT

The authors declare that there is no conflict of interest. Also, thanks to Emre KUZUGUDENLI and Canpolat KAYA for their model suggestions. This study was presented as a summary paper with the title "The Effect of Organizational Justice on Employee Motivation: An Application with Linear and Artificial Neural Network Models" at the 3rd International Conference on Applied Engineering and Natural Sciences held on 20-23 July 2022.

REFERENCES

[1] Mueller, C.W., and Wynn T., (2000), The degree to which justice is valued in the workplace, Social Justice Research, 13(1):1–24.

[2] Folger, R., and Cropanzano R., (1998), Organizational justice and human resource management, Thousand Oaks / California: SAGE Publications.

[3] Colquitt, J.A., Lepine J., and Wesson M., (2018), Organizational behavior: Improving performance and commitment in the workplace (6th Edition), New York: McGraw-Hill Education.

[4] Colquitt, J.A., (2012), Organizational justice, In: Kozlowski, S. W. (Ed.), The Oxford handbook of organizational psychology, Vol 1., New York: Oxford University Press, pp.526–547.

[5] Adams, J.S., (1963), Towards an understanding of inequity. Journal of Abnormal and Social Psychology, 67(5):422–436.

[6] Lambert, E., (2003), The impact of organizational justice on correctional staff, Journal of Criminal Justice, 31(2):155–168.

[7] Chen, W., and Lee Y., (2022), Revisiting proficiency pairing in collaborative writing from an equity theory perspective: Voices from high-proficiency efl learners, SAGE Open. April:1–11.

[8] Folger, R., (1993), Justice, motivation, and performance beyond role requirements, Employee Responsibilities and Rights Journal, 6(3):239–248.

[9] Usmani, S., and Jamal S., (2013), Impact of distributive justice, procedural justice, interactional justice, temporal justice, spatial justice on job satisfaction of banking employees, Review of Integrative Business and Economics Research, 2(1):351–383.

[10] Bucăța, G., and Rizescu A., (2022), Change management: a way of enhancing organizational efficiency, Journal of Defense Resources Management, (1):166–173.

[11] Singh, S., Mahapatra M., and Kumar N., (2022), Empowering leadership and organizational culture: Collective influence on employee flourishing, International Journal of Health Sciences, 6(S1):2983–2993.

[12] Lenka L., Miloš H., Radovan S., and Zdeněk C., (2021), Motivational preferences within job positions are different: empirical study from the Czech transport and logistics enterprises, Economic Research-Ekonomska Istraživanja, 34(1):2387–2407.

[13] Tortia EC., Gago M., Degavre F., and Poledrini S., (2022), Worker involvement and performance in Italian social enterprises: The role of motivations, gender and workload,

Sustainability, 14(2):1–20.

[14] Mbachu C., Etiaba E., Ebenso B., Ogu U., Onwujekwe O., Uzochukwu B., Manzano A., and Mirzoev T., (2022), Village health worker motivation for better performance in a maternal and child health programme in Nigeria: A realist evaluation, Journal of Health Services Research and Policy, 27(3):222–31.

[15] Pandya S., Hamal M., Abuya T., Kintu R., Mwanga D., Warren CE., and Agarval S., (2022), Understanding factors that support community health worker motivation, job satisfaction, and performance in three ugandan districts: Opportunities for strengthening Uganda's community health worker program. International Journal of Health Policy and Management, x(x):1–9. doi; 10.34172/IJHPM.2022.6219

[16] Deussom R., Mwarey D., Bayu M., Abdullah SS., and Marcus R., (2022), Systematic review of performance-enhancing health worker supervision approaches in low- and middle-income countries, Human Resources for Health, 20(1):1–12.

[17] Colquitt, J.A., (2001), On the dimensionality of organizational justice: A construct validation of a measure, Journal of Applied Psychology, 86(3):386–400.

[18] Özdaşlı, K., and Akman H., (2012), The diversification of gender and organizational statute in internal and external motivations: The research on the engineers and the technicians in Türk Telekomünikasyon a.ş., Suleyman Demirel University The Journal of Visionary, 4(7):73–81.

[19] Sposito, V. A., Hand, M. L., and Skarpness B., (1983), On the efficiency of using the sample kurtosis in selecting optimal estimators, Communications in Statistics-Simulation and Computation, 12(3):265–272.

[20] Groeneveld, R.A., and Meeden G., (1984), Measuring skewness and kurtosis, Journal of the Royal Statistical Society: Series D (The Statistician), 33(4):391–399.

[21] Marquaridt, D.W., (1970), Generalized inverses, ridge regression, biased linear estimation, and nonlinear estimation, Technometrics, 12(3):591–612.

[22] Aghbashlo, M., Hosseinpour S., and Mujumdar A.S., (2015), Application of artificial neural networks (ANNs) in drying technology: A comprehensive review, Drying Technology, 33(12):1397–1462.

[23] Kuzugüdenli, E., (2022), Relationship between the productivity of Pinus brutia Ten and site characters, the Taurus Mountains, Turkey, Journal of Mountain Science, 19(3):662–672.

[24] Kuzugüdenli, E., and Kaya, C., (2020), Relations between the productivity of Turkish red pine in Mersin region and some topographic factors, Journal of Multidisciplinary Engineering Science and Technology, 7(11): 13011–13014.

[25] Levenberg, K., (1944), A Method for the solution of certain non-linear problems in least squares. Quarterly of Applied Mathematics, 2(2):164–168.

[26] Marquardt, D., (1963), An algorithm for least-squares estimation of nonlinear parameters, SIAM Journal on Applied Mathematics, 11(2):431–441.

[27] Öztemel, E., (2016), Yapay sinir ağları, İstanbul: Papatya Bilim.

[28] Turunç, Ö., and Tabak A., (2009), The role of procedural justice, distributive justice, interactional justice and instrinsic motivation on increasing job performance, The Journal of Defense Sciences, 8(1):15–35.

[29] Karanika-Murray, M., and Cox T., (2010), The use of artificial neural networks and multiple linear regression in modelling work-health relationships: Translating theory into analytical practice, European Journal of Work and Organizational Psychology, 19(4):461–486.

[30] Erenler-Tekmen, E., Özkan-Canbolat E., and Sağlam F., (2020), Evaluation of analyzing workplace bullying from conflict perspective by linear and fuzzy logic methods, Çankırı Karatekin University Journal of the Faculty of Economics and Administrative Sciences, 10(1):349–370.

Kütahya Dumlupınar University
Institute of Graduate Studies

Journal of Scientific
Reports-A
E-ISSN: 2687-6167
Number 51, December 2022

RESEARCH ARTICLE

THEORETICAL ELECTRONIC PROPERTIES, ADMET PREDICTION, and MOLECULAR DOCKING STUDIES of SOME IMIDAZOLE DERIVATIVES

Sevtap ÇAĞLAR YAVUZ[1*]

[1*]Erzincan Binali Yıldırım University, İliç Dursun Yıldırım Vocational School, Department of Medical Services and Technicians, sevtap.yavuz@erzincan.edu.tr, ORCID: 0000-0001-6497-2907

Receive Date:05.09.2022 *Accepted Date: 21.10.2022*

ABSTRACT

Imidazole is a significant component of heterocyclic compounds and is employed in a wide range of practices. It is recognized that different imidazole-based constructions exhibit various biological activity features. Ten imidazole derivatives prepared from phenylglyoxal monohydrate and different guanylhydrazones were designed in our previous publication. This study was focused on the structural/electronic properties of these known imidazole derivatives. The molecular geometry of the compounds was calculated using Spartan 10 software and the structure was optimized using the DFT/B3LYP method with the 6-31G** basis set ground state. Also, *in silico* evaluation of imidazole derivatives was carried out using UCSF Chimera and AutoDock Vina software. The protein used in these calculations is the crystal structure of the 3SN6, beta2 adrenergic receptor-Gs protein complex, responsible for the hormonal regulation of adenylate cyclase.

Keyword: *Imidazole, DFT, Molecular docking, ADMET*

1. INTRODUCTION

Nitrogen-including heterocyclic compounds such as imidazole and benzimidazole display various biological activities. Imidazole and its derivatives are pharmacologically important scaffolds with a wide spectrum of activity, so they have attracted the attention of researchers in recent years. Imidazole-based structures indicate a wide range of biological activity features such as anticancer [1], anti-HIV [2], antitubercular [3], anti-hepatitis [4], antiinflammatory [5], antibacterial [6], antihypertensive [7], antioxidants [8], antiprotozoal [9] antimicrobial [10], antiviral [11], antifungal [12], and diverse enzyme inhibitors [13]. In the medical area, many imidazole-based compounds such as dacarbazine, temozolomide, mercaptopurine, nilotinib, and tipifarnib as clinical drugs have been commonly used to cure diverse types of cancers [14].

Relative to some heterocyclic molecules, imidazoles readily connect to protein molecules, and some imidazole drugs directly obstruct the synthesis of essential cell membrane components in high concentrations [15,16].

JSR A
Journal of Scientific Reports

Physicochemical features, over the few decades, have emerged as one of the important stages in drug discovery. The pharmaceutical descriptors provide a variety of suitable "drug-like" traits that can be advanced into structure-property collaboration [17]. Owing to imidazole compounds' unique optical, structural, and electronic properties, their applications have gradually attracted interest in recent years [18-20]. In here, the theoretical evaluation of synthesized imidazole compounds was made in the previous study [21]. The geometry of the molecules was determined theoretically by using the DFT method with the Spartan 10 package program. For the chemical stability of the structure, various parameters were calculated in the gas phase such as the highest occupied (E_{HOMO}) and lowest unoccupied molecular orbital (E_{LUMO}) energies, ovality, dipole moment (μ), electronegativity (χ) and chemical hardness (η) values. *In silico* studies such as DFT (Density Functional Theory) calculations, molecular modeling, and ADME predictions have been accomplished and debated to achieve more comprehensions into the structure-activity relationship of the imidazole derivative compounds. In this context, the physico-chemical and ADMET features were predicted. It was done molecular docking analysis of the imidazole derivative compounds using G protein-coupled receptors (GPCRs) as responsible for the majority of cellular responses.

2. MATERIALS AND METHODS

2.1. Theoretical Studies

All quantum chemical calculations were accomplished using the Spartan 10 program. Compounds (**1-10**) were computed by using the DFT method with B3LYP/6-31G** basic set. The molecular structures were visualized depending on the output data of the DFT computations again using the identical program. The general chemical structure and structural features of the studied compounds are given in Figure 1 and Table 1.

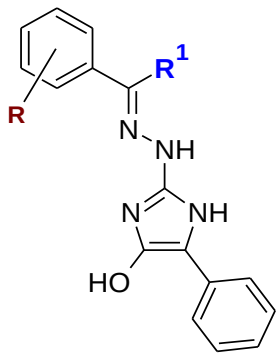

Figure 1. The chemical structure of studied compounds **(1-10)**.

Table 1. Structural features of studied compounds **(1-10)**.

Compounds	**R**	**R^1**
1	4-CH_3	H
2	H	H

JSR A
Journal of Scientific Reports

3	4-NO_2	H
4	2,4-*di*CH_3O	H
5	2-Cl-6-F	H
6	2-Cl	H
7	4-CH_3CH_2O	H
8	2,4-*di*Cl	H
9	4-Cl	H
10	H	CH_3

2.2. Docking and *In Silico* ADMET Studies

The inhibitory effect of the imidazole derivatives on the human beta2 adrenergic receptor-Gs protein was studied. Docking analyzes were performed using AutoDock Vina software and UCSF Chimera. The 3D structure of the beta2 adrenergic receptor (PDB code: 3SN6) in PDB format at 3.20 Å resolution was downloaded from the RSCB PDB website. The 2D structures of the ligands were drawn on ChemDraw Ultra 12.0 and optimized with Spartan 10 software [22]. The optimized structures were loaded into the UCSF Chimera tool. The docking analyzes of related compounds were operated utilizing the confirmed procedure present in the literature [23]. Interactions were visualized owing to Biovia Discovery Studio Visualizer [24]. The predicted ADMET properties were researched by way of the SwissADME website (http://www.swissadme.ch/). In addition, the estimated toxicity features of the compounds were studied by OSIRIS property Explorer (https://www.organic-chemistry.org/prog/peo/).

3. RESULTS AND DISCUSSION

3.1. Theoretical Studies

The visuals of the molecules obtained as a result of the calculations made with the Spartan 10 program are demonstrated in Figure 2. Frontier molecular orbital (FMO) analysis is extensively used to elucidate the optical and electronic features of organic compounds [25]. Notice of the HOMO and LUMO, and their properties is considerably helpful to evaluate the chemical reactivity of compounds [26]. A molecule with a high HOMO-LUMO energy gap has high kinetic stability and low chemical reactivity. In this way, it is distinctly from Table 2 that compound **2** (R and R'=H) is hard and more stable (less reactive), while compound **3** (R=4-NO_2 and R'=H) is soft and the least stable (more reactive). The calculation of HOMO displays that the surfaces are situated over imidazole and hydroxyl groups. The calculations of LUMO of the compound were seen on the aromatic ring attached to the Schiff base. Also, the electrostatic potential maps (EPM) with transparent shape are given in Figure 2. The electrostatic potentials at the surface are symbolized by diverse colors; red, blue, yellow, orange, and green. The fields with yellow, orange, and green are responsive to a low nucleophilic and electrophilic attack. It shows the high electron density (red in color) inside the aromatic ring attached to the imidazole ring. On the other hand, the electron density of the other aromatic ring in the compound varies according to the substituent attached to the ring (electron acceptor-electron donor). The dipole moment is an extensively utilized parameter to describe the chemical and physical properties of molecules associated with molecular stability [27,28]. In this work, the experimental dipole moment is not known. The computed dipole moments are demonstrated

JSR A
Journal of Scientific Reports

in Table 2. Among the calculated compounds **1–10**, compound **5** (R=2-Cl, 6-F, R'=H substituents) has the highest dipole moment.

1	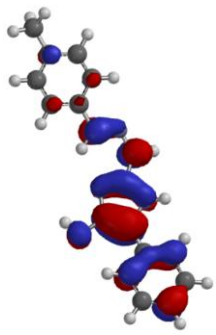	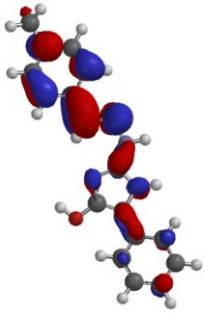	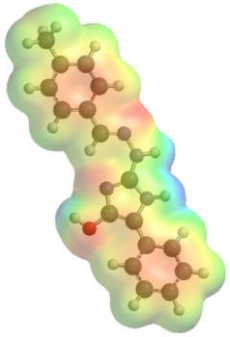
2	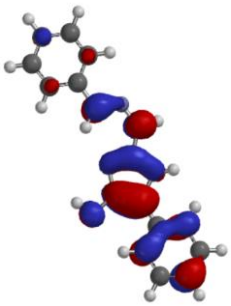	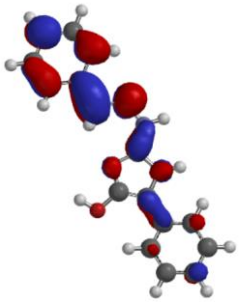	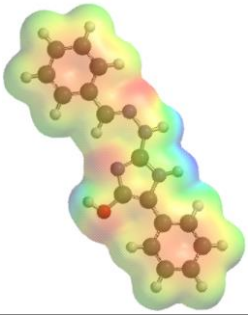
3	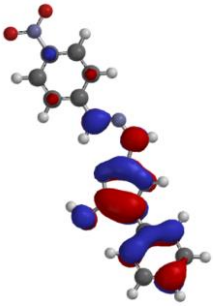	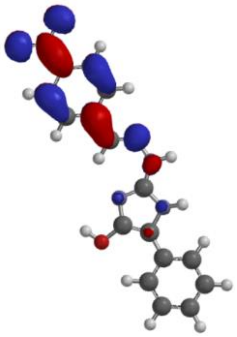	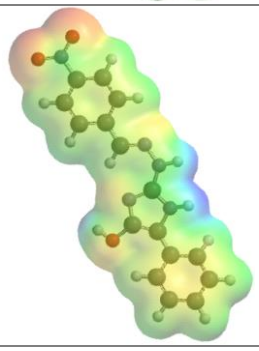

JSR A
Journal of Scientific Reports

4	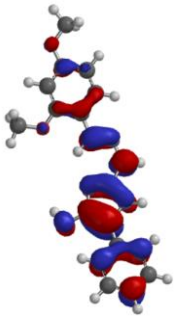	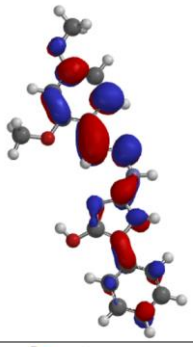	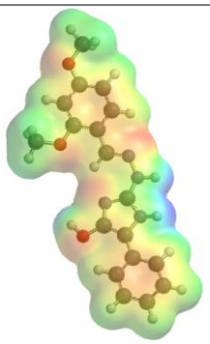
5	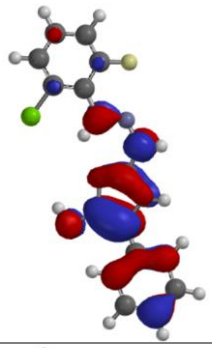	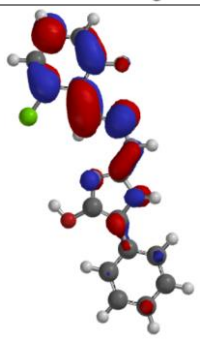	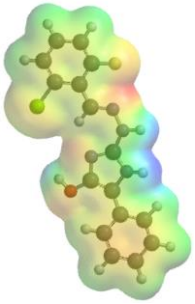
6	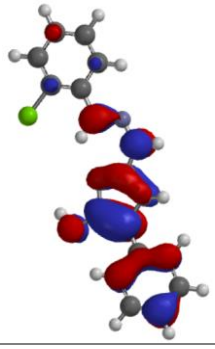	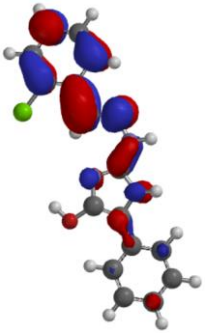	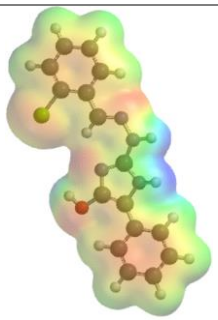

JSR A
Journal of Scientific Reports

7	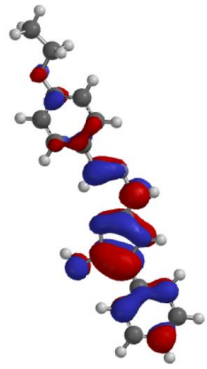	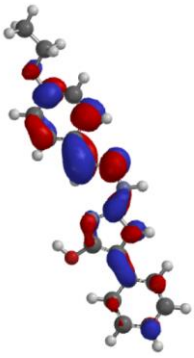	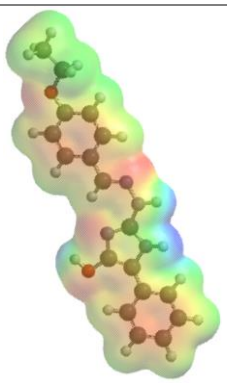
8	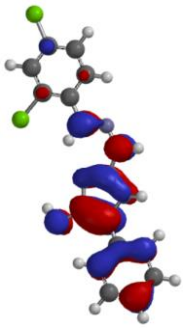	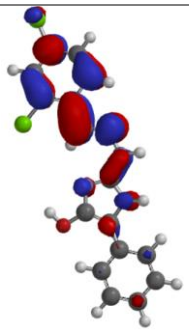	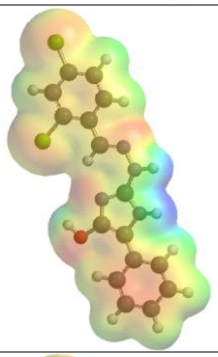
9	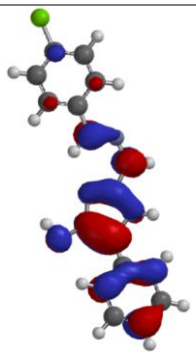	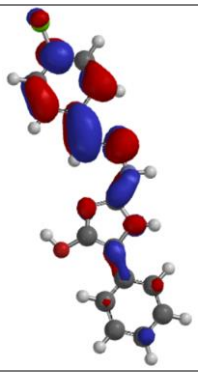	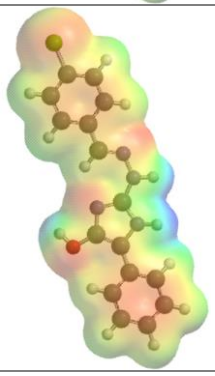

JSR A
Journal of Scientific Reports

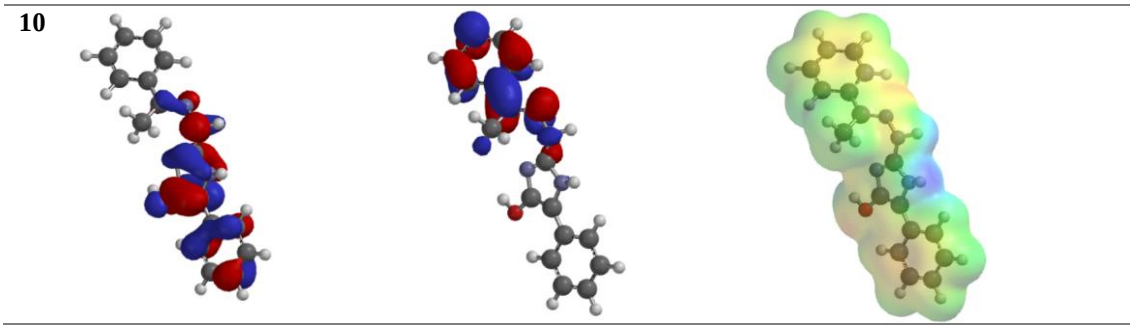

Figure 2. HOMO, LUMO and electrostatic potential maps as transparent for compounds (**1-10**).

Table 2. Some calculated electronic parameters of the optimized structure of compounds **(1-10)**.

Compound	*Energy*	E_{HOMO}	E_{LUMO}	ΔE	*Chemical Hardness (η)*	*Electronegativity (χ)*	*Ovality*	*Dipole moment (μ)*
1	-951.675560	-0.1735	-0.0383	0.1352	0.07	0.11	1.499	1.72
2	-912.354634	-0.1786	-0.0407	*0.1379*	0.07	0.11	1.467	1.71
3	-1516.85641	-0.1881	-0.0897	*0.0984*	0.05	0.14	1.513	4.36
4	-1141.40444	-0.1662	-0.0309	0.1353	0.07	0.10	1.554	2.03
5	-1471.17287	-0.1775	-0.0515	0.1260	0.06	0.11	1.493	5.09
6	-1371.94708	-0.1770	-0.0491	0.1279	0.06	0.11	1.487	3.82
7	-1066.20235	-0.1696	-0.0334	0.1362	0.07	0.10	1.547	3.00
8	-1431.54060	-0.1808	-0.0568	0.1240	0.06	0.12	1.514	3.98
9	-1371.94963	-0.1789	-0.0490	0.1299	0.06	0.11	1.494	3.24
10	-951.669185	-0.1734	-0.0404	0.1330	0.07	0.11	1.479	3.35

3.2. Molecular Docking Studies and ADMET Properties

The one of the great membrane proteins, GPCRs are assigned in signal transduction.These receptors have an important role various physiological and pathological conditions [29]. As mentioned above, imidazole derivative compounds which excellent pharmacological properties against beta2 adrenergic receptor-Gs protein complex investigated the molecular docking behavior. Binding affinity values were calculated to determine the inhibitory effects of compounds (**1-10**) on the human beta2 adrenergic receptor-Gs protein. According to this, compounds showed pretty good binding affinities.

JSR A
Journal of Scientific Reports

The binding affinities of the imidazole derivatives (**1-10**) were calculated as -8.9, -9.5, -7.3, -9.3, -9.6, -9.4, -7.4, -9.1, -6.8 and -8.4 kcal/mol, respectively. Compound **5** gave the lowest binding energy value (Table 3). The best interaction of the compound **5** was displayed as π-cation interaction (PHE R:320), π- π T-shaped interaction (PHE R:392), π-alkyl interaction (ILE R:411 and VAL R:247), and hydrogen bond interactions (ASN R:395 and TYR R:410). The three-dimensional interaction, the 2D structure, and the best binding pose of all of the compounds are shown in Figure 3. In this pose, compound **5** occurs salt bridges among the NH of the hydrazone and the carbonyl groups of residues ASP R:243 and PHE R:320. TYR R:410 and ASN R:395 form two hydrogen bonds with the hydroxyl attached to the imidazole group. In addition, TRP R:239 and CYS R:318 residues with the chlorine group attached to the aromatic ring form two halogen interactions.

Table 3. The docking results of imidazole derivatives, **1-10**.

Compounds	**Docking Score (kcal/mol)**	**RMSD (Å)**
1	-8.9	1.073
2	-9.5	1.608
3	-7.3	0.79
4	-9.3	1.341
5	-9.6	1.562
6	-9.4	1.551
7	-7.4	1.205
8	-9.1	1.15
9	-6.8	1.212
10	-8.4	1.285

JSR A
Journal of Scientific Reports

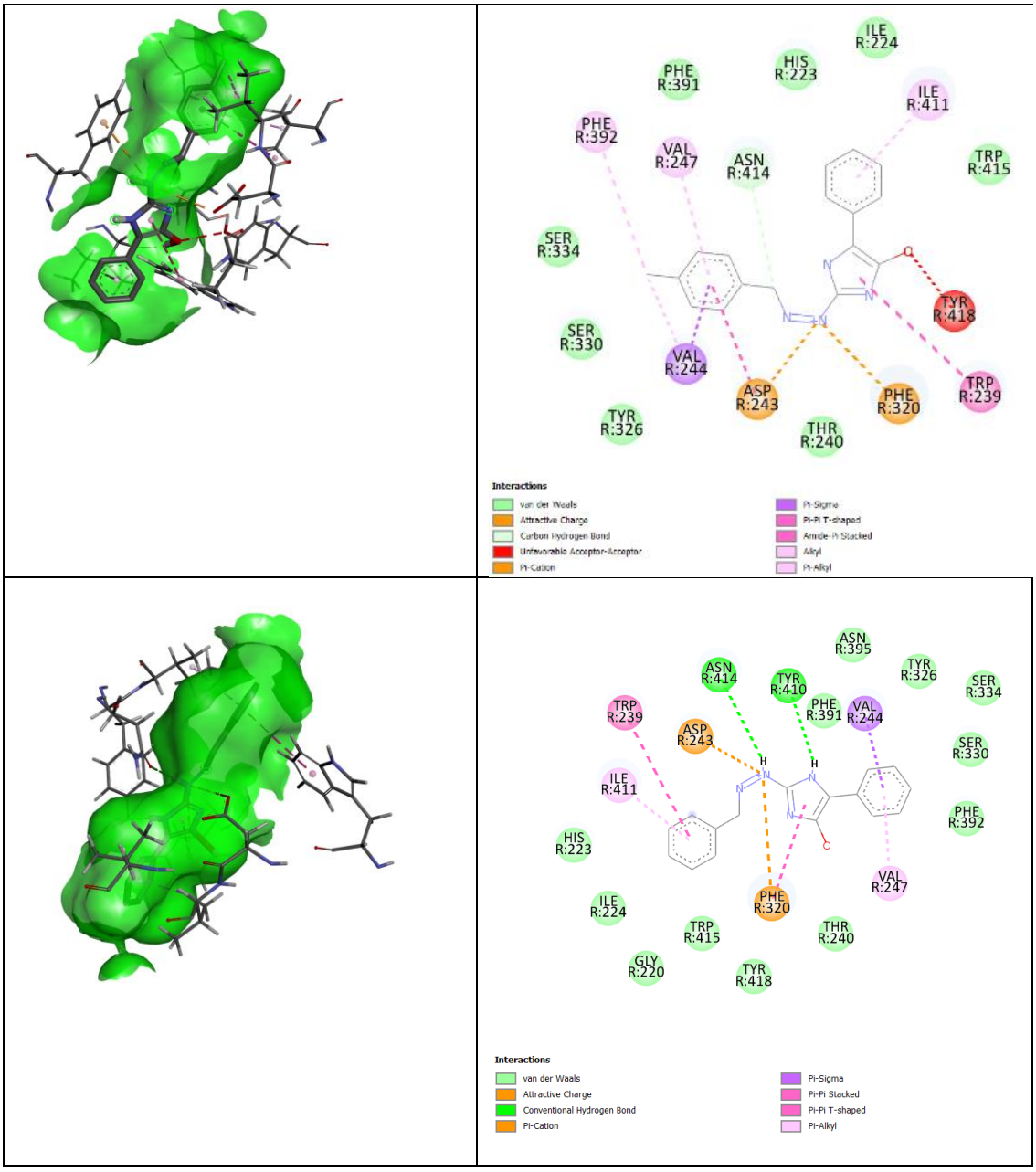

JSR A
Journal of Scientific Reports

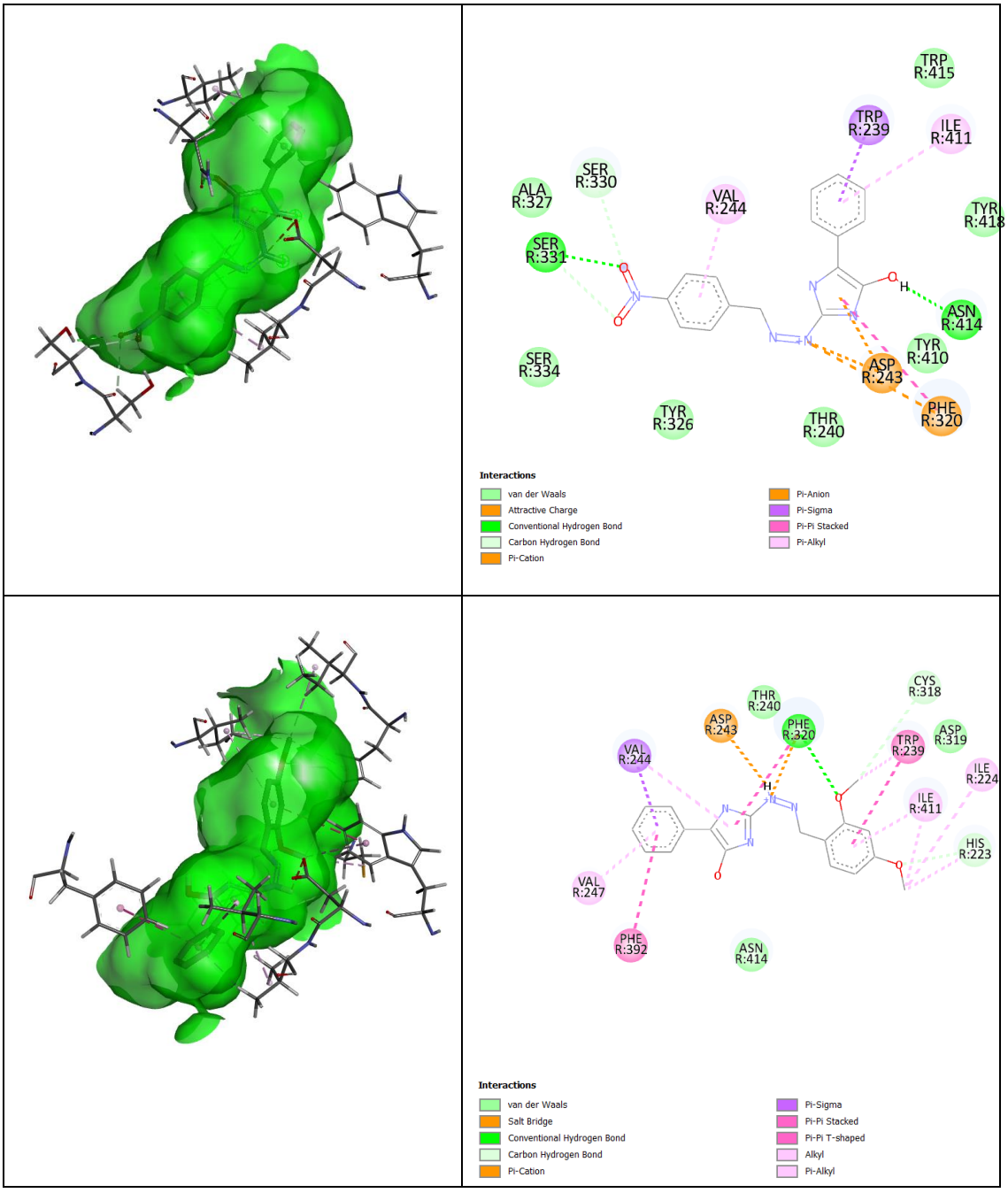

JSR A
Journal of Scientific Reports

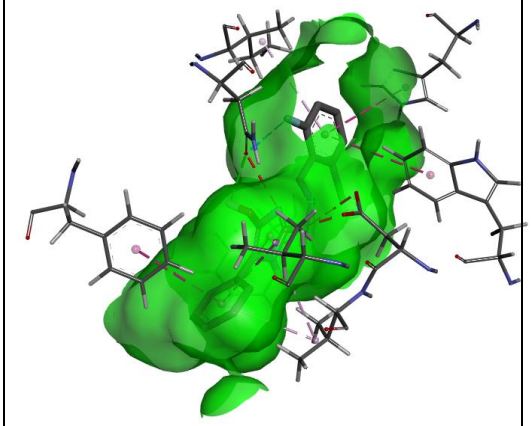

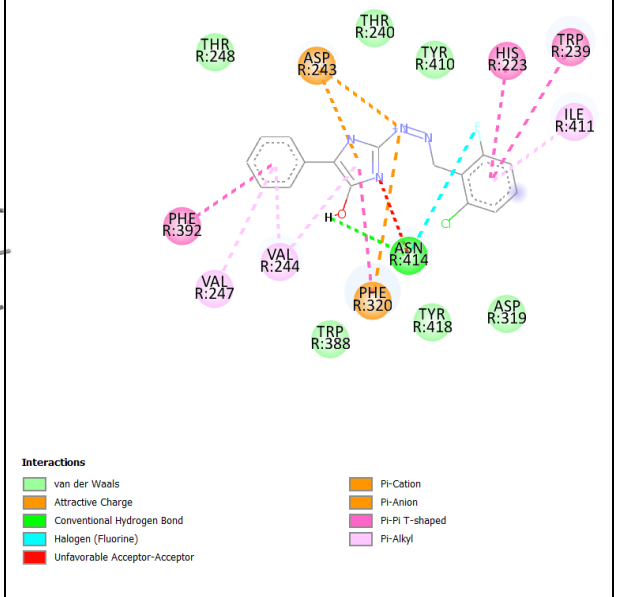

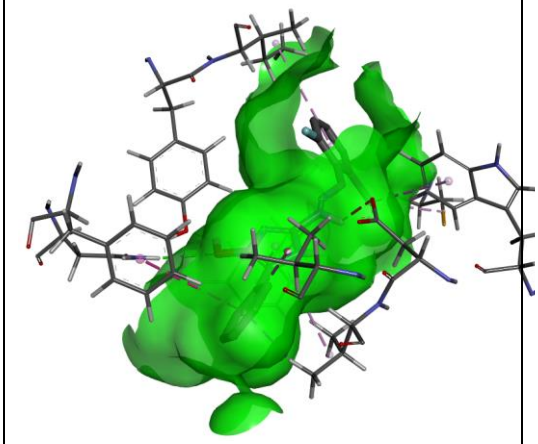

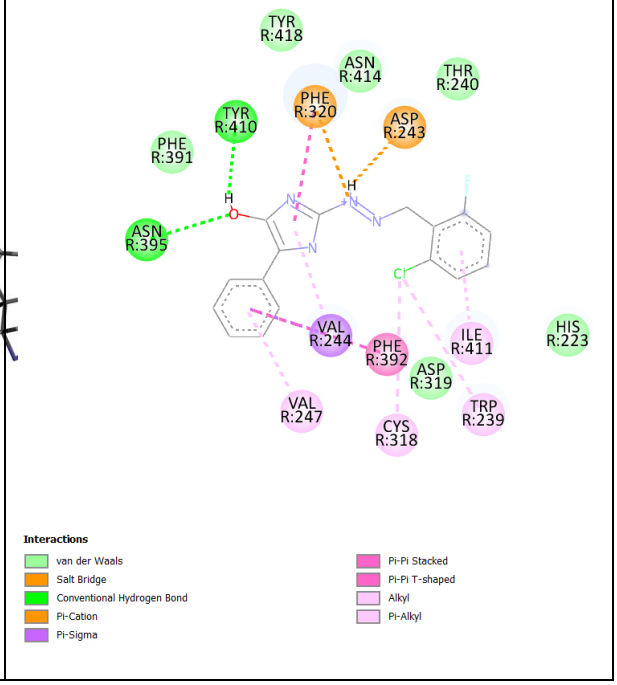

JSR A
Journal of Scientific Reports

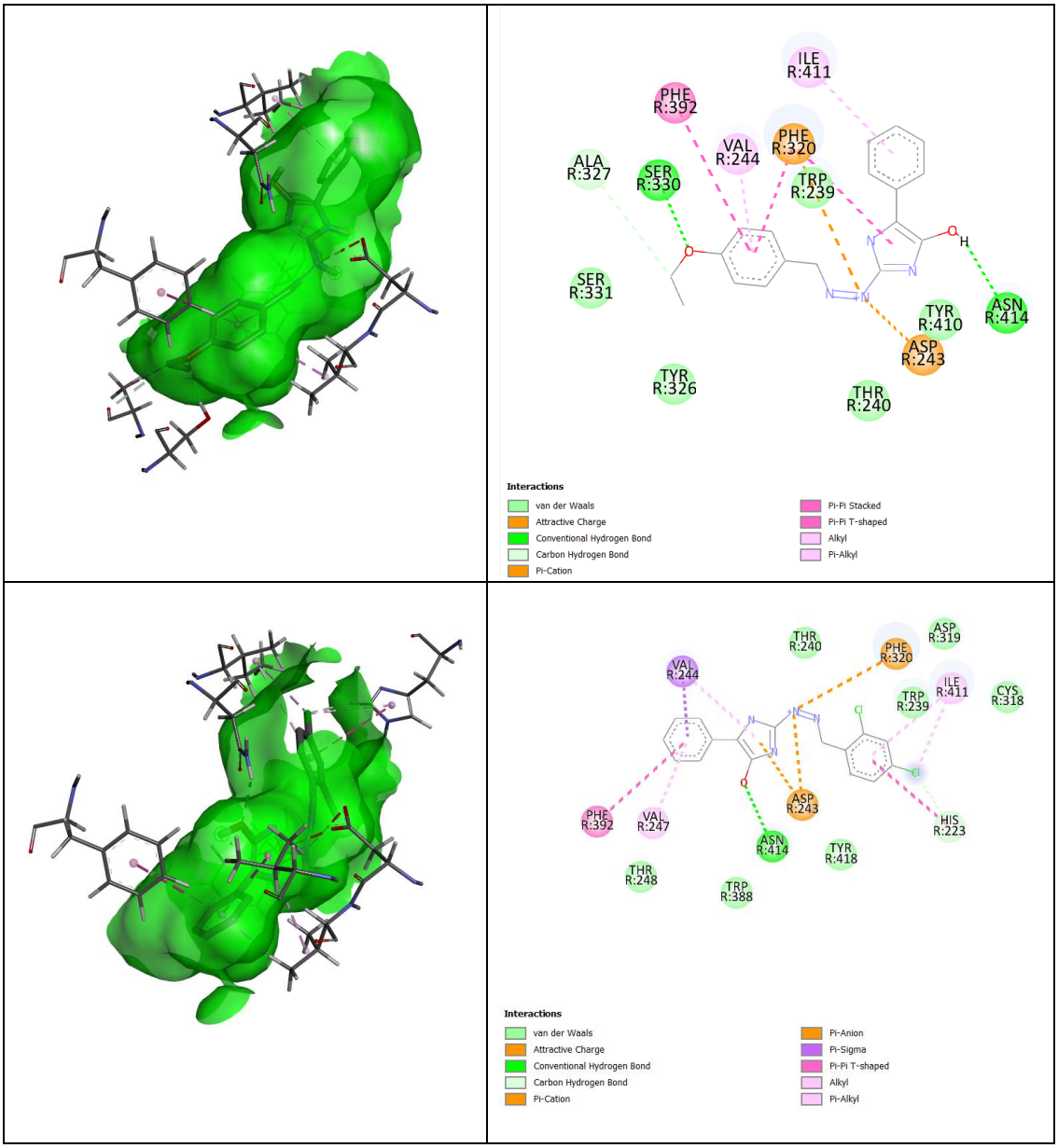

JSR A
Journal of Scientific Reports

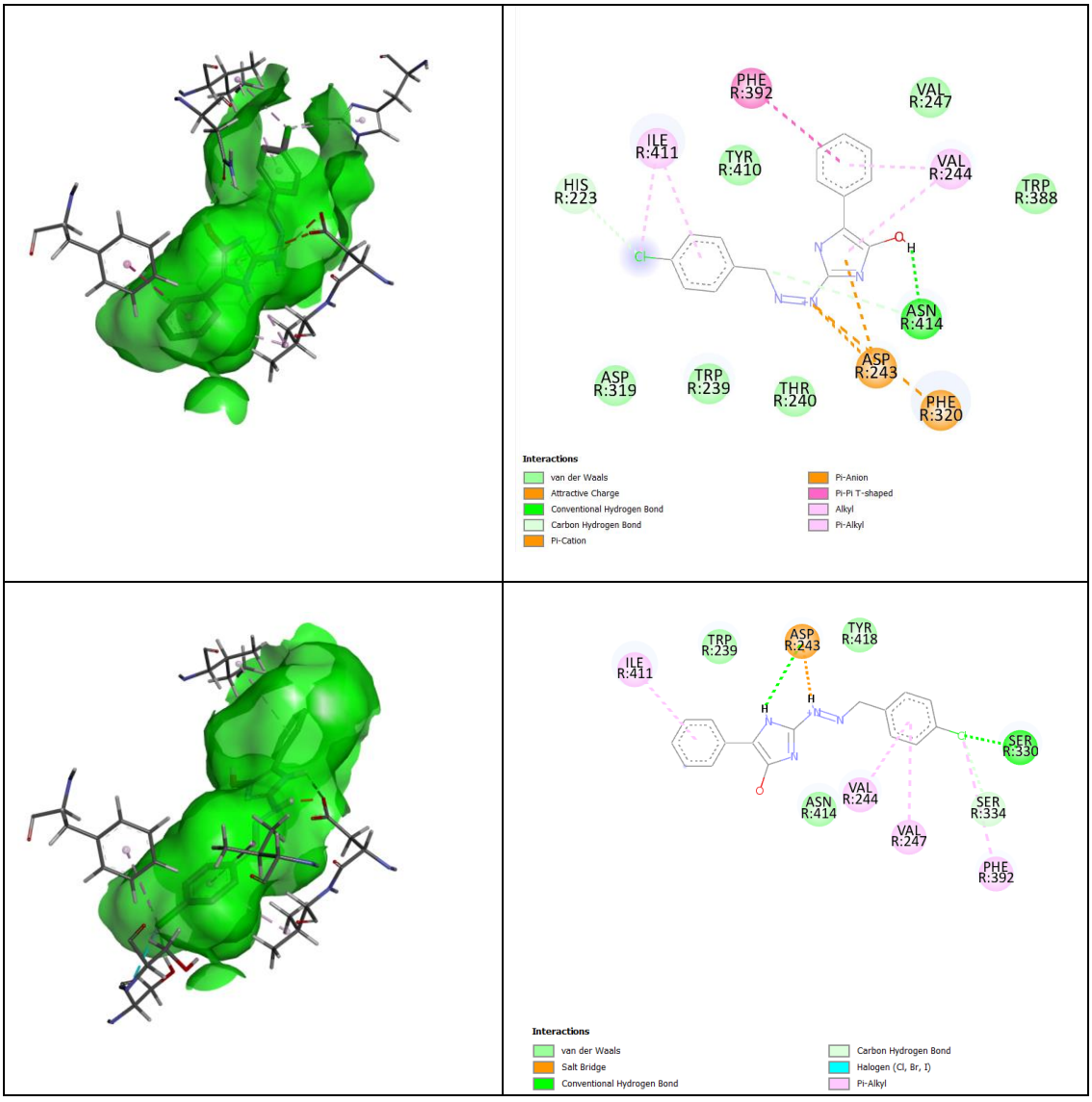

Figure 3. The three-dimensional interaction, the 2D structure, and the best binding pose of all of the compounds.

Some ADME properties were given in Table 4. According to the SwissADME website, the target compounds are appropriate with regards to bioavailability and drug-likeness. The bioavailability scores of the compounds were 0.55. Log S (ESOL) values of the compounds range from -5.37 to -

JSR A
Journal of Scientific Reports

4.20. All compounds are moderately soluble. According to the OSIRIS, the compounds are predicted to be safe in terms of mutagenic, tumorigenic, irritant, and reproductive. Also, topological polar surface area (TPSA) values of the imidazole derivatives were calculated at lower than 140 Å (Angstrom). When the TPSA values of the compounds are investigated, it can be deduced that they demonstrate drug-likeness properties.

Table 4. Some in silico ADME properties predicted by way of the SwissADME website of compounds **(1-10)**.

Some ADME properties	**Compounds**									
	1	**2**	**3**	**4**	**5**	**6**	**7**	**8**	**9**	**10**
Molecular weight (g/mol)	292.34	278.31	323.31	338.36	330.74	312.75	322.36	347.20	312.75	292.34
Rotable bonds	4	4	5	6	4	4	6	4	4	4
H-bond acceptors	3	3	5	5	4	3	4	3	3	3
H-bond donors	3	3	3	3	3	3	3	3	3	3
TPSA (Å^2)	73.30	73.30	119.12	91.76	73.30	73.30	82.53	73.30	73.30	73.30
Log $P_{o/w}$ (XLOGP3)	4.02	3.65	3.48	3.59	4.38	4.28	3.99	4.91	4.28	3.87
Log K_p	-5.23	-5.41	-5.80	-5.82	-5.21	-5.17	-5.43	-4.93	-5.17	-5.34
Log *S* (ESOL)	-4.49	-4.20	-4.23	-4.31	-4.93	-4.78	-4.48	-5.37	-4.78	-4.40
Drug likeness (Lipinski)	Yes	Yes	Yes	Yes	Yes	Yes	Yes	Yes	Yes	Yes

4. CONCLUSIONS

In this study, the electronic and molecular properties of synthesized ten heterocyclic compounds were theoretically assigned and discussed. Also, it was focused on the analysis of molecular docking on main the β-adrenergic receptors utilized for the treatment of asthma, cardiovascular and more many diseases. For this purpose, the previously designed and synthesized imidazole ring containing ligands were investigated for their molecular docking behaviors against on beta2 adrenergic receptor-Gs protein complex. According to obtained results, especially, compound 5 containing having chloro (2-) and fluoro (6-) at orto positions on phenyl ring functioned as the electron-withdrawing groups had lowest binding energy value (-9.6 kcal/mol). In silico ADMET analysis of the compounds was accomplished to assign drug-likeness, physicochemical, water-solubility, lipophilicity and toxicity properties. Log S (ESOL) values of the compounds were ranged between -5.37 to -4.20. All compounds were moderately soluble. Owing to toxicity calculations, the compounds were estimated to be safe in the way of mutagenic, tumorigenic, irritant, and reproductive. The predicted results proposed suitable ADMET values for the studied compounds. As a result of ADMET calculations, it was seen that molecules could theoretically be drugs. In addition, the docking conclusions showed

that these compounds inhibited through interactions including H-bonds, salt bridge, p-p stacking, halogen bond, and hydrophobic interaction. The theoretical consequences will be an major lead for designing drugs as anticancer agents and future in vivo experiments. Imidazole derivative compounds provide encouraging starting points for the improvement of new biologically active compounds.

ACKNOWLEDGEMENT

The author would like to thank for all referees for their valuable contributions and recommendations.

REFERENCES

[1] Ghosh, N., Chatterjee, S., Biswal, D., Pramanik, N. R., Chakrabarti, S., and Sil, P. C. (2022). Oxidative stress imposed in vivo anticancer therapeutic efficacy of novel imidazole-based oxidovanadium (IV) complex in solid tumor. Life Sciences, 301, 120606.

[2] Shirvani, P., Fassihi, A., Saghaie, L., Van Belle, S., Debyser, Z., and Christ, F. (2020). Synthesis, anti-HIV-1 and antiproliferative evaluation of novel 4-nitroimidazole derivatives combined with 5-hydroxy-4-pyridinone moiety. Journal of Molecular Structure, 1202, 127344.

[3] Fan, Y. L., Jin, X. H., Huang, Z. P., Yu, H. F., Zeng, Z. G., Gao, T., and Feng, L. S. (2018). Recent advances of imidazole-containing derivatives as anti-tubercular agents. European Journal of Medicinal Chemistry, 150, 347-365.

[4] Zong, X., Cai, J., Chen, J., Wang, P., Zhou, G., Chen, B., Li, W., and Ji, M. (2015). Design and synthesis of imidazole N–H substituted amide prodrugs as inhibitors of hepatitis C virus replication. Bioorganic & Medicinal Chemistry Letters, 25(16), 3147-3150.

[5] Puratchikody, A., and Doble, M. (2007). Antinociceptive and antiinflammatory activities and QSAR studies on 2-substituted-4, 5-diphenyl-1H-imidazoles. Bioorganic & Medicinal Chemistry, 15(2), 1083-1090.

[6] Hu, Y., Shen, Y., Wu, X., Tu, X., and Wang, G. X. (2018). Synthesis and biological evaluation of coumarin derivatives containing imidazole skeleton as potential antibacterial agents. European Journal of Medicinal Chemistry, 143, 958-969.

[7] Zhang, Y., Xu, J., Li, Y., Yao, H., and Wu, X. (2015). Design, synthesis and pharmacological evaluation of novel no-releasing benzimidazole hybrids as potential antihypertensive candidate. Chemical Biology & Drug Design, 85(5), 541-548.

[8] Abdel-Wahab, B. F., Awad, G. E., and Badria, F. A. (2011). Synthesis, antimicrobial, antioxidant, anti-hemolytic and cytotoxic evaluation of new imidazole-based heterocycles. European Journal of Medicinal Chemistry, 46(5), 1505-1511.

[9] Manjusha, P., Prasana, J. C., Muthu, S., and Rizwana, B. F. (2020). Spectroscopic elucidation (FT-IR, FT-Raman and UV-visible) with NBO, NLO, ELF, LOL, drug likeness and molecular docking analysis on 1-(2-ethylsulfonylethyl)-2-methyl-5-nitro-imidazole: An antiprotozoal agent. Computational Biology and Chemistry, 88, 107330.

[10] Prabhala, P., Savanur, H. M., Sutar, S. M., Naik, K. N., Mittal, M. K., and Kalkhambkar, R. G. (2021). In silico molecular docking and in vitro antimicrobial evaluation of some C5-substituted imidazole analogues. European Journal of Medicinal Chemistry Reports, 3, 100015.

[11] Mermer, A., Keles, T., and Sirin, Y. (2021). Recent studies of nitrogen containing heterocyclic compounds as novel antiviral agents: A review. Bioorganic Chemistry, 114, 105076.

[12] Altındağ, F. D., Sağlık, B. N., Çevik, U. A., Işıkdağ, İ., Özkay, Y., and Gençer, H. K. (2019). Novel imidazole derivatives as antifungal agents: Synthesis, biological evaluation, ADME prediction and molecular docking studies. Phosphorus, Sulfur, and Silicon and the Related Elements.

[13] Lohitha, N., and Vijayakumar, V. (2021). Imidazole Appended Novel Phenoxyquinolines as New Inhibitors of α-Amylase and α-Glucosidase Evidenced with Molecular Docking Studies. Polycyclic Aromatic Compounds, 1-13.

[14] Ali, I., Nadeem Lone, M., A Al-Othman, Z., Al-Warthan, A., and Marsin Sanagi, M. (2015). Heterocyclic scaffolds: centrality in anticancer drug development. Current Drug Targets, 16(7), 711-734.

[15] Groessl, M., Reisner, E., Hartinger, C. G., Eichinger, R., Semenova, O., Timerbaev, A. R., Jakupec, M. A., Arion, V. B., and Keppler, B. K. (2007). Structure− activity relationships for NAMI-A-type complexes (HL)[trans-RuCl4L (S-dmso) ruthenate (III)](L= imidazole, indazole, 1, 2, 4-triazole, 4-amino-1, 2, 4-triazole, and 1-methyl-1, 2, 4-triazole): Aquation, redox properties, protein binding, and antiproliferative activity. Journal of Medicinal Chemistry, 50(9), 2185-2193.

[16] Ali, I., Lone, M. N., and Aboul-Enein, H. Y. (2017). Imidazoles as potential anticancer agents. MedChemComm, 8(9), 1742-1773.

[17] Al-Blewi, F., Shaikh, S. A., Naqvi, A., Aljohani, F., Aouad, M. R., Ihmaid, S., and Rezki, N. (2021). Design and synthesis of novel imidazole derivatives possessing triazole pharmacophore with potent anticancer activity, and in silico ADMET with GSK-3β molecular docking investigations. International Journal of Molecular Sciences, 22(3), 1162.

[18] Yadav, S. B., Sonvane, S. S., and Sekar, N. (2020). Novel blue-green emitting NLOphoric triphenylamine-imidazole based donor-π-acceptor compound: Solvatochromism, DFT, TD-DFT and non-linear optical studies. Spectrochimica Acta Part A: Molecular and Biomolecular Spectroscopy, 224, 117421.

[19] Dinda, J., Ray, U., Mostafa, G., Lu, T. H., Usman, A., Razak, I. A., Chantrapromma, S., Fun, H. K., and Sinha, C. (2003). Copper (I)–azoimidazoles: a comparative account on the structure and electronic properties of copper (I) complexes of 1-methyl-2-(phenylazo) imidazole and 1-alkyl-2-(naphthyl-(α/β)-azo) imidazoles. Polyhedron, 22(2), 247-255.

[20] Wang, Y., Shen, S. Q., Zhou, J. H., Wang, T., Wang, S. N., and Liu, G. X. (2013). Synthesis, structural diversities and properties of a series of transition metal-organic frameworks based on asymmetric dicarboxylic acid and N-donor auxiliary ligand. Inorganic Chemistry Communications, 30, 5-12.

[21] Yavuz, S. Ç., Akkoc, S., and Sarıpınar, E. (2019). The cytotoxic activities of imidazole derivatives prepared from various guanylhydrazone and phenylglyoxal monohydrate. Synthetic Communications, 49(22), 3198-3209.

[22] Spartan'10, version 1.1.0. Wavefunction, Inc. Irvine, CA. 2010.

[23] Khodja, I. A., Boulebd, H., Bensouici, C., and Belfaitah, A. (2020). Design, synthesis, biological evaluation, molecular docking, DFT calculations and in silico ADME analysis of (benz) imidazole-hydrazone derivatives as promising antioxidant, antifungal, and anti-acetylcholinesterase agents. Journal of Molecular Structure, 1218, 128527.

[24] D.S.J.S.D. Biovia, CA, USA, Discovery Studio Visualizer, (2017) 936.

[25] Padmaja, L., Ravikumar, C., Sajan, D., Hubert Joe, I., Jayakumar, V. S., Pettit, G. R., and Faurskov Nielsen, O. (2009). Density functional study on the structural conformations and intramolecular charge transfer from the vibrational spectra of the anticancer drug combretastatin-A2. Journal of Raman Spectroscopy: An International Journal for Original Work in all Aspects of Raman Spectroscopy, Including Higher Order Processes, and also Brillouin and Rayleigh Scattering, 40(4), 419-428.

[26] Bilkan, Ç. Determination of structural properties of some important polymers used as interfacial layer in fabrication of schottky barrier diodes (SBDs). Journal of the Institute of Science and Technology, 10(1), 225-233.

[27] Wojciechowski, A., Raposo, M. M. M., Castro, M. C. R., Kuznik, W., Fuks-Janczarek, I., Pokladko-Kowar, M., and Bureš, F. (2014). Nonlinear optoelectronic materials formed by push–pull (bi) thiophene derivatives functionalized with di (tri) cyanovinyl acceptor groups. Journal of Materials Science: Materials in Electronics, 25(4), 1745-1750.

[28] Ioakimidis, L., Thoukydidis, L., Mirza, A., Naeem, S., & Reynisson, J. (2008). Benchmarking the reliability of QikProp. Correlation between experimental and predicted values. QSAR & Combinatorial Science, 27(4), 445-456.

[29] Soriano-Ursúa, M. A., Trujillo-Ferrara, J. G., Álvarez-Cedillo, J., & Correa-Basurto, J. (2010). Docking studies on a refined human β2 adrenoceptor model yield theoretical affinity values in function with experimental values for R-ligands, but not for S-antagonists. Journal of Molecular Modeling, 16(3), 401-409.

Kütahya Dumlupınar University
Institute of Graduate Studies

Journal of Scientific
Reports-A
E-ISSN: 2687-6167
Number 51, December 2022

RESEARCH ARTICLE

IN HEALTHCARE APPLICATIONS of MACHINE LEARNING ALGORITHMS for PREDICTION of HEART ATTACKS

Tansu SESLİER[1], Mücella ÖZBAY KARAKUŞ[2,*]

[1]Yozgat Bozok Universirty, Graduate Education Institute, Yozgat, tansu.sslr@gmail.com, ORCID: 0000-0002-8990-1512
[2]Yozgat Bozok University, Faculty of Engineering-Architectury, Department of Computer Engineering, Yozgat, mucella.karakus@yobu.edu.tr, ORCID: 0000-0003-0599-8802

Receive Date:19.10.2022 *Accepted Date: 16.11.2022*

ABSTRACT

Due to changing lifestyles in the world and in our country, the account of chronic diseases (CD) is rising day after day. CD is one of the most widespread reason of death. About 46% of the death of people in the world, excluding communicable diseases and accidents, are because of cardiovascular diseases (CVDs), according to this study, and 7.4 million of her 17.5 million deaths from these diseases are due to heart attacks. It was something. The number of deaths from cardiovascular disease is estimated to reach 22.2 million in 2030. The fact that most of the agents that are the reasons of the heart disease (HD) that can be prevented and treated is an important phenomenon in reducing cardiovascular disease deaths. Accurate and timely diagnosis of HD is therefore plenty important. Used machine learning (ML) techniques to determine heart attack risk in this study. Therefore, heart attack risk assessment was performed with a less expensive and effective approach. In this study, Logistic Regression, Support Vector Machines (SVM), Nearest Neighbor Algorithms, NaiveBayes, and Random Forest, ML techniques were applied to a data set containing 303 patient records and 14 variables. As a result of the application, the SVM technique achieved the best accuracy outcomes as 87.91%.

Keywords: *Machine Learning, Heart Attack Prediction, SVM*

1. INTRODUCTION

CVDs are involve the way of the blood is pumped and circulated throughout the body, which unfavorably affects the vessels and heart. In Cardiovascular diseases, the decisions which are wrong or delayed, are likely to cause death [1]. Coronary heart disease (CHD) is caused by narrowing of the coronary arteries, reduced blood flow to the heart, and decreased oxygen supply. The purpose of this study was to investigate the condition known as "heart attack" and the factors that cause it [2]. CVD is the leading cause of death worldwide, killing approximately 17.9 million people each year. More than 80% of cardiovascular deaths are owing to strokes and heart attacks, and and more than 30% of these deaths consist of people that under 70 years old. The World Health Organization (WHO) identifies

those at highest risk for CVD and ensures that appropriate treatment can prevent premature death [3]. When examining cardiovascular diseases, patients' age, gender, hypertension, high blood cholesterol, feeding habits, physical inactivity, smoking, alcohol use, obesity, diabetes takes into account the same qualities as CVDs can be due to various characteristics. According to the literature studies, it has been seen that reducing the risk factors that cause heart disease (HD) can actually help in the prevention of heart diseases [4].

Today, the diagnosis of CVDs is mostly made by following complex and high-priced medical processes carried out in well accoutred hospitals and health institutions. In addition, these processes often oblige the implementation of invasive procedures by highly skilled medical proficients. Although this method gives excessive diagnostic accuracy, the number of sufferers with get entry to this approach may be very restricted. Therefore, it is highly desirable to develop new, economical and easily reachable techniques for diagnosing cardiovascular diseases [5]. Convenient computerized knowledge and/or decision support systems can assist in performing clinical testing at lower cost. The efficient and correct implementation of the automated system requires a comparative study of the various available techniques [6].

It is intelligent computational process of huge knowledge sets employing a integration of machine learning, applied math analysis, and information technology. It conjointly aims to get helpful patterns and rules to guide choices concerning future actions. Machine learning can be identified as a scientific technique for planning and developing algorithms that enable computers to meet and develop reeltime problems based on historical statistics and solve real-time problems under specific instructions and rules [7].In our study, type of chest pain, ECG results, slope of ST, fasting blood glucose, sex, resting blood pressure, age, cholesterol level, resting maximum heart rate, angina that exercise-welding, ST depression that exercise-welding, defect type, and major vessel the target variable in the quantity is used in machine learning. There are many researches on the prevention of heart disease risk. More studies in the field of heart diseases will provide more opportunities to prevent heart diseases [4].

To determine coronary heart disease, a subset of variables was selected with K-Means clustering and Particle Swarm Optimization algorithms by Verma et al. [8]. In the study, a mixed model was created Logistic Regression Fuzzy by using Artificial Neural Network, unordered precept reduction and C4.5. In this model, the researchers tested on clinical data consisting of 26 variables and 335 patient records. The highest classification accuracy with 88.4% was obtained from the polynomial logistic regression algorithm [8].

Pandy et al. [9] were developed a model that predict heart disease to help healthcare proficients estimate the situation of HD based on patients' medical data. There are 14 variables. A prediction model was obtained by using J48 decision tree to classify HD according to variables. Different pruning approaches have been applied in the development of the system. An accuracy rate of 75.73% was obtained from the decision tree algorithm with reduced error pruning [9].

Kim et al. [10] tried to predict coronary heart disease. There were a total of 10 variables in the study, including 9 input variables and 1 output variable, with 748 patient records. Variables such as HDL, cholesterol, LDL, smoke, blood pressure that systole-induced, age, blood pressure that diastole-

JSR A
Journal of Scientific Reports

induced, gender and presence of diabetes were included. They are important factors commonly used to predict the CHD. 525 of 748 patients were allocated as training data and 223 as test data. Fuzzy logic was used to tide over the issues related with the instability of CHD estimation. Correct answer rate and ROC analysis were used to evaluate the constructed model. The correct answer rate for the model was 69.51%, and the ROC curve value was determined to be 0.594 [10].

Ahmed et al. [1] used five common machine learning techniques based on audited learning to detect HD early. The aim of the study was finding the selected classification method's optimal performance. For this purpose, the performances of the five classifiers were interpreted for 270 data in total in the data set by using the confusion matrix and ten-fold cross-validation method. The rate of accuracy 84% was achieved as highest by using ANN method [1].

The same dataset with this study was used by Yin et al. [11], to apply with the machine learning method. Machine learning methods are frequently used for model prediction. By analyzing the collected data, extracting valid data, and making relevant adjustments to the model, an estimator capable of making high-quality predictions is generated. A decision tree has been created that can effectively predict heart disease risk. In order to create a decision tree, by creating a new dataset by randomly selecting blocks of data, and then a technique that named "decision tree forest" was created from valuable decision trees that were created plenty of times. Then 25% of the residuary records are extracted to corroborate the predictive performance of the used method. Eventually, the estimated accuracy of our method on valid dataset is obtained as 0.857. The consequences indicate that this method is a consistent and dependable prognostic model [11].

2. MATERIALS and METHOD

2.1. Data Set

The dataset that consisting of the values of individuals with high heart attack risk and low heart attack risk taken from Kaggle [12] that was collected by Rashik Rahman. The dataset includes 303 patient records and 14 variables. The variables used were chest pain, ECG results, slope of ST, fasting blood glucose, sex, resting blood pressure, age, cholesterol level, resting maximum heart rate, angina that exercise-welding, ST depression that exercise-welding, number of major vessels, type of defect, and the target is variable. An exhaustive information about the variables is given in Table 1.

Table 1. Variables and Explanations.

#Number	Variables	Variable Types	Attribute Description
1	Age	Digital	Patient's age
2	Sex	Categorical	Patient's gender
3	Cp	Categorical	Chest pain type
4	Trestbps	Digital	Resting blood pressure
5	Chol	Digital	Cholesterol value
6	Fbs	Categorical	Fasting blood sugar

JSR A
Journal of Scientific Reports

Seslier, T. and Özbay-Karakuş, M., Journal of Scientific Reports-A, Number 51, 358-370, December 2022.

7	Restecg	Categorical	Resting electrocardiographic result
8	Thalachh	Digital	Maximum heart rate
9	Exang	Categorical	Exercise-induced angina
10	Oldpeak	Digital	Exercise-induced ST depression
11	Slope	Categorical	ST segment
12	Ca	Digital	Number of main veins
13	Thal	Categorical	Defect type
14	Output	Categorical(Target Variable)	

2.2. Experimental Methods

2.2.1. Logistic regression

The model that predicts the probability of an incident occurring by fitting the graph of data to a logistic curve is called the binary logistic regression (LR) model [13]. The dependent variable determines which independent variable(s) is an important risk factor and to what extent these independent variable(s) affect the estimation of the dependent variables' values. [14]. The achieved parameters for the expository variables can be used to predict the probability ratios for each explanatory variable in the model [13].

Special form of logistic regression model:

$$\pi(x) = \frac{e^{\beta_0+\beta_1 x_1+\beta_2 x_2+\cdots\beta_p x_p}}{1+e^{\beta_0+\beta_1 x_1+\beta_2 x_2+\cdots\beta_p x_p}} \quad (1)$$

Here; β_0, the constant is the $\beta_1, \ldots, \beta_p$ regression coefficients and the $x_1, x_2, \ldots, x_p$ independent variables. The conditional probability that the $\pi(x)$ dependent variable is equal to 1, depending on x.

$\pi(x)$ Applying the logit transform to the LR model based on, the following model is obtained.

$$\ln\left[\frac{\pi(x)}{1-\pi(x)}\right] = \beta_0 + \beta_1 x_1 + \beta_2 x_2 + \cdots \beta_p x_p \quad (2)$$

Logit transform is a linear function that can take values between -∞ and +∞ depending on the range of x.

2.2.2. Support vector machine

For regression analysis and statistical classification, a popular used technique which called “SVM” is a supervised learning method [15]. Classical learning methods aim to diminish the error ratio in the training dataset. This method is termed as empirical risk minimization (ERM). These learning techniques operate the principles of ERM, and ANNs are the most widespread model of ERM. Moreover, SVMs are grounded on the Structural Risk Minimization (SRM) principle grounded on

JSR A
Journal of Scientific Reports

"statistical learning theory". With better generalization ability, SRM is achieved by minimizing an upper bound on the generalization error [16]. It allows drawing a decision boundary on the plane of the training data that is furthest from the members of the two separate classes as shown in Figure 1.

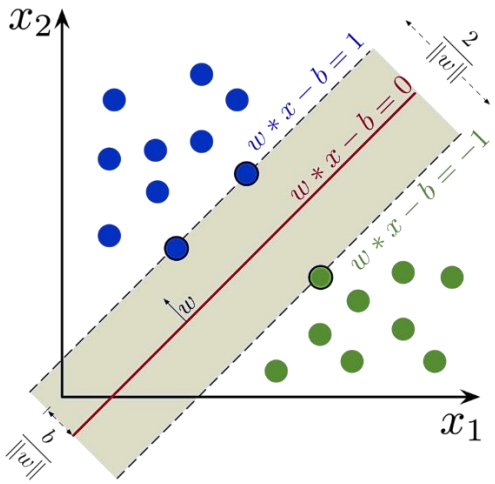

Figure 1. Margins and maximum-margin hyperplane of a trained SVM model which is trained with specimens from two separate classes [17].

Each point of the data is expressed as in Equation 3.

$$\left\{(x_i, y_i) | x_i \in R^d, y_i \in \{-1,1\}\right\}_{i=1}^{n} \tag{3}$$

Each entry in the formula, denoted by x, and y, specifies a class of data points represented by -1 or 1. Each point on the plane is wx-b indicated as a point. Here w is the normal of the multiplane and b is the trend value. The machine learning method that enables finding the separation boundary using the quadratic optimization method is the SVM [18].

2.2.3. Naive bayes

Naive Bayes strategies create the belief that everyone attributes area unit freelance. This conjecture of conditional independence is called naive because it is rarely valid in real-world applications. For this reason the algorithms characterized as naive, conversely they tend to learn quickly in many controlled classification problems [19]. They are probabilistic learning algorithms that are grounded on the theorem of Bayes.

$$P(X|Y) = \frac{P(X)P(Y|X)}{P(Y)} \tag{4}$$

In this equation (4);
Y: Attributes

X: Class

P(X\Y): It shows the probability of the X event given the Y event.

P(Y\X): It shows the probability of event Y given that event X has occurred.

P(X): It shows the probability of an X event occurring.

P(Y): It indicates Y, the probability that the event will occur.

2.2.4. Random forest

Random Forest (RF) turned into stepped forward with the aid of using Leo Bremen. RF regulations can be created as supervised classification rules [20]. However, ML (machine learning) algorithm that is one supervised, random forest, is used for regression as well as for classification, it is primarily prefered for classification goal. The Random Forest algorithm works as follows: Firstly the samples are gathered from the dataset randomly, then a decision tree is generated for each sample from the existing tree, and the tree with the best predictions is selected. The greater the number of decision trees, the more accurate the prediction results [21].

The process of improving a Random Forest algorithm consists of two steps. The first stage is creating a random forest, and the second stage is building predictions over generated Random Forest classifier. Judging by the Random Forest generation Pseudocode:

a. At first selecting the "R" attributes from the whole "m" attributes that are R<<m.
b. Secondly compute knots using the best split points among the 'R' features.
c. Thirdly, separating the knot into additional knots by using the best split.
d. In fourth step, repeating this steps from a to c till the number of nodes “l” is achieved.
e. In the last step, repeating the previous steps from a to d to create forest for number “a” to create “n” which is tree number.

Finally, when the classifier that based on Random Forest is achieved, the estimation is made.

2.2.5. K-nearest neighbor algorithm

Classification is done using the proximity between a selected feature and the closest feature. The value of K included here is expressed as a number such as 3 or 5.

The formula in Equation 5 is used to determine distances between objects.

$$(i,j) = \sqrt{\sum_{k=1}^{p}(X_{ik} - X_{jk})^2} \quad (5)$$

When a new object comes to be identified, with respect to the identified data, when examining the working style, firstly, "K" is checked. The "K" number is often selected to be odd number to prevent

equality [22]. When calculating the interval between the nearest neighbor number K and data points, Manhattan, Euclidean, Minkowski or similar methods are used [23].

2.2.6. Decision trees

Decision Trees (DT), the oldest and most important type of MLA, are tree-like structures that model decision logic, test results, and categorize data items. Nodes in a DT typically have levels that multiple, with the node which is the initial or the highest is being named the "root node". For input variants and/or characteristics, all nodes that are internal nodes, express tests. According to the results of the test, in the classification algorithm, the testing and branching procedure is repeated, until the leaf reaches the node by branching at every step to the convenient lower node. Terminal or leaf nodes correspond to the outcome of decisions. DT which is a widely used supplement in medical diagnoses has proven to be easily assess and fast learning [24].

3. RESULTS

Disease diagnosis is the most important health function. It can save lives if the disease is diagnosed before the usual or planned period. Machine learning-based classification methods can support the healthcare industry by enabling rapid and reliable disease diagnosis. As heart disease is difficult to diagnose, so it's a good time for doctors and patients. We review the indicated machine learning and image fusion classification methods. The aim of the project is understanding whether a patient who has CVD or not. For information preprocessing, data processing classification techniques were applied, especially call trees and naive Thomas Bayes to the dataset which is divided to training and test sets. This section presents the results of this classification model performed at the expense of Python programming. Results are generated for each individual coaching knowledge set and check data set.

One of the frequently applied measures in the comparison of classification methods is the accuracy criterion. Generally, confusion matrix(CM) is used to define the delicacy criteria. The CM interprets the items about the work done. The confusion matrix components for the heart disease classification process examined in the study are defined as follows;
In the proposed study, various metricals are utilized to compute the performances of MLA techniques. These metrics are calculated on CM.

TP (True Positive): Data count, which is essentially true and categorized as true.

FN (False Negative): Data count, which is essentially true but categorized as false.

FP (False Positive): Data count, which is essentially false but categorized as true.

TN (True Negative): Data count, which is essentially false and categorized as false.

Table 2, 3, 4, 5, 6, 7, 8; in the following tables, 0 means "no heart attack risk", 1 means "heart attack risk".

JSR A
Journal of Scientific Reports

Table 2. Complexity Matrix.

	0	**1**
0	TP	FN
1	FP	TN

Accuracy: Usually a measure of how often classifiers are estimated correctly. The accuracy rate of the developed algorithm is calculated according to Equation 6.

$$\text{Accuracy} = \frac{\text{TP+TN}}{\text{TP+TN+FP+FN}} \tag{6}$$

Sensitivity (Recall): Indicates the rightly classified positive values from the positive samples' total count.

$$\text{Recall} = \frac{\text{TP}}{\text{TP+FN}} \tag{7}$$

Precision: It shows how many of the values we estimated as positive are essentially positive.

$$\text{Precision} = \frac{\text{TP}}{\text{TP+FP}} \tag{8}$$

F1 Score: Precision and sensitivity are the harmonic mean, so it's a powerful metric for calculating model performance. The precision in calculating the F-Score is represented as P and R respectively.

$$\text{F1} - \text{Score} = 2 * \frac{\text{P*R}}{\text{P+R}} \tag{8}$$

There are a total of 303 records in the study. 30% of the records were used for testing and 70% for training. The confusion matrices of the algorithms in Table 3 below:

Table 3. Complexity Matrix of LR Algorithm.

	0	**1**	**Σ**
0	31	7	38
1	5	48	53
Σ	36	55	91

Table 4. Complexity Matrix of Support Vector Machines Algorithm.

	0	**1**	**Σ**
0	31	7	38
1	4	49	53

JSR A
Journal of Scientific Reports

Σ	35	56	91

Table 5. Naive Bayesian Complexity Matrix.

	0	**1**	**Σ**
0	32	6	38
1	6	47	53
Σ	38	53	91

Table 6. Random Forest Algorithm Complexity Matrix.

	0	**1**	**Σ**
0	30	8	38
1	7	46	53
Σ	37	54	91

Table 7. Complexity Matrix of K-Nearest Neighbor Algorithm.

	0	**1**	**Σ**
0	31	7	38
1	7	46	53
Σ	38	53	91

Table 8. Decision Tree Algorithm Complexity Matrix.

	0	**1**	**Σ**
0	28	10	38
1	12	41	53
Σ	40	51	91

Accuracy (Ac), Sensitivity (S), Precision (P) and F1-Score (F1-S) were used to compare classification algorithms. The results obtained using these methods in Table 9, were evaluated and the attained results.

Table 9. Application outcomes of classification algorithms.

Algorithm	**Ac**	**S**	**P**	**F1-S**
LR	0.87	0.91	0.87	0.89
SVM	0.88	0.92	0.88	0.90
NB	0.87	0.89	0.89	0.89

RF	0.84	0.87	0.85	0.86
K-NN	0.84	0.87	0.85	0.86
DT	0.76	0.77	0.80	0.79

Machine learning algorithms have an important place in determining the heart attack risk and risk factors. In our study, Logistic Regression, Support Vector Machines, Naive in determining the risk of heart attack NB, RF, K-NN and DT classification methods were utilizated. As a result of the study, 88% accuracy rate was obtained with the LR method, 88% with the SVM method, 88% with the NB method, 84% with the RF method, 84% with the k-NN method, and 76% with the DT method. The algorithm with the highest accuracy rate was the SVM algorithm. Classification algorithms; accuracy, sensitivity Precision and F1-score were compared. On the other hand, SVM method has a moderate accuracy rate, and can give physicians and researchers the opportunity to interpret. For these reasons, which model to choose in applications can be determined by considering the special conditions of the application.

4. CONCLUSION

In the long term, the operating of the raw health data to identify cardiac info will aid save lives and descry cardiac abnormalities early. In this work, machine literacy ways are used to reuse the raw data and enable new and new demarcation related to heart complaint. Predicting heart complaint is grueling and veritably important in the medical field. still, if the complaint is determined earlier and preventative evaluations are taken in no time, mortality can be greatly controlled. It's largely desirable to further expand this exploration to concentrate on datasets of reelworld, rather than just theoretical styles and simulations.

SVMs were set up to be fairly accurate in prognosticating heart complaint. unborn assignments in this exploration can be fulfilled through colorful combinations from machine literacy ways to better vaticination ways. likewise, new point selection styles can be improved to gain a broader sense of important qualifications, thereby perfecting the performance of heart complaint vaticination.

Heart attack is a vital health problem in human society. This article summarizes the existing techniques and available methods for predicting this disease. SVM, an emerging field of artificial intelligence, has shown some promising results in other fields of high-precision medical diagnosis. In heart disease prediction, it remains an open field awaiting implementation. Some ML methods that can be utilizated for heart disease prediction are discussed, as well as breakthrough machine learning algorithms. Analytical comparisons are made to find the best available algorithms for medical datasets. In the future, we aim to continue work on ad hoc medical datasets, where the dataset changes over time and requires retraining on the dataset. As a result of this study, it is thought that researchers working in the field of cardiology will guide their clinical decisions. With the developed machine learning algorithms, medical errors, unwanted application types, medical costs are reduced and patient safety and quality of life are increased. In this study, classification algorithms were applied on 14 variables in the dataset. In future studies, classification algorithms can be applied by examining the variables in the data set in more detail by using optimization algorithms.

The SVM classifier predicted cardiovascular disease patients with 88% accuracy. Therefore, we conclude this project by stating that SVMs are best and most suitable for processing medical information sets. In the future, the system designed using the machine learning algorithm classifier used will be used to predict or diagnose alternative diseases. This work can be extended or improved for automation of cardiovascular disease analysis and deep learning algorithms.

5. REMARKS

ML has been reviewed in the medical field, especially for predicting heart disease. Algorithm completion has been determined. The proposed system is available in Availability Zones. More specific feature selection methods can be used to improve algorithm accuracy and get reliable results. When certain types of heart disease are diagnosed, patient care must be tailored to that specific condition. In essence, we conclude that a dataset of reasonably collected and reliable data is used to create a predictive model of heart disease. Therefore, the most important half of preprocessing is to prepare the data set to be used in the MLA program and to preprocess the data set to get better results. Associate in Nursing Requires the use of appropriate algorithmic programs to develop predictive models that produce correct results. ANNs have been found to have meaningful implications for predicting heart conditions in most models. Therefore, it helps all caregivers and patients. It is still growing in the field of nursing, thanks to the vast access to patient information in hospitals and clinics. As far as data set standards are important, prognostic accuracy should be considered. More hospitals should be encouraged to publish high-quality datasets (while respecting patient privacy). Create a model and come up with reasonable outcomes to help people exploit and treat heart disease in its early stages.

ACKNOWLEDGEMENT

The authors received no specific grant for the research, authorship, and/or publication of this article. This paper was presented as oral in 2nd International Conference on Engineering and Applied Natural Sciences ICEANS 2022.

REFERENCES

[1] Ahmed, M. R., Mahmud, S., Hossin, M., Jahan, H., and Noori, S, (2018), A Cloud Based Four-Tier Architecture for Early Detection of Heart Disease with Machine Learning Algorithms., IEEE 4th International Conference on Computer and Communications, pp. 1951-1955.

[2] Krishniah, V. V., Sekar, D., and Rao, D., (2012), Predicting the heart attack symptoms using biomedical data mining techniques, The International Journal of Computer Science and Applications, vol. 1, no. 3, pp. 10-18.

[3] WHO, https://www.who.int/health-topics/cardiovascular-diseases#tab=tab_1 Accessed on: Jan. 24, 2022

[4] Taşcı, M. E., and Şamlı, R. (2020), Veri Madenciliği İle Kalp Hastalığı Teşhisi, Avrupa Bilim ve Teknoloji Dergisi, pp. 88-95.

[5] Caliskan, A., and Yuksel, M., (2017), Classification of coronary artery disease data sets by using a deep neural network. The EuroBiotech Journal, vol:1 no.4, pp. 271-277.

[6] Soni, J., Ansari, U., Sharma, D., and Soni, S., (2011), Predictive Data Mining for Medical Diagnosis: An Overview of Heart Disease Prediction, International Journal of Computer Applications, vol. 17, no. 8, pp. 43-48.

[7] Chandna, D., (2014), Diagnosis of Heart Disease Using Data Mining Algorithm, (IJCSIT) International Journal of Computer Science and Information Technologies, vol. 5, no. 2, pp. 1678-1680.

[8] Verma, L., Srivastava, S., and Negi, P., (2016), A Hybrid Data MiningModel to Predict Coronary Artery Disease Cases Using Non-Invasive Clinical Data, Journal of Medical Systems, vol. 40, no. 7.

[9] Pandey, A. K., Pandey, P., Jaiswal, K., and Sen, A. A., (2013), Heart Disease Prediction Model using Decision Tree, IOSR Journal of Computer Engineering (IOSR-JCE), vol. 12, no. 6, pp. 83-86.

[10] Kim, J., Lee, J., and Lee, Y., (2015), Data-mining-based coronary heart disease risk prediction model using fuzzy logic and decision tree, Healthcare İnformatics Research, vol. 21, no. 3, pp. 167-174.

[11] Yin, W., Yao, Y., Gu, Y., Bao, W., Cheng H., (2021), Prediction of Heart Disease Probability Based on Various Body Function., pp. 267-275.

[12] Available:https://www.kaggle.com/datasets/rashikrahmanpritom/heart-attack-analysis-prediction-dataset

[13] Senaviratna, N. A., and Cooray, T., (2019), Diagnosing Multicollinearity of Logistic Regression Model, Asian Journal of Probability and Statistics, vol. 5 no. 2, pp. 1-9.

[14] Kurt, İ., and Türe, M., (2005), Tıp Öğrencilerinde Alkol Kullanımını Etkileyen Faktörlerin Belirlenmesinde Yapay Sinir Ağları ile Lojistik Regresyon Analizi'nin Karşılaştırılması, Trakya Üiversitesi Tıp Fakültesi Dergisi, vol. 22 no. 3, 142-153.

[15] Zhou, J., Qiu, Y., Zhu, S., Armaghani, D., Li, C., Nguyen, H., and Yagiz, S., (2021), Optimization of support vector machine through the use of metaheuristic algorithms in forecasting TBM advance rate, Engineering Applications of Artificial Intelligence.

[16] Widodo, A., and Yang, B.-S., (2007), Support vector machine in machine condition monitoring and fault diagnosis, Mechanical Systems and Signal Processing, no. 21, pp. 2560–2574.

[17] Islam, M., Mahmud, A.A., Machine learning approaches for modeling spammer behavior, Asia information retrieval symposium, pp. 251-260, Springer, Berlin, Heidelberg.

[18] Sevli, O., (2019), Göğüs Kanseri Teşhisinde Farklı Makine Öğrenmesi Tekniklerinin Performans Karşılaştırması, Avrupa Bilim ve Teknoloji Dergisi no. 16, pp. 176-185.

[19] Saritas, M. M., and Yasar, A., (2019), Performance Analysis of ANN and Naive Bayes Classification Algorithm for Data Classification, International Journal of Intelligent Systems and Applications in Engineering, vol. 7, no. 2, pp. 88-91.

[20] K.Vijiya Kumar., (2019), Random Forest Algorithm for the Prediction of Diabetes, Proceeding of International Conference on Systems Computation Automation and Networking.

[21] Katarya, R., and Srinivas, P., (2020), Predicting Heart Disease at Early Stages using Machine Learning: A Survey, Proceedings of the International Conference on Electronics and Sustainable Communication Systems (ICESC), pp. 302-305.

[22] Kılınç, D., Borandağ, E., Yücalar, F., Tunalı, V., Şimşek, M., and Özçift, A., (2016), KNN Algoritması ve R Dili ile Metin Madenciliği Kullanılarak Bilimsel Makale Tasnifi, Marmara Fen Bilimleri Dergisi no.3, pp. 86-94.

[23] Saçlı, B., Aydınalp, C., Cansız , G., Joof, S., Yılmaz, T., Çayören, M., Akduman , İ., (2019), Microwave dielectric property based classification of renal calculi: Application of a KNN algorithm, Computers in Biology and Medicine, no.112.

[24] Uddin, S., Khan, A., Hossain, M., and Moni, M., (2019), Comparing different supervised machine learning algorithms for disease prediction, Mechanical Systems and Signal Processing, vol. 19, no. 281, pp. 1–16.

Kütahya Dumlupınar University
Institute of Graduate Studies

Journal of Scientific
Reports-A
E-ISSN: 2687-6167
Number 51, December 2022

RESEARCH ARTICLE

CRITICAL PATH METHOD with FUZZY ACTIVITY TIMES

Özlem ÇOMAKLI SÖKMEN[1*]

[1]Erzurum Technical University, Career Planning Application and Research Center, Erzurum, ozlem.sokmen@erzurum.edu.tr, ORCID: 0000-0001-8765-0038

Receive Date:26.10.2022 *Accepted Date: 28.11.2022*

ABSTRACT

The Critical Path Method (CPM) is very useful in planning and controlling complex projects when their activity times are known precisely. However, in real-life applications, the durations are foreseen in the planning phase of the project; when it is put into practice, it may vary due to various reasons such as machine breakdowns, human factors, and disruptions in material supply. Accordingly, due to the uncertainty and difficulties in estimating operating times, CPM may not be able to accurately and fully represent real projects. From this point of view, in this study, it is aimed to perform critical path analysis in a project network whose activity durations consist of triangular fuzzy numbers. In the first stage, critical path analysis and project completion time were found by using possible, optimistic and pessimistic values. Then, Yager's ranking method was used to ranking the fuzzy numbers and the project completion time and critical path were calculated with the crisp values obtained. The results were evaluated by comparing and the importance of using fuzzy numbers instead of crisp numbers in the CPM method was revealed.

Keywords: *Critical Path Method, Fuzzy Logic, Fuzzy Number, Fuzzy Project Network, Ranking Index*

1. INTRODUCTION

In today's business world, where competition is increasing, the completion of projects in the least time and with the least cost is an important factor that increases the success of enterprises in project management activities. In this competitive environment, the most effective planning of the projects and their completion within the stipulated time without delay provide a great advantage in terms of cost, time and customer satisfaction. Therefore, the need and interest in project management methods are increasing in order to ensure calendar success and maintain permanence in the sector. Various methods are used in project planning, which is an important step in project management. CPM is one of the most preferred methods for an effective management system. The critical path is the path from the start to the end of the project where all slack times are zero [1]. CPM, on the other hand, aims to identify critical activities on the critical path so that resources can be concentrated on critical activities in order to reduce the length of the project. In addition, bottlenecks in the project can be determined

JSR A
Journal of Scientific Reports

with CPM [2]. In short, CPM is a method that determines the completion time of the project by taking into account the priority relations between the activities. CPM is a useful tool for planning and managing complex projects in real-life applications [3]. This method is very effective in determining the project completion time and critical path when the activity times are known precisely. However, in real-life applications, project activity times can be uncertain due to various factors, and in this case, calculations made with classical CPM may not fully reflect real-life situations. In CPM, the fuzzy logic approach can be used to express uncertainty mathematically. Fuzzy logic, introduced by Zadeh [4] in 1965, allows extreme values of mathematics, unlike classical logic. It is difficult to model complex systems because classical logic requires precise values [5]. However, fuzzy logic, unlike classical logic, is a concept that allows the use of linguistic variables that deal with uncertain values. In this way, fuzzy logic provides an advantage in solving complex systems. Fuzzy logic is a control method based on fuzzy set theory that transforms real values into linguistic variables [6]. Fuzzy logic has wide application areas. Fuzzy logic is used in many areas such as Optimization, Operations Research, Statistics, Quality Control, Production Planning, and Process Control [7].

In real-life applications, it may not always be possible to precisely determine the duration of activities for projects. Activity durations in the project can be determined based on expert opinions and estimates. However, even for the same project, the estimations of different experts regarding the duration of activity may differ [8]. When the relevant literature is examined, it is seen that studies in which CPM is handled with the fuzzy logic approach are encountered. A bibliometric analysis of the studies in which CPM was handled with a fuzzy logic approach was made in the Web of Science (WoS) database. The studies in this field were reached by entering the word groups "Fuzzy Critical Path Problem* or Fuzzy Critical Path Method*" into the WoS database. Keyword network analysis was done using the VOSviewer (Version 1.6.16) package program. According to the bibliometric analysis made using the VOSviewer program, the most used keywords are shown in Figure 1.

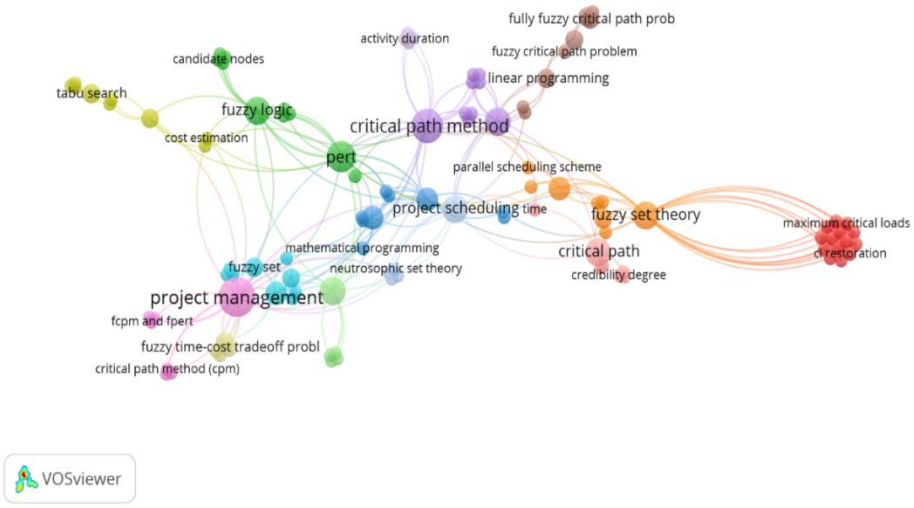

Figure 1. Keywords network analysis (VOSviewer).

As can be seen in Figure 1, among the most used keywords in studies where CPM is handled with fuzzy logic approach, "critical path method", "project scheduling", "fuzzy logic", "project management", "fuzzy set theory", "PERT" is located. In addition, it is understood that triangular fuzzy numbers and trapezoidal fuzzy numbers, which represent fuzzy activity times, are among these keywords.

Some of the studies in this area are given in this section. In some of these studies, fuzzy linear programs were used, and in some of them, activity times were represented by fuzzy numbers. The fuzzy logic approach was first applied to the scheduling problem in 1979 [9]. In [10], the authors applied a signed distance ranking method to the critical path method for activity-on-edge. This method allows the use of both positive and negative values in the ranking. In [11], the authors discussed the use of the fuzzy CPM (FCPM) method to find and improve airports' ground handling critical processes. Trapezoidal fuzzy numbers were used in the study. In [12], the author applied a linear programming formulation to calculate the lower and upper limits of the project duration in finding the critical path in a project network created using fuzzy numbers and created a membership function for the fuzzy total time. In [13], the authors proposed the expected cost model, α-cost minimization model and credibility maximization for solving fuzzy project scheduling problems. In [2], the authors discussed a project in which activity durations were expressed as trapezoidal fuzzy numbers in their study. In the study, a new analytical method and a new method for the defuzzification of fuzzy numbers are proposed. This method is applied to all float time in the project network. In [14] the authors developed a linear program and fuzzy arithmetic approach to solving the trapezoidal fuzzy action time CPM problem and proved the validity of the proposed method by comparing the methods with each other. In [15], the authors examined a project network in a fuzzy environment with activity durations normalized trapezoidal fuzzy numbers. To find the Earliest Start (ES) time and the Latest Finish (LF) time, a method is proposed to obtain the maximum and minimum of trapezoidal fuzzy numbers to be used during forward and backward transition calculations. In [8] the authors used α-cut and centroid methods to determine the critical path and completion time in a construction project with triangular fuzzy activity times and compared the results. In [16] the authors examined a fuzzy project network containing hexagonal fuzzy numbers and generalized hexagonal fuzzy numbers and obtained the fuzzy critical path by ranking method. In [17], the authors proposed a new approach in which the fuzzy numbers are ranking based on the centroid to find the critical path in a fuzzy project network where the activity times are expressed as hexagonal fuzzy numbers. In [18], the authors discussed CMP with imprecise activity time in their study. They developed a new approach to CPM based on ordered fuzzy numbers in case of uncertainty. In [19] the authors presented a new fuzzy node labeling method, taking into account the uncertainty in their work. The proposed method is quite useful for quickly identifying the critical path of fuzzy project networks. In [20] the authors propose the ranking function to solve project scheduling problems in a fuzzy environment. In the study, trapezoidal fuzzy numbers are converted to crisp values and an algorithm is presented to obtain the best result in the completion times of the fuzzy network. In[21], the authors proposed two different algorithms to find the project completion time and critical path using triangular fuzzy numbers in the activities of a construction project. Using the proposed solution algorithms, fuzzy and crisp project durations are compared. In [22] the authors used decagonal fuzzy numbers. Decagonal fuzzy numbers were converted into crisp time. In the study, the authors aimed to perform correlation and regression analysis on decagonal fuzzy numbers in comparison with the statistical mean. In [23] the authors used

FCPM and FPERT to estimate the activity completion time of a hydroelectric power project. Trapezoidal fuzzy numbers were used in the study. Project durations were obtained by using both methods and the methods were compared. In [24] the authors used neutrosophic fuzzy numbers to solve the fuzzy critical path problem. Then the mathematical model of neutrosophic CPM and a method to calculate Critical path in project network is proposed.

Based on the uncertainty in the activity durations, a project process in a enterprise operating in the production sector is discussed in this study. The situation where the duration of the activity is uncertain has been examined. Activity times were expressed with triangular fuzzy numbers. The fuzzy numbers were ranking using Yager's ranking index and the obtained results were compared with the results obtained with fuzzy values.

2. MATERIAL and METHODS

2.1. Critical Path Method

CPM is a technique for scheduling a set of activities that are interdependent in terms of start and end times and eventually converge. In this technique, the aim is to determine the critical path to be considered in order to reach the endpoint in the stipulated time and to examine the alternatives that will occur in case the activity durations change [25]. In order to understand CPM, some basic concepts should be known first. Project network is the visual that shows the activities and priority relationships in the project. Activity, any work that contributes to the completion of the project. A predecessor is an activity that must be completed before an activity can begin. ES is the earliest time an activity can start provided that all previous activities have been completed. Earliest Finish (EF) is the time found by adding the activity duration to the ES time of an activity. Latest Start (LS) is determined by subtracting the completion time of an activity from the LF. LF is the time found by adding the activity time to the LS time. Slack (S) is the time difference between the ES and LS or LF and EF times for an activity. The critical path is the path of critical activities that do not have slack time [26]. Any delay in critical activities delays the overall project completion time and the project should be managed in a way that avoids delays in any of these activities [27].

In CPM, which is one of the most widely used network methods today, the hierarchical structure of the activities in the project is determined and the process is planned according to the relationships between critical and non-critical activities and interconnected and unrelated activities. This method has many advantages such as not being mathematically complicated, having different application areas, tracking both time and cost.

2.2. Fuzzy Concept

Fuzzy logic, which was first introduced by Lotfi Zadeh [4] in 1965 and has survived to the present day, aims to describe objects and values closer to reality and more appropriately. The basic idea of this philosophy, which is called fuzzy set theory, is that the truth values (or membership values in fuzzy sets) for a judgment take not only 0 or 1 values as in the classical set approach, but also values ranging from 0 to1 and this provides the opportunity to evaluate all alternatives with the concept of likelihood [28]. Fuzzy set theory is a method that takes the solution process by formulating a model in which there is no precise information and subjectivity [14]. Fuzzy logic, while making a judgment

JSR A
Journal of Scientific Reports

about something, simultaneously talks about how much it is inside and how outside of the mathematical classifications on which it is based. Brings a new definition to that data based on the knowledge of how much the data belongs to that set of judgments and how much it does not [29]. In a fuzzy set A defined in the universal set, the membership μA; is stated as μA : E → [0,1]. For an element x in this fuzzy set A the membership degree is shown as $\tilde{A} = \{(x, \mu\tilde{A}(x)) \mid x \in E)\}$ [30].

Fuzzy numbers are expressed as a convex, normalized, finite-continuous membership function and defined as real numbers [31]. The membership function $\mu\tilde{A}(x) : X \rightarrow [0, 1]$ for a triangular fuzzy number $\tilde{A}=(a, b, c)$ is defined as follows [32]:

$$\mu_{\tilde{A}(x)} = \begin{cases} \frac{x-a}{b-a}, & a \leq x \leq b \\ \frac{c-x}{c-b}, & b \leq x \leq c \\ 0, & \text{otherwise} \end{cases} \quad (1)$$

2.3. Yager's Ranking Method

Yager [33] suggested the following procedure for ranking fuzzy sets. In addition to being robust, the Yager ranking index is a field swapping index with linearity and summability properties [8]. Let convex fuzzy number $\tilde{t}$ be defined as a fuzzy triangular number $\tilde{t}=(a, b, c)$. In this case, the ranking index $I(\tilde{t})$ will be as in Eq. 2 [34].

$$I(\tilde{t}) = \int_0^1 \frac{1}{2}(t_\alpha^L, t_\alpha^U) d\alpha \quad (2)$$

$\tilde{t}$ is the center of the mean value of the fuzzy numbers. Within the scope of this study, the ranking index formula presented in [14] and used in [21] was used to convert fuzzy numbers to crisp values. $\tilde{A}=(a, m, b)$ triangular fuzzy number, the ranking index $I(\overline{T}_{ij})$ was calculated with Eq. 3 for each activity in the process of converting fuzzy times to crisp values with Yager ranking method.

$$I(\overline{T}_{ij}) = \frac{a+m+b}{3} \quad (3)$$

Here $\overline{T}_{ij} = ij$ is the fuzzy duration of activity. The difference of this method from most other ranking methods is that it allows the crisp value return in cases where the membership degrees of uncertainty are not known [21]. The basis of Yager's ranking method is to convert the fuzzy CPM problem into the classical CPM problem with classical activity duration [14].

2.4. Experimental Analysis

The main steps in CPM include identifying the individual activities, determining the sequence of these activities, organizing the network diagram, estimating the completion time for each activity, and defining the critical path [35]. In this study, the programming of the Coordinate Measuring Machine (CMM) installation (assembly and purchasing process) project in the Mechanical Production Department of an enterprise is discussed. Table 1 lists the activities, their predecessors and their possible durations. Since the activity times cannot fully reflect the reality, they are considered as triangular fuzzy numbers instead of crisp values. This is easily explained; the setup of each machine is

JSR A
Journal of Scientific Reports

different and the department staff is not experienced in this field to provide the appropriate time under the most favorable conditions. Figure 2 shows the network diagram for the CMM project.

Table 1. The data of the considered project.

Activity no	Name of the activity	Predecessors	Activity duration time (days)
A	Deciding on the machine vendor	-	30
B	Shipping time	A	30
C	Storage of the machine until the arrival of technical sales personnel	B	45
D	Machine acceptance tests	C,J,L	2
E	Machine final assembly	D	2
F	Training of the related department engineer about the machine	E	7
G	Trial period	F	15
H	Technician internship	G	21
I	Supplier decision of ventilation (air conditioning) machine	A	60
J	Transport and assembly of the machine	I	30
K	Room design	A	15
L	Room construction	K	45

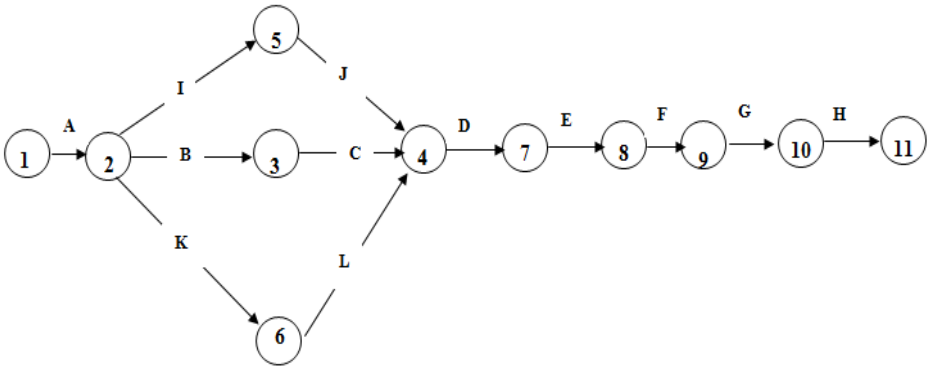

Figure 2. The network diagram of the analyzed Project.

JSR A
Journal of Scientific Reports

3. RESULTS

In the first stage, the project completion time and critical path are found by using these possible activity durations and logical relationships between activities. The results obtained are presented in Table 2. In Table 2, the first column shows the activity no, the second column shows the predecessors, and the third column shows the possible time. The fourth, fifth, sixth and seventh columns show the ES, EF, LS and LF durations of the activities, respectively. In order to be able to analyze the possible waits in the project, it is necessary to determine the slack time for each activity. Slack time; is the amount of time that a delay in the ES of a given activity does not disrupt the completion of the project. The gap time of a given activity can be calculated with = LS – ES = LF – EF. The eighth column shows the slack times. Activity without slack time; is called critical activity in the network. The ninth column shows the critical activities. According to these results, the project completion time was found to be 167 days and the critical path A – I – J – D – E – F – G – H.

Table 2. Analysis results according to possible values.

Activity no	Predecessors	Activity time/days	ES	EF	LS	LF	Slack (LF-EF)	On critical path
A	-	30	0	30	0	30	0	Yes
I	A	60	30	90	30	90	0	Yes
B	A	30	30	60	45	75	15	No
K	A	15	30	45	60	75	30	No
J	I	30	90	120	90	120	0	Yes
C	B	45	60	105	75	120	15	No
L	K	45	45	90	75	120	30	No
D	C,J,L	2	120	122	120	122	0	Yes
E	D	2	122	124	122	124	0	Yes
F	E	7	124	131	124	131	0	Yes
G	F	15	131	146	131	146	0	Yes
H	G	21	146	**167**	146	167	0	Yes

In the next stage, the project critical path and completion time were calculated by using the project activity times expressed with triangular fuzzy numbers given in Table 3. Triangular fuzzy numbers represent optimistic, possible and pessimistic situations as project duration. The possible activity duration is the activity duration used in the first stage, and similarly, the project critical path and completion time are calculated by performing the same operations for the values in other situations (best values and worst values). Afterward, triangular fuzzy numbers were converted to crisp values with Yager's ranking index and project completion time and critical path were found based on the obtained time values.

JSR A
Journal of Scientific Reports

Table 3. Durations in the context of triangular fuzzy numbers and crisp values.

Activity no	Predecessors	Activity duration time (days)			
		Best	Possible	Worst	Crisp values (Yager ranking index)
A	-	21	30	36	29
B	A	25	30	40	31,67
C	B	30	45	50	41,67
D	C,J,L	1	2	4	2,33
E	D	1	2	3	2
F	E	4	7	10	7
G	F	12	15	20	15,67
H	G	16	21	30	22,33
I	A	50	60	72	60,67
J	I	18	30	40	29,33
K	A	10	15	22	15,67
L	K	35	45	50	43,33

The results obtained for all cases are presented in Table 4. As seen in Table 4, when triangular fuzzy numbers were used, only one critical path for the project was determined for all three durations and the project durations were obtained as (123, 167, 215 days). When the analysis is made according to the crisp values obtained with the Yager ranking index, the critical path is still the same, and the project completion time has been obtained as 168.33 ≈ 168 days. According to the data obtained from the enterprise, this project was actually completed in 196 days. It is seen that the actual completion time of the project takes much more than 167 days calculated according to possible values and 168 days calculated according to the crisp values, and even closer to the maximum value of the fuzzy project duration of 215 days.

Table 4. Calculation results.

Type of activity duration		Project completion time	Critical path
Fuzzy activity times	Best Possible Worst	123 167 215	A – I – J – D – E – F – G – H
Crisp values	Crisp values (Yager ranking index)	168,33	

JSR A
Journal of Scientific Reports

Based on these results, it can be said that the fuzzy-valued CPM provides more information to the decision maker about the project completion time and that closer results to real-life can be obtained with the fuzzy logic method. As in the example discussed in this study, most real-life problems are inherently fuzzy. Even if all the conditions for the project process covered in the study are similar (such as employing personnel with the same experience and using the same equipment), the completion time of the activities may vary. For this reason, a real project process is handled with both fuzzy activity durations and crisp activity durations obtained by crisp value conversion. Completion times obtained using CPM for both cases were compared with the time the project was actually completed. The results obtained show the importance of using fuzzy-valued CPM.

4. DISCUSSION and CONCLUSIONS

In today's business world, the most effective management of projects and their completion within the stipulated time can affect the success and future of enterprise. In this context, a more realistic calculation of the completion time of the project can increase the success of the project management and thus the success of the enterprise. In today's highly competitive business environment, project management's ability to plan activities and track progress within strict cost, time and performance guidelines is becoming increasingly important to achieve competitive priorities such as on-time delivery and customization [36]. For example, in [37] the authors conducted a study on how to minimize aircraft maintenance planning time and how to create a plan with critical path analysis in a fuzzy environment. They concluded that if an aircraft maintenance operations and service system is inadequate or operational procedures are ineffective, these factors can cause flight delays that can be very costly for airlines in the long-term. Therefore, it can be said that the project planning and programming process allows the follow-up of projects not only in terms of time but also in terms of cost.

In this study, a real enterprise project is analyzed with CPM. In the study, due to uncertain situations that may arise from human and machine in project activities, crisp times could not be given and the concept of fuzzy logic was used. The use of triangular fuzzy numbers allows planning for the project by considering optimistic, possible, and pessimistic situations. In order to compare the results obtained from fuzzy CPM, crisp value conversion was performed with Yager ranking method . This method is preferred because it allows defuzzycation without the need to know the membership degrees. Yager's ranking method is based on converting the fuzzy critical path problem into a classical critical path problem with crisp activity time [34]. Although the project critical path is the same in both cases, there is a difference in terms of project completion times. It has been determined that the crisp number conversion value is very close to the possible time, but it is between the possible time and the worst time. Considering the actual completion time of the project, it is seen that it is closer to the worst time. Considering the contributions of a more realistic calculation of the project completion time to the enterprises, the importance of the studies in this field is revealed.

The results obtained from the considered problem show how real-life uncertainties can affect programming results. In the study, a real project process, which has been completed beforehand and whose completion time is known, is discussed. This provides the opportunity to compare the project completion times calculated using fuzzy and crisp values with the actual completion time of the

project. According to the results obtained, it is seen that the actual completion time of the project is closer to the maximum completion time calculated using the worst times. Therefore, in light of these results, it can be said that businesses can gain an advantage by including uncertainties in their planning in order to reduce the possibility of experiencing disruptions and delays due to programming that does not fully reflect reality and to avoid possible surprise results. Thus, this situation can make a positive contribution to businesses in terms of customer satisfaction and on-time delivery.

In future studies, project activity times can be expressed with different fuzzy numbers (L-R type, neutrosophic, trapezoidal, decagonal, etc.) and the results obtained using different defuzzification techniques for crisp value conversion can be compared. In addition, CPM can be considered in a stochastic network to express the uncertainty in activity durations.

ACKNOWLEDGEMENT

The authors received no specific grant for the research, authorship, and/or publication of this article. This paper was presented as oral in 4nd International Conference on Applied Engineering and Natural Sciences ICAENS 2022.

REFERENCES

[1] Abbasi, F. and Allahviranloo, T., (2022), Realistic solution of fuzzy critical path problems, case study: The airport's cargo ground operation systems, Granular Computing, 1-16.

[2] Shankar, N.R., Sireesha, V. and Rao, P.P.B., (2010), An analytical method for finding critical path in a fuzzy project network, International Journal of Contemporary Mathematical Sciences, 5(20), 953-962.

[3] Slyptsov, A.I. and Tyshchuk, T.A., (2003), Fuzzy temporal characteristics of operations for project management on the network models basis, European Journal of Operation Research, 147, 253-265.

[4] Zadeh, L.A., (1965), Fuzzy Sets, Information and Control, 8(3), 338-353.

[5] Mazlum, M., (2014), CPM, PERT and with Fuzzy Logic Technical Project Management and Implementation a Business, MS Thesis, Yildiz Technical University Institute of Science, Istanbul, 113p.

[6] Ozkaya, U. and Seyfi, L., (2016), A novel fuzzy logic model for intelligent traffic systems, Electronics World, 122(1960), 36-39.

[7] Çevik, O. and Yıldırım, Y., (2010), An application in milk products factory with fuzzy linear programming, Karamanoglu Mehmetbey University Journal of Social and Economic Research, 1, 15-26.

JSR A
Journal of Scientific Reports

[8] Durucasu, H., İcan, Ö., Karamaşa, Ç., Yeşilaydın, G. and Gülcan, B., (2015), Project scheduling by means of fuzzy CPM method: An implementation in Construction Sector, Ege Academic Review, 15(4), 449-466.

[9] Prade, H., (1979), Using fuzzy set theory in a scheduling problem: A case study, Fuzzy Sets and Systems, 2(2), 153-165.

[10] Yao, J.S. and Lin, F.T., (2000), Fuzzy critical path method based on signed distance ranking of fuzzy numbers, IEEE Transactions on Systems, Man, and Cybernetics-Part A: Systems and Humans, 30(1), 76-82.

[11] Han, T.C., Chung, C.C. and Liang, G.S., (2006), Application of fuzzy critical path method to airports cargo ground operation systems, Journal of Marine Science and Technology, 14(3), 2.

[12] Chen, S.P., (2007), Analysis of critical paths in a project network with fuzzy activity times, European Journal of Operational Research, 183(1), 442-459.

[13] Ke, H. and Liu, B., (2007), Project scheduling problem with mixed uncertainty of randomness and fuzziness, European Journal of Operational Research,183, 135-147.

[14] Atlı, Ö. and Kahraman, C., (2013), Fuzzy critical path analysis, Sigma, 31, 128-140.

[15] Bushan Rao, P.P. and Ravi Shankar, N., (2013), Fuzzy critical path analysis based on centroid of centroids of fuzzy numbers and new subtraction method, International Journal of Mathematics in Operational Research, 5(2), 205-224.

[16] Rajendran, C. and Ananthanarayanan, M., (2018), Fuzzy criticalpath method with hexagonal and generalised hexagonal fuzzy numbers using ranking method, International Journal of Applied Engineering Research, 13(15), 11877-11882.

[17] Adilakshmi, S. and Shankar, N.R., (2021), A new ranking in hexagonal fuzzy number by centroid of centroids and application in fuzzy critical path, Reliability: Theory & Applications, 16(2(62)), 124-135.

[18] Chwastyk, A. and Pisz, I., (2020), Critical path analysis with imprecise activities times, Sustainable Economic Development and Application of Innovation Management, 2004-2013.

[19] Liu, D. and Hu, C., (2021), A dynamic critical path method for project scheduling based on a generalised fuzzy similarity, Journal of the Operational Research Society, 72(2), 458-470.

[20] Mitlif, R.J. and Sadiq, F.A., (2021), Finding the critical path method for fuzzy network with development ranking function, Journal of Al-Qadisiyah for Computer Science and Mathematics, 13(3), 98.

[21] Değirmenci, G. and Uğural, M.N., (2022), Linear programming with fuzzy CPM: A case study in construction sector, Journal of Engineering Sciences and Design, 10(2), 466-481.

[22] Sallamal, M. and Rabinson, C., (2022), An analysis on fuzzy network path using fuzzy environment, Journal of Algebraic Statistics, 13(3), 1867-1874.

[23] Shuaibu, A.M., Muhammad, M.N. and Rabiu, N., (2022), Utilization of fuzzy critical path method and fuzzy program evaluation and review technique for building a hydroelectric power station, Dutse Journal of Pure and Applied Sciences, 8(2b), 21-32.

[24] Vijaya, V., Rajalaxmi, D. and Manikandan, H., (2022), Finding critical path in a fuzzy project network using neutrosophic fuzzy number, Advances and Applications in Mathematical Sciences, 21(10), 5743-5753.

[25] Stevens, J.D., (1988), Modified CPM-A scheduler's best friend, Cost Engineering, 30(10), 9.

[26] Akan, E., (2006), Project Management's Effect on Production Costs in Shipbuilding Industry, MS Thesis, Istanbul University Institute of Science, Istanbul, 175p.

[27] Zareei, S., (2018), Project scheduling for constructing biogas plant using critical path method, Renewable and Sustainable Energy Reviews, 81, 756-759.

[28] Kahraman, C. and İhsan, K., (2009), Using process accuracy index in fuzzy decision making environment, TÜBAV Journal of Science, 2(2), 148-156.

[29] Sağlam, F., (2008), Fuzzy Project Management and Application, MS Thesis, Yildiz Technical University Institute of Science, Istanbul, 86p.

[30] Zimmermann, H.J., (2011), Fuzzy set theory-and its applications, Springer Science & Business Media.

[31] Baykal, N. and Beyan, T., (2004), Fuzzy logic principles and fundamentals, Bıçaklar Publisher.

[32] Sireesha, V., Rao, K.S., Shankar, N.R. and Babu, S.S., (2012), Critical path analysis in the network with fuzzy interval numbers as activity times, International Journal of Engineering Science and Technology, 4(03), 823-832.

[33] Yager, R.R., (1981), A procedure for ordering fuzzy subsets of the unit interval, Information Sciences, 24, 143–161.

[34] Chen, S.P. and Hsueh, Y.J., (2008), A simple approach to fuzzy critical path analysis in project networks, Applied Mathematical Modelling, 32(7), 1289-1297.

[35] Karaca, Z. and Onargan, T., (2007), The application of critical path method (CPM) in workflow schema of marble processing plants, Materials and Manufacturing Processes, 22(1), 37-44.

[36] Kaur, P. and Kumar, A., (2014), Linear programming approach for solving fuzzy critical path problems with fuzzy parameters, Applied Soft Computing, 21, 309-319.

[37] Atli, O. and Kahraman, C., (2012), Aircraft maintenance planning using fuzzy critical path analysis, International Journal of Computational Intelligence Systems, 5(3), 553-567.